

3. SITE 1188¹

Shipboard Scientific Party²

INTRODUCTION

Principal Results

The principal objectives at Site 1188 were achieved by drilling at the Snowcap hydrothermal site. This site is characterized by extensive diffuse venting of low-temperature hydrothermal fluids. A vertical profile was delineated with mineralization and hydrothermal alteration patterns to a depth of ~400 meters below seafloor (mbsf). We found no significant occurrences of base metal sulfides or any geochemical evidence for precious metal enrichments. However, beneath an ~40-m-thick cap of unaltered dacite-rhyodacite, hydrothermal alteration was more intense and more pervasive than expected. Within this zone the rocks are very porous and highly fractured—characteristics that would facilitate diffuse fluid flow to the seafloor. The maximum borehole temperature measured was 313°C at 360 mbsf. Possible faults are indicated by uranium anomalies defined by wireline and resistivity-at-the-bit (RAB) logging. Whereas these uranium anomalies appear unrepresented in core samples, there is no evidence that they constitute major fluid pathways for the active hydrothermal system.

Using rotary core barrel (RCB) drilling, Hole 1188A was penetrated to 211.6 mbsf, although recovery was poor. While drilling, we intersected relatively unaltered vesicular dacite-rhyodacite, then at ~40 mbsf, a rapid transition to intensely altered volcanic rocks. These latter rocks continued with no further intercalations of unaltered rock to the end of Hole 1188A and then as deep as drilling penetrated in nearby Hole 1188F, which was cored with the advanced diamond core barrel (ADCB) from 218.0 to 386.7 mbsf. Recovery improved in the ADCB hole, although several significant gaps occurred in the returned core. Wireline logging and resistivity imaging with the Formation MicroScanner (FMS) of this hole from the base of casing at 195 mbsf to a blockage at ~360

¹Examples of how to reference the whole or part of this volume.

²Shipboard Scientific Party addresses.

mbsf provided valuable supplements to the core-based data. Logging while drilling (LWD) adjacent Hole 1188B with the RAB tool similarly aided the interpretation of structure and lithology in the top 72.0 m of the profile. An attempt to continue Hole 1188B as a cored hole with the ADCB failed because of bottom fill, but two wash samples collected at 66 mbsf were altered rocks comparable with those recovered at the same level in Hole 1188A. Uncored Holes 1188C, 1188D, and 1188E were unsuccessful attempts to spud a deep hole, which was eventually achieved with Hole 1188F. The difficulty in initializing Holes 1188C, 1188D, and 1188E suggests that the cap of unaltered dacite found in Hole 1188A is, in fact, quite extensive across Snowcap Knoll. This at least applies to areas with thin sediment mantles, which were the preferred sites for jetting in these holes rather than the locations where the vibration-isolated television (VIT) showed rock outcrops or presumed Fe-Mn oxide crusts.

The rate of penetration (ROP) for Hole 1188C increased from ~30 mbsf to where it terminated at 45 mbsf, indicating that it entered altered rocks at about the same depth as Hole 1188A. Accumulated cuttings from the running tool recovered after casing Hole 1188F and drilling its pilot hole to 218 mbsf were composed of both fresh rhyodacite and intensely altered rocks comparable with those profiled by Hole 1188A. Assuming this consistency at shallower subsurface levels below the Snowcap hydrothermal site continues at depth, it is reasonable to infer that the results of coring at Holes 1188A and 1188F may be combined into a single representative lithologic profile nearly 400 m deep, or 80% of the height of Pual Ridge.

A major conclusion from the shipboard studies of this profile is that to this depth (~400 mbsf) we are dealing with a sequence of felsic lavas and minor volcanoclastic horizons that originally erupted at or near the seafloor. Vesicles, microphenocrysts, microlitic groundmasses, perlitic and spherulitic textures, and flow banding have commonly been preserved in palimpsest despite the intensity of hydrothermal alteration. There is no textural evidence for the presence of slowly cooled intrusive units, but lacking identifiable contacts because of poor core recovery and alteration effects, we cannot rule out the possibility that subvolcanic dikes or sills are present. Whether any part of the drilled sequence might have formed as a high profile lava dome is also an open question. No useful limits can be placed on the number of lava flows in the sequence drilled. Only two unequivocal volcanoclastic horizons representing former seafloor positions were identified, although several more possible occurrences were noted and intersections of rocks with perlitic fabric also represent possible lava rinds. Seventy-two lithologic units were defined in core from the two holes combined. Being based on a mixture of igneous textural criteria and alteration characteristics, this figure by no means implies a succession of very thin flows. Dips of layering defined by flattened vesicles or flow banding vary randomly from horizontal to vertical, suggesting that both proximal and distal portions of flows were intersected.

The key geochemical indicator ratio Zr/TiO_2 (Zr is measured in parts per million and TiO_2 is measured in weight percent) varies between 120 and 300 in analyzed altered rocks at Site 1188. If this ratio did not change during alteration, it would suggest a dacitic (grading into rhyodacitic) parentage for the entire sequence cored. Fresh glassy and vesicular lavas near the seafloor contain scattered plagioclase and clinopyroxene microphenocrysts, and they bridge the dacite-rhyodacite

compositional boundary. A content of 70.4% wt% SiO₂ on a volatile-free basis in the shipboard analysis of one specimen is consistent with the refractive index (RI) measurements on glass in others.

Mineral assemblages arising from hydrothermal alteration vary with depth and are complicated by overprinting relationships. The profile commences with patchy films of opaline silica and smectitic clay with trace pyrite on fracture surfaces of otherwise unaltered dacite-rhyodacite. In a former perlitic glass at ~35 mbsf, this develops rapidly into pervasive alteration with an assemblage dominated by these same phases together with minor illite. Bleached lavas that follow downward to ~50 mbsf consist mainly of cristobalite and mixed-layer clays and contain minor disseminated pyrite. Anhydrite becomes a prominent phase together with pyrite as vesicle linings and in reticulate late veins as with associated pale cristobalite-pyrophyllite alteration halos. The latter create a concentrically zoned appearance to slightly darker wall rock kernels. From ~50 to ~125 mbsf, disseminated pyrite increases to a consistent several percent in former massive, vitric, vesicular, flow-banded, and brecciated lavas whose silicate component varies between two dominant assemblages. In both of these, there is a progressive downward decrease in cristobalite abundance accompanied by an increase in quartz. The first and apparently earlier or "background" assemblage, not obviously related to a recognizable veining event, is greenish clay with either cristobalite or quartz. Illite and pyrophyllite are the dominant phyllosilicates. The second assemblage is present in zones of conspicuous bleaching, which locally predominate over many meters. These are also composed of cristobalite or quartz together with whiter "clay" within which smectite, illite, chlorite, and pyrophyllite have been identified. The relative proportions of these phyllosilicates in the two alteration styles, and the role of anhydrite that also is present in places, require more quantitative studies than were possible on board. The rock products of both styles are characteristically very soft. Veins, stockworks, and vesicle fillings of anhydrite-cristobalite/quartz-pyrite are again common in this interval, and the same assemblage also is present in breccia matrices. Many smaller intervals of bleaching are clearly halos around anhydrite-dominated late-stage veins and are superimposed on the greenish silica-clay style of alteration (this being the chief evidence for relative timing).

Below 125 mbsf in Hole 1188A and throughout cores from Hole 1188F, the predominant alteration assemblage is siliceous but with subtle variations that define five depth subdivisions. Shipboard petrographic and geochemical evidence suggests that, relative to presumed precursors resembling the "background" green clay assemblages higher in Hole 1188A, these rocks are consistently enriched in silica. Quartz is present as vesicle linings and amygdules, as siliceous halos surrounding thin quartz-pyrite veins, and as finer groundmass grains accompanying or overprinting phyllosilicates. These rocks are distinctively harder than those of the higher zones in Hole 1188A and vary from pale gray to dark gray. In the uppermost silicified zone of Hole 1188A, quartz is accompanied by illite with subsidiary chlorite. The middle silicified zone has numerous remnants of greenish clay alteration and zones of superimposed bleaching. Chlorite and illite are the principal phyllosilicates, and some samples with chlorite contain magnetite and remnant igneous plagioclase. In the lower silicified zone of Hole 1188A, corrensite is the dominant clay species in some samples, denoting relatively high-temperature alteration.

Wireline logging with the spectral gamma tool delineated a uranium anomaly in the uncored gap between Holes 1188A and 1188F. Two subdivisions of siliceous alteration were recognized in Hole 1188F. The upper subdivision, from 218 to 269 mbsf, is characterized by illite clay and almost no relict plagioclase is preserved. In the lower subdivision (from 269 mbsf to the end of the hole), illite is accompanied by chlorite, relict plagioclase is common, and there are several intervals with disseminated magnetite. Disseminated and amygdaloidal pyrite is ubiquitous in the altered rocks of Hole 1188F, but its overall abundance falls from the upper to the lower subdivision, starting at slightly lower contents than in siliceous rocks from the lower part of Hole 1188A. Quartz amygdules are generally completely filled, lending the rocks a spotted appearance. Crystalline anhydrite or books of chlorite tend to line any open vesicles present. Especially in the upper subdivision of Hole 1188F, anhydrite-pyrite \pm quartz veins are common. These are again characterized by laminated or concentric alteration halos of bleached appearance, in which pyrophyllite and quartz appear to be the major phases.

The abundance of anhydrite in veins and associated alteration halos, as vesicle fill, and as breccia matrices is a noteworthy feature of Site 1188. It also is less abundant as disseminated grains associated with clays in the different alteration styles where, however, a genetic relationship with veining rather than pervasive alteration is usually evident. Chemical analyses were performed on board on 42 altered rocks from Site 1188—mostly on homogeneous rocks but also on some with anhydrite-dominated veins or breccia matrices. Some analyses of these anhydrite-bearing rocks display elevated contents of CaO. More generally, CaO is similar to or lower than its content in fresh dacites depending on whether relict igneous plagioclase has been preserved, and Na₂O shows a similar behavior. The enrichment in MgO relative to its content in likely parents is a common phenomenon, particularly in chloritic rocks. Depending on the relative abundance of illite, K₂O varies from severely depleted to modestly enriched. On a relative basis, MnO is always extremely depleted. Sulfur is distinctly enriched, reflecting the occurrence of pyrite or of pyrite and anhydrite. Both enrichment and depletion of FeO occur, but some pyritic samples have similar iron contents to those of unaltered dacites and rhyodacites, which indicates that pyrite has often formed by a sulfidation process. Immobile behavior is apparent for Al₂O₃, TiO₂, Zr, Y, and, less certainly, P₂O₅.

Fracturing as well as veining is a conspicuous feature of the altered rocks underlying Site 1188. Core recovered by ADCB showed an unhelpful tendency to disintegrate because of the pressure relief on a myriad of fractures when extracted from the barrel. This and the fracture patterns evident in resistivity imagery (discussed below) probably explain the low core recovery achieved in RCB drilling. No preferred orientation is evident for either veining or fracturing in cores. Single veins, branching veins, arrays of multiple veins, and vein networks are all present. The greater majority of veins are <1 mm in width, and only ~4% by number are >1 cm. Anhydrite, pyrite, quartz, and cristobalite are the dominant vein-filling minerals. Cristobalite-bearing veins were encountered only in the upper 126 mbsf of Hole 1188A, which is consistent with the distribution of silica polymorphs in pervasively altered rocks. Magnetite-bearing veins were observed in the two intervals where this mineral is also present in wall rock at 146–184 and 322–379 mbsf. Local alteration halos around veins, and the superimposition of

veins, are better developed deeper in Hole 1188F compared to Hole 1188A. Anhydrite-bearing veins are generally late relative to those not containing this mineral.

Pyrite is the only common sulfide mineral in the Site 1188 cores. Marcasite, sphalerite, and chalcopyrite are present locally in trace amounts, and rare pyrrhotite was identified as tiny inclusions in pyrite from a magnetite-bearing interval. Pyrite rarely exceeds 5% in abundance and is in two settings as (1) disseminations within altered rocks of all the styles described above and as (2) generally euhedral grains in anhydrite and/or silica veins or vesicle linings. A paragenetic sequence has been unraveled involving early formation of Fe oxide minerals (magnetite, spinel, ilmenite, and hematite) that are included in or replaced by the disseminated form of pyrite, which in turn may be overgrown by sphalerite or chalcopyrite. The second kind of pyrite, in anhydrite-bearing veins and vesicles, represents the final phase of sulfide deposition.

Magnetic susceptibility varies greatly over the length of the recovered core, with highs corresponding to fresh dacite and magnetite-bearing intervals. The average compressional wave velocity for all samples from this site is 4.1 km/s; however, the more massive volcanic rocks commonly have higher compressional wave velocities than the brecciated and flow-banded rocks. Thermal conductivity is higher in brecciated rocks (average >2 W/[m·K]) than in massive altered dacite (usually <2 W/[m·K]). Average measured solid density differs somewhat between Holes 1188A and 1188F (2.65 and 2.82 g/cm³, respectively). This may reflect a higher abundance of veins (anhydrite + pyrite) in samples from the lower part of the cored interval. Porosity is highly variable, from $<1\%$ to $\sim 45\%$, but with an overall trend toward decreasing porosity with depth.

The top 35 m of the cored material is characterized by high magnetic susceptibility and remanent intensity. This depth corresponds to the relatively fresh dacite-rhyodacite section at the top of the core. The magnetic measurement values show a considerable drop from 35 to ~ 135 mbsf, representing the high alteration in Hole 1188A. A sudden increase in both the susceptibility and remanent intensity is present below 135 mbsf. This is coincident with an increase in magnetite content. Thermal demagnetization experiments indicate that the dominant magnetic carrier in the upper part of the section is titanomagnetite with variable degrees of alteration. Deeper in the core, magnetite and possibly maghemite may be the important sources of magnetization. One of the most notable features in the magnetic character of this section is a sharp rise in susceptibility values below 275 mbsf. The high magnetization intensity at the bottom of the hole is consistent with the presence of magnetite, which was identified in hand specimen, by X-ray diffraction (XRD), and with optical microscopy.

Both direct bacterial counting and adenosine triphosphate (ATP) analysis established the presence of microbial biomass within core samples from ~ 34 and 49 mbsf, respectively, but not on a sample from 60 mbsf or other samples deeper in Holes 1188A and 1188F. Microbes were successfully cultivated at various temperatures under both aerobic and anaerobic conditions to 25° and 90°C from samples taken at 10 and 34 mbsf and at 25°C under anaerobic conditions from the 49 mbsf sample. Aerobic microbes were also cultivated at 25°C from very deep rock samples (222 and 225 mbsf), but these are believed to arise from seawater contamination.

Maximum borehole temperature during drilling at Hole 1188A was 4°C as recorded with the developmental Lamont-Doherty Earth Observatory (LDEO) core barrel temperature tool (CBTT). Borehole temperatures were also measured with the wireline logging temperature tool in Hole 1188F, registering 100°C a few hours after coring ended. Five days later the ultra-high-temperature multisensor memory (UHT-MSM) tool measured a maximum temperature of 304°C in the bottom of Hole 1188F. A final temperature run in Hole 1188F with the UHT-MSM tool on the last day of operations recorded a maximum of 313°C at 360 mbsf. Water samples were collected from Holes 1188B and 1188F. The sample from Hole 1188B was taken only a few meters below seafloor because of a blockage in the hole, and a concomitant temperature measurement was 6°C. Water samples also followed each UHT-MSM run in Hole 1188F, but difficulties in rapidly estimating the temperature gradient to avoid too high a temperature resulted in water samples taken at 12°C (107 mbsf) and 22°C (206 mbsf). Hole 1188B was drilled with the LWD/RAB bottom-hole assembly (BHA), and the data provide a 360° image of the borehole resistivity characteristics that might be used for lithologic correlation. Wireline logging in Hole 1188F indicated that the borehole had a much larger diameter (>17 in) than we expected from drilling with the 7.5-in diameter diamond bit. High U in spectral gamma-ray measurements was recorded between 197 and 209 mbsf, and a smaller peak was recorded between 239 and 245 mbsf.

Site Objectives

Site 1188 is located on the Snowcap hydrothermal site, which straddles a low knoll on the crest of Pual Ridge. The location is characterized by scattered outcrops of intensely altered to fresh dacite-rhyodacite and intervening areas of sediment with patches of dark Fe-Mn oxide crust and areas covered by a white material, thought to be either microbial mat or clathrate. Previous gravity coring of the sediment showed it to be composed predominantly of disaggregated altered dacite, formed by bioturbation and/or hydrothermal fragmentation. Temperatures of 6°C were measured during submersible dives at one of the many shimmering water sites, most of which are close to the edge of rock outcrops.

The principal objectives of drilling at Site 1188 were to establish subsurface alteration and mineralization patterns, and their variation with depth, beneath this area of low-temperature diffuse venting and acid sulfate alteration at the seafloor. Other objectives included defining fluid pathway structures, testing the possible existence of "subhalative" massive sulfide layers, establishing the volcanic architecture if allowed by the alteration, and delineating the extent and characteristics of subsurface microbial life. These objectives required relatively deep penetration, 500 mbsf being aimed for with the possibility of even deeper drilling if conditions were suitable.

Operations Summary

Port Call Activities

Leg 193 began 37 hr early when the first line was passed ashore to the Southwest Point fueling dock at 1700 hr on 7 November 2000. United States Territory of Guam Customs and Immigration authorities cleared the ship's complement that day, and we commenced bunkering

activities. Refueling began at 2030 hr and was completed the following morning by 0700 hr. A total of 1398.5 T of fuel was loaded.

With tug boats secured fore and aft and the pilot on board, the last line was let go at 0750 hr on 8 November 2000 and the vessel moved to Hotel (H) Berth, Ammunition Dock. The first line ashore was at 0820 hr, which began the remainder of the Guam resupply activities. Port call activities aside from the normal loading and off-loading of freight included the rearranging of the forward drill collar rack to accommodate 6.75-in drill collars to be used with the ADCB. In addition, four additional free-fall funnels (FFFs) were put on board and three hard-rock reentry system (HRRS) cones were loaded. In the riser hold, the remainder of the HRRS hardware was loaded, including 9.5-in drill collars. The SDS Digger Tools fluid hammer and some remaining HRRS hardware were placed on the riser hatch.

There were two pacing items for the port call. One was the replacement of the number 4 generator (the last of the generators in the engine room being rebuilt) and the other was the replacement of all passive heave compensator (PHC) rod and piston seals, as well as changing out the aft piston rod because of the chrome plating deterioration. In addition, the PHC rods and cylinders were measured to document the current state of wear in the system.

Texas A&M University work items included machining HRRS parts at a local shop to accommodate the installation of a float valve. All of the HRRS and ADCB hardware that had been stored in Guam after Leg 191 was transferred to the ship for possible use during Leg 193. Hardware from Singapore and Salt Lake City, where the ADCB had recently undergone land drilling tests, was also loaded. Other Transocean Sedco Forex (TSF) work items included replacement of the forward drawworks motor and installation of a new motor on the spare cement pump. A spare motor for the top drive was also loaded on board the ship during the port call. The night before departure, Catermar hosted a barbecue on the dock for the entire ship's complement. Despite intermittent rain showers, the event was a great success and served as an outstanding ice-breaker for the upcoming expedition.

Staffing for Leg 193 included several nonroutine personnel. Two Japanese engineers sailed to observe deployment of the ADCB. Three observers from Papua New Guinea (PNG) sailed as a part of the shipboard science party. An engineer from SDS Digger Tools sailed to support deployment of the hammer drill. The hammer drill engineer was replaced by another SDS employee on 14 December 2000 by helicopter transfer. Finally, a technician-in-training for the Japan Marine Science and Technology Center (JAMSTEC) sailed as a replacement of an Ocean Drilling Program (ODP) technician who could not make the cruise.

Transit to Site 1188

At 0800 hr on 14 November 2000, the last line was cast away. The pilot left the ship at 0836 hr, and the ship got under way at full speed for Site 1188. During the transit to Site 1188, we enjoyed fair weather the entire voyage, highlighted by an equator-crossing ceremony. During the trip the TSF crew completed the electrical installation of the forward drawworks motor and the spare cement pump motor. In addition, they continued to troubleshoot the active heave compensator (AHC) system. Also during the transit, efforts continued to resolve whether or not the ship would be required to officially clear customs and immigration into and out of PNG waters. The end result was, despite indications

to the contrary, that the ship did need to clear into and out of the country, which effected, albeit not severely, our operations schedule.

Upon arrival at Site 1188, arrangements for customs and immigration clearance to PNG had not been finalized. The ship continued past the Global Positioning System (GPS) coordinates of the drill site toward a point 10 nmi off Rabaul in the hope that this would expedite the clearance process. Our continued discussions with agents in Rabaul indicated that, while we should not begin coring, operations initiated to stabilize the ship while awaiting arrival of the customs officers would be possible. Based on this information, we reversed course and returned to the GPS coordinates for Site 1188. On a side note, while en route to Site 1188 (on 16 November 2000), an earthquake (M8) was reported with the epicenter located within 20–30 nmi east of the Leg 193 drilling location.

Hole 1188A

At 1730 hr on 18 November 2000, the ship was on location and we lowered thrusters and hydrophones. The precision depth recorder (PDR) depth reading for this site was 1652.4 meters below rig floor (mbrf) corrected to the rig floor dual elevator stool (DES). After spacing out the RCB and assembling the remaining 8.25-in BHA, the AHC was tested to ensure that it was performing as designed. Although vessel heave was slight to negligible, the system appeared to be functioning correctly.

During the pipe trip to the seafloor, the VIT/subsea camera system was deployed. A positioning beacon was attached to the VIT frame to allow precise placement of the beacon near our drilling target. At 0315 hr on 19 November 2000, we began a seafloor VIT survey. The beacon was released from the VIT sleeve at 0357 hr and the survey continued until 0630 hr. The VIT was recovered and operations were secured by 0730 hr, awaiting the arrival of the PNG customs officials.

At 0830 hr the helicopter arrived carrying two PNG customs agents, two PNG quarantine officers, and two logistics agents. Authorization to proceed with operations was granted at 0845 hr on 19 November 2000, and at 0930 hr the helicopter departed with the PNG officials.

The upper guide horn was pulled and the VIT/subsea TV camera was deployed once again. After picking up the top drive, an RCB was pumped down and another hour was spent viewing the seabed for a candidate spud location. At 1200 hr a 15-min jet-in test was conducted to 2.0 mbsf, indicating that there was some soft material at the seafloor. The bit was pulled clear of the seabed, and Hole 1188A (Table T1) was spudded at 1230 hr on 19 November 2000. Seafloor depth as measured by the drill string from the DES was 1651 mbrf. The bit was maintained at the seafloor while the VIT was recovered, and at 1315 hr, continuous RCB coring began.

Coring continued through Core 193-1188A-4R to a depth of 1684.6 mbrf (33.6 mbsf) before the driller experienced high torque and the pipe stuck. After working the pipe for 45 min, it was freed with 100 kilopounds (klb) of overpull. Coring resumed with Core 193-1188A-5R after reaming back to the bottom through 5.0 m of hard fill and continued until 0900 hr on 21 November 2000, when the pipe once again stuck in the borehole while recovering Core 193-1188A-23R (to 211.6 mbsf). All efforts to free the drill string, including releasing the bit, failed, which indicated that the hole had collapsed above the bit. A severing charge was rigged up and deployed, and at 2015 hr on 21 Novem-

T1. Coring summary, Site 1188,
p. 262.

ber 2000, the pipe was severed at ~1747 mbrf (96 mbsf). After the severing charge line was removed from the pipe, we determined that the pipe was still stuck, requiring deployment of a second severing charge. At 0415 hr on 22 November 2000, the second charge was successfully detonated, severing the drill string in the 5-in pipe at a depth of 1655 mbrf (4.0 mbsf). Hole 1188A ended at 0830 hr on 22 November 2000, when the severed drill pipe reached the rig floor. A total of 21.93 m of core was recovered for an overall average of 10.36% recovery (Table T1). Recovery was erratic because of the core jamming and the fractured nature of the formation.

Chemical contamination tracers for microbiological studies were injected into the number 2 mud pump suction line during deployment of Core 193-1188-11R. A Whirl-Pak plastic bag containing fluorescent microspheres (also used as a contamination tracer) was deployed with Core 193-1188A-3R. Finally, the LDEO drill string acceleration (DSA) tool housing was used to deploy maximum-reading thermometers on Core 193-1188A-4R. The unit was deployed on top of the core barrel in the sinker bar string, just as with the DSA deployments. The circulating temperature recorded was ~4°C.

The weather while drilling Hole 1188A was exceptionally calm. Day after day, the bridge log reported no roll, pitch, or heave. The ship was parked in the middle of the proverbial mill pond, with New Ireland and New Britain (including a sporadically erupting volcano at Rabaul [see [cover photograph](#)]) in sight throughout the leg. With the drill string recovered and the severed joint laid out, the crew went about assembling a new outer core barrel assembly, spacing out the RCB system, and threading 8.25-in drill collars. While this was taking place, the ship moved in dynamic positioning (DP) mode ~0.6 nmi to Site 1189 (see “[Operations Summary](#),” p. 5, in the “Site 1189” chapter). For a chronological summary of the ship operations, please see “[Operations Summary](#),” p. 8, and Table T1, p. 83, both in the “Leg Summary” chapter.

Hole 1188B

After the initial operations at Sites 1189 and 1190 (see “[Operations Summary](#),” p. 5, in the “Site 1189” chapter, and “[Operations Summary](#),” p. 2, in the “Site 1190” chapter), we made preparations to run the LWD/RAB tool and the ship was moved back to Site 1188. The RAB tool was run with a 9.875-in tricone drill bit and a standard three-stand 8.25-in BHA. The plan was to spud a hole with the RAB tool, drill a LWD hole to ~75 mbsf, deploy a FFF if the surface sediment allowed, and then reenter with the ADCB coring system. The depth of the LWD/RAB penetration was limited to 75 mbsf to keep the top of the 8.25-in drill collars above the seafloor. By doing this, we reduced the risk of getting stuck and losing another BHA.

The morning of 25 November 2000, the second rendezvous helicopter arrived bringing lithium batteries required for the RAB tool as well as an AHC service technician from Maritime Hydraulics. After a delay while the AHC was adjusted by an engineer and concluding a brief 1-hr VIT survey of the seafloor, Hole 1188B was spudded at 1500 hr in 1653 m of water. The VIT was recovered and drilling proceeded with the LWD/RAB assembly beginning at 1615 hr.

The RAB experiment required 13.0 hr to drill to a depth of 1725.0 mbrf. During the last 4 m of drilling, the ROP slowed considerably, so we decided to terminate the LWD hole at 72.0 mbsf. The drill string was brought to 17.0 mbsf, and a FFF was rigged up and released in 1.25 hr.

The VIT was deployed, and we observed the bit pulling clear of the FFF at 0945 hr on 26 November 2000. The RAB tool was disassembled, and we began preparations for deploying the ADCB coring system. The 4.5-m core barrels were spaced out, the latches adjusted, and pressure/flow tests were conducted to ensure that the proper amount of flow was passing the core shoe. Six stands of 6.75-in drill collars were made up as part of the ADCB BHA along with a diamond-impregnated bit. This bit had an outside diameter of 7.25 in and an inside diameter of 3.345 in. With the entire BHA made up and hung off at the rotary table, two wiper plugs were pumped to clear any loose rust from the inside diameter of the drill collars. In addition, we deployed and recovered a core barrel to ensure that the ADCB system was functional. The pipe trip continued without incident, and at 0100 hr on 27 November 2000, the FFF for Hole 1188B was reentered after only 37 min of vessel maneuvering.

The ADCB coring system was deployed to 1718.7 mbrf (65.7 mbsf) without much trouble. However, penetrating the 6.3 m of hard fill in the bottom of the hole proved problematic. Multiple core barrel deployments and 4.75 hr of reaming attempts with and without barrels installed resulted in no appreciable progress. Throughout the ordeal, circulating pump pressures were normal when off bottom, but ~100 psi low when on bottom. Eventually, efforts to get the ADCB system to total depth in a clean hole were abandoned. The hard rubble (identified by the recovery of two fist-sized chunks of altered volcanic rock in the ADCB wireline core barrels) prevented any viable test of the ADCB system's ability to recover core in this environment. The drill string was recovered, clearing the FFF at 1020 hr and arriving at the rig floor at 1400 hr on 27 November 2000, thus ending Hole 1188B.

Hole 1188C

While changing the BHA components after operations at Site 1191 (see "[Operations Summary](#)," p. 2, in the "Site 1191" chapter), the ship was offset in DP mode back to Site 1188. The next hole was planned as a reentry hole that would hopefully enable us to achieve the scientific target depth of 400–500 mbsf. There were several complications, however, to establishing a reentry structure on the seafloor. The terrain at the drill site, although relatively flat, contained patches of sediment interspersed with low outcrops of volcanic rock and platy crusts. To allow jetting in, the sediment patches were the preferred sites. Particularly for this deep hole, to have a chance at establishing a conventional reentry cone structure, we needed in excess of 3 m of sediment on the surface overlying the hard, fresh volcanic material that we had encountered near the surface at Holes 1188A and 1188B. Finally, it was obvious from early operations that drilling a hole deep enough to set surface casing was not going to be easy and might require several aborted attempts before achieving the goal. We expected to need at least 50–60 m of large-diameter casing in our initial deployment to offer the best chance of success for eventually casing to the approximate depth of Hole 1188A (211 mbsf). We only had two standard reentry cones and one each 16- and 10.75-in casing hangers, so we had only one opportunity for successful deployment of a conventional casing system.

Based on these limitations, we decided to deploy the reentry cone in an unconventional manner. We opted to free-fall deploy the standard reentry cone in the same manner as the FFF deployments. This deployment scenario, albeit unconventional, improved our chances for a suc-

cessful installation. First, we could pick an acceptable drilling location (i.e., flat with sediment cover and not too close to any outcropping structures) using the subsea TV system. Then we could spud the hole with the camera down and conduct a jet-in test to determine if there was enough sediment to allow 3 m of 16-in casing to be installed beneath the reentry cone. Finally, the hole could be predrilled with a 14.75-in tricone bit to establish whether hole stability would remain acceptable and allow drilling to the required depth of ~200 mbsf (total depth of the cased interval of our planned reentry hole).

This improvisational strategy required some preparatory modification to the conventional reentry system. The reentry cone panels were assembled into two halves and were not installed on the cone base. The mud-skirt extension was also not installed. Prior to running in the hole, we moved the reentry cone base over the moonpool center and installed a 16-in casing hanger with 3 m of 16-in casing. The drill string was tripped to the seafloor through the interior of the reentry cone base/16-in casing assembly.

A 14.75-in drill bit and four-stand BHA was assembled and, tripped to the seafloor, and the subsea VIT was deployed. We conducted a brief 30-min survey of the seafloor before spudding Hole 1188C ~30 m west of Hole 1188A at 1715 hr on 29 November 2000. The seafloor was tagged at a drill pipe depth measured from the rig floor DES of 1654 mbrf, similar to the predicted 3.5-kHz PDR depth of 1652.4 mbrf. A jet-in test to a depth of 1659.0 mbrf (5.0 mbsf) was successful, indicating that there was more than adequate sediment in which to deploy the reentry cone with the attached 3 m of 16-in casing. The jet-in test, conducted at 50 strokes per min (spm) and a weight on bit (WOB) of 5 klb, was completed within 10 min. The VIT was recovered, and drilling was initiated at 1815 hr that same day.

The driller was unable to advance deeper than 44.0 mbsf, well short of our goal of 200 mbsf of large-diameter borehole. Each time the driller would stop to make a connection, he would lose 10 m of hole to fill. The VIT was deployed to observe pulling out of the hole, and at 0705 hr on 30 November 2000, the bit cleared the seafloor, ending Hole 1188C.

Hole 1188D

After surveying the seafloor for 45 min, we located another candidate drill site ~40 m north of Hole 1188C. Hole 1188D was spudded at 0815 hr on 30 November 2000, and the second jet-in test reached 3.0 mbsf (1645 mbrf). Once again the VIT was recovered, and drilling commenced at 0945 hr. In 3.5 hr, the hole was advanced to a mere 15.0 mbsf. High torque and multiple reaming operations characterized drilling parameters at this location. Ultimately, the pipe stuck and then was worked free with 200 klb of overpull. However, the circulating pressure was low and indicated a problem with the BHA. The seafloor was cleared at 1345 hr, the top drive was set back, and the pipe was tripped for inspection, arriving at the rotary table by 1630 hr on 30 November 2000, ending Hole 1188D. The mechanical bit release (MBR) had failed, leaving a 14.75-in tricone bit, a bit sub crossover, and a bit disconnect in the hole.

Hole 1188E

Another 14.75-in tricone bit and MBR was made up to the four-stand 8.25-in drill collar BHA, and the pipe was tripped to bottom. The VIT

was deployed, and after a 30-min TV survey to ~30 m north of Hole 1188A, Hole 1188E was spudded at 2115 hr on 30 November 2000. The seafloor was tagged at a drill pipe depth of 1652.0 mbrf and another 3.0-m jet-in test was completed. The camera was recovered at 2200 hr, and drilling commenced. After 4.5 hr of drilling, the hole was advanced to 1668.0 mbrf (15.0 mbsf). Once again, the hole appeared to be collapsing when making connections, and drilling parameters were characterized by high torque and elevated pump pressure. The driller required 100 klb of overpull to free the drill string at depths of 15.0, 12.0, and 8.0 mbsf. Because this did not bode well for a deep hole, the bit was pulled clear of the seafloor, ending Hole 1188E at 0240 hr on 1 December 2000.

Hole 1188F

The VIT was deployed, and we spent 45 min attempting to locate another candidate drill site. At 0415 hr, we found another suitable location close to Hole 1188E, performed a 4.0-m jet-in test, and initiated Hole 1188F before recovering the VIT. At 0515 hr, drilling was initiated from a seafloor depth of 1653.0 mbrf.

From the start, the hole conditions appeared more promising than at all of the previous locations. By 2400 hr (<19 hr after starting) we had reached 78.0 mbsf, and the hole appeared stable with all drilling parameters consistent. The driller noted no excessive torque, overpull, or elevated pump pressures and had no indication of fill in the hole after making connections. By 0745 hr the following morning, the hole had been advanced to a depth of 1757.0 mbrf (104.0 mbsf; total possible depth without running the top of the BHA below seafloor). A wiper trip made it to within 15.0 mbsf and washed back to total depth. After cleaning the hole by flushing sepiolite mud, we prepared for deployment of the reentry cone. It was our opinion that the 100-m depth would be sufficient to deploy ~60 m of large-diameter casing.

The reentry cone panels (prebolted and welded into two semicircle halves) were moved onto the reentry cone base and bolted and welded together. Two snatch block sheaves were shackled on opposite sides of the cone, 180° apart. A wire rope was attached to the starboard forward tugger, run through the sheaves, and shackled to the hang-off pad eye underneath the rotary table on the aft port side. This technique was the same as that used for deploying a FFE, only we used wire rope rather than manila soft line. The cone was lowered through the splash zone below the lower guide horn, and an acetylene torch was used to cut through the wire rope. The cone was released without incident and tracked on the 3.5-kHz PDR. The cone descent was readily apparent because of the resonant ringing as it passed each tool joint. The total deployment time was just short of 9 min, and the cone was tracked at a free fall rate of 187 m/min, or ~7 mph.

Once the cone was released, the VIT was deployed and run to bottom. The cone was resting nicely on the seafloor and appeared to have much the same orientation as other reentry cones deployed in the more conventional manner.

As we expected, some loose material at the surface had fallen in on top of the bit because of the cone impact with the seafloor. However, with some overpull and back reaming, the pipe was eventually freed up enough to pull to a depth of 1659.0 mbrf (6.0 mbsf). The 14.75-in bit passed easily through the 16-in casing shoe and up into the throat of

the reentry cone; however, when lowered, the bit would consistently hang up at ~2.0 m below the casing hanger shoe.

The VIT was recovered so that we could use rotation to work/ream the bit through the trouble spot. We spent the next 8.5 hr washing/reaming the 14.75-in hole to a depth of 87.0 mbsf before retrieving the drill string, which cleared the reentry cone at 0300 hr on 3 December 2000. Although the VIT was deployed to observe the pipe withdrawal, the visibility was poor because of the turbid water from the circulated cuttings and drilling mud. The VIT was recovered and the bit cleared the rig floor at 0630 hr. The tricone bit was in excellent condition with regard to the cutting structure and bearings. However, the bit was missing two of three grease reservoirs and the third reservoir fell out on deck during handling because of the damage to the upper bit shank.

After some discussion, we decided that we would increase our chances of a successful deployment of a cased reentry hole to ~200 mbsf if the borehole diameter was 14.75 in all the way to the bottom. Another 14.75-in tricone bit was made up with a long enough BHA to allow for drilling to >200 mbsf without placing the top of the BHA below seafloor. We reentered Hole 1188F at 1315 hr on 3 December 2000 and used the elongated drilling assembly to wash and ream to a depth of 91.0 mbsf. Several tight spots were identified by high pump pressure and high drilling torque. Repeated wiper trips eventually cleaned the hole to 104.0 mbsf.

At 0230 hr on 4 December 2000, drilling began on a new 14.75-in hole and continued for 17 hr until the hole depth reached 195.0 mbsf. Two 20-bbl sepiolite mud sweeps were used to flush the borehole and the drill string was pulled. The pipe cleared the reentry cone at 2140 hr, the top drive set back, and the trip continued until the BHA reached the rig floor.

Considering the difficulties we experienced cleaning the borehole, we decided to deploy the fluid hammer with a 14.75-in dual cam underreamer bit in advance of the casing to help clear any blockage. It is important to note this is not the original deployment design for the hammer, but an innovative application choreographed as a fit-to-mission strategy. The rig crew went to work assembling five joints of 13.375-in flush joint casing. A casing shoe was not part of the assembly because the available shoes were under gauge and would not have allowed passage of the bit. The casing joints were tack welded and the entire assembly was hung in the moonpool with the casing elevators on C-plates. The first deployment challenge arose when the running tool would not slip all of the way into the 13.375-in casing hanger. After inspection and measuring, we determined that the centralizing bushing below the running tool was too big to fit in the casing hanger bore. The bushing was removed, and the running tool threaded into the casing hanger. The remaining BHA was assembled and run in the hole. The subsea TV was deployed at 2000 hr on 5 December 2000, and we reentered Hole 1188F after only 10 min of vessel maneuvering.

The hammer-assisted installation of the casing string proceeded well with the fluid hammer periodically firing as the casing encountered bridges or restrictions in the 14.75-in hole. It was a tight fit with occasional overpull and very slow progress at various trouble spots in the hole. Much to our relief, at 2330 hr, with the end of the 13.375-in casing at 61.6 mbsf, the hanger landed out and 20 klb of overpull were applied to confirm latch ring engagement.

Unfortunately, all efforts to retrieve the 14.75-in underreamer bit back through the bore of the casing proved futile. The underreamer

arms on the bit were supposed to fold back into the body, leaving a 12.35-in maximum diameter to pull back through the casing. After several hours of working the pipe and attempting to close the arms, the bit eventually stuck just inside the end of the casing. With no ability to rotate or circulate (without releasing from the casing), we had no choice at that point but to pull harder. At 150 klb overpull, the bit finally started to move up; however, after ~2.5 m of upward travel, the casing came free and the entire string began to pull out of the ground along with the bit. We surmised that the casing hanger latch ring had not fully engaged because the reentry cone was left at the seafloor. The drill string and casing assembly was tripped back to the ship, and by 1100 hr on 6 December 2000, the casing hanger was disengaged from the running tool at the rig floor. Because the bit would not move up through the casing, the 13.375-in casing joints had to be disassembled, stripped over the drill pipe, and laid out on the pipe racker (necessitating cutting the welds on the casing). Upon recovery of the shoe joint, we could see a deep, spiral-shaped groove inside the lower several inches of the casing as if it were threaded. After several inches, the groove geometry changed from spiral to axial grooves (Fig. F1). Our interpretation is that this change in groove patterns marked the point where the bit began to travel up into the casing before becoming stuck.

Undeterred by this setback, we replaced the 14.75-in dual cam under-reamer-style pilot bit with a standard 12.25-in hammer bit, believing that this deployment would be sufficient to pilot the casing into the hole. The entire casing assembly was rebuilt and run into the hole, this time with a casing shoe that had been machined on board the *JOIDES Resolution*. The casing string washed in until it encountered an obstruction at 21 mbsf; however, after 5 hr, 15 min, the casing would not advance beyond 25 mbsf. Because it was clear that no further progress was likely, we pulled the casing assembly back to the rig to deploy a reaming bit and clean out the hole again. To save time and effort, the casing was hung off with slings and placed forward in the moonpool. Each of the braided slings used in the hanging operation was rated to 8 T.

At 2210 hr on 7 December 2000, we reentered Hole 1188F with a 14.75-in tricone drilling assembly. By 1000 hr on 8 December 2000 we had washed, reamed, and cleaned the hole to a depth of 75 mbsf, well below the length of the 61-m-long 13.375-in casing string. We tripped the cleaned-out bit, rebuilt the casing running assembly (including the 12.25-in hammer bit), and ran the casing back to the bottom of the hole.

Our third attempt at deploying the casing went well at first, but progress became agonizingly slow, and the fluid hammer functioned continuously to a depth of 58.9 mbsf. At that point, the hammer ceased to function (likely because of the skin friction holding the casing and open hole beneath the hammer), and all further progress of the casing string ended ~2.5 m from the required landing point.

Recognizing that the geometry of our casing assembly (out of the throat of our reentry cone and sticking up ~2.5 m above the casing hanger) was identical in concept to the design of our HRRS, a quick adaptation to the FFF and centralizer guide was all that was required to create a nested funnel system. An HRRS cone was modified slightly by grinding on the internal landing shoulders and guide dogs to ensure passage over the running tool. At 0930 hr on 9 December 2000, the HRRS cone was deployed via free fall. A single tethered glass ball float was attached to the HRRS cone to allow recovery if should it become necessary. The subsea TV was deployed, and we verified that the HRRS

F1. Deep grooves cut into the interior of the first casing deployed in Hole 1188F, p. 99.



cone had landed properly on top of the 13.375-in casing hanger (Fig. F2). The running tool was released, and the hammer was advanced 1 m out ahead of the casing shoe to verify that everything associated with the installation was properly seated. We then recovered the drill string, which cleared the HRRS cone at 1110 hr and the rig floor at 1645 hr on 9 December 2000.

We reentered Hole 1188F at 0000 hr on 10 December 2000 after ~30 min of vessel maneuvering. Although there were several intervals of hole cleaning required, we eventually reached our target depth of 215 mbsf. A wiper trip back up inside the 13.375-in casing shoe showed no indication of hole blockage, torque, or elevated pump pressure. During what was supposed to be a final trip back to the bottom of the hole to check the status of the borehole, the drill string stuck fast. High torque and high pump pressure accompanied by high overpull indicated that the hole had started to collapse. After some tense moments, the driller was able to work the pipe free and eventually clean the hole. To convince ourselves that the hole was indeed clean and ready for deployment of our second casing string, the bit was pulled back into the 13.375-in casing shoe and lowered without rotation and minimal circulation to the bottom of the hole.

We recovered the drilling assembly and began preparations for running the 10.75-in casing string at 2315 hr on 10 December 2000. A standard cementing float shoe was attached to the shoe joint, and 13 joints of 10.75-in buttress thread casing were assembled with a standard 10.75-in casing hanger. The casing string was hung off of C-plates in the moonpool, and the subsea release assembly and 10.75-in running tool were included as part of the BHA. By 0400 hr on 11 December 2000 we were running the casing string to the seafloor.

After all our trials and tribulations to this point, the 10.75-in casing string went into the hole flawlessly. The casing shoe was cemented with 15 bbl of 15.8-lb/gal cement slurry. This is less cement than we might normally emplace, but we had experienced problems earlier in our operations when pumping mud pills that were >10 bbl. We released the pipe from the casing assembly, and the pipe cleared the rig floor at 1600 hr on 11 December 2000.

On the ensuing pipe trip, only 1 min, 7 s of maneuvering time was required to reenter the borehole. In fact, our reentry was so quick that we had to wait an additional 4.75 hr for the cement to cure before we could drill it out. It took ~4 hr to drill out the cement assembly, and by 0715 hr on 12 December 2000, we had cleaned the hole to our previous depth. To provide some initial piloting and stabilization for the ADCB coring system, we advanced the hole another 3.0 m to 218.0 mbsf and thoroughly cleaned and circulated fluid through the hole. The drill string cleared the rig floor at 1205 hr on 12 December 2000.

On our initial attempt with diamond coring, we chose to employ the 15-ft (nominal 4.5 m) ADCB for two reasons. First, it simplified core and core barrel handling (the concept of extricating 10 m of large-diameter core from a barrel without a liner seemed daunting). Additionally, the optimal operation strategy for diamond coring is to trip the core barrel whenever the throat of the bit is jammed. We expected core jamming to be a problem prior to coring even a few meters (much less for 10 m). At 1645 hr we initiated ADCB coring with slow circulation rates while the drillers and engineers monitored the drilling progress.

We intentionally kept the coring rate slow initially because the ADCB and associated 6.75-in drill collars were not supported in the larger-diameter hole. Coring parameters for the first core were 5 klb

F2. Nested HRRS funnel above a standard reentry cone, Hole 1188F, p. 100.



WOB, 50 rpm, 20 spm, and 500 psi. Conservative coring parameters were used for the first nine cores, or 20.3 m of advancement. Except for two empty core barrels, recovery ranged from 63% to 92% over this interval and averaged 75%. The average ROP over this period was 1.8 m/hr. Core blockages requiring barrels to be pulled early in the coring cycle caused the net coring rate to be even lower with the first 20 m of advancement, requiring a total of 28.5 hr. After establishing the ADCB-cored borehole, our emphasis was to optimize the penetration rate.

In many formations it is probable that rapid penetration and high recovery with the ADCB can be achieved simultaneously. During the short time we had available during Leg 193 for this operation, we did not have time to optimize both, so we sacrificed high recovery to improve the ROP. Over the next 22 cores, drilling parameters were varied as follows: 5–10 klb WOB, 60–120 rpm, 30–50 spm, and pump pressures of 700–1240 psi. Over this period we were able to nearly double the ROP to an average of 3.5 m/hr; however, core recovery suffered accordingly, dropping to only 10%. Of the first 31 cores recovered, there were nine with no recovery. Because most of the material we recovered was highly fragmented, it is likely that many of the empty barrels lost material on recovery. The lost materials could not be retained by the collet-style core catcher designed to capture full-diameter core. Alternative design core catchers did not appear strong enough to survive drilling through the rock we were recovering.

Continuous ADCB coring proceeded until reaching a depth of 327.2 mbsf. After deploying the core barrel for Core 193-1188F-32Z, the driller noted that the circulation pump pressures were too low, indicating that the barrel had not landed. Several attempts at deploying a core barrel were unsuccessful, so we decided to trip the pipe to inspect the BHA. We were nearly to our maximum penetration depth while still protecting the top of the BHA, so a pipe trip was pending in any event. The HRRS reentry cone was cleared at 1525 hr, and the bit cleared the rig floor at 1900 hr on 16 December 2000. Our inspection of the coring assembly indicated the landing ring had dislodged preventing the core barrel from seating. The inside and outside cutting structures of the bit were intact, but most of the cutting structure was severely worn. Several stabilizer pads were loose and/or missing from the drill collar stabilizer, which may have contributed to the bit failure.

A new BHA was assembled using all the available 6.75-in drill collars (341.7 m). We tripped the drill string and reentered the Hole 1188F HRRS reentry cone at 0211 hr after maneuvering the ship for 15 min. Once again we had difficulty in landing a core barrel, and after several more attempts, the ADCB landing seat was found wedged in the throat of the core lifter case.

Without a landing seat in the BHA, we had no choice but to pull the drill string, clearing the rig floor at 1545 hr on 17 December 2000. After repairs, we tripped the pipe, reentered Hole 1188F, and resumed coring. ADCB coring then continued through Core 193-1188F-47Z to a depth of 2039.7 mbrf (386.7 mbsf). Further penetration was prevented at that point by an apparent bit failure. A steadily decreasing ROP (<1.0 m/hr) and no recovery for the last three cores prompted us to terminate the ADCB coring. During the second ADCB bit run, recovery ranged from 17% to 48% and averaged 25.7%. The ROP ranged from 1.7 to 4.5 m/hr and averaged 3.0 m/hr. For the 15 cores cut with the second bit, the coring parameters were varied as follows: 5–8 klb WOB, 60–130 rpm, 30–40 spm, and pump pressures of 700–1240 psi. Upon recovery of the second diamond bit, it proved to be totally worn and devoid of diamonds.

All ADCB coring in Hole 1188F was conducted without core liners using the 15-ft core barrels. Core catchers consisted of the standard collet and spring finger types. No appreciable difference in recovery was noted, although the failure of one of the finger-type core catchers may have led to the premature bit failure. Two core barrels were recovered while reaming out the borehole with no advancement and were curated as core type "G." The recovery from these cores was not used in the accounting of recovery rates. One of the primary lessons we took from this operation was how difficult it can be to optimize bit and core catcher design as well as coring parameters in variable lithologies. Further details of the ADCB deployment in Hole 1188F can be found in the operations engineer's report for Leg 193 available from ODP.

Our first ADCB diamond bit, because it was completely worn and had no value, was converted to be used as an ADCB wireline logging clean-out bit. The remaining diamond pads on the bit interior and exterior were removed with a plasma torch, leaving the bit dimensions at ~7.125 in outside diameter and 4.00 in inside diameter. The ADCB 6.75-in drill collars and fabricated ADCB logging clean-out bit were used for the wireline logging BHA in case the pipe had to be lowered to the bottom of the hole to cool the hole for logging. For details of logging runs, the reader is referred to "[Downhole Measurements](#)," p. 86. One item of note, however, is that despite drilling the ADCB portion of Hole 1188F with a small-diameter bit, the calibrated calipers on the logging tools suggest the borehole diameter is in excess of 17 in throughout the logged interval. Once the logging tools and sheaves were rigged down, the drill string was pulled out of the hole, clearing the Hole 1188F HRRS reentry cone at 2115 hr on 21 December 2000.

Return to Hole 1188B

Because the temperature measurements during the logging run in Hole 1188F indicated a high geothermal gradient (see "[Downhole Measurements](#)," p. 86), we decided to move to nearby Hole 1188B and attempt a wireline temperature measurement and borehole water sample. This hole had been undisturbed since 27 November 2000, and we hoped that we might be able to collect at least a mixture of high-temperature fluid and borehole water as well as a temperature profile that might be repeated near the end of the leg. To ensure that the borehole temperature had not exceeded the maximum rated temperature of the batteries (65°C) and electronics (70°C) of the water-sampling temperature probe (WSTP), the temperature tool was deployed first. However, we wanted to minimize the potential for disturbance of the water column in the borehole, so the UHT-MSM temperature probe was deployed and kept just inside the end of the drill pipe prior to reentry. At 2327 hr on 21 December 2000, we reentered Hole 1188B and lowered the pipe to ~4 mbsf. The end of the pipe was unable to pass that point and the UHT-MSM tool would not pass deeper than 7 mbsf, frustrating our intentions. After recovering the temperature tool, the WSTP was deployed and a fluid sample (6°C) was taken at 3 mbsf. The drill string was pulled clear of the FFF at 0315 hr and was back on board the ship by 0745 hr on 22 December 2000.

Return to Hole 1188F

After logging operations at Hole 1189B had concluded (at ~1700 hr on 26 December 2000), we moved back to Hole 1188F (undisturbed

since 21 December 2000) to run a temperature log and attempt to sample high-temperature fluids from this hole. We experienced some difficulty in rapidly converting the time/temperature data from the UHT-MSM tool, but recognized the temperature at the bottom of the hole was much higher ($>300^{\circ}\text{C}$) than when we had measured while wireline logging ($\sim 100^{\circ}\text{C}$). A quick estimate projected the depth at which we expected to exceed the maximum temperature rating of the WSTP (65°C) at only 105 mbsf (well into the casing shoe). We collected a water sample (12°C) at that depth, but the disparity between our initial temperature gradient and the measured temperature at our sampling station initiated another temperature run with the wireline logging tool to see if we could better determine a maximum deployment depth (within its temperature limit) of the WSTP. The wireline tool returned a temperature of just over 100°C , with an erratic signal deep in the hole. The tool returned with the temperature sensor damaged, but the maximum reading thermometers in the cable head registered temperatures just higher than their calibration range (260°C). The differences in these readings made us disinclined to attempt another water sample (potentially jeopardizing the electronics of the WSTP) until we could determine with certainty a reproducible temperature profile. Later processing indicated that the data with the UHT-MSM tool indicated a similar gradient to the wireline tool to ~ 250 mbsf (see “[Downhole Measurements](#),” p. 86).

Second Return to Hole 1188F

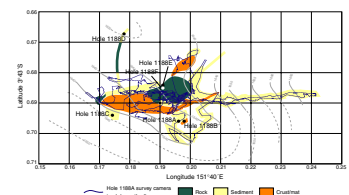
Upon completing the logging operations in Hole 1189C, we attempted a second temperature measurement and water sample in Hole 1188F. Whereas the maximum temperature recorded was close to that measured in our last temperature log ($>300^{\circ}\text{C}$), the depth vs. time file from the wireline was corrupted, making the estimation of a depth to sample within the operational limits of the WSTP challenging. We deployed the water sampler to 204 mbsf (~ 14 m below the casing shoe), where we expected the temperature not to exceed 60°C . A water sample was collected but the temperature measured with the WSTP was only 22°C . Because of an unexpected suspension of activities to clear a TSF employee through PNG customs for emergency departure (requiring a transit to the port of Rabaul), this would turn out to be the final operation of Leg 193.

Site Survey

Hole 1188A

While waiting for the *JOIDES Resolution* to be cleared by customs and receive permission to drill in PNG waters, we took the opportunity to conduct a VIT survey of the crest of Snowcap Knoll (Site 1188). Initially, the drill bit and VIT were deployed precisely on target, and we saw the expected patches of bright microbial mat and dark crusts on sediments. After hauling off bottom to fill the pipe, the bit was lowered to the same point then moved under DP in a cruciform pattern 60 m east, 40 m west, and 20 m north and south from the target point (Fig. F3). The traverse delineated a belt of flat dark crusts with bright microbial mat patches, trending west from the target point and to the immediate northwest of the target, a zone some 20 m across of outcropping rocks. Areas of pale sediment with only occasional patches of mat or crust

F3. VIT survey prior to the spudding of Hole 1188A, p. 101.



were also seen. The displayed camera depth and sonar altitude were recorded manually at various points, and these indicated that the proposed site possessed two parallel northwest-trending crests a few meters high. The VIT was withdrawn to the surface prior to the customs inspection.

The sediment patches were considered preferable by the operations manager for siting a hole. We decided to lower the VIT again after drilling operations were approved, to observe a jet-in test. This was conducted near the margin of a sediment patch ~13 m southwest of the original target. The test confirmed the suitability of the site for attempting to jet-in a modified reentry cone, if necessary, after first attempting a bare-rock spud with the RCB. After raising the VIT, Hole 1188A was spudded at this location. Additional seafloor cover information was added on subsequent camera surveys.

Subsequent Surveys

Hole 1188B

The bit and VIT were lowered to the nominal position of Site 1188A on Snowcap Knoll, landing a little north on dark crusts. A traverse south crossed quickly into sediments and within 10 m passed a large crater (severing of Hole 1188A), then a conical depression in sediment taken to be the hole location. After a farther traverse south for 10 m across sediments with scattered crusts and mat, the bit was moved 10 m west over sediments and back again.

Holes 1188C to 1188F

Additional 30- to 45-min VIT surveys were performed prior to initiation of subsequent holes. These surveys generally covered terrain mapped during the surveys for Holes 1188A and 1188B; however, in each case some new area was surveyed and the surface lithology data were added to our survey map (Fig. F3).

IGNEOUS PETROLOGY

Site 1188 is located at the low-temperature diffuse-flow Snowcap hydrothermal site within the PACMANUS hydrothermal field on Pual Ridge. Core was recovered from two drill holes. Hole 1188A was cored with the RCB system to a depth of 211.6 mbsf. Recovery averaged 10.4%. Hole 1188F, located ~30 m away from Hole 1188A, was drilled to 218.0 mbsf, where coring commenced with the ADCB to a total depth of 386.7 mbsf. The 168.7-m cored interval produced 30.89 m of core, corresponding to a recovery rate of 18.3%, which is considerably higher than that of the RCB system.

The descriptions of the igneous rock types and igneous features of altered rocks as observed in core from Holes 1188A and 1188F are based upon hand specimen and thin-section descriptions supplemented with the results of XRD analyses.

Hole 1188A

The upper part of Hole 1188A (down to ~40 mbsf) consists of fresh to slightly (or moderately) altered, black rhyodacite that has been divided into three units based on groundmass texture and phenocryst abundance. The first unit (Unit 1) is moderately plagioclase-clinopyroxene-

phyric and moderately vesicular with a glassy to microlitic groundmass. Measurements of the RI on fresh glass indicate an SiO₂ content of ~72 wt% (according to a calibration of this method using volcanic glass of andesitic to rhyodacitic composition from the Pual Ridge) (see Fig. F3, p. 42 in the “Explanatory Notes” chapter). This unit appears to extend to a depth of 34 mbsf. However, recovery was <1% in this unaltered part of the sequence, so more than one flow might be represented in Unit 1. Aphyric rhyodacite underlies Unit 1 and can be divided into a unit with a perlitic groundmass texture (Unit 2) and a moderately vesicular unit (Unit 3) with a glassy to microlitic groundmass. A rhyodacitic composition was again indicated by the results of RI measurements on Unit 3.

Alteration intensity increases sharply at a depth of ~40 mbsf, and the definition of individual units was governed by an integrated approach of recognition of primary textural features of the rocks and changes in alteration mineralogy and texture. Some units show fragmental textures that have been described as jigsaw breccia or pseudoclastic textures. These are interpreted as resulting primarily from alteration outward from fractures and/or brecciation during hydrothermal activity. However, in several units there is unequivocal evidence that at least some fragments have moved or rotated, which may indicate that the units are primary volcanoclastic rocks (hyaloclastite?). In other units, alteration is pervasive, leading to almost homogeneous replacement of the groundmass by silica-sulfate-clay alteration referred to as “bleaching” because the groundmass is light gray to white (see “Hydrothermal Alteration,” p. 33). The primary vesicles are usually preserved in bleached rocks but commonly are lined or filled by alteration minerals.

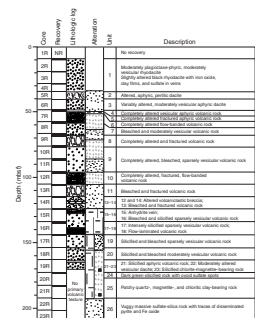
The primary composition of the altered volcanic units can generally not be determined petrographically, because phenocrysts or their pseudomorphs are absent or unrecognizable except in thin section. Most lithologic units of Hole 1188A are identified as “volcanic rock” because remnant volcanic textures including vesicles, phenocrysts, perlitic, and flow banding are common; however, because of the effect of hydrothermal alteration, the composition of the igneous precursor is difficult to constrain. It is likely that the rocks represent altered equivalents of aphyric dacite or rhyodacite equivalent to Units 2 and 3 because a gradual increase in alteration intensity has been observed (see “Hydrothermal Alteration,” p. 33). Geochemical data, especially the immobile element ratio Zr/TiO₂, provide independent evidence to substantiate this interpretation (see “Geochemistry,” p. 65).

An interval with volcanoclastic pebble breccia (Units 12 and 14) separates the upper volcanic rocks (Units 1 to 11) from a lower part consisting of variably altered volcanic rocks (Units 16 to 22). Units 23 through 26, recovered from the lower part of the drill hole, possess no remnant volcanic textures and were logged using descriptive terminology purely based on alteration mineralogy.

A full description of the various units, including lithologic characteristics and alteration mineral assemblages, is provided in Table T2. A graphic log of Hole 1188A summarizes the distribution of the units and their lithologic and alteration characteristics (Fig. F4). The modal proportions of groundmass, vesicles, and phenocrysts in Units 1, 17, 18, and 22 were determined by point counting (Table T3).

T2. Lithology and alteration of Units 1 to 26 in Hole 1188A, p. 265.

F4. Graphic summary log for Hole 1188A showing the lithologic and alteration characteristics of the various units, p. 102.



T3. Results of point counts on volcanic rock thin sections, p. 269.

Unit Summaries

The following is a brief summary of the lithologic units from Hole 1188A that have either well-preserved or remnant igneous features. Note that Units 15, 25, and 26 have no such features.

Unit 1 is black, moderately plagioclase-clinopyroxene phyric, moderately vesicular, microlite-bearing, glassy rhyodacite (Fig. F5). It is more vitreous at the top than any other lithologic unit from Hole 1188A. It contains ~72 wt% SiO₂ based upon RI measurements. Most of the vesicles are flattened as a result of flow during eruption and cooling. Thin sections show that, in addition to euhedral and subhedral plagioclase and clinopyroxene phenocrysts (generally <1.5 mm long), there are abundant smaller (to ~0.2 mm long) euhedral magnetite phenocrysts. These are commonly enclosed partially or wholly by both plagioclase and clinopyroxene. The groundmass bears numerous microlites, which include acicular transparent plagioclase, granular pyroxene, and very small (2–10 μm diameter) opaque minerals. Skeletal plagioclase in the groundmass and among the phenocrysts is rare. Some plagioclase phenocrysts are zoned, including a broad oscillatory style of zoning. Olivine from olivine-plagioclase clots (xenocrysts?) in Pieces 2 and 3 of Section 193-1188A-3R-1 is Fo₉₂ based upon RI measurements.

Unit 2 is an altered aphyric volcanic unit with well-preserved perlitic texture (Fig. F6). This indicates that it consisted of volcanic glass prior to alteration, which experienced solidification hydration. In parts, the rock shows a pseudoclastic texture because it has been altered preferentially along, and extending outward from, the perlitic cracks and away from irregular fractures.

Unit 3 is a slightly to moderately altered, moderately vesicular volcanic rock without any phenocrysts visible in hand specimen.

Unit 4 is a completely altered, bleached, aphyric, moderately vesicular volcanic rock with intervals showing remnant perlitic texture, flow banding, and/or fracturing.

Unit 5 is a completely altered, fractured volcanic rock with pseudoclastic texture. Fragments show remnant perlitic texture that is pseudomorphed by the alteration assemblage (Fig. F7).

Unit 6 is a completely altered, fractured, nonvesicular volcanic rock with incipient pseudoclastic texture. Fragments show flow banding that is pseudomorphed by the alteration assemblage (Fig. F8).

Unit 7 consists of a light gray to white bleached rock whose protolith was a sparsely to moderately vesicular aphyric volcanic rock (Fig. F9). Vesicles are typically millimeter scale in diameter and commonly are stretched into tubular shapes as long as 1 cm.

Unit 8 is a completely altered fractured volcanic rock with a pseudoclastic texture. Fragments show remnant perlitic texture that is pseudomorphed by the alteration assemblage.

Unit 9 is a bleached, sparsely vesicular volcanic rock that is very similar in appearance to Unit 7.

Unit 10 is a completely altered, fractured, intermittently perlitic and flow-banded volcanic rock. Flow banding is defined by microspherulitic bands and entirely devitrified bands. Folded flow banding has been recognized locally (Fig. F10).

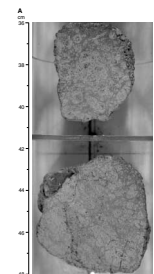
Unit 11 is another completely altered, pervasively bleached volcanic unit with sparsely vesicular patches.

Unit 12 is a completely altered, volcanoclastic, grain-supported, granule to pebble breccia with aphyric white and light gray clasts. The white clasts are completely bleached, and the light gray clasts are partially si-

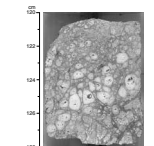
F5. Fresh, black, moderately vesicular rhyodacite, p. 103.



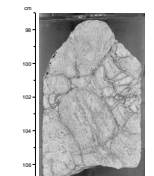
F6. Perlitic texture of aphyric dacite indicating that the groundmass consisted of volcanic glass originally, p. 104.



F7. GSC altered rock with remnant perlitic textures, p. 106.



F8. Flow banding that can be recognized in the light gray parts of Unit 6, p. 107.



licified. Locally, gray clasts show preserved vesicles (1%–3%; <1 mm diameter). The matrix consists of silica ± pyrite.

Unit 13 is a pervasively bleached, fractured volcanic rock with possible remnant flow banding and vesicles in some pieces (Fig. F11).

Unit 14 is a completely altered volcanoclastic, granule to pebble breccia (Fig. F12). This unit is indistinguishable from Unit 12.

Unit 16 is an intensely bleached and silicified, sparsely vesicular volcanic rock.

Unit 17 is an intensely silicified, sparsely vesicular volcanic rock, some pieces of which show traces of primary volcanic banding.

Unit 18 is a silicified, flow-banded volcanic rock (Fig. F13). Despite the alteration, a remnant trachytic or pilotaxitic alignment of groundmass microlites, visible in thin section, is the key to recognizing this unit as a coherent volcanic rock rather than volcanoclastic rock. Furthermore, rare plagioclase phenocrysts are evenly distributed in the groundmass rather than concentrated in particular layers. Minor, small clasts (<1 cm diameter) are interpreted as xenoliths within the flow.

Unit 19 is a silicified, bleached volcanic rock with rarely preserved perlitic texture, traces of vesicles, and some intervals of hydrothermal brecciation with silica veinlets.

Unit 20 is a silicified and bleached sparsely vesicular volcanic rock with some remnant perlitic texture.

Unit 21 is a silicified volcanic rock with a trace of vesicles and with some pieces exhibiting remnant microperlitic texture.

Unit 22 is a dark gray, moderately altered, moderately vesicular, aphyric volcanic rock. The groundmass contains ~30 modal% euhedral plagioclase microlites and rare clinopyroxene microcrysts. By comparison with fresh aphyric rhyodacite in the upper part of the hole (Unit 3), it can be inferred that this unit is also of felsic composition (dacite?).

Unit 23 is an intensely silicified, weakly to moderately chloritic magnetite-bearing volcanic rock.

Unit 24 is a distinctive dark green silicified unit with hairline silica-filled fractures and ovoid sulfate spots that may represent altered/filled vesicles.

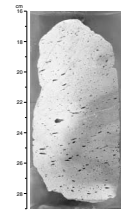
Volcanic Textures

Primary volcanic features have been recognized in many units of Hole 1188A despite the frequency of moderate to complete alteration. In particular, primary vesicles, phenocrysts, perlitic texture, spherulitic texture, and flow banding have been observed. Point counts of the thin sections of several fresh and altered volcanic rocks, which have identifiable phenocrysts and vesicles (or remnant vesicles), are given in Table T3.

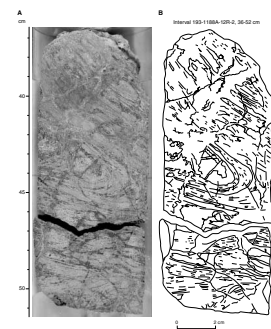
Vesicles

Vesicles are common in the rock units from Hole 1188A, including the fresh rhyodacite of Unit 1 (Fig. F5) as well as many of the altered volcanic rock units. Some specimens that exhibit the complete bleaching-type alteration nonetheless perfectly preserve empty vesicles (Fig. F9). The vesicularity of individual specimens varies from a trace to 15 vol% (except for one piece from Unit 1 that was sampled in Section 193-1188A-7R-1, which has 30 vol% vesicles). The vesicle size varies from as small as several tenths of a millimeter in diameter to several centimeters (maximum dimension) in large stretched or coalesced vesicles. Most commonly, the majority of vesicles are aligned oblate and

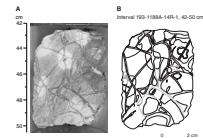
F9. Light gray to white, bleached, aphyric volcanic rock with preserved elongate vesicles, Unit 7, p. 108.



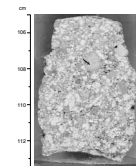
F10. Isoclinally folded flow banding in Unit 10, p. 109.



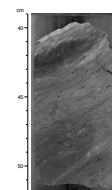
F11. Jigsaw breccia structure in completely bleached and sparsely vesicular volcanic rock, p. 110.



F12. Volcanoclastic pebble breccia, p. 111.



F13. Gray-green, flow-laminated, silicified volcanic rock, p. 112.



tube shaped, 1 or 2 mm across, and 1 or 2 cm long. These reflect stretching of originally spherical vesicles in the lava as it flowed and cooled. Other specimens contain a population of highly flattened vesicles, which can result from compaction or shearing of originally spherical vesicles in the lava as it flowed.

Phenocrysts

Phenocrysts observable in hand specimens are exclusive to the unaltered rhyodacite (Unit 1) in the upper, relatively unaltered part of Hole 1188A and are absent from 34 mbsf to the end of the hole. Although rare phenocrysts reach 10 mm, most phenocrysts are generally <1–2 mm long. They comprise both elongate lath-shaped plagioclase and equant to stubby-prismatic clinopyroxene. One thin section from Unit 1 (Sample 193-1188A-3R-1 [Piece 1, 0–2 cm]) contained enough phenocrysts that allowed us to estimate the plagioclase composition by the Michel-Levy technique. The resulting value, probably accurate only to about $\pm 5\%$ absolute, is An_{54} . Thin-section analysis of Unit 1 rhyodacite also reveals a population of euhedral to anhedral magnetite microphe-
nocrysts, which may be partly or completely enclosed in plagioclase.

Because slightly to moderately altered aphyric rhyodacite (Units 2 and 3) exists just below Unit 1, it can be inferred that the absence of large phenocrysts is a primary feature of the volcanic rocks and not necessarily caused by alteration. This is consistent with the XRD analyses that show there are significant amounts of fine-grained plagioclase in several moderately to completely altered units. Hence, any primary plagioclase phenocrysts in Units 2 and 3 should have survived hydrothermal alteration.

Plagioclase phenocrysts very similar to those in the unaltered Unit 1 are also observed in thin sections of some of the highly altered volcanic rocks deeper in the core. The plagioclase crystals preserve igneous oscillatory zoning and in places exhibit secondary overgrowths of possibly sodic plagioclase.

Perlitic Texture

Perlite is volcanic glass with arcuate and gently curved intersecting cracks that form in response to hydration. Perlitic texture is often preserved even in completely devitrified volcanic rocks and provides important evidence for the interpretation of their original composition. In Core 193-1188A-5R (Unit 2), pieces of altered, aphyric dacite(?) with well-preserved perlitic texture are present, indicating that this unit was originally glassy (Fig. F7). Furthermore, textural evidence indicates that alteration was focused along the perlitic cracks, and, hence, it is inferred that primary volcanic textures are an important control on alteration processes during hydrothermal activity (see below).

Spherulitic Texture

Well-preserved spherulites with radiating aggregates of quartz and feldspar have been recognized in thin sections of samples from Hole 1188A. This indicates that some units underwent a period of high-temperature devitrification prior to solidification, which is common in felsic lavas.

In general, if the melt is quickly chilled, it will solidify to quenched volcanic glass, whereas an equigranular to micropoikilitic microcrystalline groundmass is generated if solidification proceeds slowly enough to allow complete, homogeneous crystallization. However, depending on a variety of factors, including cooling rate, viscosity, chemical com-

position, and volatile content, undercooled felsic melts may experience a phase of high-temperature devitrification leading to the formation of spherulites instead of equigranular microcrysts (Lofgren, 1971). Individual spherulites commonly form spheres of radiating, fibrous quartz and feldspar crystals, with diameters ranging from >1 cm to <0.1 mm (micro-spherulites). They may coalesce and form completely devitrified domains within the lava.

The preserved spherulites that have been observed in thin section of samples from Unit 6 are ~1 mm in diameter and form groundmass domains consisting of coalesced radiating aggregates of quartz and feldspar (Fig. F14). Faint outlines of the spheres can be recognized under polarized light, and the radial arrangement of the microlite needles is apparent under crossed polarizers. Based on this observation, it can be inferred that parts of Unit 6 were devitrified prior to solidification, indicating relatively slow cooling rates.

In addition to these well-preserved spherulites, there are also microspherulites that typically form linear, coalesced necklacelike aggregates (Fig. F15). However, most of these structures have been altered and radiating crystal aggregates are rarely recognizable.

Flow Banding

Flow banding is a common feature of felsic lava flows. Individual bands are defined by substantial differences in microlites formed during cooling crystallization and/or differences in vesicularity. If cooling rates are low and the material remains sufficiently ductile, banded parts of the lava may become deformed and folded during flow.

Flow banding has been recognized in several altered units of Hole 1188A. In general, this primary volcanic texture is preserved in units that experienced patchy, multiphase alteration resulting in the formation of pseudoclastic textures and hydrothermal jigsaw breccia. Typically, it can be observed in the light gray, green silica-clay (GSC) altered (see “[Hydrothermal Alteration](#),” p. 33) apparent clasts and is defined by alternating light and dark, linear to fibrous domains that are interpreted to reflect the primary flow banding of the lava (Fig. F8). This texture is particularly common in Unit 10, which also includes pieces of core showing isoclinal folding of flow banding (Fig. F10). In thin section it can be observed that the flow banding is defined by variable abundances of microspherulites (Fig. F16). Light gray bands consist of coalesced microspherulites, whereas dark gray bands consist of altered glass (very fine grained clay and silica) with isolated microspherulites.

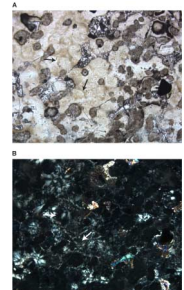
Volcaniclastic Textures

Classification of the volcanic rocks recovered from Hole 1188A is hindered by their aphyric texture and the textural and mineralogical overprint of alteration. In particular, the discrimination of primary breccia (volcanic autobreccia, hyaloclastite, or sedimentary breccia) from alteration-related brecciation or formation of pseudoclastic textures (“hydrothermal breccia”) is difficult. However, volcanic pebble breccia consisting of completely altered aphyric clasts has been recognized (Fig. F12).

Volcaniclastic Breccia

Densely packed, clast-supported volcanic pebble breccia exists in Core 193-1188A-14R (Units 12 and 14; see Fig. F12). These units are completely altered; however, the original outlines of the clasts can still

F14. Spherulitic texture from Hole 1188A, p. 113.



F15. Isolated and coalesced microspherulites forming necklacelike aggregates, p. 114.



F16. Groundmass of the flow-banded sample from Unit 10, p. 115.



be recognized. The moderate sorting of this unit, and the slight rounding of the clasts, suggests that it is a resedimented volcanoclastic deposit. All of the clasts are aphyric, and it can be inferred that they were derived from a common, local source. The clasts could have been derived from quench fragmented parts of a lava flow (hyaloclastite) and redeposited as mass-flow units. However, they show color variations (light gray and white) because of the variable intensity of silicification and clay-sulfate alteration, which may reflect differences in hydrothermal alteration at the source area. These units are important because they define paleosurfaces in the stratigraphy of Pual Ridge.

Hydrothermal Breccia with Evidence for Clast Movement

In some units logged as hydrothermal breccia, textural evidence indicates that individual fragments were moved relative to each other. This is an important observation because many rocks with fragmental appearance in Hole 1188A are jigsaw breccia, which are clearly the product of fracture-controlled alteration, generating variably developed pseudoclastic textures (Figs. F6, F7, F8, F11) (see below). However, breccia units containing clasts with laminar textures, such as flow banding, showing variable, unsystematic orientations indicate that these clasts have been moved relative to each other (Fig. F17). This textural feature may indicate a volcanoclastic origin of the particular unit (resedimented hyaloclastite?) or, otherwise, may be the result of intense fracturing during which sufficient open space was generated to allow for clast movement.

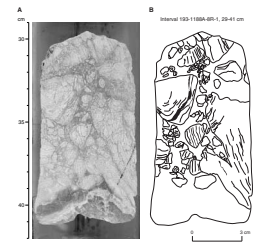
Evidence for clast movement has also been observed on a centimeter to millimeter scale. A thin section of Unit 8 (Sample 193-1188A-9R-1 [Piece 7, 68–70 cm]) shows a clastic texture with angular, locally perlitic vitriclasts generally containing $\ll 1\%$ vesicles. In parts, these clasts are separated by linear veins that are probably related to fracturing during alteration, showing a strict jigsaw-fit arrangement (Fig. F18A). However, in other areas of the thin section, the clasts are arranged in an irregular manner indicating that individual fragments have been moved relative to each other (Fig. F18B). Furthermore, there are also clasts with laminar textures (elongate tube vesicles?) that are clearly not continued in adjacent clasts, indicating that they are out of place (Fig. F18C). These textural features may be the result of hydrothermal alteration and minor fracturing in a primary volcanoclastic rock or intense fracturing associated with alteration and accompanied by substantial movement of fragments in the void space within fractures generated during brecciation.

Hydrothermal Breccia with Pseudoclastic Textures

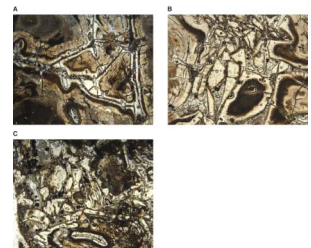
Remnant perlitic textures in slightly to moderately altered aphyric dacite (Core 193-1188A-5R [Pieces 7 and 8]) indicate that Unit 2 consisted of volcanic glass prior to alteration. The perlitic groundmass texture is best preserved in light gray siliceous domains (Fig. F6). However, large parts of the groundmass consist of interconnected networks of dark gray clay-rich alteration assemblages encircling and separating round to irregular light gray siliceous groundmass domains. Hence, the rocks show an apparent clastic texture.

It is inferred that fluid flow and alteration occurred preferentially along the previously existing perlitic cracks in the rock, which led to preferential replacement of the material in these fine fractures extending outward into the surrounding siliceous groundmass. Consequently, the light gray round to lensoidal central parts of the perlites became in-

F17. Nonsystematic orientation of flow banding in the clasts of a brecciated sample, p. 116.



F18. Various vitriclastic textures in a sample of Unit 8, p. 117.



creasingly surrounded by dark gray clay alteration forming an apparent matrix (Figs. F6, F7). However, there are also linear or irregular fractures that encircle more blocky domains (Fig. F19). Hence, the apparent clastic texture is created entirely by alteration processes and represents an excellent example of the development of “pseudoclastic textures” in coherent felsic volcanic rocks caused by hydrothermal alteration. Such features are commonly observed in the hydrothermally altered footwall of ancient massive sulfide deposits on the continents hosted by felsic lavas (Allen, 1988).

Hole 1188F

The deeper parts of Site 1188 were investigated in Hole 1188F using diamond-drilling technology. The upper portion of this hole was stabilized by inserting a casing string down to a depth of ~200 mbsf. Core was obtained from 218.0 to 386.7 mbsf. Recovery rates for individual half cores (typically 4.6 m long) varied from 0% to >90%. The overall recovery for ADCB drilling in Hole 1188F was 18.3%, compared to the 10.4% recovery experienced in Hole 1188A, which was drilled with the RCB system.

In total, 45 units (Unit 27 to 72) have been identified in Hole 1188F based on changes in the alteration mineralogy, presence or absence of plagioclase phenocrysts, remnant spheroidal textures, presence and abundance of amygdules or vesicles, and locally developed fragmental textures. Many of these units have a curated thickness of <1 m. The upper portion of the hole, down to a depth of ~340 mbsf, consists of silicified volcanic rocks, which are aphyric or slightly porphyritic with altered plagioclase phenocrysts and amygdules of variable size (ranging from submillimeter to ≤10 mm) and composition (mainly quartz, anhydrite, and/or pyrite). Below 340 mbsf, magnetite-bearing units become increasingly prominent. Hydrothermal magnetite has been observed within vesicles, in siliceous halos along anhydrite-pyrite veins, and disseminated through the groundmass. Several units are porphyritic and contain fresh, unaltered plagioclase phenocrysts in a groundmass with abundant plagioclase microcrysts. Furthermore, several units have preserved vesicles that are only partially filled or lined with alteration minerals. These features indicate that alteration of the lower part occurred under significantly different conditions than in the upper part.

The lithologic characteristics of the units recognized in Hole 1188F are provided in Table T4, and the principal features are summarized in a graphic log (Fig. F20). The units are briefly described below.

Unit Summaries

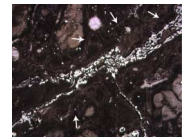
The following is a brief summary of the general characteristics of the lithologic units from Hole 1188F.

Unit 27 is a silicified, aphyric, massive volcanic rock with fine (submillimeter) quartz amygdules.

Unit 28 is similar to Unit 27 but shows a distinctive green color, which has been related to a higher abundance of chlorite. Furthermore, cyclic siliceous banding, observed along anhydrite-pyrite veins, locally encircles differently altered kernels and gives rise to an apparent clastic texture of the rock (Fig. F21).

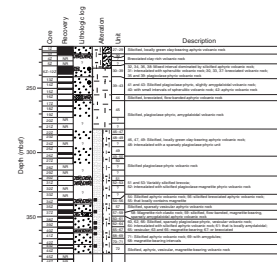
Unit 29 is a silicified, aphyric, massive volcanic rock identical to Unit 27.

F19. Fracture-controlled alteration, p. 119.



T4. Lithology and alteration of Units 27 to 72 in Hole 1188F, p. 270.

F20. Graphic summary log for Hole 1188F, p. 120.



F21. Aphyric volcanic rock representative of Unit 28, p. 121.



Unit 30 is a brecciated volcanic rock with silicified fragments embedded in a light gray clay-rich matrix (Fig. F22). This texture, though, may be a drilling-induced characteristic of the ADCB system because most of the recovered pieces consist of rubble. The fine, soft, clay-rich material may be an artifact caused by the grinding.

Unit 31 consists of one small piece that shows a prominent spherulitic texture in hand specimen (Fig. F23).

Unit 32 is a silicified, aphyric volcanic rock.

Unit 33 consists of silicified fragments of aphyric volcanic rock embedded in and/or coated by soft, gray clay similar to Unit 30.

Unit 34 is a silicified, aphyric volcanic rock. If the fragmental texture of Units 30 and 33 are drilling artifacts, then Units 32 to 34 may represent the same lithologic unit.

Unit 35 is a porphyritic, sparsely vesicular silicified volcanic rock. It contains as much as 2 vol% plagioclase phenocrysts (as long as 3 mm; commonly replaced by clay), which are locally aligned.

Unit 36 is dominantly aphyric, silicified massive volcanic rock with intervals containing pyrite-filled flattened vesicles and rare relict plagioclase phenocrysts.

Unit 37 consists of a single piece with a clastic texture. It contains abundant, rectangular to irregularly shaped light gray domains (mainly anhydrite, clay, and quartz) embedded in a tan-gray fine-grained silicified matrix.

Unit 38 is a silicified, dominantly aphyric, volcanic rock that locally contains pyrite-filled flattened vesicles and rare pseudomorphed plagioclase phenocrysts. This unit is similar to Unit 36.

Unit 39 is a porphyritic volcanic rock with clay-altered plagioclase phenocrysts (<1–1 vol%; as long as 4 mm) and as much as 3 vol% round to elongate vesicles (ranging from <1 to 5 mm, the maximum dimension). Several pieces contain quartz-rich (\pm pyrite) patches, a few millimeters to a centimeter across, that are slightly rounded.

Unit 40 is a completely altered, aphyric volcanic rock with prominent spherulitic texture in hand specimen and is identical to Unit 31.

Unit 41 is a silicified volcanic rock with fresh and clay-altered plagioclase phenocrysts (<1 to 2 vol%; as long as 4 mm). Fine amygdules (<1 mm in diameter) consist of anhydrite and pyrite. This unit contains several pieces with 1- to 2-cm-wide fragmental zones where <1-cm siliceous clasts are hosted within light gray finer siliceous material (Fig. F24).

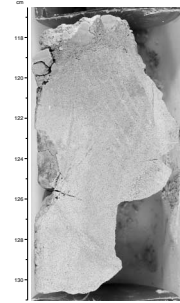
Unit 42 is a silicified aphyric volcanic rock with elongated vesicles filled or lined with pyrite-anhydrite or quartz.

Unit 43 is a silicified volcanic rock with white clay pseudomorphs of original plagioclase phenocrysts (<1–2 vol%; as long as 3 mm) and elongate vesicles (as long as 10 mm, the maximum dimension) that are lined or filled by anhydrite, pyrite, and/or quartz.

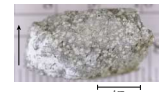
Unit 44 is a silicified, generally aphyric volcanic rock with relict flow banding and a faint clastic texture. Some pieces contain traces of white clay-altered plagioclase phenocrysts. The flow structures and fragmental textures of Unit 44 are defined by domains showing variable relative proportions of silica and clay (Fig. F25).

Unit 45 is a silicified, porphyritic, sparsely vesicular volcanic rock with as much as 3 vol% clay-altered plagioclase phenocrysts (as long as 3 mm), which are commonly replaced by bluish-white clay. The vesicles are filled by anhydrite and/or pyrite and are typically aligned, defining a flow structure. Locally, round to angular quartz-rich patches (a few millimeters to 3 cm across) are present (Fig. F26).

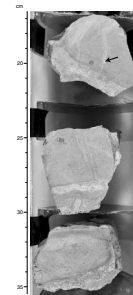
F22. Incipiently developed clastic texture, p. 122.



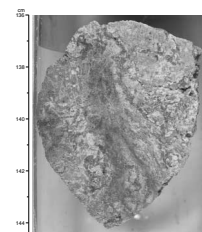
F23. Prominent spheroidal texture defined by abundant isolated and coalesced concentric domains, p. 123.



F24. Plagioclase-phyric volcanic rock of Unit 41, p. 124.



F25. Relict flow banding observed in Unit 44, p. 125.



Unit 46 is a silicified, aphyric volcanic rock with rare vesicles (partially filled by pyrite). It contains several 1- to 2-cm-wide clastic zones with <1-cm fragments in a fine, light gray matrix. Similar textures have been observed in Unit 41.

Unit 47 is a silicified, aphyric volcanic rock with rare, pyrite-filled vesicles and a distinctive greenish coloration inferred to reflect the occurrence of disseminated chlorite.

Unit 48 is a silicified, sparsely plagioclase-phyric volcanic rock, with minor, pyrite-filled vesicles.

Unit 49 is a silicified volcanic rock with a slight dark green color owing to the presence of chlorite. Locally, it contains rare plagioclase phenocrysts (some as large as 5 mm) and minor pyrite-filled vesicles. Round patches of quartz (as large as 2 cm in diameter) are present in several pieces (similar to Units 39 and 45).

Unit 50 is a silicified, slightly plagioclase-phyric volcanic rock. The unit is distinguished from Unit 49 by the absence of greenish colored clay in the groundmass of the rock. Distinct, fine (0.1–1 mm) dark spots are common, representing vesicles filled with silica (\pm pyrite).

Unit 51 is aphyric and shows a clastic texture with angular to rounded silicified fragments embedded in a dark gray quartz matrix (Fig. F27).

Unit 52 is a single piece of porphyritic volcanic rock with fresh plagioclase laths and fine titanomagnetite phenocrysts.

Unit 53 is aphyric and shows a clastic texture similar to Unit 51.

Unit 54 is a completely altered, aphyric, nonvesicular volcanic rock. Silicification is strong and pervasive, and alteration halos and clastic textures are present in some pieces.

Unit 55 is a completely altered, vuggy, clastic volcanic rock, most of which contains domains where the matrix is black and magnetite rich (Fig. F28). The domains are irregular in shape and may represent centimeter- to decimeter-scale brecciated zones in which magnetite was precipitated from hydrothermal fluids.

Unit 56 is composed of light gray, completely altered (silicified and clay altered) volcanic rocks with mottled and clastic textures.

Unit 57 is a silicified, aphyric volcanic rock with anhydrite veining and scattered fine quartz amygdules.

Unit 58 consists of one piece of magnetite-rich rock with a clastic texture.

Unit 59 is a strongly silicified, sparsely vesicular, locally flow-banded, aphyric volcanic rock with scattered fine quartz amygdules similar to Unit 57.

Unit 60 is a silicified, sparsely plagioclase-phyric, sparsely vesicular volcanic rock.

Unit 61 is a silicified, aphyric volcanic rock with fine, submillimeter amygdules.

Unit 62 is a silicified, sparsely plagioclase-phyric and sparsely vesicular volcanic rock.

Unit 63 is a silicified and locally magnetite-bearing, aphyric volcanic rock.

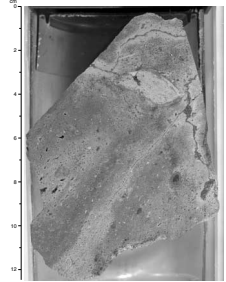
Unit 64 is a silicified, aphyric volcanic rock with fine, submillimeter amygdules.

Unit 65 is a silicified and locally magnetite-bearing, sparsely vesicular aphyric volcanic rock.

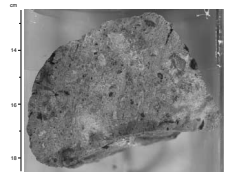
Unit 66 is a silicified, sparsely plagioclase-phyric volcanic rock with fine, submillimeter amygdules.

Unit 67 is a silicified, aphyric volcanic rock with a clastic texture.

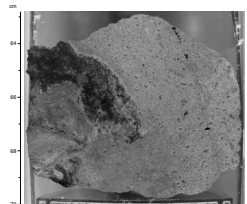
F26. Elongate amygdules and altered plagioclase phenocrysts, p. 126.



F27. Light gray and dark gray domains creating an apparent fragmental texture, p. 127.



F28. Black, magnetite-rich domain hosted within a vesicular to amygdaloidal aphyric volcanic groundmass, p. 128.



Unit 68 is a silicified volcanic rock with trace amounts of fresh plagioclase phenocrysts and finely disseminated magnetite in the groundmass.

Unit 69 is a silicified, aphyric, sparsely amygdaloidal volcanic rock.

Unit 70 is a silicified, aphyric volcanic rock with abundant amygdules consisting mainly of anhydrite.

Unit 71 consists of a single piece of silicified aphyric, sparsely vesicular volcanic rock. The vesicles are elongate (as wide as 10 mm, the maximum diameter), aligned, and typically partially filled with quartz, pyrite, chlorite, and/or anhydrite.

Unit 72 is a silicified, sparsely vesicular volcanic rock with rare, well-preserved plagioclase phenocrysts and several quartz-rich patches as wide as 2 cm in diameter. Magnetite is common in the vesicles and disseminated in the groundmass. Prominent alteration halos along the anhydrite-pyrite veins are silica and magnetite rich.

Volcanic Textures

A number of primary volcanic features are common in the rock samples from Hole 1188F. The coherent volcanic rocks are either porphyritic or aphyric and typically amygdaloidal or vesicular. Fresh or altered plagioclase microlites are generally aligned, defining a trachytic groundmass texture. Elongate vesicles and phenocrysts also show a preferred orientation. Other features such as clastic, mottled, xenolithic, and flow-banded textures have been observed less frequently. The major alteration overprint consists of silicification and clay alteration, followed by anhydrite and pyrite-rich veins (see “[Hydrothermal Alteration](#),” p. 33, “[Sulfide and Oxide Petrology](#),” p. 51, and “[Structural Geology](#),” p. 58). Note that the silicification present in Hole 1188F involves only quartz, in contrast to the shallower Hole 1188A, where silicification involves cristobalite at the top giving way to quartz at depth.

Amygdules

Amygdules, or vesicles filled with secondary minerals, are present throughout Hole 1188F (Fig. [F29](#); Table [T5](#)). Open vesicles are less abundant, yet are sporadic in core samples practically all the way to the bottom of the hole. Most amygdules are millimeter sized and give the hand specimens a spotted appearance. In some cases, amygdules are flattened and aligned, and when present, phenocrysts are aligned parallel to the same trend.

The most common amygdule-filling mineral assemblage is quartz + pyrite + anhydrite. The second most common mineral fill is any two of these three minerals or any of these minerals alone. Quartz is present as intergrown anhedral crystals, generally 0.25–0.5 mm across, forming a mosaic texture. Quartz grains exhibit undulose extinction and numerous secondary planes of fluid inclusions, giving the grains a “dirty” appearance. Pyrite and anhydrite (≤ 1 mm) are subhedral to euhedral.

Unusual amygdule filling assemblages include chlorite + chabazite(?) and pyrite + magnetite + clay. The chlorite-chabazite(?) is from Unit 55, where most amygdules are quartz filled. Other vugs are incompletely filled, with incomplete linings of radiating aggregates of chlorite and chabazite? (a clear, low-birefringence, low-RI zeolite with inclined extinction and rhombohedral cleavage).

The pyrite + magnetite + clay amygdules are present in Unit 65. This dark gray to black rock contains numerous vugs that are filled with a

[F29](#). Silicified rock with quartz ± pyrite filled amygdules, p. 129.



[T5](#). Distribution and types of amygdules in Hole 1188F, p. 276.

soft black magnetic material and a central pyrite crystal. Other vugs contain anhydrite. The soft black material is clay with inclusions of tiny bladed magnetite crystals.

Phenocrysts

Plagioclase is the only phenocryst type observed in Hole 1188F (Table T6). Fresh plagioclase is present in 13 of the 45 units identified. Plagioclase phenocrysts pseudomorphed by secondary minerals are recognized in 12 units, and 20 units are totally aphyric.

Fresh phenocrysts are euhedral and lath shaped, with both stubby laths and, more commonly, elongated laths occurring together. Zoning is sporadic, with a few phenocrysts that have rounded core zones overgrown by euhedral mantles. This feature suggests that the phenocryst at some point in its history became unstable and began to corrode, which is commonly interpreted to reflect a former magma mixing event. When fresh plagioclase laths are in a sample, the groundmass microcrysts commonly are also at least partly fresh (Fig. F30). Both phenocrysts and microlites, though, may have corroded rims.

Most fresh phenocrysts are present in such small abundances that optical estimates of chemical composition are impossible. However, some determinations by the Michel-Levy technique (which gives a minimum for the anorthite content and is probably accurate to $\pm 5\%$ absolute) gave An_{64} , An_{51} , and An_{62} . These results all reflect labradorite compositions, similar to other determinations from fresh dacites sampled during Leg 193 (An_{54} from Section 193-1188A-3R-1, An_{59} from Section 193-1190A-1R-1, and An_{50} from Section 193-1190B-2R-1).

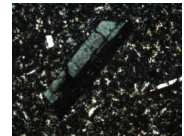
Plagioclase phenocrysts are commonly recognized as pseudomorphs, with characteristic stubby lath shapes and similar sizes compared to the fresh phenocrysts (i.e., 0.5–2.0 mm; average = ~1 mm). Plagioclase is replaced, in order from highest to lowest frequency, by quartz, clay (usually illite), clay + halloysite, clay + anhydrite, quartz + anhydrite, quartz + clay, chlorite + illite, and chlorite + illite + anhydrite (Table T6). The identification of halloysite is tentative. This is a fine-grained micallike material with low birefringence and sweeping extinction. It has been described as “silica,” probably because Hole 1188A contained an abundance of fine-grained cristobalite (i.e., silica) with low birefringence. However, as Hole 1188F is otherwise devoid of cristobalite in favor of quartz (with the exception of the spheroidal Unit 31; see below), it seems unlikely that cristobalite would persist as an alteration of plagioclase.

Spheroidal Nodules with Randomly Oriented Plagioclase Microlites

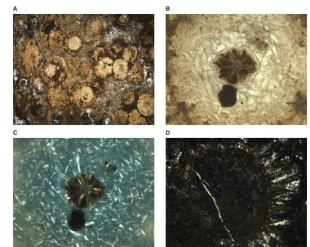
Hand specimens of Units 31 and 40 (each of which consists of only one small piece) show a prominent spherulitic texture with abundant isolated or coalesced, white, round aggregates (as wide as 1 mm in diameter). In thin section, these aggregates correspond to brown, round to irregular, coalesced domains with bulbous margins (Fig. F31A). They are rimmed by dark brown, clay-rich material, which also outlines individual spheroids in aggregated domains. Internally, they consist of randomly oriented, very fine grained plagioclase microlites (Fig. F31B, F31C). Generally, the characteristic radiating arrangement of feldspar needles, diagnostic for spherulites generated during high-temperature devitrification, is lacking. Only in rare cases have small, concentric dark brown zones with radiating feldspar crystal aggregates been observed in the core of the spheroids. The groundmass between the spheroids consists mainly of fine-grained cristobalite; however, some coarser-grained

T6. Distribution and types of plagioclase phenocrysts in Hole 1188F, p. 277.

F30. Fresh plagioclase phenocryst, p. 130.



F31. Spheroidal texture observed in Unit 31, p. 131.



radiating feldspar crystal aggregates are locally attached to the outer margins of some spheroids (Fig. F31D).

Even though the textures observed are somewhat ambiguous, it is inferred that the spheroids represent a primary volcanic feature related to high-temperature devitrification of a lava. Plagioclase microlites are well preserved within the spheroids, but generally altered in the surrounding cristobalite-rich domains, suggesting that they were protected from hydrothermal alteration in devitrified domains.

Flow Banding

Remnant, poorly preserved flow banding has been locally recognized in Units 44 and 59. Laminar textures are defined by subtle variations in the proportions of quartz and clay minerals. In thin section, the contacts between these domains are gradational. It is inferred that minor differences between individual flow bands (e.g., microvesicles, microlites, and ratio of glassy to devitrified groundmass) are reflected in the changes in alteration mineralogy.

Quartz-Rich Patches

Gray, generally rounded siliceous patches are present in several units of Hole 1188F (e.g., Units 39, 45, 49, and 72). These are embedded within the altered volcanic groundmass and consist of relatively coarse, interlocking, anhedral quartz crystals forming a mosaic texture, which are locally accompanied by interstitial pyrite and minor anhydrite and chlorite. Contacts to the surrounding groundmass are generally sharp (Fig. F32).

The origin of these patches is enigmatic. Their mineralogical composition is similar to many amygdules, which, however, rarely exceed 1 or 2 mm in diameter, except for elongated vesicles/amygdules that may be up to 10 mm long and 2 mm wide. Hence, if these quartz-rich patches represent large amygdules, there would be a significant gap in the size distribution of the vesicles.

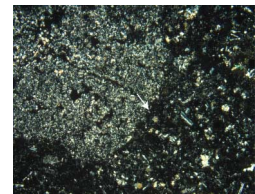
Large cavities known as lithophysae may form in felsic lavas during high-temperature devitrification as a result of diffusion processes associated with the formation of spherulitic aggregates of quartz and feldspar microcrysts. Lithophysae may be round, irregular, or star shaped and may reach diameters of several tens of centimeters. However, their outer margin invariably consists of fine quartz and feldspar needles. Such textures have not been observed around the quartz-rich patches, and therefore, it is unlikely that they represent lithophysae.

Finally, it may be possible that the quartz-rich patches represent xenolithic material that became incorporated into the lava during its passage through the subsurface or picked up from the seafloor during flow. However, it is difficult to envisage a source rock with the required, almost monomineralic composition (quartz-rich vein material?).

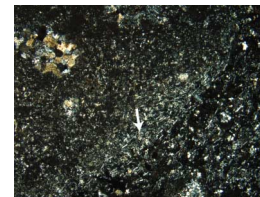
Xenoliths

Locally, isolated, round to wispy patches (as wide as 3 cm in diameter) with fine-grained igneous internal textures have been observed. They have sharp or transitional contacts to the surrounding altered volcanic groundmass. Locally, microlites in the groundmass are aligned parallel to the margins, indicating that the crystallizing lava was plastically deformed around these patches (Fig. F33). Based on their composition and the textural relationship to the enclosing volcanic groundmass, they are interpreted as xenolithic fragments, which were

F32. Rounded, quartz-rich patch domain, p. 133.



F33. Xenolith of volcanic rock embedded in microlite-rich groundmass, p. 134.



incorporated into the lava in the subsurface or from the seafloor during flow.

Thin Clastic Zones

Individual pieces of some units contain 1- to 2-cm-wide bands with clastic textures (Fig. F24). These bands contain fragments (≤ 0.5 cm) of the adjacent coherent rock, hosted in a fine-grained siliceous matrix. These zones may be interpreted as parts of autoclastically fragmented lava generated during emplacement or as fractures where brecciation of the coherent rock occurred as a result of hydrothermal and/or tectonic activity.

Pseudoclastic Texture

Silicified halos (up to 2 cm wide) are a typical feature of the veins in Hole 1188F. Where such veins intersect each other at high angles, the halos merge and encircle round to irregularly shaped groundmass domains. These kernels of less altered volcanic groundmass superficially resemble fragments and the texture of the rock may be described as pseudoclastic (Fig. F21).

Clastic/Mottled Textures

In addition to volcanic rocks with isolated quartz-rich patches, xenolithic clasts, thin clastic zones, and pseudoclastic textures, there are several units in Hole 1188F that show somewhat enigmatic mottled or fragmental textures. They contain domains with contrasting mineralogical composition mainly defined by changes in the relative proportions of microcrystalline quartz and very fine grained clays.

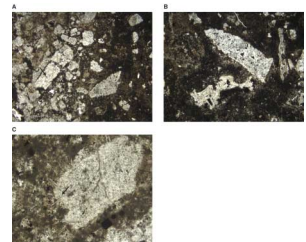
In general, quartz-rich groundmass domains, representing apparent clasts, are embedded in the surrounding slightly more clay-rich groundmass representing the apparent matrix. The contacts between these domains can be sharp or gradational and the shapes of the apparent clasts vary from angular to irregular (Fig. F34A, F34B). Locally, it can be observed that remnant plagioclase microlites are transgressing the boundary between apparent matrix and apparent clasts (Fig. F34C). Textural evidence supporting a sedimentary or volcanoclastic origin (e.g., polymict composition, clast-supported texture, phenocrysts abraded at clast margin, and grading) has not been observed.

It is possible that these fragmental units represent autoclastic zones of lava flows where the original clastic texture, defined by fragments of variable grain size of the same composition, has been subsequently enhanced during hydrothermal alteration. Alternatively, it may be argued that the textures observed are pseudoclastic, arising entirely because of the incomplete, domainal, multiphase alteration of a coherent volcanic precursor during which siliceous groundmass domains became isolated within more altered, less siliceous groundmass.

Summary

Holes 1188A and 1188F combined provide a one-dimensional view to a depth of 386.7 mbsf of the lithologic architecture beneath the low-temperature diffuse Snowcap hydrothermal site located within the PACMANUS hydrothermal field of Pual Ridge. With the lone exception of fresh volcanic rocks sampled near the surface, all of the rocks are hydrothermally altered, most of them nearly completely. Nevertheless, the majority of the rocks are demonstrably volcanic in origin and con-

F34. Unit 51 clastic textures, p. 135.



tain abundant vestiges of primary igneous features such as phenocrysts, trachytic groundmass, vesicles, amygdules, and flow banding.

The shallow, fresh volcanic rocks are rhyodacitic in composition. They contain phenocrysts of plagioclase with the optical properties of labradorite, as well as less-abundant titanomagnetite microphenocrysts. Volcanic rocks encountered deeper at Site 1188 frequently exhibit either plagioclase phenocrysts or pseudomorphs thereof. The fresh plagioclase crystals in the deeper rocks also have the optical properties of labradorite. Furthermore, some of the deeper samples contain leucoxene pseudomorphs after titanomagnetite. Thus, there is evidence that the whole volcanic section sampled at Site 1188 is essentially the same, or very similar, rhyodacite or dacite.

Most of the rocks are either vesicular or amygdaloidal, with instances of open or incompletely filled vesicles persisting to some of the deepest units. The groundmass of all the igneous rocks is uniformly fine grained, and porphyritic rocks contain relatively few and relatively small plagioclase phenocrysts (generally only 1%–2% and 1–2 mm long). Thus, all of the rocks are interpreted as volcanic, there being no coarser-grained rocks or textures, such as diabasic ones, that might indicate a hypabyssal origin.

Occurrences of perlitic texture, spherulitic texture, flow banding, volcanic brecciation, and autobrecciation all attest to the success of the coring program in sampling various coherent and brecciated portions of the volcanic rocks that built up the upper 387 m of Pual Ridge. Occurrences of hydrothermal breccia and pseudoclastic textures illustrate details about the subsequent lithologic modifications that overprint the volcanic rocks when they are subjected to subseafloor hydrothermal activity.

HYDROTHERMAL ALTERATION

Site 1188 targeted the Snowcap hydrothermal site, a zone of low-temperature diffuse venting within the PACMANUS hydrothermal field. Six attempts to drill were made at this site, resulting in three holes from which core and/or logging data were obtained. Hole 1188A, the initial hole at the site, intersected vertically extensive pervasive hydrothermal alteration, which often obscured primary textural features to the extent that it was not possible to identify individual units on the basis of igneous lithology alone. Poor hole conditions forced the abandonment of this hole at a depth of 211.6 mbsf. Hole 1188B was drilled with the LWD tool to 72.0 mbsf; an attempt to core deeper with the ADCB recovered only two wash samples. Following the abandonment of this operation, a concerted effort was made to drill a hole into the deeper part of the hydrothermal system at Snowcap. After three unsuccessful attempts, Hole 1188F provided cores from a deeper sequence of hydrothermally altered volcanic rocks from 218.0 to 386.7 mbsf.

General Overview

The following detailed description of hydrothermal alteration in coherent volcanic rocks and breccias from beneath Snowcap hydrothermal site is based primarily on visual descriptions of cores from Holes 1188A and 1188F and is supplemented by thin-section petrography and XRD analyses of bulk samples. Portable infrared mineral analyzer (PIMA) analyses were also conducted on a large number of core samples

from both holes. The spectra will be further processed on shore, but for some intervals, particularly in Hole 1188F, initial results provide additional mineralogical information that complements the XRD data. These are discussed where appropriate in the text.

Alteration was classified in drill core primarily by the visual detection under binocular microscope of the following key minerals: soft green to bluish green clay, soft white clay, hard silica polymorphs, and magnetite. Anhydrite and pyrite are present throughout the drilled section, generally as trace to minor phases. An overview of the principal alteration types is given in Table T7.

Six main types of hydrothermal alteration were delineated in cores from Site 1188:

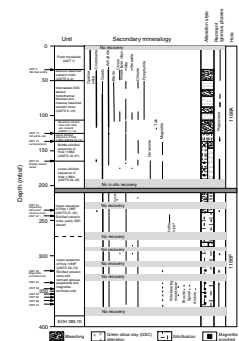
1. Patchy silica-clay and Fe oxide films developed on fracture surfaces and as vesicle linings in otherwise fresh vesicular porphyritic rhyodacite.
2. Pervasive opaline silica alteration of a single perlitic volcanic unit;
3. Pervasive blue-green to green-gray silica-clay (GSC) alteration that generally pseudomorphs textural features such as perlite and flow banding. Silica occurs as cristobalite and/or quartz.
4. Pervasive and vein-associated bleaching (whitish gray silica-clay ± anhydrite alteration) that results in the destruction of primary igneous textures other than vesicles.
5. Patchy to pervasive silicification, forming a dominant quartz-illite assemblage that shows a general trend toward quartz-illite-chlorite at depths >300 mbsf.
6. Impregnation with Fe oxides (dominantly magnetite, with minor hematite), in rare cases accompanied by hercynite, forming dark gray to black alteration patches and vein halos.

The characteristics, distribution, and relationships between each of these types of alteration are discussed in detail below. The diagnostic features of the three major alteration styles are also summarized in Table T7. In broad terms, the spatial distribution of alteration below Snowcap hydrothermal site is relatively straightforward (Fig. F35). A 34-m-thick cap of fresh rhyodacite to dacite, possibly intercalated with altered units that may not have been recovered, is underlain by a sequence of pervasively bleached vesicular volcanic rocks to a depth of ~50 mbsf. A zone of strongly anhydrite-silica (cristobalite or quartz)-pyrite veined and brecciated GSC altered rocks, intercalated with more massive bleached units and cut by late anhydrite veins with bleached halos, extends from ~50 to 105 mbsf. An additional sequence of bleached rocks with variably developed cristobalite-pyrite and quartz-pyrite stockwork veins underlies this sequence to a depth of ~125 mbsf. Between 125 and 375 mbsf (the bottom of Hole 1188F), silicification is the dominant style of alteration at Site 1188. As noted above, this style of alteration is typified by a quartz-illite assemblage, which tends toward quartz-illite-chlorite at depths >300 mbsf. Magnetite-enriched intervals are sporadic within the silicified sequence, between 135 and 185 mbsf in Hole 1188A and from 320 to 375 mbsf in Hole 1188F. The sequence of pervasively silicified rocks is crosscut by late anhydrite veins with banded gray to white bleached alteration halos. These veins are most abundant between 220 and 280 mbsf in Hole 1188F but are present in all cores below 125 mbsf.

The only two samples recovered as wash from Hole 1188B at a depth of 72.0 m are cristobalite-bearing, pervasively bleached, variably vesicu-

T7. Summary of different principal alteration types, Site 1188, p. 278.

F35. Summary of lithostratigraphic units, alteration style, and distribution of major, minor, and trace alteration phases as determined by XRD, p. 137.



lar volcanic rocks, very similar to lithologies cored between 50 and 105 mbsf in Hole 1188A. The recovery of these two samples suggests the alteration profile in Hole 1188B is similar to that in the upper part of Hole 1188A.

Tables T2 and T4 provide a summary of the distribution, lithology, and alteration features of the 26 units identified in Hole 1188A and the 46 units in Hole 1188F, respectively (refer also to Figs. F4, F20). Lithologic subdivisions were made based on remnant volcanic characteristics (e.g., the recognition of perlitic texture or flow banding and the presence or absence of phenocrysts or vesicles) and/or the dominant style of alteration within a given interval. A detailed description of the alteration of individual core pieces is presented (see the “Site 1188 Alteration Log” p. 263).

Downhole Distribution of Secondary Minerals

Thin-section and XRD investigations (Tables T8, T9, T10) reveal systematic changes in secondary mineral assemblages with depth at Site 1188, which broadly mimic the changes in alteration type outlined above (Fig. F35). The most pronounced changes are in the mineralogy of the prevailing silica polymorphs, the abundance of anhydrite, and the appearance and disappearance of particular phyllosilicate phases and magnetite.

Above 34 mbsf, opaline silica and smectitic clay are the principal secondary phases. Between 34 and 50 mbsf, cristobalite, chlorite-smectite mixed-layer phases, and anhydrite are the most abundant alteration minerals. Below 50 mbsf, pyrophyllite, occasional chlorite, illite, and barite (in trace amounts) join cristobalite and anhydrite. Barite has not been detected below 105 mbsf. With a handful of exceptions (see “Detailed Description of Hydrothermal Alteration in Lithologic Units from Site 1188,” p. 37), cristobalite is not a major alteration mineral below 120 mbsf and anhydrite becomes less abundant, whereas quartz and illite increase. Magnetite and chlorite are present in most rocks from between 140 and 185 mbsf in Hole 1188A, where quartz and illite dominate the secondary mineral assemblage, whereas anhydrite is restricted to vein and vesicle fill. In addition, corrensite is locally abundant from 165 to 185 mbsf. A quartz-illite-dominated alteration assemblage with late anhydrite veining is continued in the uppermost section of Hole 1188F (220–280 mbsf), although chlorite and magnetite are rare and corrensite is absent. PIMA analyses and thin-section observations from this interval indicate that the white clay present in the banded, bleached halos associated with these veins is pyrophyllite, although this phase was not identified in XRD spectra. Chlorite becomes abundant below 280 mbsf and is joined by sporadic magnetite below 320 mbsf. Two magnetite-bearing samples from ~350 mbsf have small amounts of brucite, alunite (in one case), and hercynite spinel.

Thin-section observations and whole-rock geochemistry (mainly Al_2O_3 , K_2O , and MgO concentrations) indicate that phyllosilicate phases commonly comprise >30 vol% of the rock in all styles of alteration and are, therefore, much more abundant than the relatively small phyllosilicate peaks in the XRD spectra might suggest. However, this phenomenon is not unusual in unoriented polymineralic powder diffraction samples and is not considered to be a significant discrepancy.

The transitions from opaline silica to cristobalite to quartz below 105 mbsf indicate a general increase in alteration temperature with depth.

T8. Minerals identified by XRD analysis, Hole 1188A, p. 279.

T9. Minerals identified by XRD analysis, Hole 1188F, p. 281.

T10. Minerals identified by XRD analysis, Hole 1188B, p. 283.

Alteration Styles and Relative Timing of Alteration Events

The alteration history of Site 1188 is multistage and complex. There are several episodes of fracturing and fluid flow, as manifested by multiple veining and alteration events.

Only small fragments of fresh to incipiently altered dacites could be recovered from the uppermost 34 m of basement at Snowcap. Below 34 mbsf, the extent of alteration is high to complete and the dominant style of alteration is pervasive replacement, although in some places alteration along veins and in patches overprints earlier pervasive alteration.

As discussed above, the most abundant secondary minerals in rocks recovered from Site 1188 are silica polymorphs (quartz or cristobalite), followed by phyllosilicates (abundant illite, with less common smectitic clay, pyrophyllite, chlorite-smectite mixed-layer phases, and chlorite), then anhydrite, pyrite, and magnetite. These phases either replace igneous material or occur as vein, vesicle, and vug fill. The common occurrence of anhydrite is remarkable. Anhydrite is most abundant as vein and vesicle fill or in breccia cement, but is also observed in thin sections replacing igneous groundmass or plagioclase, particularly in bleached units between 34 and 125 mbsf in Hole 1188A.

It is generally very difficult to associate specific alteration styles, other than bleaching, with discrete vein sets. The GSC alteration and silicification appear to be chiefly pervasive, with hydrothermal fluids percolating along microcracks, perlitic cracks, void space in breccias, and taking advantage of the generally high porosity/permeability of the fractured vesicular lavas to produce highly to completely altered rocks. In contrast, bleaching is rarely truly pervasive. Late, localized bleaching is clearly associated with anhydrite-pyrite veining in Hole 1188F, and concentric zonation of alteration halos adjacent to anhydrite-coated fractures is still recognizable even in the heavily bleached intervals between 35 and 105 mbsf in Hole 1188A.

The earliest recognizable stage of hydrothermal alteration at Site 1188 is pervasive GSC alteration, which is intercalated with and persists as remnants within bleached units in the upper part of Hole 1188A (~35–125 mbsf). The development of bleached alteration halos along anhydrite-pyrite veins, and of patches of light gray alteration within GSC altered rocks, suggests that pervasive GSC alteration preceded bleaching. Both pervasively GSC altered rocks and bleached rocks often exhibit localized silicification, either in vein halos or in and around vesicles, implying that there is a phase of silicification that postdates both GSC alteration and the early pervasive bleaching event in this part of the hydrothermal system.

Pervasive silicification is the dominant alteration type in the remainder of the cored interval (125–375 mbsf) at Site 1188. We use the active term “silicification” because the abundance of quartz as replacements and vesicle fill in most thin sections from this interval suggests that SiO₂ has been added. Also, preliminary shipboard geochemistry indicates SiO₂ enrichment in the silicified sequences relative to their precursors (Fig. F36; see “Geochemistry,” p. 65). However, these conclusions are tentative and may be modified as a result of postcruise research.

Remnant domains of GSC altered rock are preserved within pervasively silicified rocks, particularly between 150 and 185 mbsf in Hole 1188A and between 260 and 280 mbsf in Hole 1188F. We consider that an early GSC-like alteration, subsequently obscured by pervasive silicification except in remnant domains, was initially developed throughout

F36. Fluid inclusions in anhydrite, p. 139.



the entire drilled sequence and that patchy silicification higher in the sequence, where it shows a similar temporal relationship to the GSC alteration and also postdates pervasive bleaching, is likely to be related to the pervasive silicification at depth. This is the principal basis for assigning pervasive silicification to the final major stage of alteration, although postcruise research may reveal a more complex evolutionary sequence.

Additional evidence for GSCLike alteration prior to pervasive silicification in the deeper portions of the hydrothermal system is provided by the fact that, in pervasively silicified rocks, quartz typically overgrows other secondary phases such as magnetite, hematite, and, most significantly, clays pseudomorphing plagioclase microlites. Pyrite is part of all alteration assemblages, but silicified rocks are generally relatively enriched in pyrite, and quartz and pyrite are commonly intergrown.

The latest identifiable stage of hydrothermal alteration at Site 1188 is more localized and is represented by bleached and banded quartz-pyrophyllite halos associated with anhydrite (\pm quartz \pm pyrite) veins. These veins, which always cut preexisting alteration, are developed most strikingly in the upper part of Hole 1188F (~220–280 mbsf), but are present throughout the interval from 105 to 375 mbsf. The mineralogy of these veins and their associated alteration is similar to that of pervasively bleached units at shallower depths. However, these veins clearly postdate all other alteration styles at Site 1188 and are observed to cut quartz veins that are developed in pervasively bleached rocks between 105 and 125 mbsf (see “[Structural Geology](#),” p. 58), clearly demonstrating that the anhydrite veins represent a later hydrothermal event. Late anhydrite is also present throughout the silicified sequence in the centers of vesicles and vugs that are commonly lined with quartz and pyrite. Additionally, multiple late stages of anhydrite formation are inferred on the basis of silicified or bleached halos along anhydrite veins that are cut by later anhydrite veins and the presence of cyclically zoned alteration halos on many veins, implying multiple fluid pulses (see “[Structural Geology](#),” p. 58).

Detailed Description of Hydrothermal Alteration in Lithologic Units from Site 1188

Films on Fresh Porphyritic Dacite

Fresh porphyritic rhyodacite was the only lithology sampled from the upper portion of Hole 1188A (0–33.95 mbsf) (Table [T2](#)), although the very low core recovery (average <3%) in this interval means that the presence of other types of material cannot be confidently discounted. Fresh rhyodacite pebbles were also sporadically recovered farther down the hole, but this material was limited to the top of individual core intervals and was interpreted to have caved in from the upper levels.

Alteration of fresh rhyodacites is limited to the development of patchy films of grayish silica-clay and rust-colored iron oxide or oxyhydroxide on fracture surfaces and vesicle walls. Very fine grained euhedral pyrite is commonly present in trace quantities on these films. The XRD analyses (Table [T8](#)) indicate that opaline silica and smectitic clay are the dominant components of the films.

Opaline Silica

Pervasive alteration to opaline silica (confirmed by XRD analysis) is confined to Unit 2, which lies immediately beneath unaltered rhyodacite in Hole 1188A (33.95–34.08 mbsf). As it is not possible to distinguish between opaline silica and cristobalite in hand specimen, this type of alteration is included with pervasive silicification in the alteration description for the hole.

Rocks from Unit 2 have a remnant perlitic texture, cut by fine silica veinlets, along which alteration is particularly intense, resulting in a pseudoclastic texture (Fig. F37). Very fine grained pyrite is disseminated throughout the rock in trace amounts. Thin-section description and XRD analysis (Table T8) indicate that opaline silica is the dominant phase present in the unit, with minor smectite, illite, pyrite, and remnant igneous microlites of plagioclase. Silica(+clay) alteration is controlled by perlitic fractures and decreases in intensity toward the centers of perlitic pseudoclasts (Fig. F38).

Unit 2 is underlain by pervasively bleached vesicular volcanic rocks and marks a sharp increase in alteration intensity for Hole 1188A.

Green Silica-Clay Alteration

The GSC style of alteration is commonly overprinted by bleaching or silicification and is consequently interpreted to be the earliest style of pervasive alteration at Site 1188. It is most readily identified in core samples by its distinct blue-green to gray-green color and its softness when compared to silicified rocks. Although sporadically developed in most units below 49 mbsf, this style of alteration is best developed in Units 5, 6, 8, and 10, which lie in a 50-m zone of predominantly brecciated rocks between 49 and 99 mbsf (Table T2). More massive bleached units (Units 7 and 9; discussed below) are intercalated with the breccias.

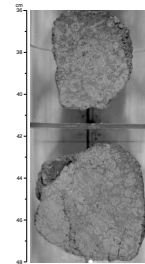
Typically, GSC alteration leaves pseudomorphs of primary igneous features, preserving perlitic textures and flow banding (Figs. F39, F40). Even where best developed, GSC altered rocks have been extensively veined (Figs. F7, F40, F41). They are cut by anhydrite-(pyrite) vein networks with rare silica-(pyrite) veins in the shallower portions of the hydrothermal system (Units 5, 6, and 8) (Fig. F42) and are cut predominantly by quartz-(pyrite) veins with associated patchy to pervasive silicification at greater depths (Unit 10) (Fig. F43). Remnant domains of soft GSC alteration are also sporadic in silicified units below 125 mbsf (Fig. F35; see the “Site 1188 Alteration Log,” p. 263), where they appear to exhibit a similar mineralogy to the main GSC altered interval between 50 and 100 mbsf, with superimposed quartz alteration.

Patchy to pervasive bleaching, associated with late anastomosing anhydrite-(pyrite) and quartz-(pyrite) vein networks, overprints the GSC altered breccias (Fig. F41). This style of bleaching is best developed in Unit 8 (Table T2), which lies between two massive bleached intervals (Units 7 and 9; see below) that are interpreted to represent the same type of alteration.

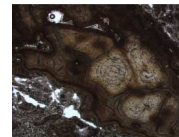
Unit 10 differs from the overlying breccias in that it is cut by a siliceous vein network, rather than the anhydrite-dominated veins that are abundant farther up the section. It exhibits well-developed silicification of altered volcanic fragments, particularly in vein halos. Scattered later anhydrite veins with bleached alteration halos cut the siliceous breccia.

Thin sections from GSC altered rocks commonly exhibit pervasive alteration of original volcanic glass to finely intergrown cristobalite and

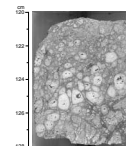
F37. Perlitic textured volcanic rock with opaline silica veinlets, resulting in a pseudoclastic texture, p. 140.



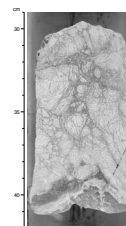
F38. Photomicrograph of remnant perlitic texture with scattered microlites surrounded by cristobalite-rich alteration products, p. 141.



F39. GSC altered rock with a remnant perlitic texture and anhydrite-(silica-pyrite) veining, p. 142.



F40. GSC altered rock with flow-banded fragments hosted in an anhydrite-(silica-pyrite) vein network, p. 143.



tan-brown clay. Where this type of alteration is developed, plagioclase microlites seem to be largely unaltered. It appears that the altering fluids used perlitic fractures and cooling cracks to invade the rock. However, original perlitic and spherulitic textures are often preserved. Spheroidal domains, where present, are typically altered to clay and surrounded by an intensely silicified matrix (Fig. F44). Vugs and vesicles are generally lined by cristobalite with blocky anhydrite in the center. Anhydrite is abundant in thin sections from Units 5, 6, and 8, but mostly as late-stage vein and vug fill. It does not seem to be a major component of the more pervasive GSC alteration style. Pyrite is present in silica \pm anhydrite veins and is abundant in patches where silicification is intense. Quartz was clearly identified in thin sections from Units 8 and 10 in the form of veins and vesicle fill together with pyrite (Fig. F45). The sections cut from Unit 10 contain quartz-pyrite-magnetite veins with chlorite-hematite halos, replacing former igneous groundmass (Fig. F46). Veins of this type were not observed in other GSC altered units.

Powder XRD investigation of GSC altered breccias indicates that silica polymorphs and anhydrite (as breccia matrix, postdating GSC alteration) are prominent alteration minerals (Table T8). The most abundant phyllosilicate phases are chlorite and illite, but pyrophyllite is also present, particularly in bluish green sections of the core. Traces of barite were also detected in most of the samples analyzed.

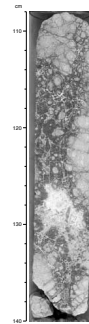
The silica polymorphs delineated by XRD show a consistent change with depth. Cristobalite is the dominant polymorph in Units 5 and 6, whereas quartz and cristobalite are both present in significant quantities in Units 8 and 10. This change from cristobalite to quartz with increasing depth is similar to the pattern recorded from the Trans-Atlantic Geotransverse (TAG) hydrothermal field (Hopkinson et al., 1999) and is consistently seen through all styles of alteration at Site 1188 (see below).

Bleaching

Pervasive bleaching is well developed in the upper part of Hole 1188A, where bleached units alternate with GSC altered units (Table T2). Unit 3 (moderately to highly altered), and Units 4, 7, 9, and 11–14 (completely altered) all exhibit bleaching, which is dominated by silica and clay with generally minor anhydrite. In contrast to the gray-green to blue-green GSC altered rocks, bleached units are typically white to light gray in appearance and may be distinguished from pervasively silicified rocks by their relative softness. Pervasively bleached units fall into three broad categories (Table T2): generally featureless to weakly vesicular units (termed massive) from shallower depths (Units 3, 4, 7, and 9; 39–97 mbsf; intercalated with GSC altered units), bleached volcanoclastic units (Units 12 and 14), and strongly veined and brecciated units with silica stockworks (Units 11 and 13; 106–117 mbsf; intercalated with the volcanoclastic units).

The lower boundary of pervasive bleaching is marked by Unit 15 (125.70–125.94 mbsf), a medium- to coarse-grained crustiform to granular anhydrite-pyrite vein set, with small fragments of bleached volcanic rock. However, bleached alteration halos associated with anhydrite \pm pyrite \pm quartz veins are present throughout all of the core recovered from Site 1188. These veins clearly postdate pervasive GSC alteration and silicification and are, therefore, interpreted to represent a later al-

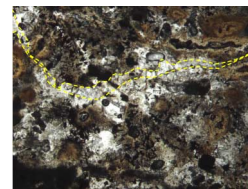
F41. GSC altered rock with a remnant perlitic texture and anhydrite-(silica-pyrite) stockwork veining, p. 144.



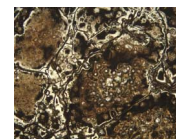
F42. Anhydrite-pyrite veining with well-developed siliceous halo hosted in GSC altered volcanic rock, p. 145.



F43. Quartz-pyrite veining with well-developed silica-chlorite alteration halos, p. 146.



F44. Clay-altered spherulites surrounded by fracture controlled silicification, p. 147.



teration event than the pervasive bleaching developed between 40 and 125 mbsf.

Massive Bleached Units

Massive bleached units exhibit pervasive replacement of volcanic rock by cristobalite, anhydrite, and clay. All igneous textures, except for vesicles, are generally destroyed. Vesicles are partially or fully filled by crustiform to bladed anhydrite and very fine grained drusy pyrite (Units 3, 4, and the upper portion of Unit 7) or by cristobalite/quartz \pm pyrite (the lower part of Unit 7 and throughout Unit 9). Late irregular anhydrite-pyrite veins are abundant in Unit 4. The pieces of core that comprise Units 5 and 9 commonly exhibit concentric zonation from white rims to gray cores (Fig. F47), representing alteration halos around fluid pathways—fractures or veins—that were not recovered.

Thin-section petrography and XRD analyses of bleached volcanic rocks indicate that anhydrite, silica polymorphs, and clays are the main alteration minerals (Table T8). Remnant microlitic igneous plagioclase is also rarely present, and barite is a minor alteration phase in some samples. Silica species show a similar zonation to that seen for the GSC altered rocks. Cristobalite is the only polymorph detected in Unit 4 and the upper part of Unit 7. The lower portion of Unit 7, as well as Unit 9, contains significant quantities of both cristobalite and quartz, with the latter mostly occurring as late silica-pyrite vesicle fill. Chlorite and smectite are the main clay phases in Unit 4, whereas illite and pyrophyllite are more abundant in the deeper bleached units.

Bleached Volcaniclastic Units

Bleached volcaniclastic lithologies (Units 12 and 14) contain soft, rounded, granule- to pebble-sized sulfate-clay altered clasts, which are cemented by quartz (Fig. F48). Variations in the color of individual clasts from white to beige and gray are interpreted to reflect compositional differences between the precursors of the clasts, meaning that the unit is polymictic. Larger clasts occasionally exhibit hard siliceous rims, implying that silicification occurred after the bleaching event. Pyrite is finely disseminated throughout the siliceous cement.

Thin-section petrography and XRD analyses (Table T8) of bleached volcaniclastic units indicate that quartz is the dominant phase, replacing the groundmass of the volcanic fragments as very fine grained intergrowths along with birefringent clay (illite, from XRD analysis) and occurring in veins with pyrite (Fig. F49). Anhydrite is present as late vug fill in Unit 14.

Brecciated Bleached Units

Units 11 and 13 comprise completely bleached, sparsely vesicular volcanic rocks that are crosscut by a strongly developed silica-anhydrite-(pyrite) stockwork vein system (Fig. F50). In Unit 11, these stockwork veins are cut by irregular, anastomosing, vuggy anhydrite veins that contain as much as 5% pyrite, mostly as drusy cavity fill. Unit 13 also displays late anhydrite veins, which are less vuggy than those in Unit 11 and have distinct narrow siliceous alteration halos. Pyrite occurs as fine disseminations throughout Units 11 and 13. The silica stockwork in Units 11 and 13 is interpreted to be equivalent to the silica cement of the intercalated volcaniclastic units and shows a similar later relationship to pervasive bleaching.

Thin-section petrography and XRD analyses indicate that silica polymorphs are the dominant alteration minerals (Table T8), occurring as

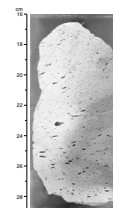
F45. Quartz-pyrite stockwork ladder vein, partly crosscutting and partly parallel to flow banding, p. 148.



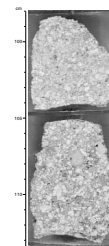
F46. Narrow quartz-pyrite-magnetite vein surrounded by a chlorite-hematite alteration halo, p. 149.



F47. Bleached vesicular rock with a zoned alteration pattern, p. 150.



F48. Bleached volcaniclastic sediment with clay-anhydrite altered clasts cemented in silica, p. 151.



granular veins and intergrown with fine clays as pervasive groundmass replacement. Cristobalite is the dominant polymorph of silica in Unit 11, whereas quartz predominates in Unit 13. Traces of talc were also detected by XRD in rocks from Unit 13, whereas remnant igneous plagioclase and disordered chlorite-smectite mixed-layer phases are present in Unit 11. Fine-grained euhedral pyrite is developed throughout, showing increased abundance toward veins. Anhydrite is present as late vein and vesicle fill in Unit 13. Relict igneous Ti magnetite shows partial breakdown to leucoxene and is often partially overgrown by pyrite.

Anhydrite Vein

Unit 15 consists of five pieces (as large as 4–5 cm across) of almost pure anhydrite, probably representing centimeter-thick anhydrite veins. These pieces are rubble from the uppermost part of Core 193-1188A-15R, and they probably represent an in situ lithologic unit (125.70 to 125.92 mbsf, curated depth), although they may also have fallen down the hole. XRD analysis (Table T8) confirms that this vein comprises near pure anhydrite. A few percent drusy quartz and pyrite accompany the anhydrite as accessory minerals.

Silicification

Pervasive silicification (quartz-illite-chlorite \pm magnetite) is the dominant style of alteration in the deeper part of Hole 1188A (Units 16–25; 125.94–184.60 mbsf) and throughout Hole 1188F (Units 27–72; 218.00–374.91 mbsf). Silicified units vary in color from light gray to almost black, and chloritic examples may be green. However, they are easily distinguished from GSC alteration and bleaching in drilled core by their relatively high hardness.

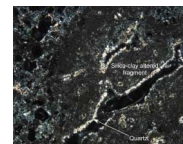
Silicified units commonly retain remnant primary textures, including vesicles (Units 16, 17, 19, 22, 27–29, 45–50, 57, 59–66, and 68–72), perlitic texture (Units 19 and 21), flow banding (Units 17, 44, and 59) and lamination (Unit 18). Thin-section observations and XRD analyses (Table T8) record the presence of preserved plagioclase phenocrysts and/or microlitic plagioclase (discussed below), implying that pervasive silicification is not strongly plagioclase destructive.

Within the silicified sequence, cristobalite is only found in Unit 21 (along with quartz) and in the less intensely altered Units 22, 31, and 40, where it is the sole silica polymorph detected. All other XRD analyses conducted on silicified units indicate that quartz is the dominant alteration mineral (Tables T8, T9). Although mostly indistinguishable in hand specimen, variability of the clay components in the secondary mineral assemblage over the 250-m-wide interval of silicification is indicated by thin-section and XRD studies. The following description of alteration styles is broken down into sections according to these changes.

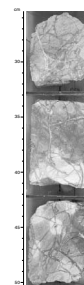
Silicification in Hole 1188A (126–185 mbsf)

Two very distinctive silicified units were intersected within the Hole 1188A silicified sequence: a finely laminated unit (Unit 18; 136.91–137.79 mbsf) and a relatively weakly altered vesicular volcanic unit (Unit 22; 164.95–165.23 mbsf). As will be outlined below, these units mark significant changes in the secondary mineralogy profile. Silicified units within the hole are accordingly divided at these horizons into an upper silicified succession (Units 16 and 17; 125.94–136.91 mbsf), a

F49. Volcaniclastic sediment, illustrating very fine grained silica-clay altered volcanic fragments rimmed by fine crystalline quartz, p. 152.



F50. Fractured, bleached volcanic rock with a strongly developed silica-anhydrite-(pyrite) stockwork veins, p. 153.



middle silicified succession (Units 19–21; 137.79–164.95 mbsf), and a lower silicified succession (Units 23–25; 165.23–184.60 mbsf).

Upper Silicified Succession (126–137 mbsf). The uppermost unit of the silicified succession within Hole 1188A (Unit 16) contains abundant anhydrite veins, as much as 1 cm in thickness, present in the rubble that makes up the core from the upper portion of the unit. These anhydrite veins in Unit 16 may be genetically related to Unit 15, which consists almost entirely of anhydrite vein material (see above). Unit 17 and the lower part of Unit 16 comprise hard, pervasively silicified vesicular volcanic rocks, which are cut by quartz-pyrite veinlets much less than 1 mm in width. These latter veins have 1-mm-wide anhydrite selvages, surrounded by well defined 2- to 5-mm quartz-rich alteration halos. Thin sections of rocks from Unit 17 show complete replacement of volcanic glass by very fine grained phyllosilicates and quartz, with patchy preservation of microlitic igneous plagioclase. Pyrite is present throughout the rock as fine-grained vesicle fill, overgrowing quartz and, on occasion, is overgrown by anhydrite. XRD analyses of Units 16 and 17 indicate that illite is the principal phyllosilicate phase, with subsidiary chlorite in Unit 17 (Table T8).

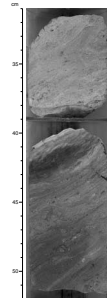
Laminated Unit (137–138 mbsf). Unit 18 is an intensely silicified, finely laminated gray-green rock (Fig. F51) that was initially thought to be a sedimentary rock. However, examination of two thin sections (Samples 193-1188A-16R-2, 12–15 cm, and 40–43 cm) reveals the unit to be a highly altered flow-banded volcanic flow. The rocks are heavily silicified, but retain aligned plagioclase microlites and scattered phenocrysts (Fig. F52). Former volcanic glass has been altered to very fine grained phyllosilicates (mostly chlorite by XRD analysis) and quartz. Pyrite is disseminated in the altered groundmass.

Middle Silicified Succession (138–165 mbsf). Units 19 to 21 exhibit pervasive silicification and patchy development of bleaching and chloritic (green) alteration. All three units are cut by fine quartz-(pyrite) veinlets. Minor (trace to 3%) very fine grained euhedral magnetite is present as patchy disseminations and on fracture surfaces in Unit 19 and in the upper part of Unit 20 (Table T2). Irregular, anastomosing to simple anhydrite-minor magnetite-trace pyrite veins, which have distinct bleached to siliceous alteration halos, are also present in Unit 18. These appear to be contiguous with the quartz-pyrite veinlets.

Two thin sections were made of rocks belonging to Unit 19 (Samples 193-1188A-17R-1, 90–93 cm, and 17R-2, 33–37 cm). Both samples are completely altered, and the igneous groundmass is replaced by quartz and very fine grained phyllosilicates (chlorite and illite, from XRD analysis) with patchy development of anhydrite. Subhedral magnetite (absent in overlying units), occurring both within anhydrite veins and in the groundmass of the rock, shows evidence of breakdown to “leucoxene” and is commonly replaced or overgrown by pyrite (Fig. F53). Although its presence in veins clearly indicates that magnetite is a product of hydrothermal deposition at Site 1188, within Unit 19 the mineral always shows evidence of breakdown and is, therefore, clearly not stable as alteration progresses. Ultimately, magnetite would be expected to break down fully. This is considered to be a possible factor contributing to the patchy distribution of magnetite throughout Hole 1188F, where magnetite is most abundant in apparently less pervasively altered rocks with remnant igneous plagioclase.

As noted above, the dominant silica polymorph present in Unit 21 is cristobalite (Table T8). This implies that metasomatism within this unit

F51. Unit 18 showing fine-scale flow lamination, p. 154.



F52. Weakly developed alignment of plagioclase microlites and a single phenocryst in a silicified laminated rock, p. 155.



F53. Anhedral former magnetite microphenocryst with remnant trellislike laths of magnetite faintly visible, p. 156.



(and the underlying Unit 22; see below) occurred at lower temperatures than those reached in the surrounding quartz-bearing lithologies. The interval probably represents a pocket of rock that avoided the passage of high-temperature fluids. As no thin section was cut from Unit 21, the textural and temporal relationships between cristobalite and quartz, which are also present in the unit (Table T8), are not known. However, it is possible that the cristobalite represents an earlier, lower temperature alteration event, which has been incompletely overprinted by quartz-dominated silicification.

Weakly Altered Volcanic Unit (165 mbsf). Unit 22 comprises fine-grained vesicular volcanic rocks that are weakly to moderately silicified and have plagioclase and magnetite microcrysts in the groundmass. Abundant silica- and anhydrite-filled microvesicles also contain traces of very fine grained euhedral pyrite. The unit is cut by rare irregular microcrystalline silica-anhydrite veins with silicified halos.

Petrography and XRD analysis of Unit 22 indicates that the main style of alteration is fine-grained cristobalite and clay (chlorite, from XRD analysis) replacement of the formerly glassy groundmass. Micro-litic and rare phenocrystic plagioclase is unaltered. Fine-grained disseminated magnetite shows evidence of incipient alteration to leucoxene. Cristobalite and later-stage anhydrite fill vesicles.

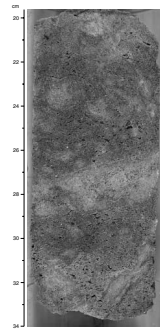
Lower Silicified Succession (165–185 mbsf). The lower silicified succession in Hole 1188A (Units 23 to 25) comprises green to black, blotchy units with remnant soft, green, clay-rich patches and intervals. The latter, interpreted to be remnant GSC alteration, are surrounded by dark-colored fine-grained quartz-(pyrite) flooding (Fig. F54), which is associated with an anastomosing network of hairline fractures. Vuggy cavities in the matrix are lined by very fine grained crystalline quartz. Very fine grained euhedral pyrite is noticeably more abundant in silicified zones, particularly in the vuggy cavities. Magnetite appears to be replaced by pyrite in the silicified zones, requiring that it predates the silica-pyrite flooding. Very rare, poorly defined quartz-anhydrite-(pyrite) veins also appear to be overprinted by the silicification. Vuggy anhydrite vesicle fill is present in Unit 24.

Thin sections from Units 23 and 25 reveal that the rocks are fine grained and heavily silicified (Fig. F55) with remnant partially altered plagioclase in the groundmass. Some samples show relict perlitic structures. Pyrite forms large subhedral crystals with inclusions of magnetite. Titanomagnetite microphenocrysts are altered to dark opaque patches with trellislike magnetite lamellae, some of which are overgrown by a lighter gray oxide (probably maghemite).

The lower silicified succession of Hole 1188A is the only interval encountered at Site 1188 where XRD analyses (Table T8) reveal corrensite as the dominant clay component. The occurrence of corrensite in this interval (165–185 mbsf) is interesting because it has been demonstrated that corrensite is indicative of a formation temperature of ~250°–270°C (Schiffman and Fridleifsson, 1991; Beaufort and Meunier, 1994; Lack-schewitz et al., 2000).

Unit 26 (193–202 mbsf). The final unit described in Hole 1188A (Unit 26; 192.70–202.29 mbsf) consists of vuggy massive sulfate-silica rubble with traces of disseminated pyrite and iron oxide spotting. It is considered likely that this unit, which most closely resembles Unit 15, is material that has fallen down the hole. It is therefore likely that an uncored vertical interval of ~30 m (192.70–218.0 mbsf) lies between the deepest in situ cores of Hole 1188A and the highest of Hole 1188F.

F54. Blotchy silicified rock with fine disseminated magnetite, p. 157.



F55. Typical photomicrograph of strongly silicified sample showing a fine-grained intergrowth of granular quartz and phyllosilicates, p. 158.



Silicification in Hole 1188F (218–375 mbsf)

The silicified units from Hole 1188F are divided on the basis of mineralogy into upper and lower sequences.

The upper sequence includes Units 27 through 45 (Cores 193-1188F-1Z to 19Z; 218–269 mbsf). It is characterized by the general absence of phyllosilicate phases other than illite in XRD spectra (Table T9) and by an almost complete absence of remnant igneous plagioclase. Two apparently spherulitic volcanic units (Units 31 and 40) show a distinctively different style of alteration to the other lithologies within the interval and are discussed separately.

The lower sequence extends from Unit 46 to Unit 72 at the bottom of the hole (Cores 193-1188F-22Z to 44Z; 282–375 mbsf). It is distinguished from the upper sequence by the widespread identification of phyllosilicate phases other than illite (most notably chlorite) in XRD spectra, the presence of remnant igneous plagioclase, and the sporadic occurrence of macroscopically visible magnetite below 320 mbsf. The magnetite-enriched lithologies are distinctive from the remainder of the lower sequence from Hole 1188 and are consequently discussed separately.

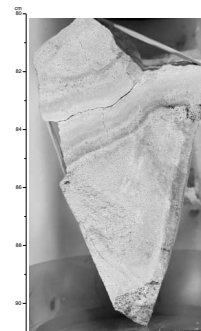
Upper Silicified Sequence (218–269 mbsf). Units 27 to 45 collectively comprise a sequence of dominantly pale to medium gray, sparsely vesicular, aphyric to weakly plagioclase-phyric volcanic rocks with occasional remnant spherulitic and flow-banded textures. Small (<1 mm) and, in some cases, large vesicles are typically filled with crystalline quartz ± pyrite, producing a distinctive spotted texture of small ovoid quartz amygdules in the more vesicular intervals. Some intervals are dark greenish gray, reflecting the presence of green chloritic clay.

The rocks of the upper sequence of Hole 1188F are cut by a network of anhydrite ± pyrite ± quartz veins, which have widths ranging from <0.1 to 10 mm, but are mostly between 1 and 3 mm wide. These veins usually exhibit cyclical alteration halos of dark and light bands, which are typically an order of magnitude wider than the associated vein (Fig. F56). Hard, dark bands contain more quartz, whereas the paler bands are softer and richer in clay. The vein network and its associated alteration appear to overprint the pervasive silicification, which is the dominant style of alteration in Units 27 to 45 (see below).

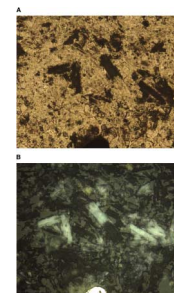
Thin-section petrography of samples from the upper sequence of Hole 1188F shows a consistent mineralogy dominated by quartz (4%–65%) and clays (25%–60%), with lesser anhydrite (<1%–17%) and pyrite (<1%–5%). Two principal clay species are present—illite and an apparently amorphous clay, which is brown when viewed in transmitted light and has a white, waxy appearance in reflected light, owing to internal reflections (Fig. F57). The distribution of this latter clay corresponds to the softer pale bands observed around anhydrite veins in hand specimen. Initial PIMA results indicate the presence of pyrophyllite, even in intervals where it could not be identified by XRD (e.g., in the upper sequence of Hole 1188F). It is considered likely that the amorphous-looking clay observed in thin section is pyrophyllite. Chlorite is also present in minor quantities in rocks with a greenish color.

The rocks of the upper sequence of Hole 1188F typically contain pseudomorphed igneous plagioclase microcrysts that are completely replaced by phyllosilicates. In weakly porphyritic intervals, palimpsest plagioclase phenocrysts are represented by fine-grained, often concentrically zoned intergrowths of illite, illite + possibly halloysite, or illite + pyrophyllite (Fig. F58). In two thin sections (Samples 193-1188F-13Z-1,

F56. Narrow anhydrite-pyrite vein with a typical cyclically banded alteration halo, p. 159.



F57. Plagioclase microlites variably replaced by colorless illite and dirty brown pyrophyllite with white internal reflections, p. 160.



F58. Plagioclase phenocryst completely replaced by fine-grained illite and possible halloysite, p. 161.



30–36 cm, and 14Z-1, 62–64 cm) remnant unaltered plagioclase was observed. Anhydrite mainly occurs as medium- to coarse-grained bladed crystals in narrow veins, which generally contain pyrite and may also contain subhedral quartz. The veins have distinct banded alteration halos, corresponding to quartz-rich and pyrophyllite-rich bands. Quartz is present throughout the rock as medium-grained crystalline aggregates filling amygdules, and as fine-grained granular groundmass intergrown with illite. Pyrite and anhydrite also are present as vesicle fill, both with and without quartz.

The gross textural relationships between minerals in rocks from the upper sequence of Hole 1188F suggest at least two stages of alteration. Early pervasive quartz-illite replacement of the primary volcanic mineralogy is overprinted by locally developed, banded quartz-pyrophyllite alteration associated with anhydrite-pyrite veining. Thin sections of core pieces that do not exhibit anhydrite veins and associated zoned alteration typically contain only subordinate pyrophyllite (Fig. F59).

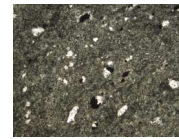
In an apparently volcanoclastic interval within Unit 27 (interval 193-1188F-1Z-2, 0–9 cm), 1-cm rounded clasts are composed of finely crystalline quartz and illite, with very little pyrophyllite and almost no pyrite. They contrast sharply with the volcanic matrix of the rock, which is very porous, contains 2%–3% plagioclase pseudomorphed by clay, and is predominantly composed of pyrophyllite and illite with very little quartz (Fig. F60). The “clasts” are, therefore, likely to be xenoliths of altered volcanic rock that were incorporated into a lava during eruption. Similar relationships are observed in surface rocks in the Snowcap hydrothermal site (Yeats et al., 2000), where altered xenoliths are hosted by fresh aphyric dacitic glass. In this case, the silica-illite altered fragments are hosted by a rock that has subsequently experienced pyrophyllite alteration.

The XRD analyses of Units 41 to 44 (Table T9) indicate the possible presence of brittle mica as a major clay phase. However, the mineral was not identified in thin section, and the samples that contain it were otherwise similar to the remainder of the upper sequence of Hole 1188F.

Spherulitic Units (234 and 242 mbsf). Units 31 and 40 are distinctly out of character with respect to the remainder of the upper sequence of Hole 1188F. Each of these intervals (193-1188F-6Z-1, 45–47 cm, and 13Z-1, 80–83 cm) is represented by single small, flat, rounded pebble-like pieces <5 cm in diameter. They are identical, so it is possible that they actually represent a single lithologic interval, one or both having fallen from higher in the hole, although neither was at the end of a core. The units have an apparent spherulitic texture with white spheroidal domains hosted in a dark green siliceous matrix.

In thin section, these rocks consist of altered, brown, isolated and coalesced subcircular domains of randomly oriented, partially devitrified volcanic glass and microlitic plagioclase, generally 0.1–1 mm in diameter, which rarely have central radiating crystal aggregates. Brown clay rims the margins and forms concentric rings in some of the domains, and many are overgrown by radiating cristobalite (Fig. F61). Although the texture is not entirely typical of spherulitic volcanic rocks, it is considered likely that it has a similar origin (see “**Igneous Petrology**,” p. 19). Similarly, the presence of volcanic glass, fresh plagioclase, and cristobalite (most likely produced by devitrification) indicates that these rocks are not strongly affected by the quartz-illite alteration that

F59. Quartz ± pyrite amygdules in a fine-grained quartz-illite groundmass, p. 162.



F60. An apparently clastic interval, p. 163.



F61. An apparently spherulitic unit, showing spherical domains in a cristobalite-clay matrix, p. 164.



is widespread elsewhere in the upper sequence of Hole 1188F. The only clay species detected by XRD analysis is chlorite.

Because Hole 1188F was cased to well below the depth of the cristobalite–quartz transition seen at ~100–110 mbsf in Hole 1188A, Units 31 and 40 must derive from an interval or intervals that escaped the otherwise pervasive quartz-illite–dominated alteration of the surrounding rocks.

Lower Silicified Sequence (282–375 mbsf). The lower sequence of Hole 1188F (Units 46 to 72; Cores 193-1188F-22Z to 44Z) immediately follows an interval from 272.9 to 282.1 mbsf of no recovery and is distinguished from the upper sequence by the common occurrence of phyllosilicates other than illite, the appearance of relict fresh plagioclase, and the sporadic occurrence of magnetite-enriched rocks. Rocks from Units 46 to 49 (interval 193-1188F-22Z-1, 0 cm, to 26Z-1, 26 cm) have <5% plagioclase in thin section, and XRD analysis only detected significant amounts of plagioclase in one of nine samples (Table T9). Minor amounts of chlorite, chlorite-smectite mixed-layer phases, and smectite were identified by XRD in this interval (Table T9).

From Units 50 to 72 (interval 193-1188F-26Z-1, 26 cm, to the end of Core 44Z), plagioclase was detected by XRD in 27 of 32 samples (Table T9), and thin-section observations suggest that up to one-third of the rock is composed of remnant fresh to slightly clay-altered igneous plagioclase. Even the most plagioclase-rich samples show complete alteration of the interstitial groundmass and incipient replacement of plagioclase by clay (Fig. F62). Fresh plagioclase is rarely identifiable in hand specimen. Consequently, Units 50 to 72 have commonly been described as completely altered in visual core descriptions (VCD) (Table T4). Thin-section examination reveals, however, that approximately half of these rocks are completely altered (>95% alteration), with the remainder being very highly to highly altered.

Illite continues as an alteration mineral in rocks of the lower sequence of Hole 1188F, as does brown clay, which, although not detected in XRD analyses, is identified as pyrophyllite, based on initial PIMA results and its optical properties. Illite abundance diminishes with increasing depth in Hole 1188F, whereas that of chlorite increases. PIMA results suggest that, overall, pyrophyllite is less abundant in rocks from the lower silicified sequence than in the upper silicified sequence and that it is restricted to rocks that have lower abundances of chlorite. Chlorite is distinguished in most XRD spectra from the lower sequence and is identified in thin section below a depth of 337 mbsf (Sample 193-1188F-34Z-1, 45–47 cm), although it is not always possible to optically distinguish chlorite from other phyllosilicates. Chlorite typically replaces groundmass and may also line or fill vugs. Where chlorite is clearly identified, it forms green, pleochroic mats with anomalous Berlin blue birefringence colors. As was observed in the upper sequence, pyrophyllite alteration is patchy or confined to banded vein halos, once again suggesting it postdates the early quartz-illite-chlorite alteration.

Similar to the upper sequence in the hole, rocks representing the lower sequence of Hole 1188F often have spotted textures, which can usually be attributed to amygdules filled with quartz ± pyrite, less common anhydrite and chlorite, and very rare magnetite. The vein mineralogy continues to be dominated by anhydrite-pyrite ± quartz, with rare quartz-clay veins. However, anhydrite-pyrite veins with centimeter-wide zoned halos—a distinct characteristic of many rocks from Units 27 to 45—are much less common in the lower sequence.

F62. Typical silicified unit from the lower sequence of Hole 1188F, p. 165.



Anhydrite is less abundant in the lower sequence of Hole 1188F than in Hole 1188A and the upper sequence of Hole 1188F. It is generally restricted to veins and late vesicle fill, and its abundance is estimated to be <2% in all thin sections representing the lower sequence. In contrast, more than half of the thin sections from the upper sequence are estimated to contain >3% anhydrite.

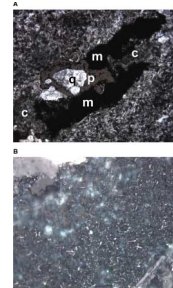
Magnetite-Enriched Lithologies (323–375 mbsf). Six magnetite-enriched units were encountered in Hole 1188F (intervals 193-1188F-31Z-1, 0–10 cm, in Unit 52; 34Z-1, 24–71 cm, in Unit 55; 37Z-1, 29–35 cm, in Unit 58; 39Z-1, 55–117 cm, in Unit 63; 40Z-1, 0–16 cm, in Unit 65; 41Z-1, 0–17 cm, in Unit 68; and 43Z-1, 56–114 cm, and Core 44Z in Unit 72). These units vary in thickness from 6 to 149 cm curated length and are often limited to single pieces intercalated with a sequence of more typical quartz-illite-chlorite altered rocks.

In hand specimen, magnetite appears to be finely disseminated and intergrown with clay and quartz, giving the rock a dark gray to black color. Magnetite also is present as vesicle fill (e.g., in Unit 65), where it is intergrown with clay and overgrown by pyrite filling the centers of amygdules (Fig. F63). In Unit 55, a slightly brecciated volcanic rock, magnetite contents are highest in the quartz-rich cement that hosts silicified angular clasts. Yet different modes of magnetite occurrence are revealed in Unit 58 (magnetite-rich halos around quartz-anhydrite-pyrite-rich domains) and Unit 72 (magnetite-rich halo along a diffuse pyrophyllite-quartz vein with a discontinuous anhydrite-pyrite core) (Fig. F64).

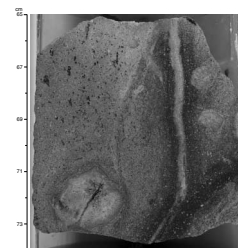
Although magnetite modes of up to 15% were estimated while preparing the VCDs, thin-section examination suggests there is <5% magnetite in the rocks. However, other oxides and spinels (hematite, maghemite, and hercynite) are in some places associated with magnetite. Thin sections of Units 55 and 58 (intervals 193-1188F-34Z-1, 45–47 cm, and 37Z-2, 31–33 cm, respectively) contain as much as 3% of a green to brown spinel, tentatively identified as hercynite (Fig. F65). This spinel is often rimmed by magnetite, and both phases are most abundant as inclusions in matrix quartz. Hematite is commonly found as inclusions in quartz (Fig. F66A), where it is associated with granular magnetite, but it may also form clusters of bladed crystals set in a mat of chlorite and a colorless, high-birefringence phase (Fig. F66B), which may be alunite or brucite (both phases were identified by XRD in the sample).

Relatively coarse (0.1–0.5 mm) opaque aggregates, with four- and six-sided shapes, were observed in polished thin sections of magnetite-enriched rocks. These aggregates represent the dark magnetic spots observed in hand-specimen samples and comprise fine (generally <10 mm) magnetite laths enclosed in a dark opaque matrix with rare pale internal reflections in reflected light. They are most abundant in domains that contain fresh igneous plagioclase. This and their shapes suggest they may be remnant altered igneous titanomagnetite. Subhedral pyrite overgrows and replaces some of the aggregates (Fig. F67). Similar magnetite-bearing aggregates were observed in the lower units of Hole 1188A, where they are also partly replaced by pyrite.

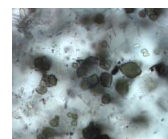
F63. Combined plane-polarized transmitted and reflected light photomicrographs of a “magnetite”-chlorite-quartz-pyrite filled vesicle, p. 166.



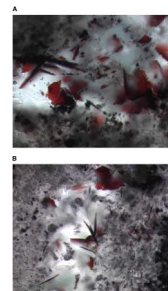
F64. Dark magnetite-bearing halo around a white quartz-clay-pyrite-(anhydrite) vein, p. 167.



F65. Fine-grained green spinel hosted in quartz, p. 168.



F66. Bladed hematite present as inclusions in quartz and as vesicle fill, p. 169.

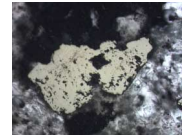


Summary of Spatial Variation of Alteration at Site 1188

The style and mineralogy of hydrothermal alteration at Site 1188 can be summarized as follows:

1. Fresh rhyodacite, with patchily developed silica-clay and iron oxide films, extends from 0 to 34 mbsf.
2. A pervasively silicified (opaline silica, with minor illite and smectite) perlitic volcanic unit (only 15 cm recovered) underlies the fresh rhyodacites and marks the upper limit of pervasive alteration at Site 1188.
3. A zone of massive bleached volcanic rocks (cristobalite-clay-anhydrite-pyrite alteration) underlies the opaline unit and extends to a depth of 49 mbsf.
4. A zone of intensely veined and fractured breccias and pseudo-breccias with veins of anhydrite-silica(cristobalite grading to quartz with increasing depth)-pyrite intercalated with more massive bleached units (cristobalite-illite-anhydrite alteration grading to quartz-illite-anhydrite alteration, with minor pyrophyllite and patchy chlorite throughout) extends from 49 to 99 mbsf. Bleaching and silicification overprint earlier GSC alteration, and quartz veining becomes more predominant toward the base of the interval.
5. A zone of hydrothermally brecciated, silica-veined, bleached units with intercalated coarse-grained volcanoclastic sediment extends from 106 to 126 mbsf. Silica veining and silica cementation of the sedimentary units postdates pervasive bleaching, but is cut by late anhydrite veins with bleached alteration halos. Cristobalite is the dominant silica polymorph at the top of the interval, but quartz dominates in the lower portion. Except for narrow anomalous units of partially altered volcanic rock, the deepest recorded occurrence of cristobalite in the hydrothermal system is within this interval, at ~116 mbsf.
6. Pervasive silicification is the dominant style of alteration in the remainder of Hole 1188A (126–185 mbsf, discounting the final two cores, interpreted to be fallen rubble) and throughout Hole 1188F (218–375 mbsf). Quartz is the most abundant alteration mineral, whereas anhydrite generally decreases in abundance with depth and is mostly confined to late veins. Disseminated and less abundant vein-related magnetite is present in units between 140 and 185 mbsf in Hole 1188A, and again below a depth of 322 mbsf in Hole 1188F. The XRD analyses (Tables T8, T9) indicate that, with the exceptions of a 20-m interval (165–185 mbsf) at the bottom of Hole 1188A, where corrensite is the only clay detected, and a 9-m interval (247–256 mbsf) of possible brittle mica within Hole 1188F, illite and chlorite (particularly in the lower part of Hole 1188F) are the dominant clay minerals associated with silicification at Site 1188. The style of hydrothermal alteration in Hole 1188F gradually changes from pervasive quartz-illite with late vein-related anhydrite-pyrophyllite to quartz-chlorite-illite-magnetite-dominated between 280 and 300 mbsf. Associated with this change is a general trend of decreasing extent of alteration from 100% to 65% going down the hole. Whereas igneous plagioclase is rarely preserved within silicified rocks in Hole 1188A or the upper portion of Hole 1188F, at

F67. Photomicrograph showing pyrite overgrowing a dark magnetite-bearing aggregate, p. 170.



depths >300 mbsf relatively calcic (An₅₁–An₆₃) plagioclase is commonly present as a remnant igneous phase. This apparent decrease in alteration intensity with depth may alternatively reflect increased stability of calcic plagioclase under the prevailing alteration conditions.

Discussion

The pervasive nature of hydrothermal alteration at Site 1188 indicates that the overall fluid fluxes below the Snowcap hydrothermal site must have been very high, implying prolonged periods of vigorous circulation of hydrothermal fluids. The spatial and temporal relationships between the different types of alteration encountered in the two successfully cored holes at Site 1188 allow a number of preliminary hypotheses to be advanced regarding the nature of the hydrothermal system at Snowcap.

In the upper portion of Hole 1188A (34–125 mbsf), pervasive GSC alteration is postdated by gray to white anhydrite-related silica-clay bleaching. Zones of pervasive bleaching and GSC alteration alternate, sometimes within single sections of core, and XRD results (Fig. F35; Table T8) indicate patchy distribution of different phyllosilicates (illite, smectite, and chlorite) and pyrophyllite. The transition from opaline silica (at 34 mbsf) to cristobalite to quartz (below 116 mbsf) also is developed in this zone. In the interval from 105 to 125 mbsf, locally developed quartz-pyrite veining and associated patchy silicification clearly overprint both these styles of alteration.

In the remainder of Hole 1188A (below 125 mbsf) and throughout the entire cored interval of Hole 1188F (218–375 mbsf), pervasive silicification is the dominant alteration type, showing a general trend from a quartz-illite to a quartz-illite-chlorite-dominated assemblage with increasing depth. The presence of domains of remnant GSC altered rocks (particularly between 150 and 185 mbsf in Hole 1188A) and microtextural observation of relatively coarse grained quartz overgrowing earlier pervasive clay alteration of igneous groundmass suggest that silicification developed as an overprint on an earlier GSC-like alteration assemblage. Similarly, sporadic magnetite-enriched lithologies show clear evidence that the iron oxides (magnetite, hematite, and/or maghemite) and, in two cases, spinel are overgrown by quartz.

Pervasive bleaching is not developed below a depth of 125 mbsf at Site 1188. However, an alteration style with a similar mineralogy to the bleached units in the uppermost 125 m is developed throughout the cored interval below this depth, as zoned pyrophyllite-quartz alteration halos along late anhydrite ± pyrite ± quartz veins, which crosscut all earlier alteration types. Similar veins are observed to cut quartz veins within bleached rocks between 105 and 125 mbsf, clearly indicating that although these veins appear to have carried similar fluids to those responsible for the pervasive bleaching in the upper portion of Hole 1188A, they represent a later phase of hydrothermal activity.

Significance of GSC Alteration and Silicification

Although individual samples may reveal textural evidence for pervasive silicification postdating earlier GSC alteration, both alteration styles are intimately related throughout the lowermost 250 m of crust intersected at Snowcap. It is usually very difficult to decide which secondary clay phase was associated with either of those alteration events.

For the sake of simplicity, we group these alteration styles together in the following discussion and separately consider the mineralogically similar, but temporally distinct, pervasive bleaching and anhydrite vein halo quartz-pyrophyllite alteration.

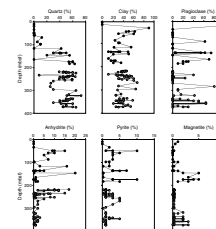
Above 125 mbsf, alteration is complex. Pervasive GSC alteration without an overprint is only represented in a few units. Below 125 mbsf, a quartz-illite-chlorite alteration assemblage is very common, sporadically accompanied by magnetite. In Hole 1188A, illite is the dominant phyllosilicate phase in GSC altered and silicified rocks to a depth of ~165 mbsf, after which corrensite and chlorite are more abundant and magnetite-bearing lithologies are more common. A similar transition is seen in Hole 1188F at a depth of 280 mbsf, below which the phyllosilicate mineralogy changes from illite to illite-chlorite to chlorite-illite. As in Hole 1188A, magnetite-rich alteration assemblages are restricted to the lowermost section of Hole 1188F. Also similar is the preferred preservation of igneous plagioclase in magnetite- and chlorite-rich units near the bottom of both holes (Fig. F35).

Magnetite, hematite, and spinel are most abundant as inclusions in quartz. Magnetite in these intervals often occurs as remnant inclusions in pyrite and as vesicle linings that have pyrite in their centers. From these observations, we infer that magnetite-bearing alteration occurred prior to the formation of late-stage quartz and pyrite. The magnetite impregnation appears to postdate an early pervasive stage of alteration, possibly equivalent to GSC alteration higher in the sequence. However, it was clearly followed by a later stage of quartz and pyrite formation, interpreted to be the main silicification event. It is interesting to note that the formation of Fe oxides did not result in significant Fe gains of the altered rock (see “**Geochemistry**,” p. 65). Conceivably, magnetite might substitute for pyrite (which is more abundant in vein halos at shallower depths) in the alteration assemblage as a consequence of variations in the $H_2S(aq)$ and $H_2(aq)$ activities of the altering fluids. The roughly antithetical relationship between pyrite and magnetite abundance in the rocks from Site 1188 (Fig. F68) is consistent with this assertion.

The transition from illite-rich to chlorite-rich rocks with increasing depth at Site 1188 is similar to a gradation from paragonitized to chloritized rocks that was documented for the basement underneath the TAG hydrothermal mound at the Mid-Atlantic Ridge (26°N) (Humphris et al., 1995). However, the appearance of chlorite/corrensite-rich and illite-poor rocks midway in the sequence as well as the sporadic developments of chlorite and illite in the upper part of Hole 1188A suggests that the basement alteration at Snowcap hydrothermal site may be more complex than underneath the TAG mound.

A general gradation upward from chlorite-rich to illite-rich rocks would be consistent with the generally accepted compositional evolution of hydrothermal fluids at mid-ocean ridges. Along the fluid flow path in a hydrothermal convection cell, it can be anticipated that Mg fixation in chlorite leads to a decrease in fluid pH, leading in turn to an increase in fluid K content, which may stabilize illite shallower in the system (Seyfried et al., 1999). The alteration mineralogy of the basement underneath Snowcap hydrothermal site does not reveal such a simple gradation in phyllosilicate mineralogy, which may suggest multiple episodes of fluid flow along dynamically changing fluid pathways. Alternatively, the low Fe and Mg contents of the dacitic volcanic sequence at the PACMANUS hydrothermal field, when compared to mid-

F68. Thin-section estimates of variation in abundance of significant minerals with depth for Holes 1188A and 1188F, p. 171.



ocean-ridge basalts, may explain the overall minor and intermittent occurrence of chlorite.

Significance of Bleaching

Pervasive and vein-related bleaching are developed throughout the altered volcanic sequence at Site 1188, showing a general decrease in intensity with increasing depth. Although sharing a similar mineralogical assemblage (quartz or cristobalite, anhydrite, illite, and pyrophyllite), the pervasive bleaching at depths <125 mbsf in Hole 1188A predates silicification and is clearly earlier than the vein-related bleached alteration halos, which are most strongly developed between 220 and 280 mbsf in Hole 1188F.

The large amount of anhydrite precipitated in bleached rocks at Snowcap hydrothermal site suggests that entrained seawater must play a major role in the evolution of the hydrothermal system. Anhydrite shows highly variable concentration downhole, particularly in the upper 250 m of the 375-m section drilled at Snowcap hydrothermal site (Fig. F68), suggesting that seawater flux within the volcanic sequence is fracture controlled and highly variable. The fact that pervasive bleaching is confined to the upper 125 m of the sequence and the generally low abundance of anhydrite below 280 mbsf (Fig. F68) indicates, unsurprisingly, that seawater circulation and mixing were more pronounced at shallow depths.

Complex crosscutting relationships between various sets of quartz-, anhydrite-, and pyrite-bearing veins (see “**Structural Geology**,” p. 58) imply episodic anhydrite-pyrite-quartz formation and consequently indicate repeated influx of different types of fluid. The width and complex banding of halos adjacent to many anhydrite-pyrite veins in Hole 1188F suggest that these veins could have been formed during repeated episodes of fluid flow with fluctuations in fluid chemistry and/or temperature.

Mixing of entrained seawater with hydrothermal fluids can be inferred from the widespread co-occurrence of anhydrite, quartz, and pyrite. These three phases will only co-precipitate in significant quantities if sulfate is supplied by seawater and if hydrothermal fluids supply Fe, SiO₂, and H₂S. The pyrophyllite present in bleached vein halos and in massive bleached units at Site 1188 requires low-pH fluids. This provides some support for the hypothesis that, despite the obvious importance of seawater, magmatic fluids may play a role in the hydrothermal system at Snowcap.

SULFIDE AND OXIDE PETROLOGY

Hole 1188A

Sulfide minerals, dominantly pyrite in a matrix of anhydrite, silica, and clay minerals, are present throughout Hole 1188A core. However, the modal percent sulfide rarely exceeds 5%, designated as the threshold for “sulfide rocks” for Leg 193 (see “**Sulfide and Oxide Petrology**,” p. 11, in the “Explanatory Notes” chapter for details). The threshold value was achieved in nine of the 23 cores recovered. Three principal sulfide modes of occurrence were identified in core from Hole 1188A: disseminated pyrite (Type 1 in Table T6, p. 66, in the “Explanatory Notes” chapter), anhydrite-silica veins with pyrite (Type 2), and silica-

anhydrite-magnetite-pyrite veins (Type 3). See “[Site 1188 Visual Core Descriptions](#),” p. 1, and “[Site 1188 Sulfide Log](#),” p. 303, for details.

Within the hydrothermally altered rocks in Section 7R-1 and below, pyrite is predominantly present at concentrations of <5% (Fig. F68) within two distinct settings: disseminated throughout the variably altered igneous protoliths (Type 1) and associated with anhydrite-silica filled fractures (Type 2). Pyrite also lines some vesicles with anhydrite ± silica (Type 2a). The greatest concentrations of macroscopically visible pyrite are within fractures (Type 2). Extremely fine grained pyrite, suspected in hand specimen and confirmed by XRD, is also present within dark GSC altered rocks.

Although pyrite is by far the most abundant sulfide in Hole 1188A, sphalerite and chalcopyrite also are present in trace amounts associated with pyrite. The sphalerite is found both in veins and vesicle linings in the uppermost part of the core (e.g., Sections 193-1188A-7R-1 [Piece 15]; 8R-2 [Piece 3]; and 9R-1 [Piece 5]). Trace amounts of chalcopyrite are found within a strongly chloritized portion of the core (Section 193-1188A-12R-1 [Pieces 9–14]).

Magnetite is present as a relict primary igneous phase (Ti magnetite) within the less altered volcanic rocks. Within the altered rocks, magnetite first appears as inclusions within pyrite and quartz, becoming evident as a discrete phase deeper within the hole where the modal percent magnetite in the altered rocks achieves 5% (Fig. F68).

Mineralization Styles

Disseminated Pyrite (Type 1)

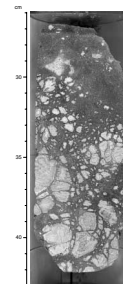
Traces of pyrite, typically <0.2 mm in size, are ubiquitous within pervasively altered rocks. Pyrite is present as disseminated euhedral to anhedral crystals and is commonly associated with very thin (<0.5 mm) Type 2 anhydrite ± quartz-pyrite veins. Extremely fine grained pyrite was encountered in the dark portions of altered rocks in Units 5, 7, 9, and 12 (e.g., Fig. F69). This pyrite, although not apparent in hand specimen, was initially identified by XRD and confirmed in thin section. From its peak height, it is estimated conservatively to constitute at least 5% of the mineral assemblage. A more accurate determination cannot be made, so all such samples are designated as containing >5% pyrite in the “[Site 1188 Sulfide Log](#),” p. 303.

Type 1 pyrite appears to be part of the alteration assemblage of anhydrite, silica, and clay minerals and is found in varying proportions, with two distinct modes. The greatest abundance of pyrite is observed within breccia stratigraphically just below fresh dacite and is associated with cristobalite and anhydrite. A second mode, found lower in the core, is principally associated with quartz and magnetite (Fig. F68).

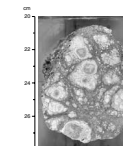
Anhydrite ± Silica-Pyrite Veins (Type 2)

Fine granular masses of pyrite are commonly found near the margins of anhydrite (±silica) veins in altered dacite (Fig. F70). The veins are typically 0.–1 mm wide but can be as much as 5 mm (Section 193-1188A-7R-2 [Piece 1]). The veins are found in the shallower sections of Hole 1188A between Sections 193-1188A-7R-2 and 16R-1. The veins have open space fill textures, with anhydrite, the main gangue mineral, showing fibrous growth at a high angle to the vein margins (Section 193-1188A-9R-1 [Piece 6B]). A particularly good example of veins with coarse-bladed anhydrite can be found in Section 193-1188A-15R-1 [Pieces 1 to 5], although these examples are devoid of pyrite. Two-phase

F69. Highly altered dacite fragments in a matrix of disseminated pyrite, p. 172.



F70. Anhydrite-quartz-pyrite veins in highly altered dacite, p. 173.



(liquid + vapor) fluid inclusions are abundant in this anhydrite (Fig. F36), and one example of a three-phase inclusion (liquid + vapor + an unidentified birefringent daughter mineral) was observed. Such barren anhydrite veins postdate the anhydrite-pyrite-silica veins (Fig. F71). Microscopic examples of Type 2 mineralization are shown in Figures F72 and F73.

Pyrite cubes, 0.1–0.35 mm in size, are present with anhydrite and silica within the vesicles of altered dacite (Type 2a). The finer-grained pyrite is found toward the margins of the vesicles within anhydrite. The coarser pyrite crystals are a druse of open space fill toward the center of the vesicles. Rare chalcopyrite crystals are also found as open space fill. Quartz crystals, showing good crystal terminations, are commonly observed near the center of the vesicles.

Silica-Anhydrite-Magnetite ± Pyrite Veins (Type 3)

Magnetite showing occasional octahedral habit and typically 0.2 mm in diameter is present in Core 193-1188A-17R (146.16–146.53 mbsf) within GSC altered and silicified volcanic rocks. The magnetite is contained within microveins, associated with bladed anhydrite crystals and variable modes of pyrite; the pyrite to magnetite ratio varies between 0 and 1. Deeper in the section (Section 193-1188A-21R-1 [Pieces 4 to 18]; 183.37–184.25 mbsf), fine network veins of quartz-pyrite-(anhydrite) produce pervasive silicification, which obliterates a magnetite-rich GSC altered volcanic rock. This pronounced increase in magnetite near the bottom of Hole 1188A is evident in the plot of magnetite against curated depth in Figure F68.

Parageneses

Some of the larger pyrite crystals within the deeper sections of Hole 1188A contain extremely small inclusions of magnetite (Fig. F74). The pyrite has clearly overgrown the magnetite and has not reacted with it, suggesting that the two phases were in equilibrium, unless there was a kinetic inhibition (low temperature) for reaction. Magnetite with the same distinctive vermicular texture as the inclusions is also present nearby in a quartz matrix (Fig. F75). Further evidence for the magnetite predating pyrite is seen in Figure F76. Within this thin section, in a region of tan-colored alteration, rhomb-shaped pyrite crystals appear to engulf magnetite. The magnetite inclusions in the pyrite are smaller toward the center of the rhomb, suggesting that pyrite is replacing magnetite. Elsewhere, however, in a less silicified part of this same thin section, there are remnants of magnetite-free pyrite. Also, in this same less altered region, there is an example of magnetite grains on the margin of and within pyrite, suggesting that, here, magnetite postdates pyrite. Taken together, it appears that at least some of the magnetite and pyrite were penecontemporaneous and a reaction such as $\text{Fe}_3\text{O}_4 + 3\text{S}_2 = 3\text{FeS}_2 + 2\text{O}_2$ may have proceeded in both directions at different times or places. Two gray minerals in this same thin section have a lamellar, latticelike texture reminiscent of magnetite-ilmenite exsolution (Fig. F77). However, from optical properties, the laths appear to be magnetite being replaced by maghemite or hematite.

Trace amounts of both black (Fe rich) and yellow (Fe poor; probably <1% Fe) subhedral sphalerite are locally developed as overgrowths on cavity-lining pyrite euhedra in vugs, and therefore are paragenetically later (Fig. F78). Thus, the paragenetic sequence observed for the opaque minerals in Hole 1188A is (early) magnetite → pyrite ± magnetite →

F71. Type 2 anhydrite-pyrite + cristobalite veins cut by a later anhydrite vein, p. 174.



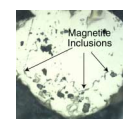
F72. Veins of anhydrite and pyrite together with disseminated pyrite in highly altered dacite, p. 175.



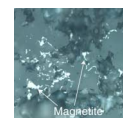
F73. Same view as Figure F72 in reflected light, p. 176.



F74. Subhedral pyrite containing vermicular inclusions of magnetite, p. 177.



F75. Vermicular magnetite in quartz, p. 178.



F76. Pyrite engulfing magnetite, p. 179.



sphalerite (late). The relative timing of deposition of the black and yellow sphalerite could not be determined. However, the apparent large differences in their iron contents, as indicated by their contrasting colors, indicate that they may have been precipitated at different times.

Hole 1188F

Pyrite is the dominant sulfide mineral within Hole 1188F. However, the modal percent sulfide never exceeds 5%; therefore, there are no new entries in the sulfide log (see the “[Site 1188 Sulfide Log](#),” p. 303). Instead, the information on sulfides and related minerals is recorded in the alteration log (see the “[Site 1188 Alteration Log](#),” p. 263). Macroscopic estimates of the abundance of pyrite range up to 4%, of which the vast majority (~88%) are $\leq 1\%$. The relatively elevated pyrite abundances (3% to 4%) are in Cores 193-1188F-8Z, 11G, 13Z, 17Z, and 34Z (see Fig. [F68](#)). The style of mineralization is similar to Hole 1188A. Pyrite is present as disseminated grains within altered volcanic groundmass (Type 1) (see Table [T6](#), p. 66, in the “Explanatory Notes” chapter), in thin veins with variable amounts of anhydrite and quartz (Type 2), and lining some vugs (former vesicles) together with clay minerals, anhydrite, and quartz (Type 2a). The veins are described in detail in “[Structural Geology](#),” p. 58.

Other opaque minerals identified macroscopically are marcasite, both yellow and black sphalerite (or wurtzite), magnetite, and hematite. Marcasite is present with anhydrite and quartz as platelike bronzy radiating crystals on fracture surfaces. The mineral was not encountered in polished thin sections. Magnetite is present in trace amounts throughout the hole, increasing in abundance below 300 mbsf (Fig. [F68](#)).

Pyrite

Pyrite is found in Type 1, 2, and 2a settings (see Table [T6](#), p. 66, in the “Explanatory Notes” chapter), as observed in Hole 1188A; however, the modal percent pyrite in Hole 1188F is generally lower than that observed in the hydrothermally altered sections of Hole 1188A. Much of the pyrite, especially in vugs (Type 2a), is euhedral (Fig. [F79](#)). Some crystals have a brassy tarnish, which was assumed to be incipient oxidation. This oxidation is particularly prevalent in Cores 193-1188F-14Z and 15Z.

In thin section, pyrite typically contains small anhedral inclusions of magnetite and quartz, with lesser pyrrhotite and rare chalcopyrite (Figs. [F80](#), [F81](#), [F82](#)). Pyrite may also contain inclusions of hematite, both as rare replacive intergrowths with magnetite (Figs. [F80](#), [F83](#)) and as platelets (Fig. [F84](#)).

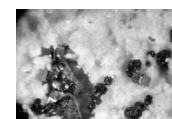
Chalcopyrite

Chalcopyrite is present in polished thin section as isolated anhedral grains and, in a few places, as partial replacements of pyrite (Fig. [F85](#)). Chalcopyrite is more obvious as a trace component within thin sections from Cores 193-1188F-6Z and below, where the mode of chalcopyrite peaked at 0.5% in Sample 193-1188F-37Z-2 (Piece 3, 31–33 cm). In this thin section, chalcopyrite is present as aggregates with pyrite and coarse quartz, and there is one example of chalcopyrite enclosed within pyrite. Elsewhere in this thin section, chalcopyrite was observed within the groundmass.

[F77](#). Lamellate magnetite partially replaced by maghemite or hematite in an altered groundmass, p. 180.



[F78](#). Subhedral Fe-rich sphalerite precipitated on euhedral pyrite in a cavity, p. 181.



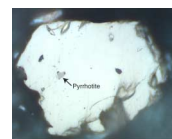
[F79](#). Vesicle filled with anhydrite, minor quartz, and pyrite, p. 182.



[F80](#). Abundant inclusions in pyrite, p. 183.



[F81](#). Pyrrhotite inclusion and smaller magnetite inclusions in pyrite, p. 184.



[F82](#). Inclusions of pyrrhotite and magnetite in pyrite, p. 185.



Pyrrhotite

Pyrrhotite was not observed in hand specimen but is a trace sulfide, typically as small, pink, anhedral to subhedral, 0.006- to 0.01-mm inclusions within pyrite grains. Pyrrhotite inclusions are observed alongside, but not intergrown with, inclusions of magnetite in the same pyrite grains (Fig. F82).

Magnetite

Present as only a trace component within much of Hole 1188F, magnetite achieves modes in excess of 3% in thin section with some hand specimen estimates as high as 10% at ~340 mbsf (Sample 193-1188F-36G-1 [Piece 3, 22–25 cm]). These magnetite-bearing samples have vugs filled with green clay, anhydrite, pyrite, and magnetite. Elsewhere, magnetite is present within veins of intergrown quartz, brown clay, and pyrite, with very rare extremely fine grained (0.005 mm) magnetite as inclusions in the quartz. These veins have a distinct dark halo, which comprises quartz and very fine granular magnetite (0.001- to 0.005-mm grains) with brown clay. This alteration type is discussed in “**Hydrothermal Alteration**,” p. 33, and “**Structural Geology**,” p. 58.

Detailed microscopic observations reveal a few examples of Ti magnetite-ilmenite exsolution (Fig. F86). This particular mineral assemblage with its characteristic texture is best represented in Sample 193-1188F-30Z-1 (Piece 2, 5–7 cm). Coarser ilmenite is intergrown with magnetite in Sample 193-1188F-37Z-2 (Piece 3, 31–33 cm) (Fig. F87). Magnetite also is present as remnants in leucoxene within the groundmass in many thin sections from Hole 1188F.

Hematite

Most of the hematite seen in thin section is present as ruby red platy inclusions in quartz (Fig. F88). It is particularly abundant (1%) in Sample 193-1188F-37Z-2 (Piece 3, 31–33 cm). In this same thin section, magnetite contains inclusions of hematite, and ilmenite is intergrown with magnetite (Fig. F87). Tiny euhedral platelets of red hematite were encountered in a vug in Sample 193-1188F-42Z-1 (Piece 5, 98–123 cm).

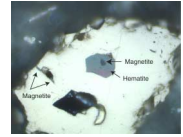
Spinel

A transparent to translucent spinel (Fig. F89) is enclosed within clear quartz in Samples 193-1188F-34Z-1 (Piece 9A, 45–47 cm) and 37Z-2 (Piece 3, 31–33 cm), respectively. The color of the mineral varies in plane-polarized transmitted light from bright apple green to a dark greenish brown. Crystals, many observed as perfectly formed and twinned octahedra with growth steps on their {111} face, are as large as 0.02 mm in size. The spinel contains tiny inclusions of what appears to be magnetite and is also rimmed by a thin film of magnetite and coarser grains of magnetite and ilmenite (Figs. F89, F90).

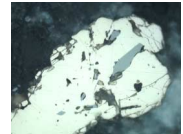
Parageneses

The dominant type of alteration within Hole 1188F is silicification (Sil), with a quartz-illite-dominated assemblage from 200 to 270 mbsf, grading into a quartz-chlorite-illite-dominated assemblage below 270 mbsf (see “**Hydrothermal Alteration**,” p. 33).

F83. Inclusion of hematite with a remnant of magnetite in pyrite, p. 186.



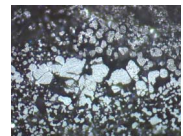
F84. Hematite inclusions in pyrite, p. 187.



F85. Chalcopyrite partially replacing pyrite, p. 188.



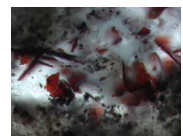
F86. Ti magnetite with ilmenite exsolution laths, p. 189.



F87. Ilmenite intergrown with magnetite surrounding spinel in a quartz matrix, p. 190.



F88. Hematite flakes in quartz, p. 191.



The parageneses of magnetite and hematite observed in samples from Hole 1188F are very complex. Magnetite (or Ti magnetite) is present both as a primary igneous phase and as a hydrothermal phase. Igneous magnetite is commonly enclosed by pyrite (Figs. F91, F92, F93), as was the case in Hole 1188A, and also as remnants in leucoxene. An excellent example of the presumed Ti magnetite precursor to the leucoxene-magnetite alteration assemblage was seen (Fig. F86). There are a few examples of igneous magnetite inclusions in pyrite that are partially replaced by hematite (Fig. F87). Elsewhere, magnetite in the groundmass contains inclusions of hematite (Fig. F90), but other magnetite grains are partially replaced by hematite. This magnetite, commonly enclosed within quartz, belongs to the hydrothermal mineralization suite that permeates some rocks.

Sample 193-1188F-26Z-1 (Piece 2, 20–23 cm) contains several examples of pyrite replacing an earlier quartz-magnetite assemblage. A first generation of quartz (quartz-1) forms euhedral crystals, some with a perfect hexagonal shape that are overgrown by magnetite (Fig. F94). Late quartz (quartz-2) overgrows this assemblage and encloses the magnetite (Figs. F94, F95). This quartz-2 has an irregular anhedral morphology. There are rare small inclusions of pyrite in quartz-2 in association with magnetite. The size and rarity of these pyrite inclusions creates problems in deciding if they represent an earlier generation of pyrite or if they are simply a consequence of a three-dimensional distribution within a larger pyrite crystal that surrounds this assemblage.

A late stage of pyrite formation overgrows and partially replaces this quartz-magnetite assemblage (Fig. F94). The pyrite contains small inclusions of magnetite crystals that have the same size and distribution as those within quartz-2. The cores of the pyrite crystals have inclusions of magnetite that are considerably smaller than those close to the edge, suggesting that there has been some replacement of magnetite as well as all of the quartz. The distribution of the magnetite inclusions in the pyrite, regardless of their size, serves to outline the shape of the original quartz-2-magnetite mass that was replaced (Fig. F95). Anhydrite that is present as thin veins with pyrite crosscuts quartz-1 (Fig. F94) and probably quartz-2.

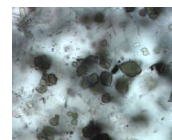
Site 1188 Summary and Paragenetic Sequence

A paragenetic diagram for Site 1188 is presented in Figure F96. Different sulfide and oxide mineral assemblages are associated with the primary igneous suite (Ti magnetite and ilmenite) as well as the superimposed predominant alteration assemblages of cristobalite-illite-pyrophyllite and quartz-chlorite-illite.

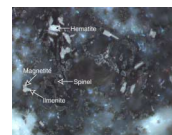
Pyrite

Pyrite is the dominant sulfide mineral at Site 1188. The first appearance of pyrite correlates with the uppermost appearance of hydrothermal alteration in dacitic volcanics in Hole 1188A. Within the hydrothermally altered rocks, Cores 193-1188A-5R and below, pyrite abundance is predominantly <5%, with four distinct settings (see Table T6, p. 66, in the “Explanatory Notes” chapter): disseminated throughout the variably altered igneous protoliths (Type 1); associated with anhydrite-silica-filled veins (Type 2); as vesicle linings associated with anhydrite ± silica (Type 2a); and in silica-anhydrite-magnetite veins (Type 3). The greatest concentrations of macroscopically visible pyrite are

F89. Spinel crystals hosted in quartz, p. 192.



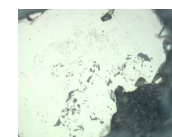
F90. Spinel, magnetite, ilmenite, and hematite, p. 193.



F91. Tiny magnetite inclusions in pyrite, p. 194.



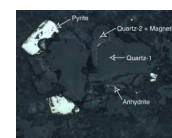
F92. Magnetite inclusions in pyrite having the same morphology as those in the neighboring quartz in the groundmass, p. 195.



F93. Pyrite enclosing magnetite in a silicified rock, p. 196.



F94. Euhedral quartz overgrown by a second quartz containing inclusions of magnetite in turn overgrown by pyrite, p. 197.



within fractures (Types 2 and 3). The downhole distribution of pyrite as observed in thin section (Fig. F68) is erratic with peaks of 5% to 10% at ~50, 140, 165, 255–270, and 345 mbsf.

Chalcopyrite

Chalcopyrite is observed at Site 1188, but only as a minor phase reported in hand specimen and thin section. Chalcopyrite first appears in trace amounts within a GSC altered portion of Hole 1188A (Section 193-1188A-12R-1), as small inclusions in quartz. Deeper within the hole, chalcopyrite is observed in thin section as isolated anhedral grains and, in a few places, as inclusions in (Fig. F80) and overgrowths on pyrite (Fig. F85). Chalcopyrite is more obvious as a trace component observed in thin section from Section 193-1188F-6Z-1 and below, where its mode peaked at 0.5% in Sample 193-2288F-37Z-2 (Piece 3, 31–33 cm; 346.12 mbsf). In this sample, chalcopyrite is observed as aggregates with pyrite and coarse quartz, with one example of chalcopyrite enclosed within pyrite. Elsewhere in this thin section, chalcopyrite is within the groundmass. Chalcopyrite is also present in vesicle fill.

Pyrrhotite

Pyrrhotite was not observed in hand specimen but is present in thin sections from Hole 1188F as a trace mineral. It is exclusively present as small (0.006 to 0.01 mm), pink, anhedral to equant subhedral inclusions within pyrite grains (Fig. F81). Pyrrhotite inclusions are found alongside but not intergrown with inclusions of magnetite in the same pyrite grains (Fig. F82). Pyrrhotite is first observed in Section 193-1188F-1Z-3 in lithologic Unit 28 at 221.9 mbsf (see “[Igneous Petrology](#),” p. 19) and is found in many of the deeper samples. It was not observed in Hole 1188A.

Sphalerite

Sphalerite is a rare mineral at Site 1188. It was observed only macroscopically in vesicles (Type 2a), in some cases perched on pyrite crystals that it clearly postdates. Fe-poor honey-yellow crystals are most common, but a black variety was also encountered, in one case in the same vesicle as the honey-yellow type. The mineral was not observed in thin section.

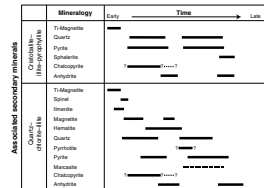
Magnetite

Ti magnetite is an accessory mineral and, in places, a liquidus phase of the relatively unaltered dacitic rock that caps the sequence of highly altered rocks. Hydrothermal magnetite, some with octahedral habit and typically 0.2 mm in diameter, first occurs in Core 193-1188A-17R (146.16–146.53 mbsf) within GSC altered and silicified volcanic rocks. The magnetite is observed within Type 3 veinlets, with hematite and hercynite, as described above, in vugs together with anhydrite, green clay, and pyrite and as inclusions within hydrothermal quartz. The downhole distribution of magnetite in thin section (Fig. F68) shows maxima at 150–165 mbsf in Hole 1188A and 355–375 mbsf in Hole 1188F.

F95. Euhedral quartz-1 overgrown by magnetite and quartz-2 overgrown by pyrite, p. 198.



F96. Paragenetic sequence, p. 199.



Paragenetic Sequence

The mineral parageneses outlined in Figure F96 consider the sulfide and oxide assemblages within the context of the two major alteration mineral assemblages recognized in Hole 1188A. The uppermost parts of Hole 1188A show cristobalite-illite-pyrophyllite-dominated alteration assemblages, crosscut by veins of predominantly anhydrite + quartz and pyrite. Pyrite is the most abundant opaque phase. Lower in Hole 1188A, as chlorite becomes a significant alteration phase along with illite and the degree of silicification increases, magnetite is present as a hydrothermal phase with modal abundances as high as 5%. Magnetite is commonly overgrown by hematite and pyrite but magnetite can, in turn, overgrow earlier formed pyrite. Similar parageneses are repeated within Hole 1188F, although hematite is commonly observed to have replaced magnetite throughout, and with pyrite that commonly contains inclusions of magnetite and pyrrhotite. As was observed in Hole 1188A, the onset of chlorite formation marks a zone of enriched magnetite values.

Observations throughout Hole 1188A suggest that there are at least two phases of pyrite-quartz precipitation, if not more. This view is consistent with the development of crosscutting vein generations observed in Hole 1188A (see “[Structural Geology](#),” p. 58) and with the observation that sulfide-oxide precipitation is predominantly a vein-controlled phenomenon. Whether or not the observed paragenetic sequence is a consequence of a single event or multiple events is open to question. Variable crosscutting vein relationships and variable mineral parageneses, especially between pyrite and magnetite, suggest that contrasting mineralization events may be coeval within the alteration sequence, depending on the nature of veining and fluid composition extant at the time of mineral precipitation.

STRUCTURAL GEOLOGY

Six attempts were made to spud holes in the Snowcap hydrothermal site, but core was recovered from only two holes (Holes 1188A and 1188F). Hole 1188A represents the shallow part of the hydrothermal system under the vent field, from 0 to 211.6 mbsf, whereas Hole 1188F represents the deeper part of the system, from 218.00 to 378.50 mbsf. The distance between the holes is only ~30 m.

The structures identified in these cores were primary volcanic layering, vein orientations, and vein relationships. We also recorded the mineralogy of the veins and, where present, the extent, intensity, and mineralogy of alteration halos around the veins. The observations were described on the structural description forms, and we entered the data in the structural log (see “[Site 1188 Structural Geology Descriptions](#),” p. 320 and “[Site 1188 Structural Log](#),” p. 305).

Hole 1188A

Orientation of Primary Layering

In the volcanic rocks, original layering was identified from the orientation of elongate flattened and stretched vesicles in some of the massive lavas and, in other parts of the core, from millimeter-scale flow banding. Individual flow bands may be defined by differences in the

abundance and size of the spherulites or microlites formed during crystallization or by differing degrees of vesicularity. This banding has commonly survived the extensive hydrothermal alteration.

Seven pieces of core contained evidence for folding (intervals 193-1188A-8R-1 [Piece 8, 65–74 cm], 12R-2 [Piece 4, 36–52 cm], 16R-1 [Piece 10, 69–79 cm], 16R-2 [Piece 3, 16–20 cm], 16R-2 [Piece 6, 31–39 cm], and 16R-2 [Piece 12, 86–94 cm]), which is defined by millimeter-scale flow banding (Fig. F97). Both upright folding and recumbent, probably intraformational folding, are evident. Boudinlike disruption of the original layering is clearly evident in interval 193-1188A-16R-1 (Piece 14, 95–102 cm) (Fig. F98). The folding and disruption of layering are most likely to have been caused by deformation during the flow of the lava, indicating a relatively viscous magma.

Twenty-five dip measurements of the volcanic layering were made on oriented pieces of core (see “Structural Geology,” p. 14, in the “Explanatory Notes” chapter). Throughout the core, the dips of the layering vary from horizontal to very steep (Fig. F99). These variations in dips could be caused by the intersection of several detached and rotated lava blocks and/or intersections of proximal to distal parts of lava flows with respect to the extrusion sites.

Vein Descriptions

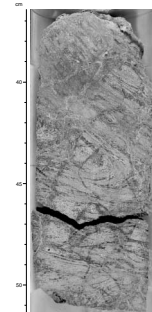
The veins in the core from Hole 1188A predominantly consist of varying proportions of anhydrite, silica minerals (cristobalite and quartz), clay minerals, pyrite, and magnetite (Fig. F100A). Chalcopyrite and sphalerite are present in trace amounts in some of the veins. According to their mineralogy and crosscutting relationships, the veins are broadly categorized as one of three types: (1) anhydrite ± pyrite veins, (2) anhydrite ± pyrite ± silica ± magnetite veins, and (3) anhydrite + silica + clay ± pyrite veins. The most common veins are those with anhydrite with or without pyrite, silica, or magnetite; these veins are present in most of the core. The anhydrite + silica + clay ± pyrite veins form a dense network, restricted to lithologic Units 10 and 11 in the curated interval at 97.38–107.39 mbsf (interval 193-1188A-12R-1, 78–91 cm, to 13R-1, 97–109 cm).

Anhydrite ± Pyrite ± Silica ± Magnetite Veins

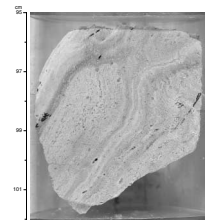
Anhydrite ± pyrite ± silica ± magnetite veins are present between Unit 4 (i.e., Section 193-1188A-7R-1, 31 cm; 48.51 mbsf) and the bottom of the core (Fig. F100A). The veins in the upper part of the core between Units 1 and 15 (i.e., above Section 193-1188A-15R-1; 125.71 mbsf) are dominated by anhydrite or cristobalite, whereas veins dominated by quartz are common in the interval between Units 15 and 25 (i.e., between Sections 193-1188A-15R-1 [126.51 mbsf] and 21R-1 [184.05 mbsf]). Magnetite is a minor to major component of the veins in lithologic Units 19–25 (i.e., between Sections 193-1188A-17R-1 [146.17 mbsf] and 21R-1 [184.05 mbsf]). These veins were plotted separately in Figure F100A, as silica-pyrite, pyrite, or magnetite-pyrite-silica-anhydrite veins.

The veins are present as single veins, branching veins, arrays of multiple veins, and as vein networks. The thickness of these veins ranges from <0.5 mm to >28 cm (see Fig. F100B). Their dips range from horizontal to vertical (Fig. F100C). The veins in volcanic rocks with well-preserved perlitic textures tend to follow the primary perlitic fracturing.

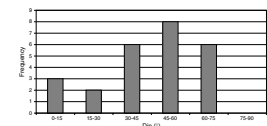
F97. Folded flow banding in pervasively altered volcanic rock, crosscut by silica-anhydrite-pyrite veins, p. 200.



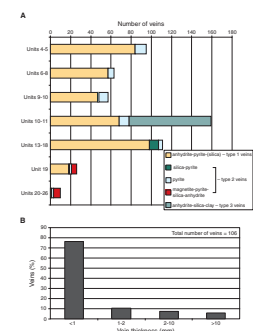
F98. Boudinlike disruption of flow lamination in pervasively altered volcanic rock, p. 201.



F99. Histogram of dips of volcanic layering, Hole 1188A, p. 202.



F100. Distribution of vein properties, p. 203.



Furthermore, in those rocks with primary flow banding, minor veins and veinlets tend to parallel individual bands, occasionally being interlinked by thicker crosscutting veins (Fig. F101A). Only one example of a vein showing multigenerational crack-seal opening was found. In this vein, two stages of anhydrite veining were recorded, both with cristobalite halos (Fig. F101B).

Most of the veins are surrounded by alteration halos of 1 mm to several centimeters thickness (Fig. F102). Soft, white halos of a clay mineral, tentatively identified as pyrophyllite, are typical around the veins in Unit 9 between 87.05 and 96.71 mbsf (i.e., Sections 193-1188A-11R-1, 15 cm, to 12R-1, 11 cm), and again around veins in Unit 11 (i.e., interval 193-1188A-13R-1, 59–138 cm [106.89–107.68 mbsf]) (Fig. F103). Silica halos are common around the veins in Units 4–8 (i.e., Sections 193-1188A-7R-1 to 9R-1) and in the deeper part of the core (i.e., from Section 193-1188A-14R-1 [116 mbsf]). In intervals of network veining, as in Unit 6 between 58.74 and 59.18 mbsf (i.e., interval 193-1188A-8R-1, 97–140 cm), silicification is pervasive around the cristobalite-pyrite bearing veins and affects the entire rock; nevertheless, the original texture of the volcanic rock is still recognizable (see Fig. F49). The rock was strongly fragmented during the stage of silica veining (Fig. F101C), which produced cristobalite in the open spaces between the rock fragments.

The anhydrite in the veins varies from very fine grained and milky-white sugary to coarse-grained with 1- to 2-mm colorless crystals. In some cases the anhydrite is present as fibrous crystals aligned perpendicular to the vein walls, suggesting growth in open fractures. Pyrite is present generally as euhedral cubes or pyritohedra of 0.1–0.5 mm size. Silica minerals are present mainly as fine-grained fibrous crystals of cristobalite or as anhedral, more coarse grains of quartz.

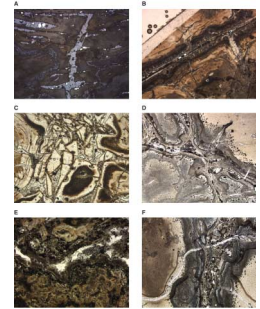
In most of the veins, as examined under the microscope, anhydrite is found in the center of the veins, whereas pyrite is in the bands along the rims of the veins. Silica (mainly cristobalite, according to XRD analysis) commonly forms selvages and alteration halos around the veins. Fine-grained pyrite defines the outermost part of these halos. Thus, pyrite is present both as coarse grains in the veins and as fine grains in the silica halos in the country rock around the veins (Fig. F101D). In thin sections from Unit 10 (i.e., Section 193-1188A-12R-1), there are highly irregular and anastomosing veins and veinlets of quartz with scattered grains of anhydrite and minor pyrite (Fig. F101E). These veins are rimmed by a brownish silica-clay halo, followed by a hematite-rutile rim with minor pyrite in the country rock farther out from the veins.

The magnetite-bearing veins in Unit 19 are found below 146 mbsf (Section 193-1188A-17R-1 and downward) and consist of coarse anhydrite (as thick as 1 mm) with scattered magnetite and pyrite. In the open vugs and the thicker veins, the anhydrite tends to be acicular, suggesting growth in a preexisting opening. Alteration halos of bleaching, which probably consist of quartz and clay minerals, extend from the veins for 5–20 mm.

Anhydrite ± Pyrite Veins

Late, thin (≤ 1 mm in thickness) anhydrite veins with or without trace pyrite cut the anhydrite ± pyrite ± silica ± magnetite veins that are surrounded by halos of alteration (Fig. F101F). These later anhydrite ± pyrite veins are characterized by having no alteration halos and the anhydrite tends to be coarse grained.

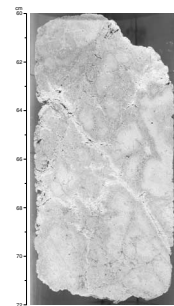
F101. Vein textures, Hole 1188A, p. 205.



F102. Anhydrite-pyrite vein with a wide halo of bleaching, p. 207.



F103. Diffuse silica-anhydrite-clay vein network and later anhydrite vein, p. 208.



Anhydrite + Silica + Clay ± Pyrite Veins

Veins of anhydrite + silica + clay are present between Unit 10 starting at 97.38 mbsf (i.e., interval 193-1188A-12R-1, 78–91 cm) and Unit 11 at 107.39 mbsf (i.e., interval 193-1188A-13R-1, 97–109 cm). The proportions of the constituent minerals vary from being predominantly anhydrite + clay minerals to predominantly silica + clay minerals. These veins form a dense network of veins <0.5–1 mm wide, overprinting earlier alteration assemblages of gray to greenish chlorite + clay minerals (Unit 10; Sections 193-1188A-12R-1 and 12R-2) (Fig. F102) and gray to white silica + anhydrite + clay (Unit 11; Section 193-1188A-13R-1) (Fig. F103). In these veins, the grain size is <0.1 mm. The network of veins is cut by anhydrite ± pyrite veins, which are especially common in Unit 11 (i.e., Section 193-1188A-13R-1) (Fig. F103).

Vein Geometries

Veins are common in Unit 4 from 48.51 mbsf (i.e., interval 193-1188A-7R-1, 31–42 cm) to the bottom of the core. The sections above Unit 4 are fresh to completely altered volcanic rocks characterized by moderate to pervasive alteration containing only very fine silica veinlets (see “Hydrothermal Alteration,” p. 33). The veins vary in thickness from hairline-thick veinlets (<0.1 mm thick) to veins thicker than 28 cm. Overall, 76% of the veins are 1 mm or less in thickness, whereas only ~6% of the veins are thicker than 1 cm (Fig. F100B). The thickest vein was found in Unit 15 and the upper part of Unit 16 (i.e., interval 193-1188A-15R-1, 0–28 cm [125.7–125.98 mbsf]), in the form of six smaller pieces of coarse anhydrite (0.1–0.5 mm grains) with minor pyrite.

The orientations of the veins, measured relative to the core axis in the oriented pieces, show that the dips of veins range from horizontal to vertical with a tendency for steeper dips in the lower part of the hole (Fig. F100C).

Vein Parageneses

The following vein parageneses are established, from oldest to youngest:

1. Anhydrite + silica + clay veins,
2. Anhydrite ± pyrite ± silica ± magnetite veins, and
3. Anhydrite ± pyrite veins.

The earliest veins formed as dense networks of anhydrite, silica, and clay minerals and postdate pervasive grayish green GSC alteration in the volcanic rocks (Figs. F102, F103). In places (despite this alteration) the original flow banding/lamination of the protolith has been preserved (Fig. F97). The network of anhydrite + silica + clay veins is cut by anhydrite + silica + pyrite veins and is overprinted by their coeval alteration halos (Figs. F102, F103). The anhydrite ± pyrite ± silica ± magnetite veins are characterized by having alteration halos of clay minerals or silica. These veins and their halos are cut by later anhydrite veins without halos.

Hole 1188F

The ADCB cores from Hole 1188F were highly fragmented, and only a few structural features could be measured. The measurements were too few to determine the general attitude of primary volcanic layering. In a few cases, structural measurements were made before the cores were split, because the high degree of core fragmentation made it impossible to preserve the structures after curation. This was especially the case for vein structures.

Primary Volcanic Structures

We observed very few primary volcanic structures in Hole 1188F. We noted alternating light gray to whitish bands in a few cases, probably representing flow banding. In other cases, we were able to define the primary layering from the orientation of flattened and stretched vesicles, typically filled by pyrite and/or anhydrite. Aligned laths of plagioclase also defined volcanic layering in some samples. The few data obtained (not plotted) (see the “[Site 1188 Structural Log](#),” p. 305) show dips ranging from subhorizontal to subvertical. As in Hole 1188A (see above), this variation can be explained by the intersection of different parts of flows, or the intersection of rotated and faulted lava blocks.

Vein Mineralogy

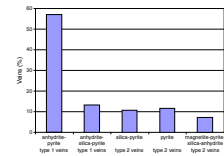
The veins in Hole 1188F consist predominantly of varying proportions of silica, anhydrite, pyrite, and magnetite (Fig. F104). About 57% of the veins are anhydrite-pyrite veins, and if the anhydrite-pyrite veins containing silica are included, this percentage rises above 70%. Approximately 11% of the veins are silica-pyrite veins, 12% are veins with only pyrite, and the remaining 7% of the veins contain magnetite with a variable content of pyrite, minor quartz, and/or anhydrite. With respect to mineralogy of the veins with depth in the hole, the amount of silica in the veins decreases downward in the hole until Unit 63, where it increases again and is present in the magnetite-bearing veins (Fig. F105). The shallowest magnetite-bearing vein is in Unit 52 (i.e., Section 193-1188F-31Z-1), and magnetite-bearing veins increase in abundance downhole. Possible marcasite was observed in a few pieces from Unit 38 (Section 193-1188F-11G-1), whereas euhedral crystals of light yellow to brown sphalerite were found associated with pyrite in veins of coarse anhydrite in Units 66 and 70 (i.e., Sections 40Z-1 and 42Z-1).

In many cases the anhydrite-pyrite veins are surrounded by silica-clay alteration halos, which, around the thicker veins (≥ 1 mm), are commonly cyclic and consist of alternating millimeter-thick layers colored different shades of gray (Fig. F106). Examination under the microscope showed that the differences between these layers are caused by variations in the proportions of clay minerals to very fine grained quartz (Fig. F107). The silica-pyrite, pyrite, and magnetite-bearing veins are usually <0.5 mm thick (hairline) and have either bleached halos of white clay minerals and minor silica or no halos.

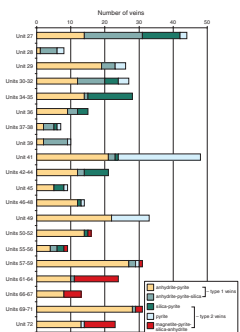
Vein Parageneses

The vein parageneses in Hole 1188F are very complex and result from several episodes of fluid infiltration. This is evidenced by the cyclic nature of the alteration halos around many of the veins and by the

F104. Distribution of veins according to mineralogy, Hole 1188F, p. 209.



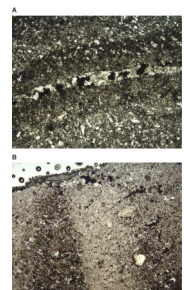
F105. Distribution of vein mineralogy vs. lithologic units, Hole 1188F, p. 210.



F106. Anhydrite-pyrite vein with a wide cyclic siliceous alteration halo, p. 211.



F107. Anhydrite-pyrite veins, Hole 1188F, p. 212.



various crosscutting relationships. However, in many cases the crosscutting veins have the same mineralogy and are surrounded by the same type of alteration halos, showing that the fluids forming the different veins had generally the same composition. This suggests that the fluids were flushed episodically through the rock during a longer period of continuing hydrothermal activity, rather than during one distinct event.

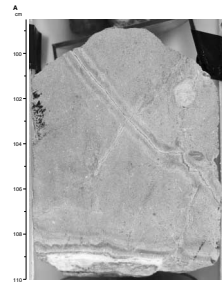
Interval 193-1188F-14Z-1 (Piece 6, 96–108 cm) in Unit 41 is a good example showing the dynamics of vein evolution in Hole 1188F (Fig. F108). The veins in this piece consist predominantly of anhydrite and pyrite. The two thicker veins, labeled Va and Vb, are surrounded by gray, 1- to 2-mm-thick, siliceous halos that grade outward into 1- to 2-mm-thick, light gray halos more rich in pyrophyllite. A thinner siliceous halo is present around vein Vc. In all veins except for the thickest vein (Va) and the thinnest veins (Vj–Vp), pyrite occupies the center of the veins and is rimmed by anhydrite. Vein Va has coarse anhydrite in the center of the vein, rimmed by thin veinlets of pyrite, followed by a thin rim of anhydrite. The thinnest veins are either pyrite veins (Vj–Vm) or veinlets of anhydrite (Vn–Vp).

Some of the thinner veins branch off from the thicker veins (e.g., Vi and Vm from Va, Vk and Vl from Vb, and Vg and Vj from Vc). Veins Vc and Vd are probably part of the same vein, crosscut by Vb. This is evinced by the anhydrite selvages of veins Vc and Vd, which are overprinted by the siliceous halo around Vb (Point A in Fig. F108B). Furthermore, the right-lateral offset between Vc and Vd matches the space of the extensional jog filled with pyrite of Vb (Point B in Fig. F108B). Finally, the anhydrite crystals are aligned east-west in the vein intersection at Point A, indicating an east-west extension. Careful examination shows that Ve cuts across the halos around both Va and Vb, indicating it to be later. Although these veins show crosscutting relationships, on the basis of their mineralogy and the nature of alteration halos, most of the veins in this specimen are considered to be part of the same main veining event, which is responsible for the formation of the abundant late anhydrite-pyrite veins that are characteristic of the cores from Hole 1188F.

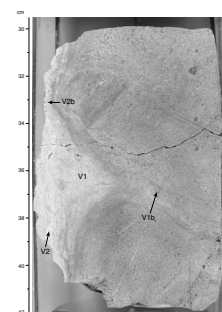
The coarse anhydrite in the center of vein Va crystallized in open space, and crystals in vugs within the vein are preferentially aligned vertically, indicating a vertical extension. The Vn, Vo, and Vp veinlets are offshoots from this anhydrite vein, and they cut the pyrite veinlets, the anhydrite layer rimming the central anhydrite, and also the surrounding alteration halos. This shows that the coarse anhydrite veining represents a late-stage event, opening up the preexisting vein Va, which had formed, as had the other veins in the piece, as a pyrite-anhydrite vein with pyrite in the center rimmed by anhydrite. Similar coarse anhydrite veins were encountered in several pieces downhole until Unit 50 (i.e., interval 193-1188F-26Z-1, 31–94 cm). Another good example of late-stage coarse anhydrite veining was observed in interval 193-1188F-25Z-1 (Piece 5, 30–42 cm) (Fig. F109).

Interval 193-1188F-23Z-1 (Piece 3, 14–24 cm) in Unit 48 shows a very good example of a multiple opening of veins (i.e., it contains unequivocal crack-seal veins) (Fig. F110). The two major veins in this piece, Va and Vb, both consist of coarse anhydrite crystallized in previous openings in the rock. They are both surrounded by 4- to 5-mm-thick selvages or halos consisting of alternating silica-clay and anhydrite layers, each layer being 1 mm or less in thickness. These layers are interpreted to represent several crack-seal events, each leading to a pair of silica-clay

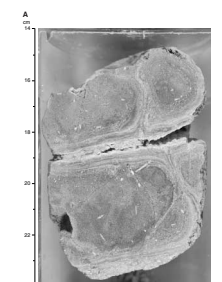
F108. Photograph and sketch of vein relationships in interval 193-1188F-14Z-1 (Piece 6, 98-110 cm), p. 213.



F109. Crosscutting anhydrite vein structures, p. 215.



F110. Close-up photograph and sketch of interval 193-1188F-23Z-1 (Piece 3, 14–24 cm), p. 216.



and anhydrite layers. The last event was the crystallization of the coarse anhydrite occupying the centers of the veins Va and Vb. Hairline veinlets of anhydrite ± pyrite (Vg, Vh, and Vi), rooted in Va and Vb, cut across the earlier couplets of anhydrite and silica-clay zoning. The vein Vc is a branch of Va, and veins Vf and probably Vd are branches of Vb. Both Vc and Vd are surrounded by cyclic selvages like those rimming Va and Vb, showing that these branches also have been opened several times. The vein Ve ends in the selvage around Va, but gets thicker away from Va, which suggests that it belongs to another vein system. Finally, the vein-forming events have led to extensive diffuse bleaching in the rocks beyond the immediate halos and selvages, which overprints pre-existing silicification. This is also evident in Unit 41 (i.e., interval 193-1188F-14Z-1 [Piece 3, 96–108 cm]) (Fig. F108).

Another example of crack-seal veining in Unit 42 was observed under the microscope in Sample 193-1188F-15Z-1, 55–58 cm (Fig. F111). Present in this sample is a 1-mm-thick quartz-pyrite vein, consisting of up to 1-mm-sized quartz grains and up to 0.5-mm-sized pyrite grains. The quartz grains show trails of numerous fine fluid and solid inclusions, both of which are subparallel to the vein margins. Some of these trails also cut across the boundaries between adjacent quartz grains. The vein is surrounded by a zoned alteration halo consisting of fine-grained quartz grading outward into a zone of brown clay minerals.

As mentioned above, magnetite is abundant in the veins from Unit 63 (i.e., Section 193-1188F-39Z-1) to Unit 72 at the end of the hole (Fig. F105). There is a piece of core in Unit 72 (i.e., interval 193-1188F-43Z-1, 56–101 cm) that contains a vertically dipping 23-cm-long and a 2- to 5-mm-thick vein consisting of anhydrite, pyrite, magnetite, quartz, and chlorite (Fig. F112). The center of the main vein (<1 mm) is occupied by quartz and clay. The iron minerals are surrounded by a thin selvage of pale chlorite. The whole assemblage is rimmed by a 2- to 4-mm quartz layer. The vein is surrounded by a magnetite-bearing siliceous halo that extends for ~10 mm out from the vein. However, a faint bleaching can be traced for another 20–30 mm out from the vein structure. Late anhydrite and pyrite-anhydrite veins cut across this vein structure at several places.

Vein Geometries

The veins in Hole 1188F are generally very thin, and >80% of the veins are <1 mm thick (Fig. F113A). Only 3.5% of the veins are thicker than 2 mm, and only one anhydrite vein is thicker than 1 cm (Unit 49; interval 193-1188F-25Z-1 [Piece 5, 30–42 cm]) (see Fig. F109). However, it is apparent from the banded halos that were noted on the ends of a large number of core pieces that many anhydrite veins of unknown thickness were not recovered by the drilling.

The orientations of the veins measured in the oriented pieces show that the dips span the range from subhorizontal to vertical (Fig. F113B). However, >42% of the veins have subvertical to vertical dips (75°–90°). There appears to be no systematic variation in dip with depth in the hole (Fig. F113C).

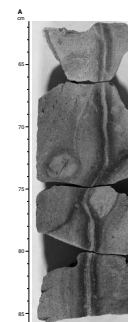
Summary

Holes 1188A and 1188F are only ~30 m apart and, therefore, together represent one vertical section of the hydrothermal system to a depth of 378.50 mbsf below the Snowcap hydrothermal site. There are several in-

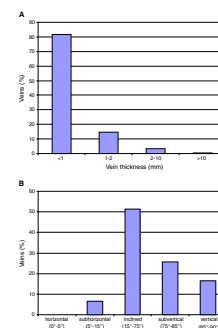
F111. Crack-seal quartz-pyrite vein, p. 218.



F112. Close-up photograph and sketch of interval 193-1188F-43Z-1 (Pieces 2–3C, 62–86 cm), p. 219.



F113. Summary of vein thicknesses and dips in Hole 1188F, p. 221.



interesting things to note with respect to vein features when comparing different parts of the hydrothermal system:

1. Cristobalite-bearing veins were only encountered in the upper part of the system, that is, above ~126 mbsf.
2. Anhydrite and pyrite are the most abundant minerals in the veins and are present from 48 mbsf in Hole 1188A to the bottom of Hole 1188F at 378.50 mbsf.
3. Magnetite-bearing veins are present at two depth intervals—between 146 and 184 mbsf in Hole 1188A and between 322 and 378.50 mbsf in Hole 1188F.
4. Crack-seal veins and alteration halos showing multiple zonations were only observed below 218 mbsf. Furthermore, the alteration halos around the veins tend to be more intense in Hole 1188F, compared to Hole 1188A.
5. Late anhydrite veins are more abundant in Hole 1188F than in Hole 1188A.
6. Brecciation and network veining are only found in Hole 1188A above 110 mbsf, and such structures were not observed in Hole 1188F.
7. There are no systematic trends with respect to dips of veins with depth.
8. More than 80% of the veins are thinner than 1 mm, whereas only 4% of the veins are thicker than 1 cm.

GEOCHEMISTRY

Methods

Inductively Coupled Plasma–Atomic Emission Spectroscopy

A subset of samples obtained from Hole 1188A were found to have 5–10 wt% total sulfur contents and were initially analyzed with the inductively coupled plasma–atomic emission spectroscopy (ICP-AES) using the Sulfur Method (see “**Geochemistry**,” p. 15, in the “Explanatory Notes” chapter). However, these samples proved mismatched to the standard reference materials for sulfides and were, therefore, reanalyzed using the method developed for igneous rocks with a dacite-rhyodacite composition (see “**Geochemistry**,” p. 15, in the “Explanatory Notes” chapter). Despite the high degree of alteration, there was, in general, a much better match of the samples with the matrix of the igneous rock standards. In most altered rocks from Hole 1188A, a major portion of the total measured sulfur is sulfate sulfur (dominantly anhydrite, with barite and possibly other minor sulfates). In addition, samples that were analyzed by ICP-AES were analyzed for their total water-soluble sulfate by a gravimetric method to better characterize the nature and abundance of the sulfates.

Ion Chromatography

A subset of samples from Hole 1188A was used to further examine the issue of sulfate dissolution (see “**Sulfate Analysis**,” p. 18, in “**Geochemistry**” in the “Explanatory Notes” chapter). The gravimetric dissolution experiments were repeated, without the addition of BaCl₂, on aliquots (0.5 g) from the cleaned and ground samples mixed with 25

mL of nanopure water. After 12 hr at 4°C, the samples were centrifuged, and the supernatant filtered through 0.45-µm Gelman polysulfone disposable filters. The extracted solutions were diluted with nanopure water to a volume of 50 mL and stored in acid-washed plastic vials for analysis. They were then analyzed using the shipboard ion chromatograph (Dionex, DX-120) to check the sulfate measurements obtained by gravimetric analysis. The waters were analyzed for Ca, Mg, K, and SO₄ following the procedures outlined by Gieskes et al. (1991) for dissolved solids. The International Association of Physical Sciences Organizations (IAPSO) standard seawater was used for calibrating the instrument. The reproducibility of these analyses, determined by repeated measurements of standards for Ca, Mg, K, and SO₄ were to within 3% to 5% on 1/200 diluted aliquots in nanopure water. It was found that the ion chromatography (IC) measurements for total dissolved cations were in good agreement with the gravimetric measurements for sulfate. However, the cation analysis of the solutions showed that other cations in addition to the Ca were also present and that not all dissolved sulfate is originally from pure anhydrite.

Following the analysis of the filtered supernatant liquid by IC, the same solutions were analyzed for Si, Mn, Al, and Na by ICP-AES. For these ICP-AES measurements, single element standards from Spex Certiprep were used. Both accuracy and precision are generally better than 1%–2% for these analyses.

Neutron Activation Analysis and Auxiliary ICP-AES

The abundance of pyrite and clay minerals in cores recovered from Hole 1188A, and the scarcity of base metal sulfides, raised the question of whether the subsurface PACMANUS hydrothermal system might be relatively enriched in gold. This analysis could not be run on board, but the opportunity arose to send samples ashore via helicopter on 25 November 2000. Samples were sent to the Commonwealth Science and Industry Research Organisation (CSIRO) Division of Exploration and Mining in Sydney, Australia, for analysis.

Three representative composite samples weighing ~150 g each were prepared. The samples from Hole 1188A were a combination of rock chips taken from bags of fine-grained “residue” that had been collected for certain cores and of an approximately equal quantity of randomly picked small fragments from the trays of cores where no residue had been retained. Because the purpose was to test the possibility of an auriferous character, these were considered to adequately represent average material, though small for typical bulk assay work. The samples covered the following intervals:

1. Cores 193-1188A-7R to 11R (48.2–96.6 mbsf);
2. Cores 193-1188A-12R to 17R (96.6–154.7 mbsf); and
3. Cores 193-1188A-18R to 23R (154.7–211.6 mbsf).

At CSIRO Exploration and Mining in Sydney, the samples were dried, ground to nominal 200 mesh in a tungsten carbide ring mill, and thoroughly homogenized. Subsamples weighing 10 g were irradiated at the Lucas Heights Nuclear Reactor (Australian Nuclear Science and Technology Organization), and the neutron activation spectra were collected for 7 days and analyzed using routine methods by Becquerel Laboratories Pty Ltd at Lucas Heights.

Separate 0.1-g subsample splits of the grab samples were retained at CSIRO Exploration and Mining in Sydney, where they were analyzed by ICP-AES. The samples were dissolved in an HF-HClO₄-HNO₃ acid mixture, evaporated to dryness, and redissolved in an HNO₃ solution for analysis by ICP-AES using a Spectro Analytical Instruments SpectroFlame instrument. The procedure normally retains all the sulfur present in the solution for whole-rock samples. Intensities were corrected for spectral interferences and referenced to synthetic calibration standards. Instrument performance was monitored with a range of standard reference soils.

Water-Sampling Temperature Probe

Surface water samples were collected off the railing of the ship by bucket grab for seawater chemistry. Two samples were collected over the drill sites. Owing to the close proximity of the drill sites, and the position of the *JOIDES Resolution* over the drill sites, the three samples were thought to represent the surface water chemistry over the drill site. These samples of surface water were used as a comparison for the samples collected by the WSTP. The sampling probe was filled with deionized water for the trip down the drill string to the sampling level. The valves were timed to open and release the deionized water to be replaced by the borehole fluids at the desired depth. After equilibration time the valves were then closed for the trip back up the drill string. Analysis of salinity, pH, and alkalinity were conducted as soon as the samples were brought to the laboratory; IC and ICP-AES measurements for anions and cations were then completed on acidified samples with a nitric acid spike.

Results

The results of the shipboard ICP-AES, NCS, IC, and gravimetric analysis of representative rock samples from Hole 1188A are given in Tables **T11**, **T12**, and **T13** with the samples listed by assigned lithologic units (see “**Igneous Petrology**,” p. 19) and in order of increasing depth. They are reported in Table **T11** ordered with respect to major element oxides expressed as weight percent. The values for total sulfur and water (by NCS) are reported in weight percent and follow the whole-rock compositions. The volatile free concentration data were recalculated to account for the abundance of H₂O, S, and SO₃ and are reported in the lower half of Table **T11**. The data for the NCS analysis of the unignited (pre-loss on ignition [LOI]) water and sulfur contents and the ignited (post-LOI) sulfur content are found in Table **T12**. The results for the four supernatant analyses by IC and ICP-AES methods are given in Table **T13**. Tables containing the data from the midcruise shore-based neutron activation analysis (NAA) and ICP-AES for the bulk samples are found in Tables **T14** and **T15**, respectively, and are presented with relevant detection limits.

Tables **T16** and **T17** present the rock data from Hole 1188F. As with the data from Hole 1188A, the samples are listed by assigned units and in order of increasing depth. They are reported in Table **T16** ordered with respect to major element oxides expressed as weight percent. The values for total sulfur and water (by NCS) are reported in weight percent and follow the whole-rock compositions at the bottom of the table. In Table **T17**, the comparison between sulfur pre- and post-LOI is presented. It was found that a modification to the LOI procedure was re-

T11. Major element oxides with selected trace elements, Hole 1188A, p. 284.

T12. Total sulfur and water measurements, Hole 1188A, p. 286.

T13. Analyses of the cations present in the supernatant and water-soluble sulfate measurements by IC and ICP-AES, Hole 1188A, p. 287.

T14. NAA analyses of the bulk samples from Hole 1188A sent to CSIRO for midcruise shore-based analyses, p. 288.

T15. ICP-AES analyses of the bulk samples from Hole 1188A sent to CSIRO for midcruise shore-based analyses, p. 289.

T16. Major element oxides with selected trace elements by ICP-AES, Hole 1188F, p. 290.

T17. Water chemistry data for WSTP sampling, Holes 1188B and 1188F, p. 292.

quired to remove the majority of the sulfur in the samples. Roasting time at 1050°C was increased from 1 to 4 hr. This increased roasting time significantly improved the efficiency of sulfur removal in the samples from Hole 1188F.

Table T18 contains the data of the water samples collected from the boreholes using the WSTP tool. A single sample was taken from Hole 1188B, and two samples were taken at different times from Hole 1188F. Temperatures recorded by the WSTP for the collected fluids range from 3° to 21°C.

Data Handling

The raw ICP-AES intensity for each element of the standard reference rocks used (see “Geochemistry,” p. 15, in the “Explanatory Notes” chapter and Murray et al., 2000) were drift and blank corrected and were then used to calculate concentrations for the ignited samples tabulated in the top half of Table T11. For all subsequent discussions, figures, and plots, the major element oxide and trace element concentrations were recalculated to the original rock composition by multiplying the ignited oxide value by 100 + LOI% then dividing by 100. Note that LOI represents the volatile content in the powdered and dried samples and consists mainly of H₂O⁺ and sulfur compounds. Trace amounts of CO₂ and other minor volatile components may also be present but are considered negligible.

Late during the Leg 193 cruise, results from a sulfate sulfur doping experiment of samples of fresh dacite and standard reference materials suggested that sulfate contents >1 wt% S affect the ICP-AES analyses, leading to an underestimation of the oxide percentages of Si, Al, Fe, Ca, and Na. Therefore, the results of the ICP-AES analyses in samples that have a reported total sulfur content >1 wt% should be considered only as approximate concentrations (see “Geochemistry,” p. 15, in the “Explanatory Notes” chapter for discussion of instrument precision and accuracy).

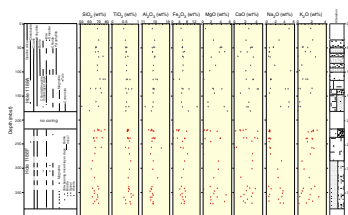
For the midcruise shore-based analyses, the NAA intensities were corrected for spectral interferences and referenced to synthetic calibration standards. The precision of the ICP-AES for a majority of the elements (i.e., K, Na, and Cr) duplicated from the NAA analysis is higher than that of NAA. Performance was monitored with a range of standard reference soils.

Hole 1188A

The variations of selected major oxide and trace element compositions are plotted against depth and are compared with the bulk mineralogy as determined by XRD in Figure F114. The observed chemical variation is generally consistent with the bulk mineralogy, including any primary minerals retained in the rock (i.e., plagioclase), as well as the alteration minerals (i.e., chlorite and illite) described in the “Site 1188 Alteration Log,” p. 263. For example, increases and decreases of MgO coincide with the appearance and disappearance of chlorite downhole, the increases of total Fe (as Fe₂O₃) correlate with the occurrences of magnetite and/or pyrite, and Na₂O is elevated in intervals containing plagioclase. The majority (14 out of 20) of the rocks sampled from Hole 1188A contain >1% total sulfur after ignition; SiO₂, Al₂O₃, FeO, CaO, and Na₂O data cited for these rocks are therefore preliminary.

T18. Major element oxides with selected trace elements, Hole 1188F, p. 293.

F114. Downhole chemical variations of selected major element oxides and trace elements, Holes 1188A and 1188F, p. 223.



Igneous Geochemistry

Only one sample analyzed from Hole 1188A represents a fresh volcanic rock (Unit 1; Sample 193-1188A-2R-1, 9–12 cm). This rock can be classified as transitional between dacite and rhyolite (i.e., rhyodacite) using the total alkalis vs. silica (TAS), or as dacite using the International Union of Geological Sciences (CIPW norm) classification. A full chemical review for this unit was deemed inappropriate based on a single sample.

Alteration Geochemistry

Three major alteration types have been identified from the cores recovered from Hole 1188A: (1) green silica-clay, (2) bleached (Bl), and (3) silicified. For more detailed descriptions of these alteration types, see “[Hydrothermal Alteration](#),” p. 33. In Table [T11](#) the alteration types assigned to each sample are noted. In Figure [F114A](#) the variation in XRD mineralogy with depth is compared with the geochemical profiles for key major elements. In general, the changes in MgO and total Fe (plotted as Fe_2O_3) correspond to the formation of chlorite, clay minerals, magnetite, and pyrite. In general, the abundance of Na, Mg, and K in the altered rocks correspond broadly with the presence of plagioclase, chlorite, and illite, respectively.

The bleached rocks show a decrease in their CaO, Na_2O , K_2O , and MgO contents relative to the fresh rock and to the GSC altered and silicified rocks. Although macroscopic and microscopic observations indicate an increase in quartz content (e.g., vesicle fill), the silicified rocks do not show elevated SiO_2 contents when compared to the fresh dacite. This apparent contradiction can be attributed to the multiple phases of alteration identified. Silica may have been lost by early GSC alteration (clay forming) and regained by later silicification. If the magnitude of the silica fluxes are similar, then no apparent net change would be observed. Based on the preliminary nature of the shipboard major element data, which is a result of high S contents, this hypothesis could not be fully tested.

Sulfate Concentrations

Comparison of total sulfur (TS) in the unignited samples to that of the ignited samples showed that traditional ignition to 1050°C does not fully remove all sulfur components (i.e., 1.09 wt% TS in ignited Sample 193-1188-14R-1, 105–108 cm [117.05 mbsf] compared to 2.98 wt% TS in the unignited [pre-LOI] sample). However, the proportion of sulfur retained during ignition varies from sample to sample, possibly indicating variable proportions of sulfur-bearing compounds that do not break down during the standard ignition procedure. A significant portion of the total sulfur found in the samples analyzed from Hole 1188A consists of soluble-sulfate sulfur, and its concentration is variable with alteration type. The values obtained for the total sulfur and calculated for the water-soluble sulfate phase are found at the bottom of Table [T11](#). Gravimetric measurements were used to determine the water-soluble sulfate concentrations. However, in many samples, there is an apparent deficiency in Ca as measured to account for all of the sulfate as anhydrite. Replicate samples measured by gravimetric analysis yielded reproducible results. Owing to this apparent disparity, the second aliquot of the liquid from soaking the powdered rock (the supernatant) was ana-

lyzed by ICP-AES and IC for Ca, Na, Si, Al, and Mn. The results are also presented in Table T13. Although the total cation concentrations are not large enough to account for all the sulfate found in the dissolution experiments, they indicate that in the supernatant solution there is a mixture of other sulfate-complexing cations, besides Ca. However, these ions do not seem to play a part in the gravimetric measurements, as the XRD spectra of the precipitate only show barite peaks.

Based on soluble-sulfate concentrations, the data suggest that many of the altered rock samples in Hole 1188A contain from 5% to 15% anhydrite. The mass of the powdered rock residues dried after soaking in comparison to their original masses indicates between 10% and 20% loss, which is in general agreement with the observed range of sulfate concentrations found in the supernatant. In contrast, no significant sulfate dissolution could be detected after soaking minicores in seawater (see “Physical Properties,” p. 21, in the “Explanatory Notes” chapter).

The sulfate-sulfur doping experiment quantified the amount of total sulfur necessary to push the error for the ICP-AES analyses outside the $\pm 2\%$ error range at 1 wt% total sulfur (pre-LOI). The presence of the sulfate was directly influencing the ICP-AES measurements by either suppressing the ionization or by forming colloids or precipitates in the solution, which were not properly transferred into an aerosol by the ICP nebulizer. Alternatively, the high S contents may cause an unusual matrix mismatch between samples and standards. In either case, the high sulfate sulfur remaining in the sample post-LOI means that measured concentrations of some of the major oxides (SiO_2 , Al_2O_3 , Na_2O , CaO , and Fe_2O_3) are markedly underestimated.

The midcruise shore-based NAA and ICP-AES analyses of samples from Hole 1188A established that the subsurface PACMANUS hydrothermal system is not enriched in gold or elements commonly associated with gold. The three NAA samples from Hole 1188A contain from 3 to 9 ppb gold (Tables T14, T15), covering the same range shown by fresh dacites and rhyodacites from Pual Ridge (Moss et al., 2001). Zinc and copper contents are low in all samples in Hole 1188A. Barium levels reported by the midcruise shore-based analyses are comparable to those obtained shipboard for Hole 1188A. In the upper 100 m of Hole 1188A, some of the Ba is associated with barite (as noted in the XRD traces). Below 100 m, the majority of the Ba is associated with silicates. This is also observed in the comparability between NAA and ICP-AES data, which imply again that the Ba is contained in silicates rather than barite. Geochemical indicator elements for an epithermal or acid sulfate style of mineralization, especially Sb and As, are exceptionally low. These data, and the low precious metal and base metal contents of the cored samples, constitute a marked contrast from the massive sulfide chimneys of the PACMANUS hydrothermal field (Parr et al., 1996).

Hole 1188B

Borehole Fluids

A single sample of fluid from Hole 1188B was taken from 3 mbsf. The data are presented below along with the fluid sample data for Hole 1188F.

Hole 1188F

The variations of selected major oxide and trace element compositions are plotted against depth and are compared with the bulk mineralogy as determined by XRD in the lower half of Figure F114B. The observed chemical variation is generally consistent with the bulk mineralogy and the alteration log, as observed in Hole 1188A. Examples of this agreement include the increases and decreases of MgO with the appearance and disappearance of chlorite, subtle increases of total Fe with increased contents of magnetite and/or pyrite, and the elevated Na₂O concentrations in intervals containing fresh plagioclase. The H₂O⁺ and TS data are presented in Table T17 and illustrate the effectiveness of the longer roasting time for removal of sulfur.

Igneous Geochemistry

Fresh volcanic rock was not encountered in Hole 1188F. The Zr/TiO₂ ratios of the altered rocks (where Zr is in parts per million and TiO₂ in weight percent) show moderate variability around 250, whereas the fresh sample from the top of Hole 1188A gives a ratio of 300 and may suggest two different parent materials, both dacitic.

Alteration Geochemistry

Two major alteration types have been identified from the cores recovered from Hole 1188F: GSC alteration and silicification. For more detailed descriptions of these alteration styles, see “Hydrothermal Alteration,” p. 33. In Table T16, the alteration types assigned to each sample are noted. The variation in XRD mineralogy with depth is compared with the geochemical profiles for key major elements. Similar to the relationship between chemical and mineralogical compositions in Hole 1188A, Na₂O, MgO, and Fe₂O₃ are low and K₂O is high where alteration is complete and illite is the dominant phyllosilicate, whereas these trends are reversed where fresh plagioclase is preserved and chlorite is abundant.

Borehole Fluids

The salinity of the surface water at Site 1188 has a value typical of that expected for Equatorial Pacific waters (35 g/kg) (Sverdrup et al., 1942). The temperature remained constant at 30°C, with a pH of 8.4. The composition of fluids collected from both boreholes is dominated by bottom seawater. The salinity of the Hole 1188B sample, at 31 g/kg, seems anomalously low. This may be caused by a dilution of the fluid by deionized water used to fill the WSTP collection coil for transfer from the rig deck to the borehole. However, the Mn is anomalously high. Concentrations of major dissolved ions in the borehole water from the WSTP from within Hole 1188F are also presented in Table T18.

MICROBIOLOGY

Samples were collected prior to curation from Holes 1188A and 1188F for shipboard studies (direct microscopic enumeration and micromorphological descriptions, ATP analysis for biomass activities, and enrichment cultures). Corresponding samples will be used for shore-

based studies (aerobic and anaerobic cultivation, biochemical and molecular typing, microscopic determination of the role of microorganisms in mineralization and alteration, and potential bioactive molecules search).

Total Bacterial Enumeration

Following the methods described in “Microbiology,” p. 19, in the “Explanatory Notes” chapter, samples were stained with 4,6-diaminodino-2-phenylindole (DAPI), and the results of direct bacterial counts are shown in Table T19. The DAPI dye binds with DNA; hence, these bacterial counts represent both the dead (provided that the DNA is intact) and the living microbial population. The uppermost core enumerated (Sample 193-1188A-5R-1, 17–21 cm; 33.7 mbsf) contains 1.5×10^7 cells/cm³, and the bacterial population decreased to 5.8×10^5 cells/cm³ in the next lower sample (Sample 193-1188A-7R-1, 55–58 cm; 48.75 mbsf). No bacteria were detected by this method in cores from deeper in Hole 1188A nor from any of the samples from Hole 1188F (Table T19). The detection limit of the direct count procedure is $\sim 1 \times 10^5$ cells/cm³, and it is possible that a more sparse bacterial population than this exists below this detection limit. A major drawback of this direct count procedure is the difficulty in distinguishing bacterial cells from mineral particles that fluoresce.

The lack of microbial habitation observed with increasing depths is most likely caused by temperature limitations. Although the temperature in Hole 1188A was not measured, it is plausible that a progressive increase in temperature occurs with increasing depth in this hydrothermal system. The temperature measurements immediately after drilling, at various depth intervals in Hole 1188F, range from $\sim 80^\circ\text{--}100^\circ\text{C}$ (see “Downhole Measurements,” p. 86). A temperature of 313°C measured at 360 mbsf in Hole 1188F 8 days after drilling indicates that the geothermal gradient at Snowcap hydrothermal site is very steep, limiting the vertical extent of any potential microbial habitat to the shallowest part of the basement.

Biomass Activities

ATP was measured to determine the biomass activity using the luciferin-luciferase method, and the results are shown in Table T19. ATP was detected only in the uppermost cores (Samples 193-1188A-5R-1, 17–21 cm [33.77 mbsf], and 7R-1, 55–58 cm [48.75 mbsf]). All samples collected from depths below 60 mbsf in Hole 1188A showed no indications of biomass activity. However, note that the detection limit of this analytical procedure is 0.5 pg/cm^3 (1×10^4 cells/cm³), and it therefore remains possible that microorganisms are present at deeper levels in amounts below the detection limit of this procedure. Because of an unavailability of reagents, ATP was not measured in samples from Hole 1188F. The results from the ATP analysis corroborate the bacterial enumeration data (Table T19); hence, we are confident that we have established a variation of biomass with depth in Hole 1188A that restricts detectable biomass to the uppermost 50 to 60 mbsf.

Enrichment Cultures

Enrichment cultivation experiments were performed to improve the yield of microorganisms in the samples. The cultivation experiments

T19. Total bacterial count and biomass activities, p. 294.

were conducted at varying temperatures and oxygen partial pressures (Table T20). Bacterial growth was determined by comparing culture medium inoculated with core samples with the uninoculated medium, where turbidity in the medium indicates growth. In cultures where it was difficult to make an assessment based on visual inspection, ATP analysis was used to test for growth.

Results from these experiments (after 1 week incubation time) are shown in Table T20. In the aerobic experiments, growth was observed at both 4°C (Sample 193-1188A-2R-1, 0–4 cm [9.60 mbsf]) and 25°C (Samples 2R-1, 0–4 cm [9.60 mbsf], and 5R-1, 17–21 cm [33.77 mbsf]). No growth was observed in any other sample. In the anaerobic cultures, growth was observed at 25°C (Samples 193-1188A-2R-1, 0–4 cm [9.60 mbsf], through 7R-1, 55–58 cm [48.75 mbsf]), and at 60°/90°C (Samples 2R-1, 0–4 cm [9.60 mbsf], and 5R-1, 17–21 cm [33.77 mbsf]). Bacteria isolated from these enriched cultures will be used in shore-based studies.

Although no bacteria were detected by direct microscopic count in any of the samples from Hole 1188F, enrichment cultivation experiments were conducted to improve the yield (and also to verify the presence) of any microorganism present at these deeper depths. In the aerobic cultures, bacterial growth was observed in both samples (Samples 193-1188F-1Z-4, 60–65 cm [222.23 mbsf], and 3Z-2, 70–75 cm [224.75 mbsf]) at 25°C. No bacteria were observed in any other cultures (Table T20). In the anaerobic cultures, bacterial growth observed was in media inoculated with Sample 193-1188F-1Z-4, 60–65 cm (222.23 mbsf), at 25°C. No bacterial growth was observed in any other sample (Table T20). In view of the high temperatures recorded at these depths (~100°C at depths >200 mbsf), the microbial mass enriched at 25°C cultures (both aerobic and anaerobic) is most likely caused by contamination from the seawater used as drilling fluid.

Micromorphological Observations

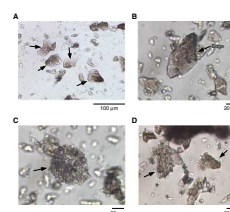
Optical and epifluorescence microscopic techniques were used to examine the interactions between microorganisms and minerals, particularly the micromorphology, size, chemical composition, and structure of minerals associated with the microorganisms. Such information is essential in establishing the biological habitat and the role of microbes in the mineralization and alteration processes in the PACMANUS hydrothermal system.

The uppermost cores (Samples 193-1188A-2R-1, 0–4 cm [9.6 mbsf], and 5R-1, 17–21 cm [33.77 mbsf]) consist of brown translucent fragments of dacitic volcanic glass (Fig. F115). The textures of these fragments range from aphanitic to microlitic (Fig. F115). When stained with DAPI, bacteria were located on the surfaces and along the edges of these fragments. Some microcrystalline domains exhibit ~20-µm spots of stray fluorescence, indicating either the presence of bacterial colonies or, more likely, autofluorescent minerals.

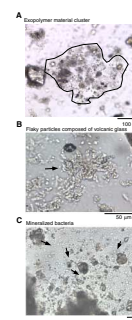
Although no bacteria were detected in core samples obtained from depths >50 mbsf (Table T19), Figure F116 shows the micromorphological observations that may suggest possible bacterial habitation at these depths (Samples 193-1188A-7R-1, 55–58 cm [48.75 mbsf], to 21R-1, 105–114 cm [184.15 mbsf]). The exopolymer clusters (clusters of material of inorganic and organic origin that contain fragments with bacterial morphology and/or are stained by DAPI), flaky particles composed of volcanic glass fragments, and mineralized bacterial particles (chains

T20. Enrichment cultivation at different culture conditions, p. 295.

F115. Mineral particles showing bacterial habitation, Hole 1188A, p. 225.



F116. Mineral particles showing possible bacterial habitation, Hole 1188A, p. 226.



of particles that have bacterial morphology and/or are stained by DAPI) are shown in Figure F116.

Fresh plagioclase phenocrysts and magnetite embedded in volcanic glass are common in core materials from Hole 1188A, but no bacterial habitation was associated with these minerals. Samples 193-1188F-1Z-4, 115–130 cm (222.23 mbsf), to 26Z-1, 62–65 cm (304.53 mbsf), from Hole 1188F were composed mostly of quartz, plagioclase, pyrite, anhydrite (Fig. F117A), and volcanic glass. No bacteria were apparent within these mineral particles. Assemblages of clay minerals and plagioclase fragments also showed no definitive bacterial mass (Fig. F117B).

Further shore-based studies using high-resolution microscopic techniques will be needed to verify the bacterial habitation within these samples.

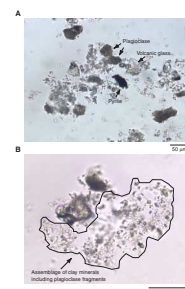
Contamination Test

The chemical tracer test was conducted while coring with the RCB (Core 193-1188A-11R) at this site. To estimate the amount of fluid intrusion into the recovered cores, a chemical tracer was deployed as previously described (Smith et al., 2000). Perfluoro(methylcyclohexane) was used as the perfluorocarbon tracer (PFT). Calibrations of the gas chromatograph (HP 5890) with standard solutions yielded a slope of 4.05×10^{12} area units/g of PFT. The detection limit of the samples was 0.01 μL of drilling fluid. The tracer was detected on the outer edge of the core, indicating a successful delivery. Estimates of drilling fluid intrusion in this sample range from below detection to 0.5 $\mu\text{L/g}$. The drilling fluid intrusion into the center of the core was below the detection limit.

PHYSICAL PROPERTIES

Physical properties measurements taken on core recovered from Site 1188, also known as Snowcap hydrothermal site, include magnetic susceptibility, natural gamma radiation, compressional wave velocity, thermal conductivity, and standard index properties. In most cases, measurements were made at least once per lithologic section. In areas of large-scale heterogeneity and when recovery allowed, sample density was increased. The magnetic susceptibility meter and natural gamma radiation device were run on Cores 193-1188A-10R through 21R, using the multisensor track (MST). Because the remaining cores from this hole were particularly fragmented, incomplete, or disturbed, they did not lend themselves to the continuous automated measurements of the MST. The cores from Hole 1188F were collected using the ADCB system, so they were too large to run through the MST. Additionally, because in most cases the cores were extremely fragmented, they were inappropriate for MST measurements and so no magnetic susceptibility or natural gamma radiation data were obtained. In both Holes 1188A and 1188F, compressional wave velocity measurements were made on discrete samples where possible in one direction and at ambient pressure. Thermal conductivity was measured on almost every lithologic unit from both holes, except where recovery was too low or rock pieces were too small for the measurement procedure (<5 cm). Index properties for both holes, also measured in every lithologic unit when recovery allowed, were measured on minicores, rock fragments, or both.

F117. Mineral fragments showing no bacterial habitation, Hole 1188F, p. 227.



Magnetic Susceptibility

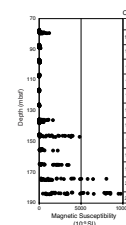
Figure F118 shows the magnetic susceptibility profile of Hole 1188A from 70 to 190 mbsf. Magnetic susceptibility varies greatly over the length of recovered core, ranging from -2.0×10^{-5} to 9736.0×10^{-5} SI, with an average value of $\sim 575 \times 10^{-5}$ SI. Generally, magnetic susceptibility increases toward the bottom of the hole. The interval from 85 to 130 mbsf has a relatively low magnetic susceptibility, ranging from -1.9×10^{-5} to 154.1×10^{-5} SI. Although Core 193-1188A-10R (77–87 mbsf) has a small magnetic susceptibility peak, the majority of the highly magnetic cores are below 135 mbsf, at and below Core 193-1188A-16R. The magnetic peak at Core 193-1188A-10R corresponds to an interval with small amounts of disseminated magnetite. The increasing magnetic susceptibility toward the bottom of the hole also coincides with an increasing amount of magnetite in the core. Varying amounts of sulfide minerals may affect the magnetic susceptibility as well, but more detailed measurements and analyses are necessary to discriminate between minerals, and will be discussed elsewhere (see “[Rock Magnetism](#),” p. 77).

Natural Gamma Radiation

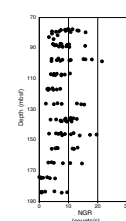
Natural gamma radiation (NGR) records are summarized in plots of total counts per second (cps) vs. curated depth (see Fig. F119). Values range from 0 to 21.5 cps, averaging 8 cps. The data from each core cover a broad range of values. Much of this variation is most likely caused by errors in the measurement process. All cores, at least over certain intervals, did not fill the core liner completely. Because NGR measurements depend on a fixed volume that is equal to that of a full core liner, the intervals where the recovered material was less than the full volume of the liner have lower than expected values. Elsewhere in the same core, the core liner may have been more completely filled, giving a higher NGR reading. Therefore, apparent trends in the data may be more indicative of recovery than of any fluctuation in radioactive elements.

Regardless of these recovery-related uncertainties, when coupled with the geochemistry data from Snowcap hydrothermal site, some information can still be extracted from the NGR values. K is the major element that produces a radioactive signal in the fresh dacites of the PAC-MANUS hydrothermal field (1.7%–1.8% K_2O) (see “[Geochemistry](#),” p. 65). As increased bleaching, alteration, and silicification of the rocks occur, the potassium is commonly leached from the rock, producing lower NGR values. Similarly, higher values may be indicative of less or a different style of alteration. As many of the cores are heterogeneous, some of the scatter in the data from each core likely represents variations in the amount or style of alteration between the individual measurement locations. Although illite is common throughout the hole as an alteration product, the region from ~ 125 to 155 mbsf has a relatively high NGR count and corresponds to the largest amounts of illite identified by XRD. The core with one of the lowest NGR measurements (Core 193-1188A-14R; 116–125 mbsf) has no illite present in XRD scans. However, when compared to the overall silicification and alteration trends, the peaks in NGR data do not consistently correspond to the amounts of silicification or other types of alteration. Therefore, variations measured by the NGR device may be a result of measurement error as well as a result of heterogeneity within lithologic units.

F118. Magnetic susceptibility, p. 228.



F119. Natural gamma radiation, p. 229.



Compressional Wave Velocity

Compressional wave velocities are shown in Table T21 and plotted in Figure F120. Values range from ~3.5 to 6.3 km/s, and average 4.6 km/s. Velocity values tend to increase with depth. Lithologic variations, vesicularity, amount of alteration, and structural features may account for some of the variance in velocity values. In many cases, the more massive volcanic rocks have higher compressional wave velocities than the brecciated and flow-banded rocks.

Thermal Conductivity

Thermal conductivity data for Holes 1188A and 1188F are shown in Figure F121. Values for Hole 1188A range from 1.05 to 4.44 W/(m·K). Most of the values are between 1.5 and 2.5 W/(m·K), with an average of 2.22 W/(m·K). One sample lies outside of this range, at ~125 mbsf, with a value of 4.44 W/(m·K). This sample was taken from a wide anhydrite vein, and thus the thermal conductivity value is closer to that of pure anhydrite (5.61 W/[m·K]) (Clark, 1966). The remaining data have a slight trend, with low values from ~50 to 85 mbsf and from ~135 to 180 mbsf, and high values in between, from ~90 to 130 mbsf. However, the trend variations are relatively small compared to the overall scatter in the data. The values seem to follow the amount of GSC alteration (see “Hydrothermal Alteration,” p. 33); as the alteration increases the thermal conductivity decreases and vice versa.

Thermal conductivity values in Hole 1188A generally seem to be higher for brecciated volcanics than for fresh and altered dacites. All of the brecciated pieces from this hole have thermal conductivity values >2.0 W/(m·K). The altered dacites have values that range from 1.0 to 2.6 W/(m·K), but within this group the majority of rocks with values >2.0 W/(m·K) have anhydrite veins or pyrite-filled vesicles, which may account for the increased thermal conductivity values.

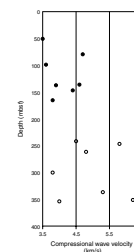
Thermal conductivity values for Hole 1188F range from 2.01 to 4.53 W/(m·K) and average 2.82 W/(m·K), which is significantly higher than for Hole 1188A. Throughout Hole 1188F, most of the vesicles are filled with quartz ± anhydrite ± pyrite, whereas in Hole 1188A most vesicles are unfilled. This should contribute to the higher thermal conductivity values in Hole 1188F, particularly in the altered dacites where most vesicles are found. This can be seen in the data by the lack of any thermal conductivity values below 2.0 W/(m·K) in Hole 1188F. The wide variety of thermal conductivity values at each depth reflects the heterogeneity of the core.

Index Properties

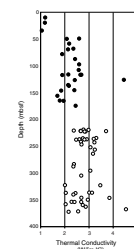
The data for water content, bulk density, dry density, grain density, porosity, and void ratio are displayed in Table T22. Grain densities of powder samples prepared for ICP-AES are given in Table T23. Figures F122 and F123 show grain density and porosity values for both holes, respectively. In Hole 1188A, grain density values range from 1.98 to 2.80 g/cm³, with an average of 2.65 g/cm³. In cases where index properties were measured on both rock fragments and minicores, values were consistent for both types of samples. Similarly, when grain density was measured on both ICP-AES powders and whole samples, values determined were also consistent. The low density value of 1.98 g/cm³ from Section 193-1188A-5R-1 may be due to the presence of opaline silica, as

T21. Compressional wave velocity, Site 1188, p. 296.

F120. Compressional wave velocity, p. 230.



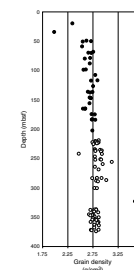
F121. Thermal conductivity, p. 231.



T22. Index properties, Holes 1188A and 1188F, p. 297.

T23. ICP powder densities, p. 299.

F122. Grain density, p. 232.



identified by XRD. For Hole 1188F, grain density values range from 2.47 to 3.59 g/cm³ and average 2.82 g/cm³. Agreement between measurements on rock fragments and minicores was not as good in Hole 1188F as it was in Hole 1188A. This could be caused by a sampling bias toward vein material over surrounding rock in rock fragment samples. Vein material, which is generally denser than surrounding material because of the enrichment in anhydrite and pyrite, tends to fracture into small pieces more easily, which is more suitable for rock-fragment sampling. Over the interval spanned by the two holes, grain density increases with depth until it reaches its peak between ~230 and 290 mbsf. Below 280 mbsf, grain density decreases slightly to a constant value between 2.7 and 2.8 g/cm³. The region between 230 and 290 mbsf is an area of increased anhydrite and pyrite content. The increase in these two minerals contributes to the higher grain density values. Additionally, because the majority of samples in this region are rock fragments, the sampling bias toward vein material in rock fragments may be partially responsible for the increase in grain density. Toward the bottom of the hole, both anhydrite content and grain density decrease again. Density values from ~290 to 400 mbsf are still higher than in Hole 1188A, possibly due to an increase in chlorite.

Porosity values for Hole 1188A are quite variable over the length of the hole, scattered from 0.4% to 44.7%. The average porosity for the hole is 25%. Hole 1188F has a smaller range in porosity, with values between 11.7% and 27.8% and an average of 18%. There is an overall trend of decreasing porosity with depth. This correlates with an increase in alteration and filling of vesicles with depth. Although the amount of silica stays relatively constant throughout Holes 1188A and 1188F, much of the silica in the upper part of Hole 1188A is in the form of cristobalite as opposed to quartz. Generally, cristobalite only coats vesicle walls, whereas quartz tends to fill the vesicles completely. As the quartz content increases with depth, more vesicle openings may be filled resulting in a decrease in porosity.

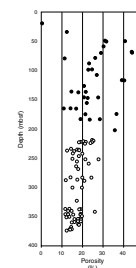
For both holes, the calculated sample porosities are higher than the vesicle space estimates made from visual core inspections. This may mean that small pore spaces in the rock framework make up a large portion of the porosity, which would possibly allow penetrative fluid flow throughout the rock.

ROCK MAGNETISM

Overall recovery from Site 1188 (Snowcap hydrothermal site) was <20%, and all of the cores have significant gaps between pieces. Because, in many cases, the recovered material was not cylindrical, the split cores commonly did not fill the core liners. Furthermore, in the case of Hole 1188F, some of the routine measurements on the whole- and archive-half cores could not be performed because the new ADCB has a larger diameter (~95 mm) compared to the standard ODP core barrel (~56 mm). Shipboard analyses of Site 1188 cores, however, reveal a distinctive variation of magnetic properties with depth. This variation defines several zones, which may be an important observation for understanding the fluid flow and alteration process of this hydrothermal system.

In addition to routine ODP measurements, the relatively low core recovery at Site 1188 made it possible for us to conduct a series of rock magnetic measurements on discrete minicores sampled for shipboard

F123. Porosity, p. 233.



analyses. The results of isothermal remanent magnetization (IRM) acquisition and subsequent thermal demagnetization experiments reveal quite distinct patterns among samples or groups of samples and may provide an important insight into the nature of magnetic carriers of the rocks from Site 1188.

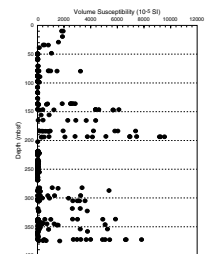
Archive-Half Core Measurements

Susceptibility

Susceptibility measurements were first conducted on whole cores using the magnetic susceptibility meter mounted on the MST. These results are described in “[Physical Properties](#),” p. 74. The whole cores were then split, and the susceptibility was measured on the archive halves. Because there were many significant gaps in the cores, instead of taking continuous measurements, we decided to make measurements of the archive half by setting the point susceptibility meter on the archive multisensor track (AMST) in manual mode and placing the probe in contact with the piece of core where we wanted a measurement. The susceptibility probe on the AMST has a depth range of 2 cm. We took point susceptibility measurements on pieces that were at least several centimeters long and a few centimeters thick. In addition, measurements were taken across intervals where there appeared to be changes in lithology or alteration style. The point susceptibility measurements proved to be quite useful at Site 1188 because most of the recovered rock samples were fragmented. Furthermore, the ADCB has a bigger diameter than ODP standard cores, and therefore, susceptibility measurements could not be performed on whole cores recovered from Hole 1188F. A total of 421 intermittently spaced susceptibility measurements were taken from Cores 193-1188A-2R through 22R and from Cores 193-1188F-1Z through 44Z.

Figure F124 shows the resultant downhole profile of magnetic susceptibility for Holes 1188A and 1188F combined. All susceptibility values in this report are given in SI units. Volume susceptibility measurements range between 10^{-4} and the upper limit of the susceptibility meter of 0.1 SI. The core recovered from the top 35 m of Hole 1188A that is dominated by relatively fresh dacite and rhyodacite has a moderately high susceptibility of 0.018 SI. The susceptibilities of most paramagnetic minerals are <0.01 SI (Collinson, 1983), and therefore, the susceptibility of this section (0–35 mbsf) cannot be explained without a contribution from ferromagnetic minerals, such as titanomagnetite and magnetite. In the interval between 35 and 135 mbsf, the susceptibility becomes extremely low and in some places it becomes even slightly negative, suggesting the presence of diamagnetic minerals such as quartz. This section of core coincides with intense alteration. There are locations where susceptibility increases sharply (e.g., in Sections 193-1188A-7R-1 [48.27 mbsf] and 10R-2 [79.42 mbsf]). However, in both cases the intervals of high susceptibility do not extend very far downhole. Then there is a large increase in susceptibility below 135 mbsf, down to almost the bottom of Hole 1188A. Peak susceptibility values in this interval (Cores 193-1188A-1R to 22R) range from 0.06 to 0.095 SI. In addition to an increase in peak values, there is also a greater degree of variability in the susceptibility values. This is in contrast with measurements from the higher sections, especially the top 35 mbsf, where there is relatively little scatter. The cause of high susceptibility values between 135 and 211 mbsf is discussed later in this chapter.

F124. Volume susceptibility, p. 234.



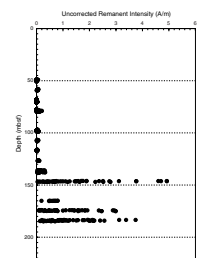
The susceptibility measurements of archive-half cores from Hole 1188F show two zones with different patterns. The susceptibility between 220 and 270 mbsf is almost two orders of magnitude lower than that between 280 and 375 mbsf, where the peak susceptibility ranges from 0.06 to 0.08 SI. The susceptibility shows a greater variability between 280 and 375 mbsf than above 270 mbsf. Although there is an ~10-m gap in the core section where no rock samples were recovered, the transition from the low- to high-susceptibility region appears to be quite sharp. The relationship of this transition between susceptibility and alteration style in Hole 1188F is again discussed later in this chapter.

Remanent Intensity

At Site 1188 we were only able to perform remanent intensity measurements and alternating-field (AF) demagnetization on cores recovered from Hole 1188A. Most of the samples recovered from Hole 1188F were too fragmented and/or the diameter of the core was too large to pass through the magnetometer. The information regarding the remanent intensity of Hole 1188F came solely from the measurements that we conducted on minicore samples.

The natural remanent magnetization (NRM) of most of the archive halves from Hole 1188A was measured using the pass-through cryogenic magnetometer. The cores were then progressively AF demagnetized at peak values of 10, 15, 20, and 30 mT. The remanent intensity was measured after each step. Both the NRM and remanent intensity were measured at 2-cm intervals. Again, because of the poor recovery and significant gaps in the sequence of rock samples, the remanent intensity data were not downloaded to the Janus database directly. The purpose of these measurements was to look at the overall trend in the NRM of archive halves. The cryogenic magnetometer has response curves whose half-power points are ~7–10 cm wide. Therefore, data from core pieces <10 cm long should be excluded from processing. Several postprocessing steps were taken to remove the outliers and bad measurement points from the data. Despite this effort, however, many erroneous data points remain. In general, they are lower than the true values because they correspond to places where the rock sample did not fill the core liner or to measurements that were taken near the edge of the rock samples. Figure F125 shows the postprocessed downhole profile of the NRM taken from the archive halves for Holes 1188A and 1188F combined. Again, we note that this profile includes uncorrected measurements because the exact volume of rock samples that passed through the cryogenic magnetometer is not known; the purpose of showing this plot is only to look at the general trend of values. Some of the core sections, especially those from the upper part of the hole, were not measured at all because they contained insufficiently long rock samples. Overall, the intensity measurements of the half cores show a similar pattern to that of susceptibility (Fig. F124). A zone of high intensity appears below 135 mbsf (Fig. F125). However, in the case of the magnetization intensity, the increase is more abrupt. Also, there appears to be some decay toward the bottom of the hole, which is not seen in the susceptibility profile of Hole 1188A.

F125. Remanent intensity, Hole 1188A, p. 235.



Discrete Measurements

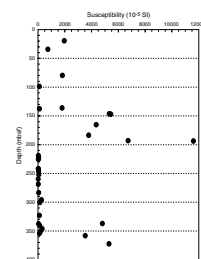
A total of 40 discrete minicore samples were taken from Holes 1188A and 1188F. Table T24 summarizes the location, dimensions, and brief descriptions of the color, texture, and hardness of these minicores. For Hole 1188A, all of the minicores were from oriented pieces of the core and cut perpendicular to the core axis except for the first two samples from the very top of the core (Samples 193-1188A-3R-1, 14 cm, and 5R-1, 45 cm) where no oriented pieces were recovered. In the case of Hole 1188F, many of the minicore samples from below 300 mbsf were from unoriented fragments of core. Before any demagnetizing steps were taken, we measured the anisotropy of magnetic susceptibility (AMS) at 15 different positions using the Kappabridge, and the data were processed with the program ANI20 supplied by Geofyzika Brno. The susceptibility of some samples was too low to be accurately measured on board the ship (Table T24). For instance, we were not able to measure the susceptibility of Samples 193-1188A-7R-1, 74 cm, and 9R-1, 25 cm, and we only report the average susceptibility values for a couple of positions for Samples 193-1188A-7R-2, 78 cm; 10R-1, 118 cm; and 14R-1, 103 cm; and 193-1188F-43Z-1, 4 cm. Figure F126 shows a downhole profile (combining Holes 1188A and 1188F) of the mean susceptibility of all the discrete samples. The magnetic susceptibility of minicores varies by several orders of magnitude. Minicores taken above 135 mbsf generally have magnetic susceptibility values <0.020 SI. Between 135 and 200 mbsf, the average susceptibility is much higher, ~ 0.060 SI. A maximum susceptibility of 0.115 SI was measured in Section 193-1188A-21R-1 (~ 194 mbsf). The susceptibility drops to <0.001 SI in the upper half of Hole 1188F. Sections 193-1188F-1Z-1 through 22Z-1 represent the low-susceptibility region of Site 1188. The susceptibility begins to increase below 295 mbsf, and there are rock samples with susceptibility values almost as high as those at the bottom of Hole 1188A. In general, the pattern is quite similar to that of point measurements taken on archive halves (Fig. F124). As in the archive halves, the high susceptibility values are found near the bottom of both Holes 1188A and 1188F.

The isotropy of magnetic susceptibility (AMS) of a rock sample is caused by a number of different factors (Tarling and Hrouda, 1993). However, in general, the mineral composition (Borradaile et al., 1987), grain shape (Uyeda et al., 1963), and mineral-preferred orientation are thought to be some of the important factors that affect the anisotropy. If the sample is dominated by magnetite, AMS may provide information on the grain shape, or if not, its crystallographically preferred orientation. Table T25 summarizes the magnitudes and principal axes of the AMS that were derived from the susceptibility tensor. There appears to be only a slight degree of anisotropy of magnetic susceptibility ($P = k_{\max}/k_{\min}$) in the samples from Site 1188. The maximum anisotropy determined is 1.16 from Sample 193-1188A-17R-2, 30 cm (~ 147 mbsf). Figure F127 is a Flinn-type diagram representing the susceptibility ellipsoid in two-dimensional space. Except for Sample 193-1188A-17R-2, 30 cm, the shape of the ellipsoids is close to spheroidal, which means that there is no evidence for a strongly preferred orientation of susceptibility.

The NRM of minicore samples (Fig. F128) was measured using the cryogenic magnetometer. Again, the NRM profile of Site 1188 shows a similar pattern to that of susceptibility (Figs. F124, F126). For Hole 1188A, where we also have the NRM intensity (Fig. F126) of the archive-half cores, the profiles match quite well. The minicores from the

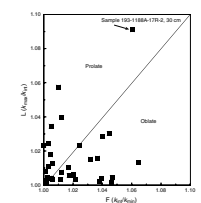
T24. Magnetic properties of minicores, p. 300.

F126. Magnetic susceptibility of minicore samples, p. 236.

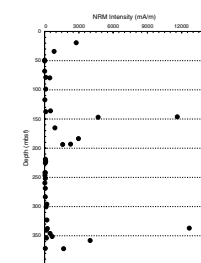


T25. Anisotropy of magnetic susceptibility, p. 301.

F127. Anisotropy of magnetic susceptibility, p. 237.



F128. Natural remanent magnetization intensity of minicore samples, p. 238.



top 35 m of the hole exhibit high intensities, whereas those taken between 35 and 135 mbsf show very low intensities. The intensity of NRM increases dramatically between 135 and 211 mbsf. A very high intensity value of 11 A/m is present at 146 mbsf (Sample 193-1188A-17R-1, 109 cm). Unlike susceptibility, however, the NRM intensity values tend to decrease toward the bottom of Hole 1188A. A corresponding decrease is shown by the archive-half NRM measurements (Fig. F126). Therefore, it is most likely a true trend and not an artifact caused by insufficient sample points. The remanent intensities were measured by performing progressive AF demagnetization at peak fields of 10, 15, 20, 25, 30, 40, 50, 60, and 80 mT. Table T24 shows the NRM intensity and stable inclination and declination of the minicore samples. The changes in magnetization intensity, inclination, and declination of the minicore samples with progressive AF demagnetization are summarized in Table T26. Figure F129 is an inclination plot of the stable magnetization. Directions are reported using the conventional ODP core orientation. Inclination generally ranges between -30° and 5° in the upper 200 m of the hole. In Hole 1188F, because of the fragmented nature of the rock samples, we were only able to conduct reliable magnetization direction measurements on 5 samples out of 23. However, the inclination values of those few measurements fall within the range measured in cores from Hole 1188A. The low negative inclination values in the upper 200 m of the hole are consistent with the fact that our drill site lies just south of the magnetic equator. In Hole 1188F, the sample taken near the bottom of the hole (Sample 193-1188F 43Z-1, 56–89 cm) has an inclination of -16° , which is reasonably consistent with the present-day Earth field. According to the International Geomagnetic Reference Field (IGRF), our drill site has declination and inclination values of 5.5° and -7.7° , respectively.

We also computed the Koenigsberger ratio (Q) of the minicore samples, which compares the relative contribution of the remanent magnetization against the magnetization induced in the cores by Earth's magnetic field. The Koenigsberger ratios range from 5 to as high as 184 (Table T24), which indicates that the in situ magnetization of these rocks is dominated by a remanent magnetization rather than magnetization induced by Earth's magnetic field.

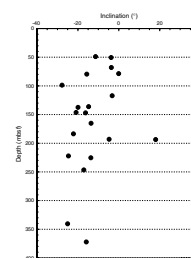
Overall, the AF demagnetization appears to be quite effective in removing the secondary magnetization. Figure F130 includes two examples from Hole 1188A (Samples 193-1188A-10R-1, 118 cm, and 17R-2, 30 cm) showing the decay in intensity and convergence toward the origin in the vector end-point diagrams with progressive demagnetization. Figure F131 shows an example of a strong secondary magnetization (Sample 193-1188A-16R-2, 46 cm). In this case, the initial declination and inclination values of 308° and -28° changed to 198° and -20° , respectively, after AF demagnetization (Table T26). This sample derives from a strongly altered, layered unit, where the presence of a secondary magnetization might be expected.

IRM Measurements

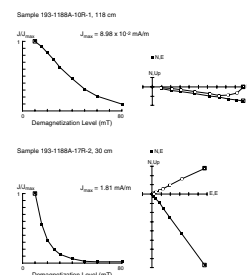
Besides standard shipboard analyses, we conducted a few additional experiments on the minicore samples to examine the magnetic properties of Site 1188. IRM and backfield isothermal remanent magnetization (BIRM) data are often used to discriminate between high- and low-coercivity magnetic phases. The field was applied at increasing steps of 50, 100, 150, 200, 250, 300, 400, 500, 800, and 1100 mT. In general, low-

T26. Magnetic properties of minicores after alternating-field demagnetization, p. 302.

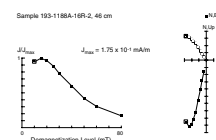
F129. Stable inclination of minicore samples, p. 239.



F130. Zijdeveld plots and intensity-decay curves of two samples, Hole 1188A, p. 240.



F131. Zijdeveld plot and intensity-decay curve of a sample from Hole 1188A with strong secondary magnetization, p. 241.



coercivity minerals include magnetite and titanomagnetite, whereas minerals such as hematite fall in the high-coercivity group. However, the grain size and oxidation and domain states also affect the coercivity.

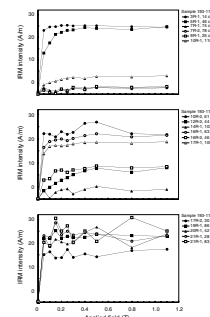
All 40 minicore samples from Site 1188 were imparted with an IRM using impulse fields. For Hole 1188A, the experiment was performed on three groups of five to six samples each. Most of the samples exhibit a steep gradient of IRM acquisition up to the saturation level (defined as 95% of the maximum IRM intensity), after which no significant increase in intensity occurs with increasing applied field (Fig. F132). The maximum remanence that is acquired is referred to as the saturated isothermal remanent magnetization (SIRM). The sample from near the top of the core (Sample 193-1188A-3R-1, 14 cm) became saturated at a low field (<100 mT), which probably suggests that the magnetic carrier is predominantly magnetite or titanomagnetite. The saturation of Sample 193-1188A-5R-1, 46 cm, occurred at a much higher field (300–400 mT). Similarly, Samples 193-1188A-10R-1, 118 cm; 12R-2, 44 cm; and 16R-2, 46 cm, exhibited relatively high coercivity (500 mT). The high coercivity may be in part caused by a subtle change in the style of alteration or alteration minerals. The presence of hematite was noted in Sample 193-1188A-16R-2, 46 cm (see “[Hydrothermal Alteration](#),” p. 33). In general, there appears to be a quite close relationship between the NRM and SIRM values. Samples with high NRM tend to have high SIRM. For example, all the minicore samples between 135 and 211 mbsf exhibit relatively high SIRM intensities.

Another notable feature is that some samples exhibit high variability of IRM intensity values as a function of applied field. The fluctuation is especially noticeable for Samples 193-1188A-17R-2, 30 cm, through 21R-1, 83 cm (Fig. F132). The high variability in IRM is an instrumental effect. The 2G Enterprises cryogenic magnetometer used in this study is an extremely sensitive instrument, but the measurements tend to become unstable at high magnetization values.

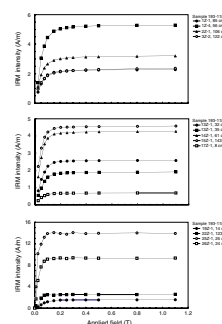
We measured IRM intensities of all 23 samples collected from Hole 1188F. Some of these samples were also measured for BIRM intensities. To examine the behavior of magnetic minerals at low fields (<100 mT), we added 10, 25, and 70 mT to the impulse field steps. Figure F133 shows the results of IRM measurements conducted for Hole 1188F samples. The experiment was performed in five groups, using four to five samples per group. As in Hole 1188A, we see correlation between NRM and SIRM values, with samples with relatively high NRM values having high SIRM values (Fig. F133). Samples 193-1188F-1Z-1, 85 cm, through 19Z-1, 14 cm, which roughly correspond to the depth interval 218–270 mbsf, exhibit a monotonous rise in IRM intensity with increase in applied field. Below this depth, from 270 to ~325 mbsf (Samples 193-1188F-2Z-1, 123 cm, through 31Z-1, 36 cm), there is a small deviation from the monotonous curve observed above. A significant change occurs below 325 mbsf. The rock samples start to show an immense fluctuation in the IRM intensity, similar to what we saw near the bottom of Hole 1188A.

In addition to variability in IRM intensities, the samples from Hole 1188F exhibit a range of coercivity fields. In general, coercivity decreases with increasing depth. Samples 193-1188F-1Z-1, 85 cm, through 3Z-2, 122 cm, show relatively high coercivity (>400 mT). The fact that there is no significant increase in IRM intensity beyond 500 mT suggests that the high coercivity in these samples is not caused by the presence of hematite but rather by other factors that affect coercivity such as grain size and oxidation and domain states. The coercivity decreases

F132. Intensity of impulse isothermal remanent magnetization, Hole 1188A, p. 242.



F133. Intensity of isothermal remanent magnetization, Hole 1188F, p. 243.



to 200–250 mT for Samples 193-1188F-13Z-1, 32 cm, through 19Z-1, 14 cm. It diminishes further to ~100 mT for Samples 193-1188F-22Z-1, 123 cm, through 26Z-1, 24 cm, and becomes extremely low in the samples that exhibit high IRM fluctuations.

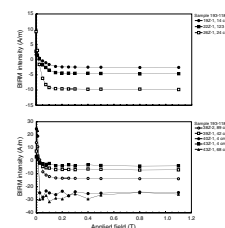
Figure F134 shows the BIRM measurements that were performed on some of the groups of samples. BIRM intensity measurements were conducted to make sure that some of the features that we observed in the IRM experiment appear in the BIRM experiment as well. In general, the characteristics that we observed in the IRM experiment can be seen in the BIRM results. Very high coercivity minerals such as hematite do not seem to be dominant in any of the samples from Hole 1188F.

Thermal Demagnetization

Another additional experiment that was conducted on the shipboard minicore samples was to monitor the magnetization intensity with increasing temperature. By examining the thermal demagnetization curves, one may be able to determine the magnetic minerals in the minicore samples based on their Curie temperature. Table T27 summarizes the Curie temperatures of some of the more common magnetic minerals. We chose four minicore samples from Hole 1188A (193-1188A-5R-1, 46 cm; 7R-1, 74 cm; 17R-1, 109 cm; and 21R-1, 28 cm) that were already saturated with IRM magnetization. The samples were progressively heated up to 700°C, with smaller temperature intervals beyond 500°C. Figure F135 shows the variation in remanent intensity as a function of temperature. A sharp drop in intensity was observed for Sample 193-1188A-5R-1, 46 cm, at 350–400°C, which suggests that the remanence is carried by a single magnetic phase. This phase is most likely titanomagnetite. In general, the Curie temperature falls with increasing titanium content as well as other impurities such as Mg, Ca, Al, Cu, V, and Si (Thompson and Oldfield, 1986). However, if the magnetic carrier were a single-phase titanomagnetite, the Curie temperature of 400°C would correspond to a composition of roughly 35% Fe₃O₄ and 65% FeTiO₄. Sample 193-1188A-7R-1, 74 cm, shows a feature similar to Sample 5R-1, 46 cm. However, it has a much more subdued intensity. This probably suggests a greater degree of low-temperature alteration in which titanomagnetite became oxidized to tinohematite. The Curie temperatures of tinohematite and titanomagnetite are almost identical within the range of titanium concentrations that we have observed.

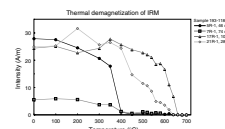
Samples 193-1188A-17R-1, 109 cm, and 21R-1, 28 cm, exhibit somewhat complex thermal demagnetization curves. Sample 193-1188A-17R-1, 109 cm, shows an increase in the remanent intensity between 200° and 350°C and a small drop at 560°C followed by a larger drop between 600° and 680°C. The first decrease of intensity at 560°C corresponds to the Curie temperature of magnetite, whereas the second decrease at 680°C corresponds to that of hematite. However, hematite has a much lower value of saturation magnetization. For instance, at room temperature (20°C) it is only ~5% and 9% of that of magnetite and maghemite, respectively. Therefore, a dominance of hematite does not explain the high remanent intensity of Sample 193-1188A-17R-1, 109 cm. One possible explanation may be that maghemite converted to hematite upon heating. The conversion to hematite at 300°C is one of the characteristic properties of maghemite. If so, this conversion may explain the drop of intensity of Sample 193-1188A-17R-1, 109 cm, above 300°C (Fig. F135). In this case, the dominant magnetic carriers in the preheated original sample would have been magnetite and maghemite.

F134. Intensity of back-field isothermal remanent magnetization, Hole 1188F, p. 245.



T27. Magnetic properties of remanence-carrying natural minerals, p. 305.

F135. Thermal demagnetization curves for representation samples from Hole 1188A of isothermal remanent magnetization, p. 246.



The thin-section analysis shows no original hematite in Sample 193-1188A-17R-1, 109 cm. However, IRM measurements taken on the same sample after it was thermally demagnetized show the possible presence of hematite. Figure F136 shows the results of IRM intensity measurements taken on samples after they were thermally demagnetized to over 700°C. Sample 193-1188A-17R-1, 109 cm, is characterized by a sharp rise in IRM below 100 mT and a gradual increase beyond 500 mT. The sharp increase may be caused by a small amount of magnetite or maghemite that was not converted to hematite, whereas the latter increase may be caused by converted hematite. Another notable feature is the large drop in the IRM intensity before and after the heating. Considering that Sample 193-1188A-17R-1, 109 cm, has one of the highest NRM intensities of Hole 1188A and thus a very high IRM intensity, the drop in IRM intensity after thermal demagnetization is significant.

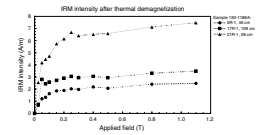
Sample 193-1188A-21R-1, 28 cm, does not show a single drop in intensity but instead a series of decays (Fig. F135). Therefore, it appears to be a mixture of different magnetic minerals. On the basis of the thermal demagnetization curve, it appears that this sample may have as many as four different phases of magnetic minerals. Still, the predominant magnetic carriers appear to be titanomagnetite and magnetite. Beyond 640°C, the sample loses all its remanent intensity, so it is unclear whether or not it contains hematite. However, thin-section study of the original sample shows a small amount of hematite.

The IRM measurement taken on Sample 193-1188A-21R-1, 28 cm, after it was thermally demagnetized shows three small steps of increase in IRM intensity in a relatively low field (<350 mT), followed by a gradual increase in IRM in the higher field (>400 mT) (Fig. F136). Such features are not seen in the IRM measurements of the preheated sample. One possible explanation of this difference in the IRM behavior of samples before and after heating is that the extremely low coercivity mineral in Sample 193-1188A-21R-1, 28 cm, may be affecting the initial IRM measurements. Upon heating to 700°C and then cooling, the extremely low coercivity mineral has disappeared or been reduced to some other form. The exact Curie temperature of this magnetic carrier is uncertain.

Discussion and Summary

Both the archive-half susceptibility and the discrete remanent intensity and susceptibility measurements of Site 1188 show consistent patterns (Figs. F124, F128). Based on magnetic properties, Hole 1188A may be divided into three intervals. The top 35 m of the cored material is characterized by high magnetic susceptibility (0.018 SI) and remanent intensity (0.82–2.76 A/m). This depth roughly corresponds to the relatively fresh dacite-rhyodacite section at the top of the hole. The degree of alteration of the recovered rhyodacite ranges from none to slight. The susceptibility of 0.018 SI is consistent with the presence of ~1% magnetite (Hrouda and Kahan, 1991). The magnetic measurement values show a considerable drop from 35 to ~135 mbsf. This section represents a highly altered interval in Hole 1188A. There are small intervals within this section where magnetization and susceptibility are elevated. These intervals are coincident with more intense silicification, and magnetite was commonly reported from silica-rich intervals (see “Hydrothermal Alteration,” p. 33). A marked increase in both the susceptibility and remanent intensity occurs below 135 mbsf. In this interval, NRM intensities are as high as 11 A/m and susceptibility increases as much as three orders of magnitude compared to the interval above.

F136. Intensity of isothermal remanent magnetization after thermal demagnetization, Hole 1188A, p. 247.



Magnetite-bearing veins are found throughout this interval (see “[Structural Geology](#),” p. 58), which would account for the increased values. However, the remanent intensity and susceptibility vary in different manners. Magnetic susceptibility shows higher values toward the bottom of Hole 1188A, whereas remanent intensity actually decreases. This feature is unlikely to be a sampling artifact because it is apparent in the archive-half as well as minicore sample measurements. The discrepancy between the magnetic susceptibility and remanent intensity trends is reflected in the relatively low Koenigsberger ratio ($Q = 5$) of Sample 193-1188A-21R-1, 83 cm. The cause of this difference is unclear. Whereas the presence of paramagnetic minerals such as pyrite can increase the magnetic susceptibility, and Sample 193-1188A-21R-1, 83 cm, is from an interval that includes pyrite veins, there is no notable increase in pyrite abundance in the core descriptions from this interval.

The investigation of minicore samples shows that remanence dominates the magnetization induced by Earth’s field. The inclinations of samples with high Koenigsberger ratios ($Q > 20$) range between -22° and -7° , which is slightly steeper than that predicted by the present-day Earth field reference model for zero-age material. Acquisition of IRM suggests that minicore samples from the top of Hole 1188A (Sample 193-1188A-3R-1, 14 cm) and from below 149 mbsf (samples taken from Sections 193-1188A-17R-2 through 21R-1) have relatively low coercivity (<200 mT) (Fig. [F132](#)). A number of minicore samples in between (20–149 mbsf) show much higher coercivity (300–500 mT), which may be caused by alteration or the presence of high-coercivity minerals such as hematite. This could not routinely be checked on shipboard samples because of a limit on the number of thin sections that could be prepared. However, for one sample (193-1188A-12R-2, 44 cm) that has a very high coercivity (400–500 mT), hematite was identified in thin section. The SIRM values among the minicore samples are similar to those of the NRM.

Thermal demagnetization performed on four representative minicore samples suggests that at least in the top 50 m of the hole the dominant magnetic carrier is titanomagnetite with variable degrees of alteration (Fig. [F135](#)). At 146 mbsf (Sample 193-1188A-17R-1, 109 cm), magnetite and possibly maghemite may be the magnetic carriers. Sample 193-1188A-21R-1, 28 cm (193 mbsf), shows a complex demagnetization with a gradual decrease between 300° and 640°C . Our interpretation is that this sample contains a mixture of magnetic minerals, including magnetite and titanomagnetite, probably in various phase and domain states.

In Hole 1188F, the diameter of the recovered ADCB samples was larger than the standard ODP core, preventing long-core remanence measurements on the archive-half cores. In addition, most of the samples that were recovered were either rubble or rocks broken into short pieces. As a result, we were not able to obtain reliable estimates of the magnetization direction from many of the minicore samples. The few samples that were long enough for orientation measurements have inclination values similar to those of Hole 1188A.

One of the most notable features of Hole 1188F is a sharp rise in the susceptibility values below 275 mbsf (Fig. [F124](#)). The zone between 211 and 275 mbsf is uniformly low in magnetic susceptibility (<0.002 SI). Below 275 mbsf, the peak susceptibility increases by almost two orders of magnitude. The change in magnetic susceptibility corresponds to a major change in the alteration style in Hole 1188F (see “[Hydrothermal Alteration](#),” p. 33). The NRM shows a similar pattern to susceptibility,

although the most significant rise in the remanence occurs at a greater depth (>330 mbsf) (Fig. F128). The maximum NRM value of 12.66 A/m occurs at 336 mbsf in Hole 1188F. The high magnetization intensity at the bottom of the hole is consistent with the presence of magnetite, which was identified by XRD and optical microscopy (see “**Hydrothermal Alteration**,” p. 33). As in Hole 1188A, there is a large contrast in IRM behavior between the upper and lower parts of Hole 1188F. A dramatic increase in the variability of SIRM values occurs below ~330 mbsf (Fig. F133). We attribute this behavior to extremely low coercivity magnetic minerals present in the rock samples. Because we have not done any thermal demagnetization experiments on these samples, we are not certain of the nature of this low-coercivity magnetic mineral. One characteristic of Hole 1188F, which distinguishes it from Hole 1188A, is that there is a fairly steady decrease in the coercivity from top to bottom.

DOWNHOLE MEASUREMENTS

Hole 1188A

Temperature Measurements

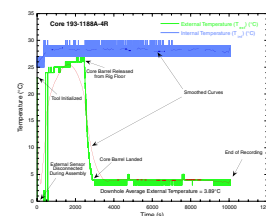
The CBTT was deployed on the fourth core barrel during the initial drilling stages of Hole 1188A. The deviation from the initial plan for CBTT deployments (see “**Downhole Measurements**,” p. 27, in the “Explanatory Notes” chapter) was necessary because of the difficulties in communicating and initializing the CBTT using a serial line connection with a DB9 communication port (COM1) in the downhole measurements laboratory PC data acquisition system.

One of the tools did not respond to several communication attempts, and the second tool finally began responding after several attempts and diagnostic checks were made. The batteries were revived by connecting a 100-Ω resistor for several minutes and monitoring the increasing voltage. In addition, resetting the tattletale controller prior to any communication attempt was necessary. Once several bench tests were satisfactory, the tool was prepared for deployment.

After initialization, the tool was placed in a dewar with 320 mL of glycerin that was used as a thermal sink. The purpose of using glycerin was to protect the electronics from excessive temperatures, as they were rated to ~100°C and the downhole conditions were not well known. Shortly after initializing the tool, the external sensor was briefly disconnected for final assembly. After reconnecting the thermocouple and placing the tool in the pressure case, TSF core technicians assisted in placing the tool assembly on top of the core barrel and it was released as soon as the previous core was on deck. The tool was downhole for 3.2 hr, and it recorded data for 2.8 hr (Fig. F137). The discrepancy in time is believed to be similar to the original problems described above.

The temperature vs. time record from Core 193-1188A-4R (28.9–33.6 mbsf) shows profiles for both the internal (T_{int}) and external (T_{ext}) temperature sensors. The time of initialization, a period of ~6 min during which T_{ext} was disconnected, a heating period when the tool was at the rig floor, a cooling trend as the core barrel was released from the rig floor, and, finally, the bottom-hole profile, were all recorded (Fig. F137). T_{ext} shows an average bottom-hole temperature of $3.9^{\circ} \pm 0.4^{\circ}\text{C}$, whereas T_{int} shows an average temperature of $28.2^{\circ} \pm 0.8^{\circ}\text{C}$. These measurements imply either effective cooling of the borehole through

F137. CBTT temperature measurements obtained while drilling Core 193-1188A-4R in the Snowcap hydrothermal site, p. 248.



pumping an average of 50 strokes per min (spm), which is ~250 gallons per min (gpm), or very cool, shallow subsurface conditions for this area.

The tool was disassembled and cleaned thoroughly after retrieval. Several checks were made to determine the erratic behavior in data recording times and communication. In the meantime, the DSA/CBTT pressure case was deployed in Sites 1189 and 1191 with maximum temperature thermometers to provide an idea of downhole temperature conditions while troubleshooting the CBTT electronics continued. The maximum temperature measurements recorded with the thermometers showed that the conditions were favorable for attempting an LWD hole at Site 1189 (see “[Downhole Measurements](#),” p. 59, in the “[Site 1189](#)” chapter). During the deployment of the DSA/CBTT pressure case at the Satanic Mills hydrothermal site (Site 1191), the bit, core barrel, and DSA pressure case were lost at this site (see “[Operations Summary](#),” p. 2, in the “[Site 1191](#)” chapter), ending any other potential deployment of the CBTT during Leg 193.

Hole 1188B

Temperature Measurements

On 21 December 2000, Hole 1188B was reentered and the UHT-MSM temperature probe from the University of Miami was deployed (see “[Downhole Measurements](#),” p. 27, in the “[Explanatory Notes](#)” chapter). The bottom of the drill pipe encountered a restriction at 3 mbsf, and the UHT-MSM penetrated to a logging total depth (TD) of 7 mbsf. The tool recorded a maximum temperature of 4.8°C during a 15-min stationary measurement (Fig. [F138A](#)).

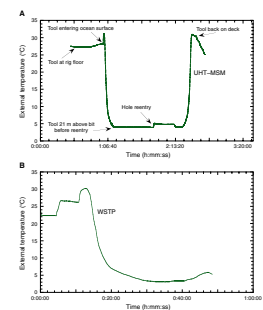
Following the UHT-MSM deployment, the WSTP was lowered to a depth of 6 mbsf for a 15-min station (Fig. [F138B](#)). The maximum recorded temperature was 5.8°C, and a water sample was obtained, although problems with the valve were reported (see “[Geochemistry](#),” p. 65).

LWD Operations

On 25 November 2000, drilling operations for the first ODP deployment of the LWD RAB tool began soon after the lithium batteries arrived from Rabaul, New Britain (PNG). The batteries did not arrive in Guam before our departure on 14 November 2000, consequently, they were shipped to Rabaul where they were transported to the *JOIDES Resolution* on a helicopter. Upon arrival, they were promptly tested and revived with a 150-Ω resistor for several minutes prior to assembling the RAB. After the batteries were installed, the tool was initialized and the Anadrill engineer began the assembly of the 9.875-in RAB BHA (see “[Downhole Measurements](#),” p. 27, in the “[Explanatory Notes](#)” chapter) with the assistance of the rig floor crew. Once the RAB was within several meters of the seafloor, the VIT camera was lowered and a suitable location was found for beginning drilling operations in Hole 1188B. Spudding was delayed by ~1.5 hr because drilling engineers were servicing and calibrating the AHC system that had not been operational until this time.

Drilling began with a very high penetration rate (≥ 40 m/hr) in the upper 8 mbsf. At 13 mbsf, a hard formation was encountered as it stalled the top drive and required ~100,000 klb of overpull to get free. Two more difficult-to-drill zones were encountered at 27 and 64 mbsf.

F138. Temperature measurements, Hole 1188B, p. 249.



The penetration rate slowed down to ~2 m/hr at 68 mbsf, and finally at 72 mbsf, the LWD operations were terminated. The decision to stop 3 m short of the original target depth was based on our previous experiences in Holes 1188A and 1189A (see “Site 1188,” p. 8, and “Site 1189,” p. 9, both in “Operations Summary” in the “Leg 193 Summary” chapter) as well as the significant decrease in penetration rates toward the bottom of the hole.

A FFF was deployed after LWD operations were finished and before pulling out of the hole with the intent of reentering with the ADCB and deepening the hole (see “First Return to Site 1188,” p. 9, in “Operations Summary” in the “Leg 193 Summary” chapter). After retrieving the RAB, we noticed that the tool was in good condition with only a few scratches and slight wear on the resistivity buttons.

LWD Data Quality

Sepiolite mud was used to flush drill cuttings out of the hole. The mud weight was determined to be 8.9 pounds per gallon (ppg), and mud resistivity was determined to be 0.183 Ωm using the Schlumberger mud resistivity meter. These parameters, along with the bit size, were used for applying environmental corrections to the data.

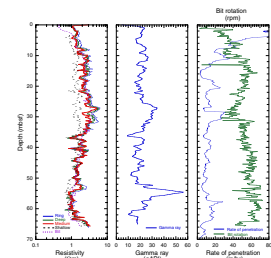
The RAB tool in memory mode records data as a function of time. At the surface during deployment, time and depth data were recorded with the depth from Geolograph. The time-depth file was corrected for heave as explained in “Downhole Measurements,” p. 27, in the “Explanatory Notes” chapter. The corrected surface time-depth file was then used to match the recorded downhole time file with the surface depth data, thus generating a depth file for the RAB data.

The RAB tool provides electrical images of the borehole wall with three different levels of investigation (deep, medium, and shallow), as well as individual log curves of electrical resistivity at the same three depths of investigation and of natural radioactivity. The RAB tool records the total gamma radiation but not its spectrum. Therefore, the contribution of the main radioactive elements, such as potassium, thorium, and uranium, cannot be individually separated from the total spectrum measurements. The log curves of electrical resistivity and gamma ray are displayed together with the ROP and bit rotation in Figure F139.

At the beginning of the LWD operations, the optimal ROP was determined to be 20–27 m/hr based on a sampling interval of 20 s. However, in the upper 32 m, the ROP was high and erratic. These data may provide an estimate of formation hardness or fracture zones because the resistance of the rocks to drilling fluctuated and made conditions difficult to maintain a constant penetration rate.

The quality of the electrical images of Hole 1188B are greatly influenced by artifacts causing stripes in the images, especially in the top and bottom intervals. There are several possible explanations that will require additional processing and a detailed look at the raw data and drilling parameters. First, errors during the time-depth conversion and filtering techniques applied to the time-depth file for removing the effects of vertical motion of the bit might be potential reasons for these problems. Second, the sea state was relatively calm (~0.5-m heave) during LWD operations, but the active heave compensator was used. Although the Geolograph should correct for the motion of the drawworks, the operation of the active heave compensator may also have contributed to the problems since the weight on bit is not accurately

F139. Log curves obtained from the resistivity-at-the-bit tool, Hole 1188B, p. 250.



known and the system was being calibrated minutes prior to spudding the hole. Third, a problem with the RAB time-frame file was found when the memory data were downloaded at the end of the run. The RAB tool acquisition time was 28.5 hr from the time of initializing to the time of download, and the RAB time frame file had recorded over 95 hr of data.

LWD Formation Evaluation

Electrical resistivities range from 0.2 Ωm for the shallow button (R_B) to 6.4 Ωm for the ring measurement (R_{RING}). These values tend to be low for volcanic rocks with rhyolite and dacite compositions. Young water-bearing volcanic rocks typically have values between 10 and 200 Ωm (Keller, 1966). The relatively low resistivity values may indicate a formation with either a high degree of alteration, exhibiting a significant amount of fracturing, or having high porosity. Gamma-ray values range from 1 to 56 gAPI with an average value of 21 gAPI. Both the average resistivity and gamma-ray log curves from the RAB were used for characterizing the lithostratigraphy of Hole 1188B. Figure F140 shows deep resistivity and gamma-ray curves, the logging units identified from the logs, and the core lithostratigraphic units found in the upper 75 m of neighboring Hole 1188A.

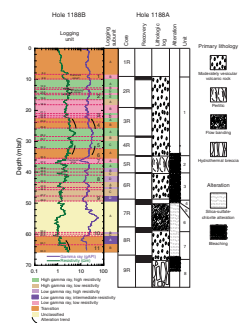
Eleven logging units were identified from five different relationships found in the electrical resistivity and gamma-ray measurements (Fig. F140). These relationships are high gamma ray–high resistivity, high gamma ray–low resistivity, low gamma ray–low resistivity, transitional responses, and unclear relations that are labeled unclassified.

Based on log responses and core observations, the high gamma-ray and high resistivity values of logging Units 2, 5, and 8 may reflect less fractured and/or less altered sections of rhyodacite lava flows. In many cases, this is supported by a decreasing ROP (Fig. F139) in logging units with high resistivity, which may be indicative of harder layers. Logging units characterized by low resistivities are interpreted to represent altered or fractured layers (logging Units 3, 7, and 9). The presence of both seawater or conductive clay minerals causes the resistivity to decrease. The higher gamma-ray values of logging Unit 9 may be explained by the presence of K- or U-bearing minerals as seen in the wireline logs from Holes 1188F, 1189B, and 1189C. Logging Unit 7 shows a sharp decrease in resistivity and low gamma-ray values that may represent a fractured zone, but it may also correspond to a high-porosity zone with abundant vesicles.

Logging Units 1, 4, 6, and 11 are interpreted as transitional layers. Logging Unit 1 represents the transition between a softer seafloor cover, also characterized by a high-penetration rate, and the harder layers of logging Unit 2. Logging Units 4 and 6 are interpreted as transitions in alteration and fracturing from a more massive logging Unit 5. Logging Unit 11 is a transitional layer at the bottom of the hole, where the rock properties or style of alteration seem to be changing.

Logging Unit 10 does not show a clear correlation between resistivity and gamma-ray measurements. The upper part of this unit is characterized by high resistivities that decrease with depth and the highest gamma-ray values of the entire upper 65 m, where the drop in resistivity occurs. This logging unit seems to represent a transition between a massive upper part of a flow to considerable alteration toward its base. The gamma-ray response in Hole 1188B suggests the presence of K- or U-rich minerals in logging Unit 10 (~52–60 mbsf). This is consistent

F140. Preliminary interpretation of the logging curves from the resistivity-at-the-bit tool, p. 251.



with core observations from Hole 1188A, suggesting higher clay concentrations in lithostratigraphic Units 6 and 7 at a similar depth (50–68 mbsf). The XRD mineralogical analyses and core observations also suggest the presence of illite and/or chlorite, which generally have high potassium and thorium contents (see “[Hydrothermal Alteration](#),” p. 33).

Variations within the 11 logging units were subdivided into 31 logging subunits (Fig. F140). These subdivisions are based on the same relationships used to describe the 11 logging units described above. In these subdivisions, two more relationships were recognized, low gamma ray–high resistivity and low gamma ray–intermediate resistivity. The logging subunits represent small-scale variations of the log responses within the logging units (e.g., the thin layers of low resistivity identified in logging Subunits 2B and 2D). Interpretation of the additional logging data relationships awaits postcruise research.

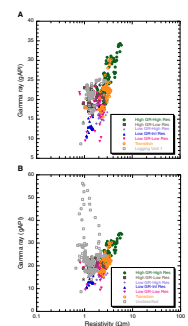
In the upper 39 m of the hole, there is a positive correlation between the electrical resistivity and gamma ray (Fig. F140). Most of the rocks in this interval are characterized by high resistivity and gamma-ray values or low resistivity and gamma-ray values. One exception is logging Subunit 3A, which shows low resistivity and high gamma-ray values. This log response may be indicative of a layer rich in conductive K- or U-bearing minerals. Two factors may explain the predominantly positive correlation between resistivity and gamma ray above 39 mbsf. Alteration (i.e., bleaching) may lead to a decrease in radioactive elements; thus, gamma-ray values will be low in an altered zone. However, a predominance of seawater in fractures and voids may also cause the same effect. Lithologic units from the equivalent section of Hole 1188A show that in the upper 39 m, rocks tend to vary from relatively fresh to strongly bleached (see “[Hydrothermal Alteration](#),” p. 33). Unfortunately, because of the poor core recovery, only a few physical properties, petrological, and geochemical analyses exist from this section, and the contribution of the radioactive elements to the gamma-ray radiation is not known.

Below 39 mbsf, a correlation between resistivity and the gamma-ray logs is not as clear, especially in logging Unit 10 (Fig. F140). Most of the logging units below this depth exhibit an opposite trend to the one observed above 39 mbsf (i.e., many units are either characterized by high resistivity and low gamma-ray values or vice versa). The highest gamma-ray values are recorded in logging Unit 10, but there is no apparent correlation with resistivity measurements. The correlation between electrical resistivity and gamma-ray measurements exhibits a relatively linear trend for most of the logging units, with the exception of logging Unit 10 (Fig. F141).

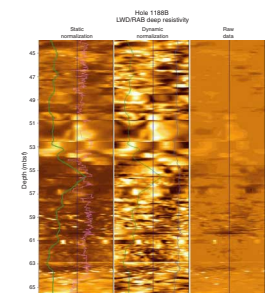
LWD Borehole Images

Figure F142 shows the image of the deep resistivity between 44.5 and 65.5 mbsf after different steps of image processing. For the raw data image, the electrical resistivity values were distributed into 18 classes, each with a different color. An equalized histogram method was used for enhancement of the other two images. This method optimizes the use of a given number of colors (N) in a given interval of the image by determining the color thresholds ($N - 1$) that will partition the data values into (N) equal populations—32 in this particular case. The processing module BorNor, which is part of the GeoQuest Geoframe software package, was used for providing two types of image normalization for the

F141. Covariation of electrical resistivity vs. gamma ray, p. 252.



F142. Images of the deep resistivity from the resistivity-at-the-bit tool, p. 253.



Leg 193 RAB data—static and dynamic. Static normalization is a computation where a window covering the entire depth interval is specified. In contrast, dynamic normalization requires a separate set of computations repeated at regularly spaced positions over the specified depth interval. This method uses a sliding window of relatively short length, which for this case was the default value of 0.6 m. The successive windows have an overlap of 75%, and color thresholds are interpolated between the windows so that a continuous movement of the normalization is simulated.

The raw data image gives an overview of the section but the least amount of detail. Static normalization allows for better interpretation than the raw data image as contrast is enhanced and details are highlighted. The dynamically normalized image shows the most detail and fine features. However, it is only suitable for interpretation on a small scale. As the color thresholds are computed in a sliding window, the same color at two widely separated depth points does not necessarily have the same resistivity. With increasing levels of processing, the problems outlined previously in the data quality are magnified. The raw image data show problems only locally, the statically normalized image shows more problematic sections, and the dynamically processed image shows the greatest effects of data degradation. Not much information was gained from the dynamic image after shipboard processing, and further work is needed before the image is suitable for structural analyses.

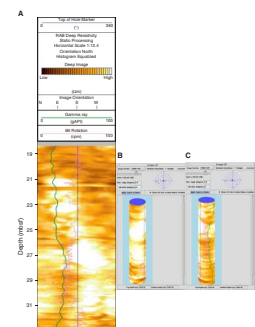
The static image may be suitable for correlation with the results of the formation evaluation. The light-colored (highly resistive) layers between 50 and 54 mbsf (Fig. F142) correlate with the upper, highly resistive zone of logging Unit 10. In Figure F143, the depth interval between 18.7 and 32 mbsf is shown as two-dimensional and three-dimensional image representations. The light-colored features correspond to the high resistivity layers of logging Units 3, 4, and 5. Although the resistivities for the entire logged section tend to be low, the high resistivity contrast and patchy nature of this subvertical feature may imply higher concentrations of anhydrite, as the reported resistivity values for this calcium sulfate are in the range of 10,000 Ωm or higher (Serra, 1972a, 1972b; Rider, 1996). The low resistivity and gamma-ray values found in logging Subunits 3B and 3D also appear as darker colors or conductive features in Figure F143.

Hole 1188F

Operations

On 21 December 2000, wireline logging operations in Hole 1188F began with the deployment of a high-temperature/pressure telemetry gamma-ray cartridge (HTGC) and dual induction resistivity (DIT-E) tool string combination with real-time cable head temperature capabilities (MTEM). The water depth was estimated from pipe measurements at ~1653 mbrf. The first casing string (13.375 in) was set to a depth of 58.9 mbsf, and the base of a second casing string (10.75 in) was at 190.4 mbsf (see “Introduction,” p. 1). The drill pipe was placed at ~185 mbsf. A wiper trip to the bottom of the hole was done ~12 hr before logging operations began, and 15 bbl of sepiolite mud was circulated at the end of that hole-cleaning operation. A sepiolite mud weight of 8.9 ppg and a mud resistivity of 0.183 Ωm were used to apply corrections to the logging data.

F143. Detail color image of deep resistivity between 18.7 and 32 mbsf using a static normalization technique, p. 254.



The MTEM-HTGC-DIT-E tool string was deployed, but the wireline heave compensator (WHC) was not used because the system would not power up. A problem was found with the limit switch as the piston extended to a maximum position sending a current imbalance (current flowing on the ground line) to the ground fault interrupt (GFI) and causing the GFI to shut the system down. An external power supply was used to manually move the piston to a middle position where the limit switch would not affect the system. The WHC was then used during the second and third tool string deployments.

The second wireline deployment included the MTEM, the hostile environment natural gamma-ray sonde (HNGS), the accelerator porosity sonde (APS), and the hostile environment lithodensity sonde (HLDS). The third tool string combination consisted of the MTEM, the natural gamma-ray tool (NGT), the dipole sonic imager (DSI), and the FMS. During the last two logging runs, heave measurements were recorded with the guideline tensionometer encoder that was installed on the WHC for LWD operations. These records show <1-ft average heave during the second deployment and <1-m average motion for the third run (Fig. F144).

Drilling operations achieved a TD of 386.7 mbsf in Hole 1188F, and all wireline tool deployments reached a logging TD of 356 mbsf. An obstruction was encountered 30 m above the hole's TD, and all attempts to get past this were unsuccessful. Prior to the beginning of the logging operations, a borehole restriction was encountered at 362 mbsf during a wiper trip, and, although this spot is 6 m deeper than the logging TD, the hole problems are probably related.

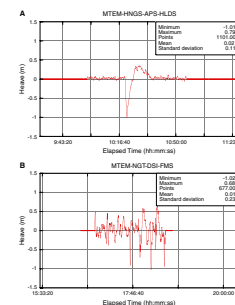
On 26 December 2000, 5 days after the hole was drilled, the UHT-MSM temperature probe was lowered on the sand line to a depth of 20 m above the seafloor, and then Hole 1188F was reentered. Core barrel sinker bars were placed on top of the tool to add weight, and the UHT-MSM was deployed prior to reentering the hole to minimize the disturbance in the water column by displaced fluids as the tool was descending. The pipe was lowered 8 mbsf, and downlog temperatures were recorded at a sampling rate of 1 s and a logging speed of 250 m/hr until a logging TD was reached at 361 mbsf. The uplog was recorded using the same parameters and logging speed. Following the temperature log, the WSTP was deployed to a depth of 104 mbsf. On 29 December 2000, once again Hole 1188F was reentered and the UHT-MSM probe and WSTP were deployed following the similar procedures. The logging speed for the UHT-MSM was 300 m/hr, and the depth for the WSTP measurement was 207 mbsf.

Borehole Condition and Data Quality

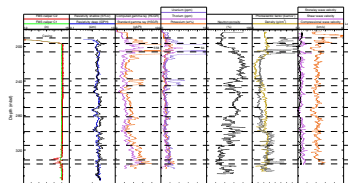
Caliper measurements show that Hole 1188F is oversized (Fig. F145). The caliper from the HLDS measured 17.26 in throughout the entire logged interval, whereas the FMS calipers measured 15.14 in throughout the same interval. The maximum extension of these calipers is 17.75 and 15.5 in, respectively. The less-than-maximum extension on the FMS caliper lead us to question the accuracy of the borehole measurements. To confirm the accuracy of the borehole measurements, the second tool string was run inside the 10.75-in casing with the HLDS caliper open. The caliper measured 10.39 in, suggesting that the borehole measurements with this caliper (>17 in) were correct.

The HLDS and FMS calipers were calibrated at 8 and 12 in before the logging runs because of the 7.25-in ADCB bit that was used to drill Hole

F144. Heave measurements recorded with the guideline tensionometer encoder during the second and third wireline run, Hole 1188F, p. 255.



F145. Overview of the wireline logs, Hole 1188F, p. 256.



1188F. However, nonlinear changes may occur as the maximum aperture is reached; hence, the calipers were checked after logging operations concluded. On deck, the maximum extension of the HLDS caliper measured at 17.75 in, a 0.49-in difference with the recorded downhole data, and the FMS caliper arms measured at 15.5 in, a 0.36-in difference with the borehole measurements. Therefore, we interpret the diameter of the borehole to be in excess of 15 in and probably ≥ 17 in.

The enlarged diameter of the borehole affects several of the measurements. The FMS produced only several short intervals with high-resolution images, and most of the borehole has intervals where only a range of one to three pads were in direct contact with the borehole walls. In most instances, the neutron porosity data are high and density readings are low with values approaching 1 g/cm^3 between 210 and 240 mbsf, which can also be explained by an enlarged borehole.

Electrical Resistivity Measurements

Electrical resistivity values measured in Hole 1188F are low throughout the entire logged interval. Deep resistivity measurements range from 0.4 to 2.3 Ωm , and the shallow-resistivity log shows variations between 1.0 and 3.4 Ωm (Fig. F145). The medium-resistivity log shows isolated spikes with higher resistivity values that range up to 43 Ωm . These spikes do not show any correlation with the other logs and are probably caused by a malfunction of the medium-resistivity receiver. For this reason, this log was not included in the site report.

Natural Radioactivity Measurements

Formation natural radioactivity was measured during each run and with three different tools. The HTGC measured total gamma counts, whereas the HNGS and NGT provided spectral measurements. The different gamma-ray tools show good correlation between each other.

All gamma-ray curves show high values ranging up to 558 gAPI for the interval between 197.3 and 208.9 mbsf (Fig. F145). The spectral gamma-ray measurements show a significant increase in uranium within this interval. Uranium values increase up to 64 ppm. Potassium values are also slightly elevated, with values as high as 2.7 wt%. Another interval with increased gamma-ray and uranium values is present between 238.7 and 245.0 mbsf. Gamma-ray values increase to 62 gAPI and uranium values to 5.2 ppm. Besides these anomalies, gamma-ray values are between 2.8 and 80 gAPI. A good correlation between the standard gamma-ray curve and the potassium log indicates that potassium makes a significant contribution to the gamma-ray spectrum. Both the total gamma ray and the potassium values show downward increasing trends between 255 and 275 and between 300 and 338 mbsf.

Neutron Porosity and Density Measurements

Neutron porosity values range from 20% to 94% with an average value of 54%. These values are very high when compared to the core porosities measured, which range from 12% to 28% (see “Physical Properties,” p. 74). These high porosity values may be explained by the enlarged borehole, the overall high fracturing of the rocks as observed in the FMS images, and, to some degree, the presence of hydrous minerals such as clay minerals (see “Downhole Measurements,” p. 27, in the “Explanatory Notes” chapter).

Density measurements show values ranging between 1.1 and 2.7 g/cm³. The average density for the entire logged interval is 2.0 g/cm³. Densities are especially low in the depth interval between 210 and 238 mbsf, where the values decrease to slightly above 1 g/cm³. The low values are indicative of the large diameter of the borehole, where, in many cases, the tool standoff reaches values close to or >1 in. Above 210 mbsf and below 298 mbsf, density values are higher, interrupted only locally by narrow peaks of low values. The photoelectric factor (PEF) values range between 1.4 and 11.7 barn/e⁻. The highest values correlate with the gamma-ray anomaly between 197.3 and 208.9 mbsf. However, for most of the borehole, the PEF reaches a maximum of 5.0 barn/e⁻, with an average value of 2.1 barn/e⁻. Values are low between 210 and 298 mbsf and show a slight increase below 298 mbsf.

Sonic Measurements

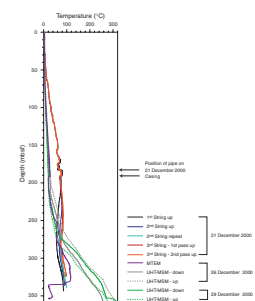
Compressional wave velocities range from 2.3 to 5.9 km/s. The mean value is 3.1 km/s. In general, these compressional wave velocities are low for dacite or rhyodacite. This may be a direct effect of the large dimensions of the borehole and the relatively high fracture density of the formation. The depth intervals between 197.3 and 208.9 mbsf and also between 270.5 and 281 mbsf show significant changes in velocity with the largest low-velocity zones of the entire logged interval. The interval between 197.3 and 208.9 mbsf is especially unique because the porosity is low, whereas density, gamma-ray, and photoelectric effect values tend to be high. Postcruise processing and detailed analysis of the shipboard slowness time coherence processing will determine if the low-velocity zone is not a processing artifact. Stoneley and shear wave velocities are also low (Fig. F145). The shear wave velocity profile shows a high of 2.5 km/s at the top of logging Unit 2 that corresponds to highs in both bulk density and PEF. However, for most of the hole, the recorded shear wave velocities are below 2.0 km/s.

Temperature Measurements

Temperature measurements were made during wireline operations on 21 and 22 December 2000, as well as 5 and 7 days later with the UHT-MSM temperature probe. These profiles are displayed in Figure F146. The MTEM located in the cable head was used in every wireline deployment during the 20 to 21 December 2000 logging operations. The profiles show an average steady increase in temperature from inside the 13.375-in casing string starting at 30 mbsf to ~234 mbsf. Temperature lows were recorded inside the 10.75-in casing from 156 to 160 mbsf and from 174 to 183 mbsf. A temperature high was also recorded from 184 to 191 mbsf. The high corresponds to the transition between the logging BHA and the 10.75-in casing. The low from 174 to 183 mbsf corresponds to the tool entering the logging BHA, whereas the low at 156–160 mbsf is well inside the pipe.

The interval from 234 to 289 mbsf shows that all 20 and 21 December 2000 temperature profiles have a decreasing trend followed by increasing temperatures until reaching the logging TD at 357 mbsf. The maximum recorded temperature in these runs was 99.6°C. This temperature was recorded with the second string at the bottom of the hole during the repeat section. The second pass with the FMS showed a maximum temperature of 98.4°C at ~15 m shallower than the previous high-temperature reading.

F146. Temperatures recorded in Hole 1188F during wireline logging operations and with the UHT-MSM temperature probe, p. 257.



The temperature profile recorded 5 days later using the UHT-MSM probe shows a much smoother profile than the temperature measurements from the wireline operations, especially because the drill pipe was placed at 20 mbsf. In the upper part of Hole 1188F, temperatures are lower than those obtained with the wireline temperature sensor down to 250 mbsf. However, a sharp increase in temperature is observed starting from 250 mbsf to the bottom of the hole. The maximum recorded temperature is 304°C, which is an increase of 204°C over the previous wireline measurements. There were concerns about the reliability of these measurements, especially after a WSTP measurement at 107 mbsf recorded only 12°C and faulty pressure readings were obtained with the UHT-MSM probe during the previous run. This uncertainty led to the deployment of the wireline telemetry cartridge that was used during the previous wireline measurements. This tool recorded increases with depth until it failed at ~338 mbsf (Fig. F146), where the temperature readings dropped from 118° to ~20°C. When the tool was back on deck, maximum-temperature thermometers that were placed in the cable head prior to deployment provided measurements >260°C. These measurements and the state of the wireline sensor, which had the electrical leads fused together, confirmed the previous measurements made with the UHT-MSM temperature probe.

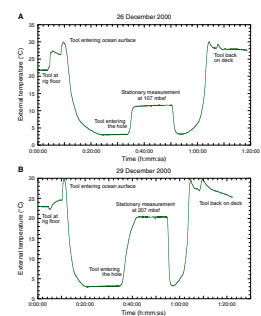
Additional temperature measurements were planned for 29 December 2000 to determine the amount of thermal rebound in Hole 1188F and to estimate a suitable depth for obtaining water samples. The UHT-MSM tool recorded temperature and pressure as a function of time. To obtain depth, the internal tool clock was synchronized with rig floor time and the computer in the subsea shop. The computer in the subsea shop was then used to obtain time-depth records of the sand line as the tool was being lowered in the hole. Attempts to match times proved to be a time-consuming task because of the different sampling rates between the tool (1 sample/s) and the subsea computer (1 sample every 4 or 5 s). In addition, in many instances the depth files from the subsea shop contained records from previous deployments; hence, depth matching required detailed inspection of several thousand data points before a correlation was possible. This process proved to be too lengthy; therefore, quick depth estimates based on pressure records and previous temperature profiles were made for determining the WSTP depth estimates. After downloading the time-temperature measurements from the UHT-MSM and filtering the time-depth files from the subsea shop, times were matched and the two files were merged to get the temperature measurements as a function of depth (Fig. F146). The maximum temperature recorded during this deployment was 313°C.

WSTP deployments in Hole 1188F were made to depths of 107 and 207 mbsf. The profiles show maximum temperatures of 12° and 20°C (Fig. F147) that correlate well with the UHT-MSM profiles made shortly before the WSTP measurements. Unfortunately, estimates from previous records failed to provide higher-temperature water samples because the depth of the cold water front seemed to be increasing as a function of time, and estimates using pressure records were 70 m shallower than the desired 60°C temperature range.

Formation Evaluation

Eleven logging units were defined in Hole 1188F (Fig. F145). The top-most unit (logging Unit 1) is characterized by increasing values in potassium, thorium, and uranium concentrations with depth. High values

F147. Temperatures recorded in Hole 1188F during deployment of the WSTP, p. 258.



of electrical resistivity and density and low values of neutron porosity suggest a low degree of fracturing (Fig. F145). FMS images show that this unit corresponds to the part of the borehole that was cemented during casing operations (Fig. F148). FMS images also show that the interval below the cemented part corresponds to a highly fractured interval followed by a zone showing breccias composed of high resistivity clasts and horizontal to subhorizontal fractures (Fig. F148). The zone between 202 and 207.5 mbsf is >15.5 in, and no FMS images were acquired; whereas, below this interval one pad shows glimpses of a brecciated zone suggesting that the brecciation is continuous for the entire interval from 196 to ~211 mbsf. This brecciated interval corresponds to the high uranium anomaly in logging Unit 2 (Fig. F145) and may correspond to a zone of predominantly lateral fluid flow or the presence of a low-angle fault. Total gamma-ray values in logging Unit 2 reach 558 gAPI, and uranium values go up to 64 ppm. Potassium and thorium are high, with values reaching 2.7 wt% for potassium and 4.8 ppm for thorium. The PEF is also high in this zone with a maximum value of 11.7 barn/e⁻.

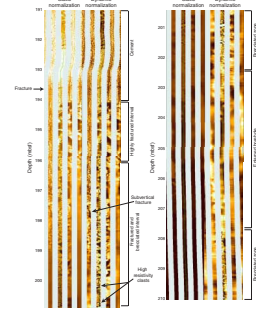
Very high neutron porosity and low density values characterize logging Unit 3. Log responses in this logging unit are probably strongly influenced by an enlarged borehole as shown in Figure F148. Electrical resistivities, which are less sensitive to variations in the size of the borehole than the neutron porosity and density measurements, show intermediate to high values that correlate with changes in porosity. Gamma-ray values are low, as well as photoelectric factor values.

A decrease in neutron porosity and an increase in density characterize logging Unit 4. Electrical resistivities are at an intermediate level, slightly decreasing downward. The upper part of logging Unit 4 (logging Subunit 4A) corresponds to a second anomaly in the gamma ray and uranium (Fig. F145).

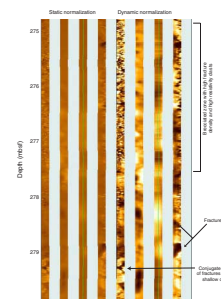
Logging Units 5 and 7 show intermediate to high electrical resistivity, neutron porosity, density, and compressional wave velocity values as well as low gamma-ray values. Partial FMS images of logging Unit 5 show a high degree of brecciation that features a high fracture density predominantly exhibiting horizontal to subhorizontal orientations. Logging Units 5 and 7 are separated by logging Unit 6, which is characterized by low electrical resistivity and sonic velocity values and high neutron porosity values. Partial FMS images show a highly brecciated zone composed of high-resistivity clasts and high fracture density (Fig. F149).

The transition to logging Units 8 to 11 is marked by a slight but sharp increase in the photoelectric factor log at 298 mbsf. Logging Units 8 and 9 are identified by high electrical resistivity and density values and intermediate to high compressional wave velocities. Gamma ray values increase downward in both units. FMS images of this unit show that although there is a high fracture density, there is a small amount of brecciation in this unit (Fig. F150). The difference between these two units is in the neutron porosity, which is lower in logging Unit 9 and confirms the FMS measurements. Logging Unit 10 is a thin unit with slightly lower electrical resistivities than logging Units 8 and 9 and with increased values of the total gamma-ray and potassium log and of the photoelectric factor log. Logging Unit 11 is the lowest logging unit. It shows intermediate to high electrical resistivity, neutron porosity, and density values.

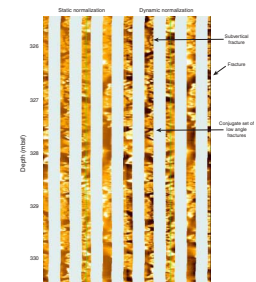
F148. FMS images showing a 19-m interval immediately below the 10.75-in casing shoe in Hole 1188F, p. 259.



F149. An FMS section of Hole 1188F showing numerous fracture patterns and brecciation within logging Unit 6, p. 260.



F150. The bottommost part of the Hole 1188F showing the best FMS images of the entire logged interval, p. 261.



REFERENCES

- Allen, R.L., 1988. False pyroclastic textures in altered silicic lavas, with implications for volcanic-associated mineralization. *Econ. Geol.*, 83:1424–1446.
- Beaufort, D., and Meunier, A., 1994. Saponite, corrensite and chlorite/saponite mixed-layer minerals and saponite in the Sancerre-Couy deep drill hole (France). *Clay Miner.*, 29:47–61.
- Borradaile, G.J., Keeler, W., Alford, C., and Sarvas, P., 1987. Anisotropy of magnetic susceptibility of some metamorphic minerals. *Phys. Earth Planet. Inter.*, 48:161–166.
- Clark, S.P. (Ed.), 1966. *Handbook of Physical Constants*: Spec. Publ.—Mem. Geol. Soc. Am., 97.
- Collinson, D.W., 1983. *Methods in Rock Magnetism and Palaeomagnetism: Techniques and Instrumentation*: London (Chapman and Hall).
- Gieskes, J.M., Gamo, T., and Brumsack, H., 1991. Chemical methods for interstitial water analysis aboard *JOIDES Resolution*. *ODP Tech. Note*, 15 [Online]. Available from World Wide Web: <http://www-odp.tamu.edu/publications/tnotes/tn15/f_chem1.htm>. [Cited 2001-11-07]
- Hopkinson, L., Roberts, S., Herrington, R., and Wilkinson, J., 1999. The nature of crystalline silica from the TAG submarine hydrothermal mound, 26°N Mid-Atlantic Ridge. *Contrib. Mineral. Petrol.*, 137:342–350.
- Hrouda, F., and Kahan, S., 1991. The magnetic fabric relationship between sedimentary and basement nappes in the High Tatra Mountains, N. Slovakia. *J. Struct. Geol.*, 13:431–442.
- Humphris, S.E., Herzig, P.M., Miller, D.J., Alt, J.C., Becker, K., Brown, D., Brüggemann, G., Chiba, H., Fouquet, Y., Gemmell, J.B., Guerin, G., Hannington, M.D., Holm, N.G., Honnorez, J.J., Itturino, G.J., Knott, R., Ludwig, R., Nakamura, K., Petersen, S., Reysenbach, A.-L., Rona, P.A., Smith, S., Sturz, A.A., Tivey, M.K., and Zhao, X., 1995. The internal structure of an active sea-floor massive sulphide deposit. *Nature*, 377:713–716.
- Keller, G., 1966. Electrical properties of rocks and minerals. In Carmichael, R.S. (Ed.), *Handbook of physical properties*, Spec. Publ.—Mem. Geol. Soc. Am., 97:553–577.
- Lackschewitz, K.S., Singer, A., Botz, R., Garbe-Schönberg, D., Stoffers, P., and Horz, K., in press. Formation and transformation of clay minerals in the sedimentary sequence of Middle Valley, Juan de Fuca Ridge, ODP Leg 169. *Econ. Geol.*, 95:361–390.
- Lofgren, G., 1971. Experimentally produced devitrification textures in natural rhyolitic glass. *Geol. Soc. Am. Bull.*, 82:111–124.
- Moss, R., Scott, S.D., and Binns, R.A., 2001. Gold content of eastern Manus Basin volcanic rocks: implications for enrichment in associated hydrothermal precipitates. *Econ. Geol.*, 96:91–107.
- Murray, R.W., Miller, D.J., and Kryc, K.A., 2000. Analysis of major and trace elements in rocks, sediments, and interstitial waters by inductively coupled plasma–atomic emission spectrometry (ICP-AES). *ODP Tech. Note*, 29 [Online]. Available from World Wide Web: <<http://www-odp.tamu.edu/publications/tnotes/tn29/INDEX.HTM>>. [Cited 2001-11-07]
- Parr, J.M., Binns, R.A., and Gemmell, J.B., 1996. Sulfide chimneys from the Satanic Mills site in the PACMANUS hydrothermal field, eastern Manus basin, Papua New Guinea. *Eos Trans. Amer. Geophys. Union*, 77:W120.
- Rider, M., 1996. *The Geological Interpretation of Well Logs* (2nd ed.): Caithness (Whittles Publishing).
- Schiffman, P., and Fridleifsson, G.O., 1991. The smectite-chlorite transition in drill-hole Nj-15, Nesjavellir geothermal field, Iceland: XRD, BSE and electron microprobe investigation. *J. Metamorph. Geol.*, 9:679–696.
- Serra, O., 1972a. Review of well-logging methods. Spec. Publ.—Mem. Bur. Rech. Geol. Min., 77:769–773.

- , 1972b. Well-logging and stratigraphy. Spec. Publ.—Mem. Bur. Rech. Geol., 77:775–797.
- Seyfried, W.E., Jr., Ding, K., Berndt, M.E., and Chen, X., 1999. Experimental and theoretical controls on the composition of mid-ocean ridge hydrothermal fluids: *Rev. Econ. Geol.*, 8:181–200.
- Smith, D.C., Spivack, A.J., Fisk, M.R., Haveman, S.A., Staudigel, H., and the Leg 185 Shipboard Scientific Party, 2000. Methods for quantifying potential microbial contamination during deep ocean coring. *ODP Tech. Note*, 28 [Online]. Available from the World Wide Web: <<http://www-odp.tamu.edu/publications/tnotes/tn28/INDEX.HTM>>. [Cited 2001-11-07]
- Sverdrup, H.U., Johnson, M.W., and Fleming, R. (Eds.), 1942. *The Oceans: Their Physics, Chemistry and General Biology*: Englewood Cliffs (Prentice-Hall).
- Tarling, D.H., and Hrouda, F., 1993. *The Magnetic Anisotropy of Rocks*: London (Chapman and Hall).
- Thompson, R., and Oldfield, F., 1986. *Environmental Magnetism*: London (Allen and Unwin).
- Uyeda, S., Fuller, M.D., Belshé, J.C., and Girdler, R.W., 1963. Anisotropy of magnetic susceptibility of rocks and minerals. *J. Geophys. Res.*, 68:279–291.
- Yeats, C.J., Binns, R.A., and Parr, J.M., 2000. Advanced argillic alteration associated with actively forming, submarine polymetallic sulfide mineralisation in the Eastern Manus Basin, Papua New Guinea. *Geol. Soc. Aust.*, 59:555. (Abstract)

Figure F1. Deep grooves cut into the interior of the first casing deployed in Hole 1188F. The underreamer arms on the fluid hammer appear to have gouged out metal while rotating up into the casing until they were wedged. Continued overpull changed the patterns of the grooves from a radial to an axial geometry.



Figure F2. Video photograph from VIT of the nested HRRS funnel (with bright albedo on the far right side of the image) above a standard reentry cone at Hole 1188F.

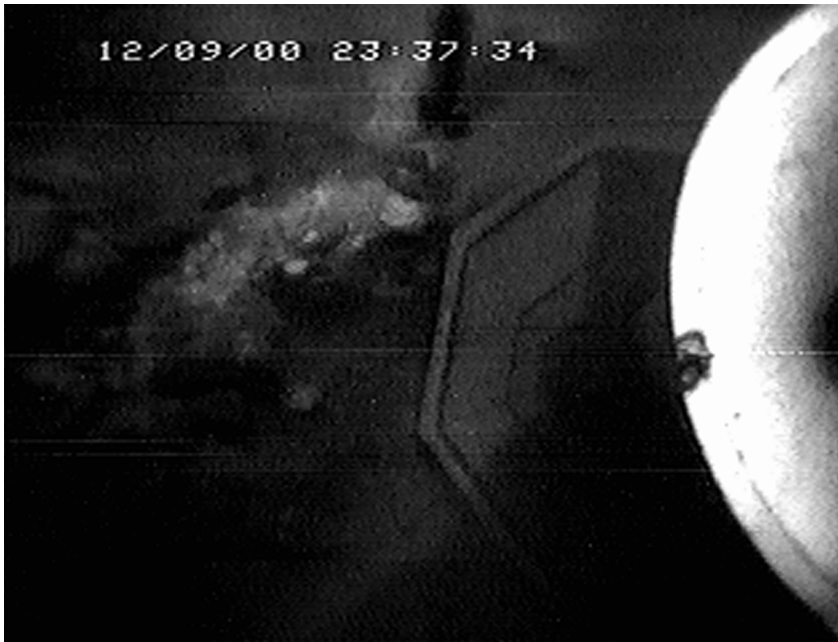


Figure F3. Calculated course of the vibration-isolated television (VIT) during the site survey prior to the spudding of Hole 1188A, and observed seafloor character. Bathymetric contours (5-m intervals) within the survey area are based on VIT cable measurement and sonar altimetry, calibrated to the actual drill pipe measurement depth of Hole 1188A. Contours outside the survey area are derived from submersible dives and have been added to show the general topography of the Snowcap hydrothermal site. Only the track from the initial survey is shown, but additional seafloor cover information from other surveys has been added. The Global Positioning System averaged locations for all of the holes at Site 1188 are also shown.

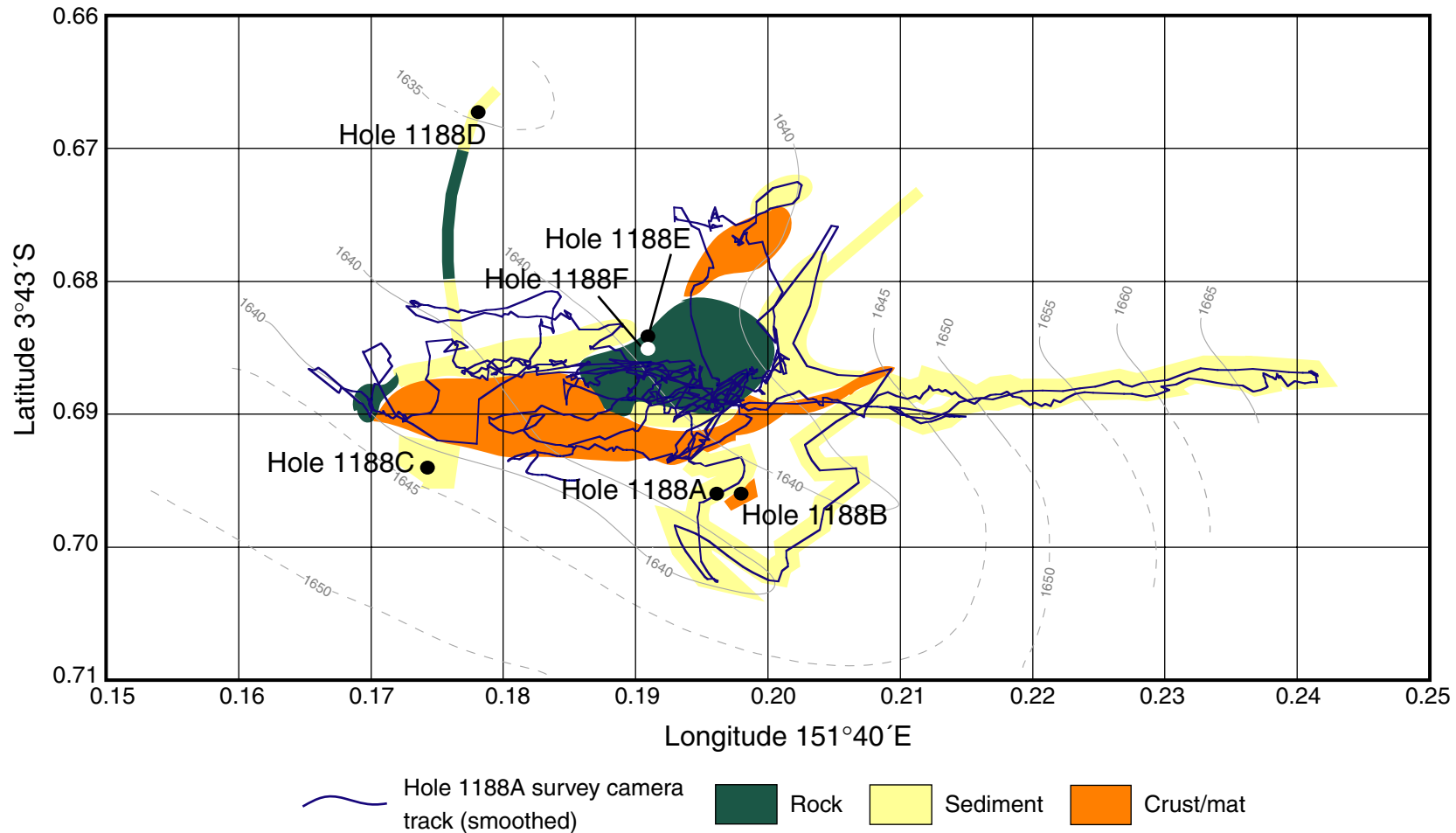


Figure F4. Graphic summary log for Hole 1188A showing the lithologic characteristics of the various units including alteration. See Figure F6, p. 45, in the “Explanatory Notes” chapter for the lithologic key. NR = no recovery.

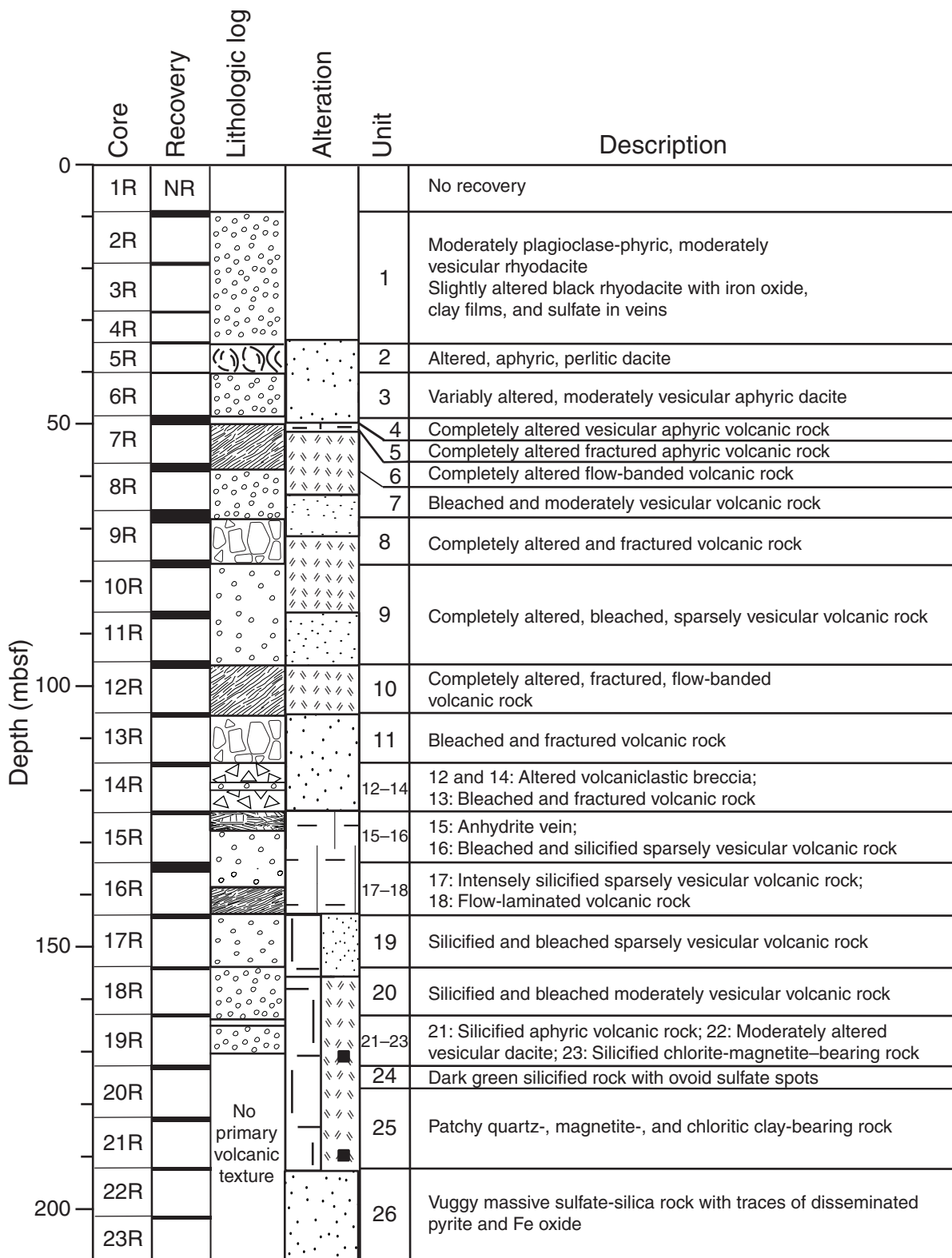


Figure F5. Close-up photograph of fresh, black, moderately vesicular rhyodacite from the upper part of Hole 1188A (Unit 1) (interval 193-1188A-4R-1, 0-13 cm).

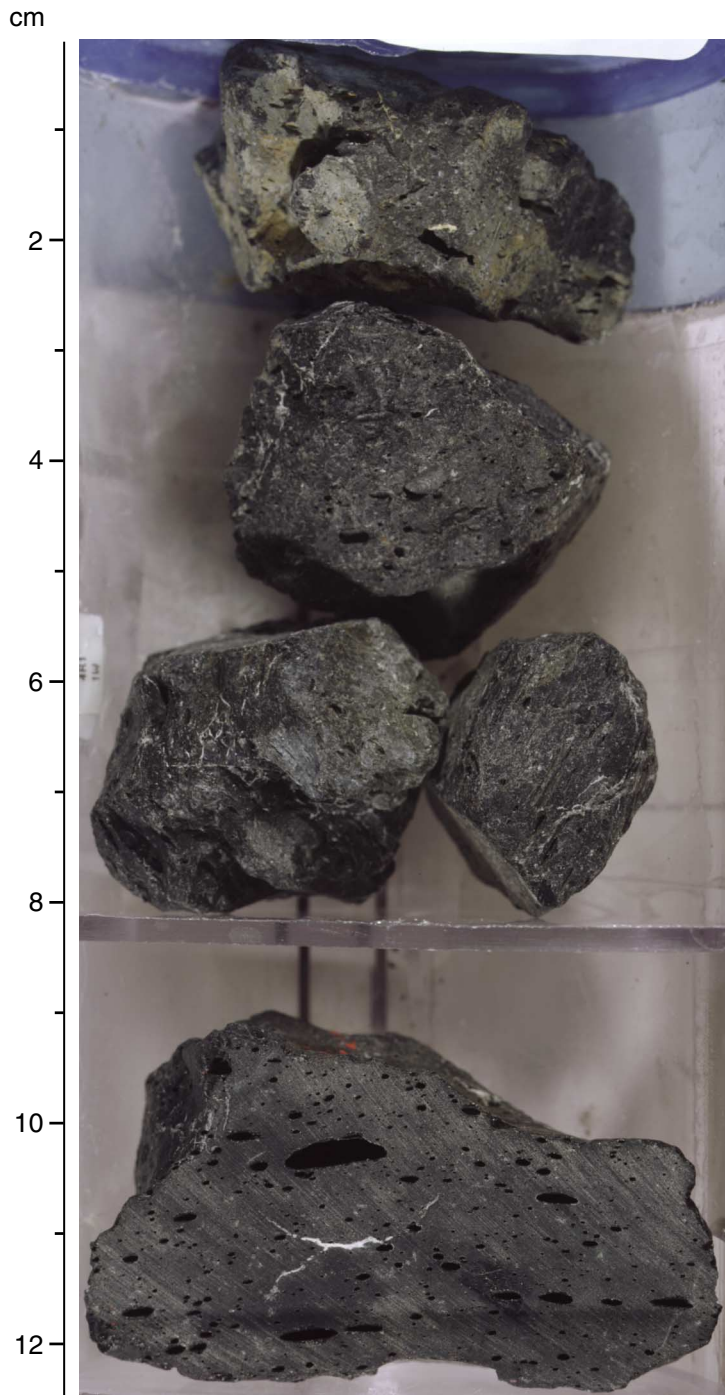


Figure F6. A. In this close-up photograph, the perlitic texture of aphyric dacite (Unit 2) indicates that the groundmass consisted of volcanic glass originally. Alteration proceeded preferentially along and outward from the perlitic cracks generating a pseudoclastic texture in some domains of the sample. In hand specimen, this unit has a sugary appearance. The arcuate perlitic cracks are enhanced by alteration generating light gray “islands” in a dark gray, irregular network of clay, opaline silica, and minor pyrite forming an apparent matrix (interval 193-1188A-5R-1, 36–48 cm). (Continued on next page.)

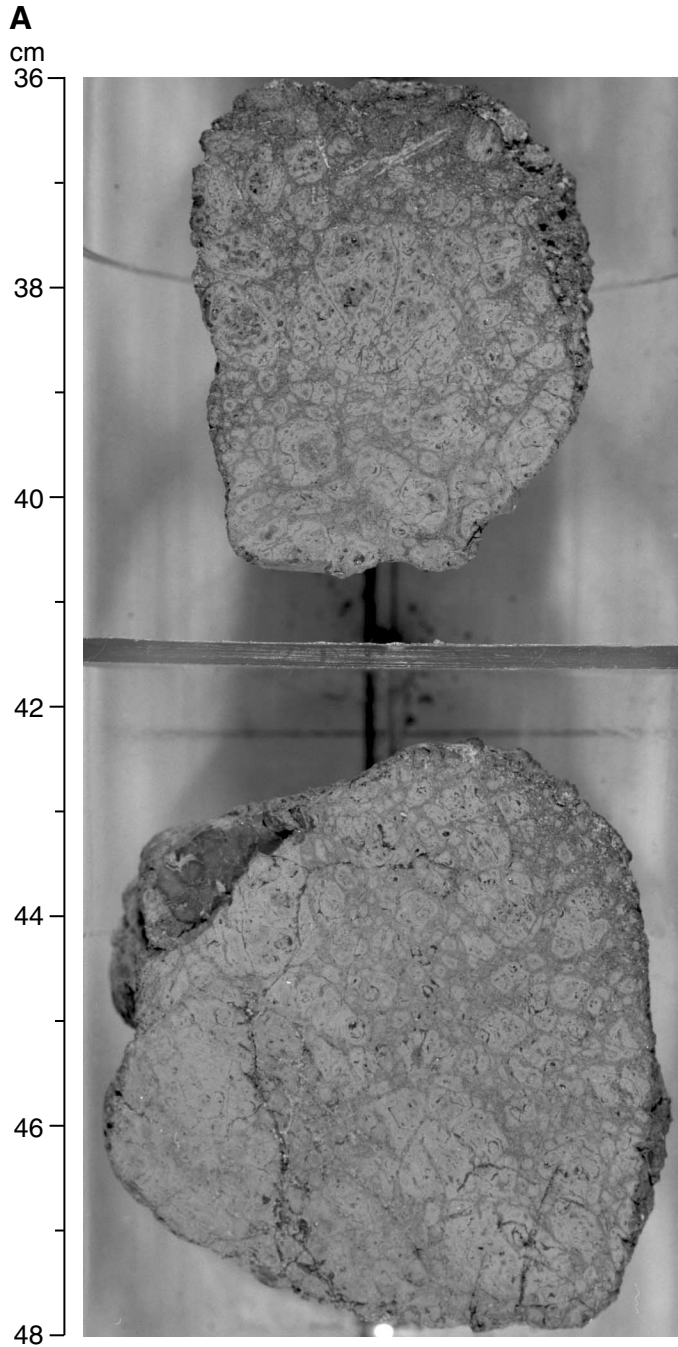


Figure F6 (continued). B. In thin section, well-preserved perlitic texture with scattered microlites is present within the “islands,” which are surrounded by alteration products. Width of view = 2.75 mm (Photomicrograph ID# 1188A_13; **thin section 3**).

B

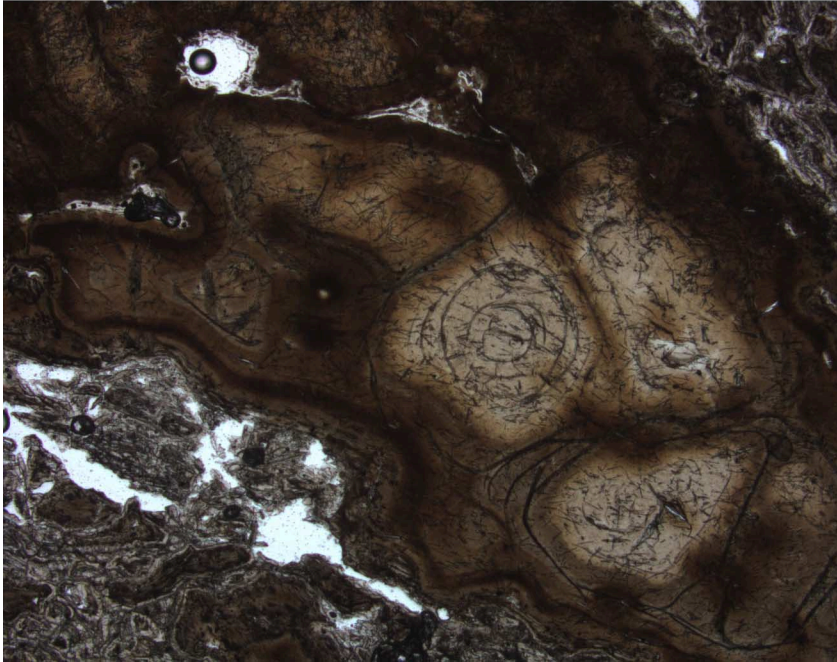


Figure F7. Close-up photograph of GSC altered rock (Unit 5) with remnant perlitic textures and anhydrite-(silica-pyrite) stockwork veining. We infer that the pseudoclastic texture of this sample is caused by the preferential replacement of perlitic cracks by dark alteration assemblages (interval 193-1188A-7R-1, 120–128 cm).

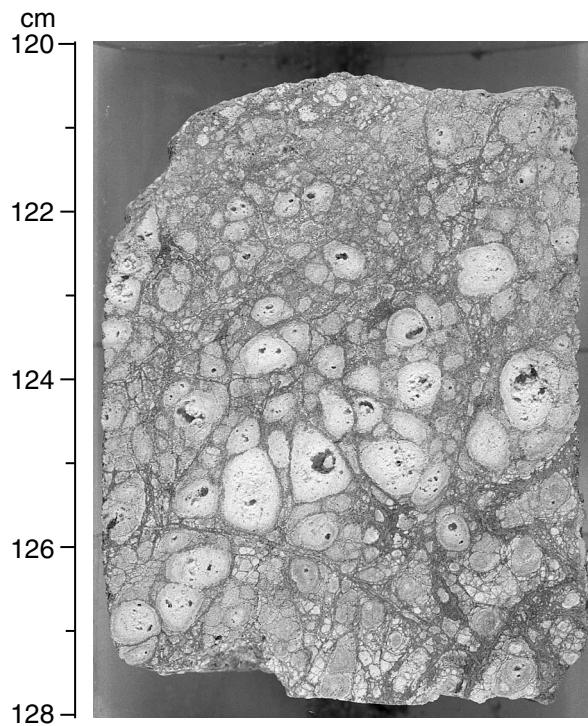


Figure F8. Close-up photograph in which flow banding can be recognized in the light gray parts of Unit 6 and is defined by alternating dark gray and light gray linear to fibrous domains preserving the primary igneous texture of the rock. Subsequent fracturing and alteration along irregular veins generated the brecciated, jigsaw-fit texture (interval 193-1188A-8R-1, 97-107 cm).

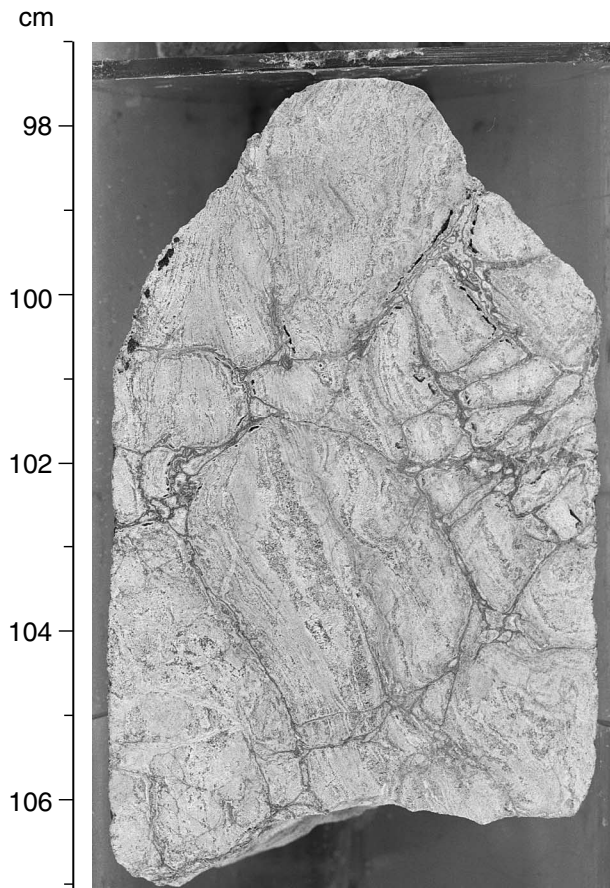


Figure F9. Close-up photograph of Unit 7, which consists of light gray to white, bleached, aphyric volcanic rock with preserved elongate vesicles. The core sample is pervasively bleached with a zoned alteration pattern toward a darker gray, less strongly bleached kernel (interval 193-1188A-9R-1, 16–29 cm).

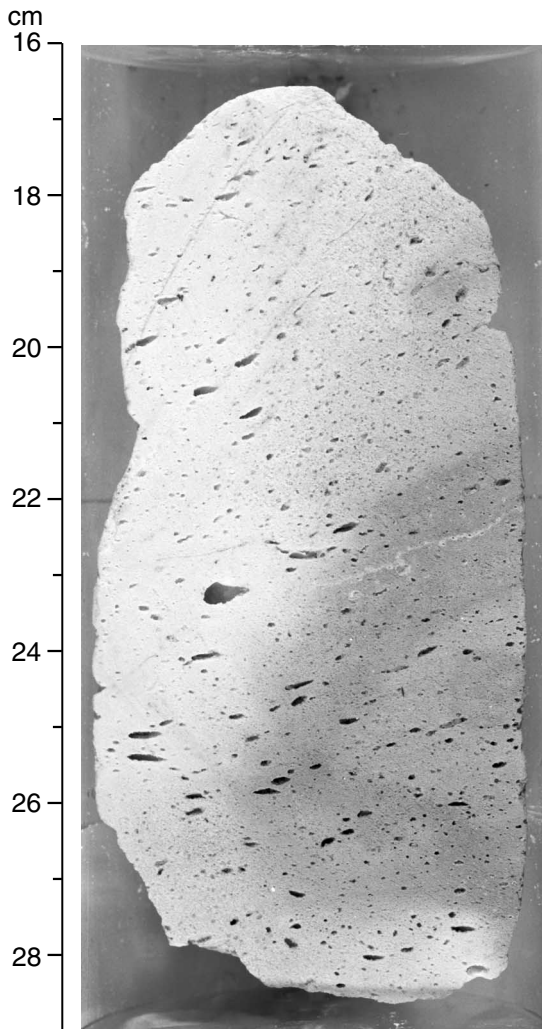
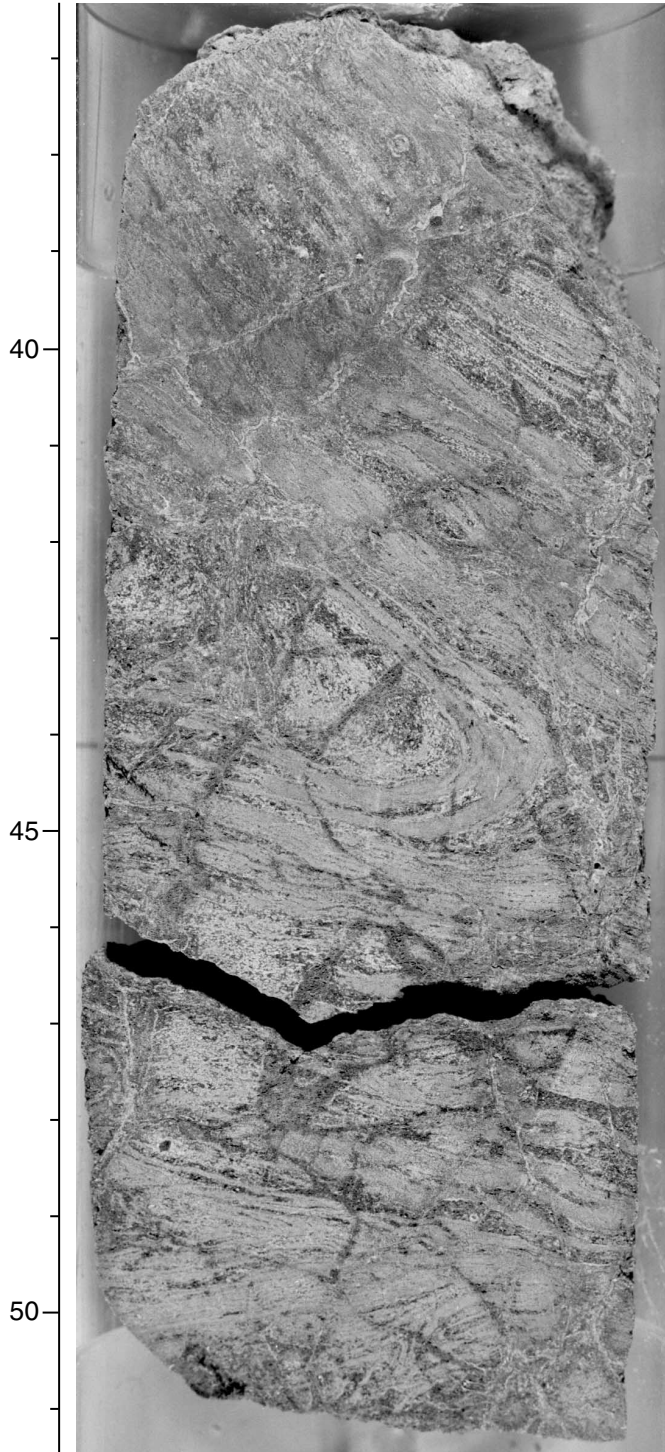


Figure F10. Flow banding in Unit 10 is locally deformed into isoclinal folds (interval 193-1188A-12R-2, 36–52 cm). A. Close-up photograph of hand specimen. B. Line drawing sketch of hand specimen highlighting folds and fractures.

A

cm



B

Interval 193-1188A-12R-2, 36-52 cm



0 2 cm

Figure F11. Unit 13 consists of completely bleached and sparsely vesicular volcanic rock that shows jigsaw breccia texture caused by the fracturing and silicification in the vein halos (interval 193-1188A-14R-1, 42–50 cm). **A.** Close-up photograph of hand specimen. **B.** Line drawing sketch of hand specimen highlighting fractures and alteration halos.

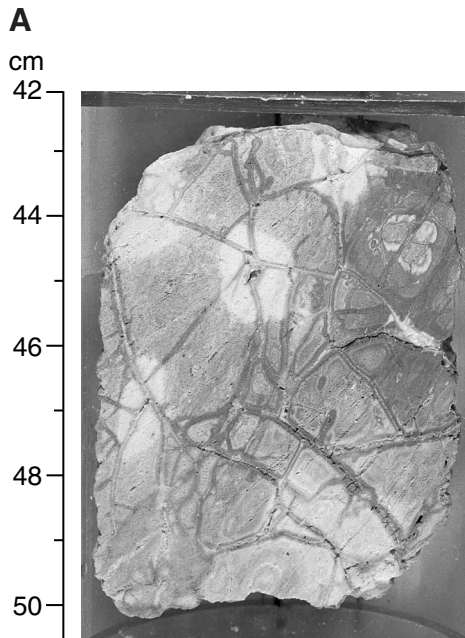


Figure F12. Close-up photograph of volcanoclastic pebble breccias (Units 12 and 14) that separate the volcanic rocks in the upper part of Hole 1188A from volcanic rocks in the lower part. They are grain supported and consist of completely altered, white and light gray, aphyric clasts. White clasts are bleached (sulfate-clay altered) and gray clasts are (partially) silicified. Arrow = clast that is sparsely vesicular (Unit 14; Interval 193-1188A-14R-1, 105–113 cm).

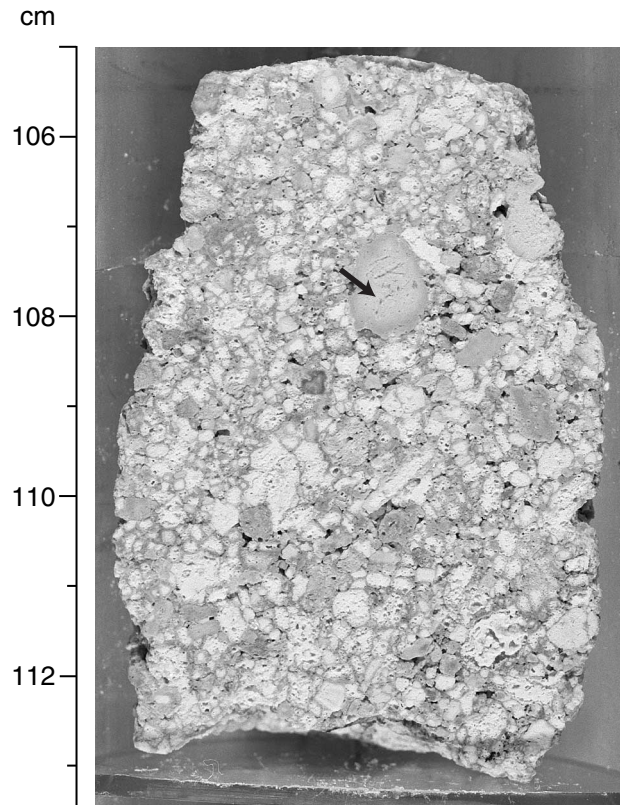


Figure F13. Close-up photograph of the gray-green, flow-laminated, silicified volcanic rock (Unit 18) with minor volcanic clasts (xenoliths?) located above the lower volcanic units of Hole 1188A and below the volcanoclastic pebble breccia. Plagioclase phenocrysts and microlites are oriented subparallel to the lamination, defining a remnant trachytic texture (interval 193-1188A-16R-2 [Piece 7, 39–52 cm]; 137.25 mbsf).

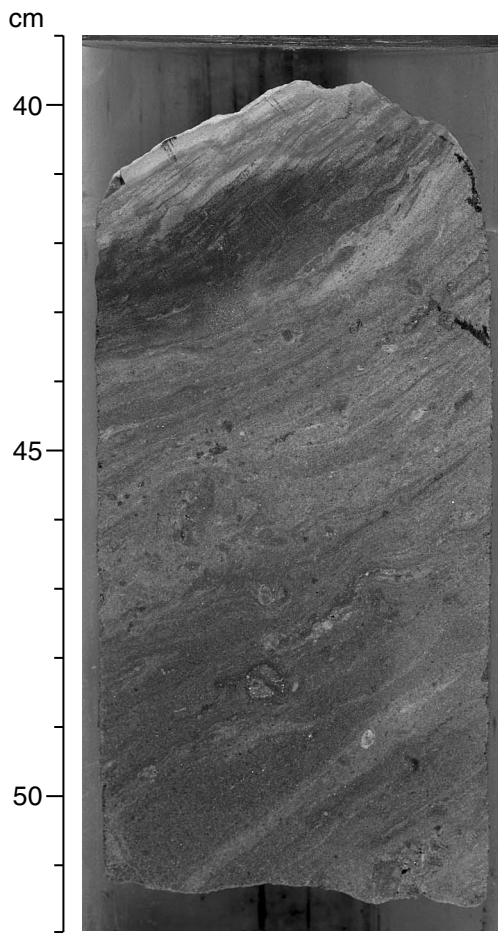
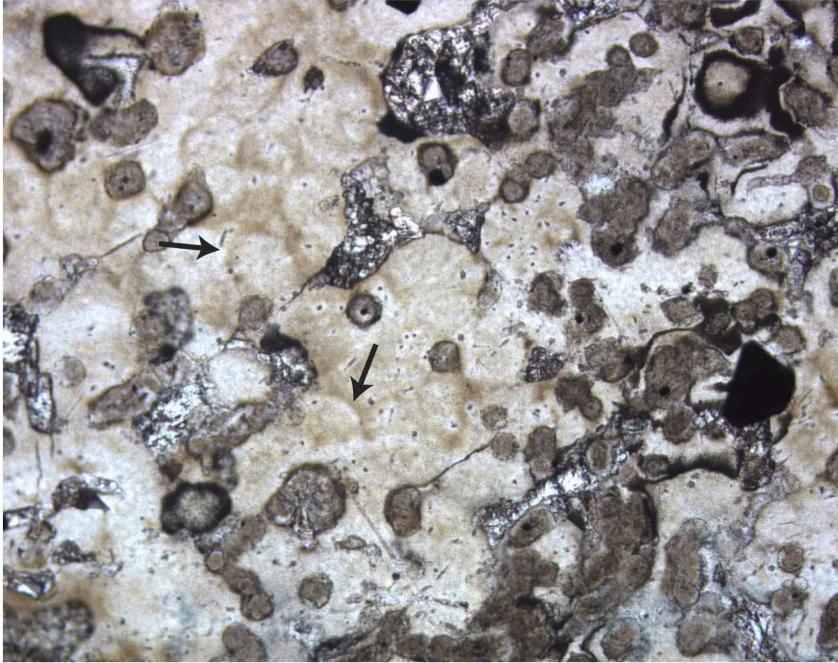


Figure F14. Spherulitic texture can be observed in some thin sections of samples from Hole 1188A. **A.** Parts of the groundmass of Unit 6 consist of coalesced spherulites indicating that the unit underwent high-temperature devitrification prior to solidification. Arrows = faint circular features that outline the margins of individual spherulites in plane-polarized light (interval 193-1188A-7R-2 [Piece 2, 39–41 cm]; width of view = 1.40 mm. Photomicrograph ID# 1188A_37; [thin section 6](#)). **B.** Radiating aggregates of fine quartz and feldspar needles can be recognized in the area shown in (A) when the polarizers are crossed (width of view = 1.40 mm. Photomicrograph ID# 1188A_38; [thin section 6](#)).

A



B

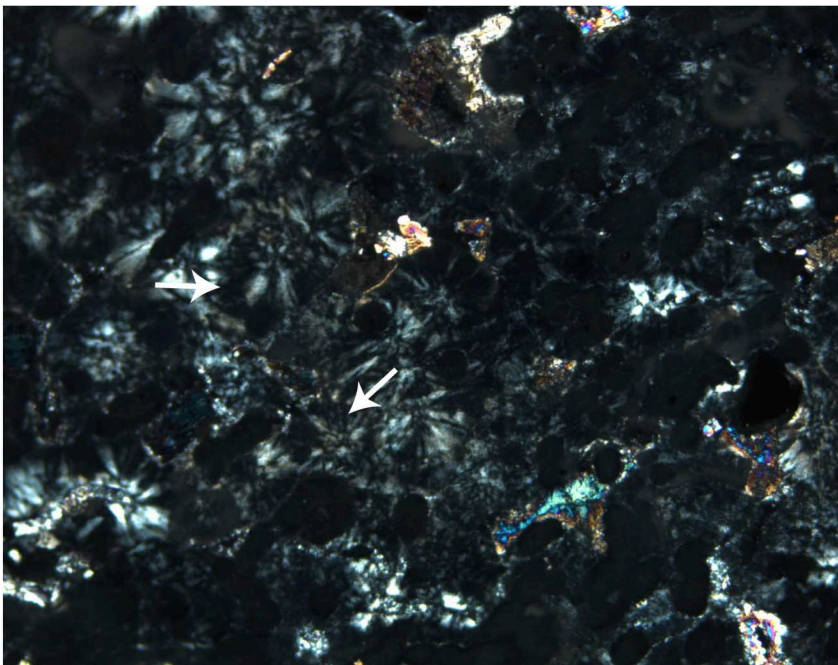


Figure F15. Isolated and coalesced microspherulites forming necklacelike aggregates (arrows) are dispersed in a silica-clay-rich groundmass. Because of the alteration, most microspherulites lack any internal structures (interval 193-1188A-8R-1 [Piece 8, 66–69 cm], Unit 6, in plane-polarized light; width of view = 1.40 mm. Photomicrograph ID# 1188A_33; [thin section 7](#)).

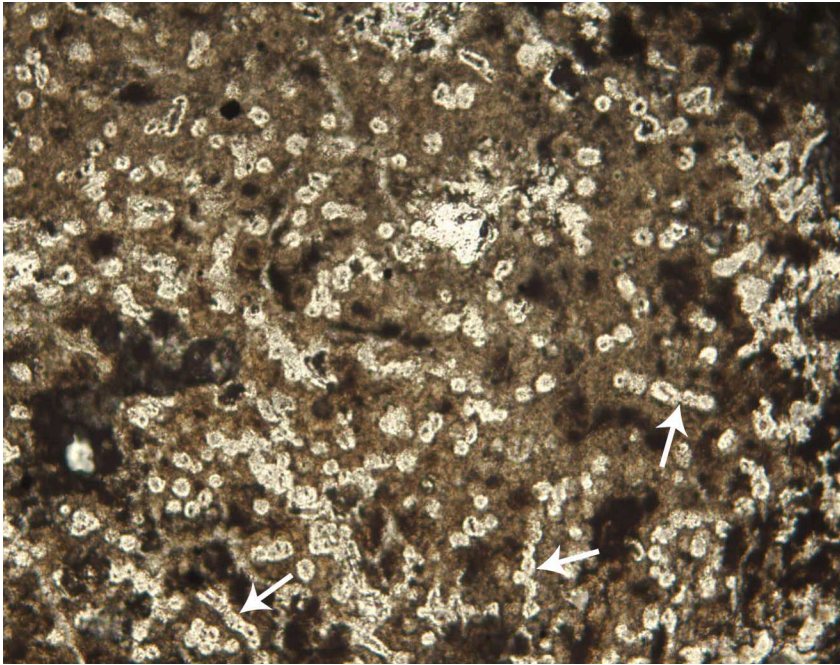


Figure F16. The groundmass of the flow-banded sample from Unit 10 consists of domains of completely coalesced microspherulites and domains with isolated microspherulites in altered glass (fine-grained clay and silica) corresponding to the light gray and dark gray bands in hand specimen. The arrow indicates the bulbous outer margin of the devitrified domain (interval 193-1188A-12R-1 [Piece 12, 123-124 cm]; in plane-polarized light; width of view = 5.5 mm. Photomicrograph ID# 1188A_55; [thin section 11](#)).

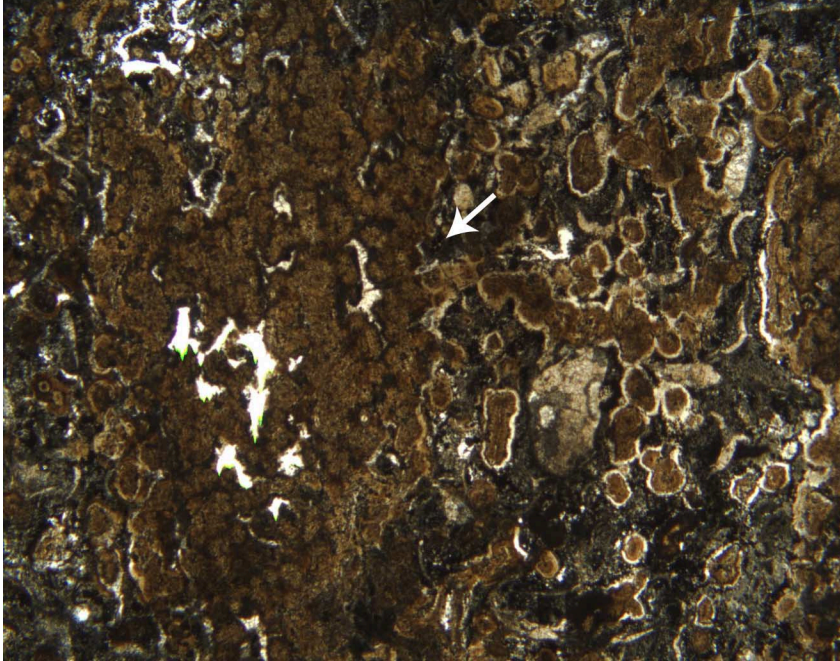


Figure F17. The nonsystematic orientation of laminar flow banding in the clasts of this brecciated sample indicated that the individual clasts have moved relative to each other (interval 193-1188A-8R-1, 29–41 cm; Unit 6). **A.** Close-up photograph of hand specimen. **B.** Line drawing showing the essential textural characteristics of the sample.

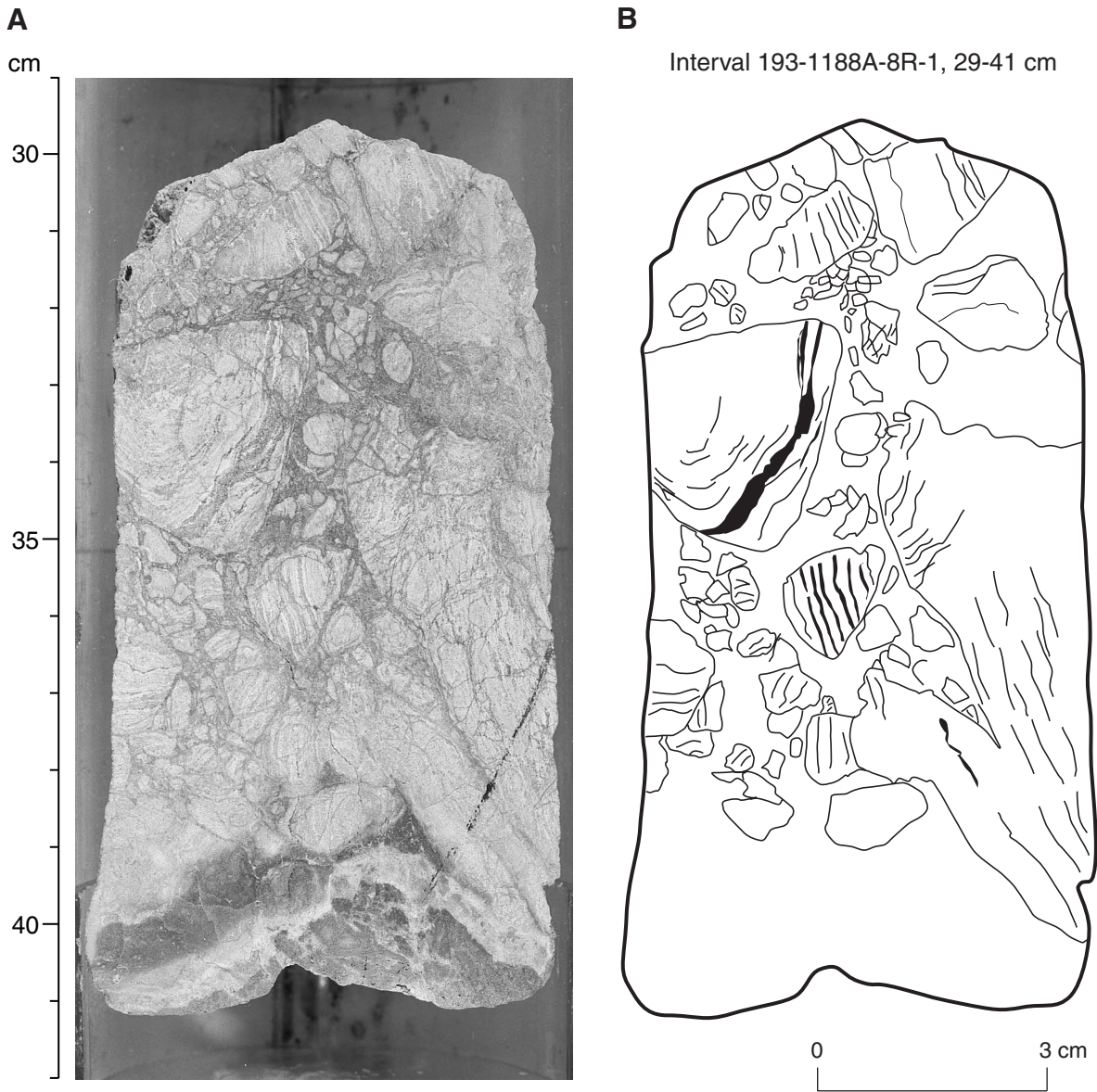
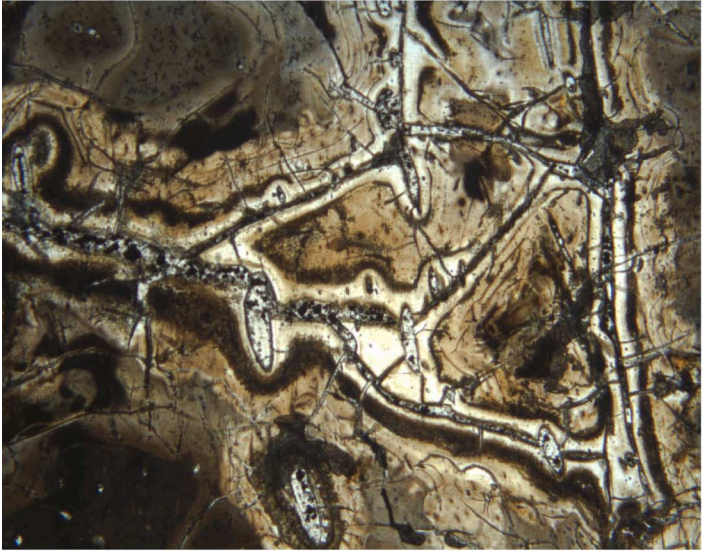


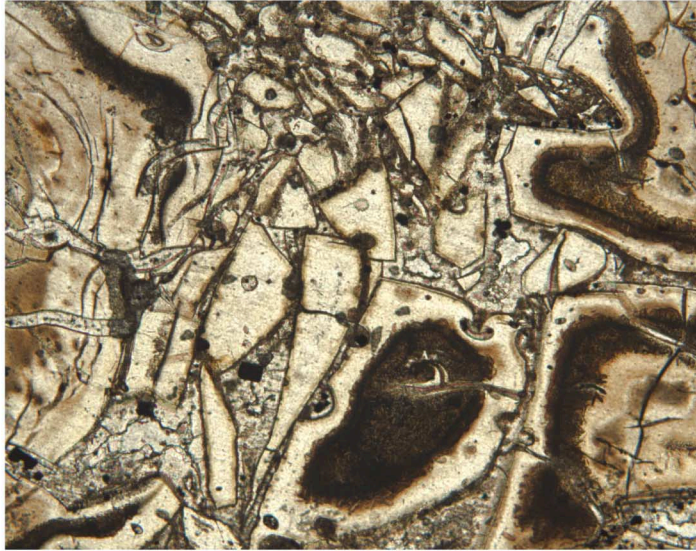
Figure F18. Thin sections of various vitriclastic textures in one sample of Unit 8 (interval 193-1188A-9R-1 (Piece 7, 68–70 cm). **A.** Locally the clasts show jigsaw-fit texture with fractured vesicles continuing on either side of the vein. This arrangement indicates that fracturing during alteration generated these clasts and that relative movement was minimal (in plane-polarized light; width of view = 5.5 mm. Photomicrograph ID# 1188A_44; **thin section 9**). **B.** Vitric clasts with locally preserved perlitic cracks are irregularly arranged in this part of the thin section. Therefore, they must have moved relative to each other prior or during hydrothermal activity (in plane-polarized light; width of view = 2.75 mm. Photomicrograph ID# 1188A_45; **thin section 9**). **C.** One of the clasts in this area of the thin section shows a laminar texture that could be remnant, elongate tube vesicles. This texture is not continued in the adjacent clasts, which indicates that this clast is out of place (in plane-polarized light; width of view = 5.5 mm. Photomicrograph ID# 1188A_98; **thin section 9**). (**Figure shown on next page.**)

Figure F18 (continued). (Caption shown on previous page.)

A



B



C

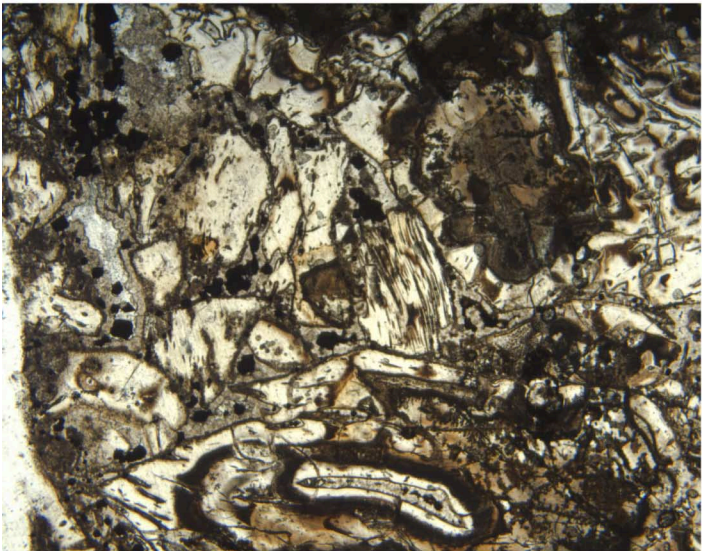


Figure F19. Thin section of fracture-controlled alteration that has generated a jigsaw breccia texture on a centimeter to millimeter scale. Arrows = remnant, arcuate perlitic cracks enclosed around fragments that represent remnants of perlitic kernels and angular fragments defined by linear, quartz-filled veins (Unit 5; interval 193-1188A-7R-1 [Piece 18, 120-124 cm]; in crossed polarized light; width of view = 2.75 mm. Photomicrograph ID# 1188A_32; **thin section 5**).

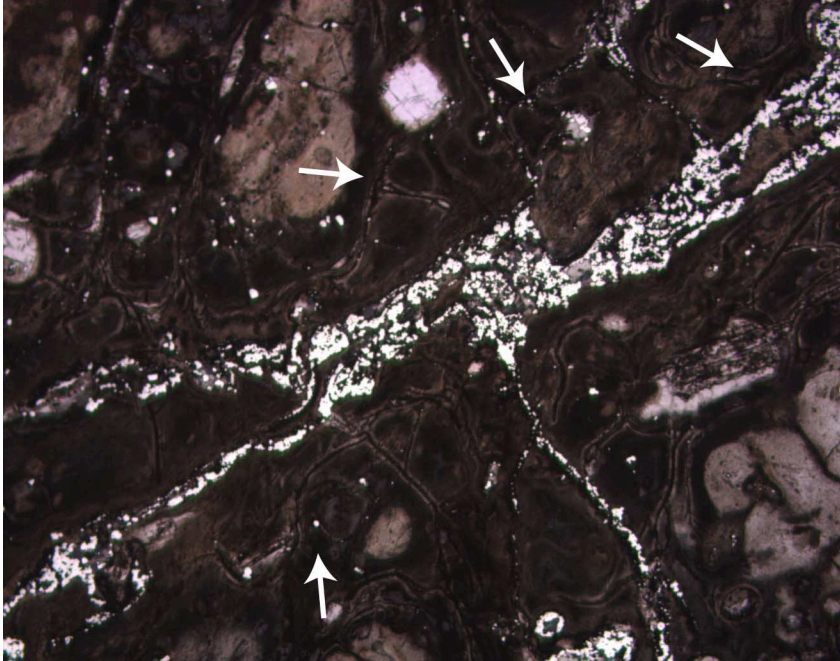


Figure F20. Graphic summary log for Hole 1188F showing the lithologic characteristics, including alteration, of the various units. See Figure F6, p. 45, in the "Explanatory Notes" chapter for the lithologic key. NR = no recovery.

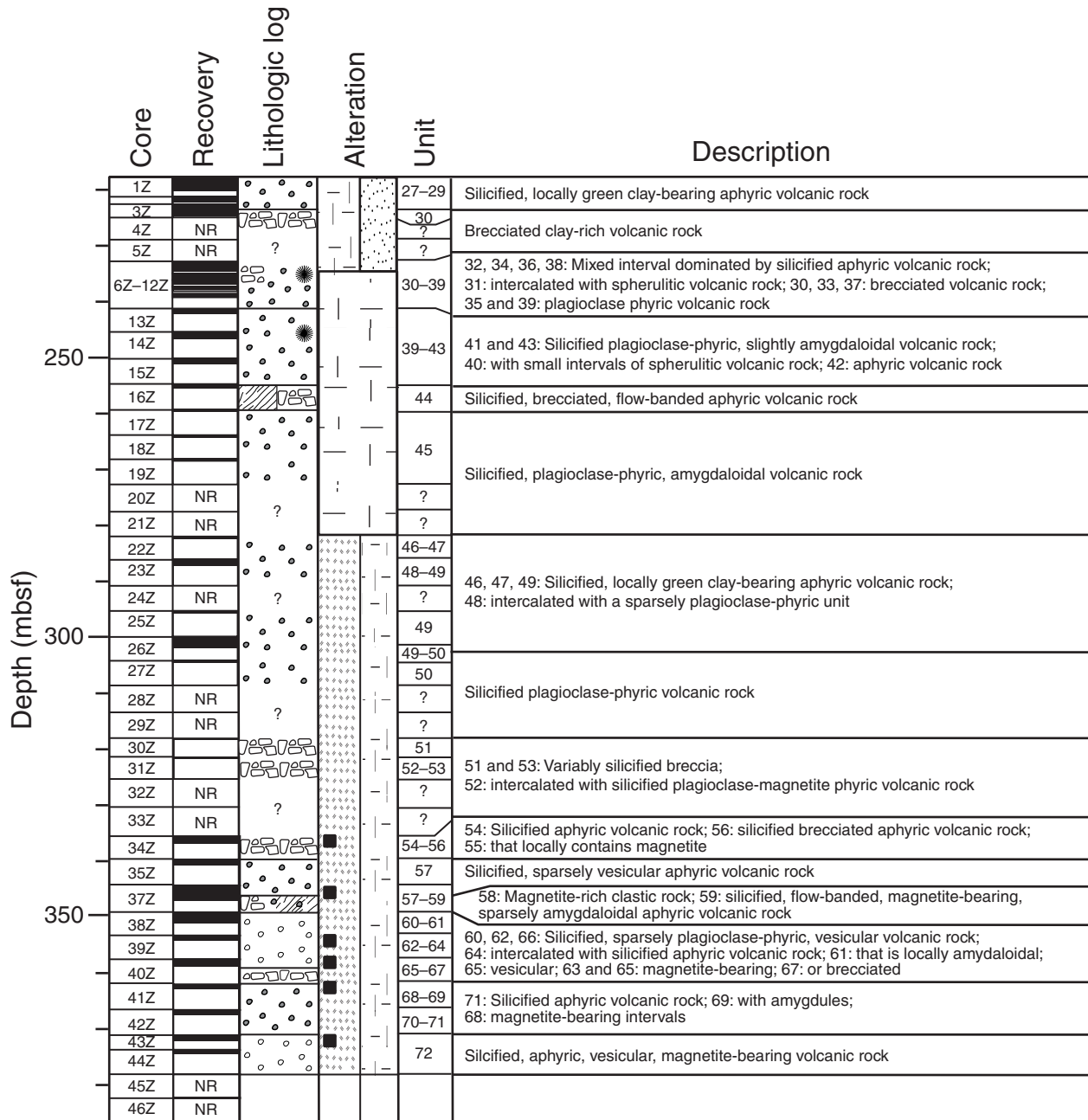


Figure F21. Close-up photograph of aphyric volcanic rock representative of Unit 28. Siliceous banded alteration halos are related to anhydrite-pyrite veins and produce an apparent clastic texture (interval 193-1188F-1Z-4, 43-60 cm).

cm

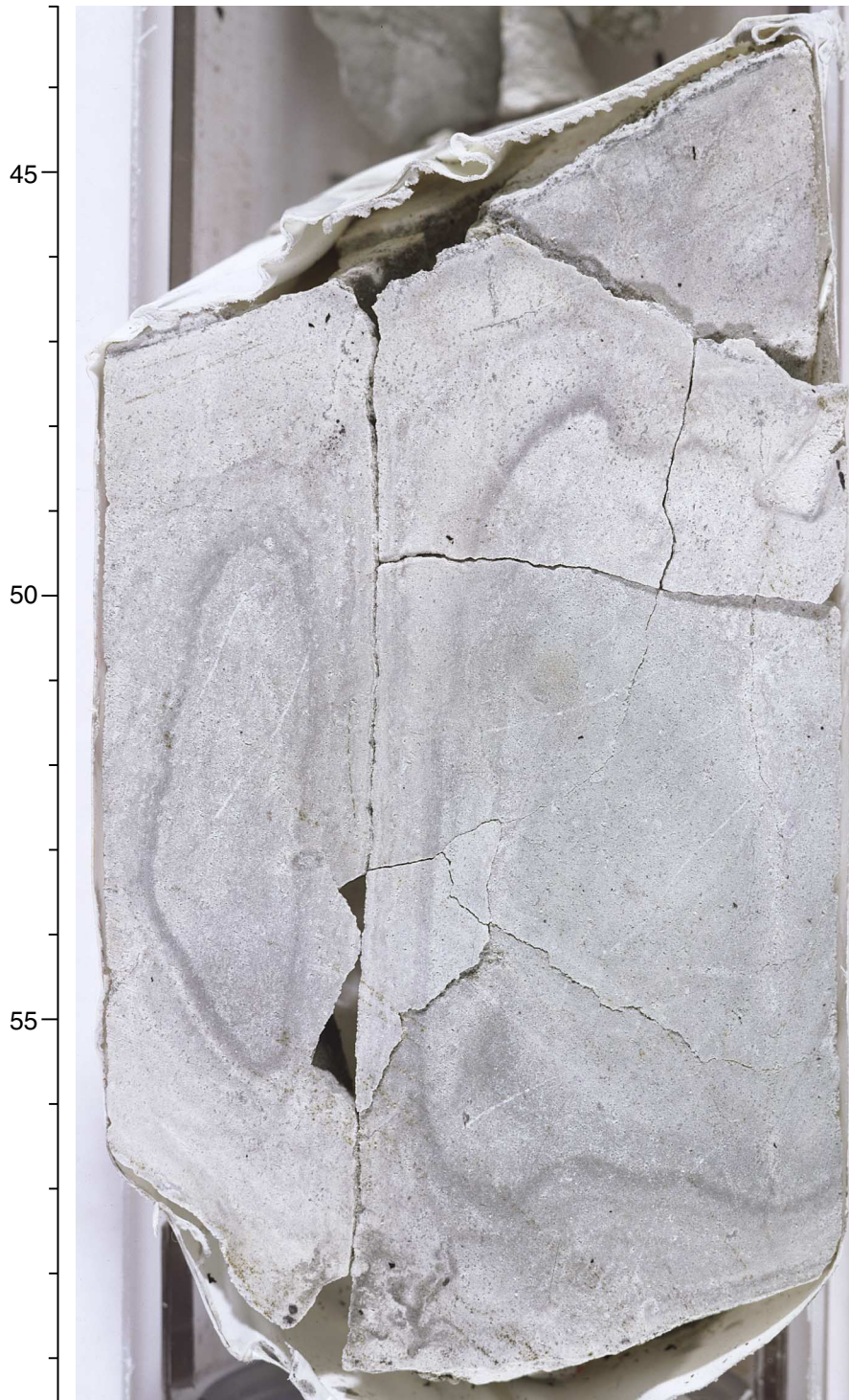


Figure F22. Close-up photograph of a piece from Unit 30 with incipiently developed clastic texture on the margin. The round, angular, and irregular siliceous fragments are embedded in a clay-rich matrix (interval 193-1188F-3Z-2, 117-131 cm).

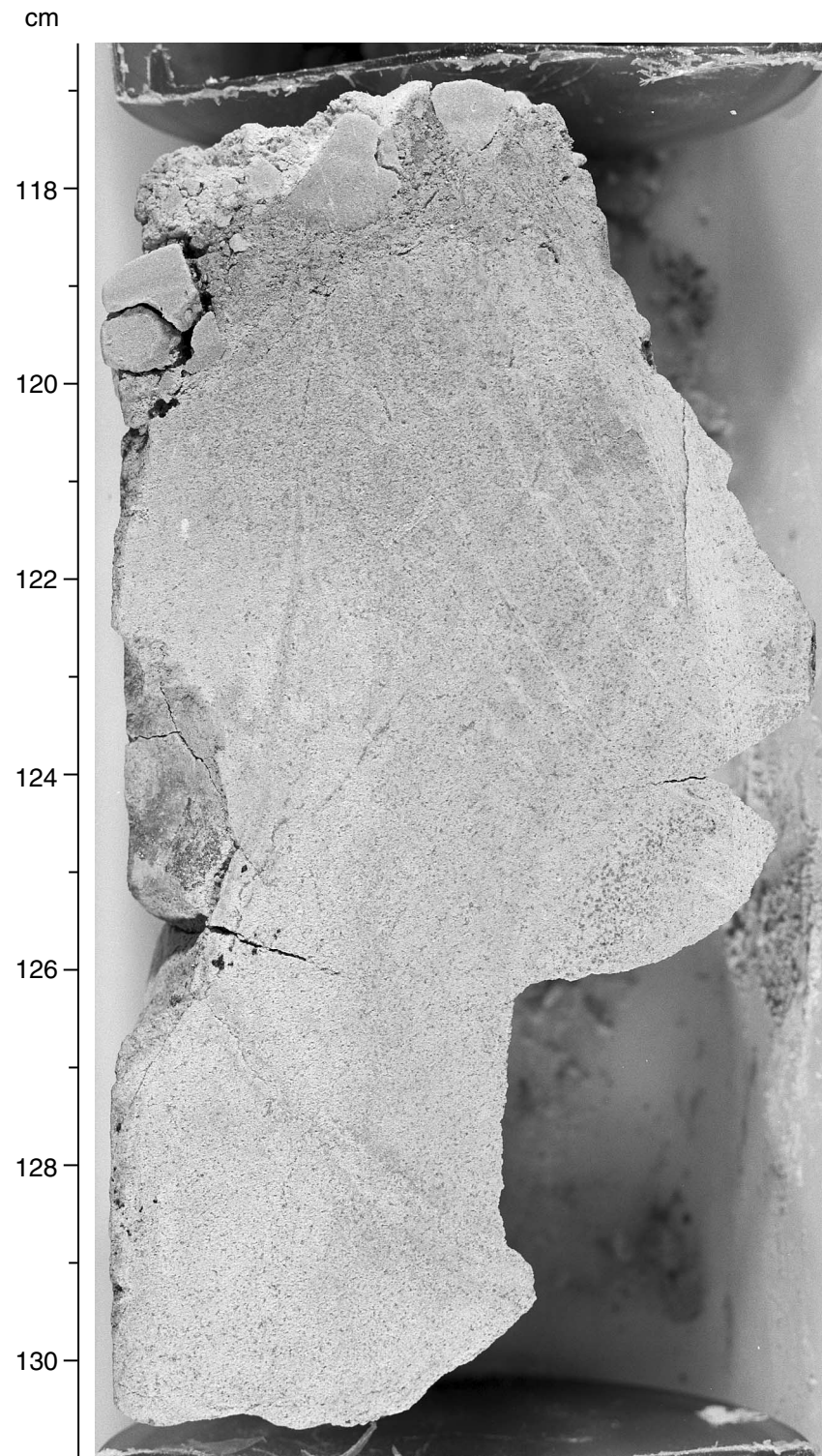


Figure F23. Close-up photograph of a prominent spheroidal texture defined by abundant isolated and coalesced white concentric domains within a dark groundmass. It is inferred that this texture represents a remnant volcanic feature related to high-temperature devitrification processes in Unit 31 (interval 193-1188F-6Z-1, 45-47 cm).



1 cm

Figure F24. Close-up photograph of plagioclase-phyric volcanic rock of Unit 41. Individual 1- to 2-cm-wide zones with fragmental textures are present in several adjacent pieces of Unit 41. These zones are compositionally identical to the coherent volcanic rock on either side. It is inferred that these zones may be the product of autobrecciation during flow or brecciation caused by faulting. Note the lath-shaped plagioclase phenocrysts; one phenocryst is dissected by an anhydrite-pyrite veinlet (arrow) (interval 193-1188F-14Z-1, 16.5–35.5 cm).

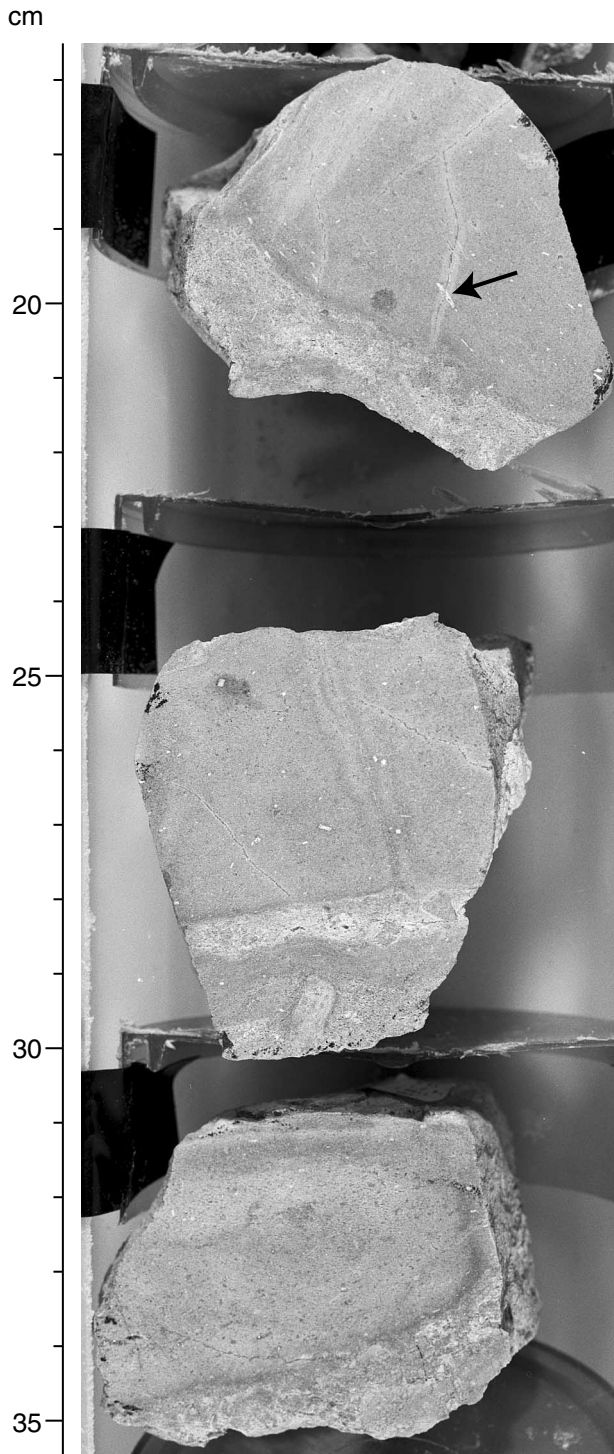


Figure F25. Close-up photograph of relict flow banding observed in Unit 44, defined by fine bands with variable proportions of silica and very fine-grained clay minerals. This example consists of one comparatively homogeneous domain in the center of the hand specimen, which is enveloped by domains with mottled or clastic appearance. These domains may reflect primary textural differences with the central part representing coherent facies and the outer parts representing clastic facies of one lava (interval 193-1188F-16Z-1, 136–144 cm).

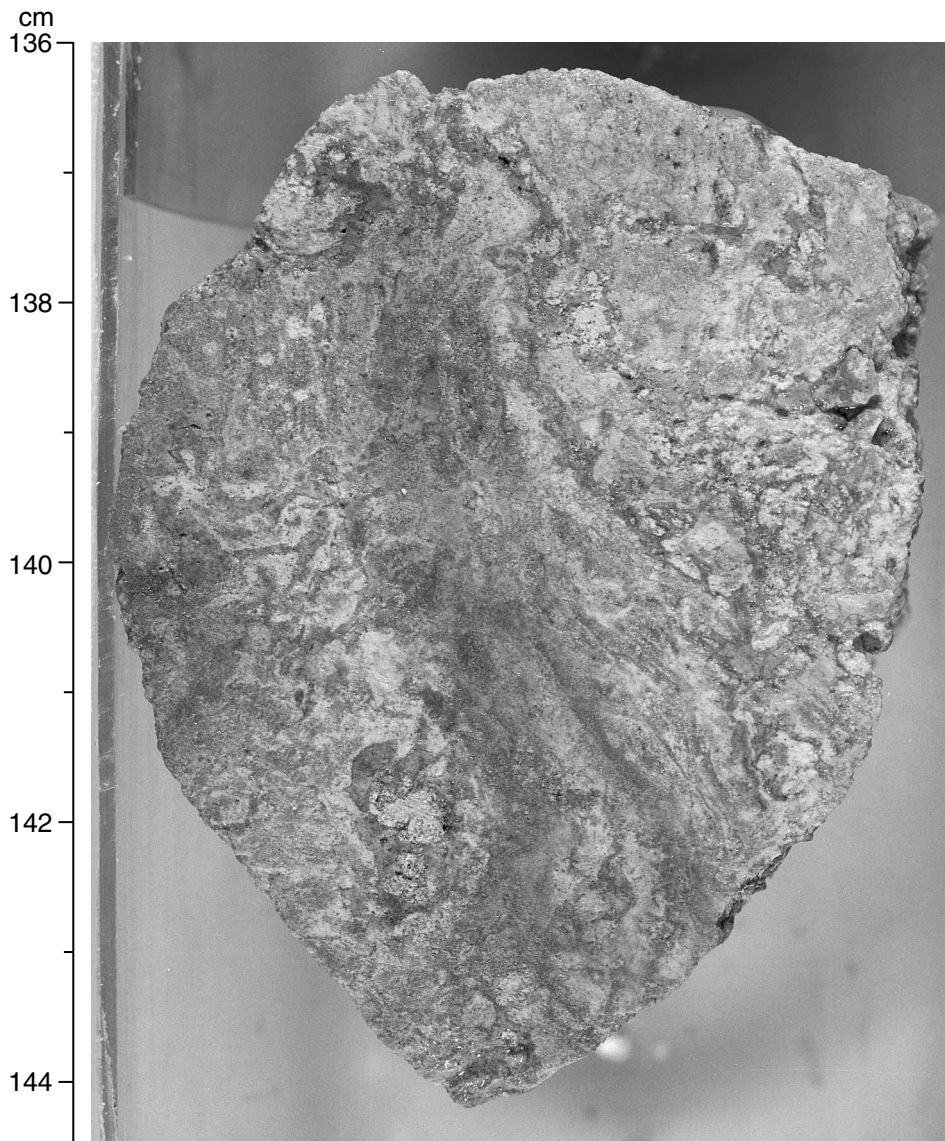


Figure F26. Close-up photograph of elongate amygdules (up to 5 mm) that are aligned, defining a flow structure in Unit 45. Plagioclase phenocrysts are clay altered but clearly recognizable in hand specimen. Locally, slightly rounded quartz-rich patches are hosted within the volcanic groundmass. The origin of these patches is enigmatic, and they may represent xenoliths, amygdules, or alteration features (interval 193-1188F-17Z-1, 0-12 cm).

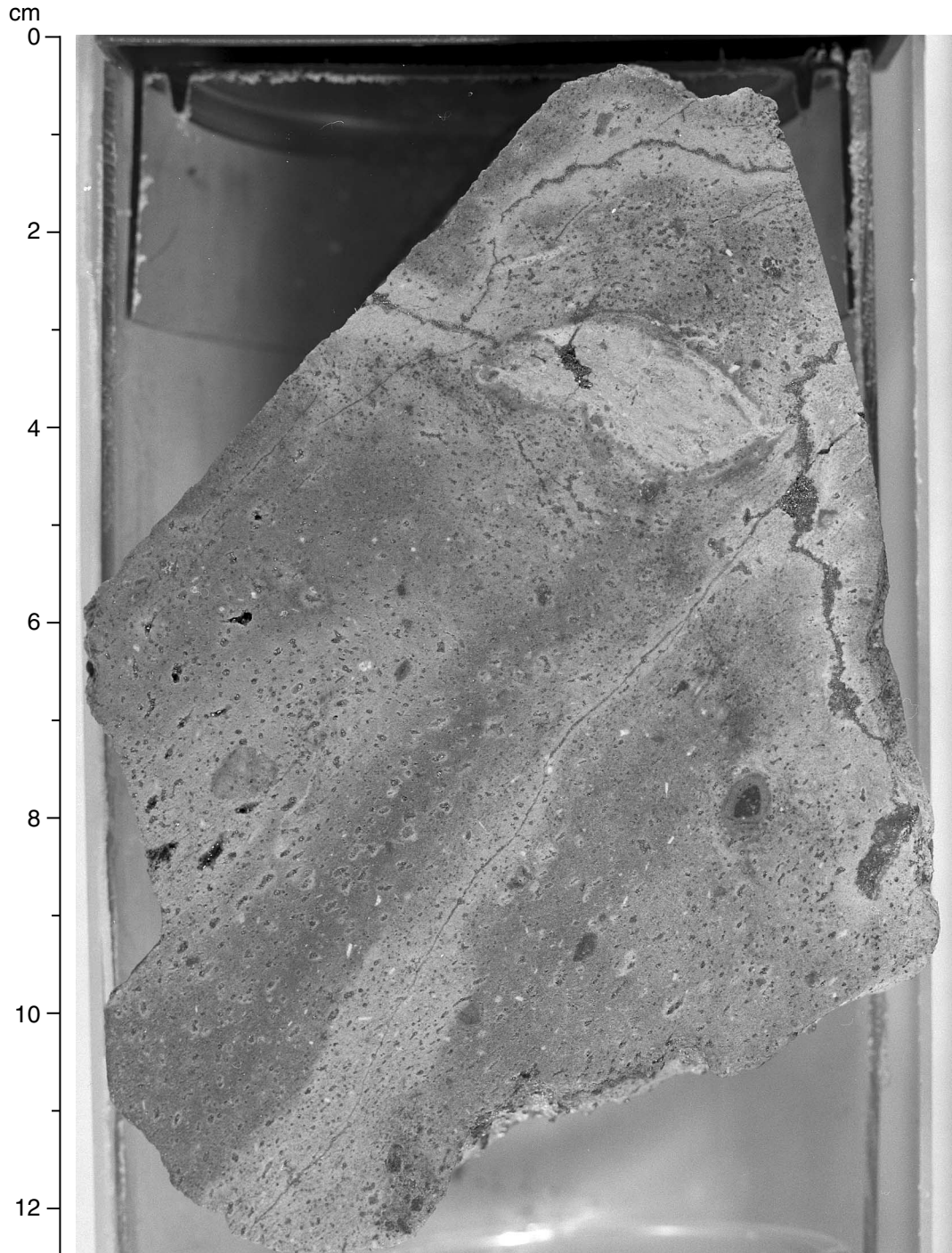


Figure F27. Close-up photograph of angular to round, light gray and dark gray domains irregularly distributed in a siliceous groundmass giving rise to apparent fragmental texture in Unit 51 (interval 193-1188F-30Z-1, 12-19 cm).

cm

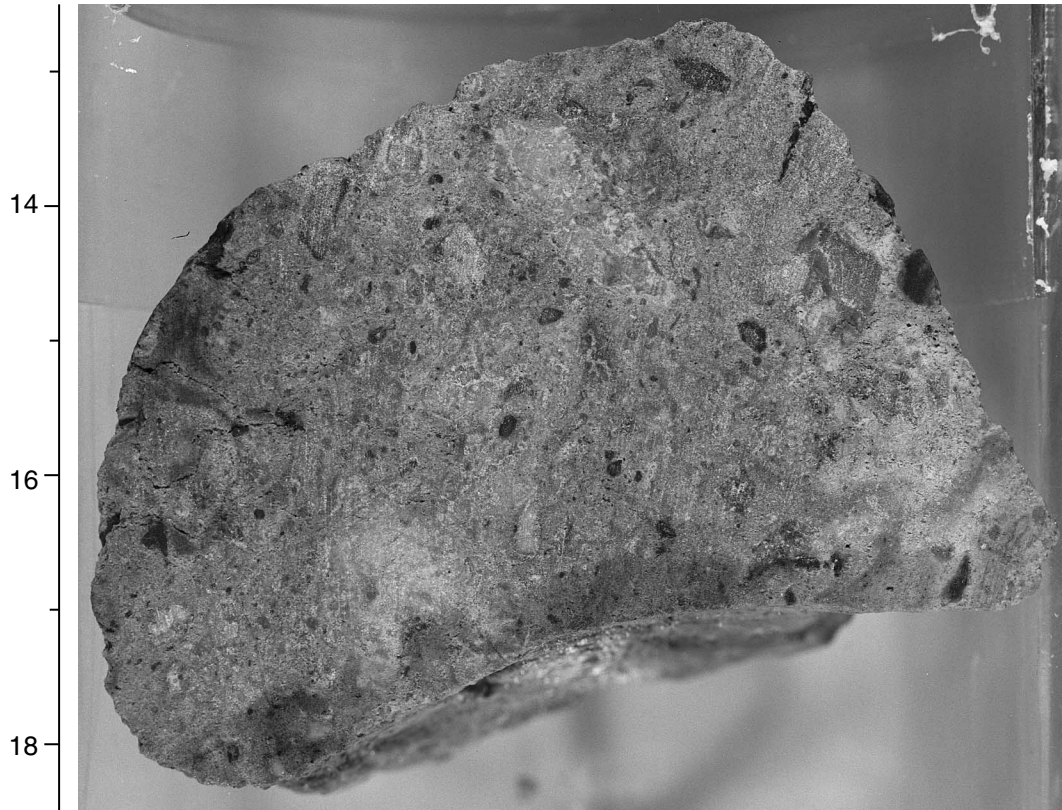


Figure F28. Close-up photograph of a black, magnetite-rich domain that is hosted within a vesicular to amygdaloidal aphyric volcanic groundmass. The origin of these domains is uncertain; however, it is apparent that particular parts of the rock provided more favorable conditions for hydrothermal fluid flow and magnetite precipitation than others (interval 193-1188F-34Z-1, 63–70 cm).

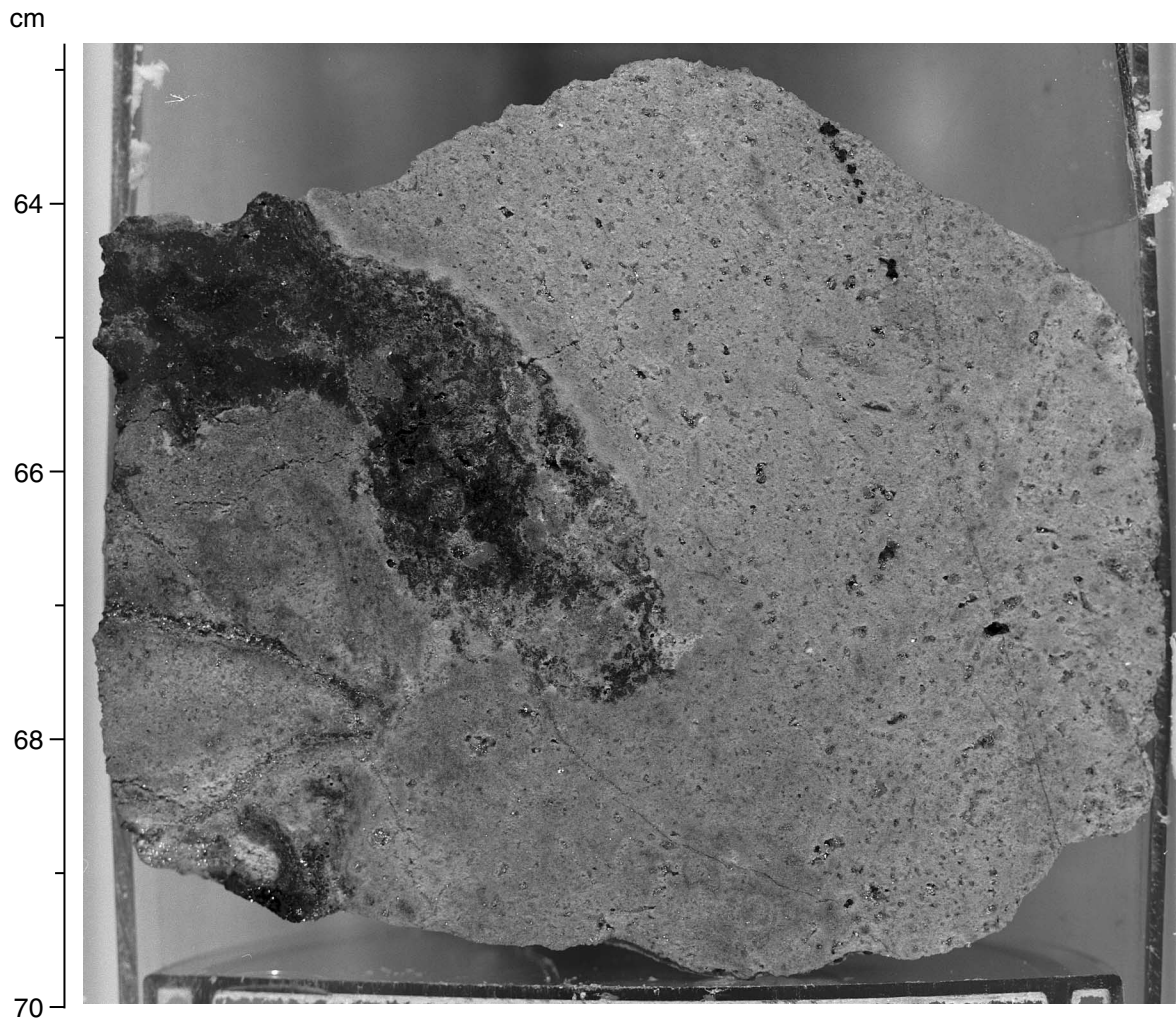


Figure F29. Thin-section photomicrograph of a silicified unit without anhydrite veining (Unit 28) showing quartz \pm pyrite amygdules in a fine-grained quartz-illite groundmass. Amygdules are <1 mm long, and elongate examples are preferentially oriented (interval 193-1188F-1Z-3, 86–89 cm; width of view = 2.75 mm. Photomicrograph ID# 1188F_12; [thin section 61](#)).

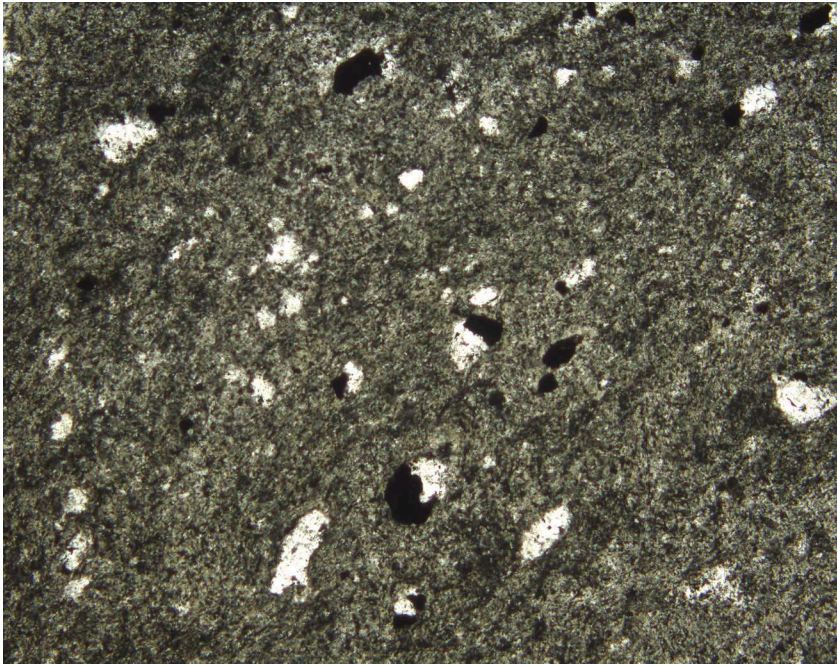


Figure F30. Fresh plagioclase phenocryst set in groundmass containing 35 vol% fresh plagioclase microli-
tes, 35 vol% quartz, 25 vol% brown clay, and 5 vol% pyrite. (Unit 51, interval 193-1188F-31Z-1, 1-3 cm; in
crossed polarized light; width of view = 2.75 mm. Photomicrograph ID# 1188F_78; **thin section 92**).

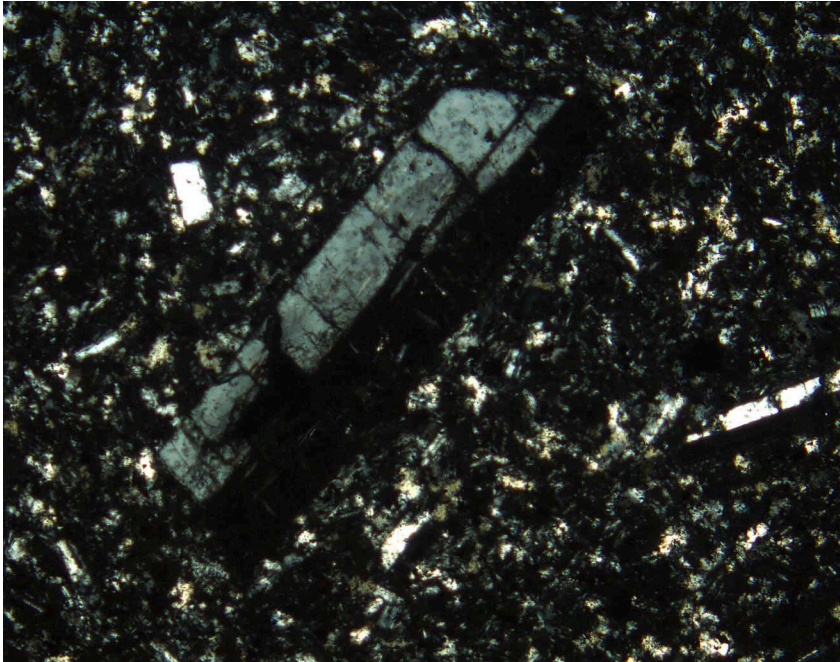
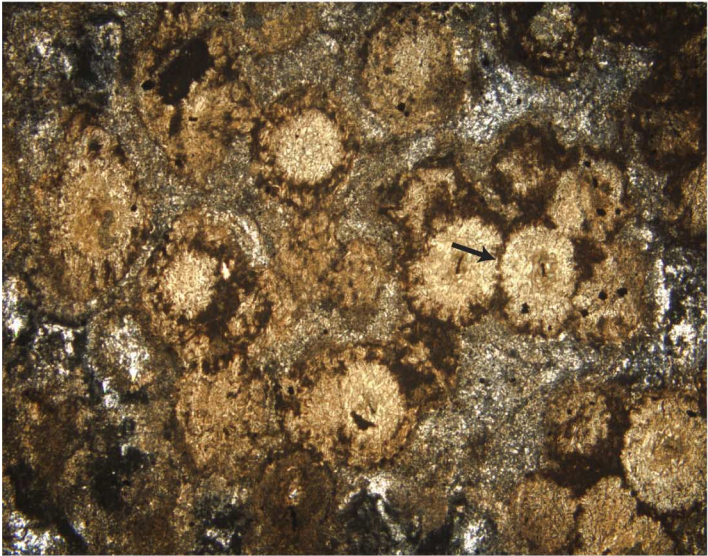


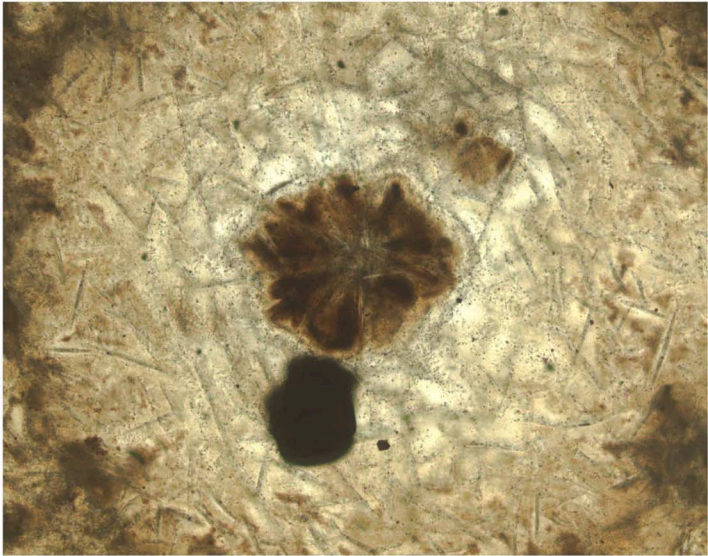
Figure F31. The spheroidal texture observed in hand specimen of Unit 31 (interval 193-1188F-6Z-1, 45–47 cm) (see Fig. **F23**, p. 123) is reflected by round to bulbous, coalesced brown domains surrounded by gray, cristobalite-rich groundmass in thin section. **A.** Brown spheroidal domains outlined by dark brown rims, which also encircle individual spheroids in coalesced aggregates. Arrow = coalesced spheroids (in plane-polarized light; width of view = 5.5 mm. Photomicrograph ID# 1188F_16; **thin section 67**). **B.** The spheroids consist of very fine, randomly oriented plagioclase needles. However, locally radiating crystal aggregates can be observed in the center of these structures (in plane-polarized light; width of view = 0.7 mm. Photomicrograph ID# 1188F_18; **thin section 67**). **C.** The generally feltlike internal texture of the spheroids and a small central domain with radiating crystal aggregates can be recognized using crossed polarizers and the condenser lens (in cross-polarized light; width of view = 0.7 mm. Photomicrograph ID# 1188F_19; **thin section 67**). **D.** The groundmass between the spheroids consists dominantly of fine-grained cristobalite; however, there are some coarser crystal aggregates that are attached to the outer surface of the spheroids (in cross-polarized light; width of view = 1.4 mm. Photomicrograph ID# 1188F_26; **thin section 67**). (**Figure shown on next page.**)

Figure F31 (continued). (Caption shown on previous page.)

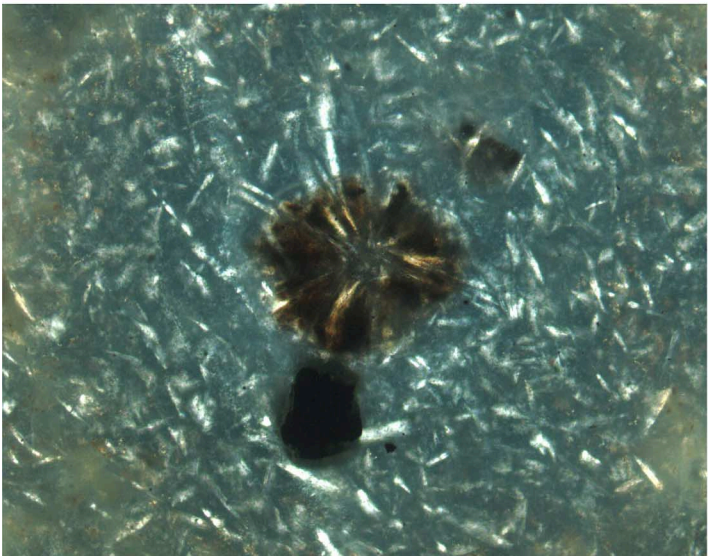
A



B



C



D

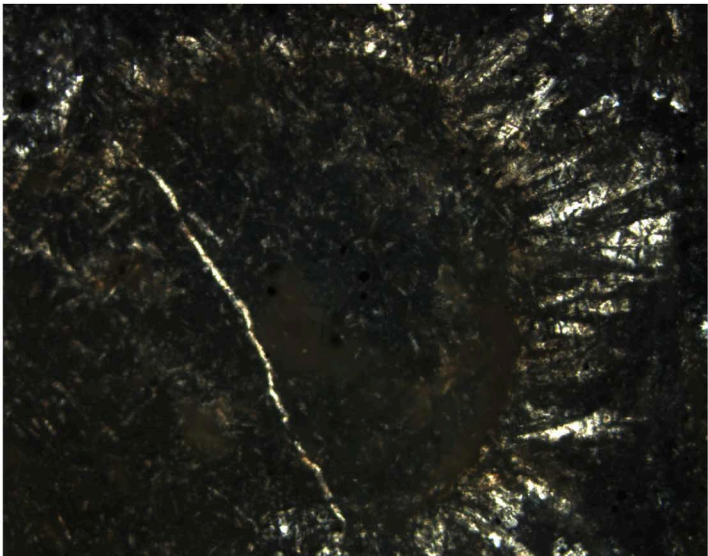


Figure F32. Rounded, quartz-rich patch representative of those in several units in Hole 1188F. These domains consist of relatively coarse, mosaic quartz aggregates and have sharp margins with the enclosing volcanic groundmass, which in this sample consists of fresh plagioclase, secondary quartz, and a trace of anhydrite (Unit 72; interval 193-1188F-43Z-1, 67–69 cm; width of view = 5.5 mm. Photomicrograph ID# 1188F_112; [thin section 111](#)). Arrow = boundary between patch (left) and groundmass (right).

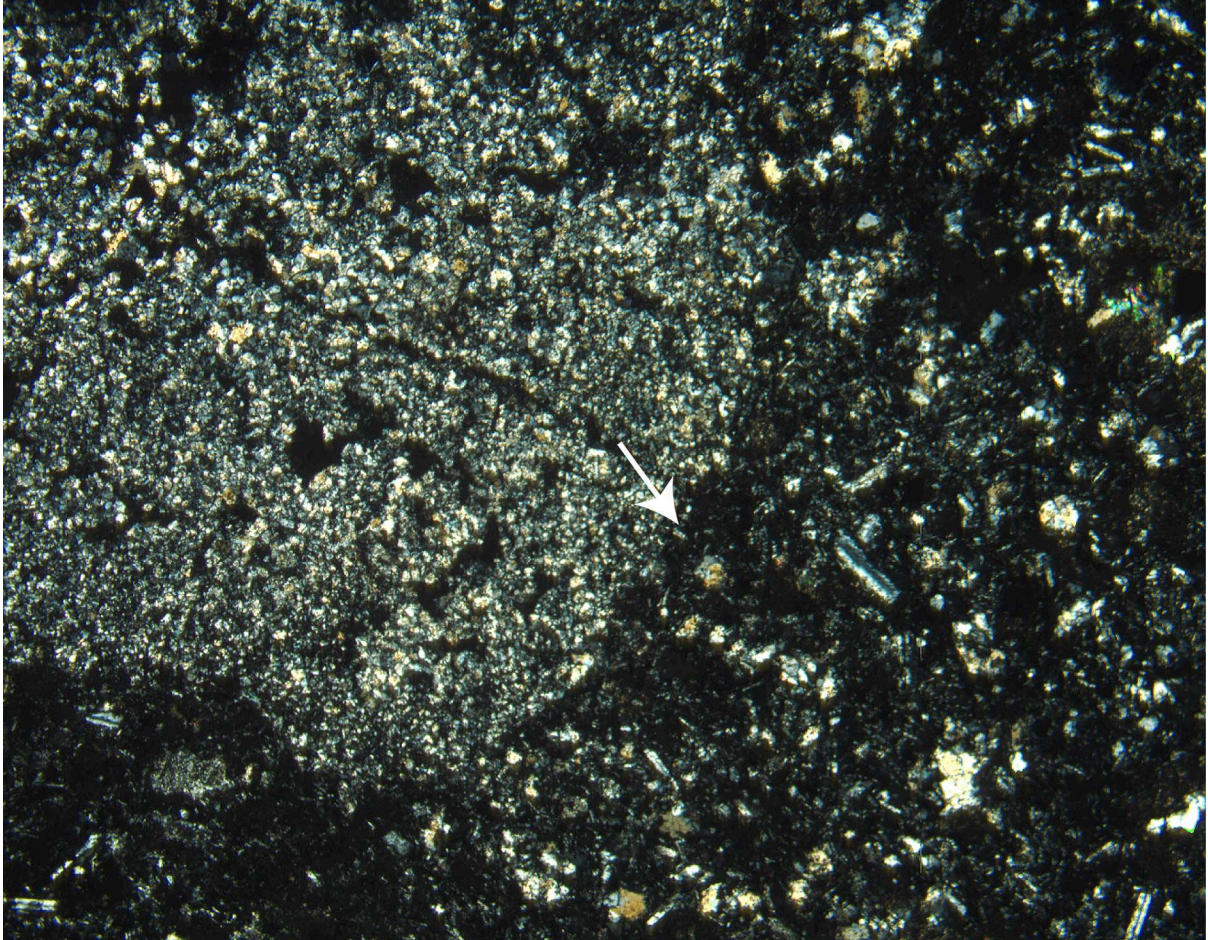


Figure F33. A xenolithic fragment of volcanic rock embedded in the microlite-rich groundmass of Unit 72. The xenolith consists of very fine grained quartz and clay minerals and contains an aggregate of mosaic quartz crystals that probably represent an amygdale. Arrow = the enclosing volcanic groundmass is occupied by abundant, aligned plagioclase microlites, which wrap around the margin of the xenolith (interval 193-1188F-43Z-1, 67–69 cm; width of view = 5.5 mm. Photomicrograph ID# 1188F_111; [thin section 111](#)).

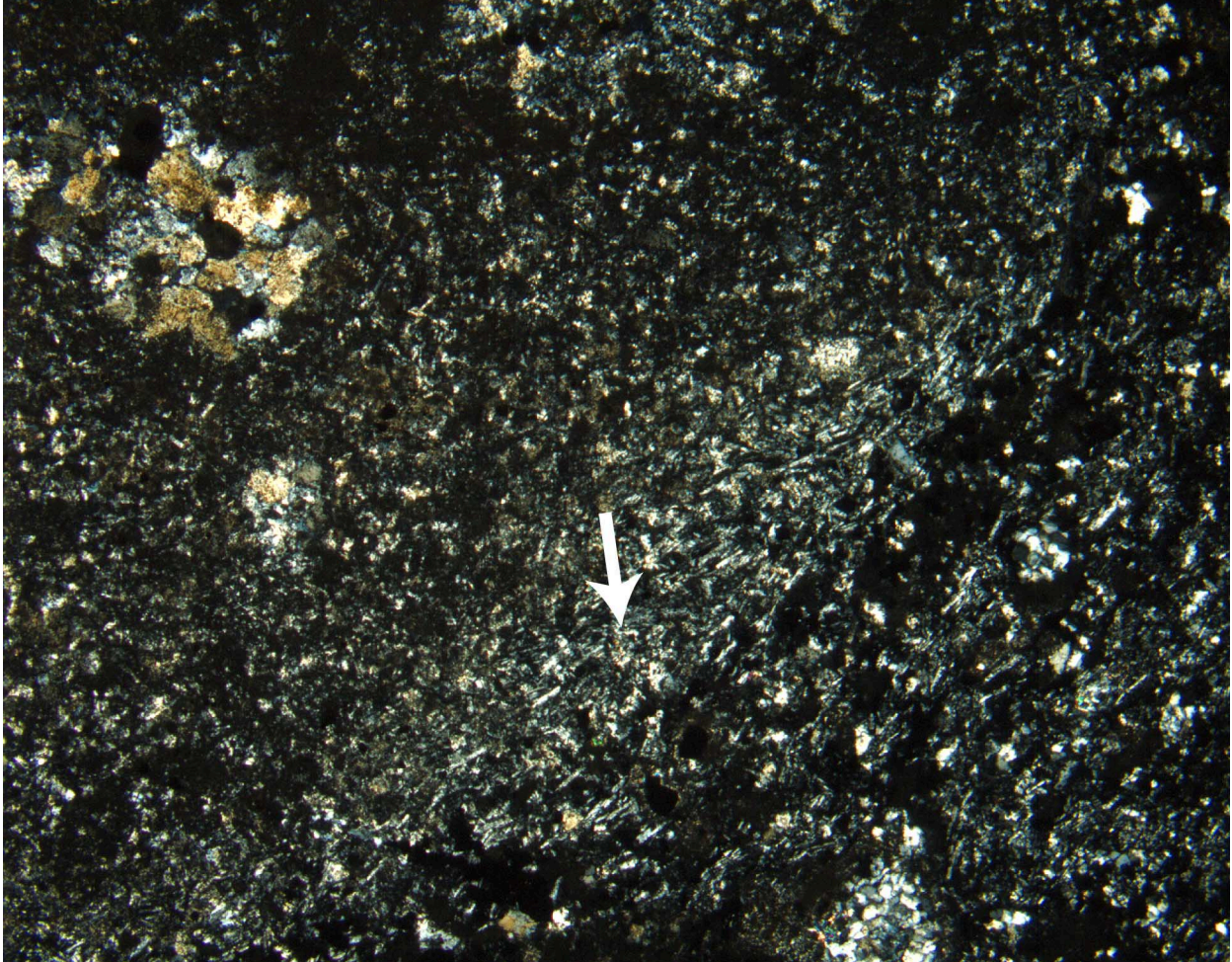
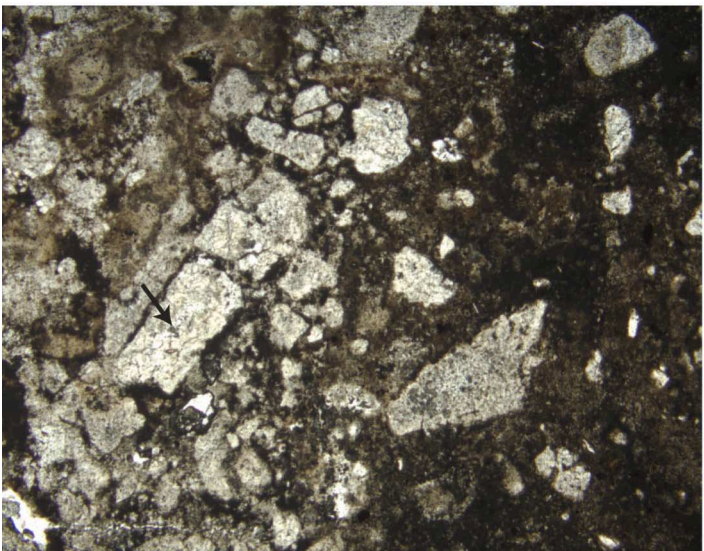


Figure F34. Unit 51 has an apparently clastic texture in hand specimen (Fig. F27, p. 127), which is defined by siliceous groundmass domains embedded in a dark gray apparent matrix enriched in clay minerals. Remnant plagioclase phenocrysts and microlites are in both types of groundmass (all photomicrograph images are from interval 193-1188F-30Z-1, 5–7 cm). **A.** The contact between a large, siliceous domain and a clay-rich domain with isolated siliceous apparent clasts is gradational. Arrow = altered plagioclase phenocryst (width of view = 5.5 mm. Photomicrograph ID# 1188F-B-46; [thin section 91](#)). **B.** The shapes of siliceous apparent clasts vary between angular and highly irregular (width of view = 2.75 mm. Photomicrograph ID# 1188F-B-47; [thin section 91](#)). **C.** Locally, plagioclase microlites are transgressing the boundary between apparent clasts and apparent groundmass (width of view = 0.70 mm. Photomicrograph ID# 1188F_48; [thin section 91](#)). ([Figure shown on next page.](#))

Figure F34 (continued). (Caption shown on previous page.)

A



B



C

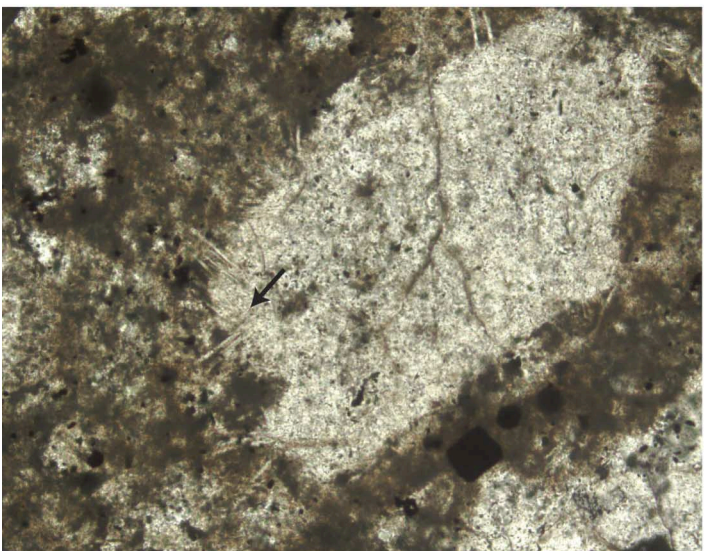


Figure F35. Summary of lithostratigraphic units, alteration style, and distribution of major (heavy lines) and minor to trace (light lines) alteration phases at Site 1188. Shaded intervals = cores where there was no recovery or no in situ recovery. Intervals where remnant igneous plagioclase was detected by X-ray diffraction (XRD) are also indicated on the right hand side. Pyrite is present in all samples analyzed and is not included in the plot. Note the variation in silica species with depth. Clay and phyllosilicate phases are indicated where detected in XRD analyses; no indication of their abundance relative to other phases is implied. It is anticipated that detailed postcruise investigation will extend the distribution ranges for some of these minerals. The terms major, minor, and trace as used here apply to XRD peaks and do not imply quantitative abundances (see **“Hydrothermal Alteration,”** p. 8, in the “Explanatory Notes” chapter). As the data are still under evaluation, mineral distribution indicated by portable infrared mineral analyzer (PIMA) is not included in the plot. EOH = end of hole. Ch/Sm = chlorite/smectite. **(Figure shown on next page.)**

Figure F35 (continued). (Caption shown on previous page.)

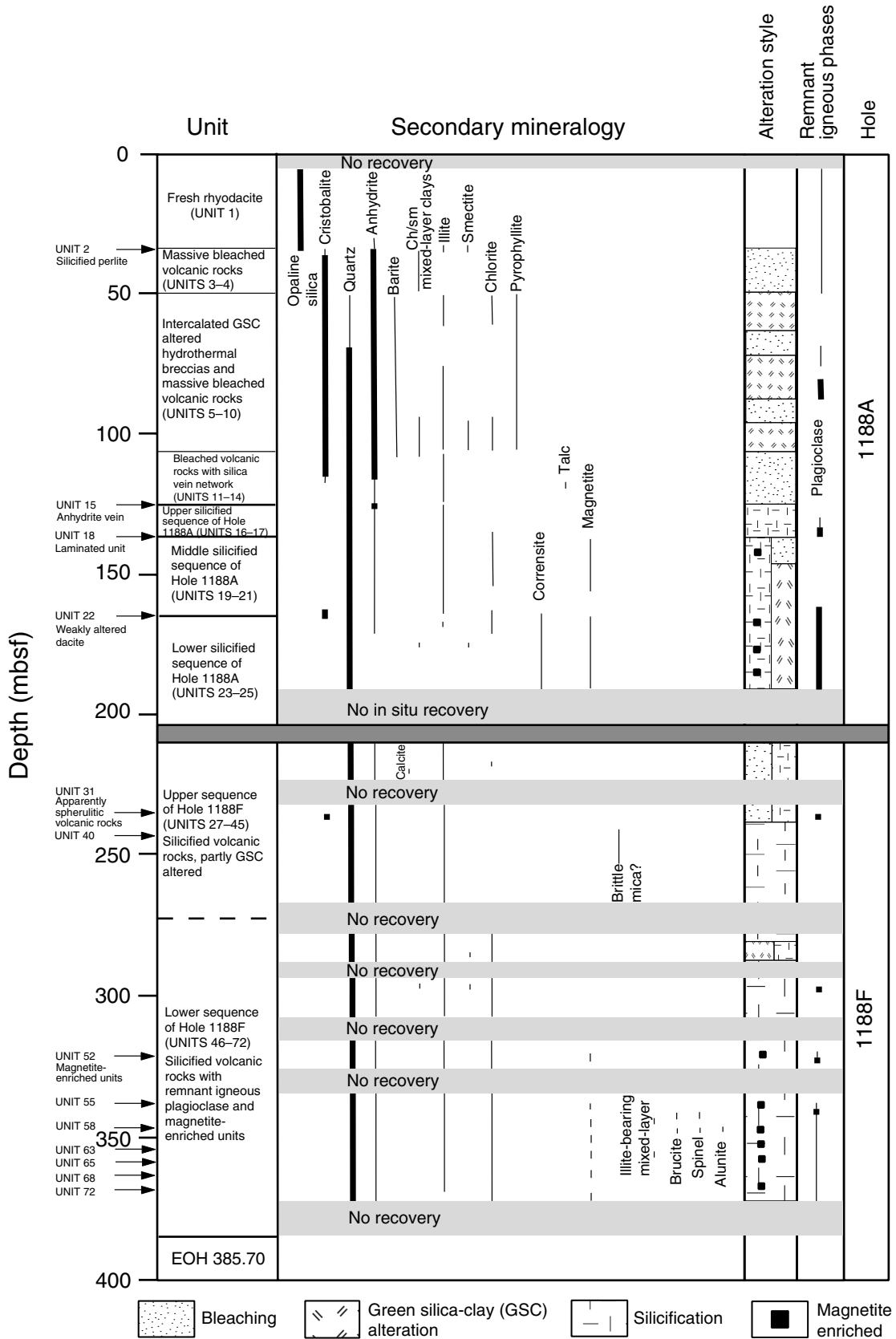


Figure F36. Fluid inclusions in anhydrite (Sample 193-1188A-7R-2 [Piece 2, 39–41 cm] in plane-polarized transmitted light; width of view = 0.275 mm. Photomicrograph ID# 1188A_5; [thin section 6](#)).

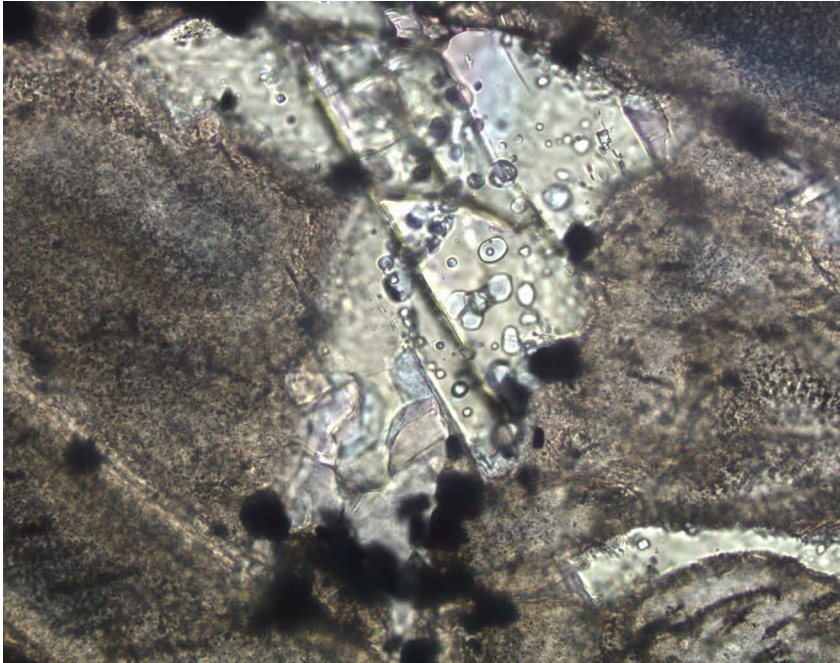


Figure F37. Close-up photograph of Unit 2 showing a perlitic textured volcanic rock with opaline silica veinlets, resulting in a pseudoclastic texture (interval 193-1188A-5R-1, 36–48 cm).

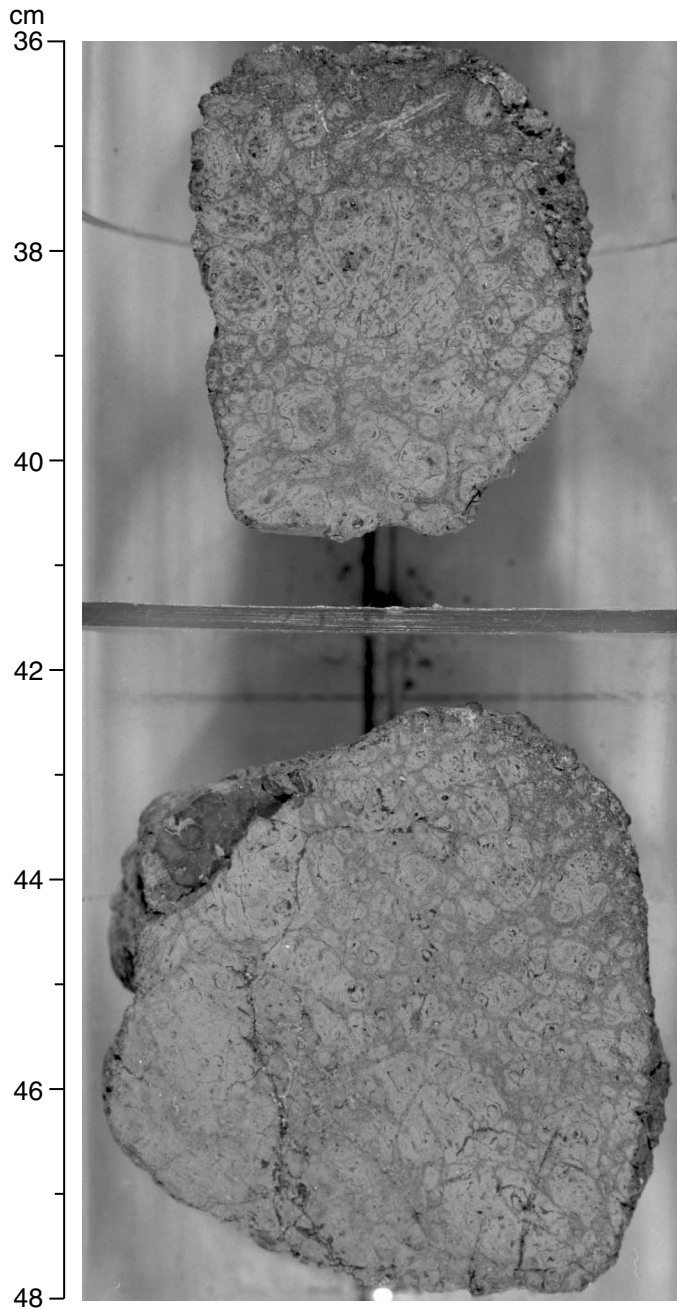


Figure F38. Photomicrograph of Unit 2 showing remnant perlitic texture with scattered microlites surrounded by alteration products (Sample 193-1188A-5R-1, 35–38 cm, in plane-polarized light; width of view = 2.75 mm. Photomicrograph ID# 1188A_13; **thin section 3**).

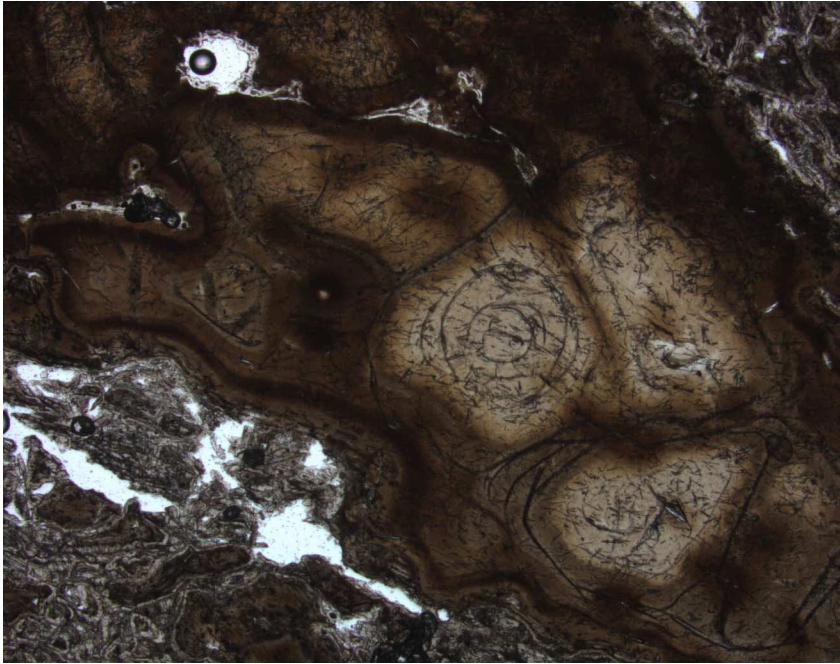


Figure F39. GSC altered rock (Unit 5) with a remnant perlitic texture and anhydrite-(silica-pyrite) veining (Sample 193-1188A-7R-1, 120–128 cm) following the perlitic cracks, generating a pseudoclastic texture.

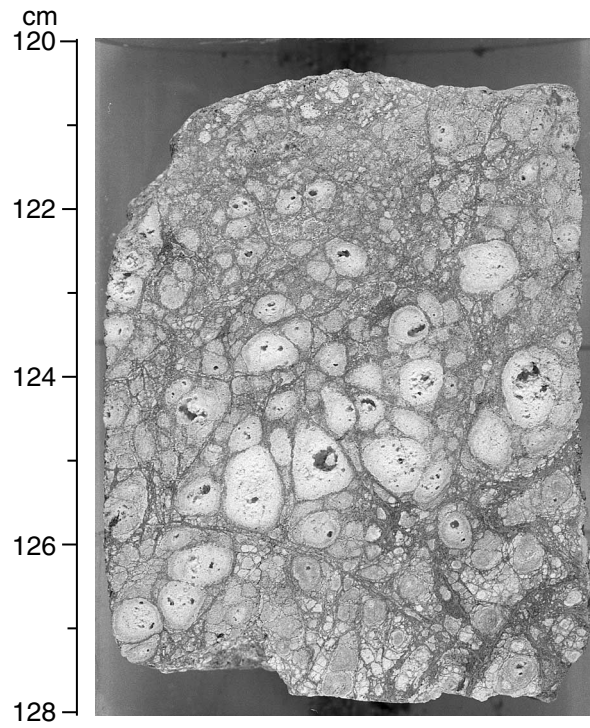


Figure F40. GSC altered rock (Unit 6) with flow-banded fragments hosted in an anhydrite-(silica-pyrite) vein network (interval 193-1188A-8R-1, 30–41 cm).

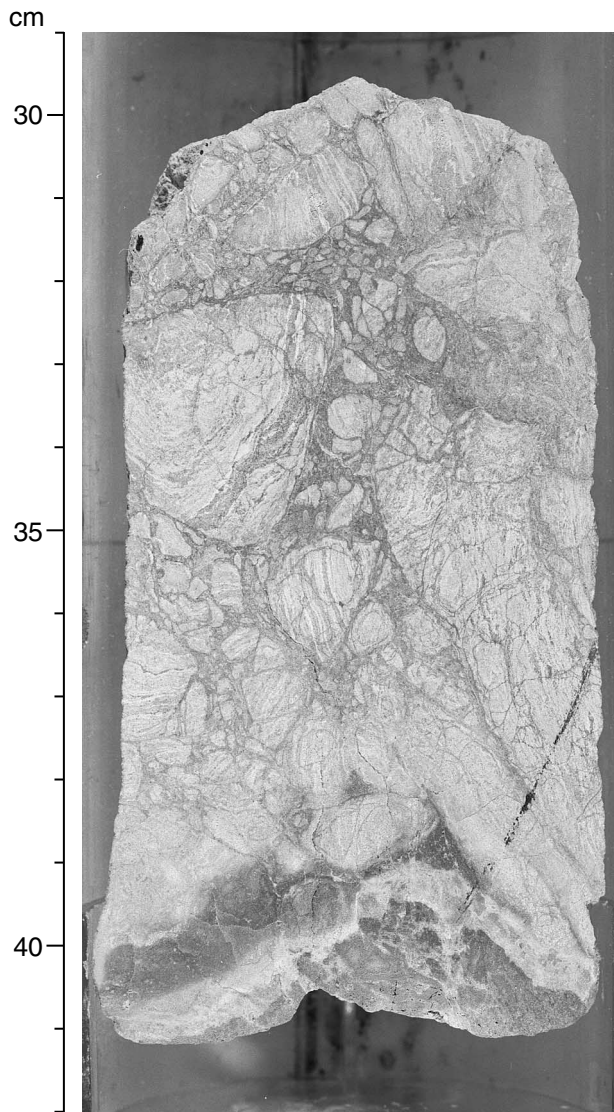


Figure F41. GSC altered rock (Unit 6) with a remnant perlitic texture with superimposed dark alteration halos composed of silica-anhydrite-dusty pyrite \pm clay and late anhydrite-(silica-pyrite) stockwork veining. The large white patch near the center of the photographed piece is late bleaching surrounding a late irregular anhydrite-pyrite vein (interval 193-1188A-8R-1, 108-140 cm).

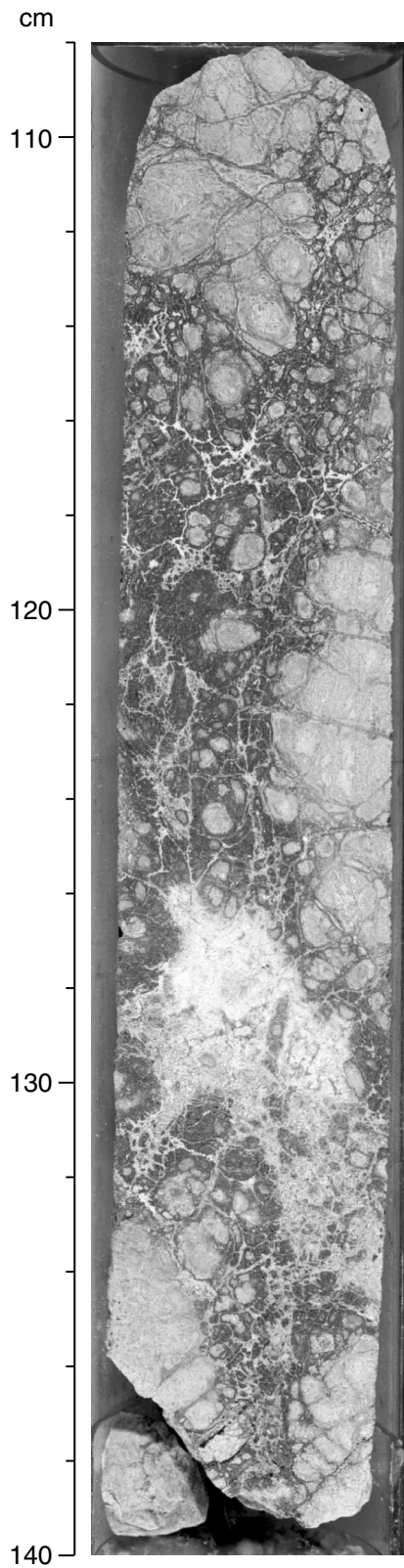


Figure F42. Anhydrite-pyrite veining with well-developed siliceous halos hosted in GSC altered volcanic rock. The vein has cut and filled two vesicles (interval 193-1188A-8R-1, 124–127 cm, Unit 6, in plane-polarized light; width of view = 0.7 mm. Photomicrograph ID# 1188A_22; [thin section 8](#)).

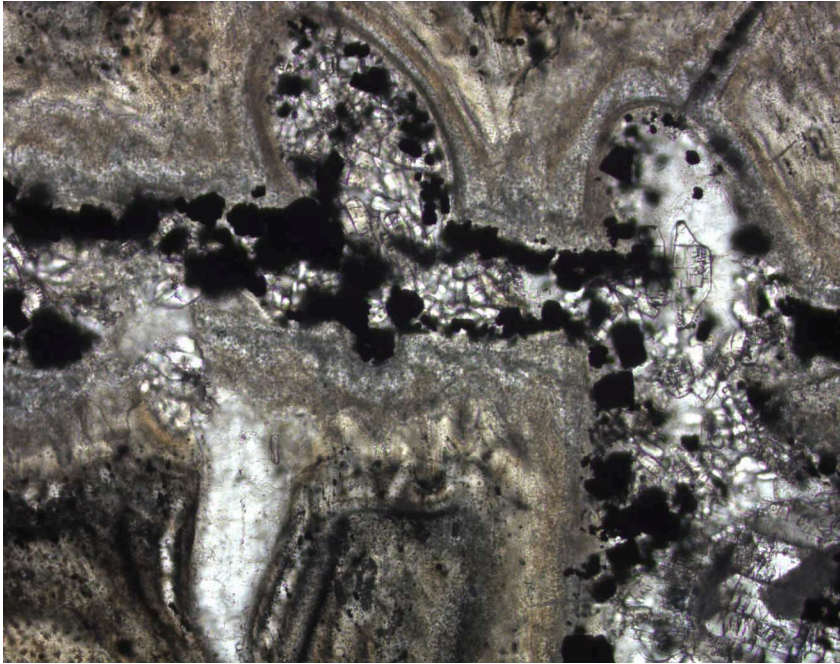


Figure F43. Quartz-pyrite veining with well-developed silica-chlorite alteration halos (interval 193-1188A-12R-2, 48–51 cm, Unit 10, in plane-polarized light; width of view = 1.4 mm. Photomicrograph ID# 1188A_111 [modified]; [thin section 12](#)). Dashed yellow lines = the main vein.

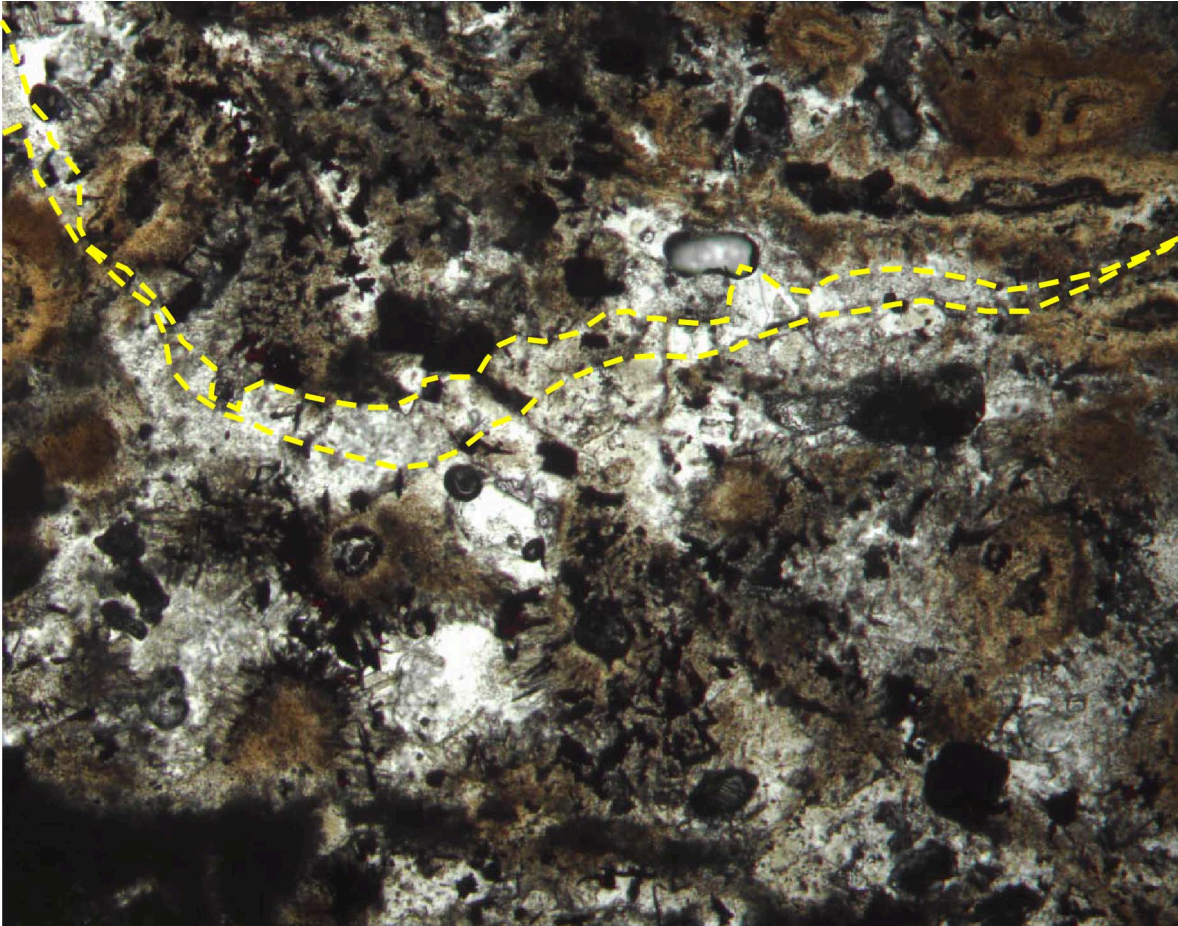


Figure F44. Clay-altered spherulites surrounded by fracture controlled silicification (interval 193-1188A-7R-1, 120–124 cm, Unit 5, in plane-polarized light; width of view = 2.75 mm. Photomicrograph ID# 1188A_36; [thin section 5](#)).

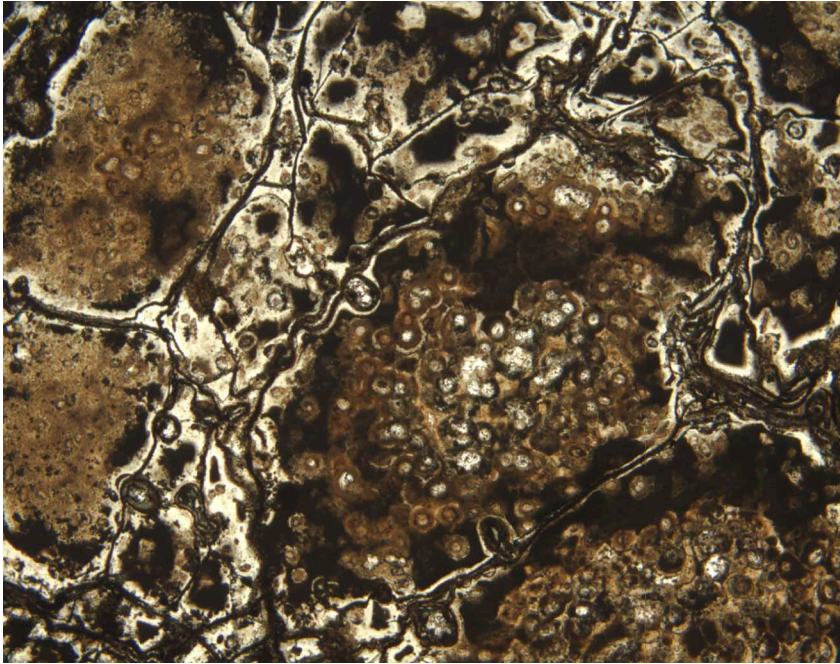
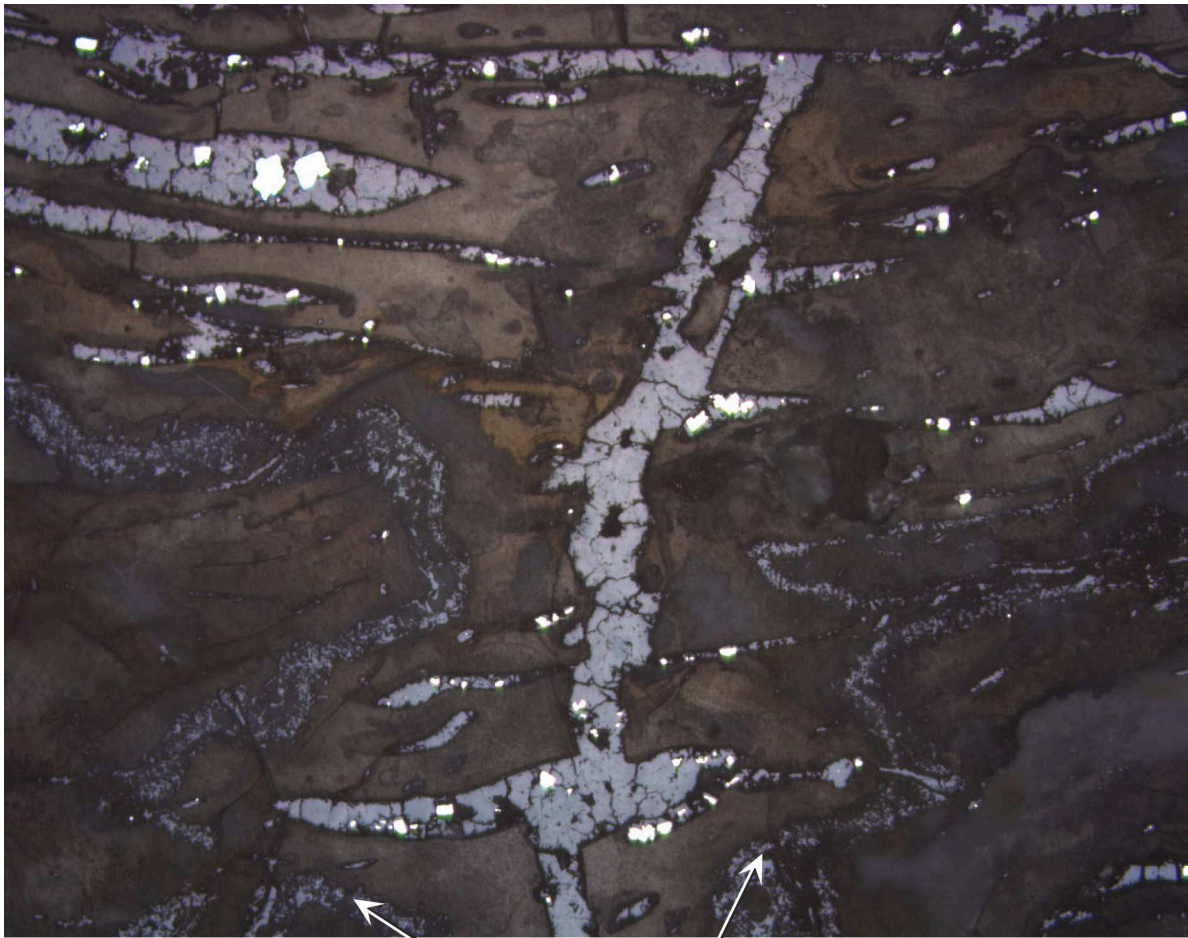


Figure F45. Quartz-pyrite stockwork ladder vein, partly crosscutting and partly parallel to flow banding. A front of silicification (irregular, granular reflective gray banding, indicated on the image) at the outer vein selvage is clearly visible (interval 193-1188A-9R-1, 68–70 cm, Unit 8, in reflected light; width of view = 2.75 mm. Photomicrograph ID#1188A_57 [modified]; [thin section 9](#)).



Fronts of silicification

Figure F46. Narrow quartz-pyrite-magnetite vein (lower center of image) surrounded by a chlorite (dark green)-hematite alteration halo. Remnant spherules of the host volcanic rock are visible at the top left and top right of the image (interval 193-1188A-12R-1, 123–124 cm, Unit 10, in plane-polarized light; width of view = 1.4 mm. Photomicrograph ID# 1188A_67; [thin section 11](#)).

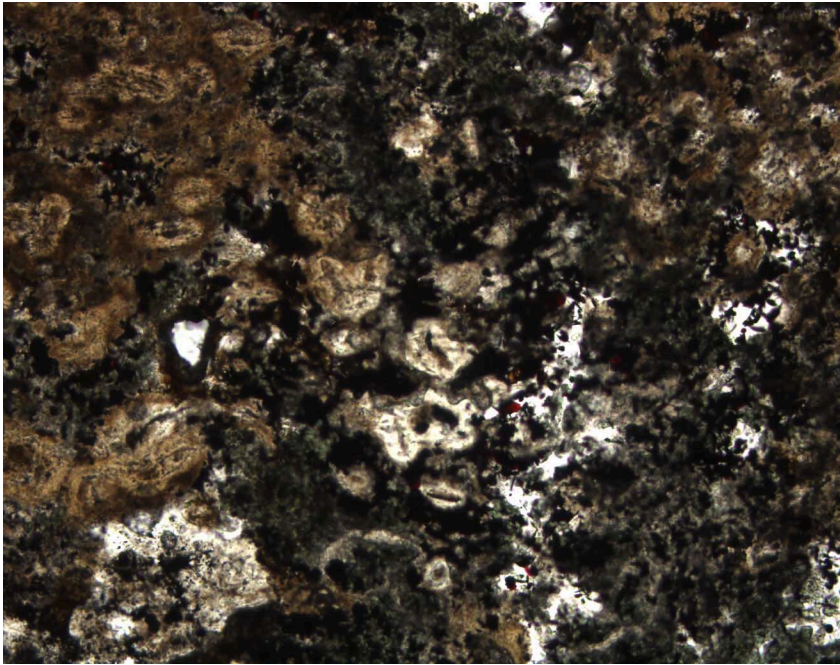


Figure F47. Pervasively bleached vesicular rock (Unit 7) with a zoned alteration pattern toward a darker gray, less strongly bleached kernel (Sample 196-1188A-9R-1, 16–29 cm).

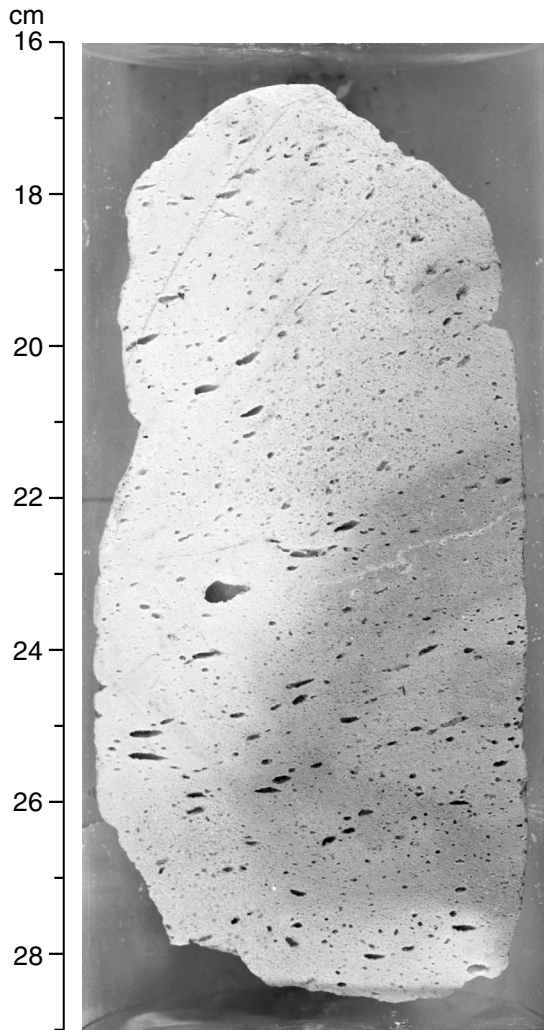


Figure F48. Bleached volcaniclastic sediment (Unit 14) with clay-silica \pm anhydrite altered clasts cemented in silica. Note the variation in grain color and the distinct dark rim (silica alteration) on the large clast in the center of the image (interval 193-1188A-14R-1, 98-113 cm).

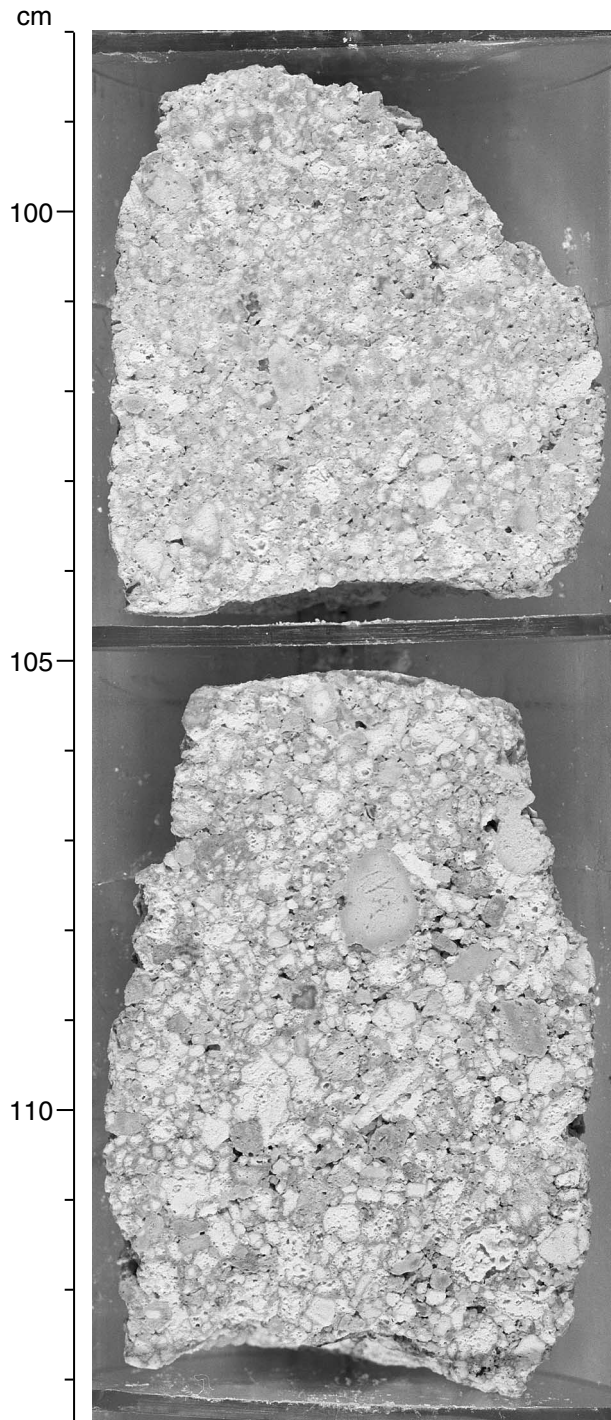


Figure F49. Photomicrograph of volcanoclastic sediment (Unit 14), illustrating very fine grained silica-clay altered volcanic fragments (dark) rimmed by fine crystalline quartz (interval 193-1188A-14R-1, 105–106 cm, in cross-polarized light; width of view = 2.75 mm. Photomicrograph ID# 1188A_63 [modified]; [thin section 14](#)).

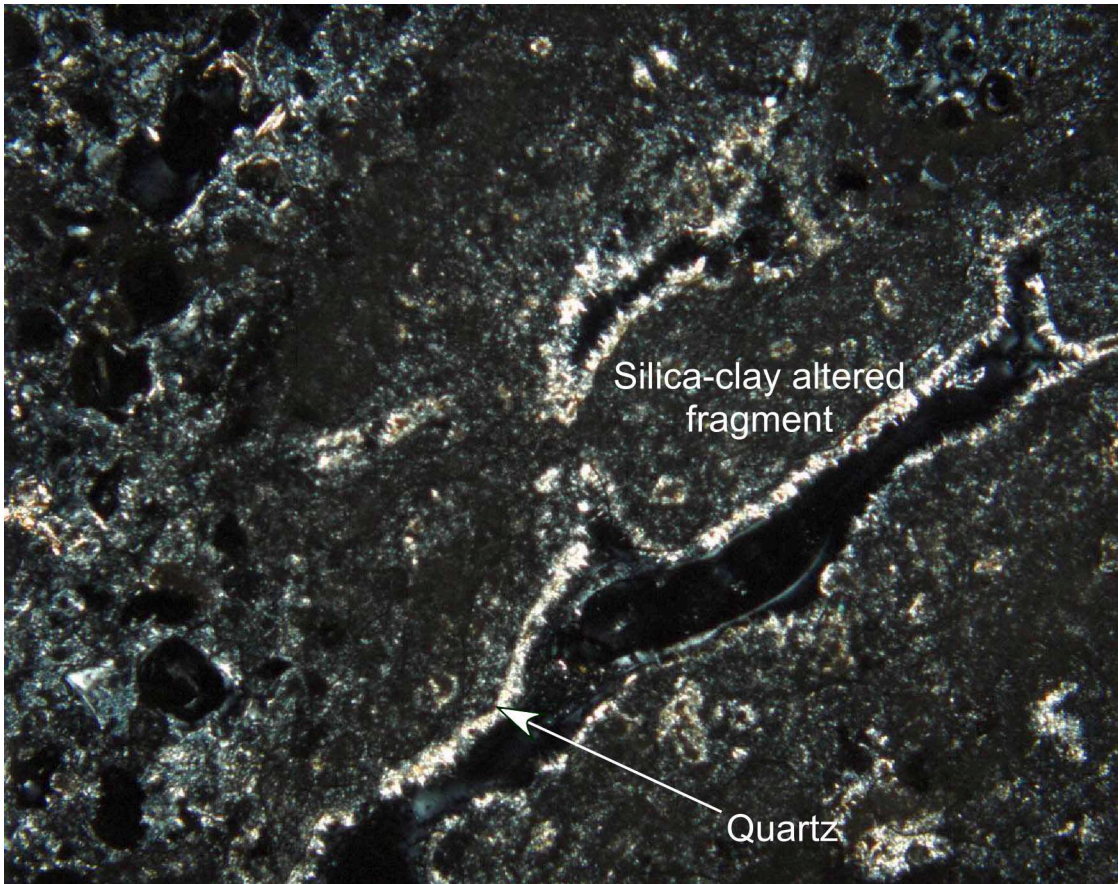


Figure F50. Fractured, bleached volcanic rock (Unit 13) with a strongly developed silica-anhydrite-(pyrite) stockwork veins (interval 193-1188A-14R-1, 25.5–50.5 cm).

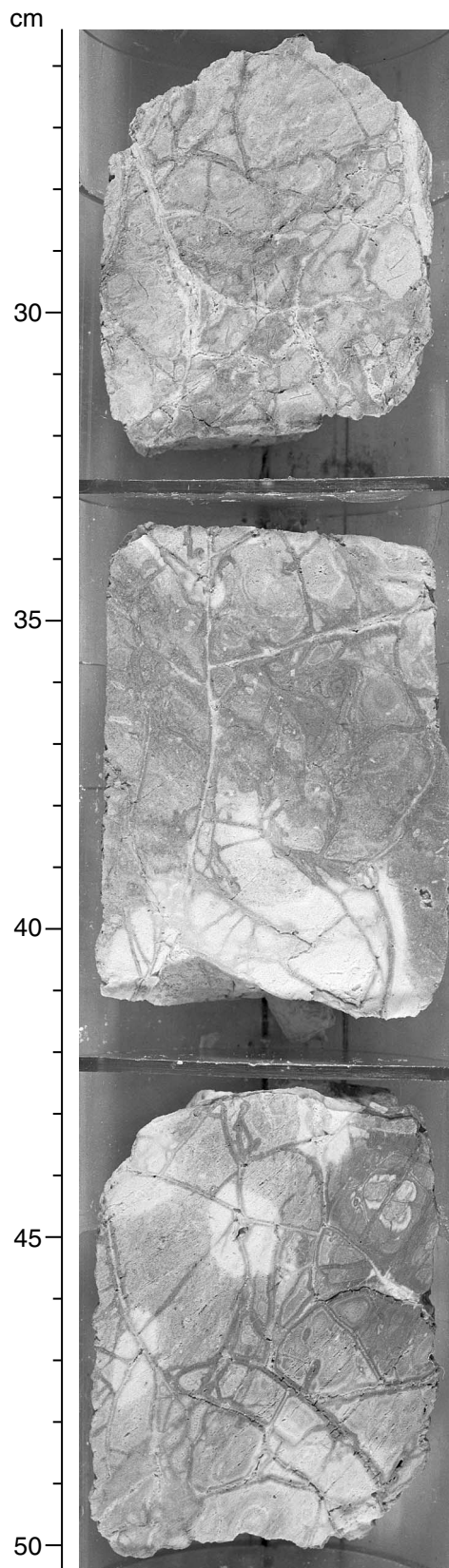


Figure F51. Unit 18 showing fine-scale flow lamination (interval 193-1188A-16R-2, 31–52 cm).

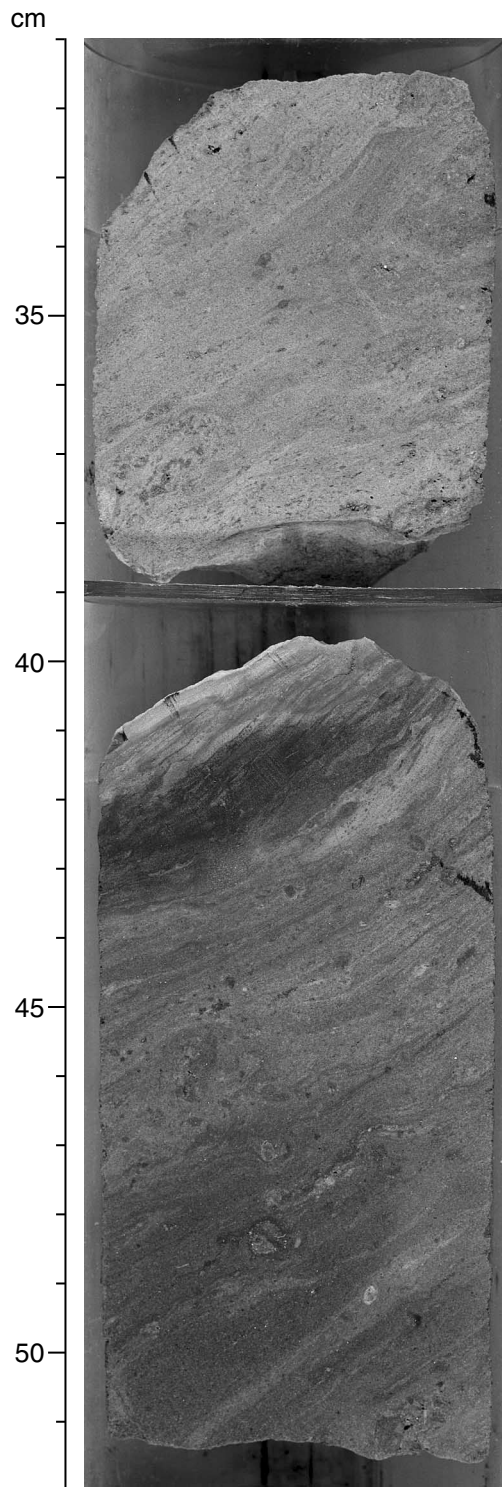


Figure F52. Photomicrograph of a section from finely laminated Unit 18 showing weakly developed alignment of plagioclase microlites and a single phenocryst. Silicification is expressed as patches of quartz masking alignment of microlites in the groundmass of the rock. Apparent high relief of plagioclase is a manufacturing artifact (interval 193-1188A-16R-2, 40–43 cm, Unit 18, in plane-polarized light; width of view = 1.4 mm. Photomicrograph ID# 1188A_77; [thin section 19](#)).



Figure F53. Anhedral former magnetite microphenocryst, which has broken down to leucoxene (dark patch in central portion of image), with remnant trellislike laths of magnetite faintly visible. A pyrite cube overgrows the magnetite (interval 193-1188A-19R-1, 73–76 cm, Unit 19, in reflected light; width of view = 0.7 mm. Photomicrograph ID# 1188A_93; **thin section 21**).

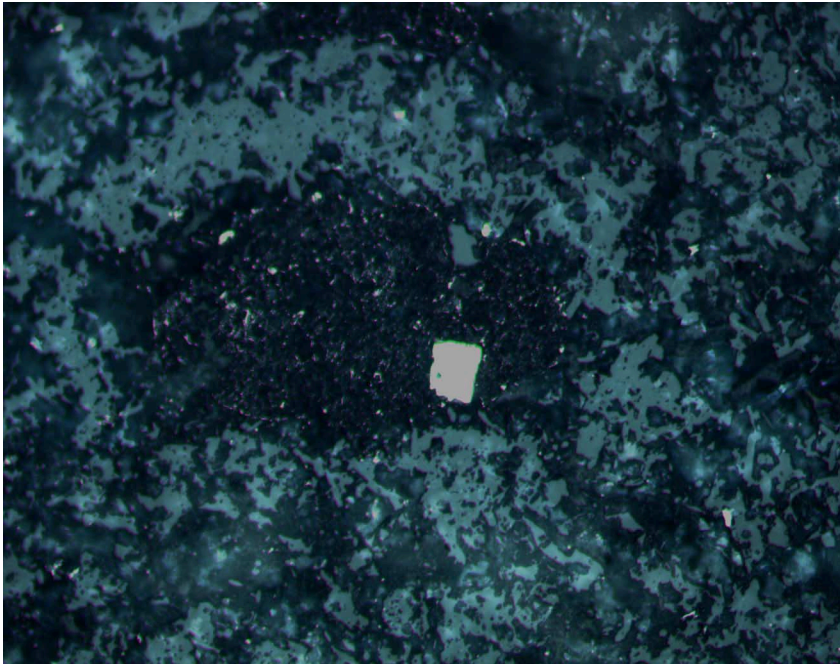


Figure F54. Blotchy silicified rock (Unit 25) with remnant pale-green patches of clay-rich material with fine disseminated magnetite (black spotting), surrounded by darker pervasively silicified material (interval 193-1188A-21R-1, 20-34 cm).

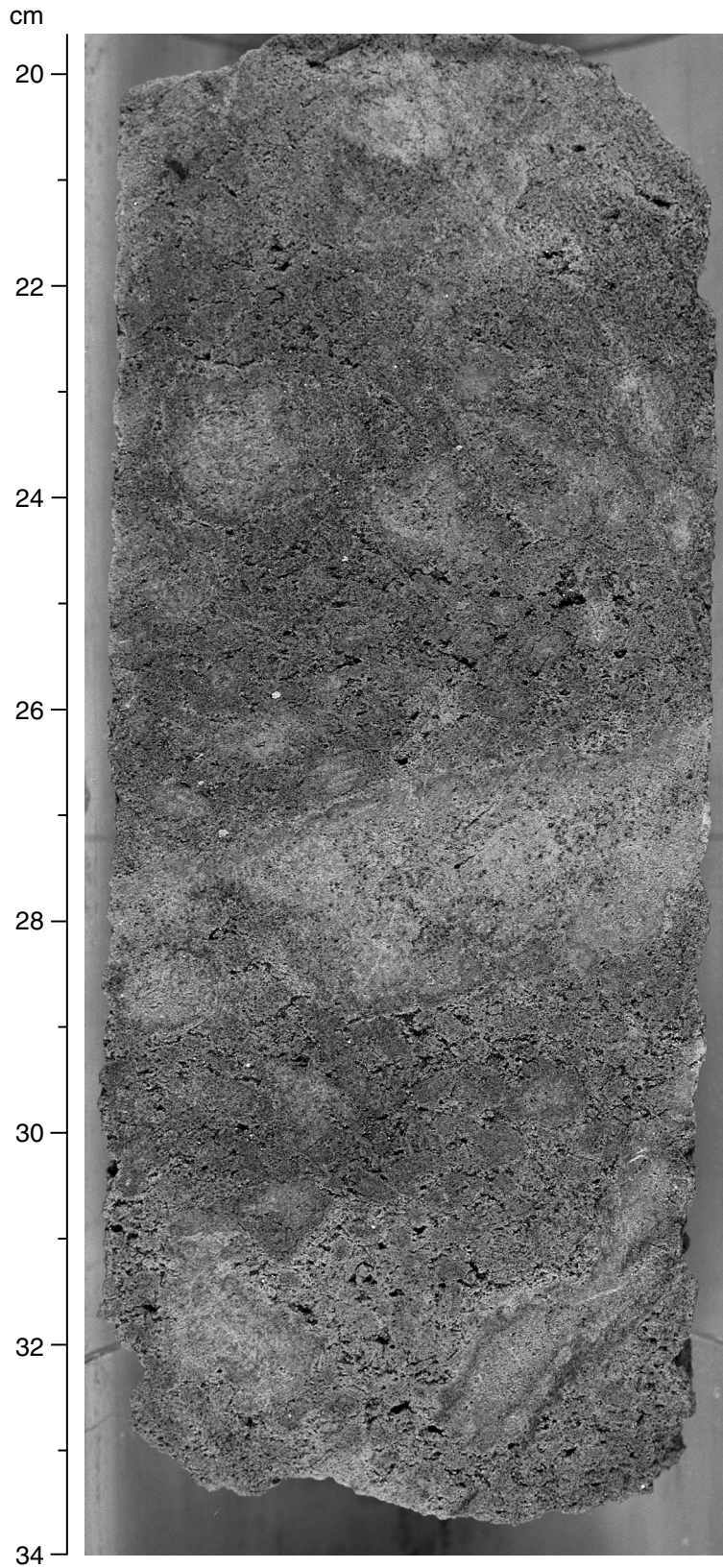


Figure F55. Typical photomicrograph of strongly silicified sample (Unit 25) from the lower portion of Hole 1188A, showing a fine-grained intergrowth of granular quartz and phyllosilicates (interval 193-1188A-21R-1, 20–24 cm, in simultaneous reflected and transmitted plane-polarized light; width of view = 0.7 mm. Photomicrograph ID# 1188A_103; [thin section 26](#)).

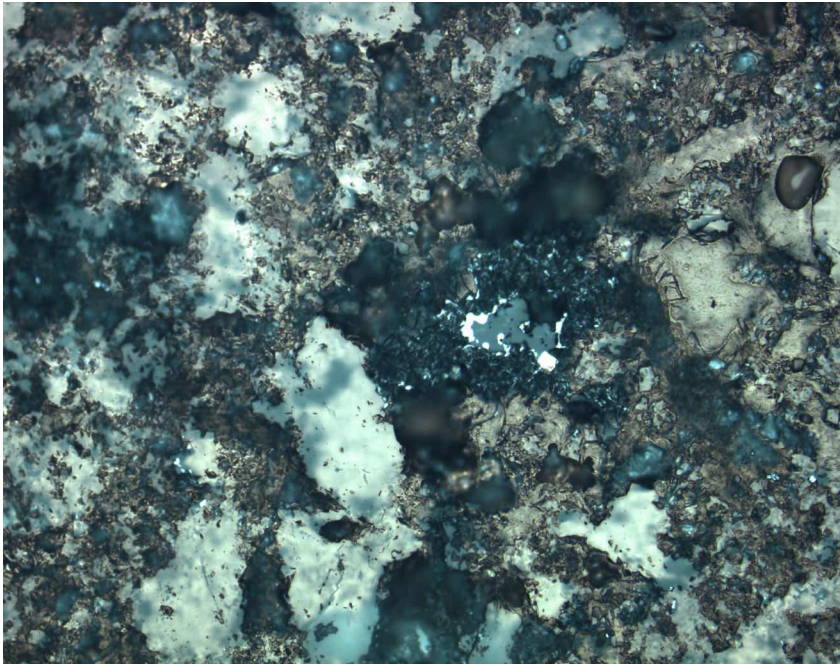


Figure F56. Narrow anhydrite-pyrite vein (1–2 mm, along fracture) with a typical 1- to 1.5-cm-wide cyclically banded alteration halo. The different shades of gray are caused by varying proportions of quartz and clay (interval 193-1188F-2Z-1, 80–91 cm; Unit 29).

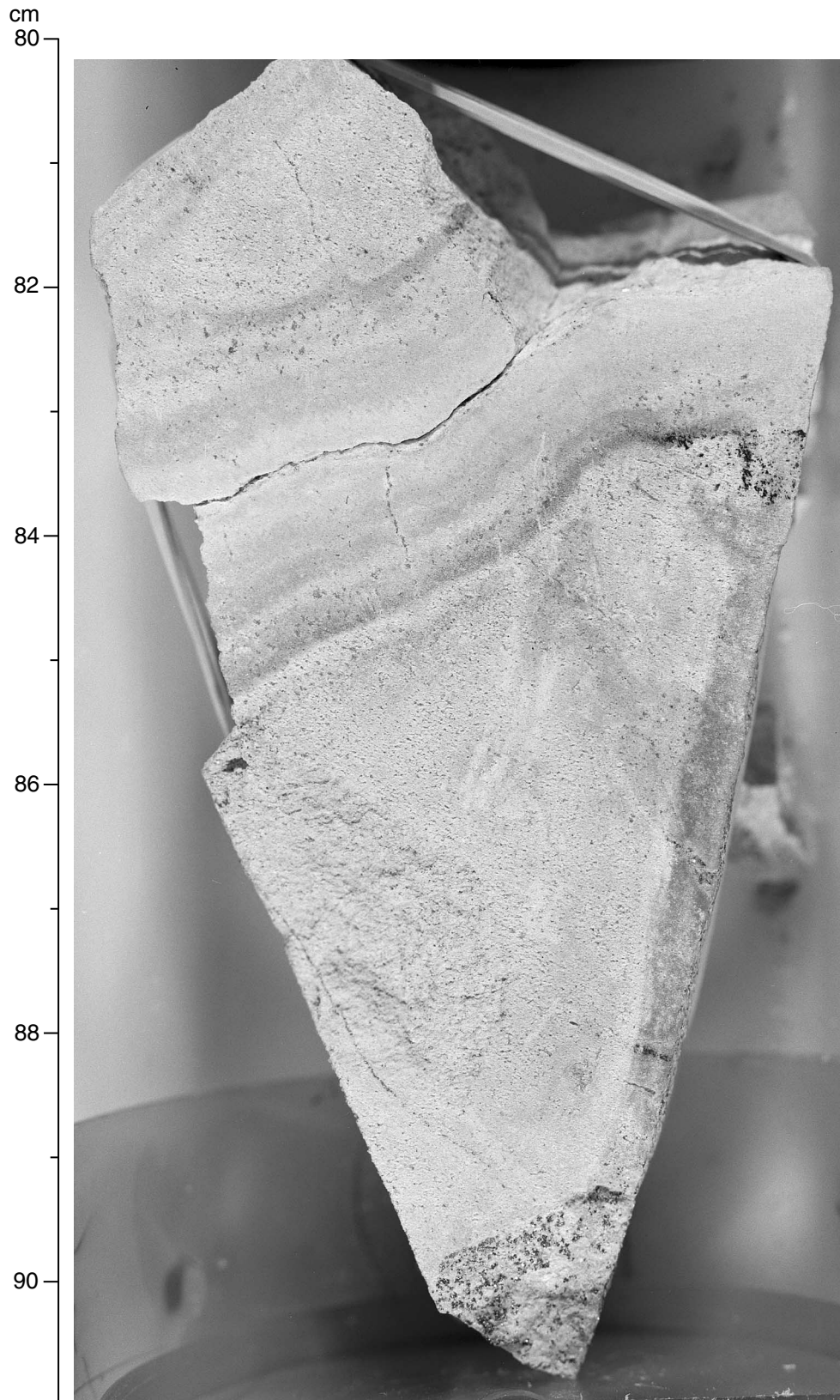
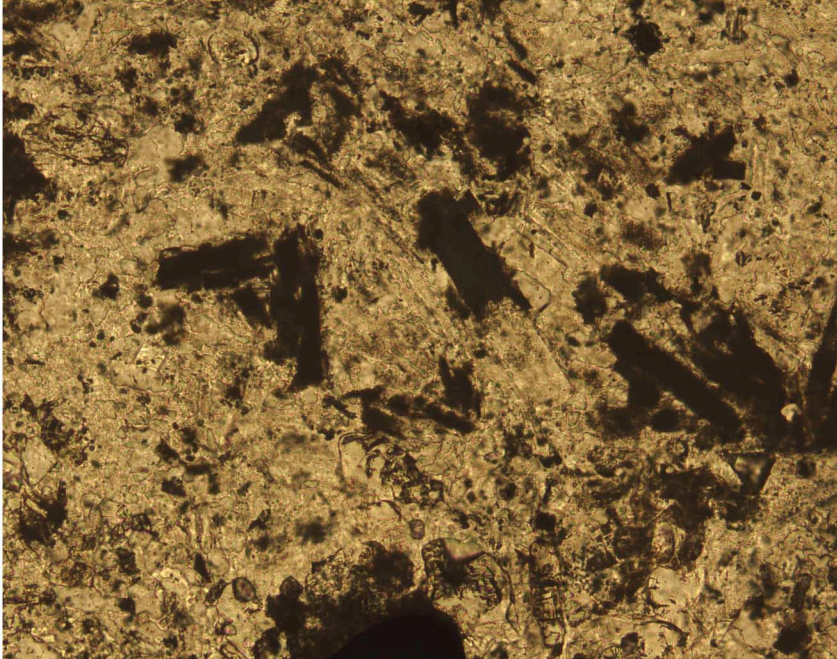


Figure F57. Photomicrographs showing plagioclase microlites variably replaced by colorless illite and dirty brown pyrophyllite. Note that the pyrophyllite shows white internal reflection under the reflected light (interval 193-1188F-11G-1, 138–141 cm, Unit 39, in (A) plane-polarized transmitted light and (B) reflected light; width of view = 0.7 mm. Photomicrograph ID# 1188F_31 and 1188F_32; [thin section 75](#)).

A



B

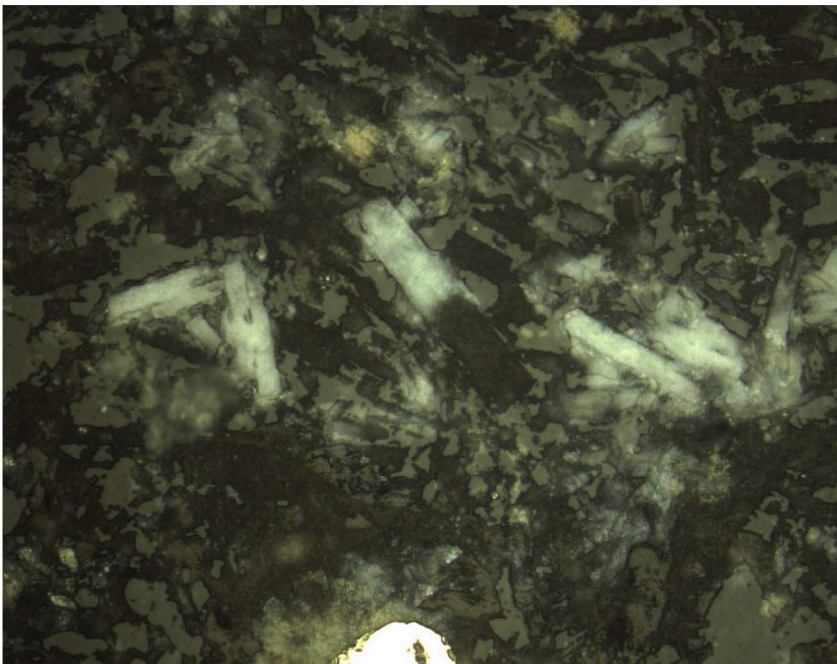


Figure F58. Plagioclase phenocryst completely replaced by fine-grained illite (birefringent mineral) and possible halloysite (gray) (interval 193-1188F-14Z-1, 102–105 cm, Unit 41, in cross-polarized light; width of view = 0.7 mm. Photomicrograph ID# 1188F_80; [thin section 80](#)).

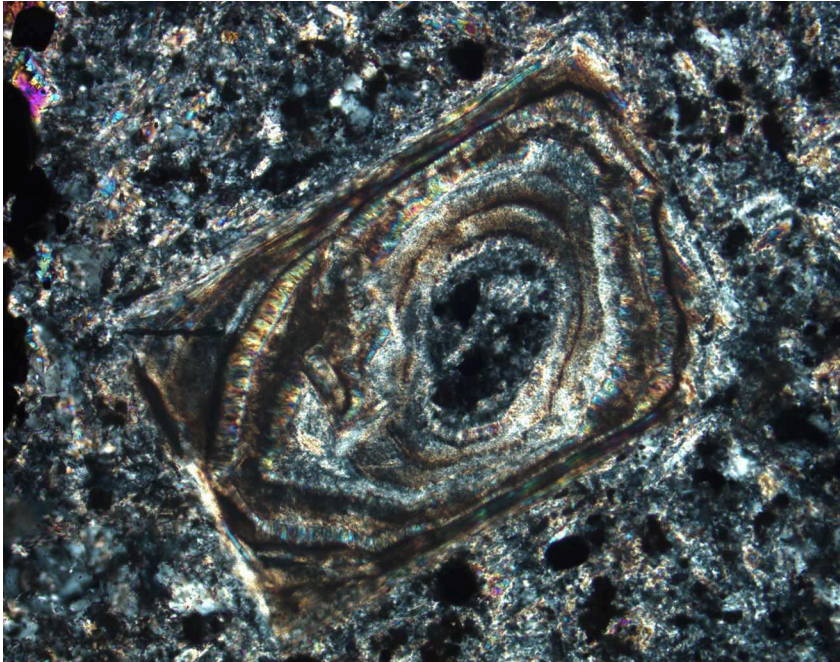


Figure F59. Photomicrograph of a thin section without anhydrite veining (Unit 28), showing quartz \pm pyrite amygdules in a fine-grained quartz-illite groundmass (interval 193-1188F-1Z-3, 86–89 cm, in plane-polarized light; width of view = 2.75 mm. Photomicrograph ID# 1188F-12; [thin section 61](#)).

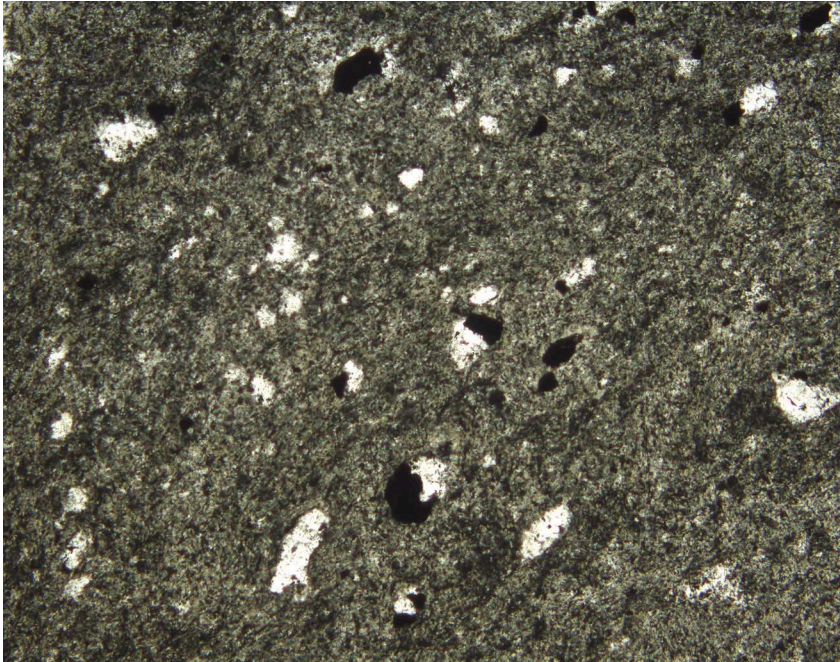


Figure F60. Thin-section photomicrograph of an apparently clastic interval within Unit 27. The image shows the contact between a fine-grained quartz-illite altered “clast” (top right) and the dark clay rich matrix of the rock (interval 193-1188F-1Z-2, 8-10 cm, in plane-polarized light; width of view = 2.75 mm. Photomicrograph ID# 1188F_11; **thin section 58**).

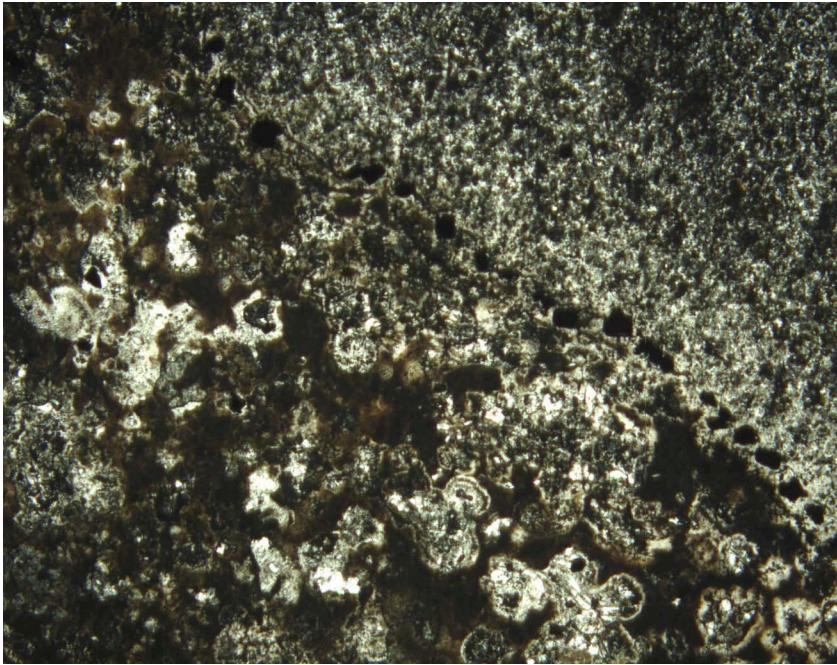


Figure F61. Photomicrograph of an apparently spherulitic unit, showing spherical domains in a cristobalite-clay matrix (interval 193-1188F-6Z-1, 45–47 cm, Unit 31, in plane-polarized light; width of view = 5.5 mm. Photomicrograph ID# 1188F_16; [thin section 67](#)).

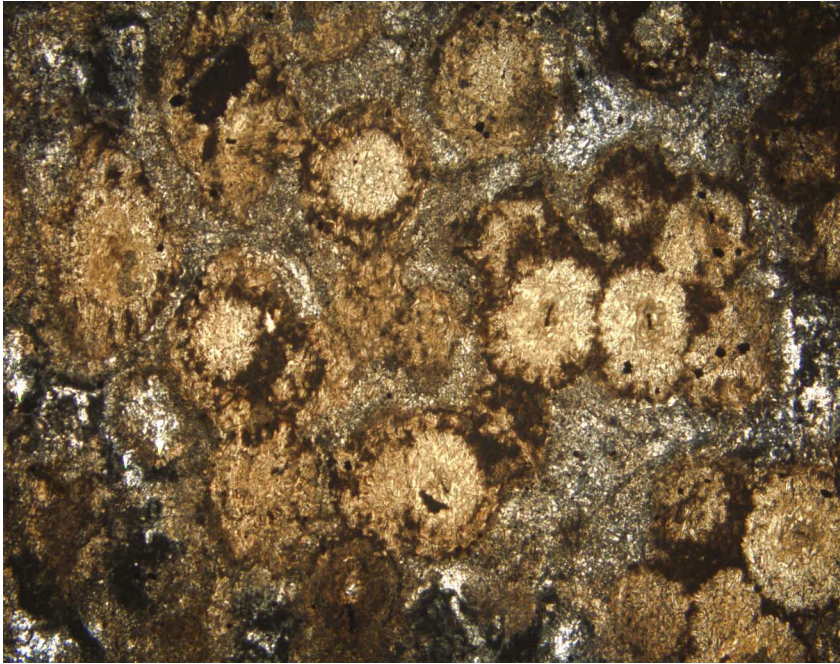


Figure F62. Photomicrograph of a typical silicified unit from the lower sequence of Hole 1188F. Remnant corroded plagioclase microcrysts show a trachytic alignment and are hosted in a fine-grained alteration assemblage of quartz and illite. The coarsely crystalline quartz fills original vesicles. (interval 193-1188F-37Z-2, 18–20 cm, Unit 57, in cross-polarized light; width of view = 5.5 mm. Photomicrograph ID# 1188F_107; [thin section 100](#)).

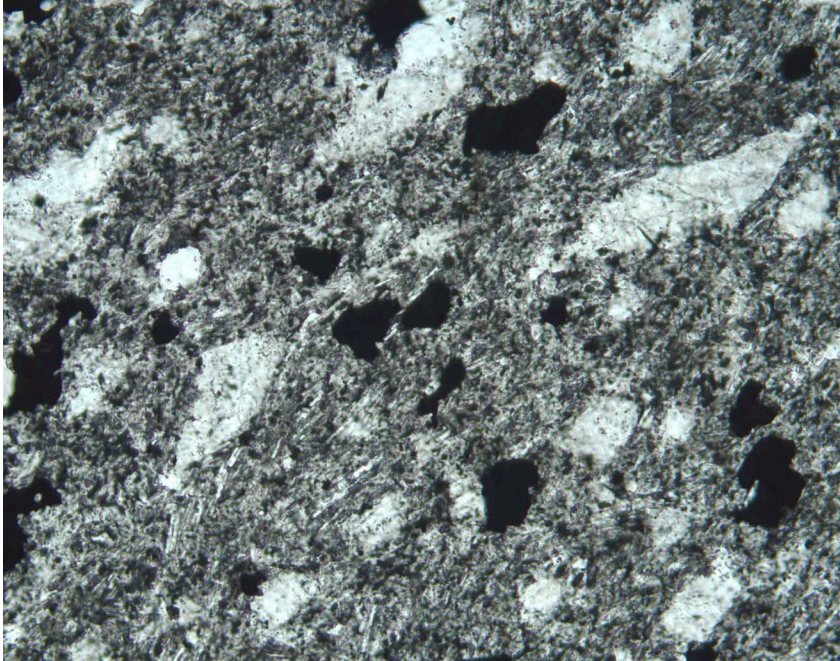
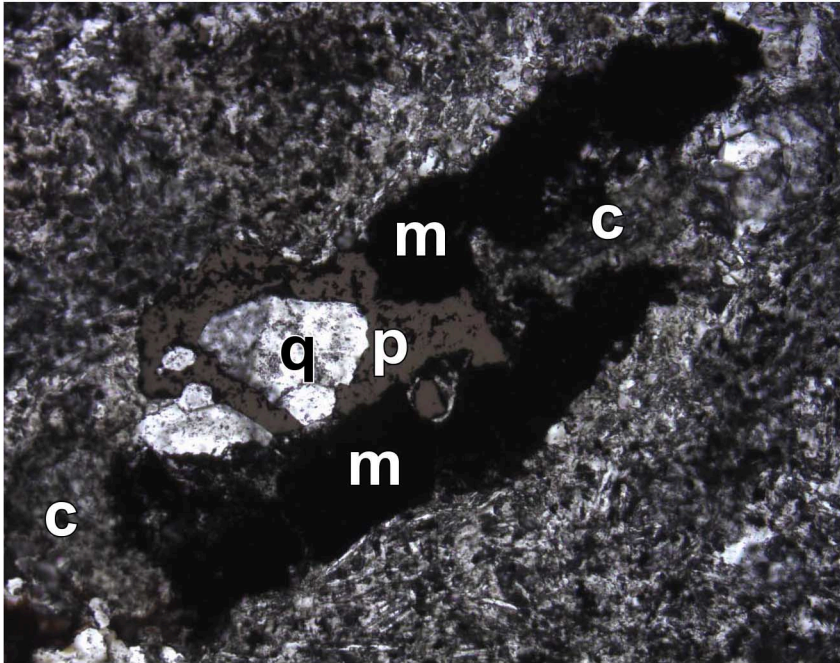


Figure F63. A. Combined plane-polarized transmitted and reflected light photomicrograph of a “magnetite” (m)-chlorite (c)-quartz (q)-pyrite (p) filled vesicle. Width of view = 1.4 mm. B. High-magnification reflected light image of the opaque portion (m) of the amygdale in (A). It consists of fine, spongy remnant magnetite in a matrix of clay (white internal reflections) and dark opaque material. Width of view = 0.275 mm (interval 193-1188F-40Z-1, 3–5 cm; Unit 65). Photomicrograph ID# 1188F_94 and 1188F_95; [thin section 106](#)).

A



B

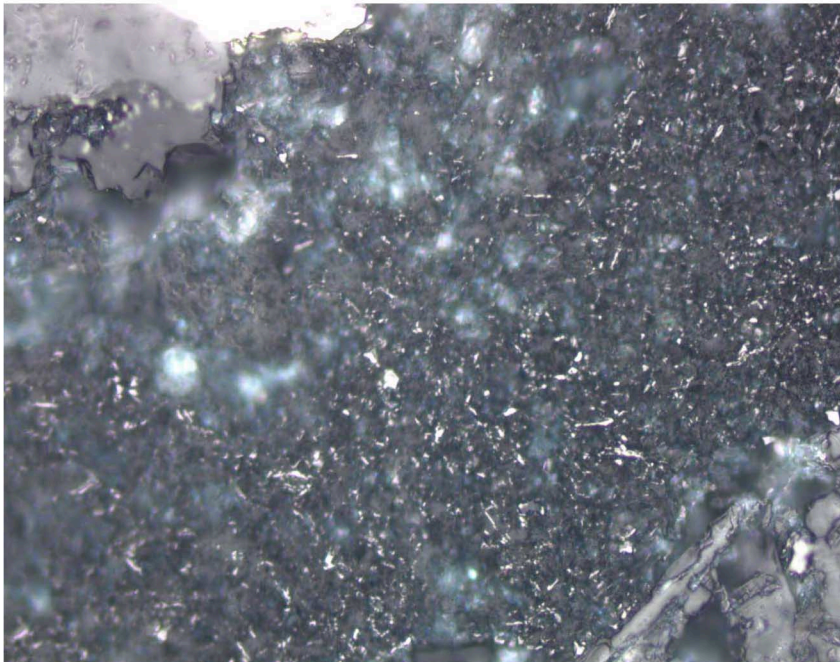


Figure F64. Close-up photograph (wet) of part of Unit 72, the final unit of Hole 1188F. Note the dark magnetite-bearing halo around the white quartz-clay-pyrite-(anhydrite) vein that runs along the core. Dark magnetite can also be seen partially filling vesicles in the top left of the photograph (interval 193-1188F-43Z-1, 65–74 cm).

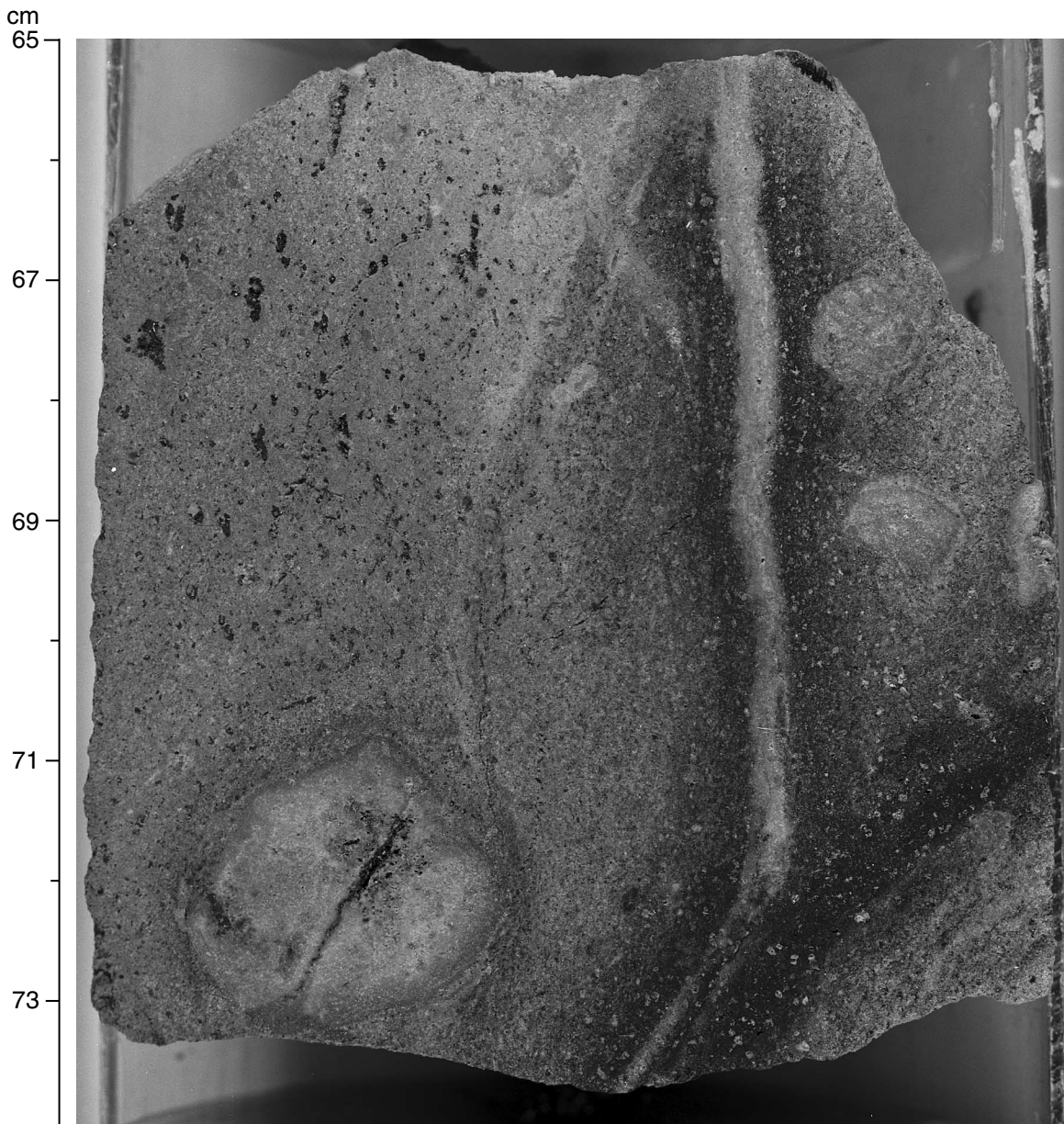


Figure F65. Fine-grained green hercynite spinel crystals hosted in quartz from Unit 55. (Sample 193-1188F-34Z-1 [Piece 9A, 45–47 cm] in plane-polarized light; width of view = 0.70 mm. Photomicrograph ID# 1188F_85; [thin section 95](#)).

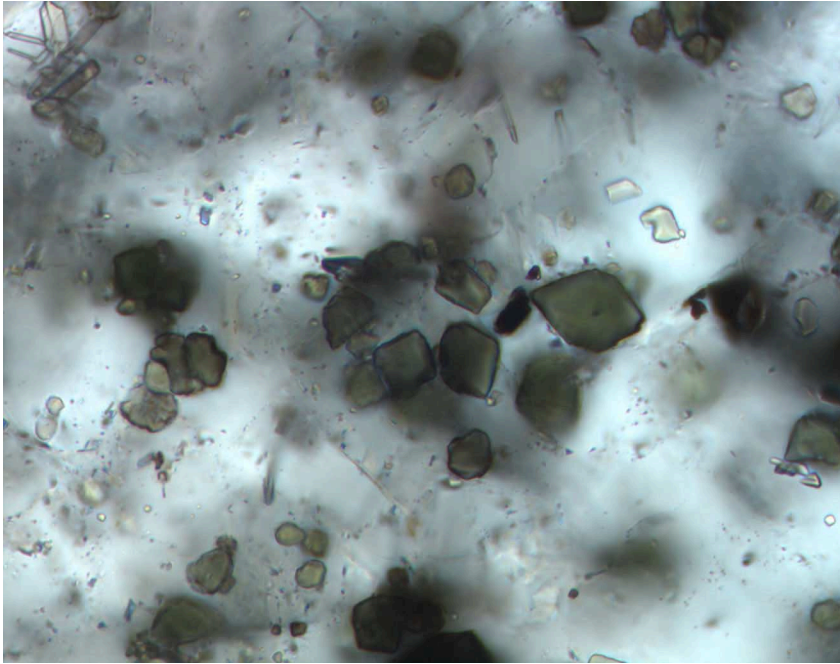
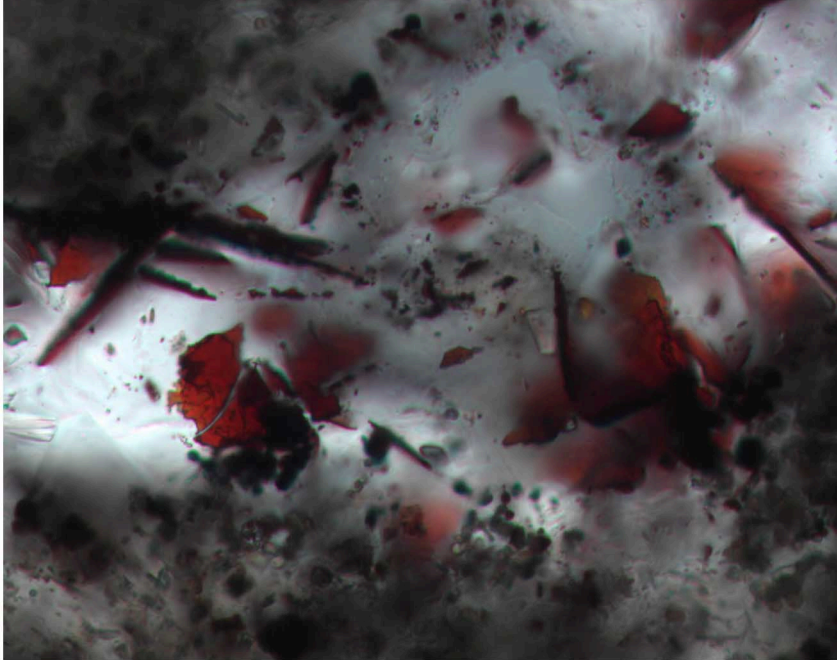


Figure F66. Photomicrograph of hematite in Unit 58. **A.** Bladed crystals of hematite in quartz, associated with bladed magnetite (in plane-polarized light [oil immersion]; width of view = 0.14 mm). **B.** Hematite as vesicle fill, with colorless alunite or brucite and pale green chlorite (interval 193-1188F-37Z-2, 31–33 cm, in plane-polarized light; width of view = 0.275 mm. Photomicrograph ID#s 1188F_75 and 1188F_89; [thin section 101](#)).

A



B

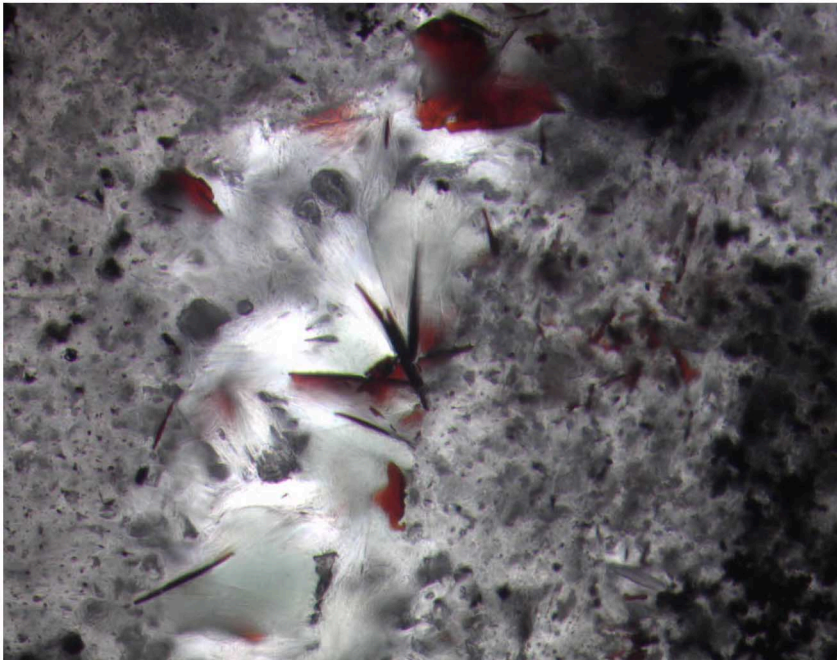


Figure F67. Combined plane-polarized transmitted and reflected light photomicrograph showing pyrite overgrowing a dark magnetite-bearing aggregate. Note the fine lamellae of magnetite in the opaque area of the slide and the magnetite inclusions in pyrite (interval 193-1188F-40Z-1, 3–5 cm; Unit 65; width of view = 0.7 mm. Photomicrograph ID# 1188F_96; [thin section 106](#)).

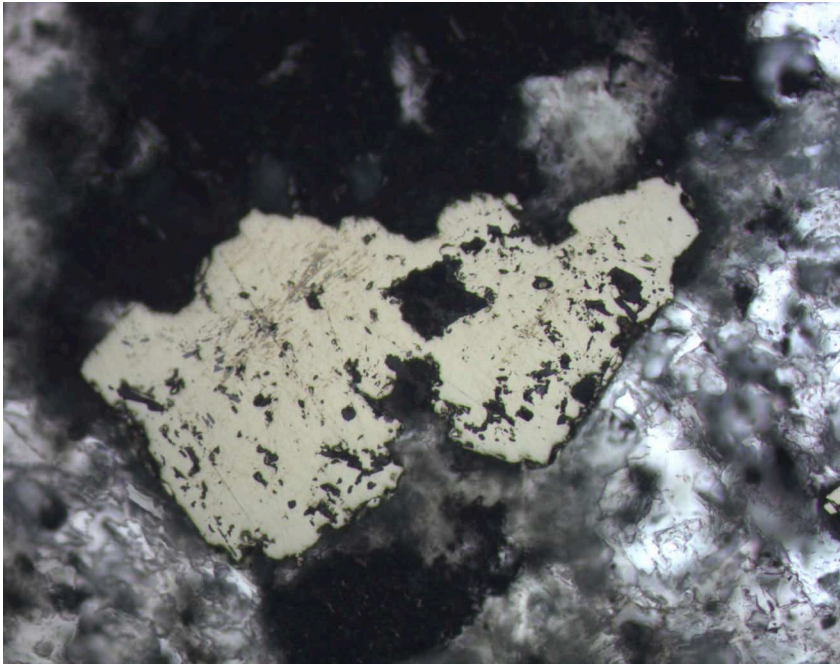


Figure F68. Variation in abundance of significant minerals with depth at Site 1188, as estimated in thin section for Hole 1188A (solid circles) and Hole 1188F (open circles).

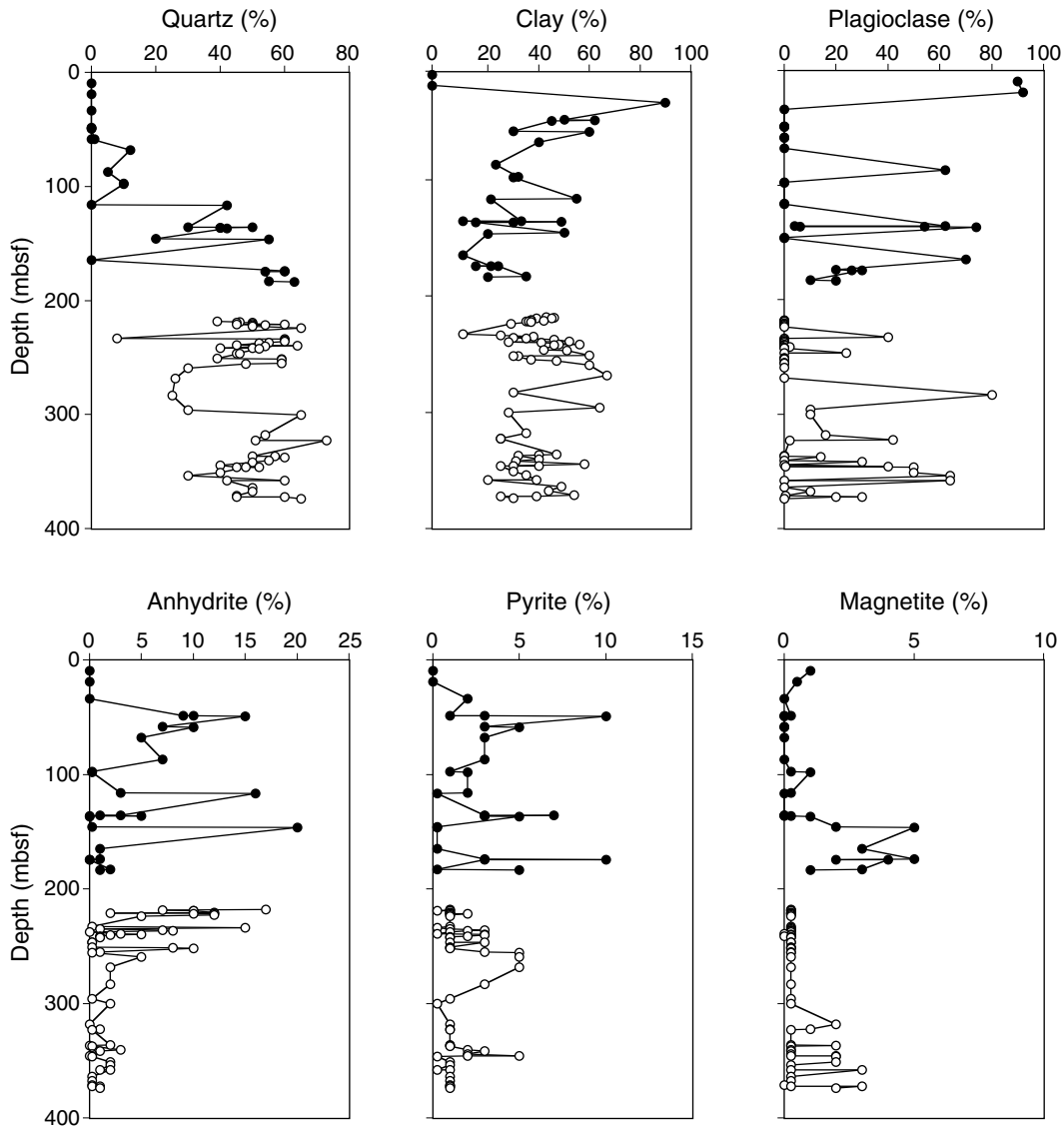


Figure F69. Highly altered dacite fragments in a matrix of Type 1 disseminated pyrite. Very fine grained pyrite (identified as a minor phase by X-ray diffraction) is sufficiently abundant to darken the encompassing anhydrite-silica-clay host (interval 193-1188A-7R-2, 26–42 cm).

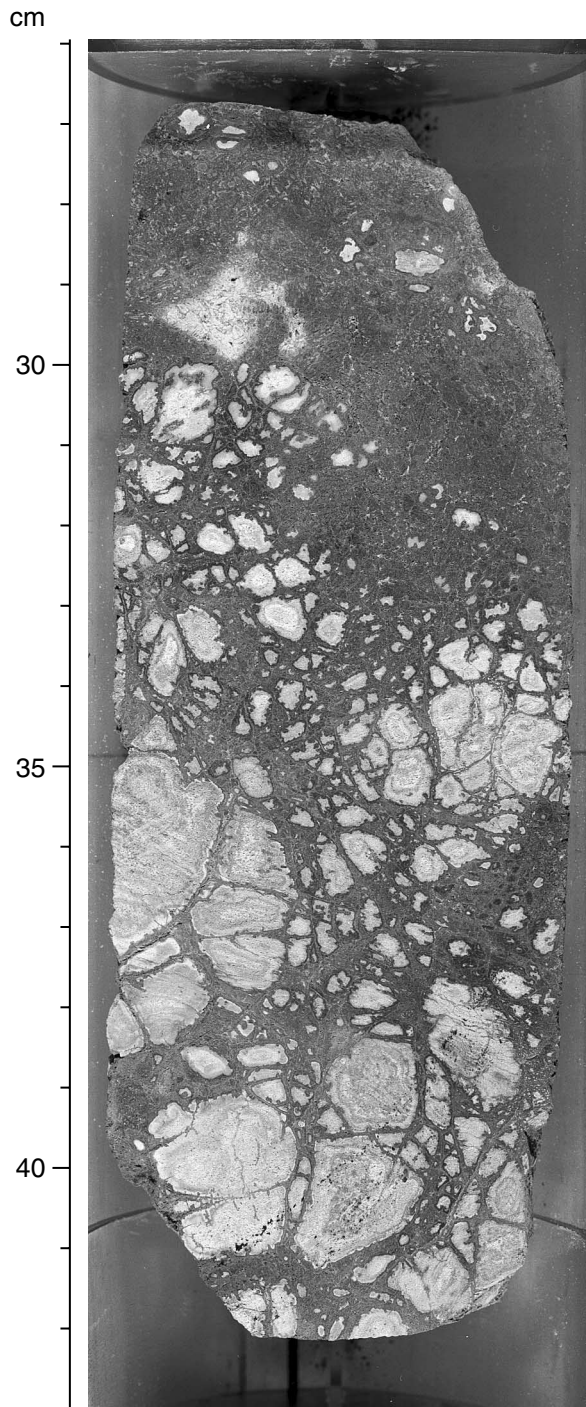


Figure F70. Type 2 anhydrite-quartz-pyrite veins in fractured and highly altered dacite (interval 193-1188A-8R-1, 20-28 cm).

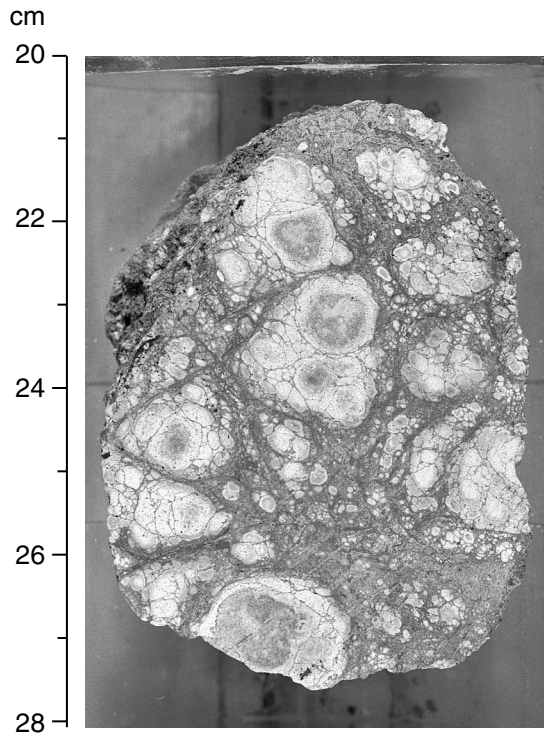


Figure F71. Type 2 anhydrite-pyrite + cristobalite veins cut by a later barren anhydrite vein (Sample 193-1188A-7R-2 [Piece 2, 39–41 cm] in plane-polarized transmitted light; width of view = 1.4 mm. Photomicrograph ID# 1188A_4; [thin section 6](#)).



Figure F72. Veins of anhydrite and pyrite together with Type 1 disseminated pyrite in highly altered dacite. The altered fragments are compositionally zoned with a silica-rich rim and clay- and anhydrite-rich interior. Note the absence of pyrite in the silicified rim and the zonal arrangement of very fine pyrite within the fragment at bottom right (Sample 193-1188A-7R-2 [Piece 2, 39–41 cm] in plane-polarized transmitted light; width of view = 0.275 mm. Photomicrograph ID# 1188A_1; [thin section 6](#)).

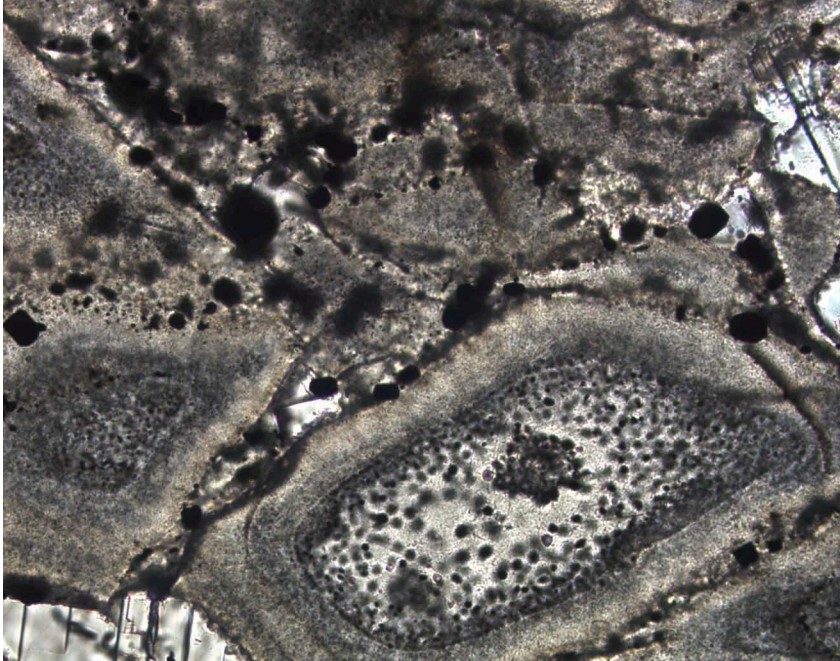


Figure F73. Same view as Figure F72, p. 175, in reflected light (Sample 193-1188A-7R-2 [Piece 2, 39–41 cm]; width of view = 0.275 mm. Photomicrograph ID# 1188A_2; [thin section 6](#)).

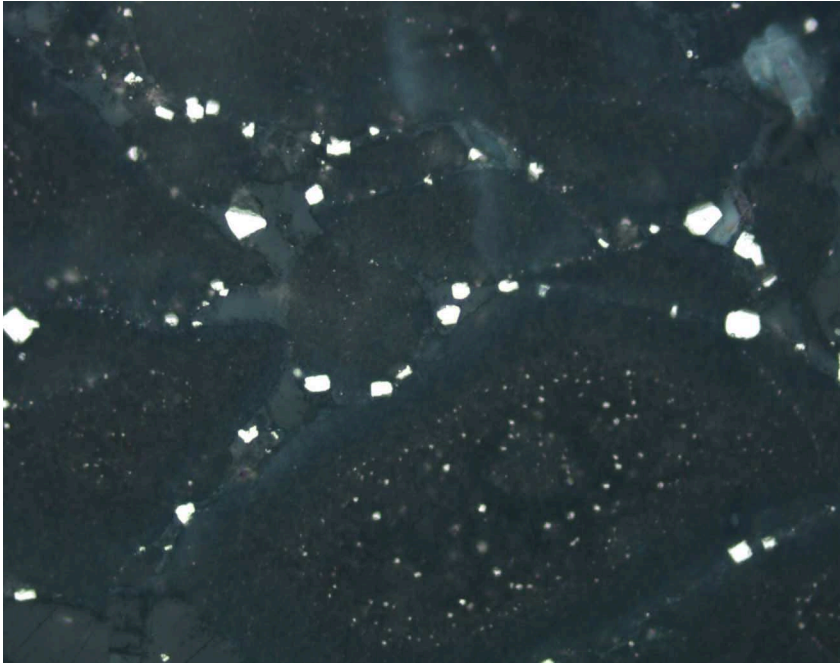


Figure F74. Subhedral pyrite (yellow) containing vermicular inclusions of magnetite (indicated) (interval 193-1188A-20R-1, 74–76 cm, in reflected light; width of view = 0.167 mm. Photomicrograph ID# 1188A_6; thin section 24).

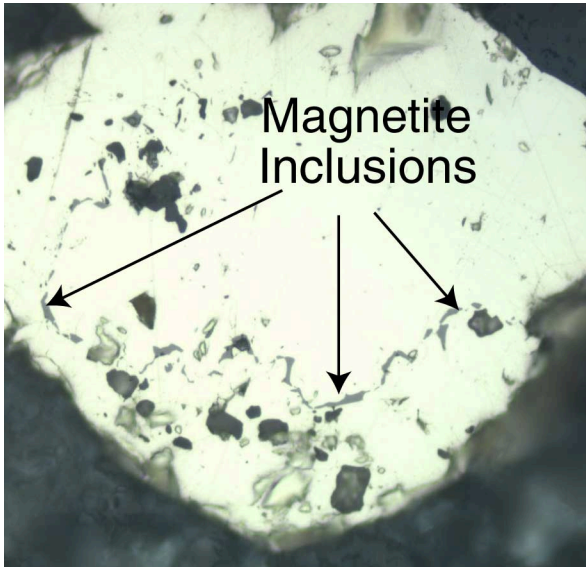


Figure F75. Vermicular magnetite (light gray) in quartz (dark gray, smooth) (interval 193-1188A-20R-1, 74–76 cm, in reflected light; width of view = 0.167 mm. Photomicrograph ID# 1188A_9; [thin section 24](#)).

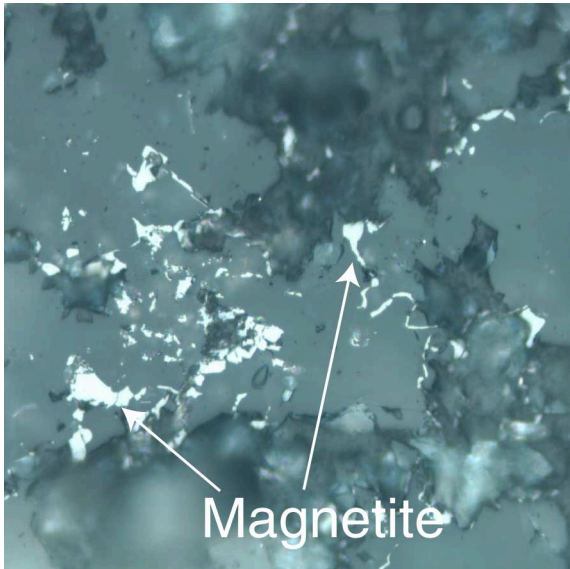


Figure F76. Pyrite (white) engulfing magnetite (medium gray). Note magnetite inclusions in pyrite (interval 193-1188A-20R-1, 92–95 cm, in reflected light; width of view = 0.275 mm. Photomicrograph ID# 1188A_106; [thin section 25](#)).

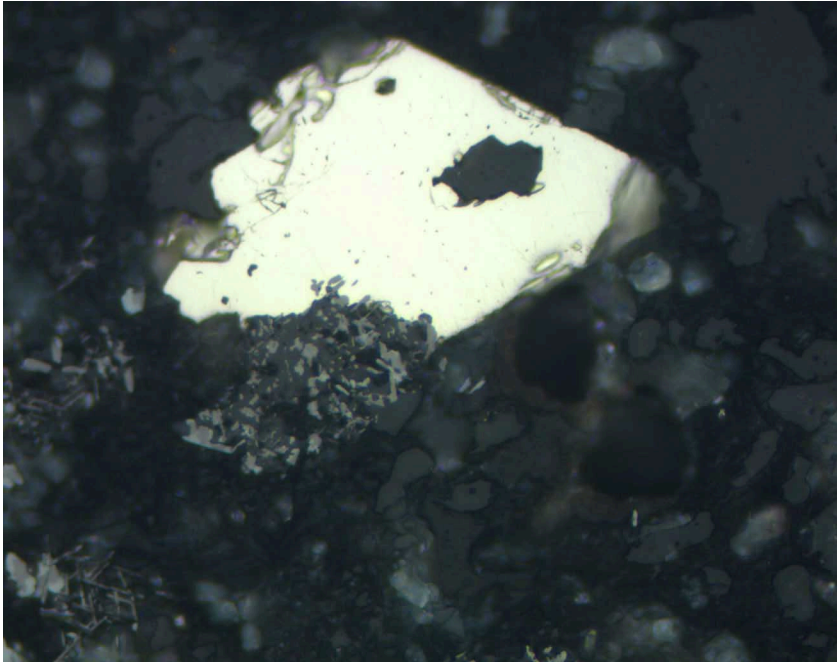


Figure F77. Lamellae in lattice textured magnetite (medium gray) partially replaced by maghemite or hematite (light gray) in an altered groundmass (Sample 193-1188A-20R-1 [Piece 5, 92–95 cm] in reflected light; width of view = 0.275 mm. Photomicrograph ID# 1188A_105; [thin section 25](#)).

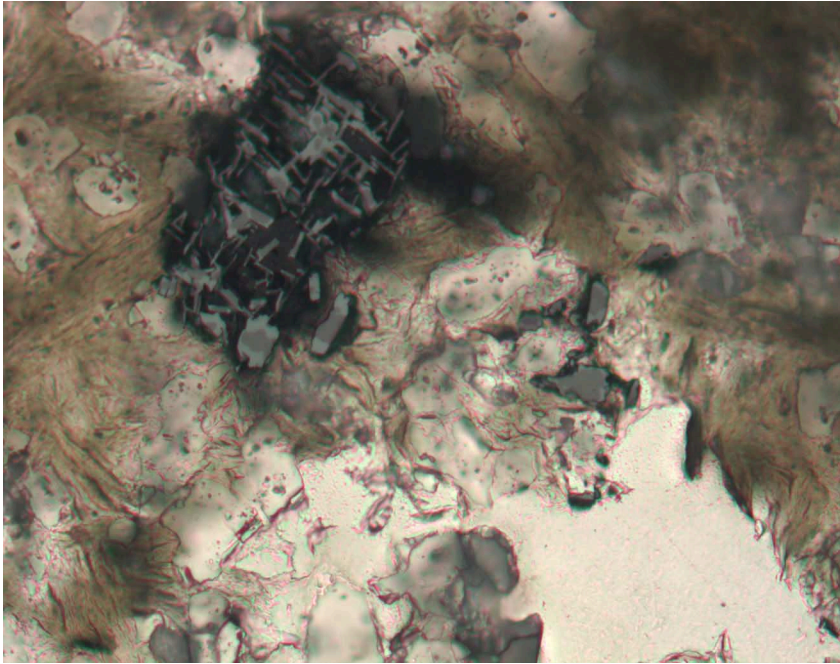


Figure F78. Close-up core photograph of subhedral Fe-rich sphalerite (black) precipitated on euhedral pyrite in a cavity (Sample 193-1188A-9R1 [Piece 5, 30–40 cm]; width of view = 5 mm).

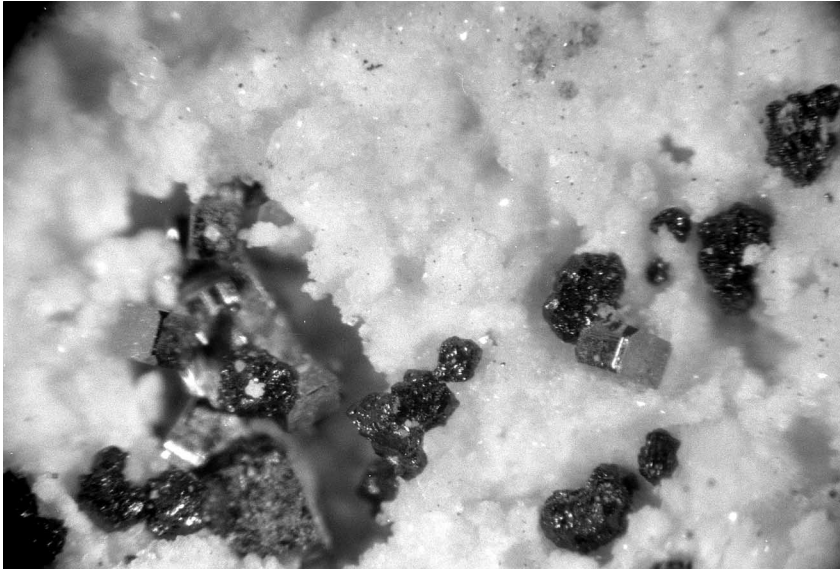


Figure F79. Vesicle filled with anhydrite (high relief, with cleavage), minor quartz (low relief), and euhedral pyrite (opaque) (Sample 193-1188F-15Z-1 [Piece 16, 142–144 cm] in plane-polarized transmitted light; width of view = 1.40 mm. Photomicrograph ID# 1188F_44; [thin section 83](#)).

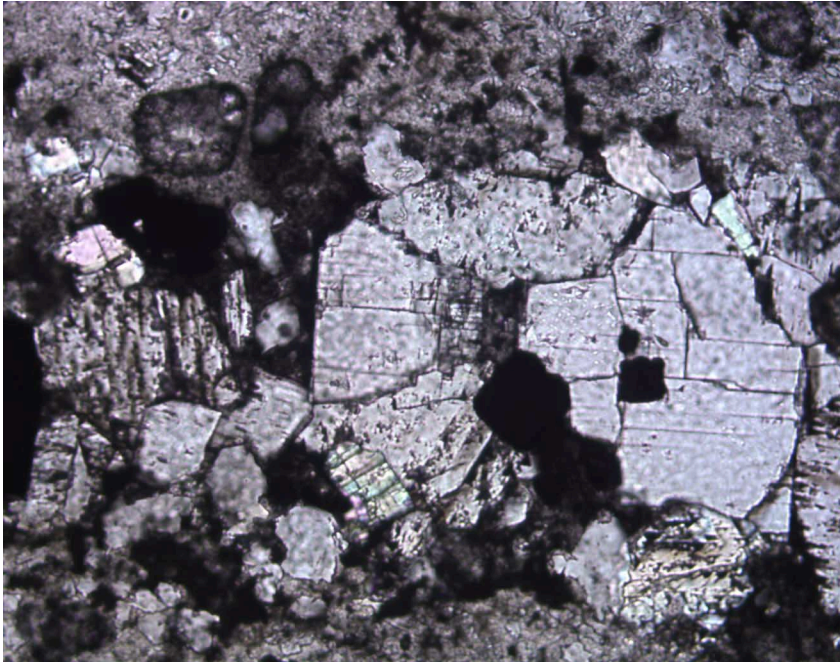


Figure F80. Pyrite with abundant magnetite and quartz and rare hematite and chalcopyrite inclusions (Sample 193-1188F-15Z-1 [Piece 12, 111–114 cm] in reflected light; width of view = 0.70 mm. Photomicrograph ID# 1188F_24; [thin section 82](#)).

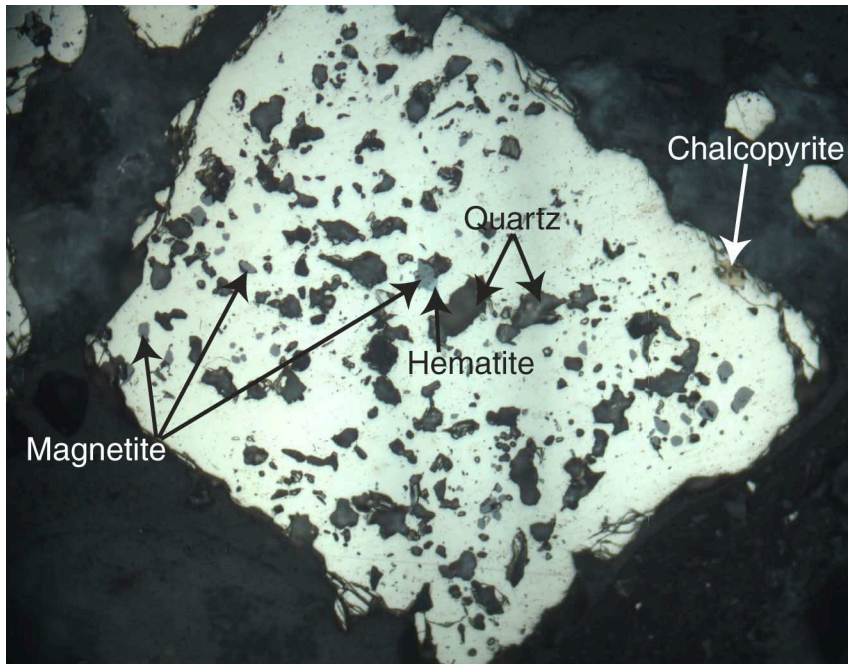


Figure F81. Pyrrhotite inclusion (0.006 mm in diameter) and smaller magnetite inclusions in pyrite (Sample 193-1188F-1Z-3 [Piece 3, 86–89 cm] in reflected light; width of view = 0.14 mm. Photomicrograph ID# 1188F_6; **thin section 61**).

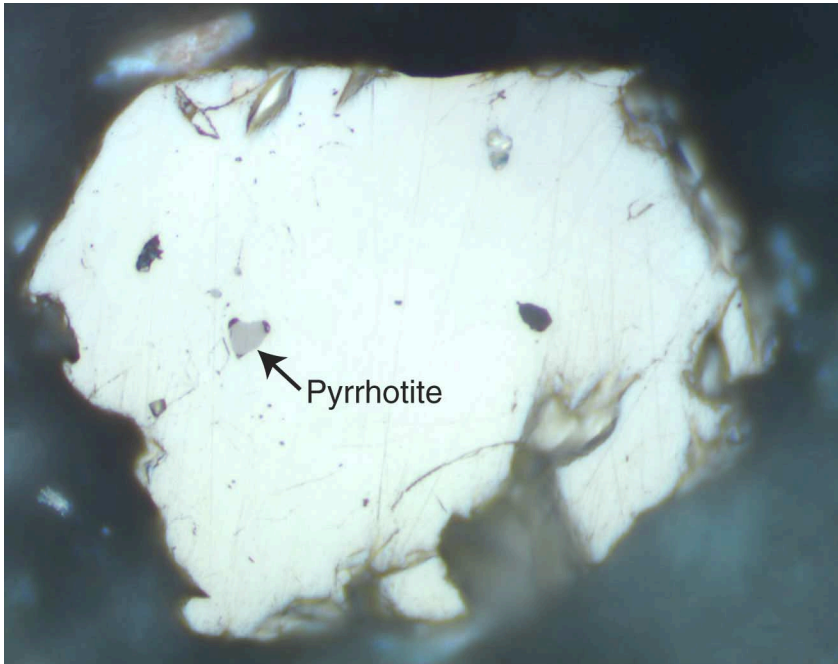


Figure F82. Inclusions of pyrrhotite and magnetite in pyrite (Sample 193-1188F-11G-1 [Piece 9, 108–111 cm] in reflected light; width of view = 0.275 mm. Photomicrograph ID# 1188F_23; [thin section 74](#)).

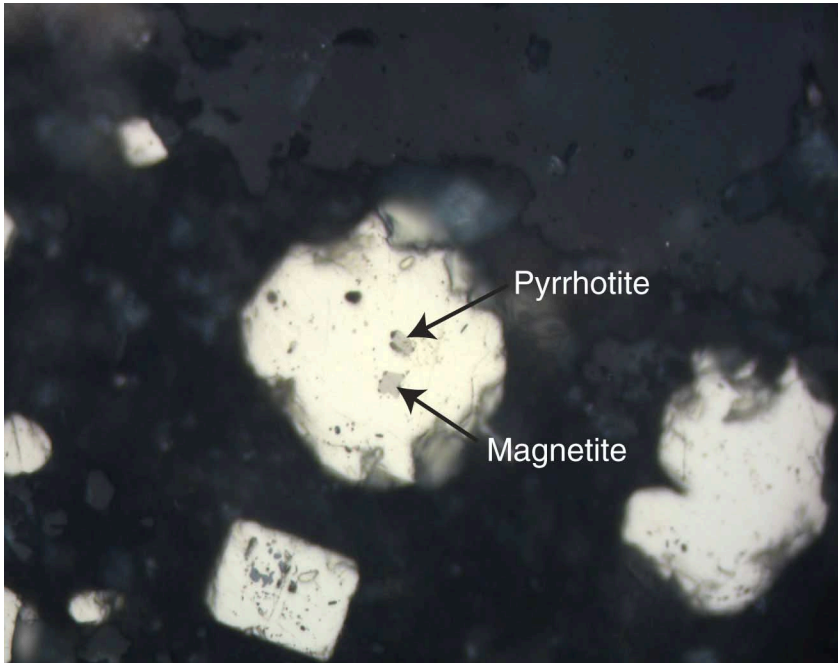


Figure F83. Inclusion of hematite (medium gray) with a remnant of magnetite (dark gray) in pyrite (white) (Sample 193-1188F-35Z-1 [Piece 2D, 44–46 cm] in reflected light; width of view = 0.14 mm. Photomicrograph ID# 1188F_106; **thin section 98**).

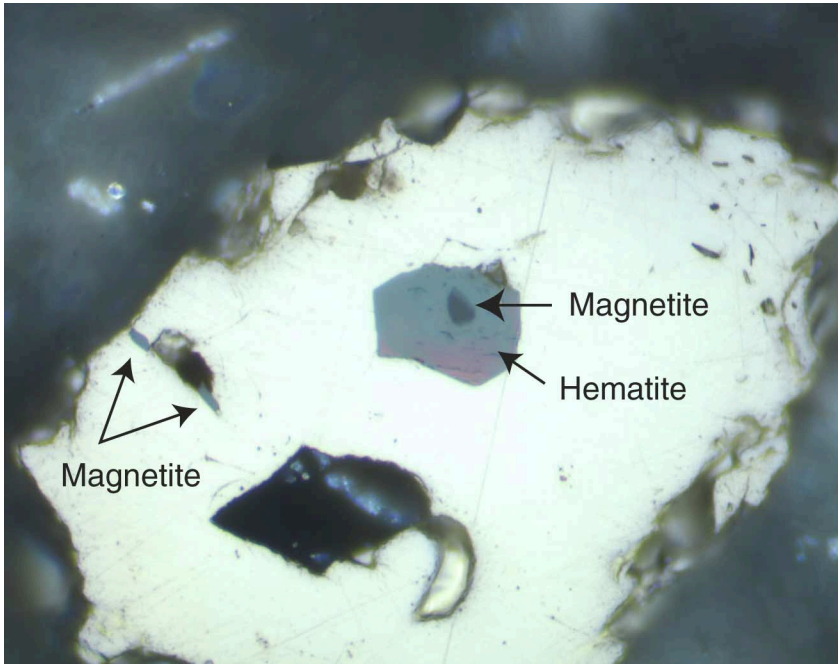


Figure F84. Hematite inclusions (medium gray) in pyrite (white) (Sample 193-1188F-9Z-1 [Piece 1B, 9–12 cm] in reflected light; width of view = 0.70 mm. Photomicrograph ID# 1188F_40; [thin section 72](#)).



Figure F85. Chalcopyrite (yellow) partially replacing pyrite (white) (Sample 193-1188F-37Z-2 [Piece 3, 31–33 cm] in reflected light; width of view = 0.28 mm. Photomicrograph ID# 1188F_109; **thin section 101**).



Figure F86. Ti magnetite with ilmenite exsolution laths (Sample 193-1188F-30Z-1 [Piece 2, 5–7 cm] in reflected light; width of view = 0.14 mm. Photomicrograph ID# 1188F_65; [thin section 91](#)).

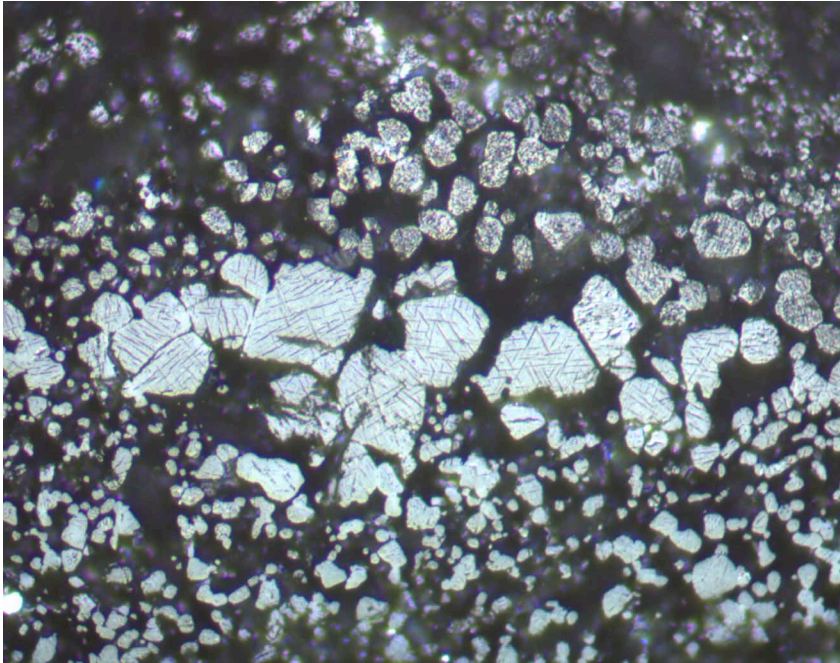


Figure F87. Ilmenite (light gray) intergrown with magnetite (medium gray) surrounding spinel (dark gray) in a quartz matrix. The magnetite grain at the top edge of the photomicrograph has hematite inclusions (Sample 193-1188F-37Z-2 [Piece 3, 31–33 cm] in reflected light; width of view = 0.14 mm. Photomicrograph ID# 1188F_105; **thin section 101**).

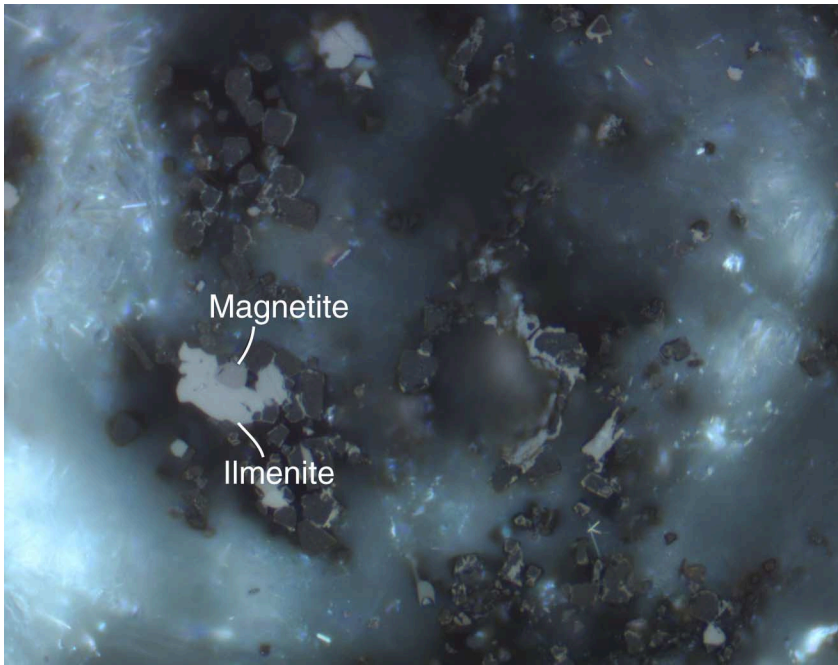


Figure F88. Hematite flakes (ruby red to opaque) in quartz (Sample 193-1188F-37Z-2 [Piece 3, 31–33 cm] in plane-polarized light; width of view = 0.14 mm. Photomicrograph ID# 1188F_75; [thin section 101](#)).

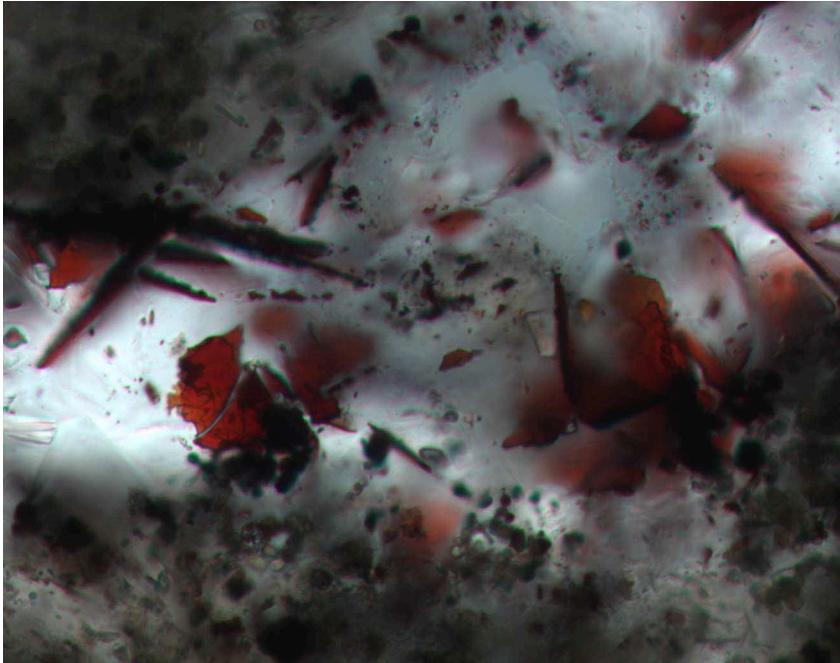


Figure F89. Spinel crystals hosted in quartz (Sample 193-1188F-34Z-1 [Piece 9A, 45–47 cm] in plane-polarized light; width of view = 0.70 mm. Photomicrograph ID# 1188F_73; [thin section 95](#)).

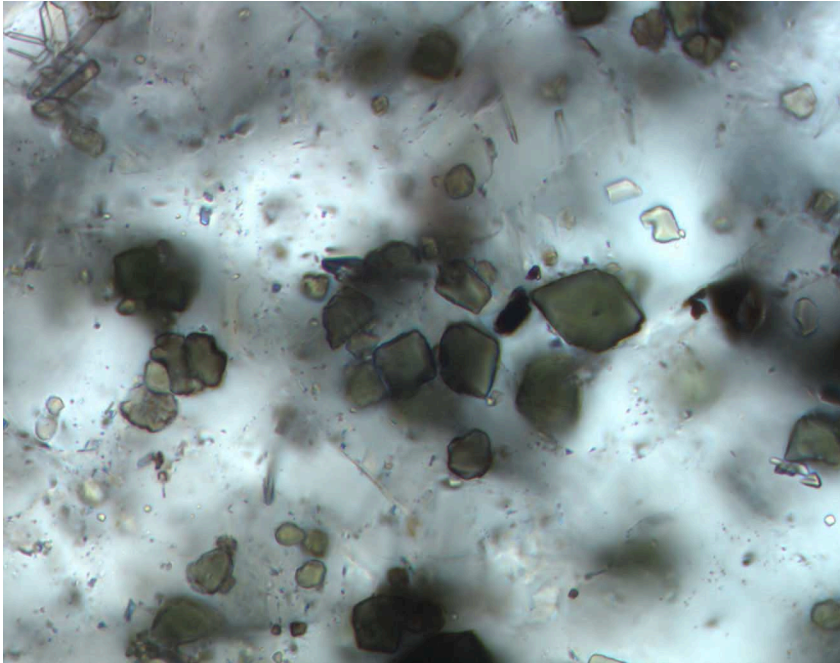


Figure F90. Spinel (dark gray), magnetite (medium gray), ilmenite (light gray), and hematite (white). Spinel has a thin coating of magnetite. Magnetite contains inclusions of hematite. Magnetite-ilmenite intergrowth on the left side of the photomicrograph (Sample 193-1188F-37Z-2 [Piece 3, 31–33 cm] in reflected light; width of view = 0.14 mm. Photomicrograph ID# 1188F_101; [thin section 101](#)).

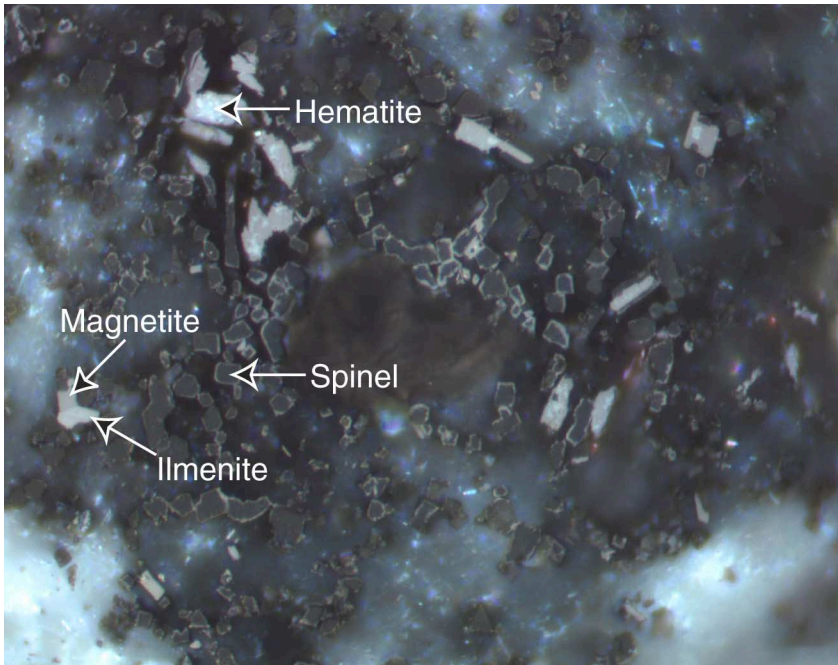


Figure F91. Tiny magnetite (gray) inclusions in pyrite (white). Groundmass contains magnetite grains within quartz that are the same size and shape as the magnetite inclusions in the pyrite (Sample 193-1188F-13Z-1 [Piece 3B, 47–50 cm] in reflected light; width of view = 0.275 mm. Photomicrograph ID# 1188F_62; [thin section 77](#)).



Figure F92. Magnetite (gray) inclusions in pyrite (white) having the same morphology as those in the neighboring quartz (black) in the groundmass. Magnetite inclusions in the center of the pyrite grain are smaller than those near the edge suggesting that the former have been partially replaced (Sample 193-1188F-25Z-1 [Piece 4, 24–26 cm] in reflected light; width of view = 0.275 mm. Photomicrograph 1188F_71).

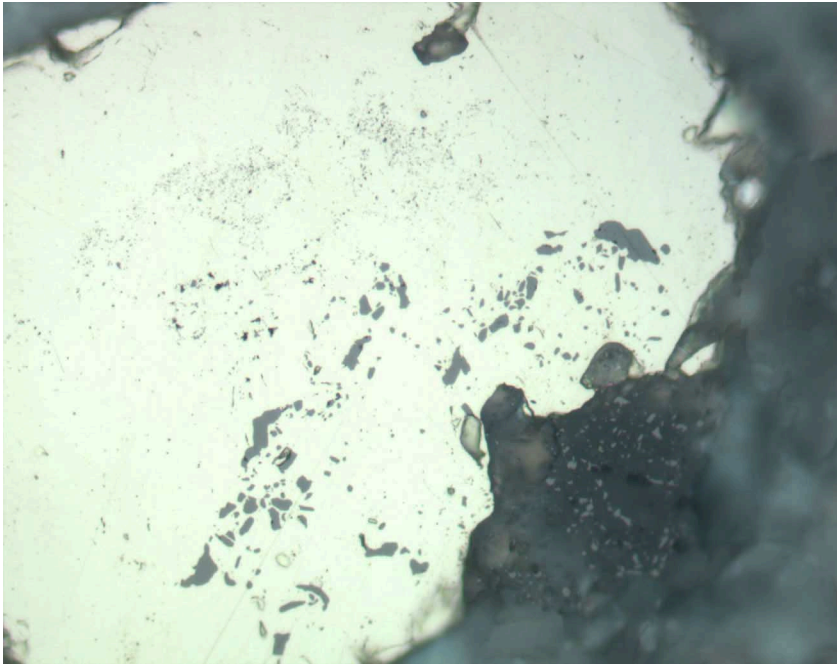


Figure F93. Pyrite (white) enclosing magnetite (medium gray) in a silicified rock (Sample 193-1188F-34Z-1 [Piece 9A, 45–47 cm] in reflected light; width of view = 0.275 mm. Photomicrograph ID# 1188F_73; [thin section 95](#)).

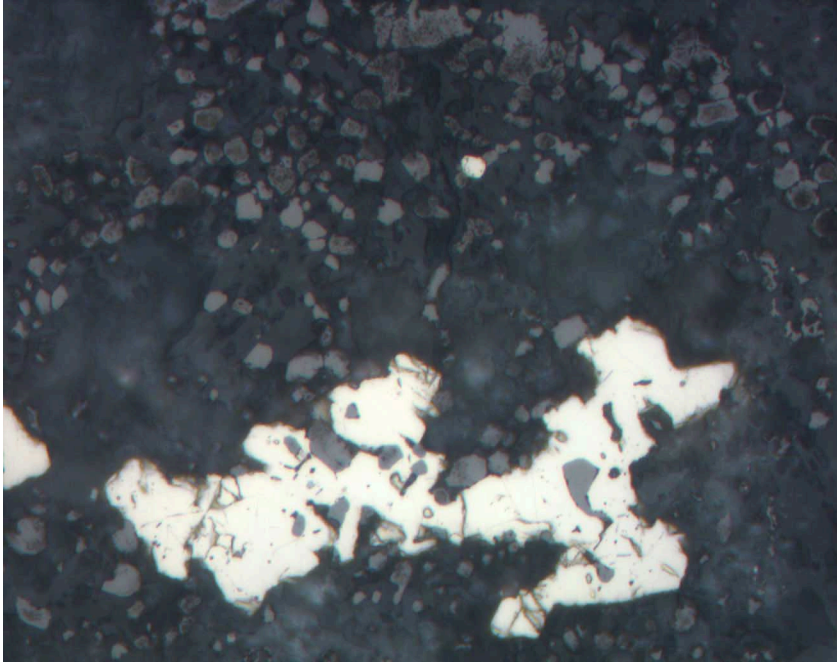


Figure F94. Euhedral quartz (quartz-1, dark gray) overgrown by a second quartz (quartz-2, gray) containing inclusions of magnetite (medium gray), which are in turn overgrown by pyrite (white). An anhydrite vein (high relief, mottled gray) is present in a fracture in quartz-1 near the center of the photomicrograph (Sample 193-1188F-26Z-1 [Piece 2, 20–23 cm] in reflected light; width of view = 0.70 mm. Photomicrograph ID# 1188F_37; [thin section 90](#)).

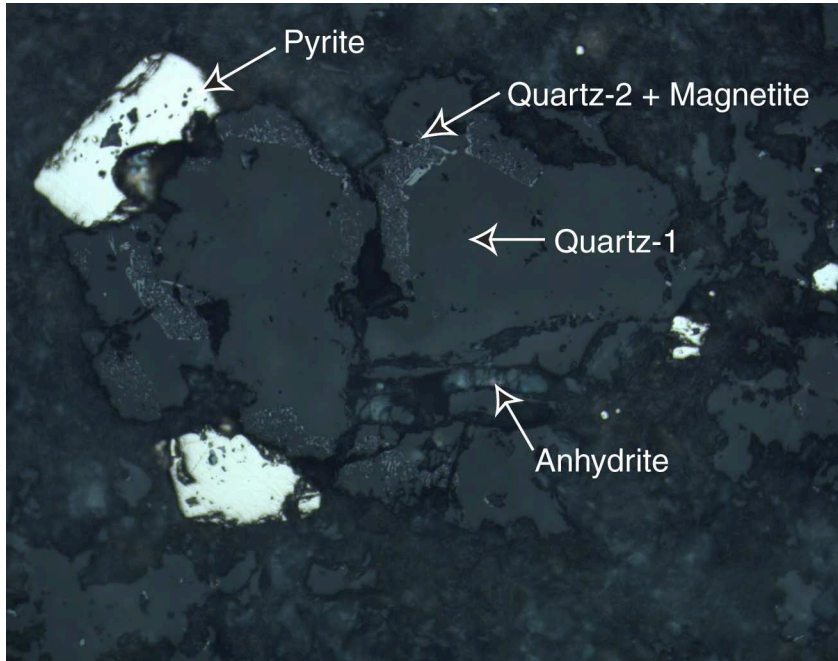


Figure F95. Euhedral quartz-1 overgrown by magnetite and quartz-2 overgrown by pyrite. The pyrite contains inclusions of magnetite from quartz-2 (Sample 193-1188F-26Z-1 [Piece 2, 20–23 cm] in reflected light; width of view = 0.275 mm. Photomicrograph ID# 1188F_36; **thin section 90**).

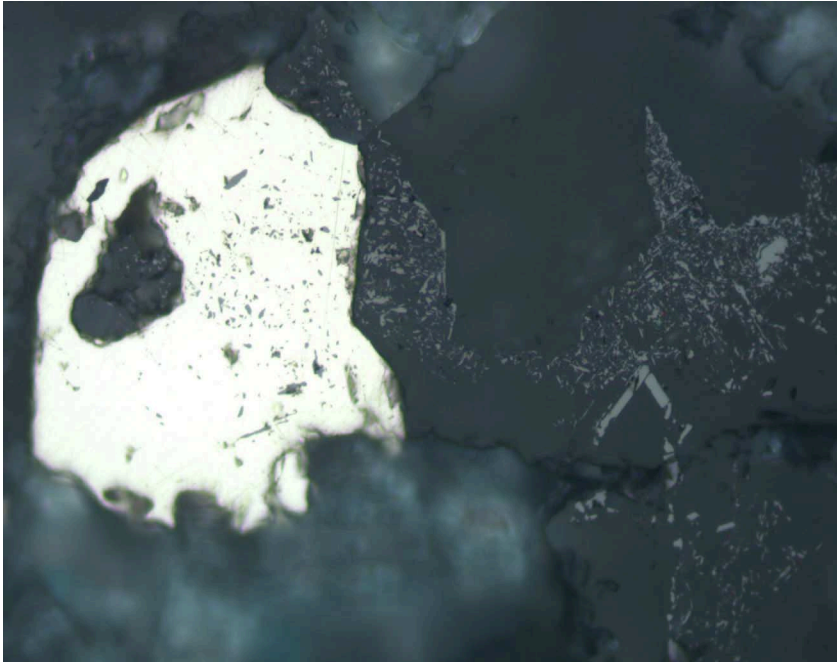


Figure F96. Paragenetic sequence for Site 1188. Intervals flagged with a question mark indicate uncertainty in the time of beginning and/or end of crystallization.

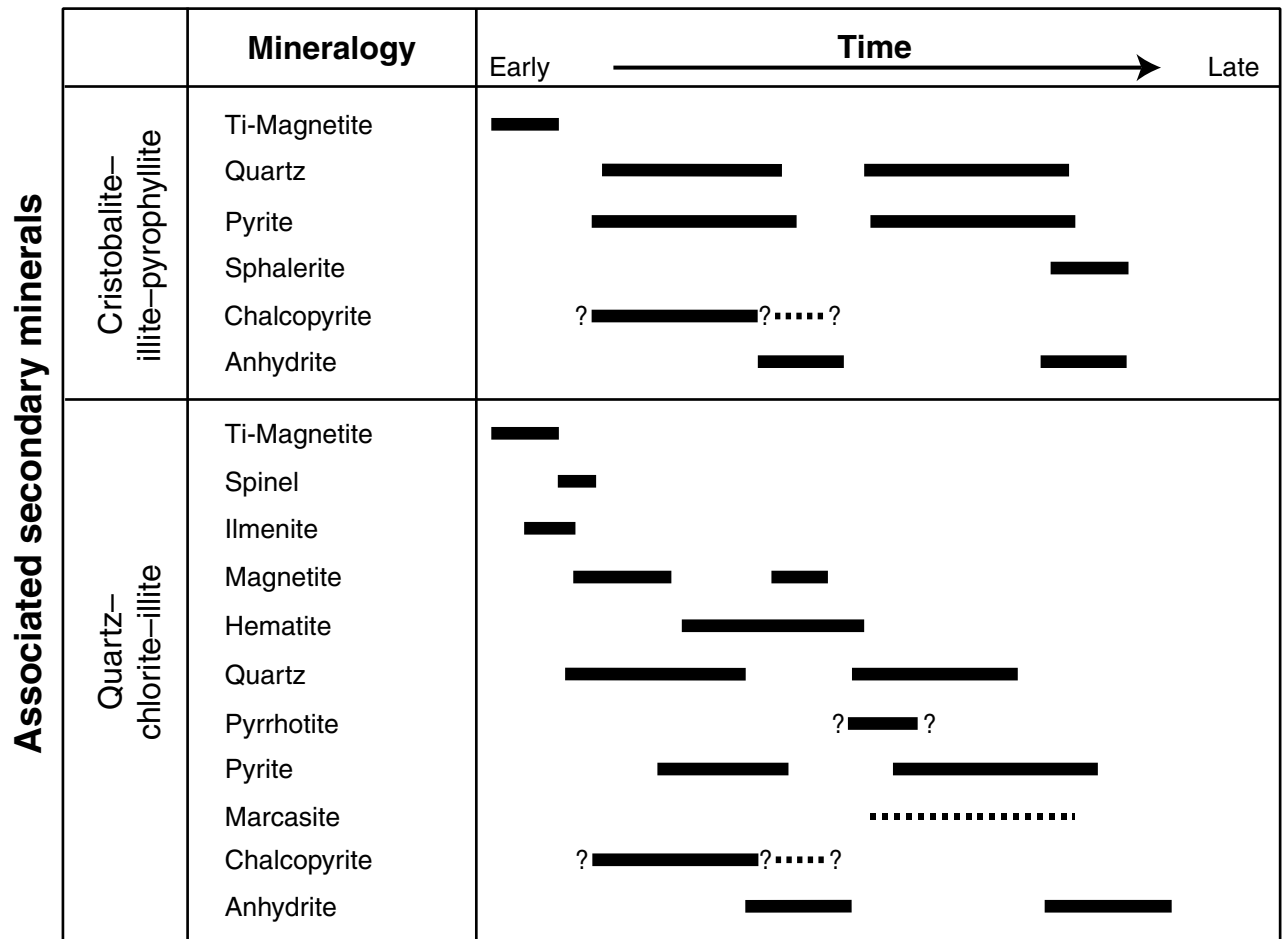


Figure F97. Close-up photograph of folded flow banding in pervasively altered volcanic rock, crosscut by silica-anhydrite-pyrite veins (Unit 10; interval 193-1188A-12R-2 [Piece 4, 37–51 cm]; 98.44 mbsf).

cm

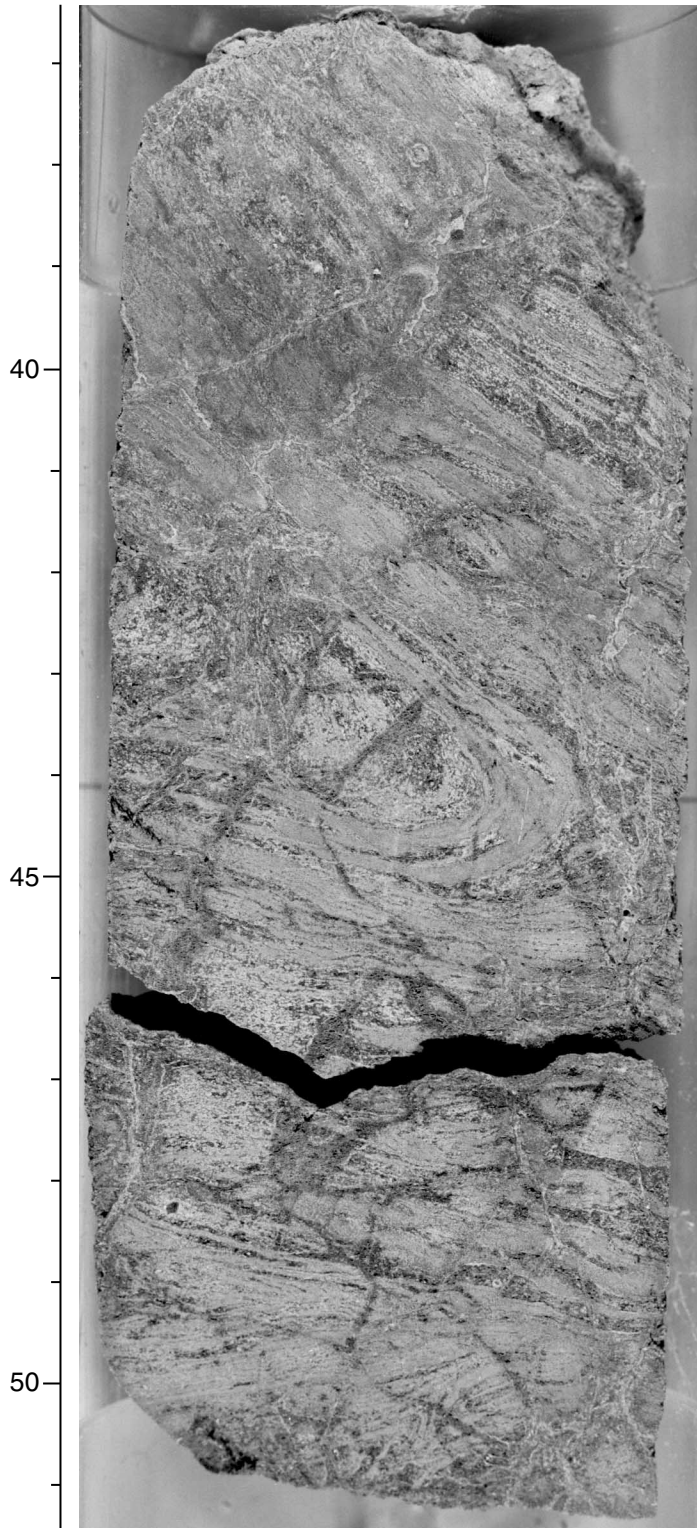


Figure F98. Close-up photograph of the boudinlike disruption of original layering in a pervasively altered flow-laminated volcanic rock. A thin silica-pyrite vein with a bleached halo crosscuts the lamination (interval 193-1188A-16R-1 [Piece 14, 95–101 cm]; 136.34 mbsf).

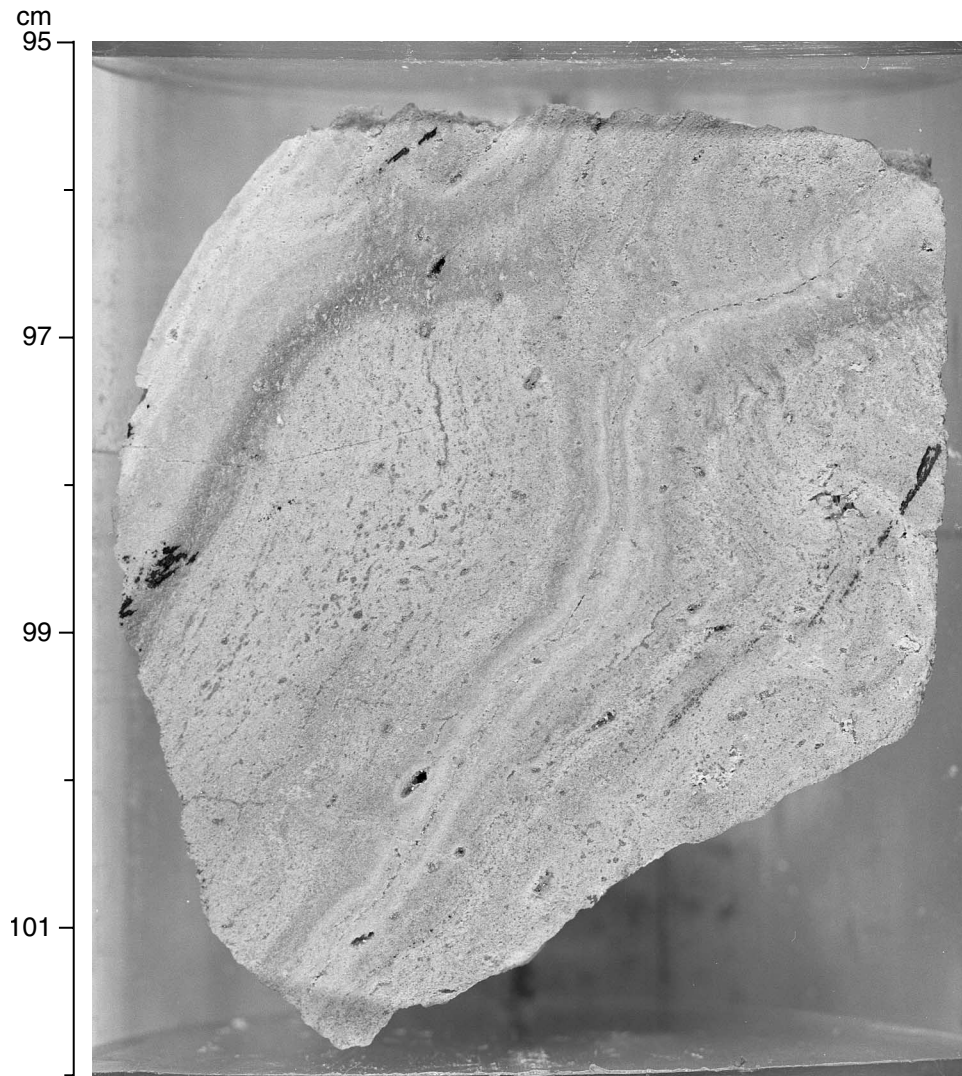


Figure F99. Histogram of dips of volcanic layering, Hole 1188A.

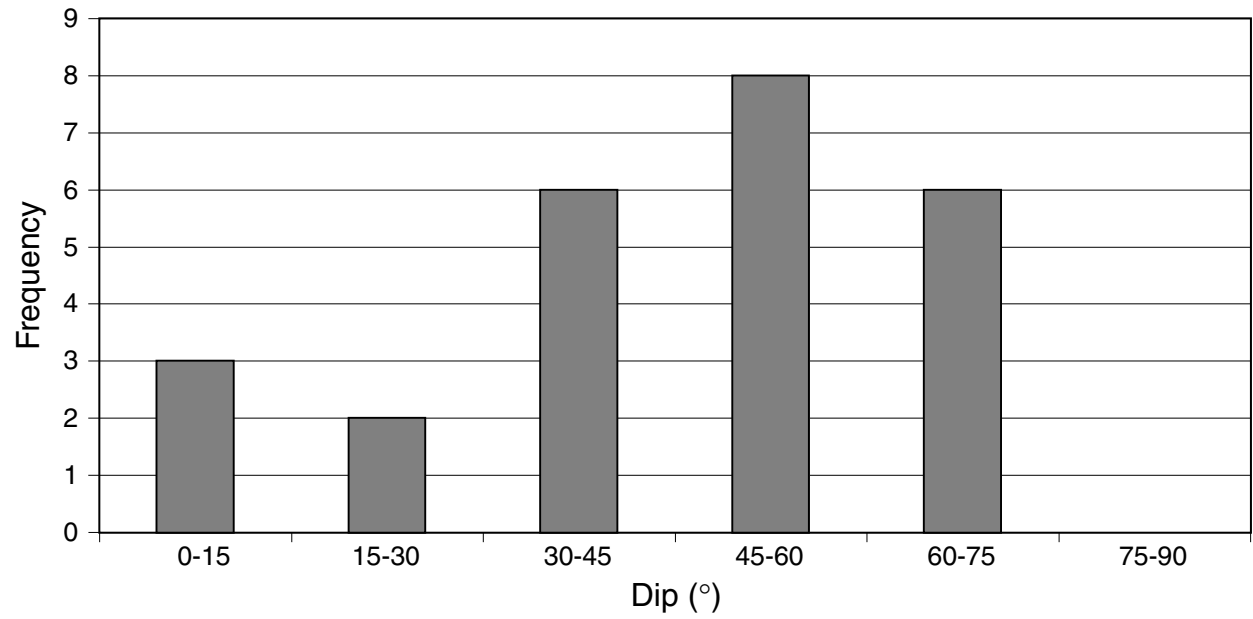
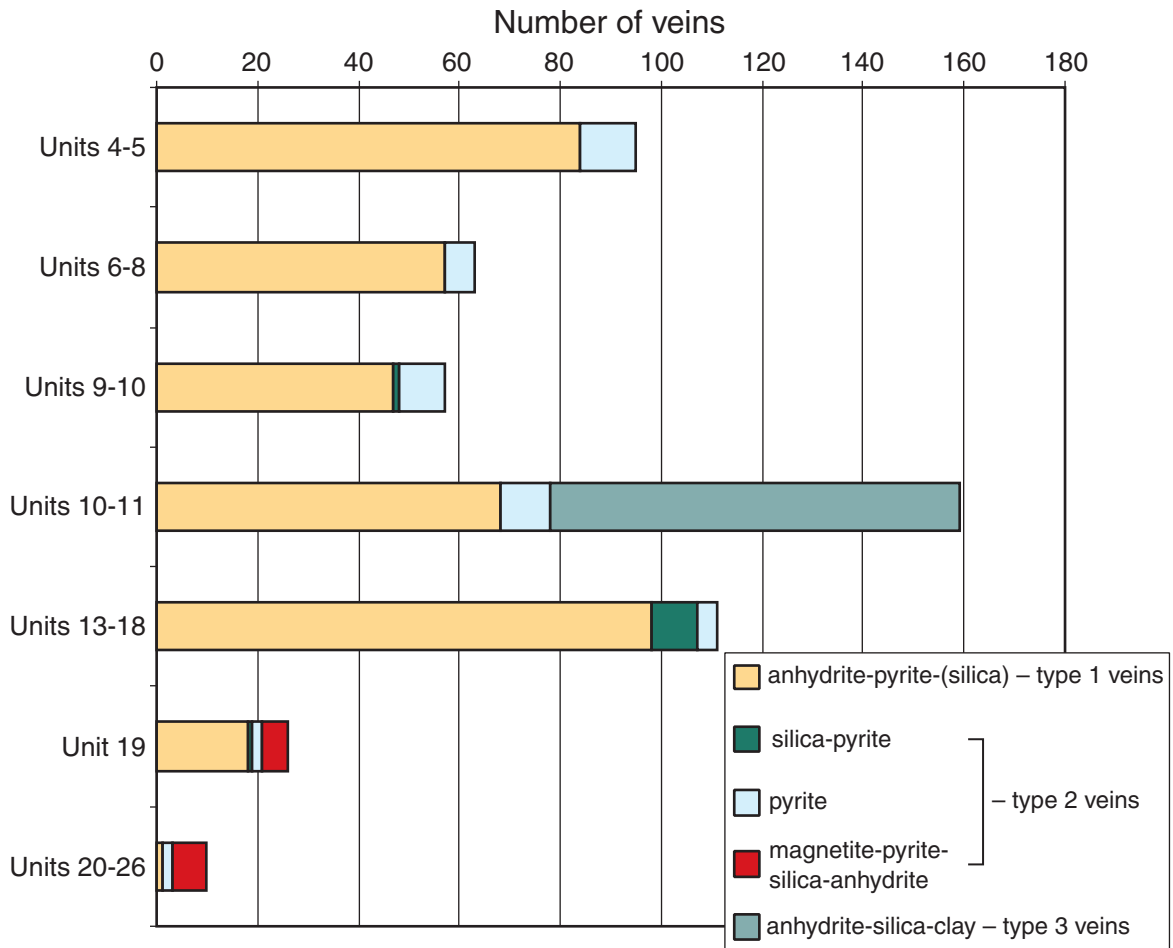


Figure F100. A. Distribution of vein mineralogy vs. lithologic units in Hole 1188A. B. Distribution of all vein thicknesses in Hole 1188A. Types 1, 2, and 3 correspond to the categories discussed in the text (Continued on next page.)

A



B

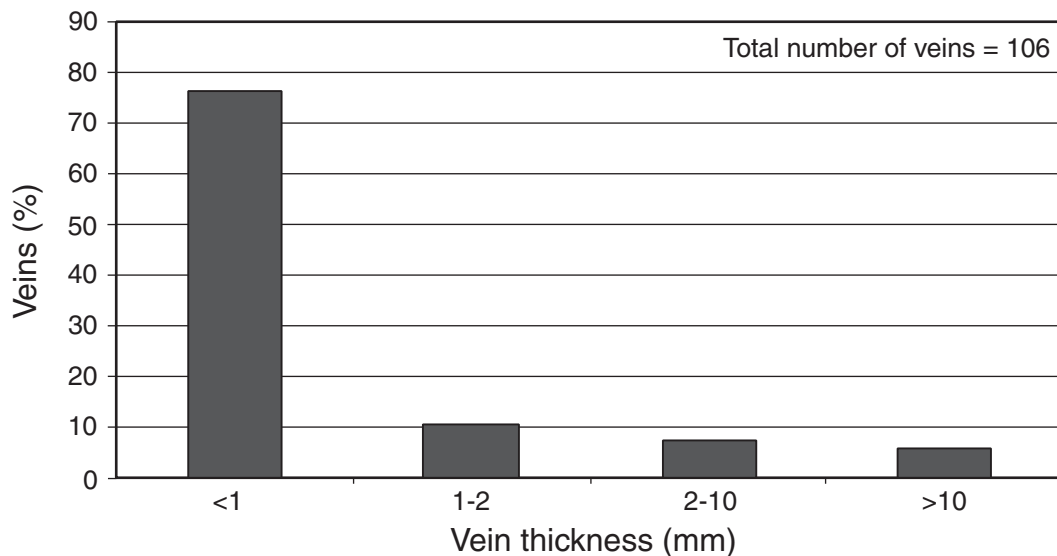


Figure F100 (continued). C. Distribution of dips of veins vs. depth in Hole 1188A.

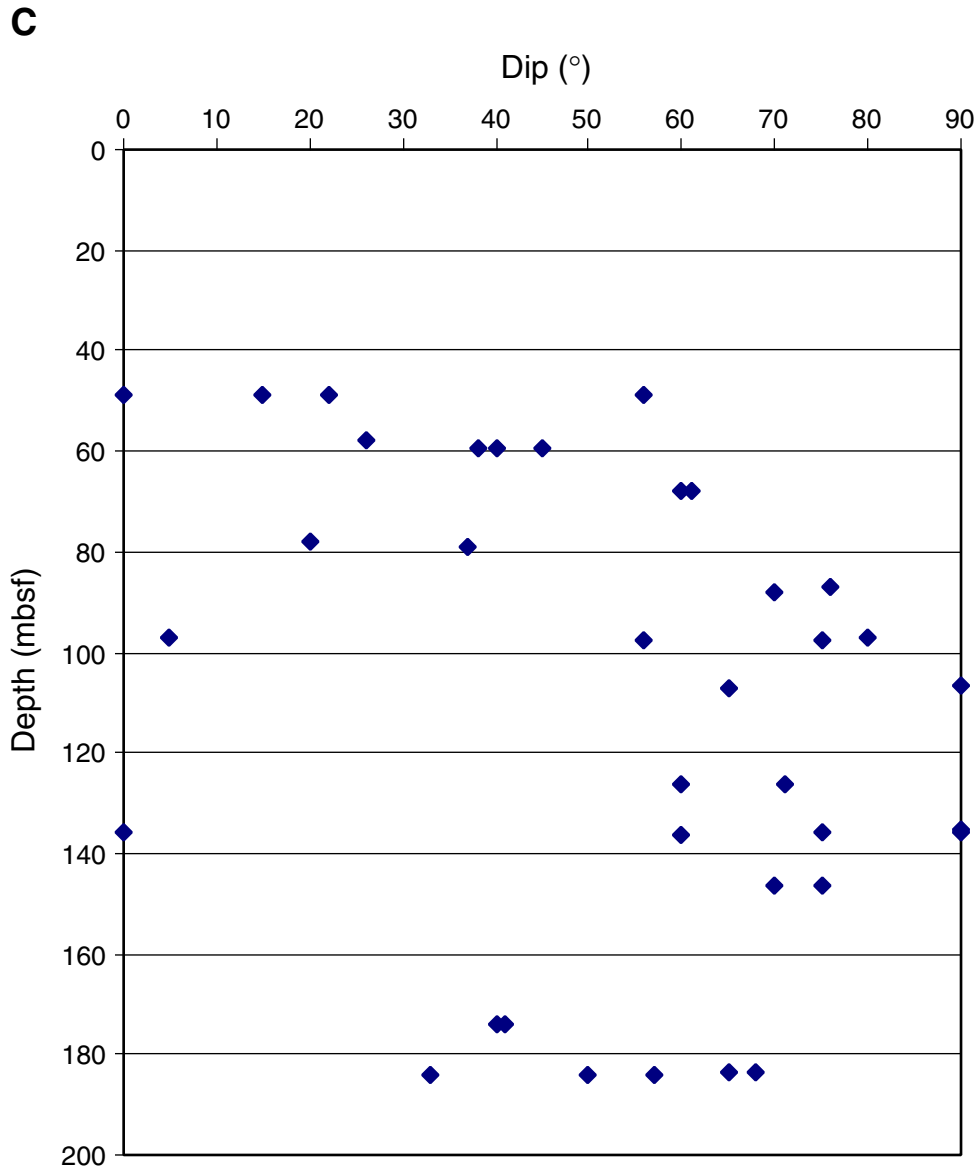
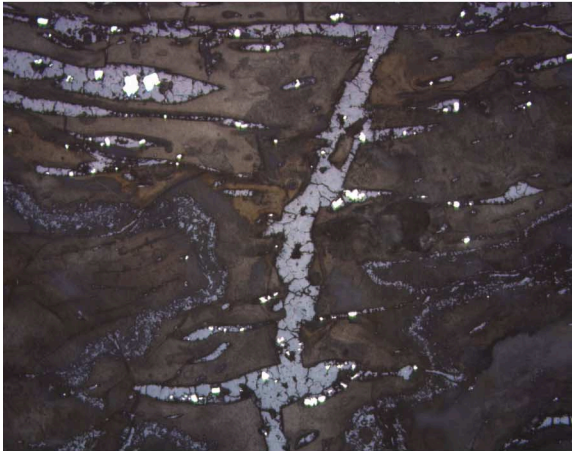


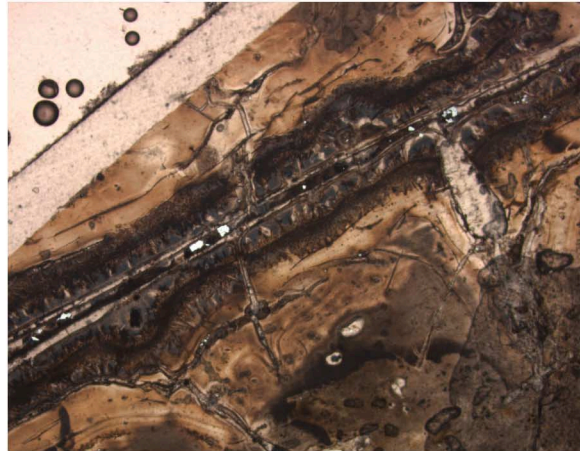
Figure F101. Photomicrographs of vein textures, Hole 1188A. **A.** Silica-pyrite vein cutting altered volcanic rock with offshoots parallel to flow banding (Sample 193-1188A-9R-1 [Piece 7, 68–70 cm] in reflected light; width of view = 2.75 mm. Photomicrograph ID# 1188A_57; **thin section 9**). **B.** Anhydrite-pyrite vein with cristobalite halos demonstrating two episodes of opening. Note the vein offshoot crosscutting the first halo in the upper right of the photo (Sample 193-1188A-9R-1 [Piece 7, 68–70 cm] in plane-polarized transmitted light; width of view = 2.75 mm. Photomicrograph ID# 1188A_16; **thin section 9**). **C.** Fragments of strongly silicified volcanic rock in a cristobalite-pyrite vein. Note the open-space growth on the fragments (Sample 193-1188A-9R-1 [Piece 7, 68–70 cm] in plane-polarized transmitted light; width of view = 2.75 mm. Photomicrograph ID# 1188A_45; **thin section 9**). **D.** Anhydrite-pyrite vein with pyrite surrounding anhydrite. Note the fine-grained pyrite at the outer fringes of the gray halo of silica around the veins (Sample 193-1188A-7R-2 [Piece 2, 39–41 cm] in plane-polarized transmitted light; width of view = 1.40 mm. Photomicrograph ID# 1188A_40; **thin section 6**). **E.** Quartz vein rimmed by brown clay-cristobalite and farther outward by a band of hematite and rutile with minor pyrite (Sample 193-1188A-12R-1 [Piece 12, 123–124 cm] in plane-polarized transmitted light; width of view = 1.40 mm. Photomicrograph ID# 1188A_108; **thin section 11**). **F.** Anhydrite-silica-pyrite vein with pronounced silica alteration halo, crosscut by later anhydrite vein. Note the fine-grained “dusty” pyrite at the outer fringes of the silica alteration halo (Sample 193-1188A-7R-2 [Piece 2, 39–41 cm] in plane-polarized transmitted light; width of view = 1.40 mm. Photomicrograph ID# 1188A_04; **thin section 6**). (**Figure shown on next page.**)

Figure F101 (continued). (Caption shown on previous page.)

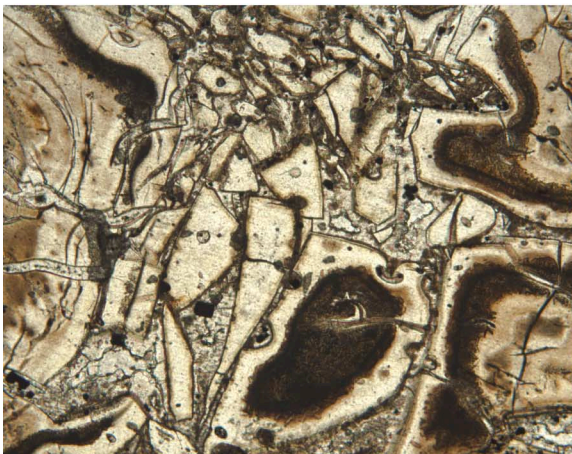
A



B



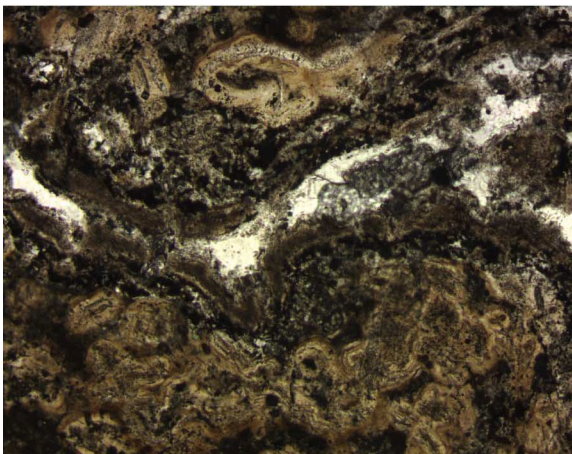
C



D



E



F



Figure F102. Close-up photograph of an anhydrite-pyrite vein (at 76 cm) with a wide halo of bleaching, overprinting an earlier vein network of anhydrite-silica-clay veins, which crosscut pervasively GSC altered volcanic rocks (Sample 193-1188A-12R-1 [Pieces 7–8, 71–90 cm]; 97.17 mbsf).

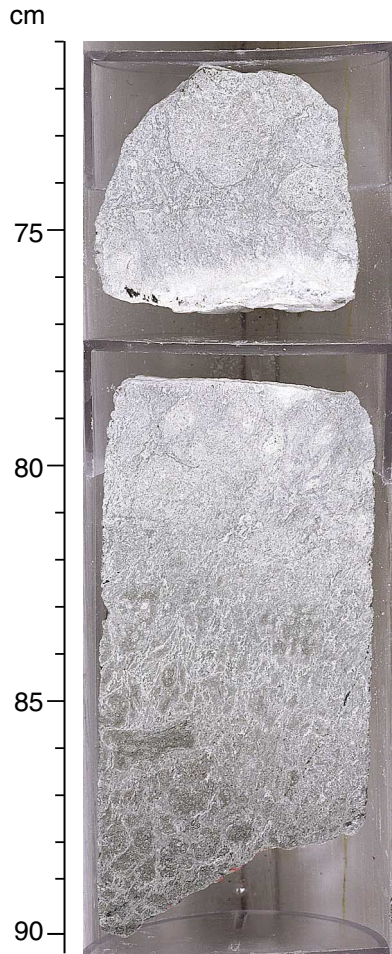


Figure F103. Close-up photograph of a diffuse silica-anhydrite-clay vein network and patches, overprinting completely anhydrite-clay altered volcanic rock. Late anhydrite veins with white clay \pm silica halos crosscut both the alteration and the vein network (Sample 193-1188A-13R-1 [Piece 9, 60–72 cm]; 106.90 mbsf).

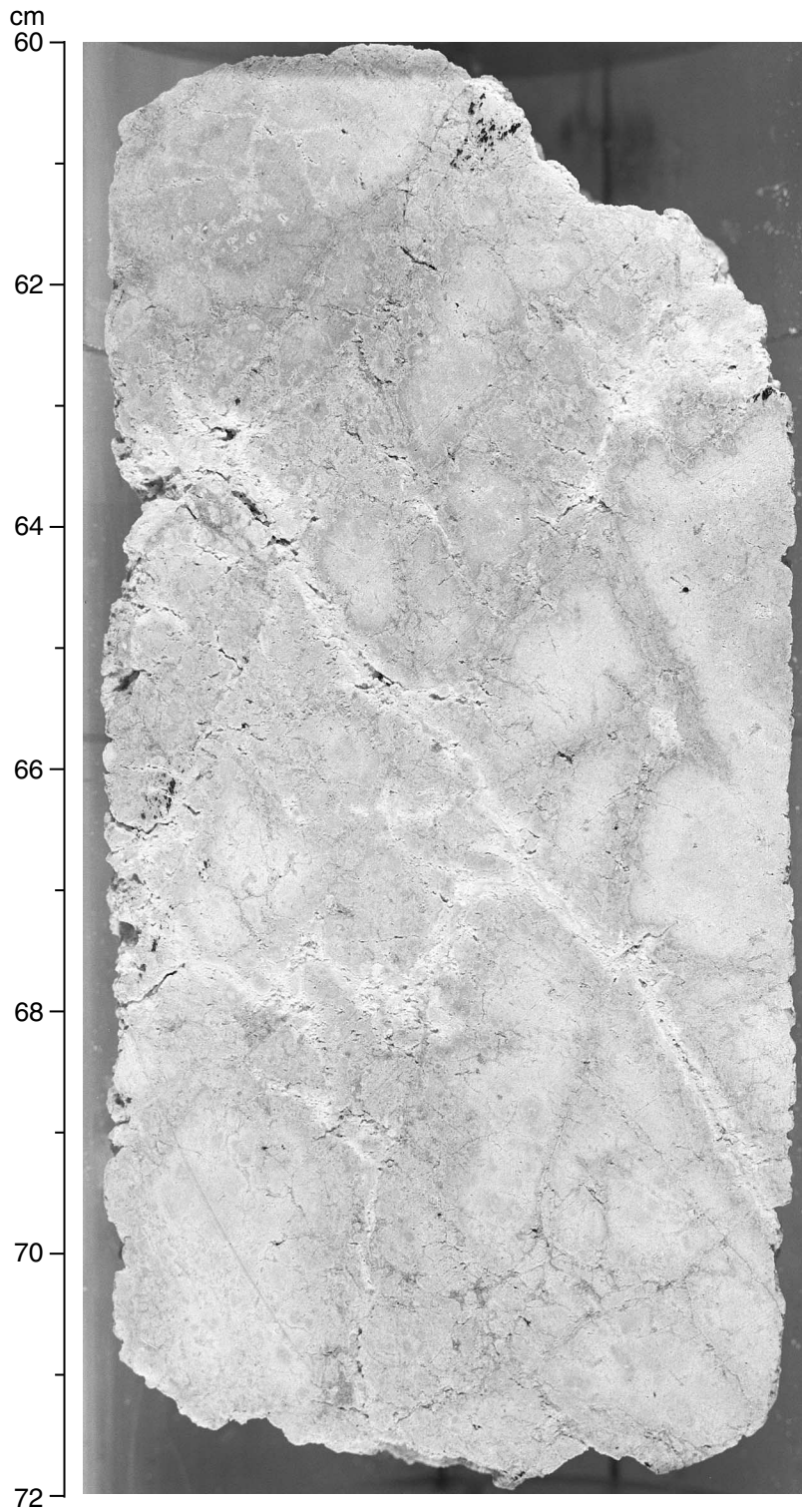


Figure F104. Distribution of veins according to mineralogy in Hole 1188F. Types 1 and 2 correspond to vein categories discussed in the text.

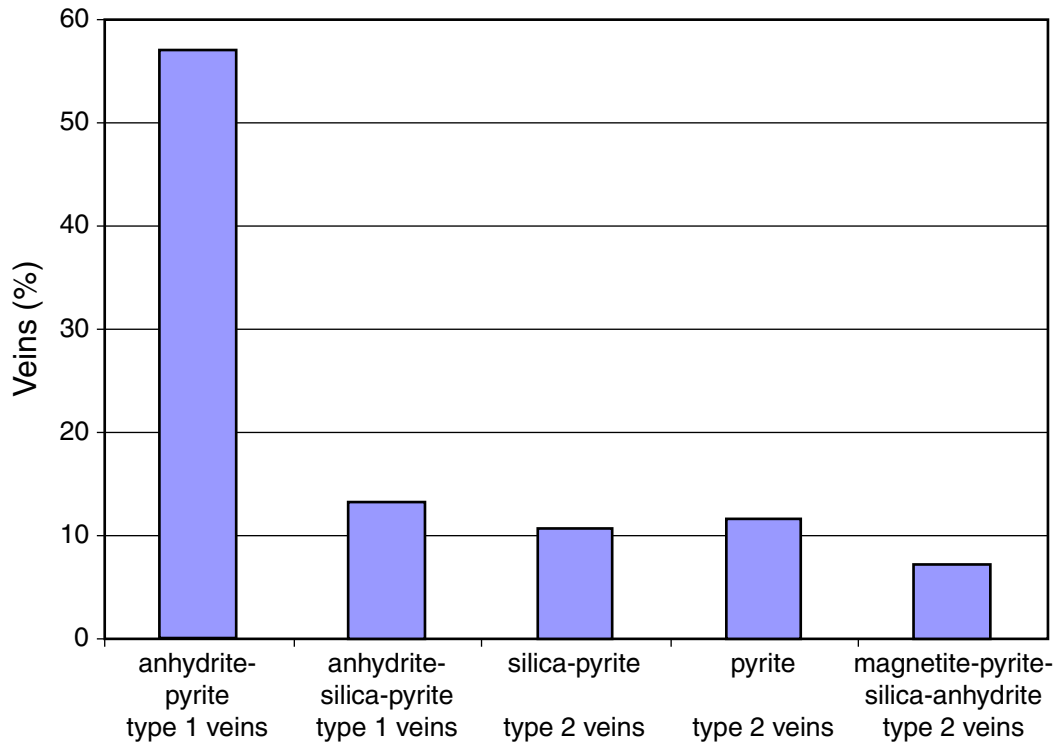


Figure F105. Distribution of vein mineralogy vs. lithologic units in Hole 1188F. Types 1 and 2 correspond to categories discussed in the text.

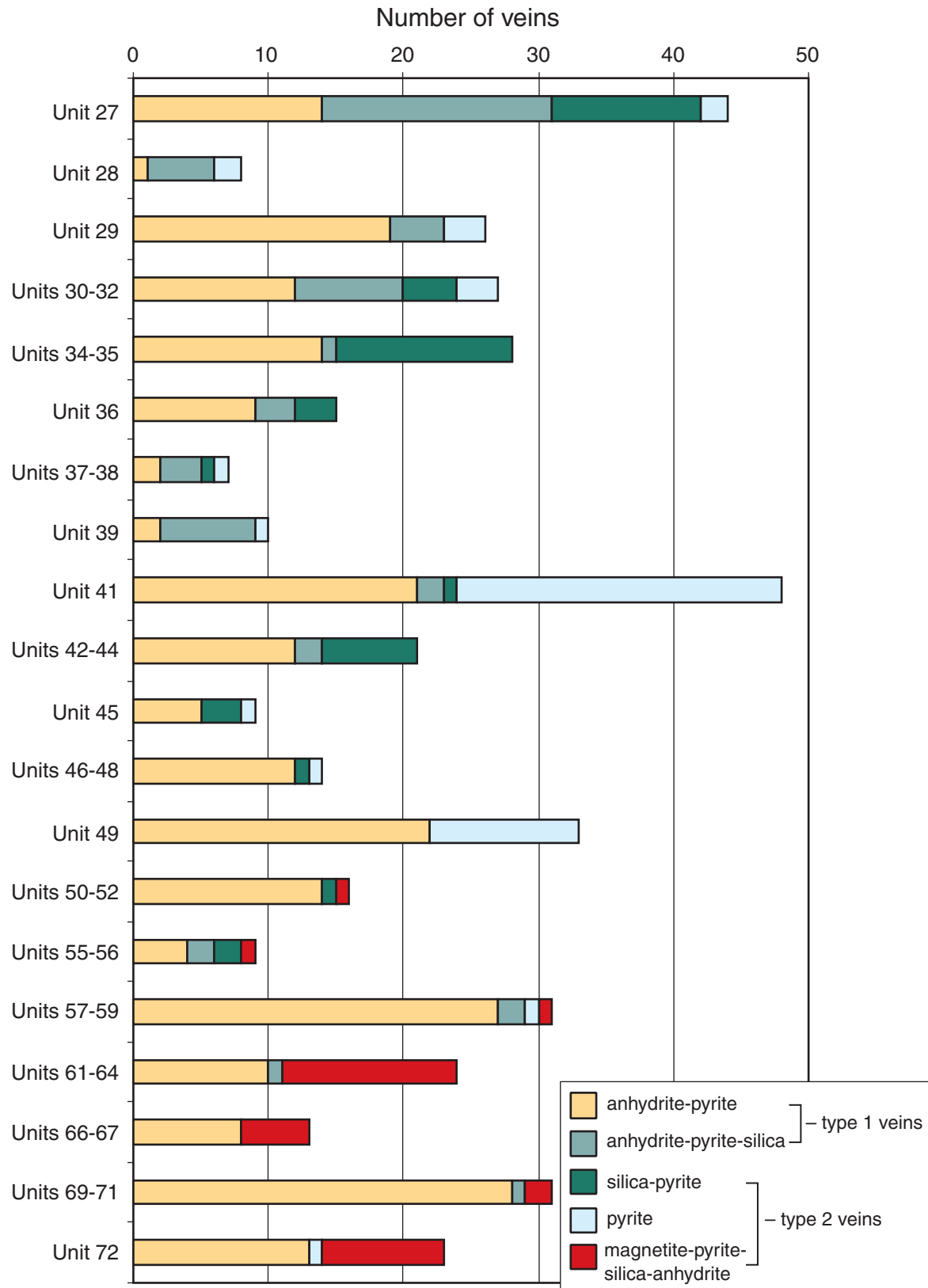


Figure F106. Anhydrite-pyrite vein (at 84 cm) with a wide cyclic siliceous alteration halo. The different shades of gray are due to varying proportions of quartz and clay minerals (interval 193-1188F-2Z-1, 80–91 cm [Piece 2G]; 222.30 mbsf).

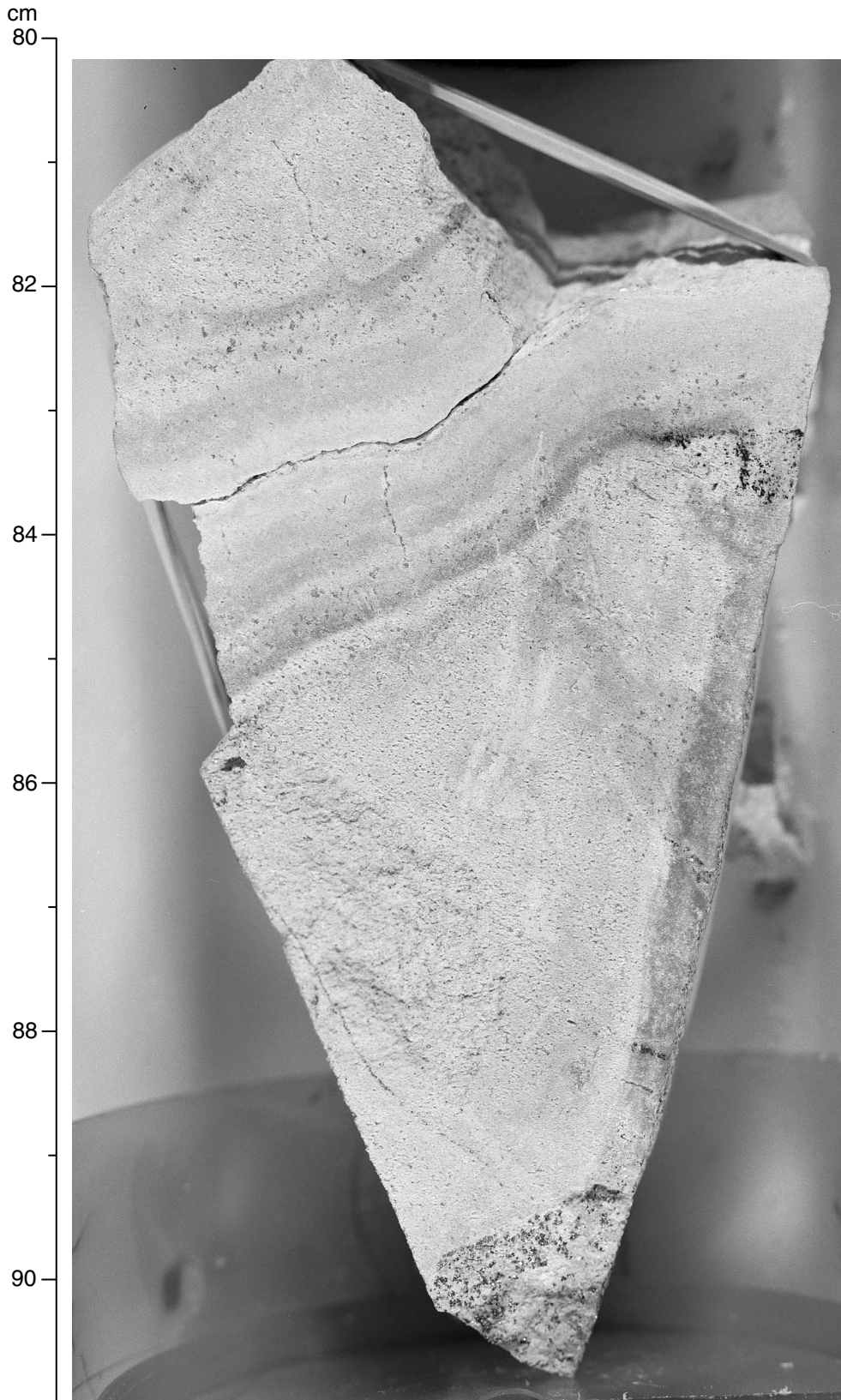
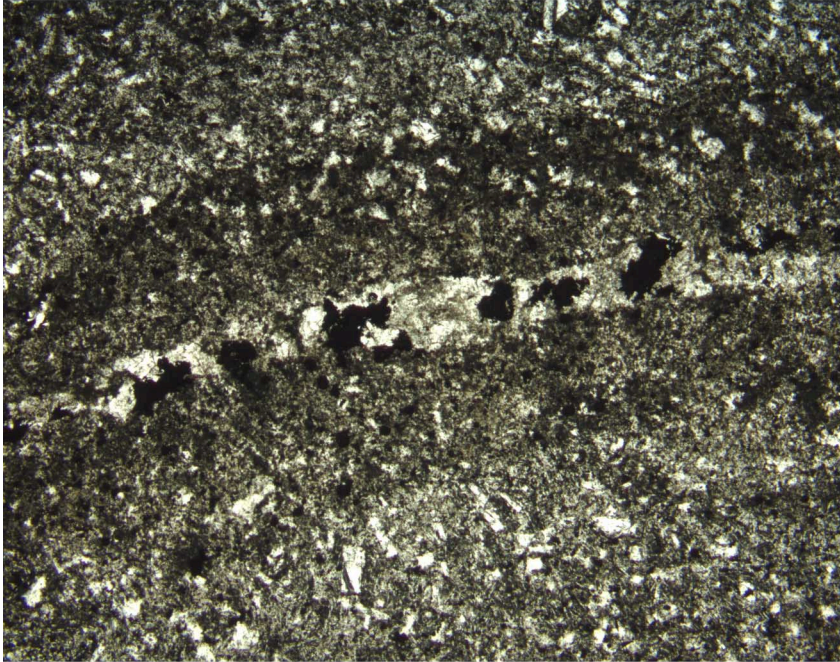


Figure F107. A. Anhydrite-pyrite vein with a zoned alteration halo of very fine grained quartz grading outward into a zone of brownish clay minerals (Sample 193-1188F-31Z-1 [Piece 1, 1–3 cm] in plane-polarized transmitted light; width of view = 5.5 mm. Photomicrograph ID# 1188F_84; **thin section 92**). B. Anhydrite-pyrite vein crosscutting alternating quartz- and clay-dominated bands, which formed around another anhydrite-pyrite vein (Sample 193-1188F-14Z-1 [Piece 6, 102–105 cm] in plane-polarized transmitted light; width of view = 5.5 mm. Photomicrograph ID# 1188F_67; **thin section 80**).

A



B

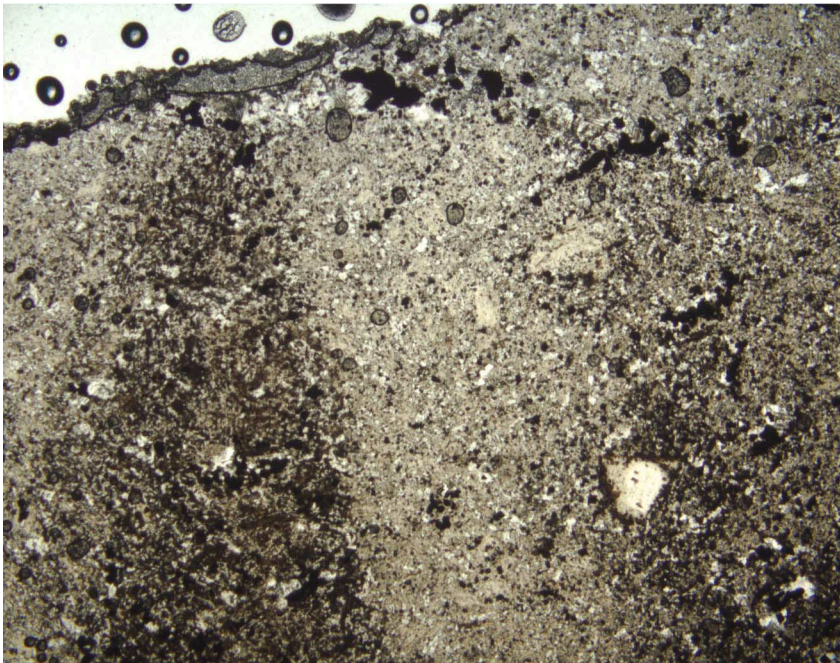


Figure F108. A. Close-up photograph of interval 193-1188F-14Z-1 (Piece 6, 98–110 cm). (Continued on next page.)

A

cm

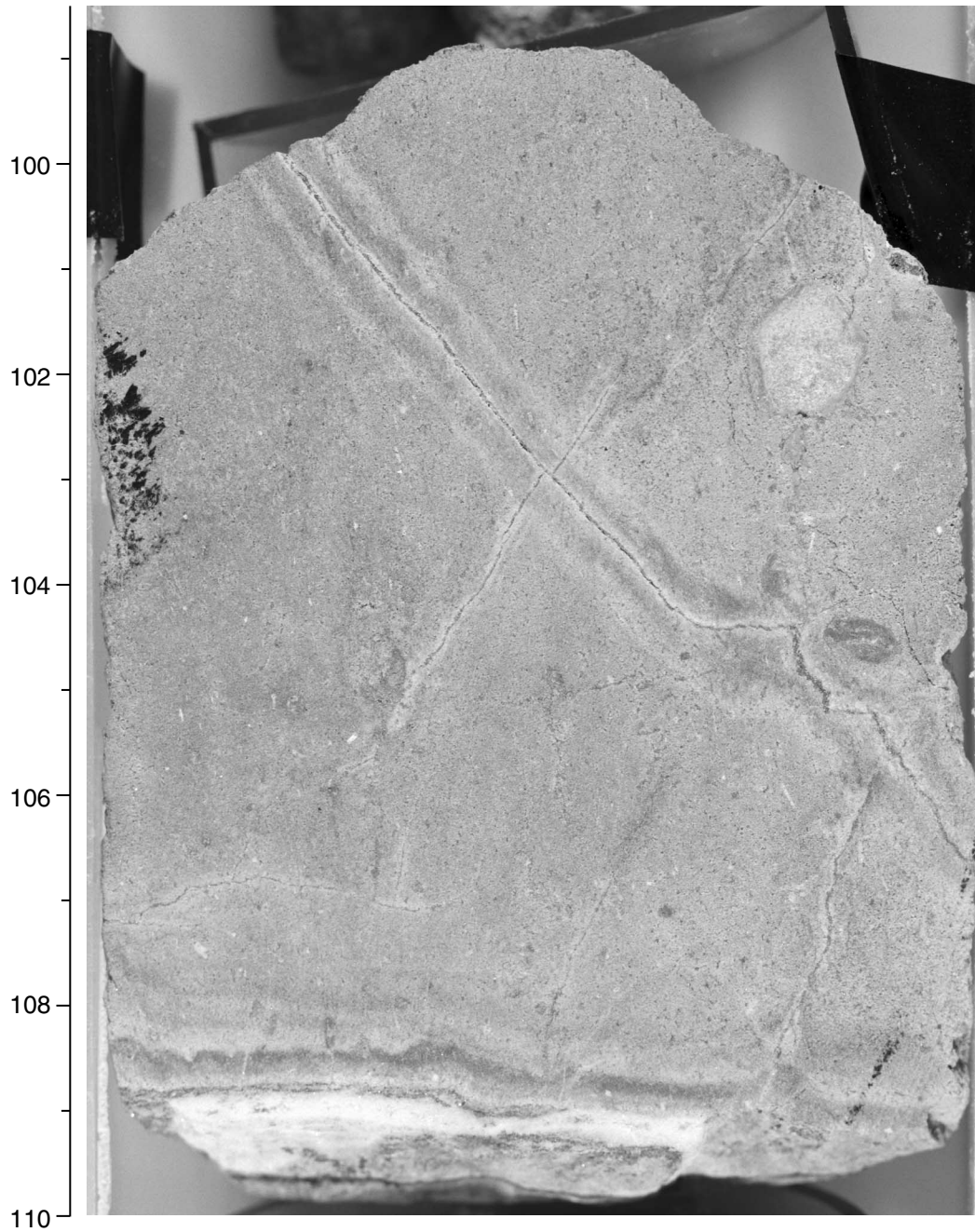


Figure F108 (continued). B. Sketch of the complex vein relationships in interval 193-1188F-14Z-1 (Piece 6, 98–110 cm); 246.86 mbsf. See “Vein Parageneses,” p. 62, in “Structural Geology” for explanation.

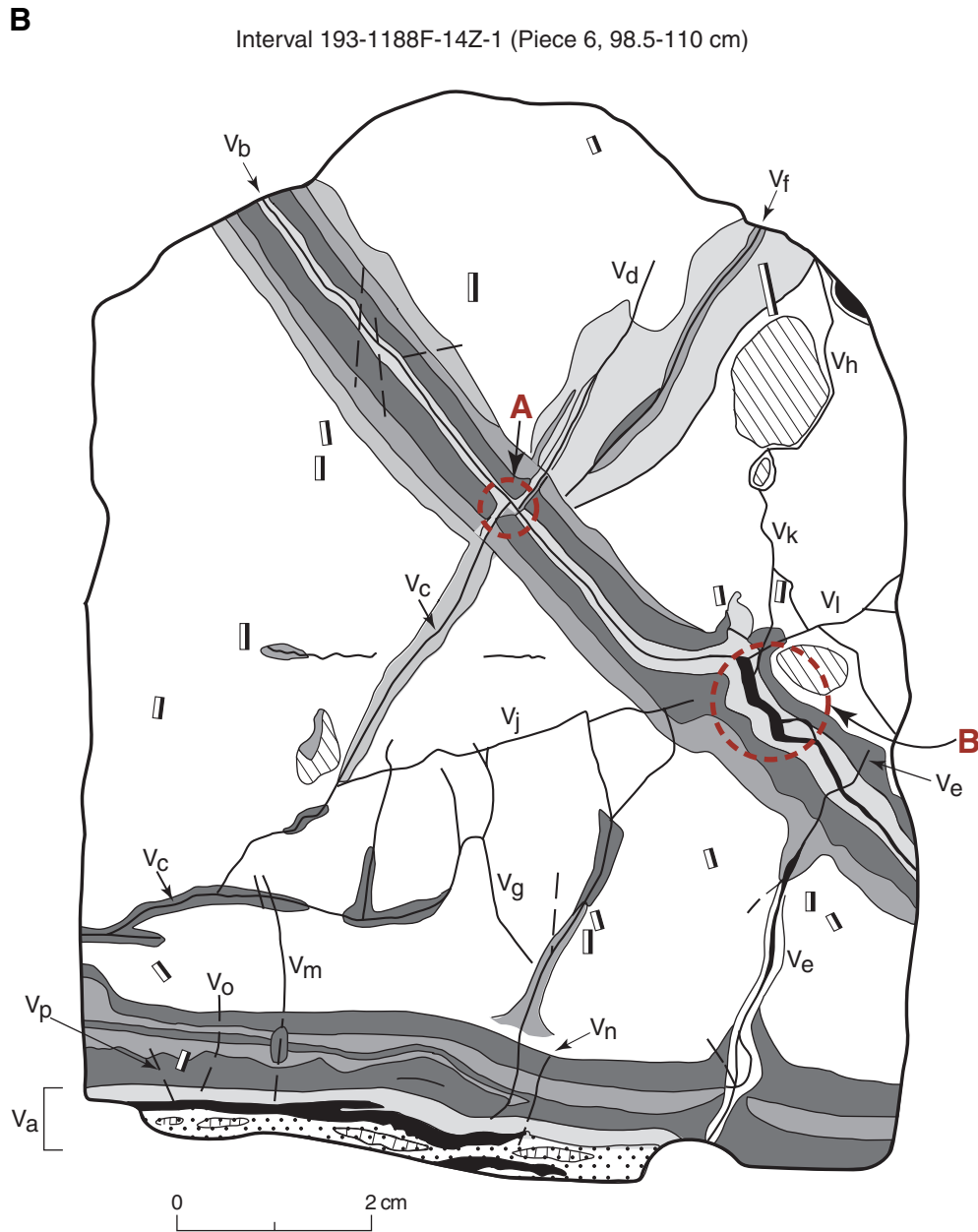


Figure F109. Close-up photograph of an earlier formed anhydrite vein structure (V1–V1b) crosscut by later anhydrite vein with coarse-grained anhydrite as open-space fill (V2). A thinner vein, V2b, branching off the main vein V2 in the upper part of the piece, can be seen (at 32 cm) cutting across another member of the earlier formed vein structure and its siliceous halo (interval 193-1188F-25Z-1 [Piece 5, 30–42 cm]; 295.88 mbsf).

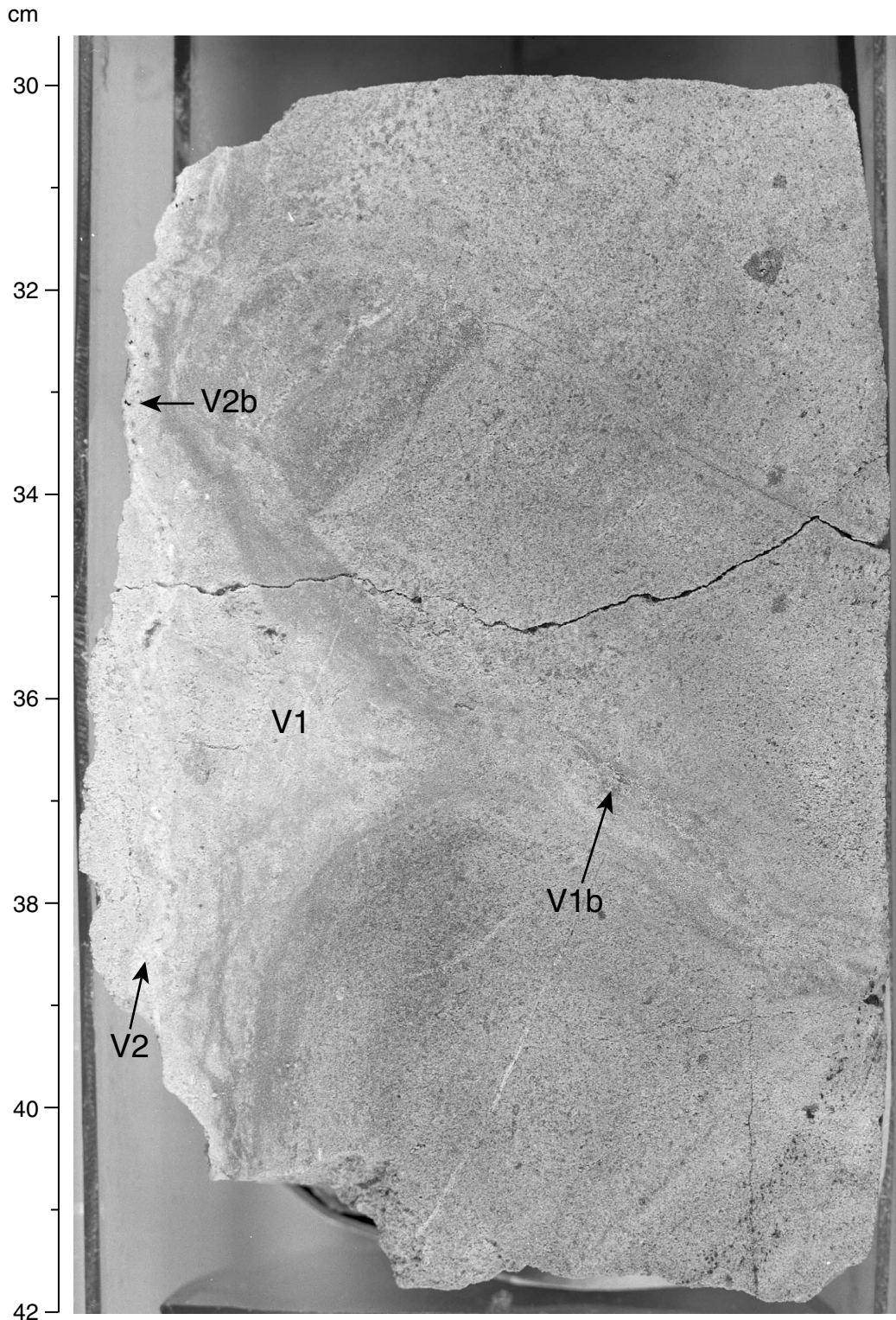


Figure F110. A. Close-up photograph of interval 193-1188F-23Z-1 (Piece 3, 14–24 cm); 286.74 mbsf. (Continued on next page.)

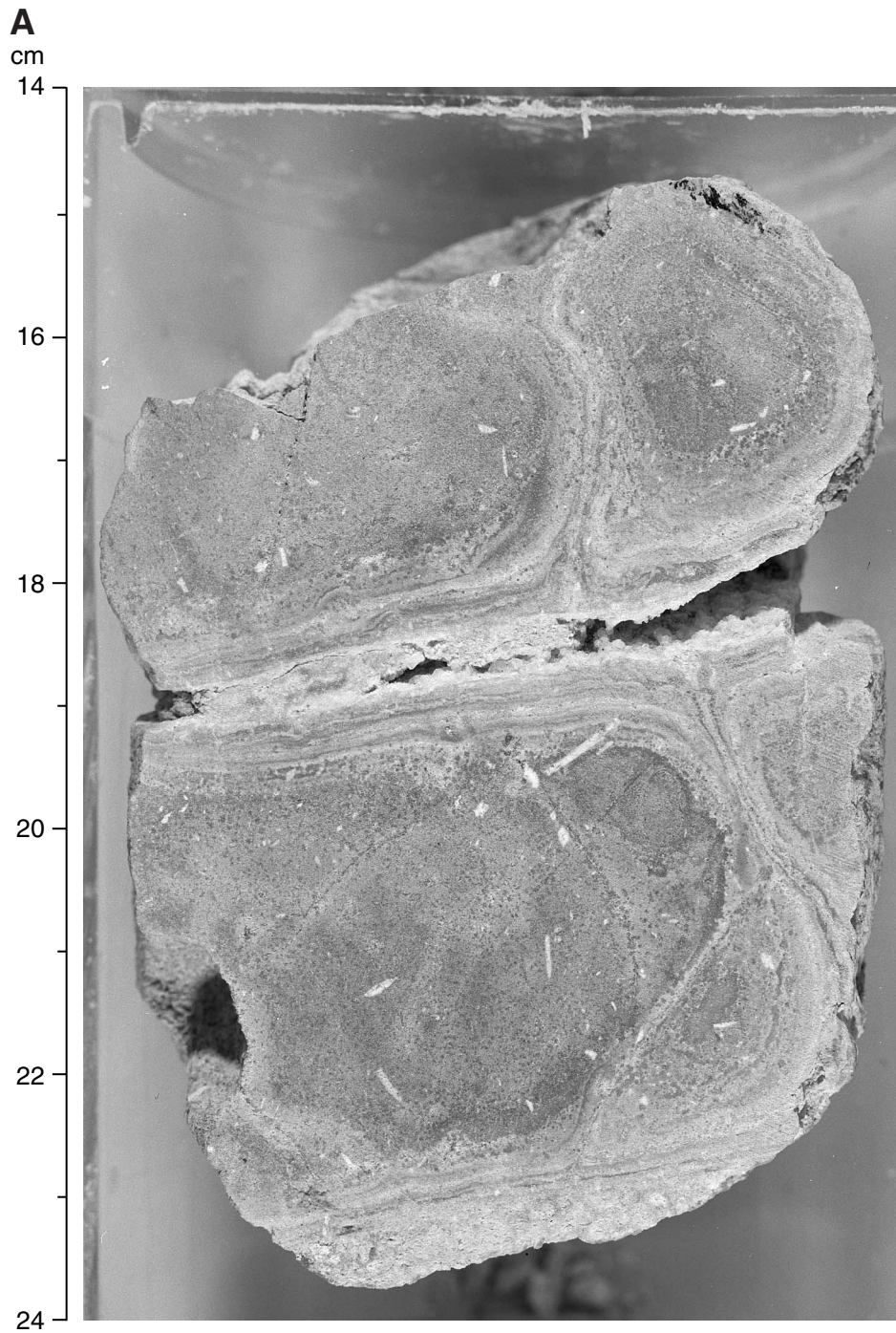


Figure F110 (continued). B. Sketch of multiple opening of a vein system. See "Vein Parageneses," p. 62, in "Structural Geology" for explanation.

B

Interval 193-1188F-23Z-1, 14-24 cm

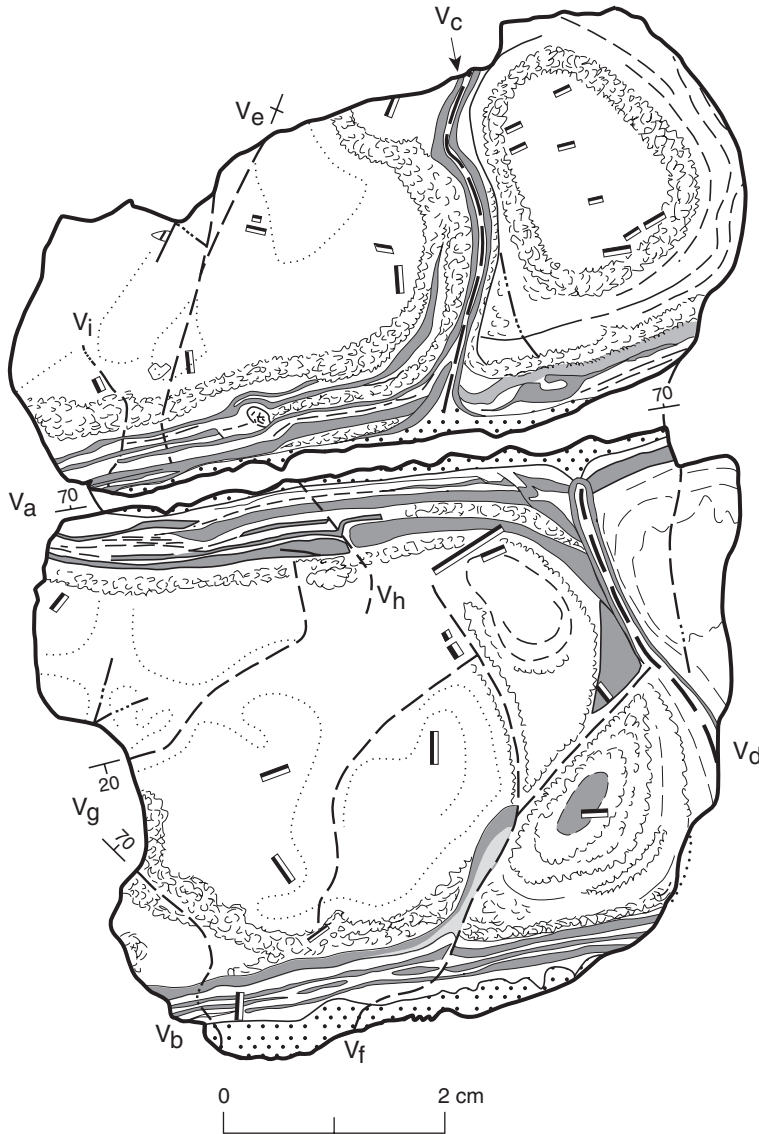


Figure F111. Photomicrograph of a quartz-pyrite vein. The quartz grains contain dark trails subparallel to the vein margins. These trails are defined by fine fluid and solid inclusions and strongly suggest that this vein was formed by crack-seal mechanism (Sample 193-1188F-15Z-1 [Piece 8, 55–58 cm] in cross-polarized transmitted light; width of view = 5.5 mm. Photomicrograph ID# 1188F_82; [thin section 81](#)).

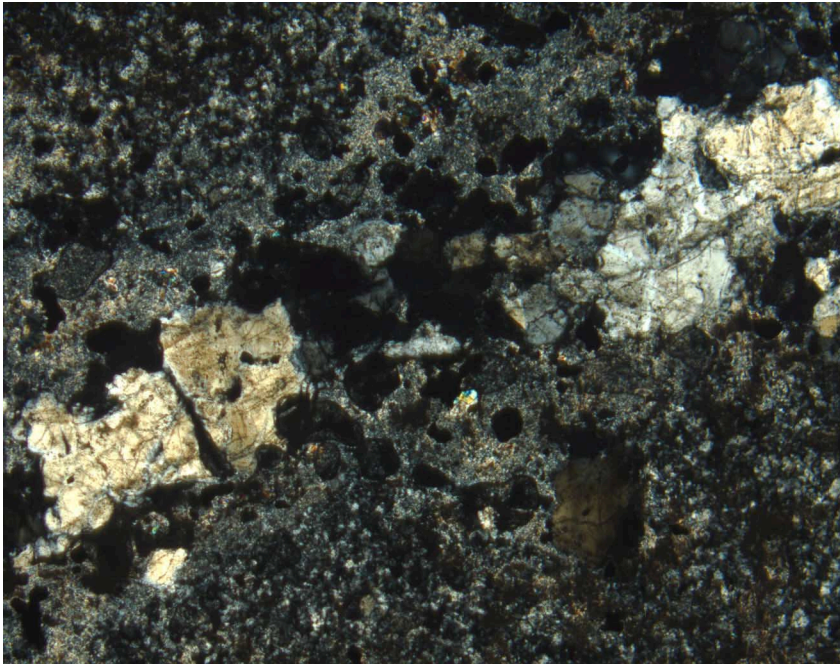


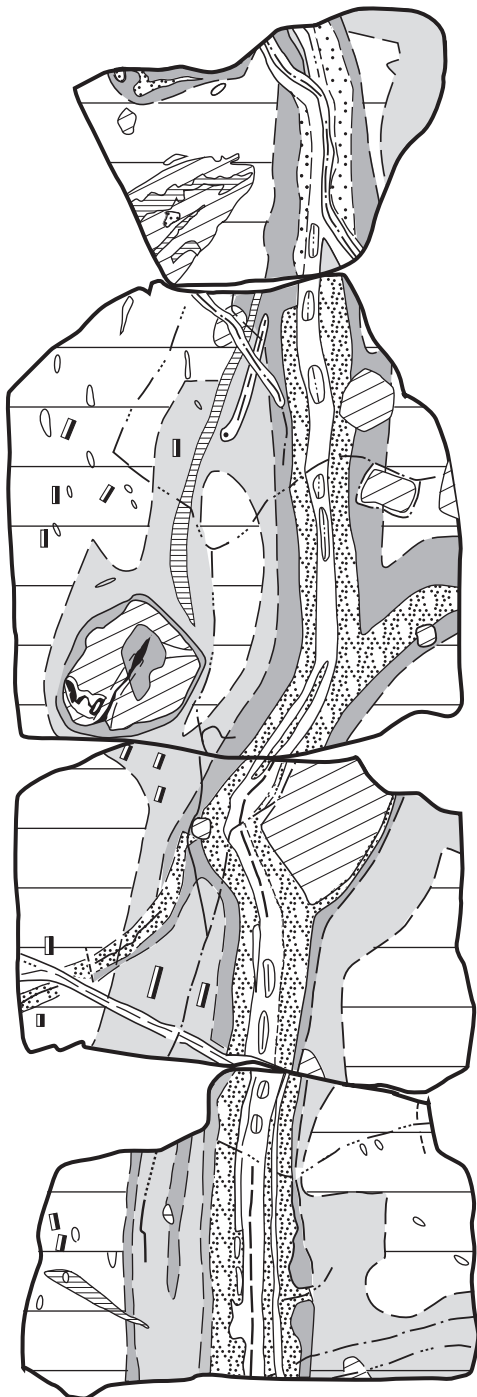
Figure F112. A. Close-up photograph of interval 193-1188F-43Z-1 (Pieces 2-3C, 62-86 cm); 372.06 mbsf. Quartz-clay vein with a pronounced dark, magnetite-bearing siliceous alteration halo. Several thin anhydrite and anhydrite-pyrite veins cut across this main vein structure, as highlighted in the sketch. (Continued on next page.)



Figure F112 (continued). B. Sketch of Sample 193-1188F-43Z-1 (Pieces 2-3C, 62-86 cm); 372.06 mbsf.

B

Interval 193-1188F-43Z-1, 62-86 cm



-  Gradational boundary
-  Clast
-  Vesicle/amygdule
-  Feldspar phenocryst
-  Pyrite + anhydrite + chlorite
-  Pyrite + anhydrite
-  Anhydrite (\pm silica)
-  Pyrite + quartz
-  Pyrite + quartz + chlorite/clay
-  Magnetite (\pm quartz)
-  Vein as vugs
-  Strong silicification
-  Weaker silicification
-  Vein-fill (silica + clay)
-  Altered host rock
-  Magnetite + silica halo
-  Clay-silica alteration

0 2 cm

Figure F113. A. Distribution of vein thicknesses in Hole 1188F. B. Veins in Hole 1188F are grouped according to their dips: horizontal = 0°–5°, subhorizontal = 5°–15°, inclined = 15°–75°, subvertical = 75°–85°, vertical = 85°–90°. (Continued on next page.)

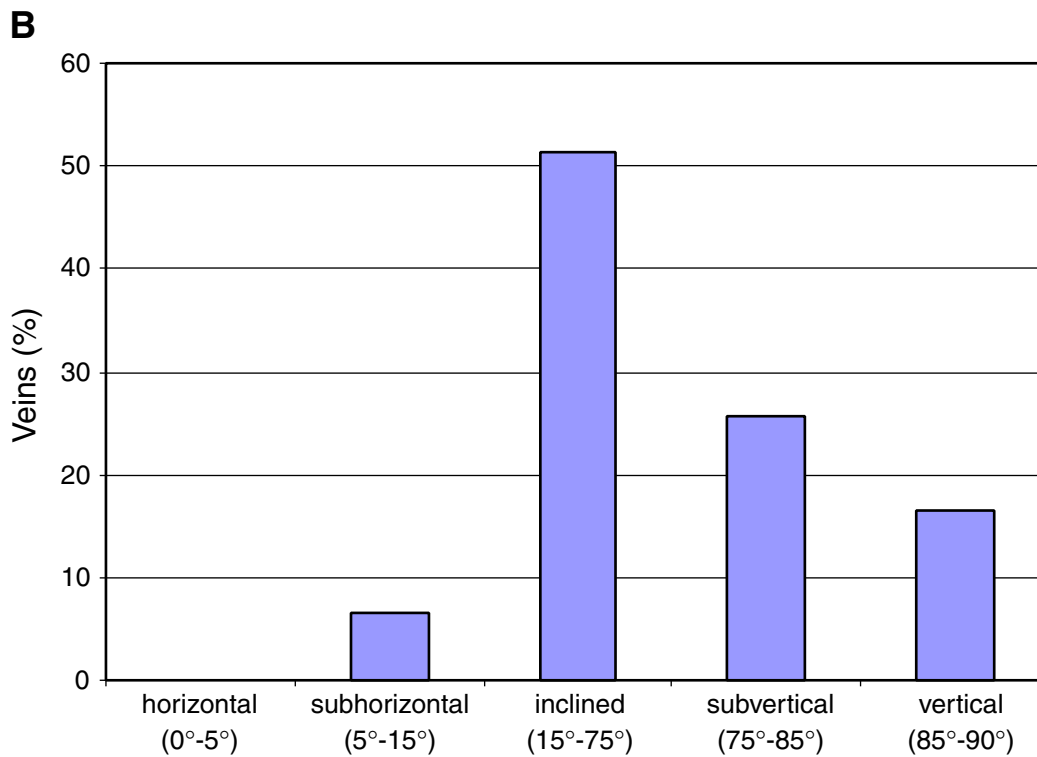
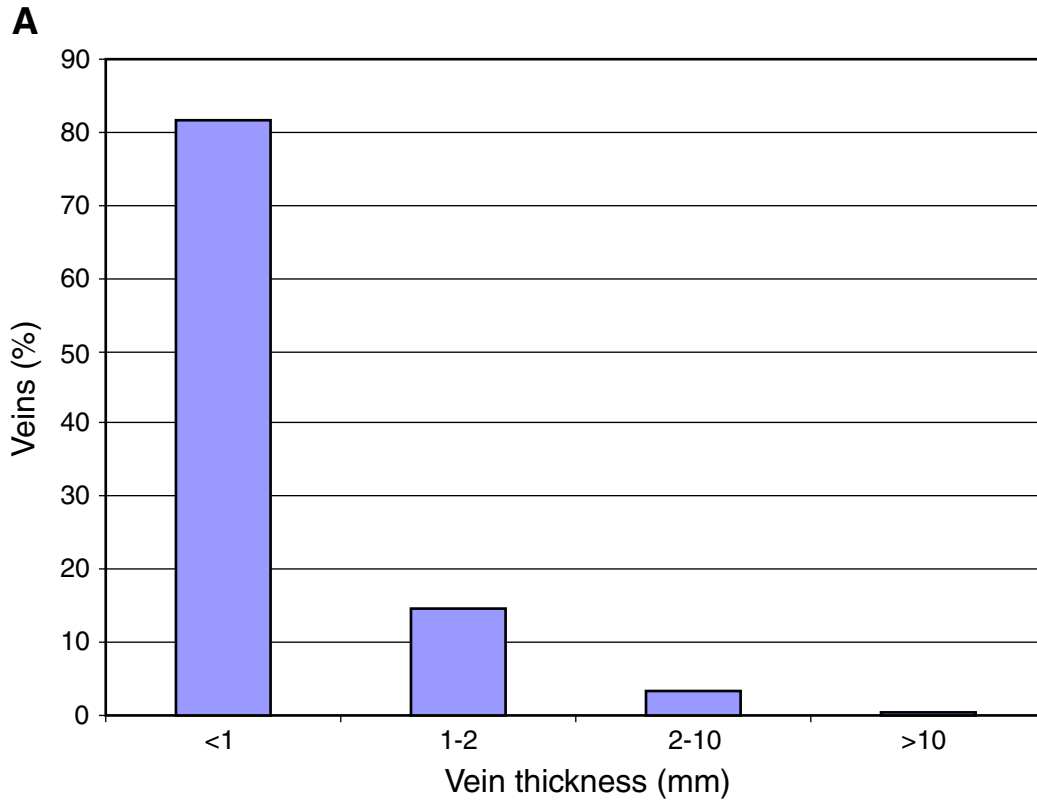


Figure F113 (continued). C. Dips of veins vs. dip in Hole 1188F.

C

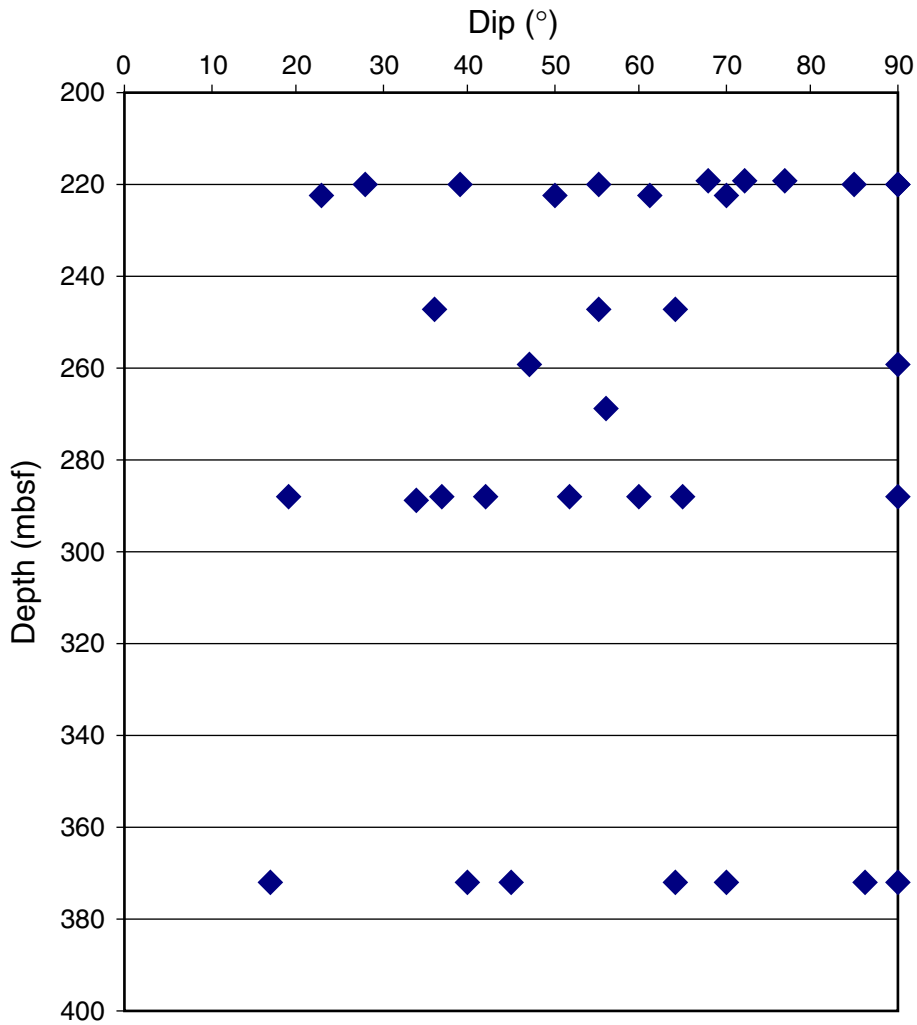


Figure F114. A. Downhole variations of selected major element oxides plotted together with the significant mineral phases from X-ray diffraction, and the alteration and unit logs for Holes 1188A and 1188F. The alteration symbols used are from Figure F8, p. 47, in the “Explanatory Notes” chapter. (Continued on next page.)

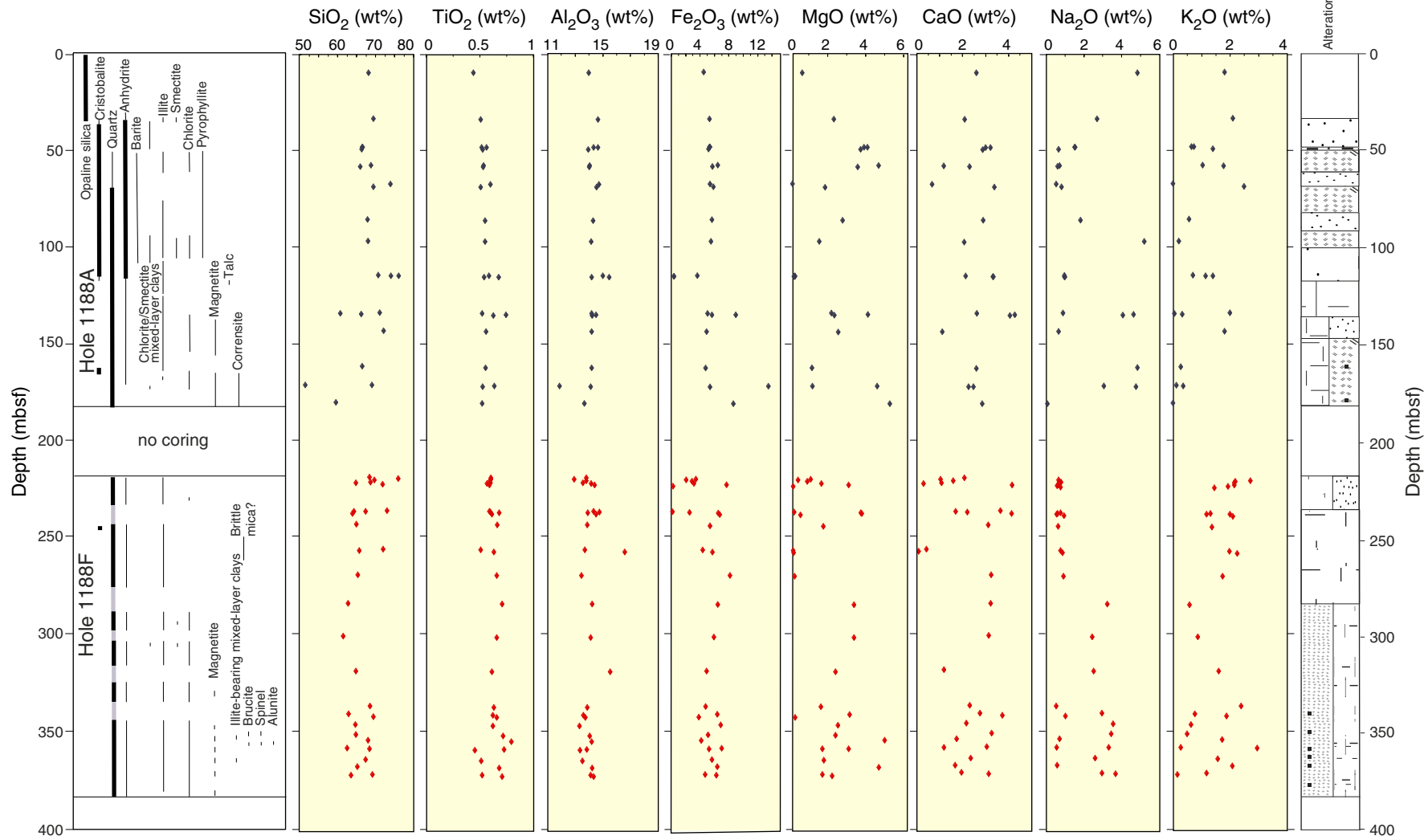


Figure F114 (continued). B. Downhole variations of selected trace elements and total S and water, plotted together with the significant mineral phases from X-ray diffraction, and the alteration and unit logs for Holes 1188A and 1188F.

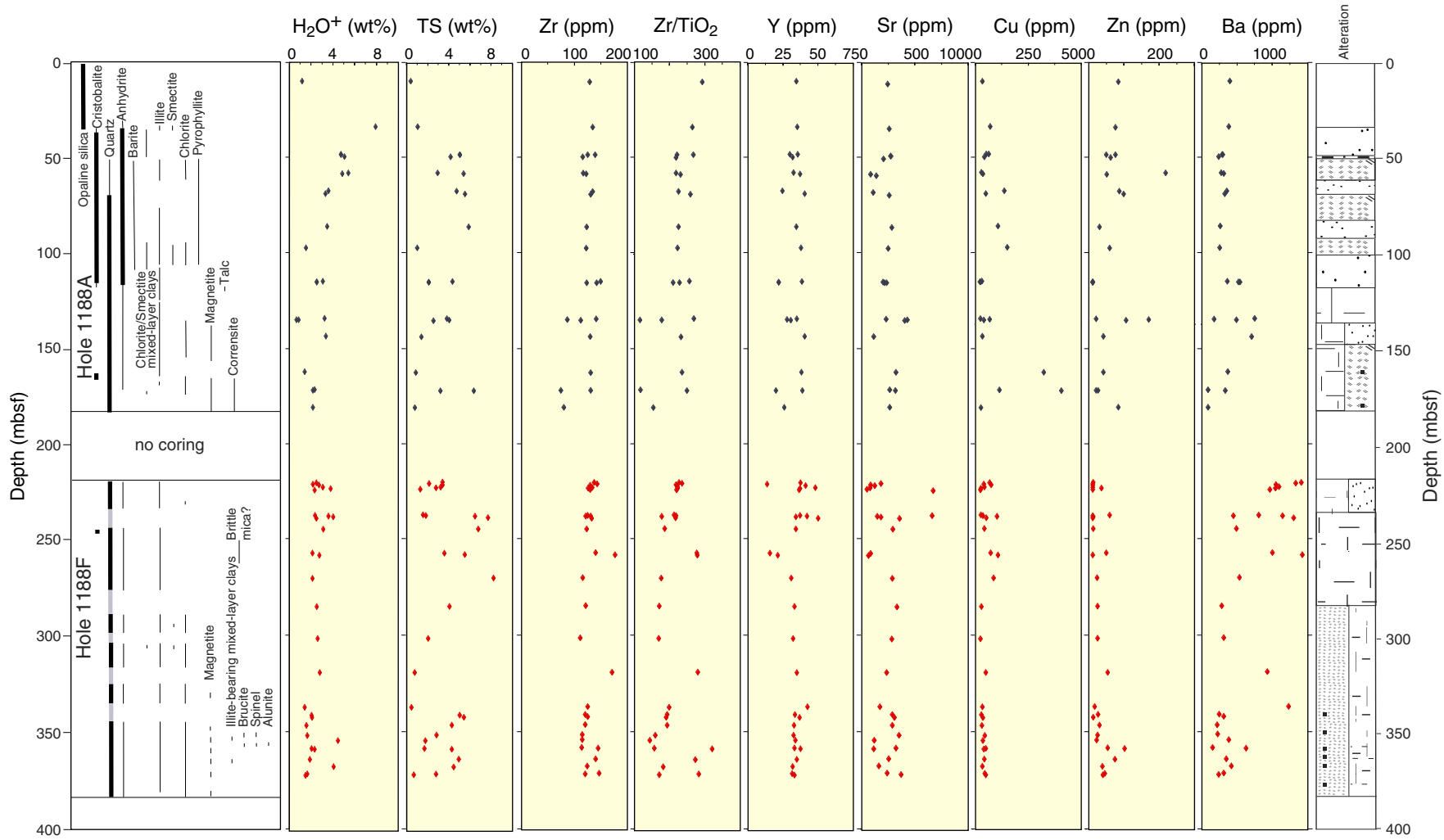


Figure F115. Photomicrographs of mineral particles from Hole 1188A showing bacterial habitation. Ground samples (<100 μm ; Sample 193-1188A-5R-1, 17–21 cm; 33.77 mbsf) of translucent fragments of dacitic volcanic glass with (A, B) plagioclase microlites (arrows) and microcrystalline domains with (C, D) spheroidal crystallites (arrows) are shown. DAPI-stained bacteria are located on the surface, flat planes, and edges of these fractures.

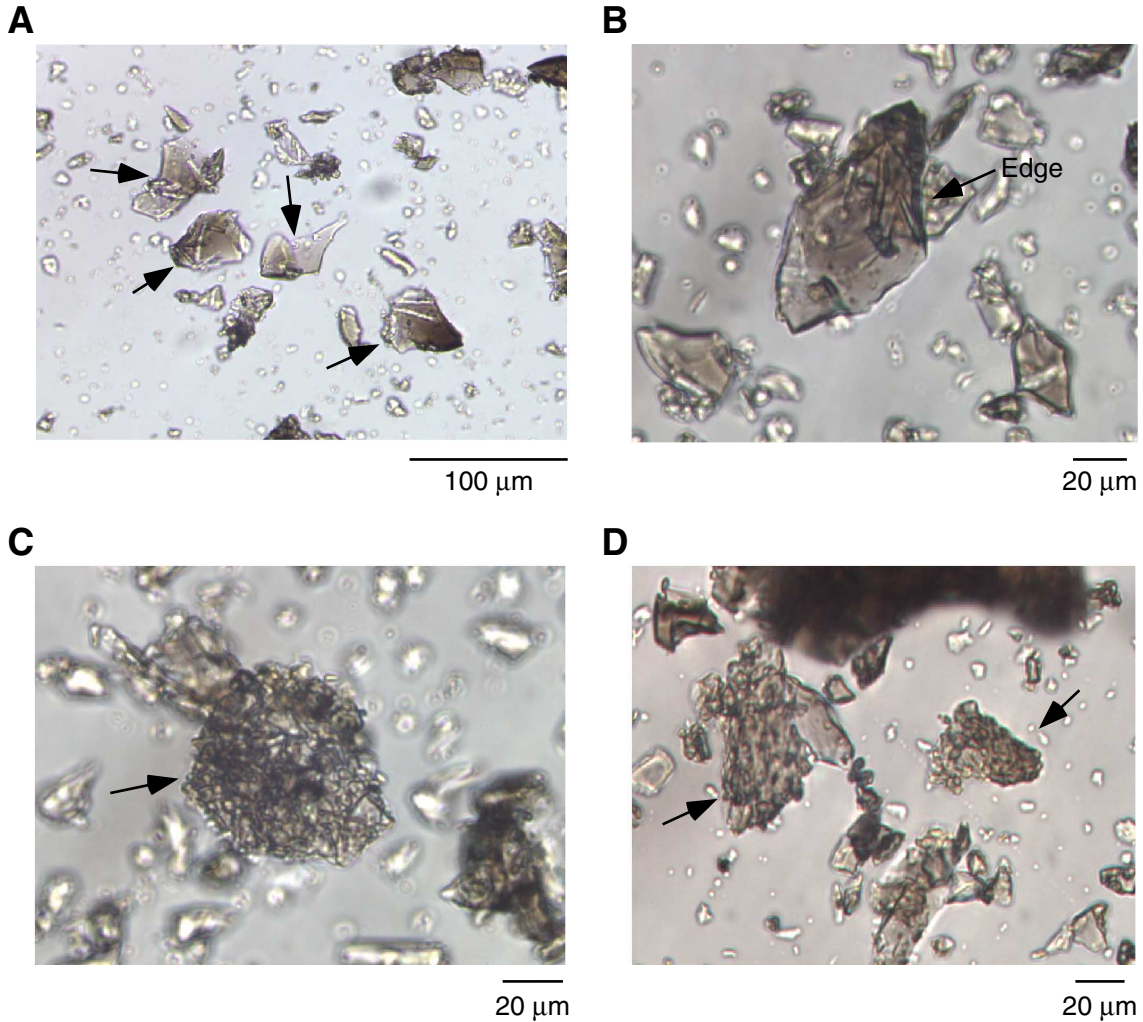


Figure F116. Photomicrographs of mineral particles from Hole 1188A showing possible bacterial habitation. Ground samples (<100 μm) of (A) exopolymer cluster (Sample 193-1188A-8R-1, 18–20 cm; 59.58 mbsf), (B) flaky particles composed of volcanic glass (Sample 193-1188A-9R-1, 137–140 cm; 68.97 mbsf), and (C) mineralized bacteria (Sample 193-1188A-13R-1, 50–53 cm; 106.8 mbsf) are shown.

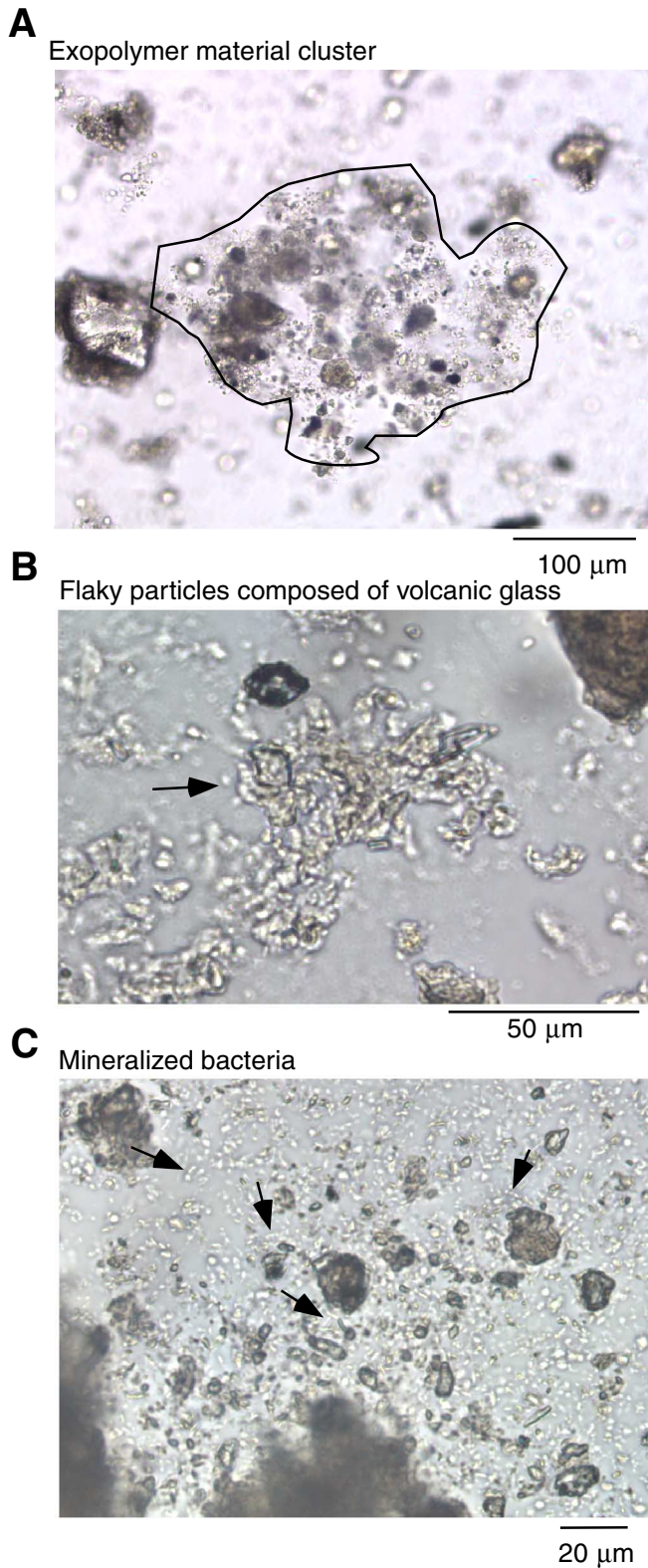
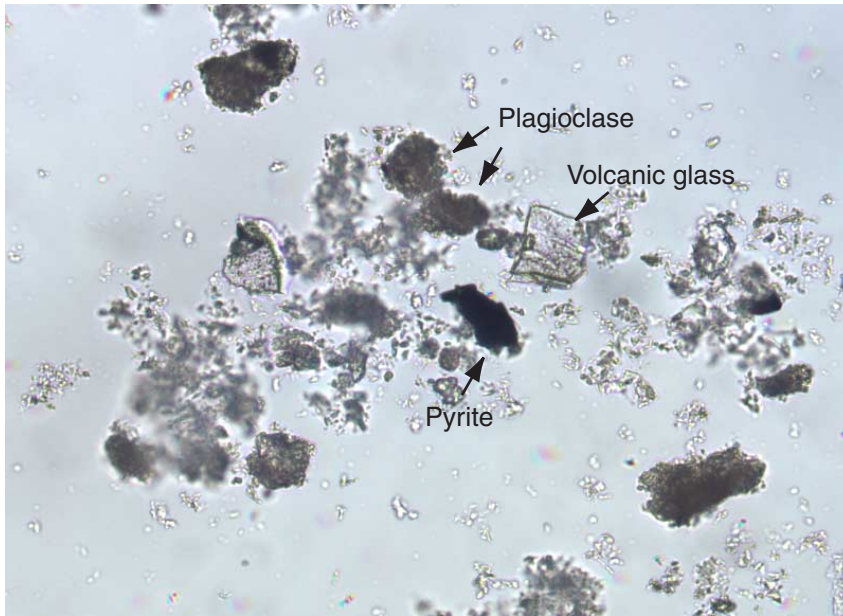


Figure F117. Photomicrographs of mineral fragments from Hole 1188F showing no bacterial habitation. A. Sample 193-1188F-16Z, 88–90 cm, (255.78 mbsf) showing plagioclase, pyrite, and volcanic glass fragments with no stained bacteria. B. Sample 193-1188F-1Z-4, 63–63 cm (222.23 mbsf), showing assemblages of clay minerals and plagioclase fragments with no definitive bacterial mass.

A



B

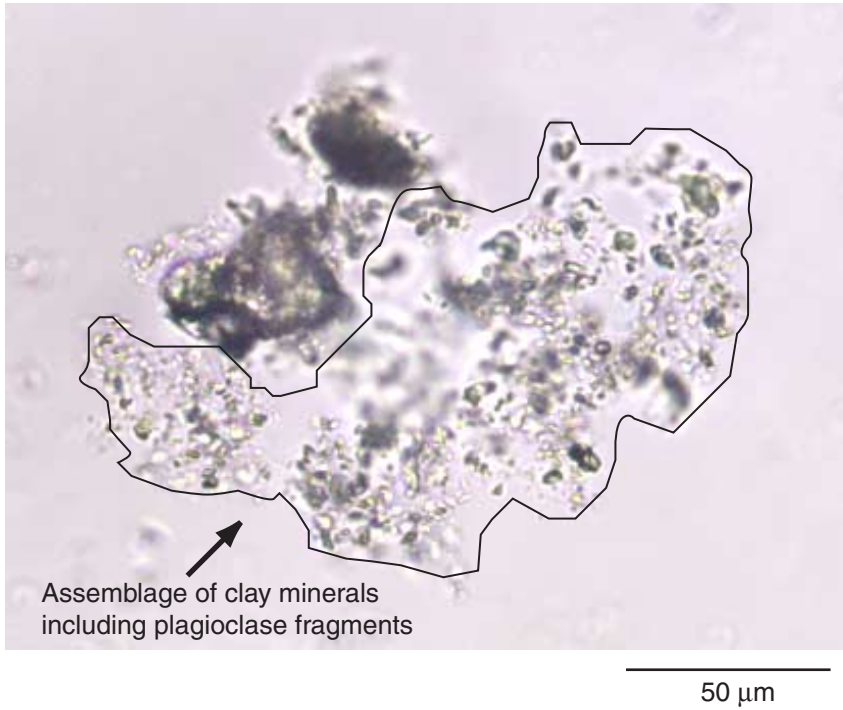


Figure F118. Magnetic susceptibility, Hole 1188A.

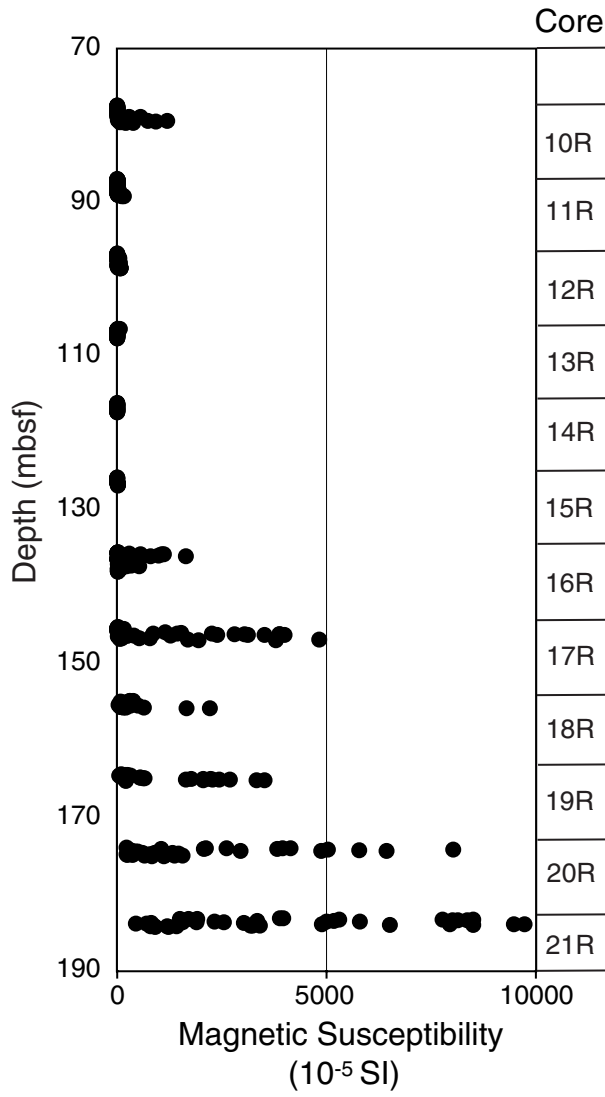


Figure F119. Natural gamma radiation (NGR), Hole 1188A.

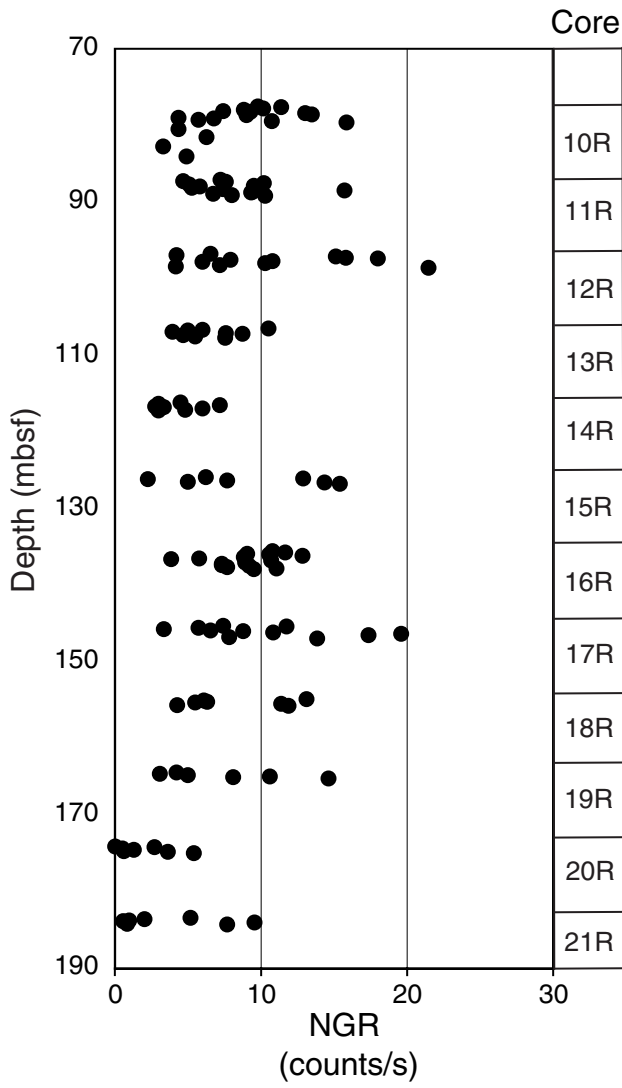


Figure F120. Compressional wave velocity, Site 1188. Solid circles = Hole 1188A, open circles = Hole 1188F.

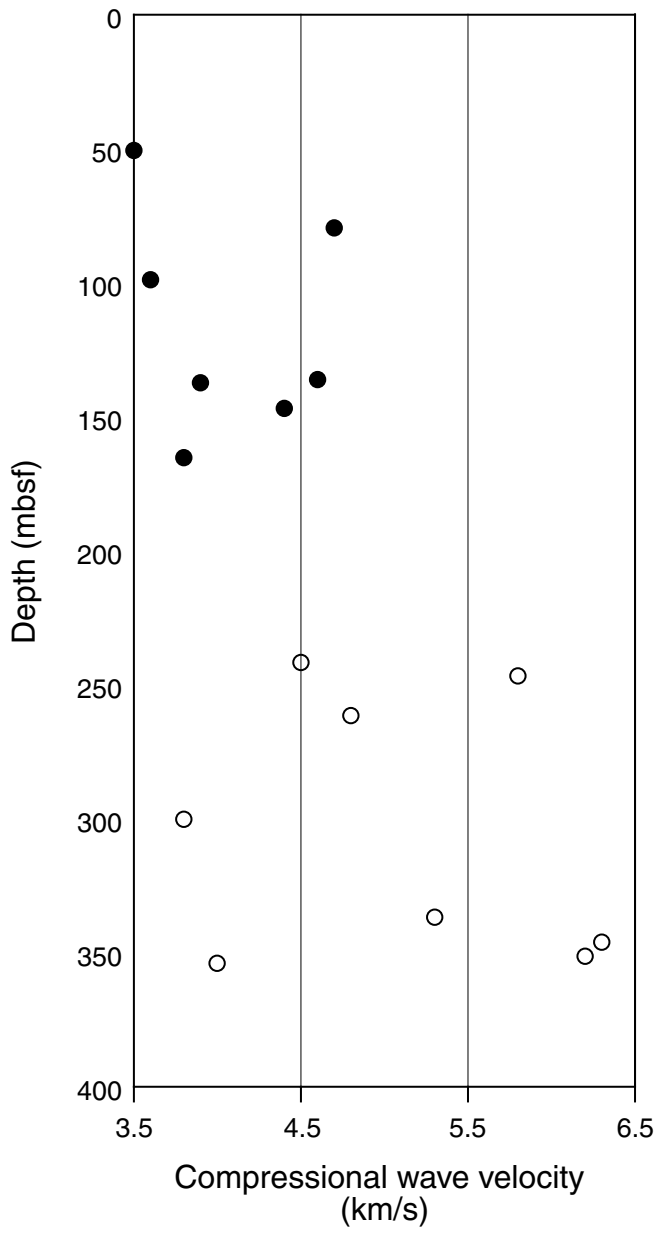


Figure F121. Thermal conductivity, Site 1188. Solid circles = Hole 1188A, open circles = Hole 1188F.

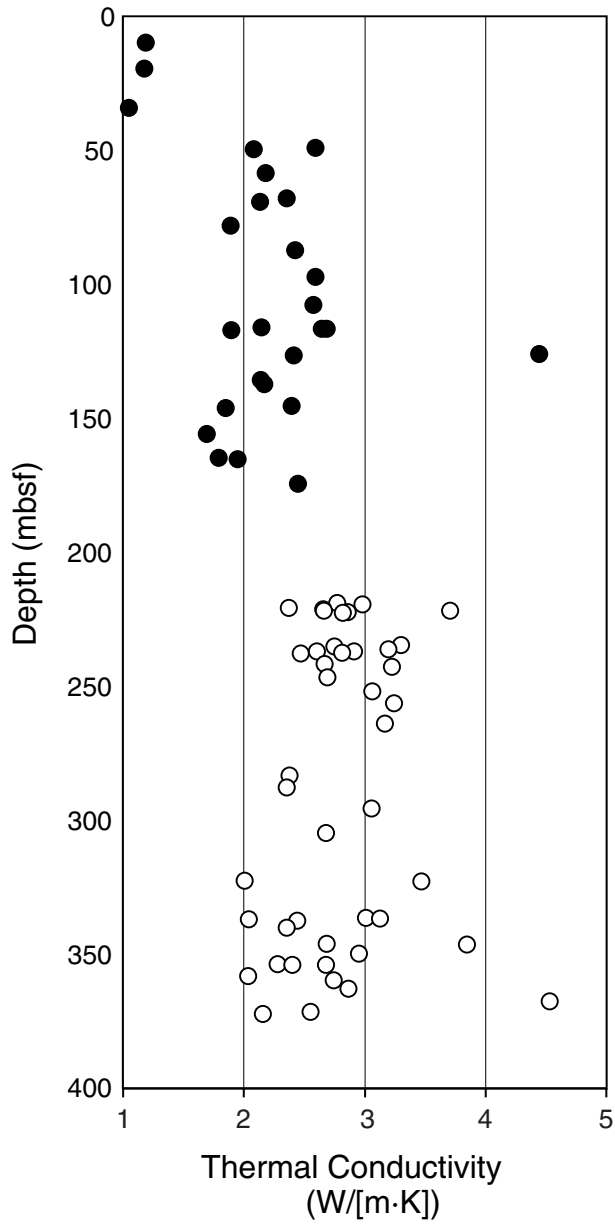


Figure F122. Grain density, Site 1188. Solid circles = Hole 1188A, open circles = Hole 1188F.

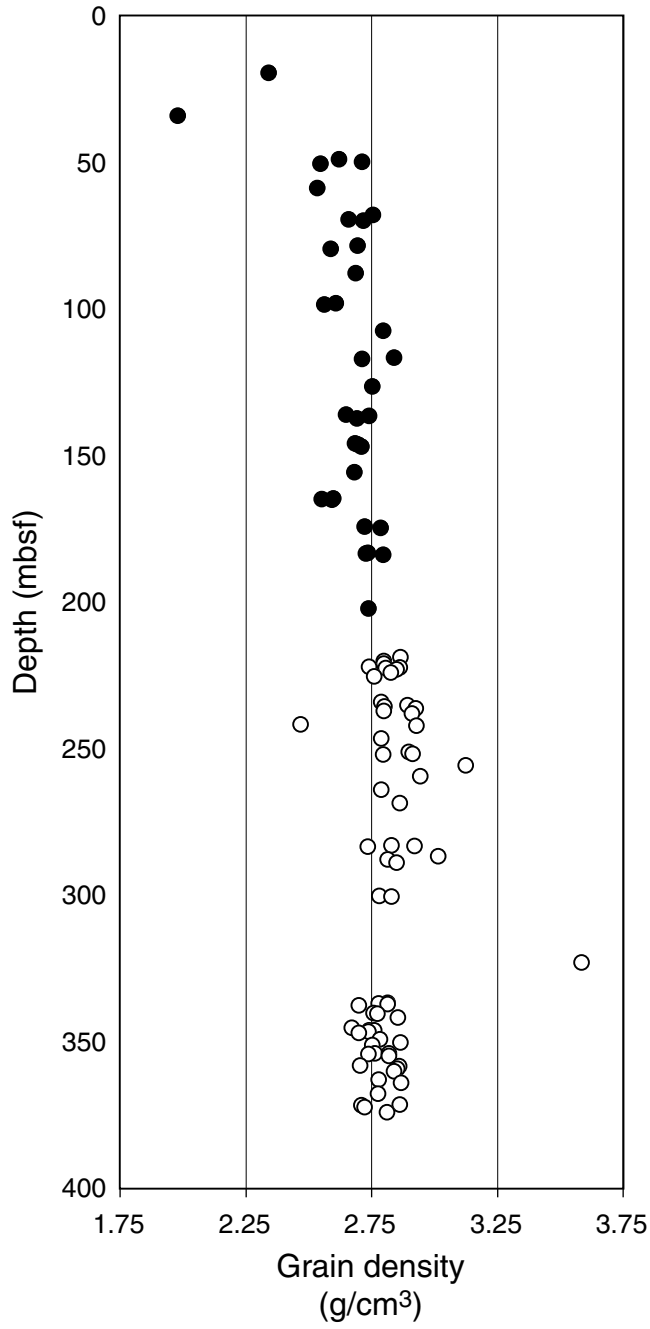


Figure F123. Porosity, Site 1188. Solid circles = Hole 1188A, open circles = Hole 1188F.

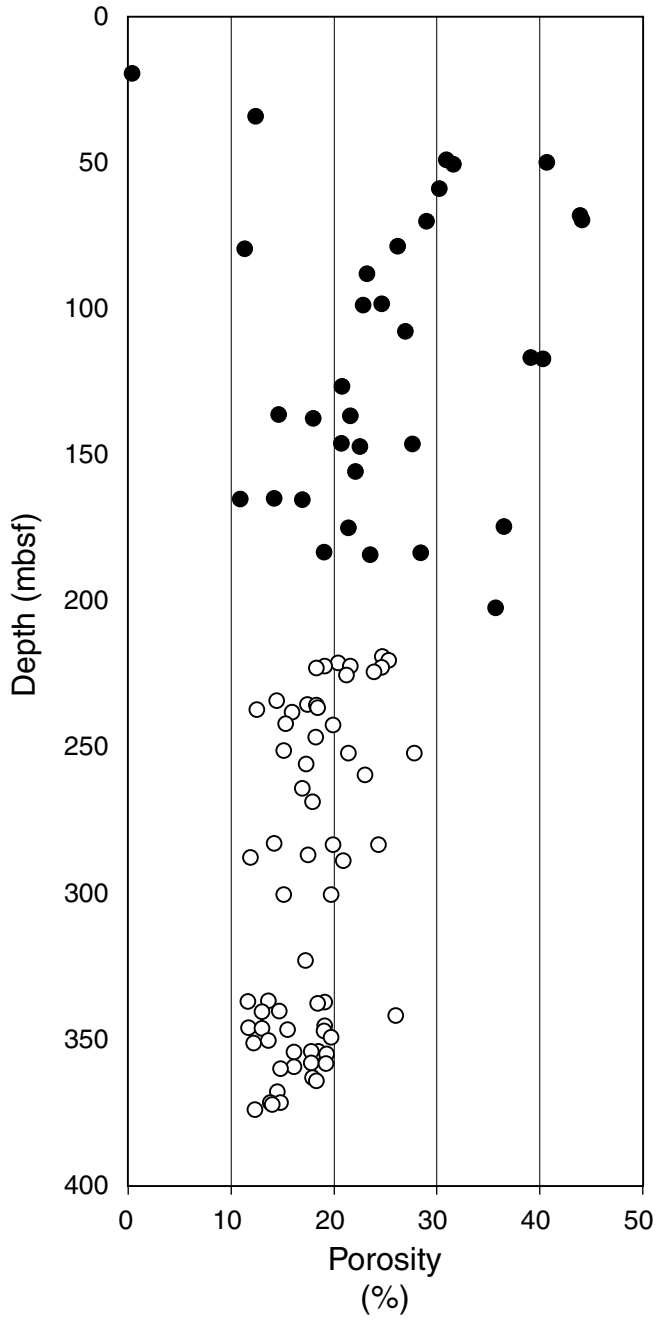


Figure F124. Volume susceptibility vs. depth of archive-half core samples. Holes 1188A and 1188F are combined into one profile. The susceptibility represents point measurements taken using the archive multisensor track in manual mode.

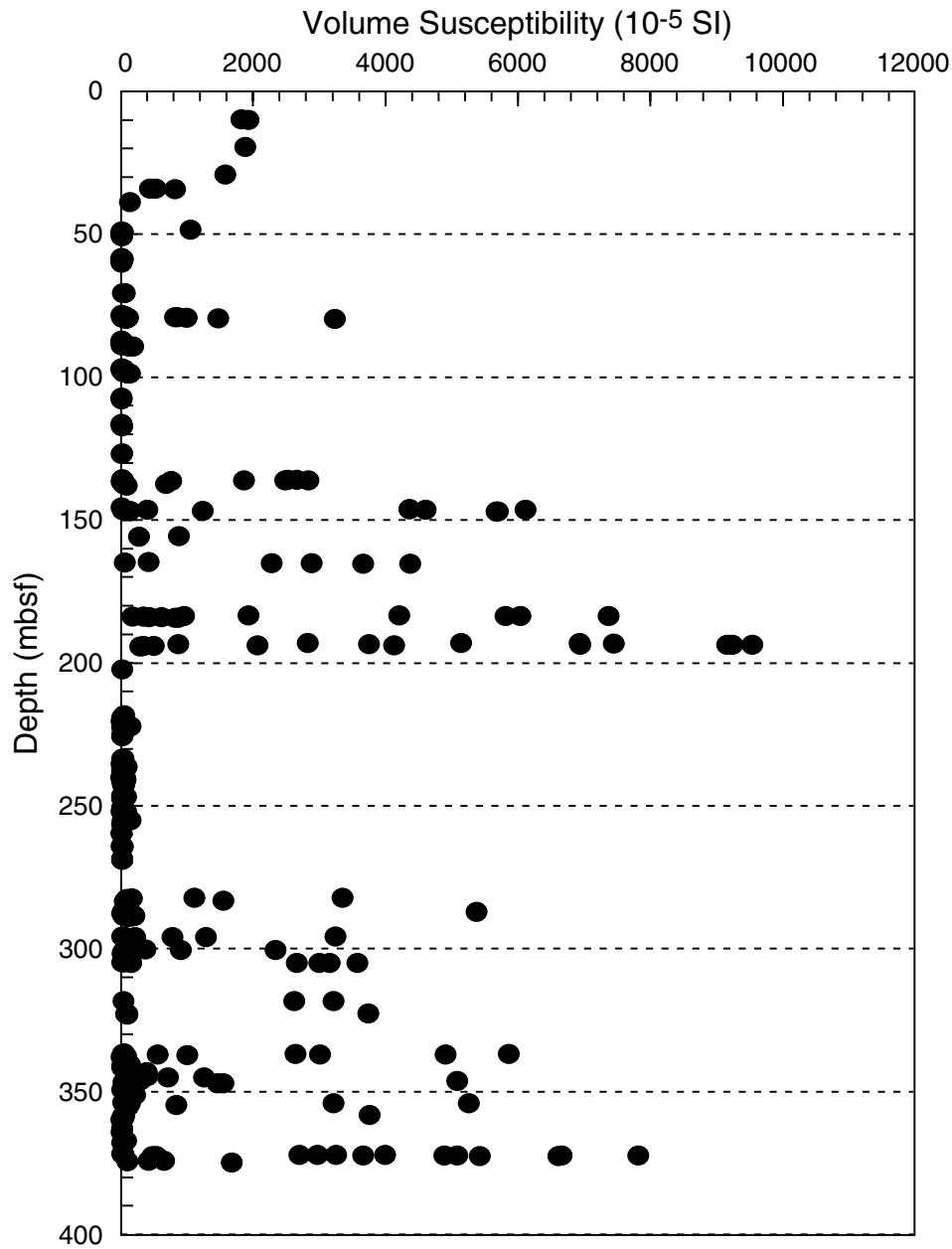


Figure F125. Uncorrected remanent intensity vs. depth of archive-half core samples, Hole 1188A. Similar measurements could not be made for Hole 1188F because of the larger diameter of the recovered samples.

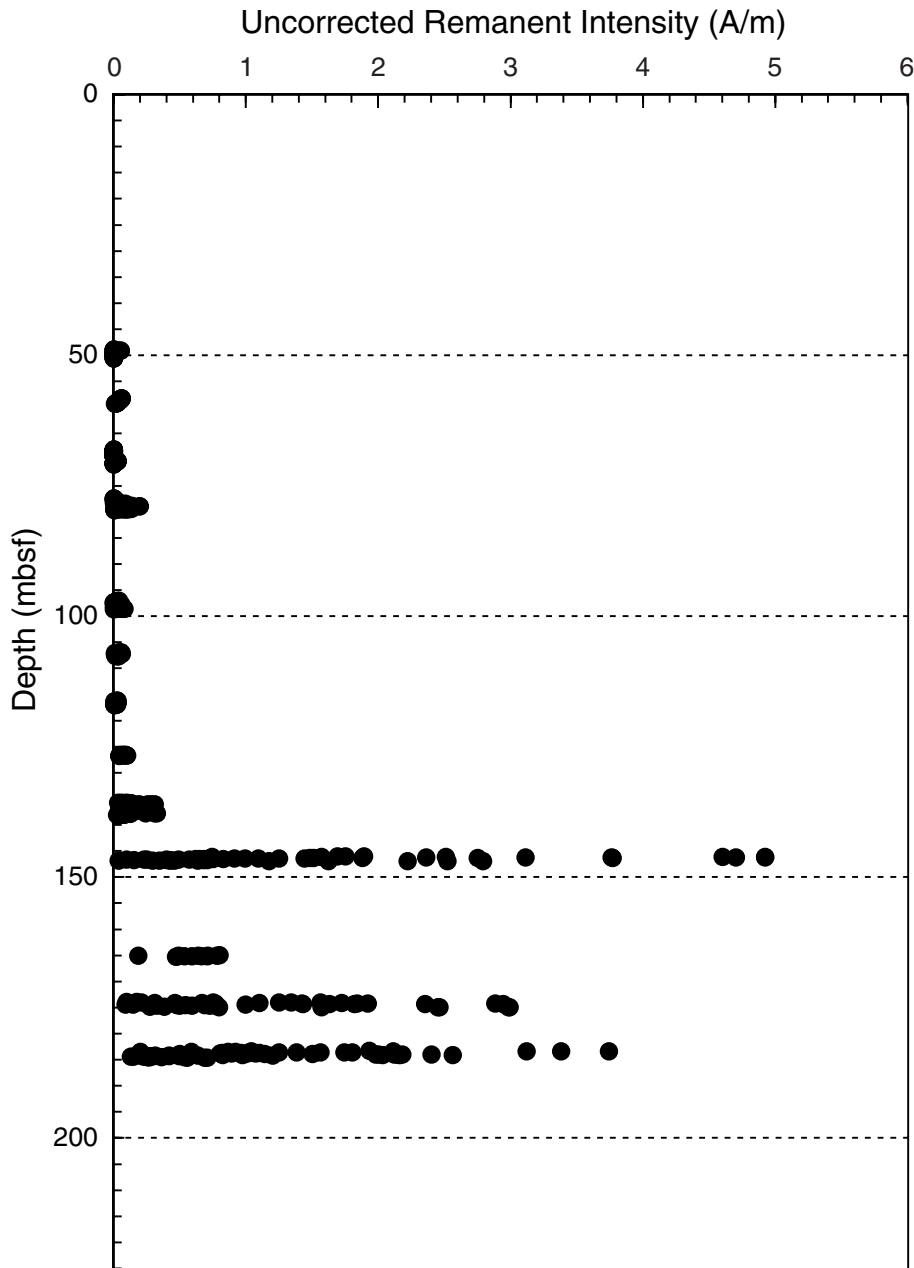


Figure F126. Magnetic susceptibility vs. depth of 40 minicore samples. Holes 1188A and 1188F are combined into one profile.

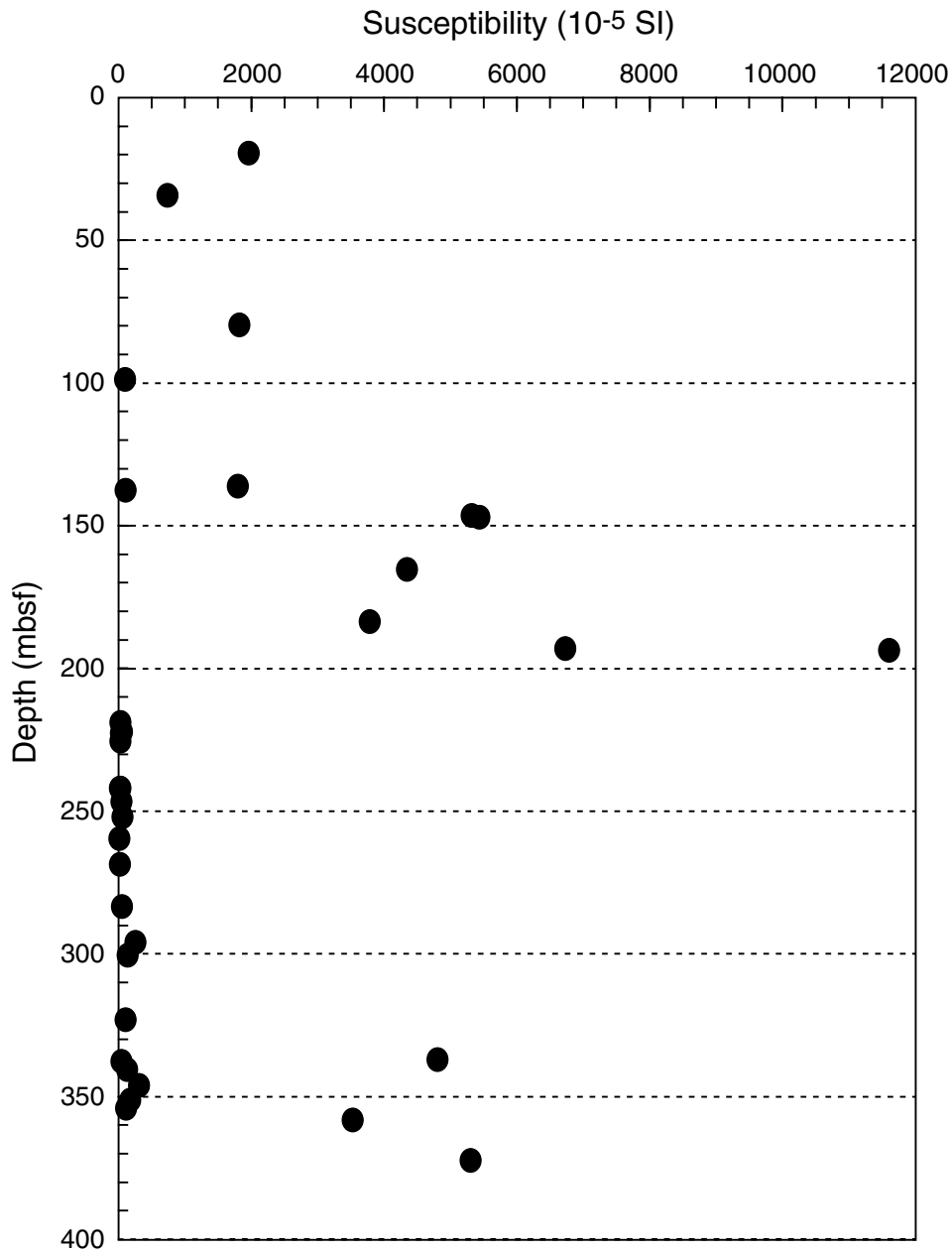


Figure F127. Flinn-type diagram of the anisotropy of magnetic susceptibility ellipsoid showing magnetic fabric foliation (F) and lineation (L), Site 1188.

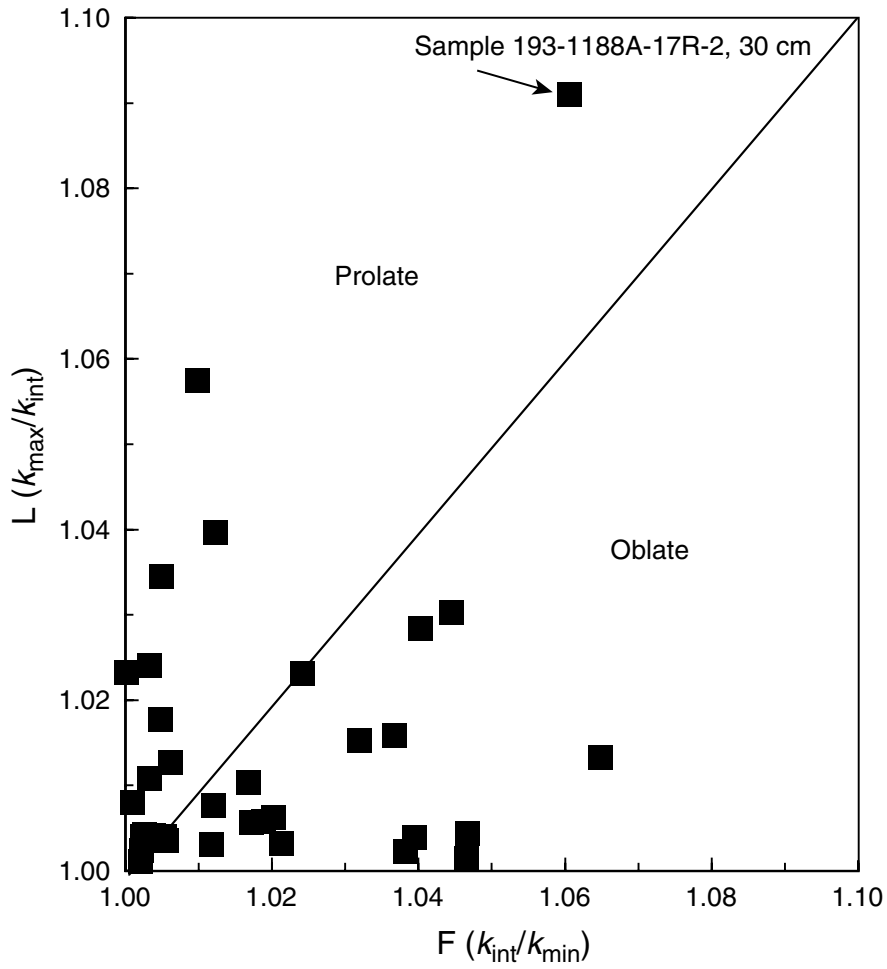


Figure F128. Natural remanent magnetization (NRM) intensity vs. depth of 40 minicore samples. Holes 1188A and 1188F are combined as a single profile.

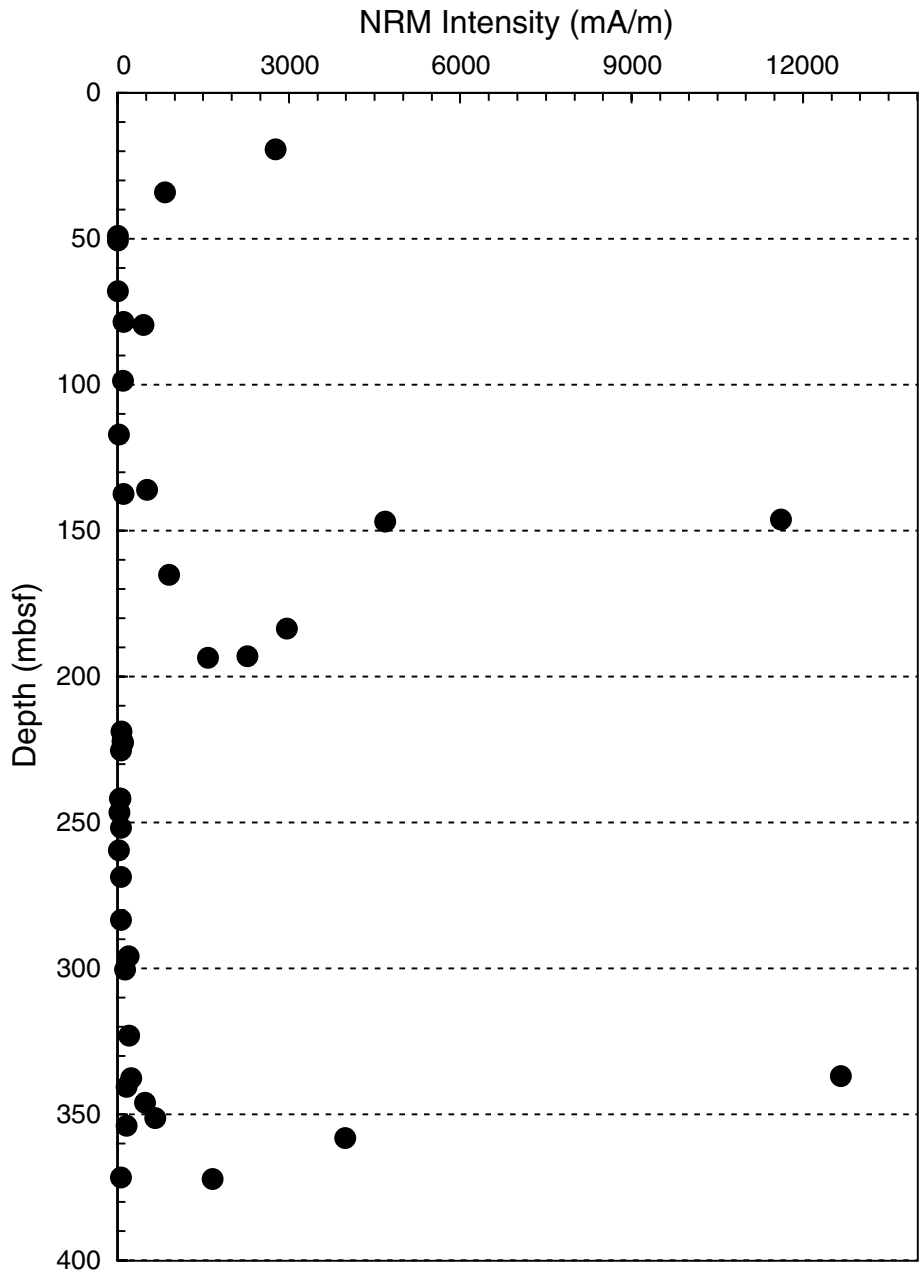


Figure F129. Stable inclination vs. depth of minicore samples, Site 1188. Holes 1188A and 1188F are combined as a single profile.

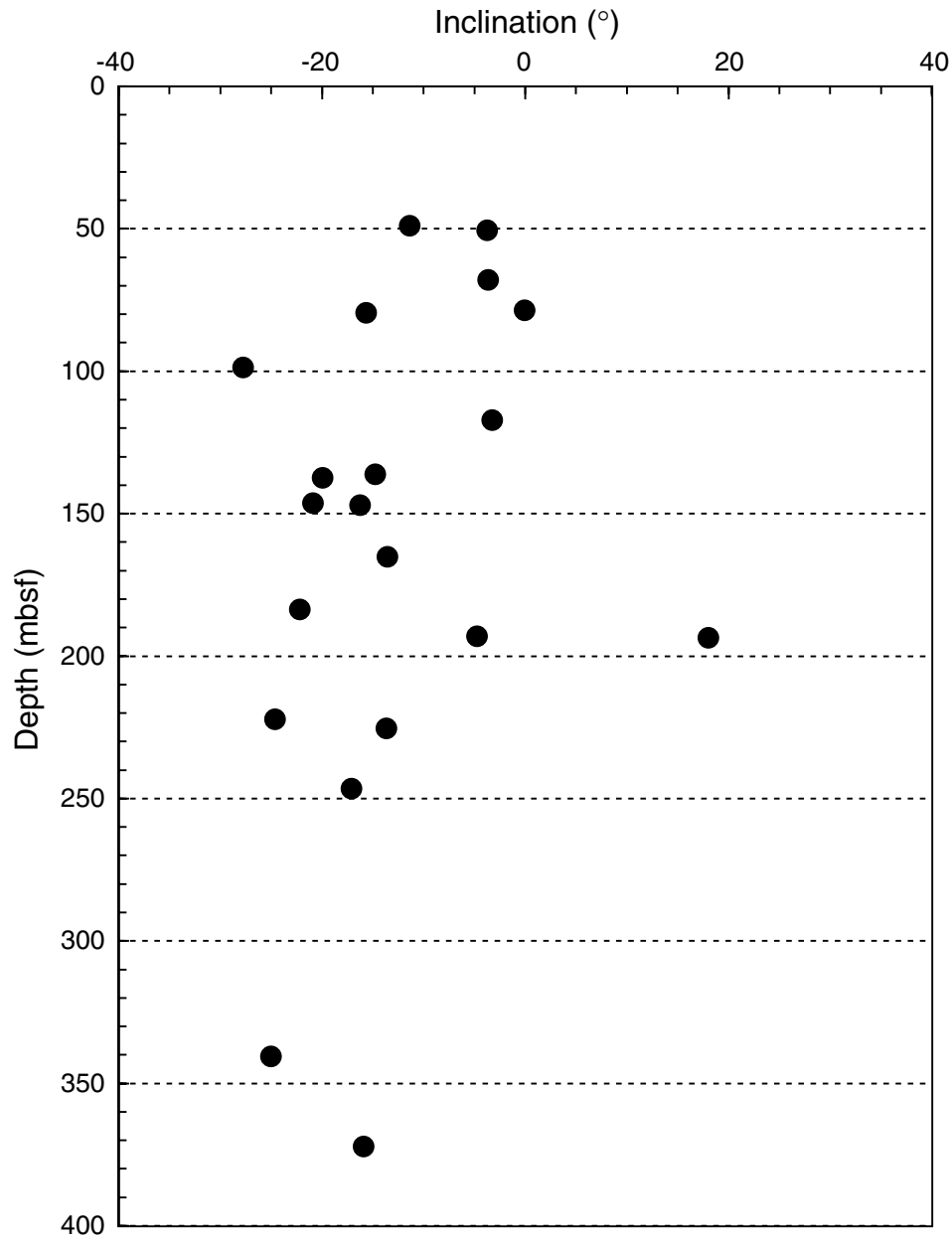
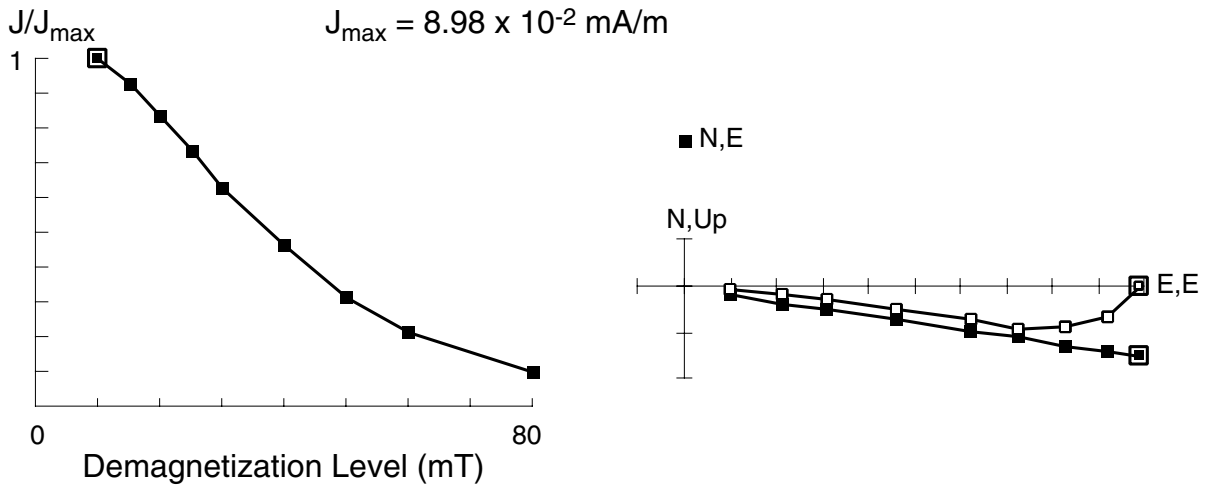


Figure F130. Zijderveld plots and intensity-decay curves of Samples 193-1188A-10R-1, 118 cm, and 17R-2, 30 cm, showing component decay toward the origin during progressive alternating-field demagnetization.

Sample 193-1188A-10R-1, 118 cm



Sample 193-1188A-17R-2, 30 cm

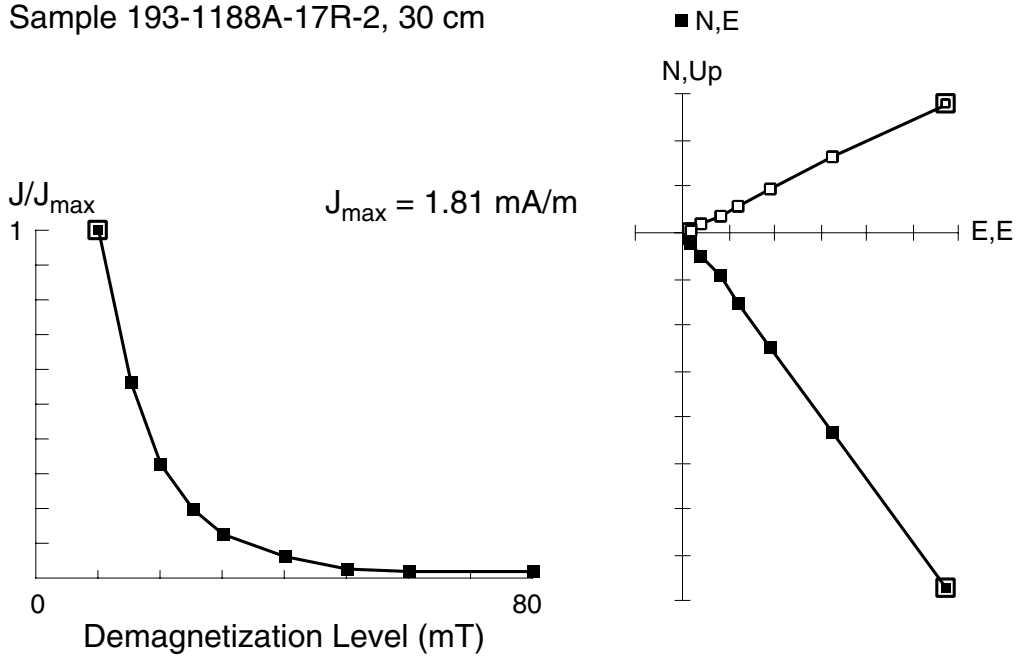


Figure F131. Zijderveld plot and intensity-decay curve of Sample 193-1188A-16R-2, 46 cm, showing the presence of a strong secondary magnetization that was effectively removed by alternating-field demagnetization.

Sample 193-1188A-16R-2, 46 cm

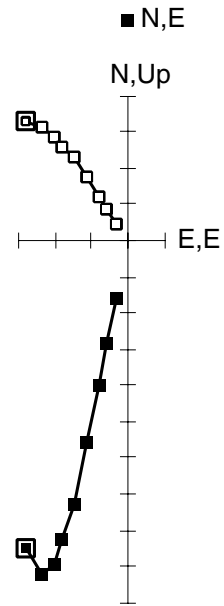
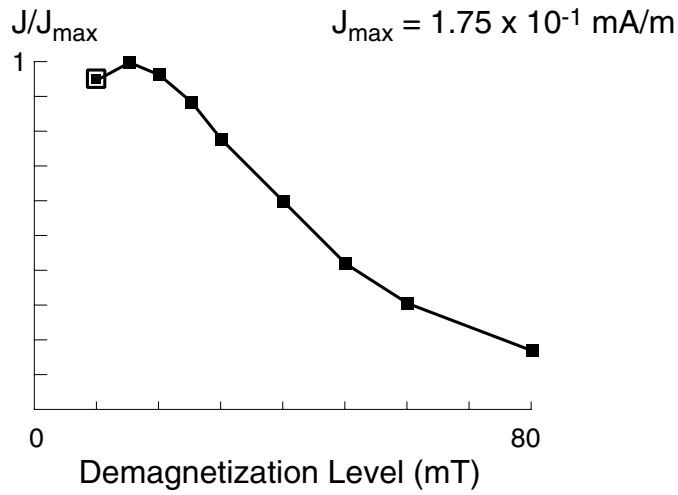


Figure F132. Intensity of isothermal remanent magnetization (IRM) as a function of applied impulse field for 17 minicores, Hole 1188A. The high variability in IRM is a result of instrumental effects.

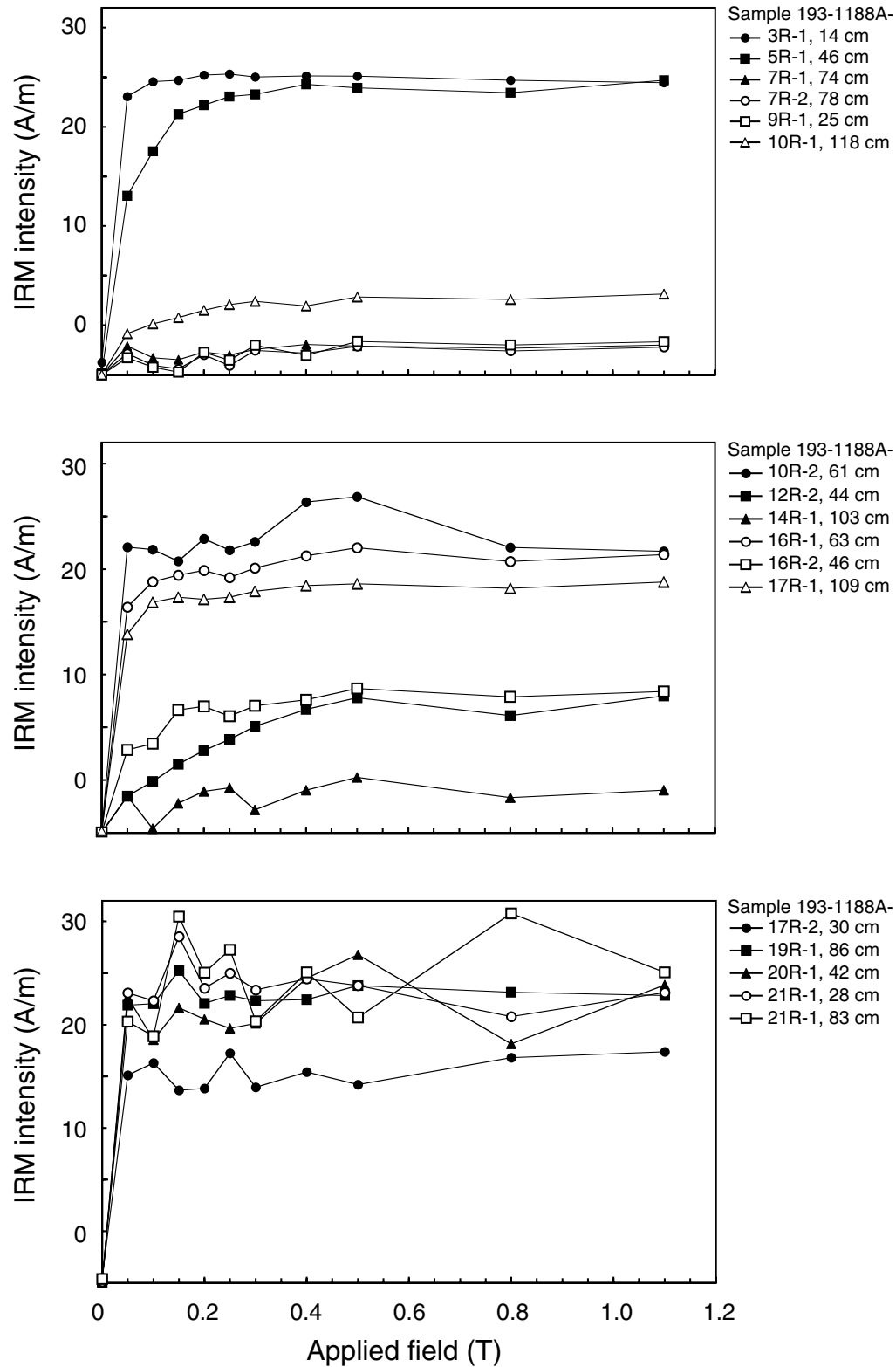


Figure F133. Intensity of isothermal remanent magnetization (IRM) as a function of applied impulse field for 23 minicores, Hole 1188F. The high variability in IRM is a result of instrumental effects. (Continued on next page).

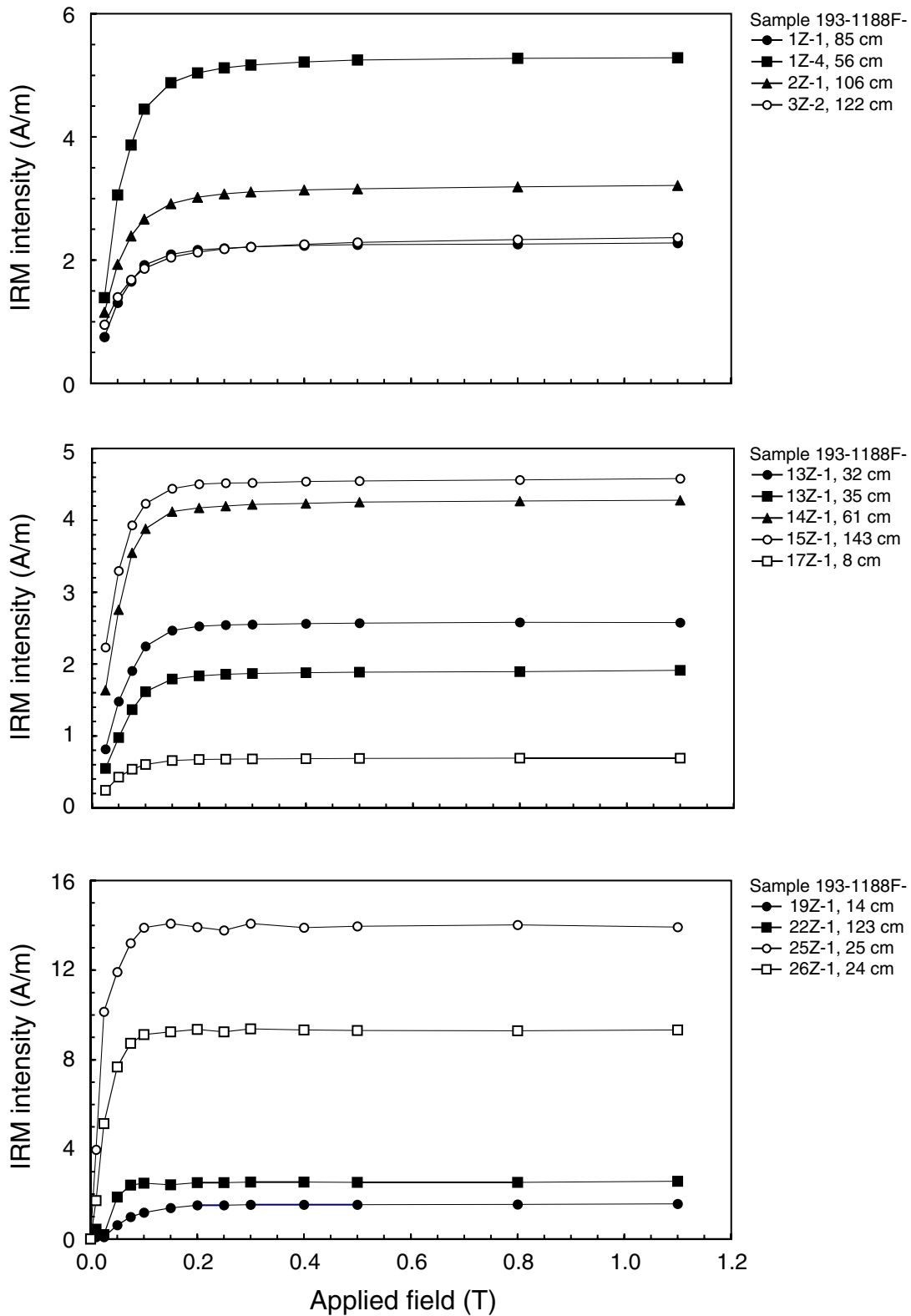


Figure F133 (continued).

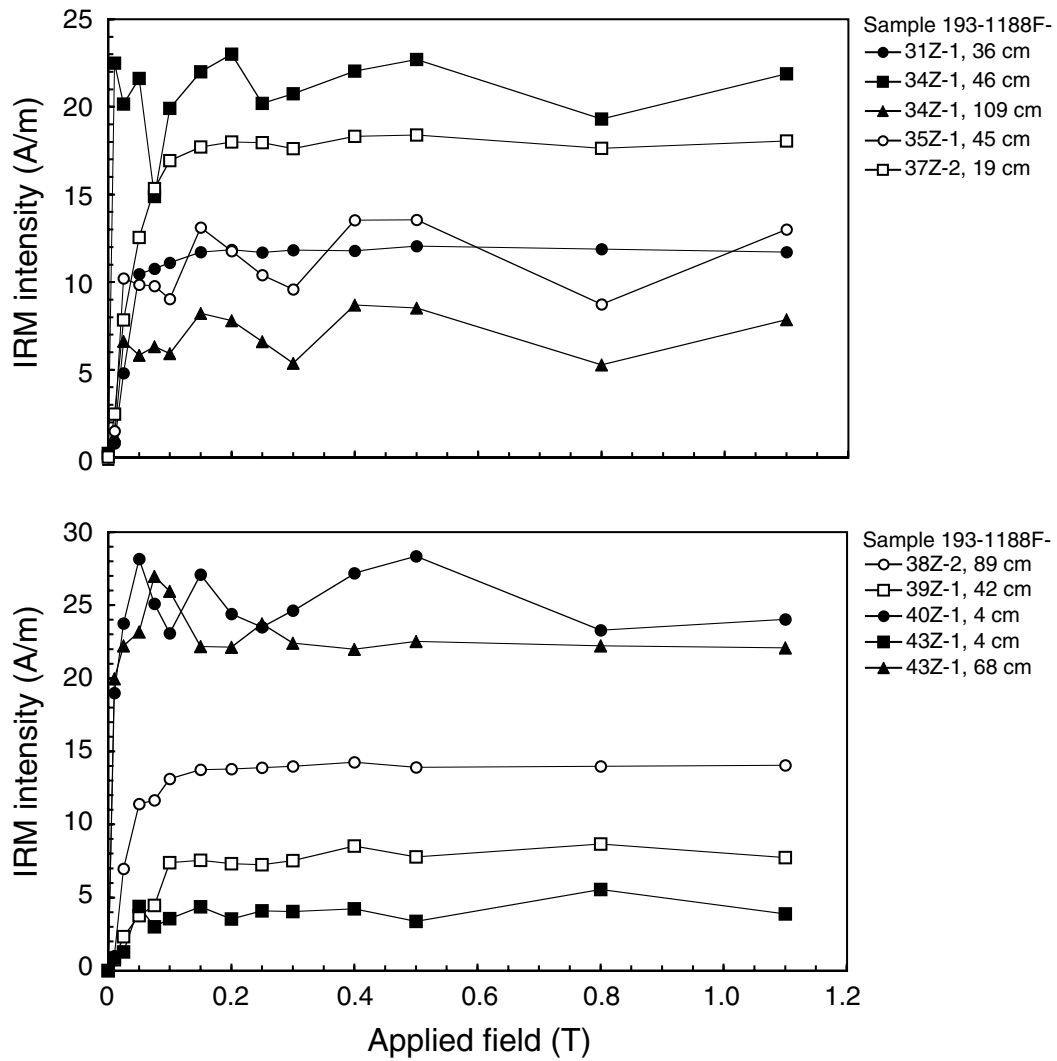


Figure F134. Intensity of backfield isothermal remanent magnetization (BIRM) as a function of applied impulse field showing the contrasting behavior of samples from Hole 1188F. These samples correspond to some of the samples in Figure F133, p. 243. The high variability in BIRM is a result of instrumental effects.

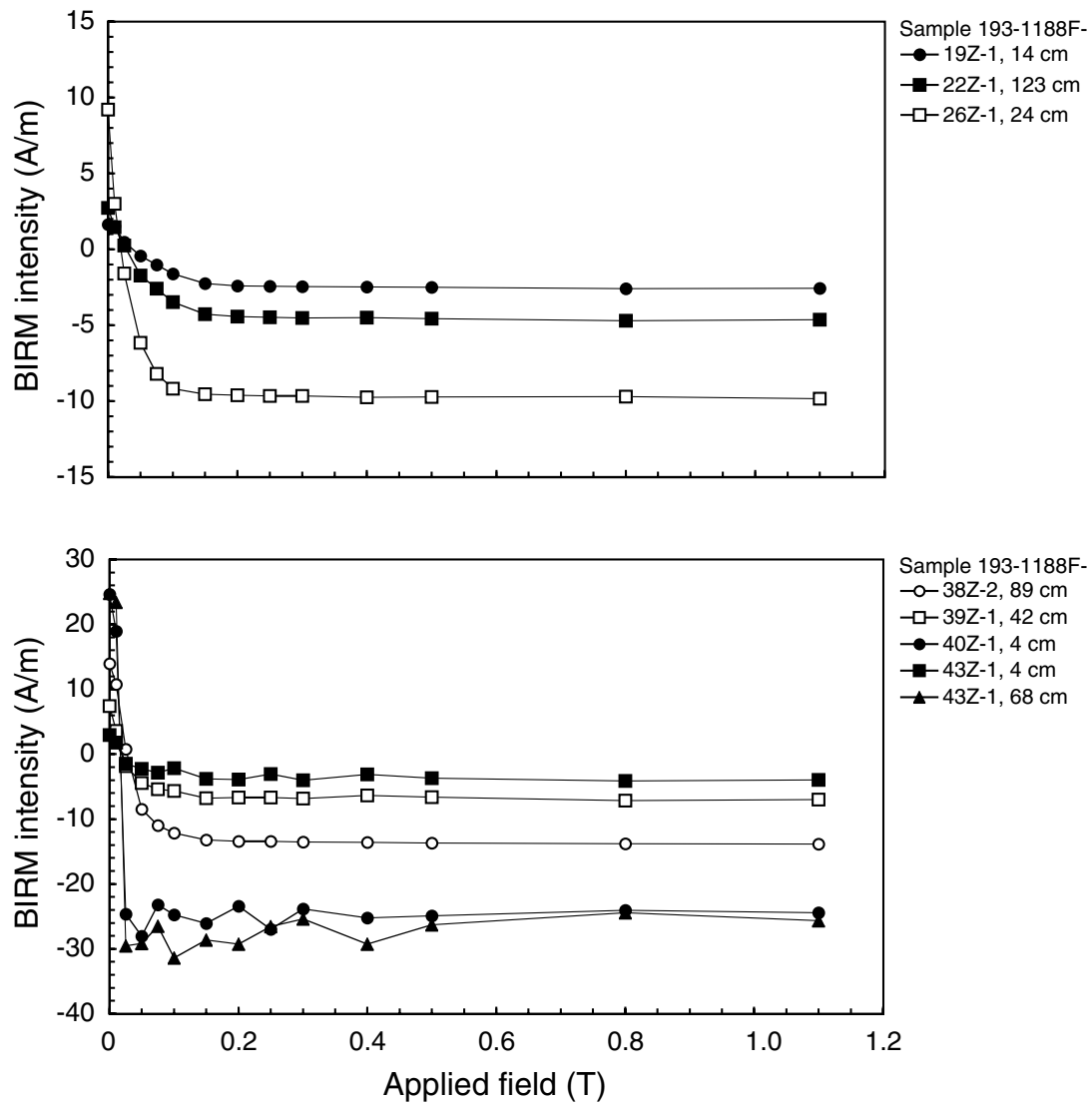


Figure F135. Thermal demagnetization curves of four representative samples from Hole 1188A. The samples were imparted with an isothermal remanent magnetization (IRM) at an impulse field of 1.1 T.

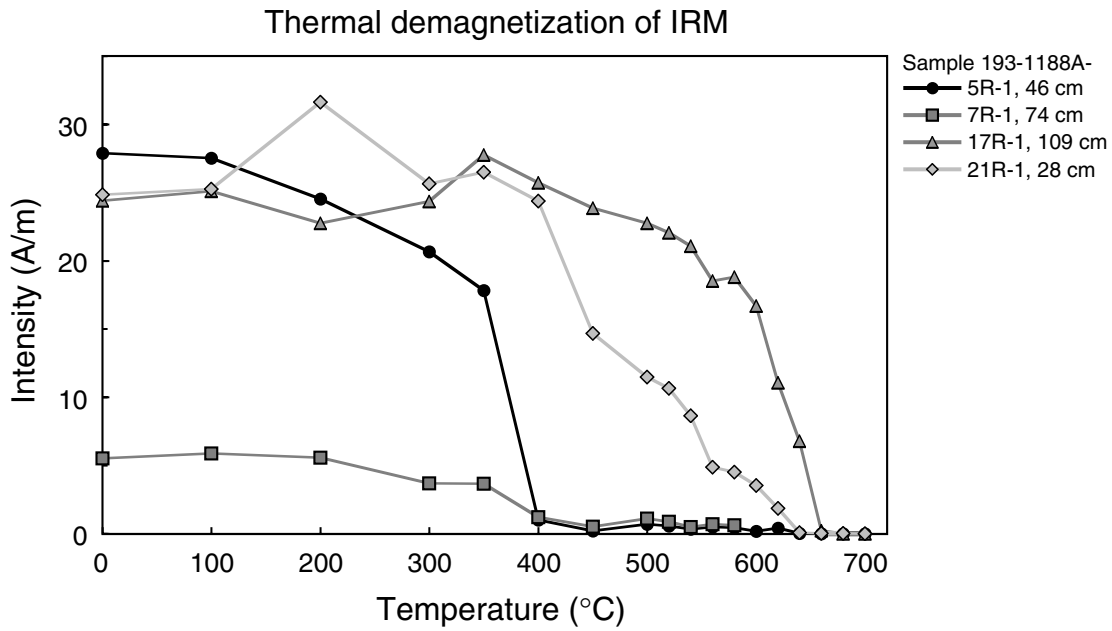


Figure F136. Intensity of isothermal remanent magnetization (IRM) as a function of applied impulse field after thermal demagnetization, Hole 1188A.

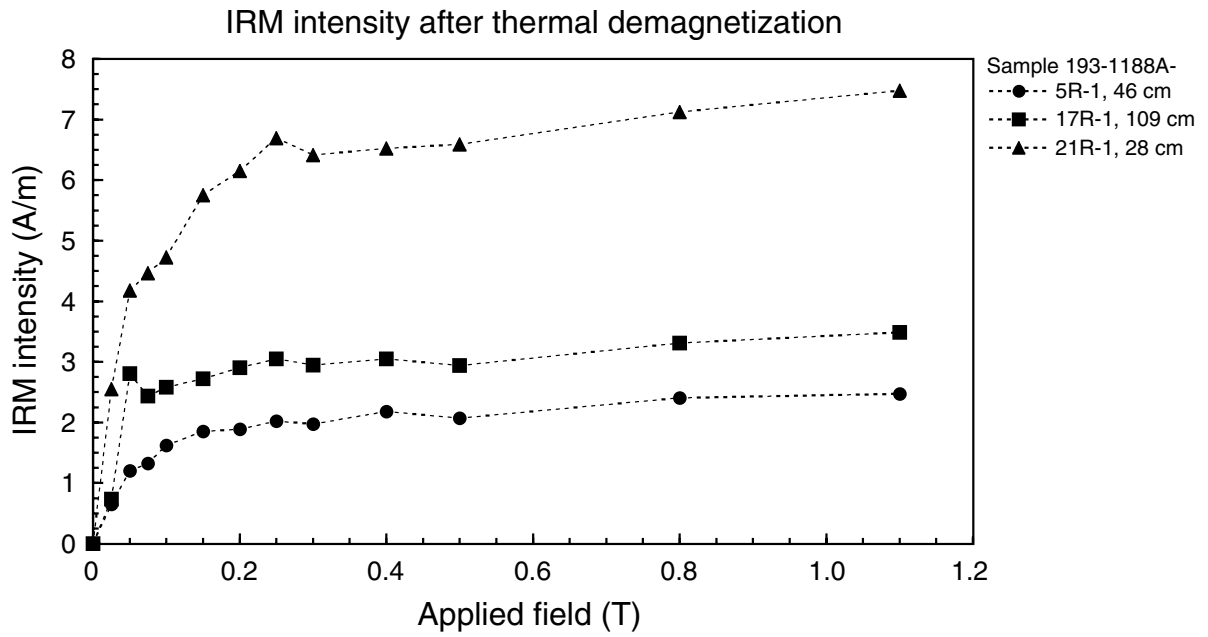


Figure F137. Core barrel temperature tool measurements obtained while drilling Core 193-1188A-4R at the Snowcap hydrothermal site.

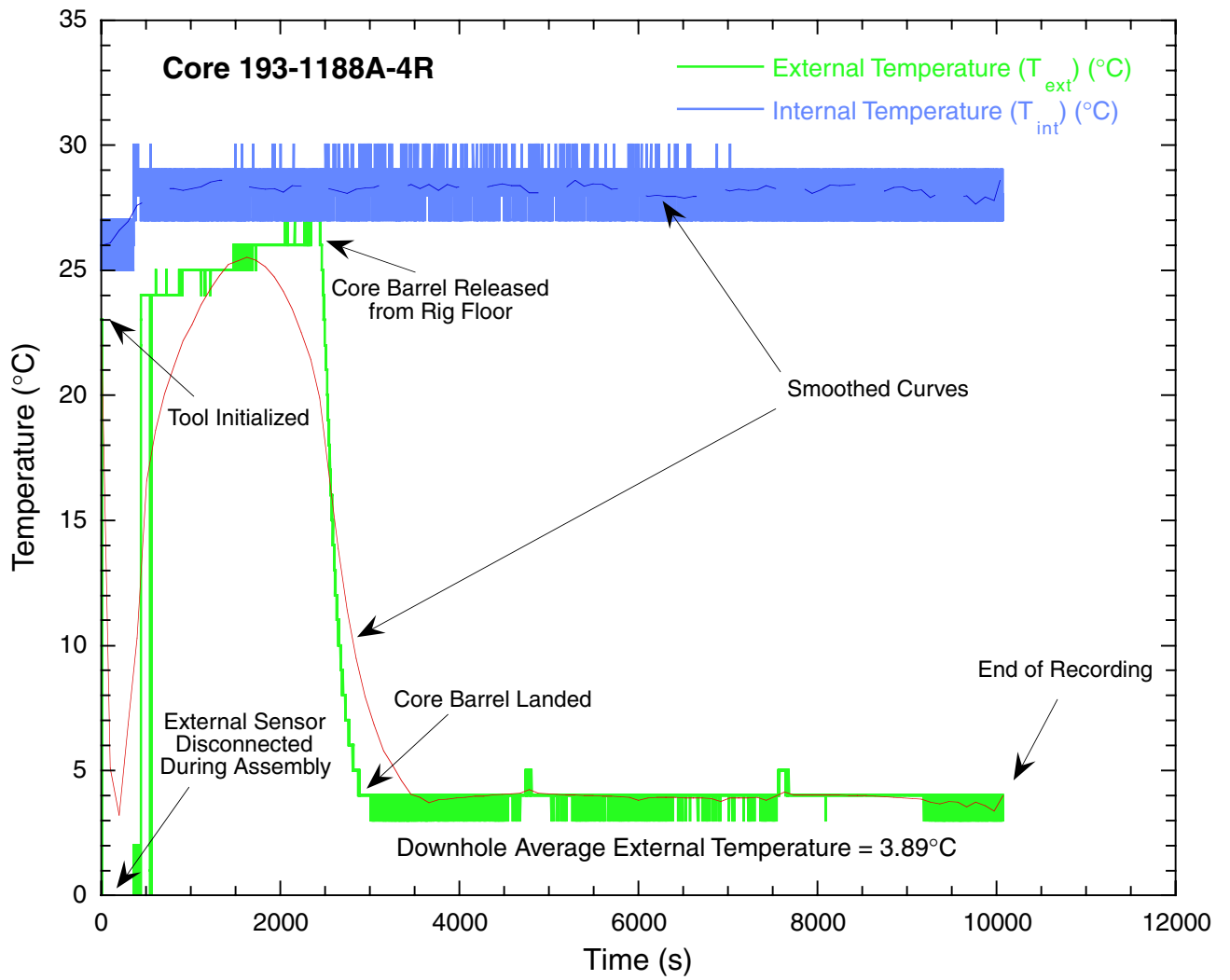


Figure F138. Temperature measurements made in Hole 1188B. A. Measurements recorded with the UHT-MSM on 21 December 2000. The tool was lowered to a depth of 7 mbsf and recorded a maximum temperature of 4.8°C during a 15-min stationary measurement. B. Temperature profile recorded with the WSTP following the deployment of the UHT-MSM in Hole 1188B. The tool recorded a maximum temperature of 5.8°C.

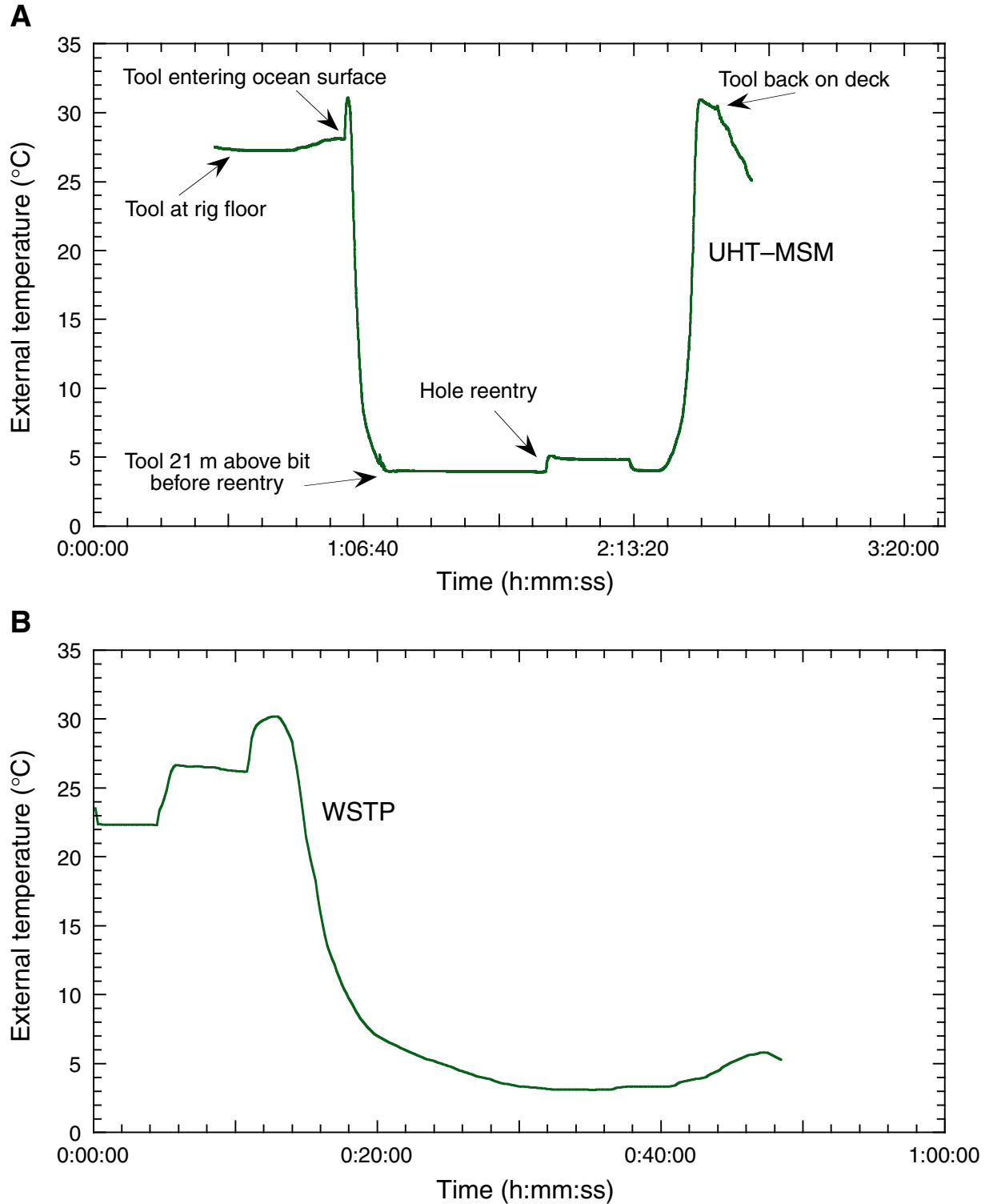


Figure F139. Log curves obtained from the resistivity-at-the-bit (RAB) tool in Hole 1188B. The left panel shows five logs of electrical resistivity with different depths of investigation and vertical resolution. In the middle, the gamma-ray log is displayed. The right plot exhibits the rate of penetration and bit rotation.

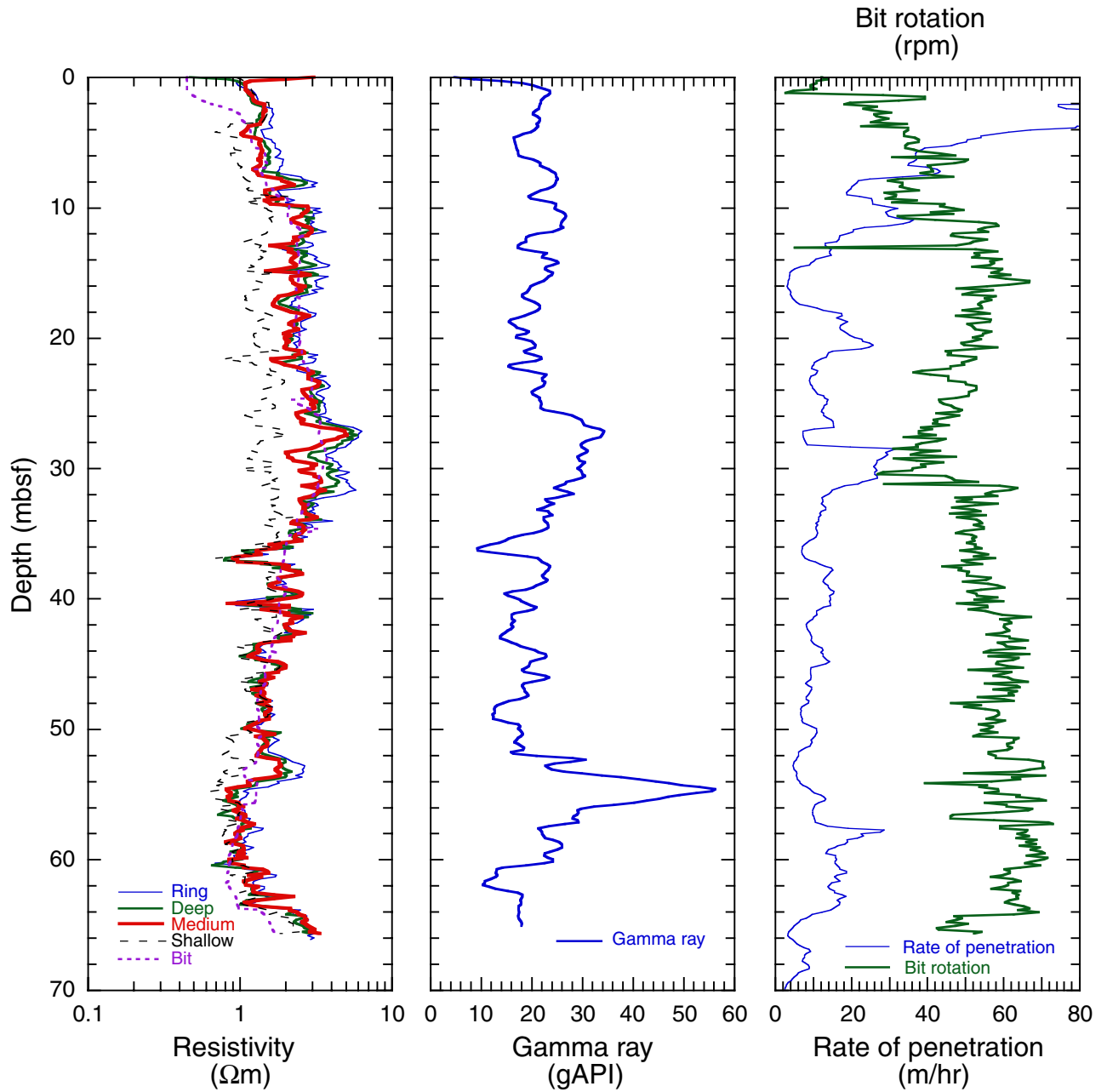


Figure F140. Preliminary interpretation of the logging curves from the resistivity-at-the-bit (RAB) tool in Hole 1188B. The deep electrical resistivity and gamma-ray logs were used to identify 11 logging units that are divided into 31 logging subunits. A comparison to the core lithostratigraphic units identified in Hole 1188A shows a larger degree of detail in structural features and variations in alteration derived from the logs mainly because of the low core recovery in the shallow portions of the Snowcap hydrothermal site.

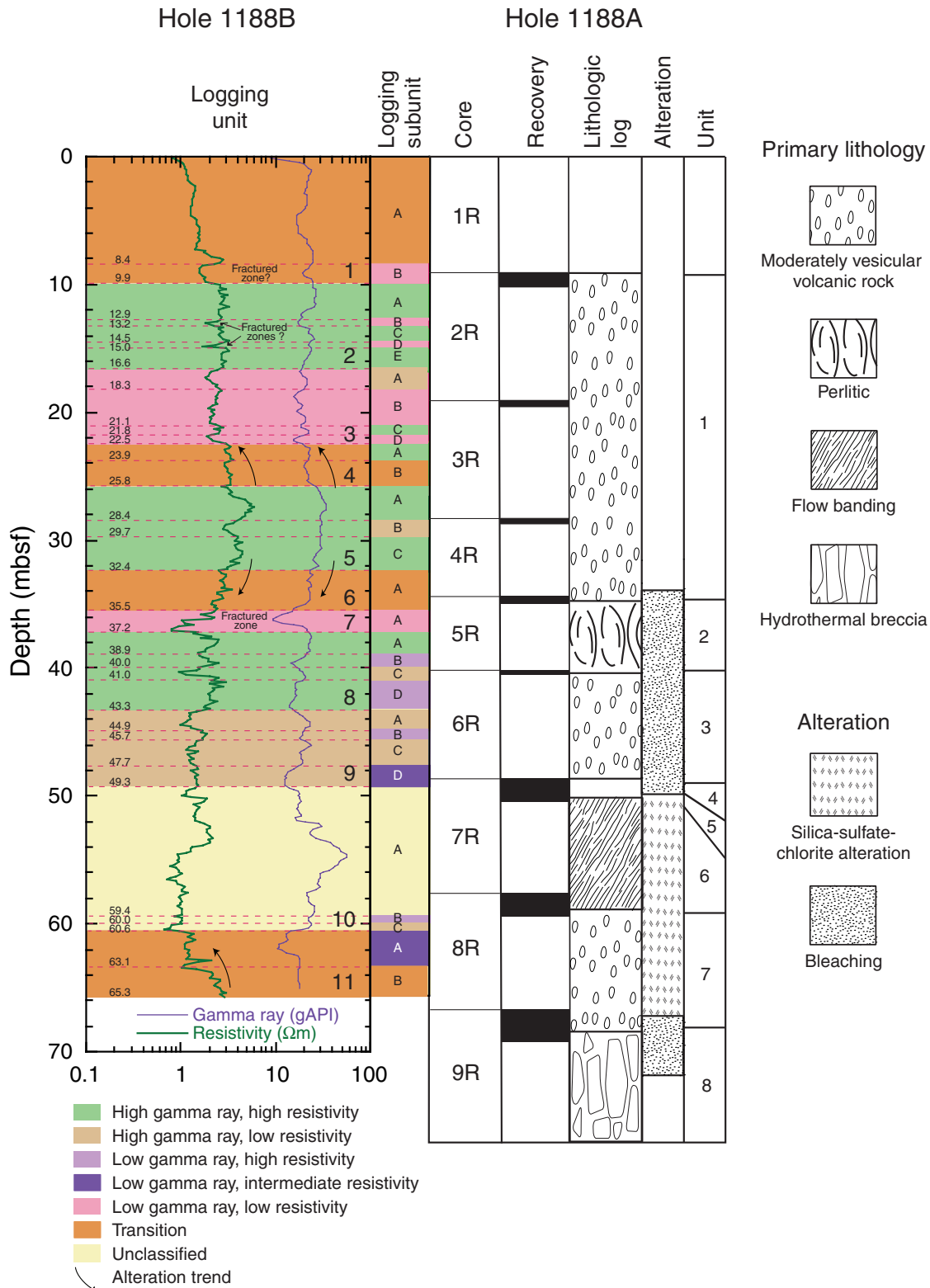


Figure F141. A. Covariation of electrical resistivity vs. gamma ray showing the different logging units displayed in Figure F140, p. 251, with the exception of logging Unit 10. The relationship between resistivity and gamma ray shows a good correlation for most of the logging units in Hole 1188B. B. A similar covariation diagram including data from logging Unit 10, which shows large variability within this 11-m-thick zone.

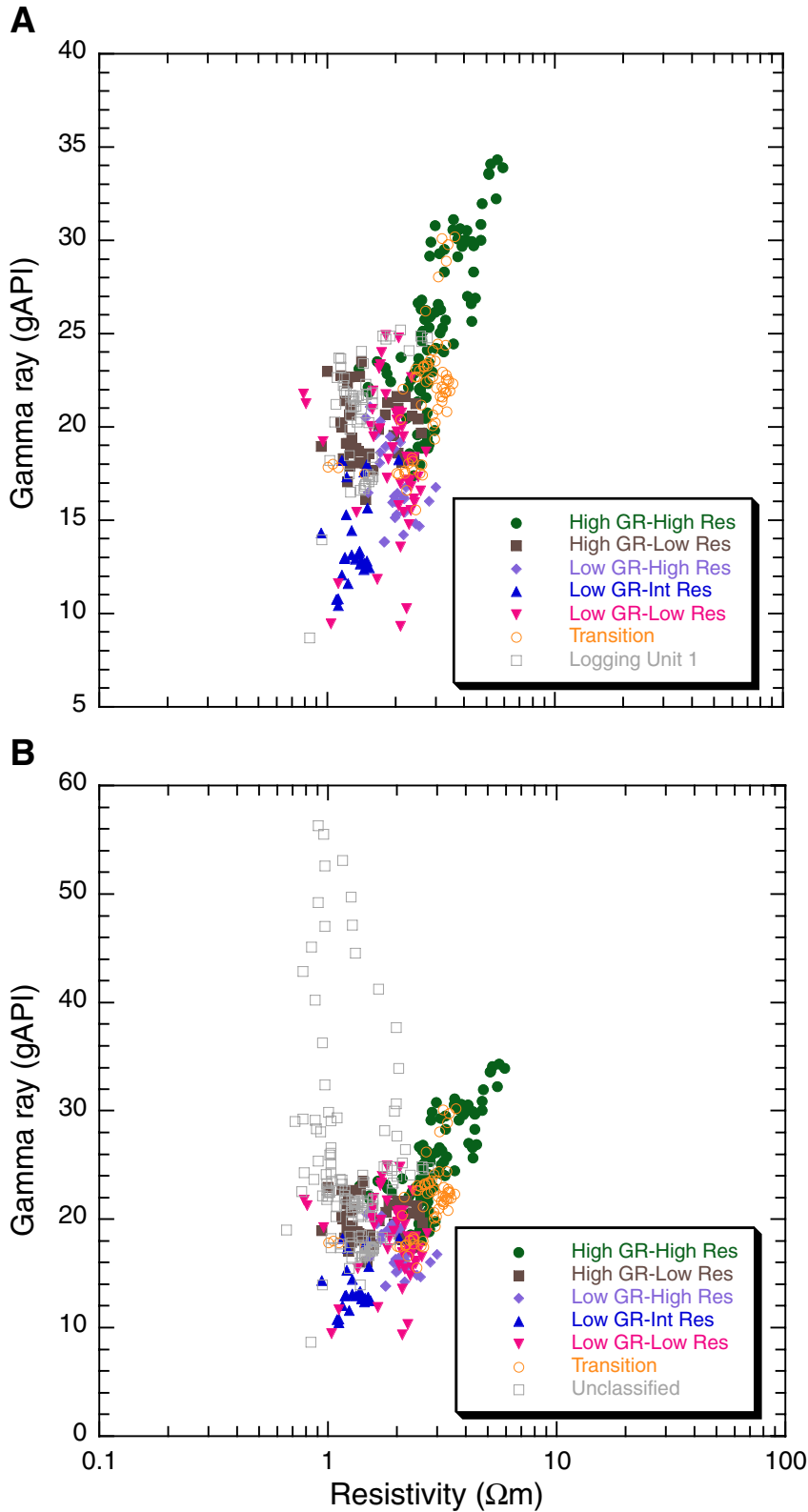


Figure F142. Images of the deep resistivity from the resistivity-at-the-bit (RAB) tool. Light colors correspond to resistive features, dark colors to conductive ones. All images are oriented toward the north. The figure shows three different ways of image processing. The left column shows an image from static processing, using 32 colors. The assignment of colors to resistivity values is valid for the entire hole. The column in the middle gives the result of dynamic processing with 32 colors. The assignment of colors to resistivity is changed within a sliding window. The right column shows the image of the raw data. The green line (low frequency fluctuation) in the static and dynamic column gives the gamma ray. The pink image (high frequency fluctuation) in the static window corresponds to the rotation of the bit, and the blue curve (high frequency fluctuation) in the dynamic image is a resistivity log.

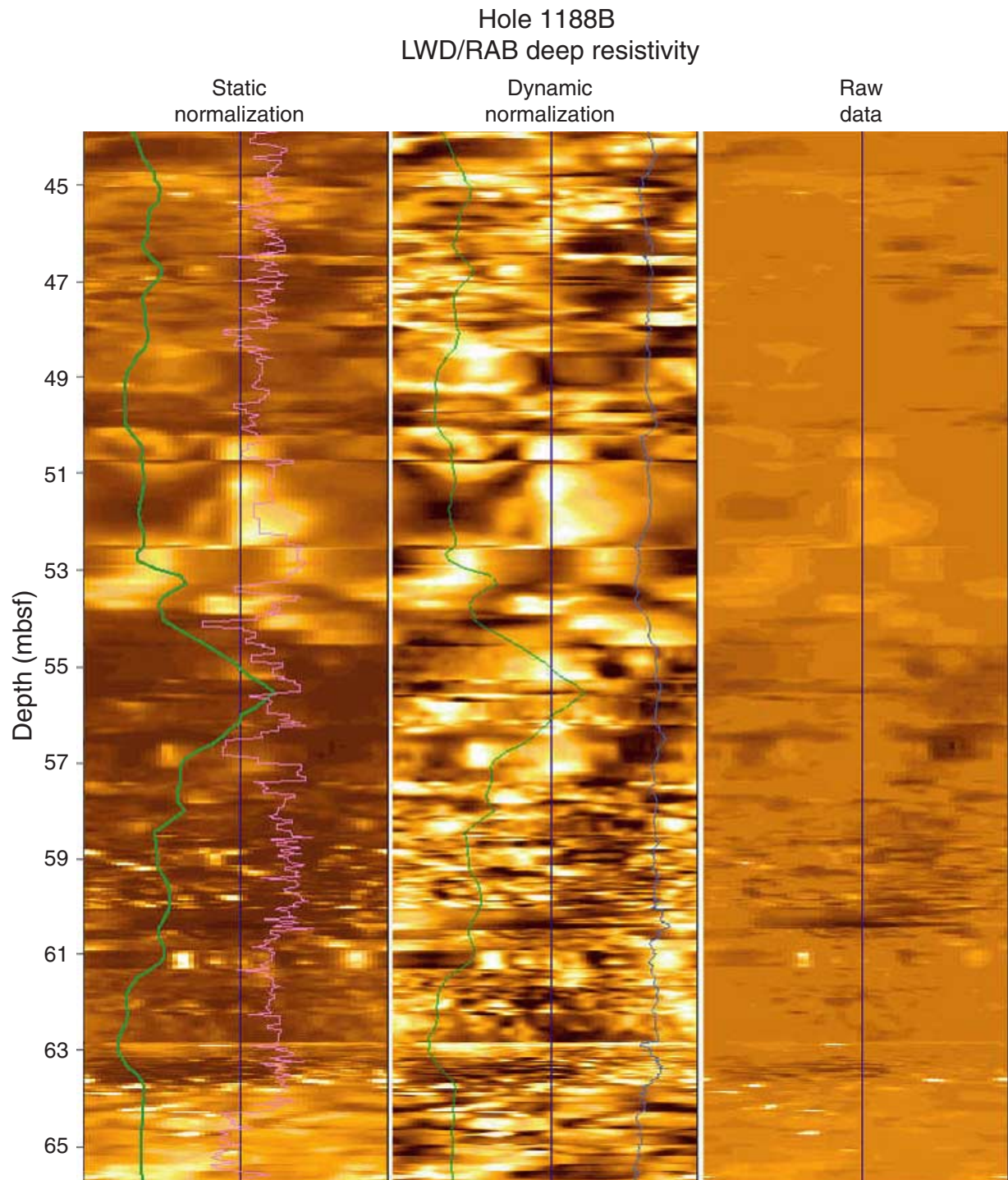


Figure F143. A. Detail image of deep resistivity from Hole 1188B between 18.7 and 32 mbsf using a static normalization technique and 32 colors. B, C. Panels showing the same depth interval displayed in three dimensions, but in two different orientations.

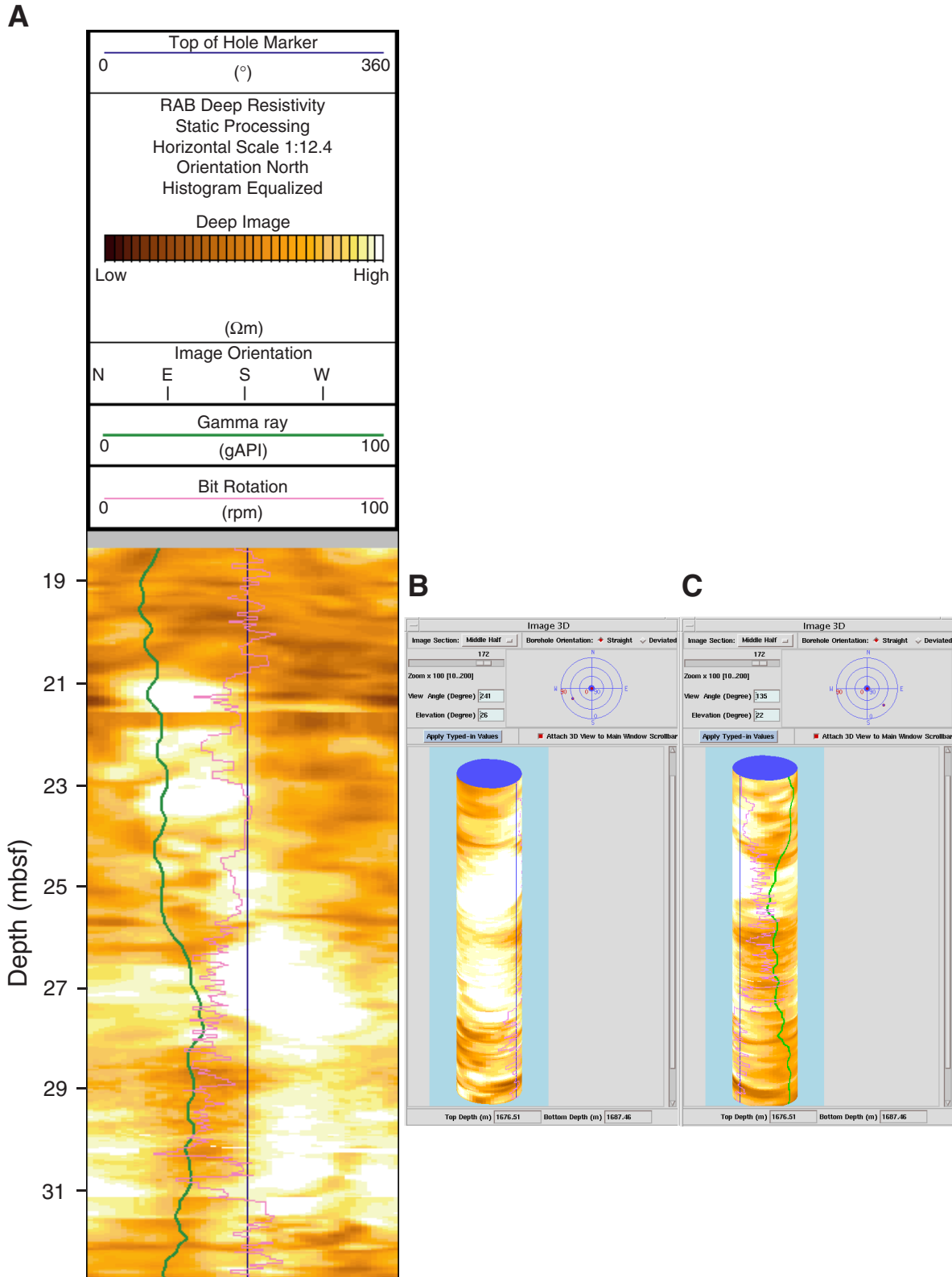


Figure F144. Heave measurements recorded with the guideline tensionometer encoder during the second (MTEM-HNGS-APS-HLDS) and third (MTEM-NGT-DSI-FMS) wireline run in Hole 1188F. Heave was very low during logging operations, averaging <0.3 m during the second and <1.0 m during the third run.

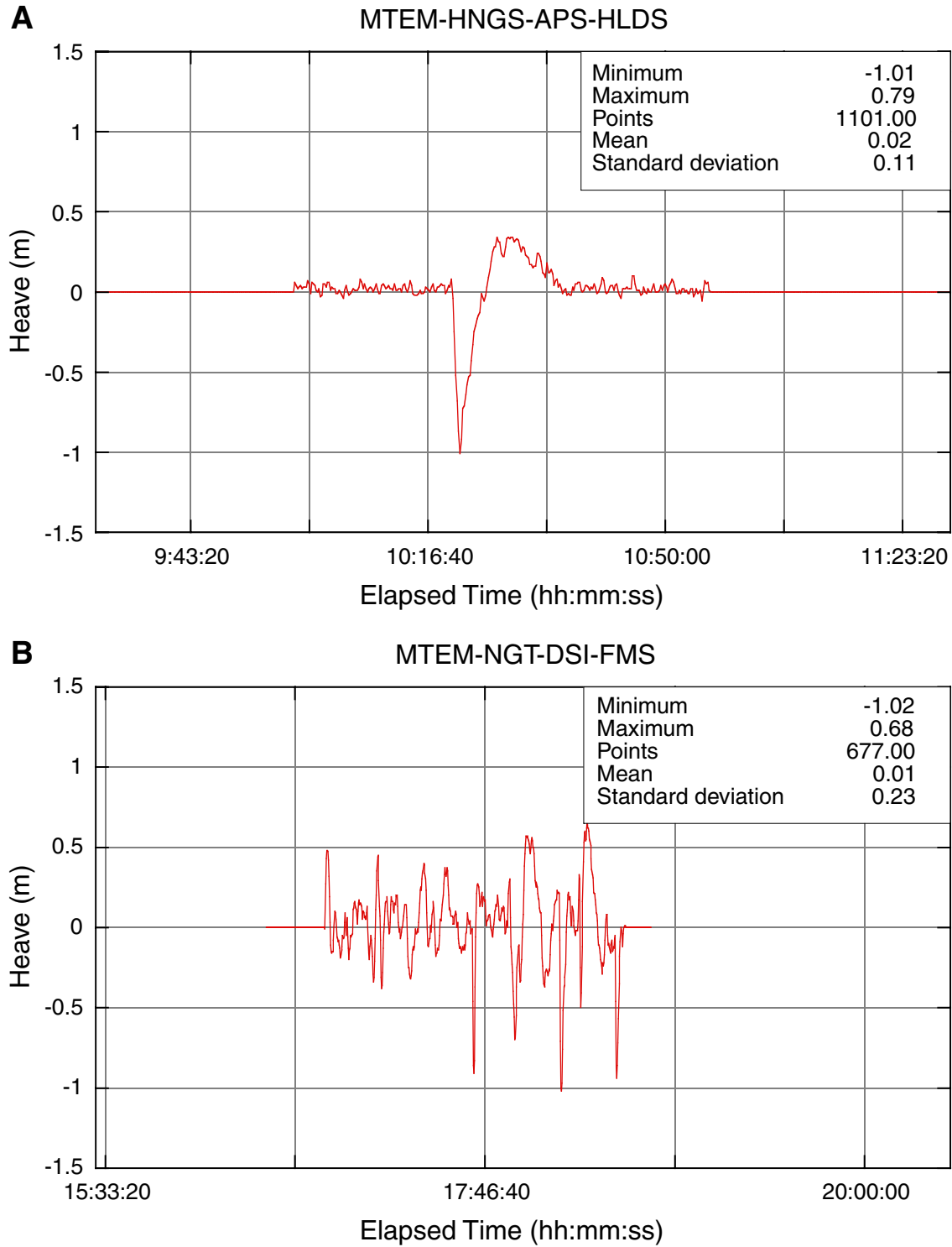


Figure F145. Overview of the wireline logs from Hole 1188F. For better displaying purposes of the lower intervals, the total gamma-ray log is cut off at 100 gAPI, the uranium at 10 ppm, and photoelectric factor log at 5 barn/e⁻. A total of 11 logging units were identified from the downhole measurements.

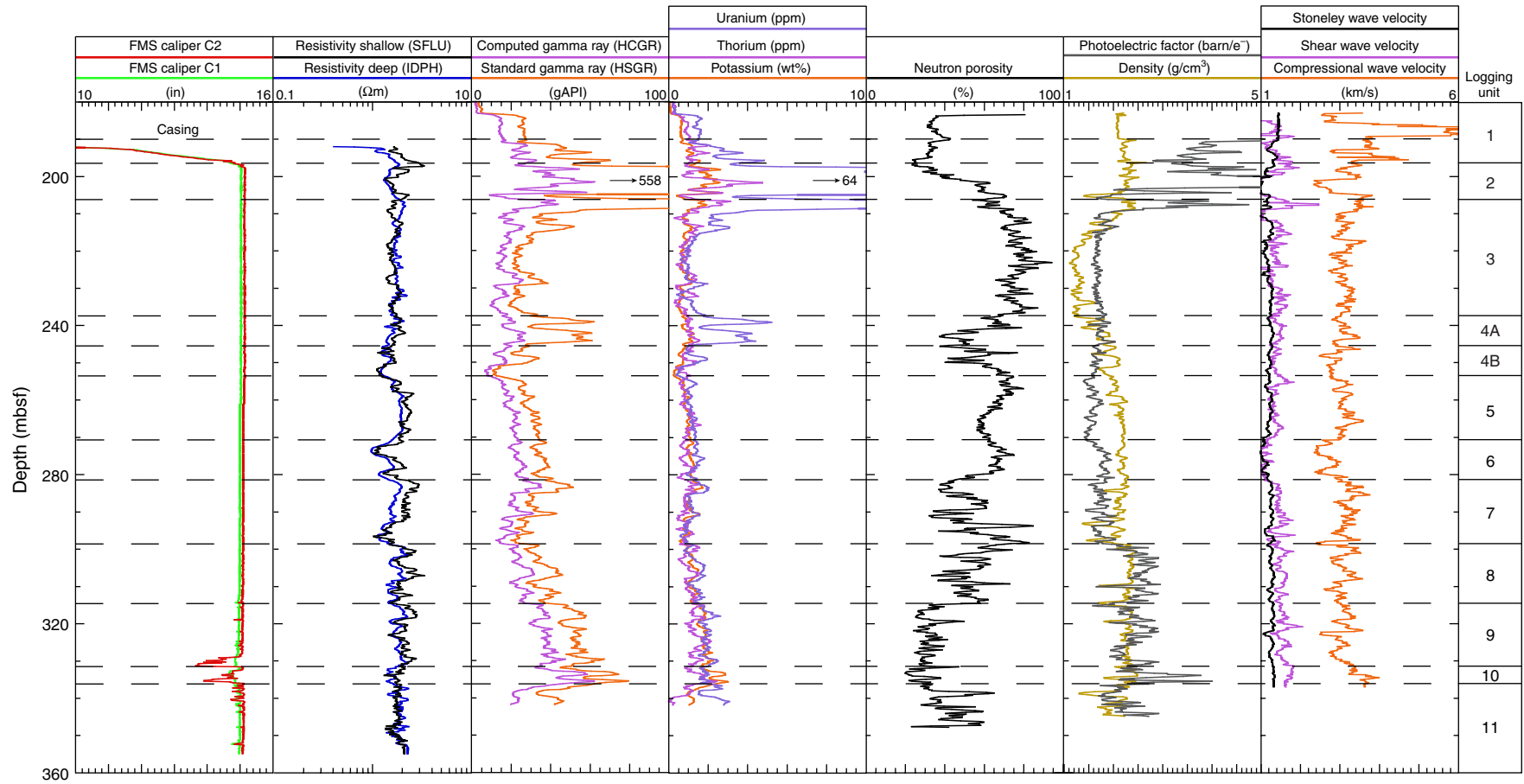


Figure F146. Temperatures recorded in Hole 1188F during wireline logging operations and with the UHT-MSM temperature probe. Temperatures measured during wireline operations on 21 and 22 December 2000 show the immediate postdrilling disturbance of the temperature gradient with a maximum recorded at 99.6°C. Measurements with the UHT-MSM 4 and 7 days later show the changes in the temperature field while equilibrating. The maximum recorded temperature was 313°C. The 26 December 2000 measurements obtained with the MTEM sensor are lower toward the bottom of the hole because of the tool failure at high temperatures.

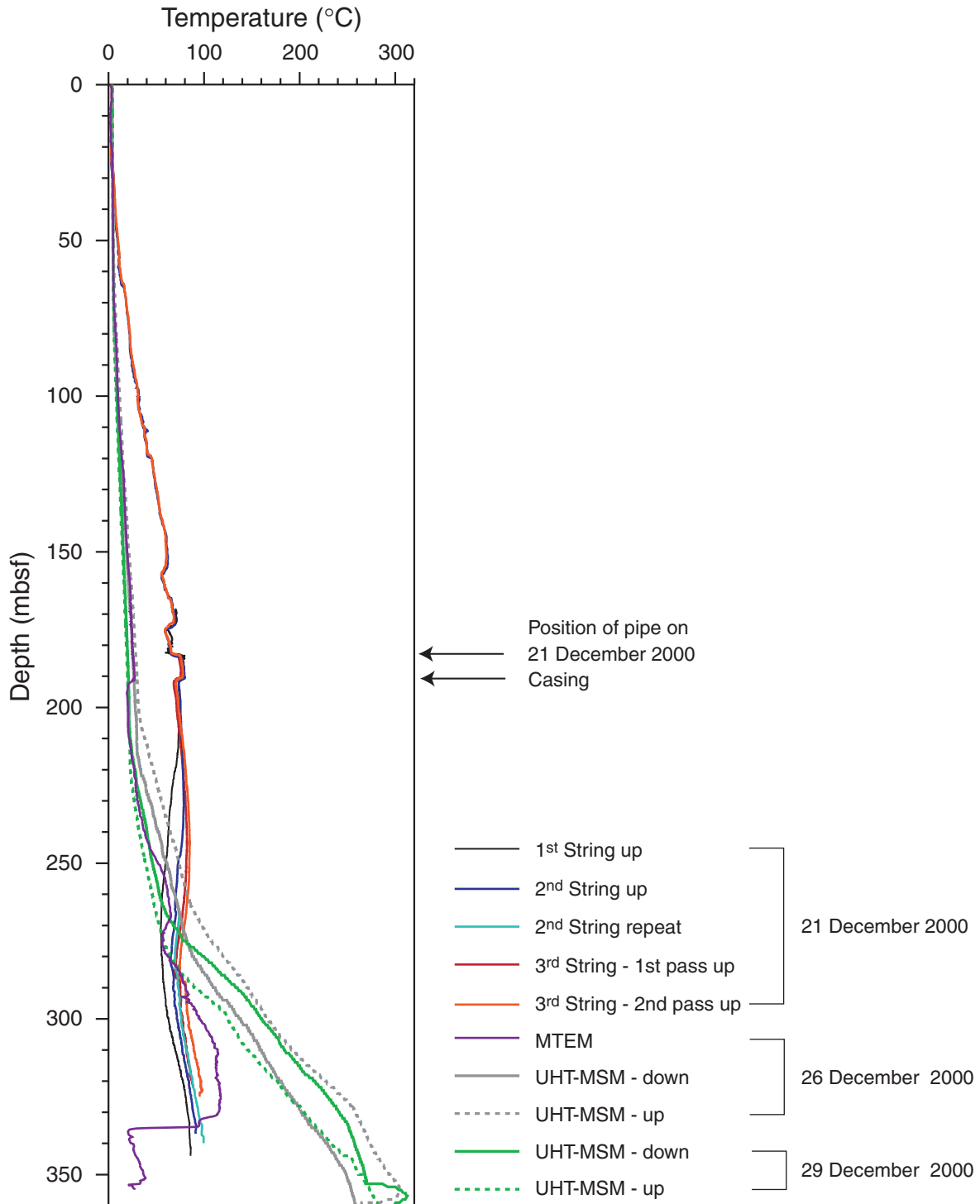


Figure F147. Temperatures recorded in Hole 1188F during deployment of the WSTP. A. The WSTP was lowered to a depth of 107 mbsf on 26 December 2000. The maximum-recorded temperature was 12°C. B. During the second WSTP deployment, the tool was lowered to a depth of 207 mbsf, where it measured a maximum temperature of 20°C.

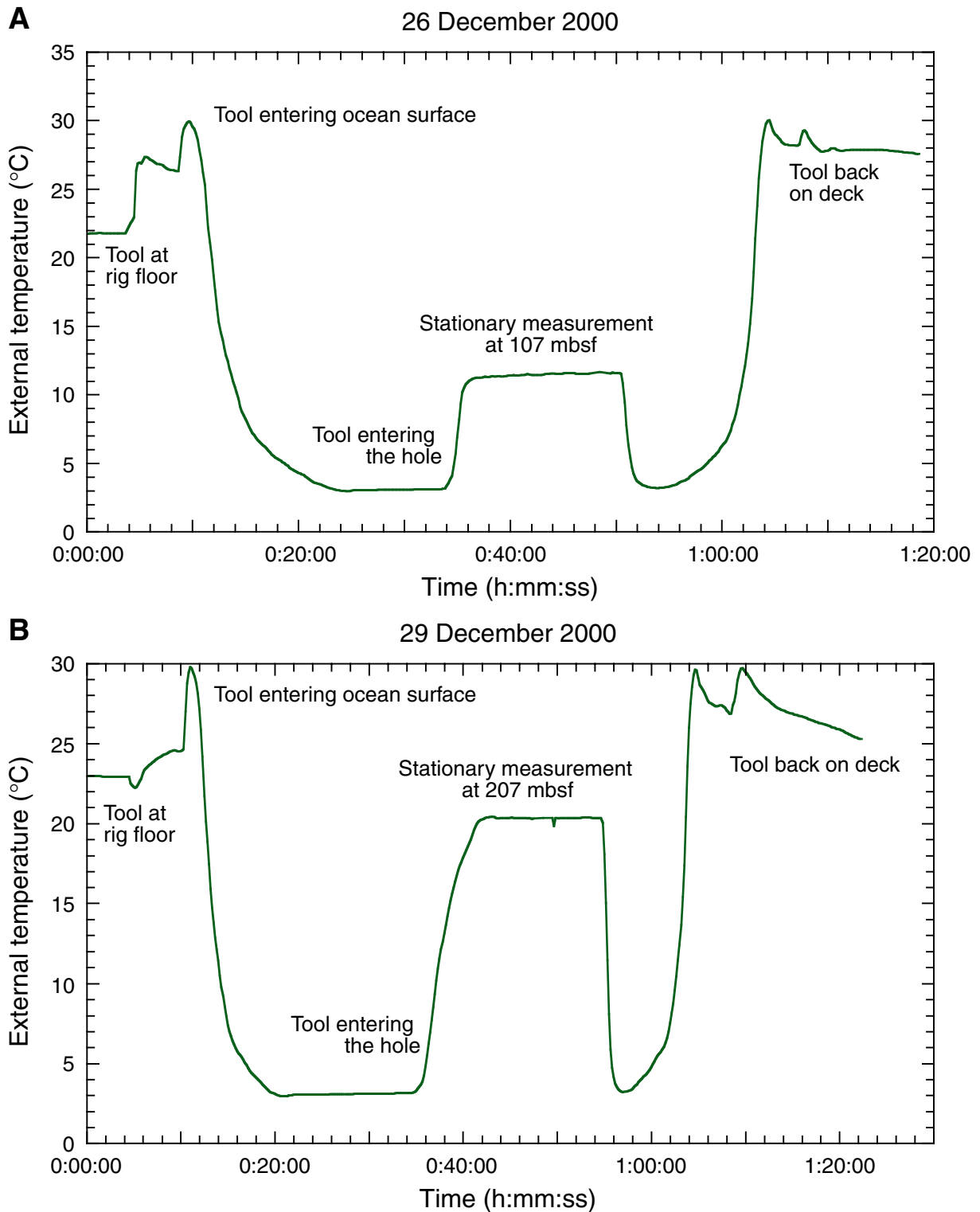


Figure F148. FMS images showing a 19-m interval immediately below the 10.75-in casing shoe in Hole 1188F. The cement extends for 3 m below the casing shoe. Below this depth, high fracture density and brecciated zones are displayed as well as an enlarged section of the borehole. The leftmost four strips were statically normalized; whereas, the four panels on the right represent a dynamic normalization.

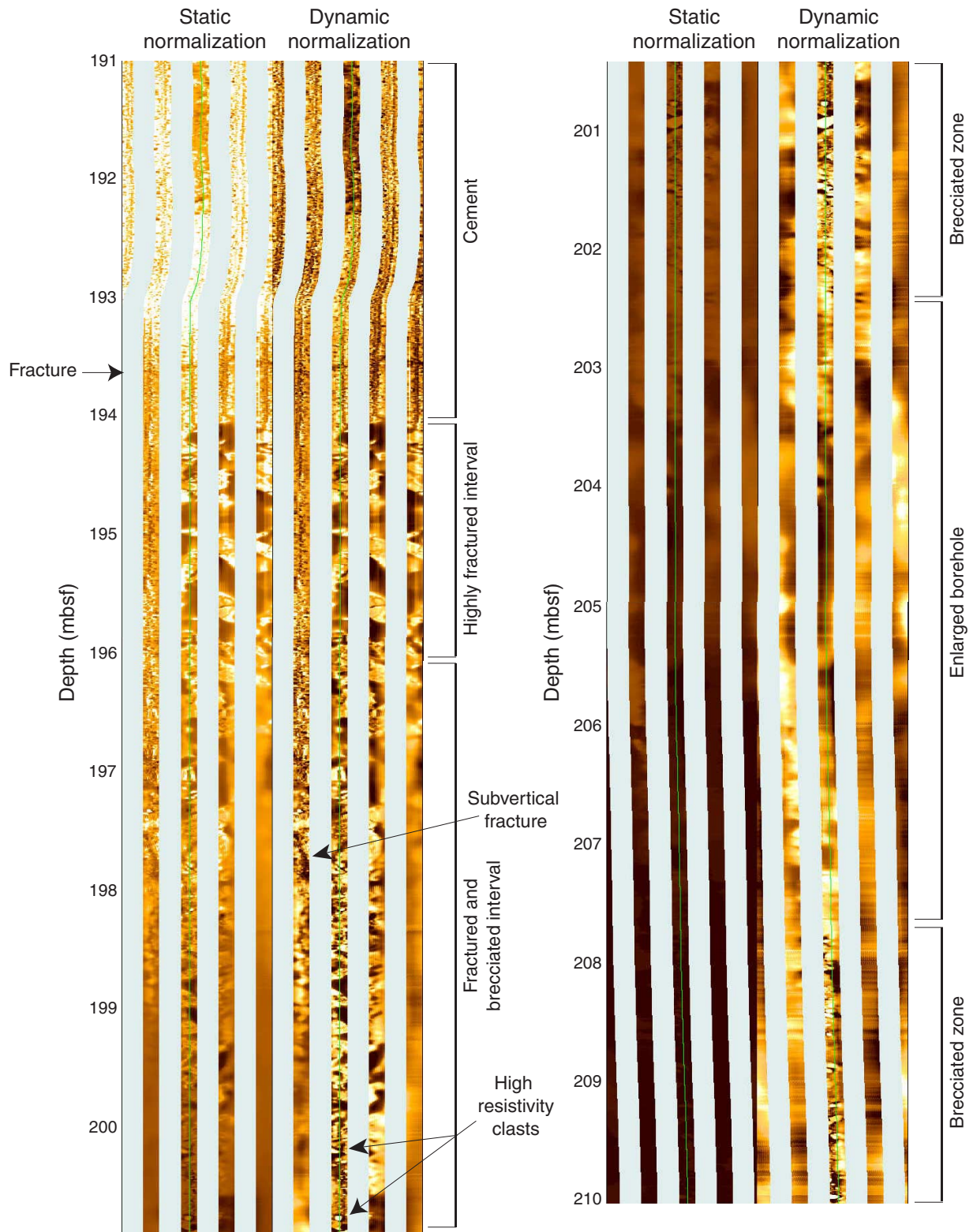


Figure F149. An FMS section of Hole 1188F showing numerous fracture patterns and brecciation within logging Unit 6.

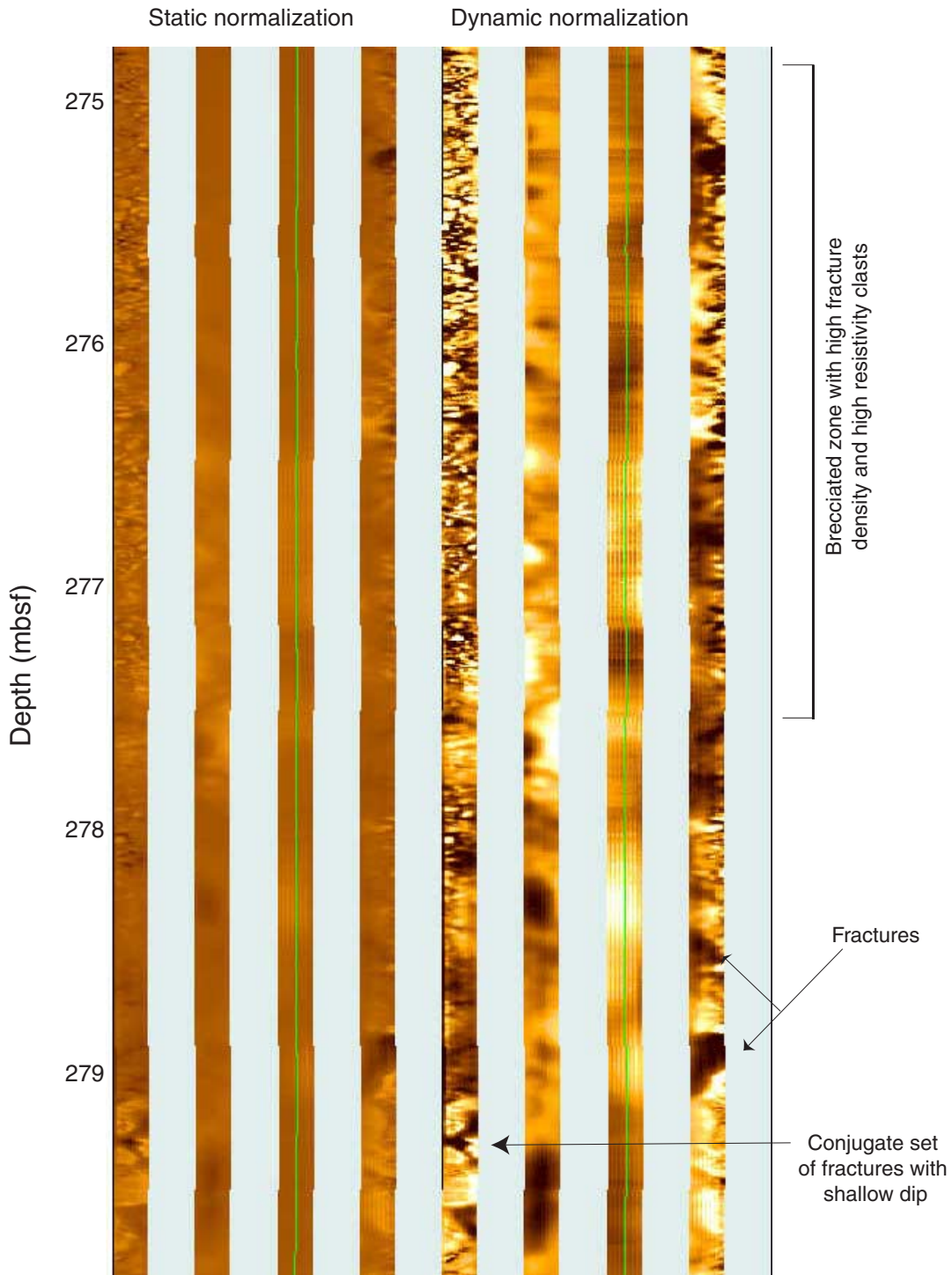


Figure F150. The bottommost part of the Hole 1188F showing the best FMS images of the entire logged interval. Mostly, fracture patterns have a horizontal to subhorizontal orientation and the degree of brecciation is lower than in shallower sections.

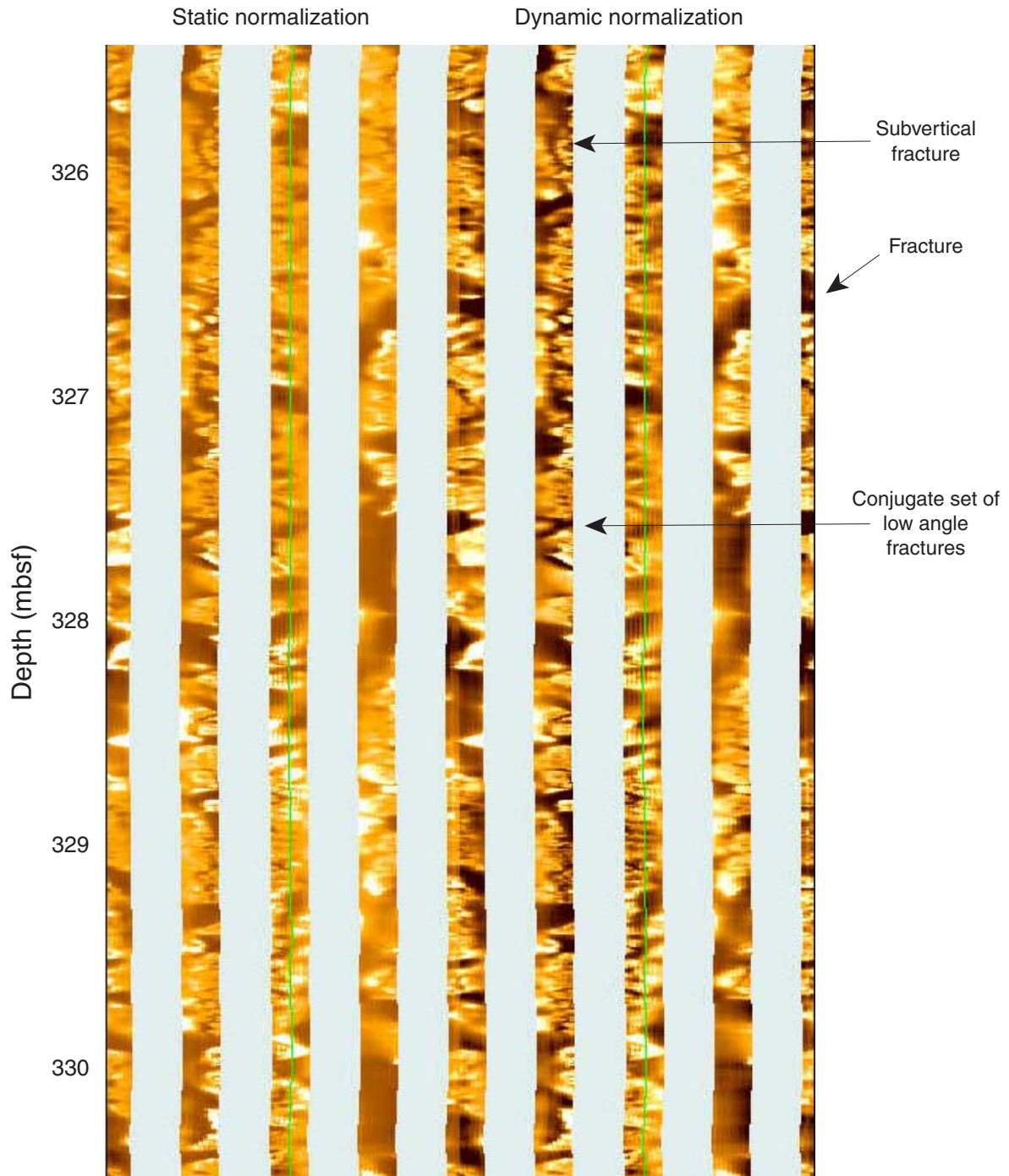


Table T1. Coring summary, Site 1188. (See table notes. Continued on next two pages.)

Hole 1188A

Latitude: 3°43.6962'S
Longitude: 151°40.1964'E
Time on site (hr, min): 530, 15
(1730 hr, 18 Nov 2000–0830 hr, 22 Nov 2000;
0530 hr, 25 Nov 2000–1400 hr, 27 Nov 2000;
1100 hr, 29 Nov 2000–0700 hr, 30 Nov 2000;
0700 hr, 30 Nov 2000–1630 hr, 30 Nov 2000;
1630 hr, 30 Nov 2000–0245 hr, 1 Dec 2000;
0245 hr, 1 Dec 2000–2115 hr, 21 Dec 2000;
2115 hr, 21 Dec 2000–0745 hr, 22 Dec 2000;
1700 hr, 26 Dec 2000–1200 hr, 27 Dec 2000;
1515 hr, 29 Dec 2000–0400 hr, 30 Dec 2000)
Time on hole (hr): 87 (1730 hr, 18 Nov 2000–0830 hr, 22 Nov 2000)
Seafloor (drill pipe measurement from rig floor, mbrf): 1651.0
Distance between rig floor and sea level (m): 10.8
Water depth (drill pipe measurement from sea level, m): 1640.2
Total depth (from rig floor, mbrf): 1862.6
Total penetration (mbsf): 211.6
Total length of cored section (m): 211.6
Total core recovered (m): 21.93
Core recovery (%): 10.4
Total number of cores: 23

Hole 1188B

Latitude: 3°43.6962'S
Longitude: 151°40.1981'E
Time on hole (hr, min): 64, 15 (0530 hr, 25 Nov 2000–1400 hr, 27 Nov 2000)
Additional time on hole (hr, min): 10, 50 (2115 hr 21 Dec 2000–0745 hr 22 Dec 2000)
Seafloor (drill pipe measurement from rig floor, mbrf): 1653.0
Distance between rig floor and sea level (m): 10.9
Water depth (drill pipe measurement from sea level, m): 1642.1
Total depth (from rig floor, mbrf): 1725.0
Total penetration (mbsf): 72.0
Comments: LWD and ADCB only; no coring done.

Hole 1188C

Latitude: 3°43.6940'S
Longitude: 151°40.1741'E
Time on hole (hr): 20 (1100 hr, 29 Nov 2000–0700 hr, 30 Nov 2000)
Seafloor (drill pipe measurement from rig floor, mbrf): 1654.0
Distance between rig floor and sea level (m): 10.9
Water depth (drill pipe measurement from sea level, m): 1643.1
Total depth (from rig floor, mbrf): 1698.0
Total penetration (mbsf): 44.0
Total length of cored section (m): 0.0
Total length of drilled intervals (m): 44.0
Comments: No coring done.

Hole 1188D

Latitude: 3°43.6672'S
Longitude: 151°40.1780'E
Time on hole (hr, min): 9, 30 (0700 hr, 30 Nov 2000–1630 hr, 30 Nov 2000)
Seafloor (drill pipe measurement from rig floor, mbrf): 1645.0
Distance between rig floor and sea level (m): 10.9
Water depth (drill pipe measurement from sea level, m): 1634.1
Total depth (from rig floor, mbrf): 1660.0
Total penetration (mbsf): 15.0
Total length of cored section (m): 0.0
Total length of drilled intervals (m): 15.0
Comments: No coring done.

Hole 1188E

Latitude: 3°43.6842'S
Longitude: 151°40.1907'E
Time on hole (hr, min): 10, 15 (1630 hr, 30 Nov 2000–0245 hr, 1 Dec 2000)
Seafloor (drill pipe measurement from rig floor, mbrf): 1652.0
Distance between rig floor and sea level (m): 10.9
Water depth (drill pipe measurement from sea level, m): 1641.1
Total depth (from rig floor, mbrf): 1668.0
Total penetration (mbsf): 16.0
Total length of cored section (m): 0.0
Total length of drilled intervals (m): 16.0

Table T1 (continued).

Comments: No coring done.

Hole 1188F

Latitude: 3°43.6850'S
 Longitude: 151°40.1909'E
 Time on hole (hr, min): 498, 30 (0245 hr, 1 Dec 2000–2115 hr, 21 Dec 2000)
 Additional time on hole (hr, min): 19 (1700 hr, 26 Dec 2000–1200, 27 Dec 2000);
 12, 45 (1515 hr, 29 Dec 2000–0400, 30 Dec 2000)
 Seafloor (drill pipe measurement from rig floor, mbrf): 1653.0
 Distance between rig floor and sea level (m): 11.3
 Water depth (drill pipe measurement from sea level, m): 1641.7
 Total depth (from rig floor, mbrf): 2039.7
 Total penetration (mbsf): 386.7
 Total length of cored section (m): 168.7
 Total length of drilled intervals (m): 218.0
 Total core recovered (m): 30.89
 Core recovery (%): 18.3

Core	Date (2000)	Time (local)	Top depth (mbsf)	Length (m)		Recovery (%)
				Cored	Recovered	
193-1188A-						
1R	19 Nov	1425	0.0	9.6	0.00	0.0
2R	19 Nov	1640	9.6	9.6	0.20	2.1
3R	19 Nov	2025	19.2	9.7	0.10	1.0
4R	19 Nov	2310	28.9	4.7	0.09	1.9
5R	20 Nov	0225	33.6	5.0	0.29	5.8
6R	20 Nov	0350	38.6	9.6	0.07	0.7
7R	20 Nov	0545	48.2	9.7	1.67	17.2
8R	20 Nov	0715	57.9	9.7	1.87	19.3
9R	20 Nov	0835	67.6	9.7	2.60	26.8
10R	20 Nov	1055	77.3	9.6	1.69	17.6
11R	20 Nov	1300	86.9	9.7	1.72	17.7
12R	20 Nov	1505	96.6	9.7	1.64	16.9
13R	20 Nov	1630	106.3	9.7	1.14	11.8
14R	20 Nov	1915	116.0	9.7	1.13	11.6
15R	20 Nov	2210	125.7	9.7	0.80	8.2
16R	21 Nov	0010	135.4	9.7	1.96	20.2
17R	21 Nov	0220	145.1	9.6	1.07	11.1
18R	21 Nov	0400	154.7	9.6	0.75	7.8
19R	21 Nov	0515	164.3	9.6	0.69	7.2
20R	21 Nov	0615	173.9	9.2	0.93	10.1
21R	21 Nov	0710	183.1	9.6	1.23	12.8
22R	21 Nov	0805	192.7	9.4	0.11	1.2
23R	21 Nov	0930	202.1	9.5	0.18	1.9
193-1188B-						
1O	26 Nov	0500	0.0	0.0	0.00	NA
1Z	27 Nov	0940	72.0	0.0	0.15	0.0
193-1188C-						
1O	30 Nov	0530	0.0	0.0	0.00	NA
193-1188D-						
1O	30 Nov	1400	0.0	0.0	0.00	NA
193-1188E-						
1O	1 Dec	0230	0.0	0.0	0.00	NA
193-1188F-						
1Z	12 Dec	2020	218.0	3.5	2.50	71.4
2Z	12 Dec	2250	221.5	1.1	0.75	68.2
3Z	13 Dec	0145	222.6	2.5	2.15	86.0
4Z	13 Dec	0530	225.1	3.3	0.00	0.0
5Z	13 Dec	1130	228.4	4.7	0.00	0.0
6Z	13 Dec	1425	233.1	1.9	1.55	81.6
7Z	13 Dec	1720	235.0	1.2	1.05	87.5
8Z	13 Dec	1945	236.2	1.5	0.95	63.3
9Z	13 Dec	2130	237.7	0.6	0.55	91.7
10Z	13 Dec	2315	238.3	0.6	0.00	0.0
11G	13 Dec	0000	238.9	0.0	0.00	NA
12Z	14 Dec	0615	238.9	2.5	0.00	0.0
13Z	14 Dec	0905	241.4	4.5	1.10	24.4
14Z	14 Dec	1140	245.9	4.5	1.10	24.4
15Z	14 Dec	1400	250.4	4.5	0.95	21.1

Table T1 (continued).

Core	Date (2000)	Time (local)	Top depth (mbsf)	Length (m)		Recovery (%)
				Cored	Recovered	
16Z	14 Dec	1635	254.9	4.5	0.65	14.4
17Z	14 Dec	1900	259.4	4.5	0.11	2.4
18Z	14 Dec	2145	263.9	4.5	0.20	4.4
19Z	15 Dec	0025	268.4	4.5	0.32	7.1
20Z	15 Dec	0225	272.9	4.7	0.00	0.0
21Z	15 Dec	0500	277.6	4.5	0.00	0.0
22Z	15 Dec	0730	282.1	4.5	0.40	8.9
23Z	15 Dec	1020	286.6	4.5	1.20	26.7
24Z	15 Dec	1300	291.1	4.5	0.00	0.0
25Z	15 Dec	1555	295.6	4.5	0.30	6.7
26Z	15 Dec	1940	300.1	4.5	2.10	46.7
27Z	15 Dec	2220	304.6	4.5	0.31	6.9
28Z	16 Dec	0145	309.1	4.5	0.00	0.0
29Z	16 Dec	0445	313.6	4.5	0.00	0.0
30Z	16 Dec	0725	318.1	4.5	0.10	2.2
31Z	16 Dec	1030	322.6	4.6	0.30	6.5
32Z	18 Dec	0635	327.2	4.7	0.00	0.0
33Z	18 Dec	1010	331.9	4.5	0.00	0.0
34Z	18 Dec	1245	336.4	3.6	1.20	33.3
35Z	18 Dec	1650	340.0	4.5	0.85	18.9
36G	18 Dec	2130	344.5	0.0	0.00	NA
37Z	18 Dec	2340	344.5	4.5	2.61	58.0
38Z	19 Dec	0255	349.0	4.5	2.15	47.8
39Z	19 Dec	0815	353.5	4.5	1.00	22.2
40Z	19 Dec	1045	358.0	4.5	1.15	25.6
41Z	19 Dec	1310	362.5	4.5	0.75	16.7
42Z	19 Dec	1540	367.0	4.5	0.75	16.7
43Z	19 Dec	1845	371.5	2.5	0.99	39.6
44Z	19 Dec	2215	374.0	4.5	0.80	17.8
45Z	20 Dec	0245	378.5	4.5	0.00	0.0
46Z	20 Dec	0645	383.0	2.6	0.00	0.0
47Z	20 Dec	1045	385.6	1.1	0.00	0.0

Notes: LWD = logging while drilling, ADCB = advanced diamond core barrel.
 NA = not applicable.

Table T2. Lithology and alteration of Units 1 to 26, Hole 1188A. (See table note. Continued on next three pages.)

Unit	Core, section (Piece)	Curated depth (mbsf)		Curated length (m)	Lithology	Alteration
		Top	Base			
1	193-1188A-					
	2R-1 (All)	9.60	9.85	0.25	Moderately vesicular rhyodacite with scattered acicular plagioclase phenocrysts (as long as 10 mm) and clinopyroxene (as long as 0.1 mm).	Fresh unit. Patchy sulfate clay and Fe oxide films coat fracture surfaces and vesicles. Rare hairline sulfate veinlets. Trace pyrite is present as fine euhedra on films in vesicles and on fractures.
	3R-1 (All)	19.20	19.38	0.18		
	4R-1 (All)	28.90	29.03	0.13		
	5R-1 (1-6)	33.60	33.95	0.35		
	6R-1 (2)	38.67	38.73	0.06		
7R-1 (1-3)	48.20	48.35	0.15			
2	5R-1 (7-8)	33.95	34.08	0.13	Completely altered aphyric volcanic unit with remnant perlitic texture, cut by fine silica veinlets (pseudoclastic texture).	Strongly bleached, silicified (hard) gray unit. Silica veinlets give pseudoclastic texture. Trace disseminated pyrite. XRD mineralogy: opaline silica dominant, minor smectite, illite, plagioclase, and pyrite.
3	6R-1 (1, 3)	38.60	38.80	0.20	Moderately to highly altered, moderately vesicular aphyric dacite(?).	Weak bleaching. Pervasive, moderate intensity alteration. Anhydrite (+ pyrite) lines vesicles. Mineralogy otherwise unknown, but volcanic glass is pervasively replaced.
	7R-1 (4-5)	48.35	48.43	0.08		
4	7R-1 (6-16A)	48.43	49.26	0.83	Completely altered aphyric, sparsely vesicular dacite with intervals of flow banding (Pieces 6 and 14) and an interval of hydrofractured breccia (Piece 8).	Intense bleaching (silica-sulfate-clay alteration) with weakly developed patchy silicification. Medium- to coarse-grained irregular anhydrite-pyrite veins, which form the matrix in the fractured breccia. Anhydrite-pyrite vesicle fill, trace honey gold sphalerite noted in Pieces 11 and 15. XRD mineralogy: cristobalite and anhydrite dominant, minor pyrite and chlorite, trace kaolinite and hematite. Remnant igneous plagioclase also detected.
5	7R-1 (16B-20)	49.26	49.70	0.44	Completely altered hydrofractured volcanic rock with a pseudoclastic texture. Fragments show remnant perlitic texture, which is pseudomorphed by the alteration assemblage.	Greenish gray alteration (silica-sulfate-chloritic clay), grading to gray-blue silica-sulfate-clay bleaching at the base of the unit (Sections 193-1188A-7R-1 [Pieces 19 and 20] and 7R-2 [Piece 1]). Remnant volcanic texture (perlitic?) replaced by silica and rimmed by chloritic clay. Fragments hosted in a stockwork matrix of anhydrite-(silica-pyrite) with white sulfate alteration halos bleaching the clayey rims of many fragments. In the gray-blue portion of the unit, fragments are dominantly sulfate-bluish clay and are again hosted in an anhydrite-pyrite stockwork. Silica is present as late drusy vug fills, with trace pyrite. XRD mineralogy: anhydrite and cristobalite dominant, minor pyrite and chlorite (upper green-gray portion); anhydrite dominant, minor cristobalite, pyrophyllite, and pyrite, and trace quartz (lower bluish portion).
	7R-2 (1)	49.70	49.96	0.26		
6	7R-2 (2-6)	49.96	50.56	0.60	Completely altered fractured volcanic rock with a pseudoclastic texture. Core 193-1188A-8R-1 (Piece 1) is moderately bleached and unaltered dacite and Core 193-1188A-8R-1 (Pieces 2 and 3) (which match the lower portion of the overlying unit) are interpreted to be fragments that have fallen down the hole.	Greenish gray (silica-sulfate-chloritic clay) to gray-blue (silica-sulfate-clay) altered fragments hosted in a stockwork matrix of anhydrite-(silica-pyrite) veins with white sulfate alteration halos bleaching the clayey rims of many fragments. Fine-grained pyrite appears to be disseminated in many of the fragments, but on close examination seems more likely to be associated with fine silica veinlets as well as siliceous replaced flow bands. Scattered, 1- to 5-cm-wide, slightly nebulous, late anhydrite-silica veins cut and bleach sections of the stockwork and host minor pyrite and trace honey gold sphalerite. XRD mineralogy: anhydrite and cristobalite dominant, minor quartz, illite, pyrite, and traces of barite.
	8R-1 (1-11)	57.90	59.30	1.40		

Table T2 (continued).

Unit	Core, section (Piece)	Curated depth (mbsf)		Curated length (m)	Lithology	Alteration
		Top	Base			
7	193-1188A- 8R-1 (12-13)	59.30	59.40	0.10	Completely bleached sparsely to moderately vesicular volcanic rock with patches of silicification.	Bleached (silica-sulfate-clay altered) unit. Variation in color from pure white to medium gray may reflect silica abundance and is probably related to fluid-bearing fractures with zoned alteration halos. Vesicles are lined by anhydrite, with minor pyrite in the upper part of the unit, and silica filled farther down. XRD mineralogy: cristobalite and anhydrite dominant, minor quartz, illite, pyrophyllite, and pyrite, and traces of barite. Quartz is a major component at the base of the interval (= silica vesicle fill).
	8R-2 (1-9)	59.40	60.13	0.73		
	9R-1 (1-6)	67.60	68.13	0.53		
8	9R-1 (7-10)	68.13	69.10	0.97	Completely altered hydrofractured volcanic rock with a pseudoclastic texture. Fragments show remnant perlitic texture, which is pseudomorphed by the alteration assemblage.	Strongly bleached (silica-sulfate-clay altered) fractured unit, cut by a fine anastomosing network of anhydrite and silica-pyrite veinlets. Appears to be a more pervasively bleached equivalent to Unit 5. Pyrite is present as late vesicle and vug fill and as fine disseminations, particularly in more siliceous portions of the unit. XRD mineralogy (from an intensely bleached portion of the unit): quartz and cristobalite dominant, minor pyrophyllite and anhydrite, and traces of pyrite and barite.
	9R-2 (1-9)	69.10	70.51	1.41		
	9R-3 (1-2)	70.51	70.85	0.34		
	10R-1 (1-8)	77.30	78.15	0.85		
9	10R-1 (9-14)	78.15	78.78	0.63	Completely bleached sparsely vesicular volcanic rock with patches of silicification. This unit is nearly indistinguishable in hand specimen from Unit 7.	Bleached (silica-sulfate-clay altered) unit. Variation in color from pure white to medium gray seems to reflect silica abundance and is probably related to fluid-bearing fractures with zoned alteration halos. Vesicles are filled with silica and pyrite (dominantly) and less commonly by anhydrite. Pyrite is also associated with the zoned halos and is finely disseminated throughout the rock. XRD mineralogy: cristobalite, plagioclase (?? in a strongly leached rock), and quartz dominant, minor pyrite and anhydrite, and traces of barite.
	10R-2 (1-13)	78.78	79.66	0.88		
	11R-1 (1-10)	86.90	88.28	1.38		
	11R-2 (1-7)	88.28	89.23	0.95		
	12R-1 (1-3)	96.60	96.99	0.39		
10	13R-1 (1)	106.00	106.36	0.06	Completely altered, fractured, frequently perlitic, and flow-banded volcanic rock. Flow banding defined in part by microspherulitic bands and entirely devitrified bands.	Early pervasive gray-green silica-sulfate-chlorite alteration of the volcanic fabric, with later fracturing and pervasive flooding by silica with associated sulfide (pyrite-trace chalcopyrite). Late scattered simple to anastomosing anhydrite veins exhibit bleached and siliceous alteration halos. XRD mineralogy: cristobalite dominant throughout unit. Quartz and anhydrite, with minor pyrophyllite and pyrite, are the major components of a sampled sulfate vein. Quartz, anhydrite, and pyrite are minor to trace phases elsewhere in the unit, while illite, chlorite, and barite are present in trace concentrations. Plagioclase was detected as a major component in Sections 193-1188A-12R-1 (Piece 12) and 13R-1 (Piece 2). Subsequent careful binocular examination of these samples detected what may be remnant primary igneous plagioclase.
	12R-1 (4-14)	96.99	98.08	1.09		
	12R-2 (1-4)	98.08	98.62	0.54		
	13R-1 (2)	106.37	106.42	0.05		
11	13R-1 (3-16)	106.42	107.69	1.27	Completely altered, pervasively bleached volcanic unit with sparsely vesicular patches. The unit is cut by a poorly to strongly developed silica-sulfate stockwork vein system.	Pervasively bleached (silica-sulfate-clay altered) fractured unit. Two different styles of veining, which both appear to postdate the pervasive alteration, are present. Irregular, anastomosing vuggy sulfate veins contain up to 5% pyrite, primarily as open space fill in vugs, and postdate earlier narrow, sharply defined silica-trace pyrite stockwork veins. Pyrite also occurs as fine disseminations in the altered body of the rock. XRD mineralogy: cristobalite and plagioclase dominant, minor quartz and pyrite, traces of anhydrite, barite, and chlorite.
	14R-1 (1)	116.00	116.03	0.03		
12	14R-1 (2)	116.03	116.10	0.07	Completely altered volcanoclastic, granule to pebble breccia.	Strongly bleached, sulfate-rich altered volcanic clasts are cemented in silica. Some clasts show silica. Trace pyrite occurs disseminated in the silica.

Table T2 (continued).

Unit	Core, section (Piece)	Curated depth (mbsf)		Curated length (m)	Lithology	Alteration
		Top	Base			
13	193-1188A- 14R-1 (3-12)	116.10	117.04	0.94	Pervasively bleached and fractured volcanic rock. Possible remnant flow banding and vesicles in some pieces. The unit is cut by a very strongly developed silica-sulfate stockwork vein system.	Pervasively bleached (silica-sulfate-clay altered) fractured unit, with obvious similarities to Unit 11. Well-developed fracturing hosts a stockwork of sharply defined silica-trace pyrite veins, some of which appear to predate anhydrite veins, while others seem to be synchronous. Anhydrite veins with very distinct narrow silica halos. Pyrite also is present as fine disseminations in the altered body of the rock. XRD mineralogy: quartz and anhydrite dominant, minor pyrite and cristobalite (upper sample only), and traces of talc.
14	14R-1 (13-18)	117.04	117.31	0.27	Completely altered volcanoclastic, granule to pebble breccia. Rock resembles Unit 12.	Strongly bleached, sulfate-rich altered volcanic clasts are cemented in silica. Some clasts show silica. Trace pyrite is present disseminated in the silica.
15	15R-1 (1-5)	125.70	125.94	0.24	Crustiform anhydrite-pyrite vein.	Bleached volcanic fragments attached to the vein margin.
16	15R-1 (6-22)	125.94	126.81	0.87	Completely bleached and silicified, sparsely vesicular volcanic rock with scattered sulfate veining and fine sulfide veinlets.	Very strongly silicified unit. Anhydrite veins, 1 cm thick, are present in the rubble, which makes up the upper portion on the unit (related to Unit 15, above?). The basal part of the unit comprises hard, pervasively silicified vesicular volcanics, which are cut by <<1-mm-wide pyrite veinlets with 1-mm anhydrite selvages, surrounded by well defined 2- to 5-mm silica alteration halos. Pyrite is present throughout the rock as fine-grained vesicle fill, intergrown with anhydrite and/or quartz. Apparent extremely fine grained disseminated pyrite is probably material filling microscopic vesicles.
17	16R-1 (3-20) 16R-2 (1)	135.47 136.86	136.86 136.91	1.39 0.05	Completely silicified, sparsely vesicular volcanic rock with pale green tinges and irregular silica-anhydrite veining. Some pieces show traces of primary volcanic layering.	Very strongly silicified unit. The unit comprises hard, pervasively silicified vesicular volcanics, which are cut by <<1-mm-wide pyrite veinlets with 1-mm anhydrite selvages, surrounded by well defined 2- to 5-mm silica alteration halos (as seen in the above unit). Rare medium-grained anhydrite veins are also present. Pyrite is present throughout the rock as fine-grained vesicle fill, intergrown with anhydrite and/or quartz. Apparent extremely fine grained disseminated pyrite is probably material filling microscopic vesicles. XRD mineralogy: quartz dominant, minor plagioclase, traces of anhydrite, illite, chlorite, and pyrite.
18	16R-2 (2-12)	136.91	137.79	0.88	Finely laminated, flow-banded, gray-green volcanic rock. Strongly silicified.	Gray-green alteration, dominantly silicification, with minor chlorite. Chaotic structure at the top and base of the unit. Minor vuggy silica, laminated silica, and laminated sulfate veins. Trace very fine grained disseminated pyrite throughout rock. XRD mineralogy: quartz and plagioclase dominant, traces of chlorite, anhydrite, and pyrite.
19	16R-2 (13-15) 17R-1 (1-25) 17R-2 (1-6) 18R-1 (1-17)	137.79 145.10 146.60 154.70	138.05 146.60 146.96 156.56	0.26 1.50 0.36 1.86	Silicified, bleached volcanic rock with rarely preserved perlitic texture and vesicles. Some intervals of hydrothermal brecciation with silica veinlets.	Silicified, bleached volcanic rock with rarely preserved perlitic texture and vesicles. Cut by fine silica-trace pyrite veinlets and more abundant irregular, anastomosing to simple anhydrite-minor magnetite-trace pyrite veins, which have distinct bleached to siliceous alteration halos. There is evidence to suggest the silica veinlets and the anhydrite-magnetite veins are contiguous. Magnetite also is present as patches of very fine euhedra on fracture surfaces and, less commonly, as disseminations throughout the rock. Some intervals of hydrothermal brecciation with silica veinlets. XRD mineralogy: quartz dominant, minor anhydrite, traces of illite and magnetite.

Table T2 (continued).

Unit	Core, section (Piece)	Curated depth (mbsf)		Curated length (m)	Lithology	Alteration
		Top	Base			
20	193-1188A- 18R-1 (18-23)	156.56	156.85	0.29	Silicified and bleached moderately vesicular volcanic unit, with some remnant perlitic texture. Very fine grained disseminated magnetite present in Section 193-1188A-18R-1 (Pieces 18–23).	Silicified unit with similar alteration to overlying material. The pieces from Section 193-1188A-18R-1 probably have more in common with the lower portion of Unit 19 than with Pieces 1–4 of Section 193-1188A-19R-1. The entire unit is moderately vesicular, with fine to very coarse grained anhydrite vesicle and vug fill (\pm trace pyrite). A hairline fracture in Section 193-1188A-19R-1 (Piece 4) contains very fine grained pyrite and displays a 1-cm-wide siliceous alteration halo.
	19R-1 (1-4)	164.30	164.52	0.22		
21	19R-1 (5-13)	164.52	164.95	0.43	Silicified volcanic with some pieces exhibiting remnant microperlitic texture. Very rare vesicles.	Silicified, bleached volcanic rock with remnant perlitic texture and rare vesicles, which are silica filled. Piece 9 from Section 193-1188A-19R-1 exhibits green clay (chloritic) alteration. Very little pyrite throughout.
22	19R-1 (14-16)	164.95	165.23	0.28	Moderately altered, vesicular dacite. Some alignment of vesicles at the top of the unit—probable flow structure.	Fine-grained vesicular volcanic unit with magnetite, pyroxene and plagioclase microcrystals in the groundmass, although the magnetite may be an alteration product. Cut by rare irregular microcrystalline silica-anhydrite veins, with slightly bleached halos. Microvesicles are silica- and anhydrite-filled. Traces of very fine grained disseminated pyrite also in vesicles.
23	19R-1 (17)	165.23	165.27	0.04	Completely silicified, weakly to moderately chloritic magnetite-bearing volcanic rock.	Pervasively silicified unit with green chloritic clay-rich patches. Very fine, slightly vuggy anastomosing silica-anhydrite \pm pyrite veining is faintly visible and appears to have been overprinted by the pervasive silicification event, which also appears to be related to the ~5% very fine magnetite, which is disseminated throughout the unit. Pyrite is also disseminated throughout, but tends to be more abundant in chloritic sections of the unit. Rare poorly defined silica-anhydrite-pyrite veins are also overprinted by the pervasive silicification. XRD mineralogy: quartz dominant, minor plagioclase, anhydrite (in a sample including silica-anhydrite-pyrite veining), chlorite-smectite mixed-layer, magnetite, and pyrite, and traces of illite.
	20R-1 (3-11)	173.98	174.81	0.83		
24	20R-1 (12-13)	174.81	175.01	0.20	Distinctive dark green silicified unit with hairline silica-filled fractures and ovoid sulfate spots (perhaps after vesicles?).	Dark green, pervasively silicified unit with hairline silica filled fractures, rimmed by narrow bleached halos. Ovoid sulfate spots appear to be remnant vesicles. Very fine grained pyrite is disseminated throughout the rock, but more concentrated in vuggy, silica-lined cavities. Extremely fine grained dark spots are disseminated magnetite (2%–3%). XRD mineralogy: quartz and plagioclase dominant, minor magnetite, chlorite-smectite mixed-layer, and pyrite, and traces of anhydrite.
25	20R-1 (14-15)	175.01	175.11	0.10	Green-black unit with patches of remnant soft green clay-rich material in a zone of pervasive silica-pyrite stockworking. Very fine magnetite is disseminated throughout.	Remnant soft green clay-rich patches, containing disseminated magnetite, are surrounded by pervasive fine grained silica-minor pyrite flooding, which is associated with a network of anastomosing hairline fractures. Vuggy cavities in the silica are lined by fine crystalline quartz. Very fine grained euhedral pyrite is noticeably more abundant in silicified zones, particularly in the vuggy cavities. Magnetite appears to be replaced by pyrite in the silicified zones, suggesting it predates the silica-pyrite flooding. XRD mineralogy: quartz dominant, minor plagioclase, magnetite, chlorite-smectite mixed-layer, and pyrite.
	21R-1 (1-18)	183.10	184.60	1.50		
26	22R-1 (1)	192.70	192.86	0.16	Vuggy massive sulfate-silica with traces of disseminated pyrite and Fe oxide spotting. Probable vein material, which may be rubble from farther up the hole.	
	23R-1 (1)	202.10	202.29	0.19		

Note: XRD = X-ray diffraction.

Table T3. Results of point counts on volcanic rock thin sections, Hole 1188A.

Core, section, interval (cm)	Unit	Rock type	Number of points	Groundmass (%)	Vesicles (%)	Phenocrysts (%)		
						Plagioclase	Clinopyroxene	Opaques
193-1188A-								
2R-1 (Piece 3, 9-12)	1	Rhyodacite	750	92.5	3.6	2.6	0.8	0.4
3R-1 (Piece 1, 0-2)	1	Rhyodacite	750	92.2	4.6	2.4	0.1	0.5
16R-1 (Piece 6, 31-38)	17	Volcanic rock	750	94.8	4.5	0.4	0.0	0.2
16R-1 (Piece 10, 74-78)	17	Volcanic rock	750	95.4	3.2	0.9	0.0	0.4
16R-2 (Piece 2, 12-15)	18	Volcanic rock	565	96.4	1.9	1.0	0.0	0.5
16R-2 (Piece 7, 40-43)	18	Volcanic rock	500	98.4	0.0	1.2	0.0	0.4
19R-1 (Piece 15, 73-76)	22	Volcanic rock	500	86.5	13.3	0.1	0.0	0.0

Note: Point counts were measured using a rectangular grid with a = 0.667 mm and b = 0.8 mm.

Table T4. Lithology and alteration of Units 27 to 72, Hole 1188F. (See table note. Continued on next five pages.)

Unit	Core, section (Piece)	Curated depth (mbsf)		Curated length (m)	Lithology	Alteration
		Top	Base			
193-1188F-						
27	1Z-1 (1-5)	218.00	219.21	1.21	Completely altered, silicified, massive aphyric volcanic rock.	Intensely fractured, pervasive pale gray silicified rock with minor greenish, chloritic intervals (remnant GSC domains) and softer, more clayey pieces. Cut by irregular anhydrite-pyrite ± silica veins with cyclically zoned, 1- to 2-cm-wide siliceous alteration halos. XRD mineralogy: quartz dominant, minor anhydrite, illite, and pyrite.
	1Z-2 (1-4)	219.21	220.42	1.21		
	1Z-3 (1-2)	220.42	221.04	0.62		
28	1Z-3 (3)	221.04	221.65	0.61	Completely altered, silicified, and green clay-bearing, massive aphyric volcanic rock.	Pervasive pale gray silicification and abundant green material (remnant GSC domains?). Similar to Unit 27 but with a dominance of green material. Anhydrite-pyrite coated fractures show distinct, cyclically banded silicified alteration halos overprinting the chloritic alteration. Remnant kernels of groundmass domains encircled by such veins are green. XRD mineralogy: quartz dominant, minor anhydrite, illite, chlorite, and pyrite.
	1Z-4 (1)	221.65	222.25	0.60		
29	1Z-4 (2)	222.25	222.86	0.61	Completely altered, silicified, massive aphyric volcanic rock.	Intensely fractured, pervasive pale gray silicified intervals intercalated with creamy-colored, softer, more clay-rich material. Thin, submillimeter anhydrite-pyrite-silica veins with well-developed, 10- to 15-mm-wide, gray siliceous alteration halos. XRD mineralogy: quartz dominant, minor anhydrite, illite, and pyrite. Sample 193-1188F-2Z-1, 73–74 cm, contains, additionally, calcite and probably traces of kaolinite.
	2Z-1 (1-3)	221.50	223.00	1.50		
	3Z-1 (1-3)	222.60	224.04	0.44		
30	3Z-2 (1-3)	224.04	225.59	1.55	Completely altered, brecciated, silicified volcanic rock with a clayey matrix.	Hard, indurated, pervasively silicified and less abundant creamy-colored (more clay rich) fragments embedded in a light gray, clay-anhydrite matrix. Late pyrite-silica ± anhydrite veinlets cut larger pieces and have well-developed, banded (cyclic) siliceous alteration halos (as wide as 2 cm). XRD mineralogy: quartz dominant, minor anhydrite, illite, chlorite, and pyrite.
	6Z-1 (1)	233.10	233.55	0.45		
31	6Z-1 (2)	233.55	233.57	0.02	Highly altered, apparently spherulitic volcanic rock.	Single piece of apparently spherulitic volcanic rock. Contains 50% isolated, white, round, altered apparently spherulites (as much as 1 mm in diameter, radiating crystal aggregates). Central vugs are common and often filled by pyrite crystals. XRD mineralogy: cristobalite and plagioclase dominant, minor chlorite and pyrite.
32	6Z-1 (3-4)	233.57	234.37	0.80	Completely altered, silicified, massive aphyric volcanic rock.	Light gray indurated, silicified, and less-abundant creamy-colored more clay-rich pieces. Fracture surfaces with silica and sulfate. Trace disseminated pyrite tends to be more abundant in less strongly silicified pieces. Scattered Fe oxide spotting after sulfide. XRD mineralogy: quartz dominant, minor anhydrite and illite.
	6Z-2 (1A-1B)	234.37	234.61	0.24		
33	6Z-2 (1C-3)	234.61	235.39	0.78	Silicified volcanic fragments embedded in soft gray clay.	Pervasively silicified fragments embedded in and/or coated by soft, gray clay. Fracture surfaces are mostly coated by white silica-anhydrite with zoned cyclic alteration halos (as much as 1 cm half-width). Trace pyrite disseminated and as vug fills. Quartz-pyrite spots may be remnant plagioclase phenocrysts. Piece 3A contains rare plagioclase phenocrysts. XRD mineralogy: quartz dominant, minor anhydrite, illite, and pyrite.
34	7Z-1 (1A-1G)	235.00	236.01	1.01	Silicified, massive aphyric volcanic rock.	Rounded pebbles of silicified, sparsely microvesicular volcanic rock. Intensity of silicification decreases away from edges of pebbles, leaving less-altered kernels. Pyrite is finely disseminated in the less-silicified kernels but is absent from the intensely silicified piece margins. FeO _x spotting on white coated surfaces is after pyrite. Distinct blue amorphous surface coating (silica-clay?) on some fragments of Piece 1E. XRD mineralogy: quartz dominant, minor anhydrite and illite, and traces of pyrite.

Table T4 (continued).

Unit	Core, section (Piece)	Curated depth (mbsf)		Curated length (m)	Lithology	Alteration
		Top	Base			
35	193-1188F- 7Z-1 (2A-2D)	236.01	236.51	0.50	Silicified volcanic rock with scattered plagioclase phenocrysts.	Intensely silicified rock. White silica-sulfate coated fracture surfaces have distinct banded silicified alteration halos. Planar to convolute lamination is defined by silica and gray-greenish clay. It is unclear whether they are vein halos or possibly pseudomorphed flow banding. Remnant plagioclase phenocrysts are generally corroded to skeletal. Pyrite is present as very fine grained disseminations and as slightly coarser microvesicle fill (\pm quartz). XRD mineralogy: quartz dominant, minor anhydrite and illite, and traces of pyrite.
	7Z-2 (1-3)	236.51	237.11	0.60		
36	8Z-1 (1-2)	236.20	237.53	1.33	Silicified, massive aphyric volcanic rock.	Intensely silicified rock. Flamelike zoned to patchy halo, sometimes cut by narrow pyrite veins. Whitish to light gray elongate patches in halos are soft and consist of silica-clay with some anhydrite and pyrite. XRD mineralogy: quartz dominant, minor anhydrite and illite.
	9Z-1 (1A)	237.70	237.80	0.10		
37	9Z-1 (1B)	237.80	237.86	0.06	Silicified clastic rock.	Irregular white clasts(?) are soft, anhydrite-clay-quartz-pyrite-bearing material. The groundmass is light green and fine grained with disseminated gray silica-clay. There are dark gray completely silicified oval patches developed in the piece. XRD mineralogy: quartz dominant, minor anhydrite and illite.
38	9Z-1 (1C-1F)	237.86	238.25	0.39	Silicified, massive, aphyric volcanic rock.	Highly silicified rocks. Zoned halos consist of dark gray silicified bands alternating with softer bands that have a bleached appearance. Away from the halos, alteration is pervasive, but anhydrite-pyrite-rich as well as quartz-rich patches are developed. XRD mineralogy: quartz dominant, minor anhydrite and illite, and traces of pyrite.
	11G-1 (1-6)	238.90	239.56	0.66		
39	11G-1 (7-13)	239.56	240.40	0.84	Silicified slightly vesicular volcanic rock with scattered plagioclase phenocrysts.	Highly silicified rocks. Trace to 1% plagioclase phenocrysts are replaced by soft, white, clayey material. Pyrite is abundant in groundmass and filling vesicles together with anhydrite. Zoned halos are associated with anhydrite veins, some of which are preserved on the surfaces of some pieces. Open vesicles are lined with clay-silica and pyrite and often filled with blocky anhydrite. Piece 8 has acicular, clear crystals overgrowing anhydrite and pyrite in vugs. XRD mineralogy: quartz dominant, minor anhydrite, pyrite, and illite.
	13Z-1 (1-3C)	241.40	242.20	0.80		
40	13Z-1 (4)	242.20	242.23	0.03	Highly altered, apparently spherulitic volcanic rock.	Single piece of apparently spherulitic volcanic rock. Contains 50% isolated, white, round, altered apparently spherulites.
41	13Z-1 (5)	242.23	242.76	0.53	Silicified volcanic rock with scattered plagioclase phenocrysts.	Remnant plagioclase phenocrysts replaced by bluish white clay. Microvesicles(?) filled by anhydrite and pyrite. Hairline to several-millimeter-thick anhydrite-pyrite veins and veinlets, predominantly with millimeter- to centimeter-wide siliceous alteration halo. Occasional round to bulbous, irregular dark gray siliceous patches within the groundmass. XRD mineralogy: quartz dominant, minor anhydrite, pyrite, and illite, and traces of chlorite. Sample 193-1188F-14Z-1, 134–139 cm, additionally contains probably brittle mica or illite-bearing mixed layer.
	13Z-2 (1-4)	242.76	243.57	0.81		
	14Z-1 (1-9)	245.90	247.42	1.52		
	14Z-2 (1)	247.42	247.61	0.19		
15Z-1 (1-6)	250.40	250.84	0.44			
42	15Z-1 (7-15)	250.84	251.79	0.95	Silicified, aphyric volcanic rock.	Irregular silica void fill. Pyrite and anhydrite crystals as vesicle fill. Pyrite is disseminated throughout. XRD mineralogy: quartz dominant, minor anhydrite, pyrite, and probably brittle mica or illite-bearing mixed layer.
43	15Z-1 (16)	251.79	251.90	0.11	Silicified volcanic rock with scattered plagioclase phenocrysts.	Rocks contain 1% plagioclase phenocrysts replaced by bluish clay. Vugs and veins are filled by anhydrite and pyrite. Pyrite is also in the microvesicles.
	15Z-2 (1-2)	251.90	252.09	0.19		
	16Z-1 (1A-1B)	254.90	255.09	0.19		
44	16Z-1 (1C-3)	255.09	256.38	1.29	Silicified, brecciated, flow-banded, aphyric volcanic rock.	Dominantly nonporphyritic rubble with remnant autoclastic and flow-banded textures. Some pieces contain rare plagioclase phenocrysts replaced by bluish clay. Sulfate vesicle fill and pyrite-anhydrite vug lining. Fine pyrite-anhydrite veinlets with narrow bleached halos are present. XRD mineralogy: quartz dominant, minor pyrite, illite, and probably brittle mica or illite-bearing mixed layers, and traces of anhydrite.
45	193-1188F- 17Z-1 (1)	259.40	259.52	0.12	Silicified volcanic rock with scattered plagioclase phenocrysts.	Unit 45 is characterized by 1%–2% plagioclase phenocrysts replaced by bluish clay. Some edges show bleached silicified halos. Elongate, aligned microvesicles are filled with pyrite. Fine pyrite veinlets have anhydrite selvages and silicified halos. Pyrite content ranges from 1% to 3%.
	18Z-1 (1A-1C)	263.90	264.30	0.40		
	19Z-1 (1A-1E)	268.40	268.81	0.41		

Table T4 (continued).

Unit	Core, section (Piece)	Curated depth (mbsf)		Curated length (m)	Lithology	Alteration
		Top	Base			
46	22Z-1 (1-11)	282.10	282.98	0.88	Completely altered, silicified, aphyric, volcanic rock.	Unit 46 is characterized by several slightly brecciated rocks. Multiple dark gray bands border the brecciated zone. The remainder is often green and apparently chloritized. Pyrite is present mostly in veinlets, and fine-grained pyrite fills vesicles and voids. XRD mineralogy: quartz dominant, minor anhydrite, pyrite, illite, and chlorite.
47	22Z-1 (12-15)	282.98	283.36	0.38	Completely altered, green clay-bearing, aphyric, volcanic rock.	Highly silicified and apparently chloritized rock. Some quartz blebs with pyrite are present.
48	23Z-1 (1-10B)	286.60	287.61	1.01	Silicified volcanic rock with scattered plagioclase phenocrysts.	Silicified rocks with plagioclase phenocrysts altered to white clay. A bleached appearance is in most of the rocks. Veins and veinlets are filled by pyrite, whereas vugs are lined by pyrite-anhydrite-quartz. Halos are developed around the edges. XRD mineralogy: white halos—quartz dominant, minor anhydrite, illite, and pyrite, and small amounts of chlorite. Gray kernels—quartz dominant, minor chlorite, illite, and pyrite, and traces of anhydrite and smectite.
49	23Z-1 (11E-14)	287.61	288.09	0.48	Completely altered, silicified, green clay-bearing, aphyric volcanic rock.	Apparently chloritized rock with light gray to gray alteration halos around vugs that are partly filled with anhydrite-pyrite. Some anhydrite-quartz-pyrite vugs are present. Pyrite is present in rare hairline veinlets and as microvesicle fill. Piece 2 of Section 193-1188F-23Z-2 is covered by a white crust of anhydrite. In Piece 2 of Section 193-1188F-26Z-1 very fine grained magnetite is disseminated throughout. XRD mineralogy: quartz dominant, minor anhydrite, chlorite, illite, and pyrite. Piece 4 of Section 193-1188F-25Z-1 additionally contains major plagioclase.
	23Z-2 (1-9)	288.09	289.00	0.91		
	25Z-1 (1-6)	295.60	296.08	0.48		
	26Z-1 (1-2)	300.10	300.36	0.26		
50	26Z-1 (3-6)	300.36	301.19	0.83	Silicified volcanic rock with scattered plagioclase phenocrysts.	1%-2% plagioclase laths are partly replaced by white clay. White silica-sulfate crusts on some pieces have zoned alteration halos. Fine quartz-pyrite spotting appears to be vesicle fill (amygdules). Magnetite is present in Piece 2 of Section 193-1188F-27Z-1. XRD mineralogy: quartz dominant, minor plagioclase, chlorite, anhydrite, illite, and pyrite.
	26Z-2 (1-4)	301.19	302.27	1.08		
	27Z-1 (1-2)	304.60	304.91	0.31		
51	30Z-1 (1-4)	318.10	318.30	0.20	Completely altered, variably silicified breccia.	This is a clastic or pseudoclastic unit of completely altered rock, presumably volcanic. Clasts are variably silicified. Matrix is variably clay- and anhydrite-bearing. Piece 4 is considerably darker than the other pieces and may contain more abundant magnetite. Clasts are generally hard to very hard. Late-stage anhydrite-pyrite crystals are in veins and pockets in the matrix. XRD mineralogy: quartz dominant, minor plagioclase, illite, and chlorite, and traces of pyrite.
52	31Z-1 (1)	322.60	322.69	0.09	Silicified, magnetite-bearing volcanic rock with scattered plagioclase phenocrysts.	Pervasive silicification of the groundmass with disseminated magnetite and pyrite (very high alteration intensity). An anhydrite vein with a dark silicified halo and a magnetite-pyrite-quartz vein (1 mm wide) with a pale silicified halo are present. XRD mineralogy: quartz dominant, minor plagioclase, illite, and chlorite, and traces of pyrite.
53	31Z-1 (2-5)	322.69	323.02	0.33	Completely altered, variably silicified breccia.	Clasts are variably silicified. Matrix is variably clay- and anhydrite-bearing. Pieces 3 and 4 (3–5 cm in diameter) are massive aphyric volcanic rock with diffuse light gray and light green domains resembling previous units (such as Unit 50). XRD mineralogy: quartz dominant, minor pyrite, illite, and chlorite, and traces of anhydrite.

Table T4 (continued).

Unit	Core, section (Piece)	Curated depth (mbsf)		Curated length (m)	Lithology	Alteration
		Top	Base			
54	193-1188F- 34Z-1 (1-4)	336.40	336.64	0.24	Completely altered aphyric volcanic rock.	Silicified rock with zoned halos. Pyrite and magnetite are disseminated in the quartz-dominated clayey matrix. Vugs are filled with quartz, anhydrite, and pyrite. XRD mineralogy: quartz dominant, minor anhydrite, illite, and pyrite, and traces of plagioclase.
55	34Z-1 (5-12)	336.64	337.11	0.47	Completely altered volcanic rock and breccia with variable black, late-stage magnetite-bearing alteration.	Highly silicified, gray clasts of coarse-grained quartz ± pyrite, and tannish gray, clay-rich clasts are in a highly silicified and magnetite-impregnated matrix. Bluish fine-grained silica patches are present. Vugs are filled with pyrite, anhydrite, quartz, and red hexagonal plates of hematite. Piece 5 is a black silicified, slightly brecciated rock, which is heavily impregnated with magnetite. XRD mineralogy of Piece 5: magnetite dominant, minor di- and trioctahedral illite, quartz, plagioclase, chlorite, pyrite, and Fe spinel, and traces of brucite. XRD mineralogy of Piece 9: plagioclase and quartz dominant, minor illite, chlorite, pyrite, and magnetite, and traces of illite-bearing mixed layer.
56	34Z-1 (13-18)	337.11	337.73	0.62	Completely altered and variably silicified volcanic rock breccia.	Silicified rock with patchy distribution of light gray more clayey and gray, more silicified areas. Magnetite-rich apophysis and veins filled with magnetite-quartz-pyrite are developed. Spherical, light gray and light greenish gray spots (possible vesicle fill) could contain chlorite or green clay. XRD mineralogy: quartz dominant, minor chlorite and illite, and traces of anhydrite and pyrite.
57	35Z-1 (1-3B) 35Z-2 (1A-2B) 36G-1 (1-2) 37Z-1 (1-4) 37Z-2 (1-2)	340.00 341.50 344.50 344.50 345.81	341.50 341.99 344.75 345.81 346.10	1.50 0.49 0.25 1.31 0.29	Silicified, sparsely vesicular, aphyric, massive volcanic rock.	Sugary silicified rocks with scattered, ovoid fine grained quartz amygdules. Banded textures are common and related to anhydrite ± pyrite veins. Prominent alteration halos along margins of several pieces. Traces of disseminated magnetite are present in Pieces 1, 2D, and 2E of Section 193-1188F-35Z-1. XRD mineralogy: quartz dominant, minor plagioclase, anhydrite, illite, pyrite, magnetite, and chlorite.
58	37Z-2 (3)	346.10	346.16	0.06	Magnetite-rich, clastic rock.	Disseminated magnetite (5%–8%) is present throughout the dark siliceous groundmass. Quartz-anhydrite pyrite domains have near massive, 2-mm-wide, magnetite alteration halos. The rock is similar to Piece 5 of Section 193-1188F-34Z-1. XRD mineralogy: plagioclase dominant, minor magnetite, illite, alunite, Fe spinel, chlorite, pyrite, and brucite.
59	37Z-2 (4-9)	346.16	347.28	1.12	Silicified, flow-banded, locally magnetite-bearing, aphyric, sparsely vesicular volcanic rock.	Banded, variably colored, silicified rock with fine quartz amygdules. Darker bands and domains are magnetite-bearing. Pyrite is present as crystals in very fine unfilled vesicles. XRD mineralogy: quartz dominant, minor plagioclase, anhydrite, and magnetite, and traces of illite, chlorite, and pyrite.
60	38Z-1 (1-3)	349.00	350.30	1.30	Silicified, slightly vesicular volcanic rock with scattered plagioclase phenocrysts.	Uniformly silicified light gray to greenish gray rocks. The groundmass is dominantly quartz with clay and very minor disseminated pyrite and magnetite. Vugs are filled with pyrite-anhydrite.
61	38Z-2 (1-4)	350.30	351.22	0.92	Completely altered, aphyric, amygdaloidal volcanic rock.	Silicified, greenish gray rocks with disseminated very fine grained magnetite and pyrite (as much as 1% each) in groundmass. Groundmass is gray, greenish gray, or GSC. Plagioclase microlites are replaced by white clay. XRD mineralogy: quartz and plagioclase dominant, minor illite, chlorite, and anhydrite, and traces of pyrite and magnetite.
62	39Z-1 (1-6)	353.50	354.05	0.55	Silicified volcanic rock with scattered plagioclase phenocrysts.	Silicified gray to light gray rocks. The groundmass is dominantly quartz with clay and very minor disseminated pyrite and magnetite (as much as 1%). The zoned halos are developed in Pieces 1 and 2 and consist of gray silicified and light gray, slightly softer bands. Plagioclase phenocrysts are replaced by white clay or dark gray clay and quartz. XRD mineralogy: quartz dominant, minor anhydrite, illite, chlorite, and pyrite, and traces of plagioclase and magnetite.

Table T4 (continued).

Unit	Core, section (Piece)	Curated depth (mbsf)		Curated length (m)	Lithology	Alteration
		Top	Base			
63	193-1188F- 39Z-1 (7-10)	354.05	354.67	0.62	Completely altered, variably magnetite-enriched volcanic rock.	Abundant magnetite (as much as 5%) imposes a dark gray to black color to the rock. Magnetite is intergrown with clay and quartz. Dark spots are soft and magnetic (i.e., clay + magnetite). Vugs are filled with pyrite and clay or pyrite and anhydrite. Pyrite in groundmass is rare. Plagioclase phenocrysts are altered to white clay.
64	39Z-1 (11-12)	354.67	354.93	0.26	Completely altered, aphyric volcanic rock.	Silicified rock with quartz-clay dominated light gray groundmass. Rocks have a spotty texture, owing to pyrite + anhydrite filled vugs with clay-rich halos. Minor magnetite and pyrite disseminated in groundmass. Pieces 3 and 4 of Section 193-1188F-39Z-2 are greenish-gray rocks with tan alteration halos along anhydrite + pyrite veins (Piece 4). Plagioclase phenocrysts are replaced by white to bluish white clay. Vugs are filled/lined with pyrite and anhydrite. XRD mineralogy: quartz dominant, minor anhydrite, illite, chlorite, pyrite, and plagioclase.
	39Z-2 (1-4)	354.93	355.38	0.45		
65	40Z-1 (1)	358.00	358.16	0.16	Completely altered, magnetite-enriched, vesicular volcanic rock.	Silicified microcrystalline groundmass. Vesicles lined/filled with green clay, anhydrite, pyrite, and magnetite. Commonly, pyrite is present in the centers of magnetite-filled vesicles. XRD mineralogy: quartz dominant, minor plagioclase, anhydrite, illite, chlorite, pyrite, and magnetite.
66	40Z-1 (2)	358.16	358.82	0.66	Silicified volcanic rock with scattered plagioclase phenocrysts.	Silicified rock with quartz-clay dominated light gray groundmass. Rocks have a spotty texture, owing to pyrite + anhydrite filled vugs with clay-rich halos. Minor magnetite and pyrite disseminated in the groundmass. XRD mineralogy: quartz dominant, minor anhydrite, illite, and pyrite, and traces of plagioclase and chlorite.
67	40Z-1 (3)	358.82	359.39	0.57	Completely altered, clastic-textured volcanic rock.	Brecciated with centimeter-sized angular highly silicified clasts that are surrounded by a light gray to tannish gray silica-clay matrix. The matrix is completely recrystallized, which makes distinguishing the original texture difficult. However, relict textures suggest it is composed of clay-silica altered clasts embedded in a silica-rich cement. Minor pyrite is disseminated throughout the rock. XRD mineralogy: quartz dominant, minor anhydrite, illite, and pyrite, and traces of plagioclase and chlorite.
	40Z-2 (1-2)	359.39	360.22	0.83		
68	41Z-1 (1-2)	362.50	362.67	0.17	Completely altered, magnetite-enriched volcanic rock.	Magnetite is abundant (3%), finely disseminated in a silicified groundmass. A trace of fresh plagioclase phenocrysts (2 mm long, identified by perfect [010] cleavage reflections) is noted in Piece 2B.
69	41Z-1 (3-4)	362.67	364.05	1.42	Completely altered, aphyric, amygdaloidal volcanic rock.	Silicified rock with finely disseminated pyrite and trace magnetite. Highly silicified very fine grained gray halos. Rocks are commonly spotty, owing to quartz-clay-pyrite vug fill. XRD mineralogy: quartz dominant, minor plagioclase, pyrite, illite, and chlorite, and traces of magnetite and anhydrite.
	41Z-2 (1-6)	364.05	364.86	0.81		
70	42Z-1 (1-7)	367.00	368.46	1.46	Completely altered, aphyric, sparsely amygdaloidal volcanic rock.	Pale, silicified rocks with anhydrite veins and associated alteration halos. Banded structures are probably vein-related zoned alterations. Fine quartz ± pyrite and anhydrite ± pyrite amygdules form discrete bands. Pyrite also is present as very fine grained crystals in microvesicles. XRD mineralogy: quartz dominant, minor anhydrite, chlorite, illite, and pyrite, and traces of plagioclase.
	42Z-2 (1-3)	368.46	368.75	0.29		
71	43Z-1 (1)	371.50	372.06	0.56	Completely altered, aphyric, sparsely vesicular volcanic rock.	Silicified rock with anhydrite-chlorite or quartz-chlorite lined vesicles and small (<1 mm) quartz, quartz-pyrite, and pyrite-chlorite amygdules. XRD mineralogy: quartz dominant, minor illite, pyrite, and chlorite, and traces of anhydrite and plagioclase.

Table T4 (continued).

Unit	Core, section (Piece)	Curated depth (mbsf)		Curated length (m)	Lithology	Alteration
		Top	Base			
72	193-1188F- 43Z-1 (2-4) 44Z-1 (1-3)	372.06 374.00	372.64 374.91	0.58 0.91	Completely altered, magnetite-bearing, aphyric, sparsely vesicular volcanic rock.	Pervasive silicification. Magnetite (1%–5%) is present throughout the rock as very fine grained disseminations and as vesicle fill with blue quartz and pyrite, and occasional late anhydrite. In the vesicles magnetite-quartz represents an early assemblage followed by pyrite ± anhydrite. Magnetite increases in abundance toward anhydrite-pyrite veins. XRD mineralogy: quartz and plagioclase dominant, minor chlorite, anhydrite, pyrite, and magnetite.

Note: GSC = green silica-clay, XRD = X-ray diffraction.

Table T5. Distribution and types of amygdules,
Hole 1188F.

Unit	Mineral composition of amygdule	Remarks
27	Quartz ± anhydrite	Flattened and aligned
28	Quartz + pyrite	Flattened
29	Quartz + pyrite + anhydrite	
30	Quartz	
32	Quartz ± anhydrite	
33	Quartz	
35	Quartz + pyrite + anhydrite	
36	Quartz + anhydrite	
38	Quartz + pyrite + anhydrite	
39	Pyrite + anhydrite	
41	Pyrite + anhydrite	
42	Anhydrite	
43	Quartz + pyrite + anhydrite	
45	Quartz + pyrite ± anhydrite	
46	Quartz + anhydrite ± pyrite	
47	Pyrite	
48	Pyrite	
49	Quartz + pyrite ± anhydrite	
55	Quartz; chlorite + chabazite(?)	
57	Quartz ± pyrite ± anhydrite	Flattened
59	Quartz + pyrite	
65	Pyrite + magnetite + clay; anhydrite	
66	Quartz + pyrite + anhydrite	Flattened
70	Quartz + pyrite + anhydrite	

Table T6. Distribution and types of plagioclase phenocrysts, Hole 1188F.

Unit	Fresh plagioclase	Replaced by	Remarks
27	No	Quartz	
28	No	Quartz ± clay	Trachytic
29	No	Quartz	
35	No	Quartz, quartz + anhydrite, illite, illite + halloysite	
36	No	Illite, anhydrite, quartz, and pyrite	
39	Some fresh	Clay, quartz, anhydrite, illite + halloysite	Trachytic
41	An ₆₄ phenocrysts, microlites	Illite + anhydrite ± halloysite	
42	No	Illite + anhydrite	
43	No	Illite + halloysite	
45	No	Clay + halloysite	
46	An ₅₁ phenocrysts, microlites	Incipient quartz	
49	An _{>33} phenocrysts, microlites		
51	Phenocrysts, microlites		Clastic
52	An ₆₂ phenocrysts, microlites		
54	No	Quartz	
56	No	Chlorite + illite	
57	Phenocrysts, microlites		Trachytic
59	Phenocrysts, microlites		Trachytic
62	An _{>38} phenocrysts	Clay	
65	Phenocrysts, microlites		Trachytic
66	No	Clay; chlorite + clay + anhydrite	Trachytic
69	Phenocrysts, microlites		
70	No	Clay	
71	Phenocrysts, microlites		
72	Phenocrysts, microlites		

Table T7. Summary of different principal alteration types, Site 1188.

	Green silica-clay	Bleaching	Silicification
Color in hand specimen:	Bluish green to green	White to light gray	Gray to greenish gray
Typical mineralogy:			
Cristobalite	Abundant	Abundant	Rare
Quartz	Abundant	Abundant	Abundant
Anhydrite	Absent	Abundant	Absent
Illite	Abundant	Abundant	Abundant
Chlorite	Abundant	Rare	Absent (?)
Pyrophyllite	Rare	Abundant	Rare
Pyrite	Abundant	Abundant	Abundant
Magnetite	Rare	Absent	Locally common
Style:			
Pervasive	Abundant	Rare	Abundant
Vein/stockwork	Absent	Abundant	Rare

Table T8. Minerals identified by XRD analysis, Hole 1188A. (See table notes. Continued on next page.)

Core, section, interval (cm)	Unit	Description	XRD identification: major (minor, "trace") minerals*	Anhydrite (%)
193-1188A-				
2R-1, 9-12	1	Moderately vesicular rhyodacite	Opaline silica, plagioclase (augite, "smectite")	
5R-1, 38-40	2	Completely altered aphyric volcanic rock with perlitic texture	Opaline silica (illite, smectite, pyrite, plagioclase)	
5R-1, 42-45	2	Completely altered aphyric volcanic rock with perlitic texture	Opaline silica (plagioclase, anorthite, sepiolite, k-feldspar, pyrite, "smectite")	
7R-1, 62-64	4	Gray rock with anhydrite-pyrite veins	Cristobalite, anhydrite (pyrite, plagioclase)	
7R-1, 92-93	4	Flow-banded rock with anhydrite-pyrite veins	Cristobalite (anhydrite, pyrite, plagioclase, smectite, "chl/sm mixed-layer clays, hematite")	
7R-1, 119-120	5	Jigsaw breccia with textures replaced by anhydrite and chlorite	Anhydrite, cristobalite (pyrite, chlorite, illite)	
7R-1, 145-147	5	Rock with a pseudoclastic texture	Anhydrite (cristobalite, pyrite, pyrophyllite, "quartz")	
7R-2, 39-41	6	Completely altered fractured volcanic rock	Cristobalite (anhydrite, pyrite, chlorite, illite, "barite")	
7R-2, 51-53	6	Completely altered fractured volcanic rock	Anhydrite, cristobalite (pyrite, quartz, illite, "barite")	
8R-1, 66-69	6	Completely altered fractured volcanic rock	Cristobalite (anhydrite, pyrite, chlorite, illite, "barite")	
8R-1, 124-127	6	Completely altered fractured volcanic rock	Cristobalite (anhydrite, pyrite, illite, "chlorite, barite")	
8R-1, 147-148	7	Completely bleached vesicular volcanic rock with silicification	Cristobalite, anhydrite (pyrite, quartz, illite, "barite")	
9R-1, 13-14	7	Completely altered fractured volcanic rock	Cristobalite, anhydrite, quartz (pyrophyllite, "pyrite, barite")	
9R-1, 66-70	8	Completely altered fractured volcanic rock	Cristobalite (pyrophyllite, pyrite, anhydrite, "barite")	
9R-2, 79-81	8	Completely altered fractured volcanic rock	Cristobalite (anhydrite, quartz, pyrite, illite)	
10R-1, 35-37	8	Completely altered fractured volcanic rock	Quartz, cristobalite (pyrophyllite, "barite, pyrite")	
11R-1, 35-38	9	Completely bleached vesicular volcanic rock with silicification	Cristobalite (plagioclase, quartz, anhydrite, pyrite, "chlorite")	
11R-1, 56-57	9	Completely bleached vesicular volcanic rock with silicification	Cristobalite, plagioclase, quartz (pyrite, anhydrite, "illite, barite")	
12R-1, 51-52	10	Completely altered fractured perlitic and flow-banded rock	Quartz, cristobalite, anhydrite (pyrophyllite, pyrite)	
12R-1, 69-70	10	Completely altered fractured perlitic and flow-banded rock	Cristobalite (anhydrite, pyrite, "illite, chlorite, chl/sm mixed-layer clays, smectite, barite")	
12R-1, 117-118	10	Completely altered fractured perlitic and flow-banded rock	Cristobalite, plagioclase (quartz, "pyrite, anhydrite, barite")	
12R-2, 48-51	10	Completely altered fractured perlitic and flow-banded rock	Cristobalite, plagioclase (quartz, pyrite, "anhydrite, barite, chlorite")	
13R-1, 9-12	11	Completely altered, pervasively bleached volcanic rock	Cristobalite, plagioclase (quartz, pyrite, "anhydrite, barite, chl/sm mixed-layer clays")	
14R-1, 4-10	12	Completely altered volcanoclastic, granule to pebble breccia	Quartz (illite, "pyrite")	
14R-1, 44-45	13	Pervasively bleached fractured volcanic rock	Quartz (cristobalite, anhydrite, pyrite, illite, "talc")	2-5
14R-1, 92-93	13	Pervasively bleached fractured volcanic rock	Quartz, anhydrite (pyrite, illite, "talc")	5-10
14R-1, 105-108	14	Completely altered volcanoclastic breccia	Quartz (anhydrite, illite)	2-5
15R-1, 14-21	15	Anhydrite vein	Anhydrite	100
15R-1, 76-80	16	Completely bleached and silicified, vesicular volcanic rock	Quartz (illite, pyrite, "anhydrite")	<2
16R-1, 77-78	17	Completely silicified, sparsely vesicular volcanic rock	Quartz (anhydrite, plagioclase, illite, "pyrite, chlorite")	2-5
16R-1, 95-98	17	Completely silicified, sparsely vesicular volcanic rock	Quartz (anhydrite, plagioclase, illite, "chlorite")	2-5
16R-2, 12-15	18	Gray-green finely laminated, strongly silicified volcanic rock	Quartz, plagioclase (pyrite, "chlorite, anhydrite")	<2
16R-2, 40-43	18	Gray-green finely laminated, strongly silicified volcanic rock	Quartz, plagioclase (pyrite, "chlorite, anhydrite")	<2
16R-2, 51-52	18	Gray-green finely laminated, strongly silicified volcanic rock	Quartz, plagioclase (chlorite, "anhydrite, pyrite")	<2
16R-2, 68-69	18	Gray-green finely laminated, strongly silicified volcanic rock	Quartz, plagioclase ("chlorite, pyrite, anhydrite")	<2
17R-1, 90-93	19	Silicified, bleached volcanic rock	Quartz (illite, "pyrite, anhydrite, chlorite")	<2
17R-1, 123-124	19	Silicified, bleached volcanic rock	Quartz (anhydrite, "illite")	5-10
18R-1, 28-29	19	Silicified, bleached volcanic rock	Quartz, anhydrite (magnetite, "illite")	15-20
18R-1, 87-97	20	Silicified and bleached, moderately vesicular volcanic rock	Quartz (anhydrite)	2-5
19R-1, 51-57	21	Silicified volcanic rock	Cristobalite, plagioclase (quartz, chlorite)	
19R-1, 73-76	22	Moderately altered, vesicular volcanic rock	Cristobalite, plagioclase (chlorite)	
20R-1, 46-47	23	Silicified, moderately chloritic magnetite-bearing volcanic rock	Quartz (plagioclase, anhydrite, corrensite, magnetite, illite, "pyrite")	2-5
20R-1, 75-76	23	Silicified, moderately chloritic magnetite-bearing volcanic rock	Quartz, plagioclase (magnetite, pyrite, chlorite)	0
20R-1, 92-95	24	Distinctive dark green silicified rock	Quartz, plagioclase (magnetite, pyrite, smectite, "anhydrite, chl/sm mixed-layer clays")	<2
20R-1, 102-103	24	Distinctive dark green silicified rock	Quartz, plagioclase (magnetite, pyrite, corrensite, "anhydrite")	<2
21R-1, 20-21	25	Green-black rock with green clay in a silica-pyrite stockwork	Quartz (plagioclase, magnetite, corrensite, "pyrite")	0

Table T8 (continued).

Notes: XRD = X-ray diffraction. * = the terms major, minor, and trace are applied to XRD analyses as explained in “**Hydrothermal Alteration,**” p. 8, in the “Explanatory Notes” chapter and do not imply quantitative abundances. Anhydrite abundances are estimated for quartz-bearing assemblages as described in “**Hydrothermal Alteration,**” p. 8, in the “Explanatory Notes” chapter. This procedure probably results in an overestimation of the anhydrite abundance because the effect of clays is ignored. In the absence of a suitable calibration, it is not possible to estimate anhydrite abundance from XRD spectra. Chl/sm mixed-layer clays = chlorite/smectite-mixed layer clays.

Table T9. Minerals identified by X-ray diffraction analysis, Hole 1188F. (See table notes. Continued on next page.)

Core, section, interval (cm)	Unit	Description	XRD identification: major (minor, "trace") minerals*	Anhydrite (%)
193-1188F-				
1Z-1, 4-5	27	Completely altered massive rock	Quartz (anhydrite, illite, "pyrite")	5-10
1Z-1, 29-30	27	Completely altered massive rock	Quartz (anhydrite, illite, pyrite)	2-5
1Z-1, 87-88	27	Completely altered massive rock	Quartz (anhydrite, illite, pyrite)	5-10
1Z-2, 4-5	27	Completely altered massive rock	Quartz (anhydrite, illite)	2-5
1Z-2, 37-38	27	Completely altered massive rock	Quartz (anhydrite, illite, "pyrite")	5-10
1Z-3, 20-21	27	Completely altered massive rock	Quartz (anhydrite, illite)	5-10
1Z-3, 34-35	27	Completely altered massive rock	Quartz (anhydrite, illite)	10-15
1Z-3, 35-36	27	Completely altered massive rock (including anhydrite vein)	Quartz (anhydrite, illite)	50-60
1Z-3, 85-86	28	Completely altered, silicified and green clay-bearing massive rock	Quartz (chlorite, illite, anhydrite, pyrite)	<2
1Z-3, 106-108	28	Completely altered, silicified and green clay-bearing massive rock	Quartz (anhydrite, illite, pyrite, "chlorite")	2-5
1Z-4, 90-91	28	Completely altered, silicified and green clay-bearing massive rock	Quartz (anhydrite, illite, "pyrite")	5-10
2Z-1, 44-45	29	Completely altered, silicified aphyric massive rock	Quartz (anhydrite, illite, pyrite)	2-5
2Z-1, 73-74	29	Completely altered, silicified aphyric massive rock	Quartz, calcite (anhydrite, illite, "kaolinite?")	5-10
3Z-1, 6-7	29	Completely altered, silicified aphyric massive rock	Quartz (illite, anhydrite, "pyrite")	<2
3Z-2, 40-41	30	Completely altered, brecciated, clay-rich rock	Quartz (anhydrite, illite, pyrite)	10-15
3Z-2, 144-145	30	Completely altered, brecciated, clay-rich rock	Quartz (anhydrite, chlorite, illite)	2-5
3Z-2, 150-151	30	Completely altered, brecciated, clay-rich rock	Quartz (anhydrite, illite, pyrite)	10-15
6Z-1, 20-21	30	Completely altered, brecciated, clay-rich rock	Quartz (anhydrite, illite, chlorite, pyrite)	<2
6Z-1, 46-47	31	Highly altered volcanic rock	Cristobalite, plagioclase (chlorite, pyrite)	0
6Z-1, 77-78	32	Completely altered, silicified massive aphyric rock	Quartz (anhydrite, illite)	2-5
6Z-2, 47-48	33	Silicified volcanic fragments embedded in soft gray clay	Quartz (illite, pyrite, anhydrite)	<2
7Z-1, 41-45	34	Silicified massive aphyric rock	Quartz (anhydrite, illite, "pyrite")	5-10
7Z-1, 104-107	35	Silicified, plagioclase-phyric rock	Quartz (anhydrite, illite)	2-5
7Z-2, 3-6	35	Silicified, plagioclase-phyric rock	Quartz (anhydrite, illite, "pyrite")	<2
8Z-1, 68-71	36	Silicified massive aphyric rock	Quartz (anhydrite, illite)	5-10
9Z-1, 9-12	37	Silicified clastic rock	Quartz (anhydrite, illite)	2-5
11G-1, 53-56	38	Silicified massive aphyric rock	Quartz (anhydrite, illite, "pyrite")	5-10
11G-1, 138-141	39	Silicified plagioclase-phyric, slightly vesicular volcanic rock	Quartz (anhydrite, pyrite, illite)	10-15
13Z-1, 118-121	41	Silicified plagioclase-phyric volcanic rock	Quartz, anhydrite, pyrite, illite)	2-5
13Z-2, 51-55	41	Silicified plagioclase-phyric volcanic rock	Quartz (anhydrite, illite, "pyrite")	5-10
13Z-2, 55-70	41	Silicified plagioclase-phyric volcanic rock	Quartz (anhydrite, pyrite, illite, "chlorite")	2-5
14Z-1, 134-139	41	Silicified plagioclase-phyric volcanic rock	Quartz (anhydrite, brittle mica?, pyrite)	2-5
15Z-1, 66-69	42	Silicified, aphyric rock	Quartz (anhydrite, brittle mica?, pyrite)	2-5
15Z-1, 90-95	42	Silicified, aphyric rock	Quartz (anhydrite, illite, brittle mica?, pyrite)	5-10
16Z-1, 41-43	44	Silicified, brecciated, flow banded, aphyric rock	Quartz (illite, pyrite, "anhydrite")	<2
16Z-1, 139-141	44	Silicified, brecciated, flow banded, aphyric rock	Quartz (pyrite, illite, brittle mica?, "anhydrite")	<2
22Z-1, 63-67	46	Completely altered, silicified, aphyric, volcanic rock	Quartz (anhydrite, pyrite, illite, chlorite)	2-5
23Z-1, 25-26	48	White halo of Piece 3	Quartz (anhydrite, illite, pyrite, chlorite)	5-10
23Z-1, 26-27	48	Gray kernel of Piece 3	Quartz (chlorite, illite, pyrite, "anhydrite, smectite")	<2
23Z-1, 102-103	49	Silicified, green clay-bearing aphyric volcanic rock	Quartz (anhydrite, chlorite, illite, "pyrite")	2-5
23Z-2, 13-14	49	White crust of Piece 2 (anhydrite vein)	Anhydrite ("quartz")	>95
23Z-2, 24-25	49	Silicified, green clay-bearing, aphyric volcanic rock	Quartz (anhydrite, chlorite, illite, pyrite)	2-5
23Z-2, 45-46	49	Silicified, green clay-bearing, aphyric volcanic rock	Quartz (anhydrite, chlorite, illite, "pyrite")	2-5
25Z-1, 24-26	49	Silicified, green clay-bearing, aphyric volcanic rock	Quartz, plagioclase (chlorite, pyrite, "anhydrite")	<2
26Z-1, 20-23	49	Silicified, green clay-bearing, aphyric volcanic rock	Quartz (anhydrite, pyrite, illite, chlorite, chl/sm mixed-layer clays, "smectite")	5-10
26Z-2, 60-61	50	Silicified, plagioclase-phyric volcanic rock	Quartz (chlorite, illite, anhydrite, pyrite)	2-5
27Z-1, 22-23	50	Silicified, plagioclase-phyric volcanic rock	Quartz (anhydrite, pyrite, plagioclase, illite, chlorite)	2-5
30Z-1, 5-7	51	Completely altered, variably silicified breccia	Quartz (plagioclase, illite, chlorite, "pyrite")	0

Table T9 (continued).

Core, section, interval (cm)	Unit	Description	XRD identification: major (minor, "trace") minerals*	Anhydrite (%)
31Z-1, 1-3	52	Silicified, slightly plagioclase-magnetite phyric volcanic rock	Quartz, plagioclase (chlorite, magnetite, pyrite, "anhydrite")	<2
31Z-1, 39-42	53	Completely altered, variably silicified breccia	Quartz (pyrite, illite, chlorite, "anhydrite")	<2
34Z-1, 22-23	54	Completely altered aphyric volcanic rock	Quartz (anhydrite, illite, pyrite, "plagioclase")	5-10
34Z-1, 27-28	55	Completely altered volcanic rock and breccia with variable black, late-stage magnetite-bearing alteration	Magnetite (di- and trioctahedral illite, quartz, plagioclase, chlorite, pyrite, Fe spinel, "brucite")	0
34Z-1, 40-41	55	Completely altered volcanic rock and breccia with variable black, late-stage magnetite-bearing alteration	Plagioclase, quartz (illite, chlorite, pyrite, magnetite, "illite-bearing mixed layer clays")	0
34Z-1, 89-90	56	Completely altered and variably silicified volcanic rock breccia	Quartz (chlorite, illite, "anhydrite, pyrite")	<2
35Z-1, 5-6	57	Silicified, sparsely vesicular, aphyric, massive volcanic rock	Quartz (plagioclase, pyrite, magnetite, illite, "anhydrite, chlorite")	<2
35Z-1, 46-48	57	Silicified, sparsely vesicular, aphyric, massive volcanic rock	Quartz (plagioclase, pyrite, chlorite, "illite, anhydrite, magnetite")	<2
35Z-1, 140-141	57	Silicified, sparsely vesicular, aphyric, massive volcanic rock	Quartz (anhydrite, illite, "pyrite, chlorite")	2-5
35Z-2, 48-49	57	Silicified, sparsely vesicular, aphyric, massive volcanic rock	Quartz (anhydrite, illite, pyrite, "plagioclase")	2-5
37Z-1, 6-7	57	Silicified, sparsely vesicular, aphyric, massive volcanic rock	Quartz, plagioclase (illite, "anhydrite, pyrite, magnetite, chlorite")	<2
37Z-2, 18-20	57	Silicified, sparsely vesicular, aphyric, massive volcanic rock	Quartz (plagioclase, illite, pyrite, anhydrite, chlorite)	2-5
37Z-2, 31-33	58	Magnetite-rich, clastic rock	Plagioclase (magnetite, illite, alunite, Fe spinel, chlorite, pyrite, brucite)	0
37Z-2, 65-68	59	Silicified, locally magnetite-bearing, aphyric volcanic rock	Quartz (plagioclase, anhydrite, magnetite, "illite, chlorite, pyrite")	2-5
38Z-2, 90-92	61	Completely altered, aphyric, amygdular volcanic rock	Quartz, plagioclase (illite, chlorite, anhydrite, "pyrite, magnetite")	2-5
39Z-1, 7-8	62	Completely altered, sparsely plagioclase-phyric volcanic rock	Quartz (anhydrite, illite, "chlorite, plagioclase, pyrite")	5-10
39Z-1, 41-43	62	Completely altered, sparsely plagioclase-phyric volcanic rock	Quartz (anhydrite, illite, chlorite, "pyrite")	2-5
39Z-2, 18-19	64	Completely altered, aphyric volcanic rock	Quartz (anhydrite, illite, chlorite, pyrite, plagioclase, illite-bearing mixed layer clays)	2-5
40Z-1, 3-5	65	Completely altered, magnetite-enriched, vesicular volcanic rock	Quartz (plagioclase, anhydrite, illite, chlorite, pyrite, magnetite)	2-5
40Z-1, 36-38	66	Completely altered, sparsely plagioclase-phyric volcanic rock	Quartz (anhydrite, illite, pyrite, "plagioclase, chlorite")	2-5
40Z-2, 35-36	67	Completely altered, clastic-textured volcanic rock	Quartz (anhydrite, illite, pyrite, "plagioclase, chlorite")	2-5
41Z-1, 46-47	69	Completely altered, aphyric, amygdular volcanic rock	Quartz (plagioclase, pyrite, illite, chlorite, "magnetite, anhydrite")	<2
41Z-2, 7-10	69	Completely altered, aphyric, amygdular volcanic rock	Quartz (plagioclase, pyrite, illite, chlorite, "magnetite, anhydrite")	<2
42Z-1, 30-31	70	Completely altered, aphyric, sparsely amygdaloidal volcanic rock	Quartz (anhydrite, illite, "pyrite")	5-10
42Z-1, 72-74	70	Completely altered, aphyric, sparsely amygdaloidal volcanic rock	Quartz (anhydrite, chlorite, illite, pyrite, "plagioclase")	5-10
43Z-1, 6-8	71	Completely altered, aphyric, sparsely vesicular volcanic rock	Quartz (illite, pyrite, chlorite, "anhydrite, plagioclase")	<2
43Z-1, 67-69	72	Completely altered, magnetite-bearing, aphyric volcanic rock	Quartz, plagioclase (chlorite, pyrite, magnetite, "anhydrite")	<2
43Z-1, 90-91	72	Completely altered, magnetite-bearing, aphyric volcanic rock	Quartz, plagioclase (chlorite, anhydrite, "pyrite, magnetite")	2-5
44Z-1, 85-86	72	Completely altered, magnetite-bearing, aphyric volcanic rock	Quartz, plagioclase (chlorite, anhydrite, "pyrite, magnetite")	2-5

Notes: XRD = X-ray diffraction. * = the terms major, minor, and trace are applied to XRD analyses as explained in "Hydrothermal Alteration," p. 8, in the "Explanatory Notes" chapter and do not imply quantitative abundances. Anhydrite abundances are estimated for quartz-bearing assemblages as described in "Hydrothermal Alteration," p. 8, in the "Explanatory Notes" chapter. This procedure probably results in an overestimation of the anhydrite abundance because the effect of clays is ignored. In the absence of a suitable calibration, it is not possible to estimate anhydrite abundance from XRD spectra. Chl/sm mixed-layer clays = chlorite/smectite-mixed layer clays.

Table T10. Minerals identified by X-ray diffraction analysis, Hole 1188B.

Core, section, interval (cm)	Unit	Description	XRD identification: major (minor) minerals*
193-1188B-			
1Z-1, 0-15	1	Completely altered, bleached, locally sparsely vesicular volcanic rock	Cristobalite (plagioclase, anhydrite, pyrite, illite, chlorite)
1Z-1, 16-31	1	Completely altered, bleached, locally sparsely vesicular volcanic rock	Cristobalite (pyrite, illite, quartz, anhydrite)

Note: XRD = X-ray diffraction. * = the terms major and minor are applied to XRD analyses as explained in **“Hydrothermal Alteration,”** p. 8, in the **“Explanatory Notes”** chapter and do not imply quantitative abundances.

Table T11. Major element oxides with selected trace elements, Hole 1188A. (Continued on next page.)

Core, section: 193-1188A-:	2R-1	5R-1*	7R-1	7R-1*	7R-2	8R-1	8R-1	9R-1	9R-2*	11R-1	12R-2	14R-1	14R-1	14R-1	14R-1*	16R-1	16R-1	
Interval (cm):	9-12	42-45	62-64	62-64	39-41	66-69	124-127	67-70	79-81	34-38	48-51	47-51	105-108	105-108	105-108	95-98	95-98	
Curated depth (mbsf):	9.69	34.02	48.82	48.82	50.09	58.56	59.14	68.27	69.89	87.25	98.56	116.47	117.05	117.05	117.05	136.35	136.35	
Rock type:	FD	AD	AD	AD	BR	BR	BR	BR	BR	AD	BR	BR	BR	BR	BR†	BR	AD	AD†
Alteration style:	F	BI	Sil/BI	Sil/BI	Sil/GSC	GSC	GSC	BI	BI	Sil/BI	Sil/GSC	BI/Sil	BI/Sil	BI/Sil	BI/Sil	Sil	Sil	
Ignited rock powder composition*:																		
Major element oxide (wt%):																		
SiO ₂	69.24	70.51	67.68	67.55	67.31	69.81	66.96	74.98	70.50	68.99	69.11	71.82	75.17	75.75	77.22	72.18	71.71	
TiO ₂	0.45	0.52	0.57	0.53	0.54	0.54	0.54	0.61	0.51	0.56	0.56	0.59	0.55	0.58	0.69	0.53	0.55	
Al ₂ O ₃	14.19	14.89	14.56	14.87	14.15	14.28	14.24	14.93	14.75	14.50	14.37	15.22	14.40	14.63	15.71	14.41	14.40	
Fe ₂ O ₃	4.61	5.44	5.50	5.44	5.30	6.61	5.84	5.46	5.97	5.76	5.65	3.72	0.40	0.31	0.40	5.17	4.82	
MnO	0.11	0.16	0.03	0.04	0.06	0.15	0.05	0.01	0.03	0.02	0.08	0.00	0.00	0.01	0.01	0.03	0.04	
MgO	0.68	2.37	3.98	4.17	3.79	4.76	3.65	0.17	1.90	2.82	1.58	0.28	0.23	0.24	0.29	2.23	2.31	
CaO	2.65	2.14	3.27	3.04	2.92	1.21	2.34	0.69	3.45	2.94	2.11	2.17	3.40	3.27	3.37	2.67	2.52	
Na ₂ O	4.90	2.74	1.53	1.56	0.67	0.74	0.62	0.56	0.84	1.84	5.27	0.98	1.01	0.99	1.01	0.91	0.88	
K ₂ O	1.83	2.13	0.65	0.75	1.42	1.05	1.80	BD	2.53	0.57	0.22	0.71	1.16	1.39	1.42	2.04	2.08	
P ₂ O ₅	0.08	0.17	0.12	0.11	0.11	0.12	0.17	0.07	0.18	0.16	0.15	0.11	0.14	0.14	ND	0.10	0.08	
Total (wt%):	98.75	101.08	97.89	98.07	96.27	99.28	96.20	97.47	100.67	98.17	99.10	95.61	96.46	97.31	100.10	100.27	99.37	
LOI (wt%):	1.42	8.39	7.07	7.76	7.21	6.09	7.58	6.44	8.77	6.39	1.74	5.85	4.69	5.41	7.31	5.41	2.95	
Trace element (ppm):																		
Zr	130	135	126	140	116	118	123	136	132	124	123	150	124	138	142	141	151	
Y	35	35	36	30	32	33	37	25	40	35	38	39	22	23	22	35	38	
Sr	247	260	278	279	208	87	141	113	263	289	255	204	218	226	236	234	235	
Zn	73	64	64	39	51	207	40	76	87	20	47	BD	BD	8	BD	9	45	
Cu	15	51	44	32	24	9	15	118	31	89	131	12	3	4	5	4	4	
Ba	405	389	301	293	241	280	319	356	330	269	258	364	545	483	522	752	688	
Whole-rock composition																		
Major element oxide (wt%):																		
SiO ₂	68.26	64.59	62.90	62.31	62.46	65.56	61.88	70.15	64.32	64.58	67.91	67.62	71.64	71.65	71.57	68.27	69.59	
TiO ₂	0.44	0.47	0.53	0.49	0.50	0.51	0.50	0.57	0.47	0.52	0.55	0.56	0.52	0.55	0.64	0.50	0.53	
Al ₂ O ₃	13.99	13.64	13.53	13.72	13.13	13.41	13.16	13.97	13.46	13.58	14.12	14.33	13.72	13.84	14.56	13.63	13.98	
Fe ₂ O ₃	4.55	4.98	5.11	5.02	4.92	6.21	5.40	5.11	5.45	5.39	5.55	3.50	0.39	0.29	0.37	4.89	4.68	
MnO	0.11	0.15	0.03	0.04	0.06	0.14	0.04	0.01	0.03	0.02	0.08	0.00	0.00	0.01	0.00	0.03	0.04	
MgO	0.67	2.17	3.70	3.85	3.52	4.47	3.37	0.16	1.74	2.64	1.55	0.26	0.22	0.22	0.26	2.11	2.24	
CaO	2.62	1.96	3.04	2.81	2.71	1.14	2.16	0.64	3.15	2.75	2.07	2.04	3.24	3.09	3.13	2.53	2.44	
Na ₂ O	4.83	2.51	1.42	1.44	0.62	0.69	0.57	0.52	0.77	1.73	5.18	0.93	0.96	0.94	0.93	0.86	0.85	
K ₂ O	1.81	1.95	0.61	0.69	1.32	0.99	1.67	BD	2.31	0.54	0.21	0.67	1.11	1.31	1.32	1.93	2.02	
P ₂ O ₅	0.08	0.16	0.11	0.10	0.10	0.12	0.16	0.06	0.16	0.15	0.15	0.10	0.13	0.14	0.00	0.10	0.07	
Total S (%):	0.02	0.65	4.66	4.66	3.78	2.53	5.00	4.33	5.14	5.47	0.63	3.95	1.73	1.73	1.73	3.42	3.42	
Total H ₂ O ⁺ (wt%):	1.21	7.93	4.75	4.75	5.09	5.42	4.90	3.63	3.34	3.49	1.54	3.08	2.53	2.53	2.53	3.24	3.24	
S _{water-soluble sulfate} (wt%):	0.04	ND	5.15	ND	4.24	1.20	4.93	4.50	ND	5.68	0.14	0.92	2.08	ND	ND	3.42	ND	

Notes: Upper portion of the table contains the oxide abundances in ignited powders, while the lower portion is the original rock compositions. The analyses of samples containing >1 wt% total S should be used as general compositional guides, and not as absolute values. * = samples ignited for 6 hr at 600°C followed by 4 hr at 1050°C; all other samples were roasted only for 1 hr at 1050°C; † = duplicate. Rock types: AD = altered dacite, BR = breccia, GD = green dacite, FD = fresh dacite. Alteration types: F = fresh, BI = bleached, Sil = silicified, GSC = green silica-clay. BD = below detection, ND = not determined. Water, total sulfur, and loss on ignition (LOI) are reported in weight percent of the unignited powders for Hole 1188A.

Table T11 (continued).

Core, section: 193-1188A-:	16R-2	16R-2	17R-1	17R-1	19R-1	20R-1	20R-1	21R-1	21R-1
Interval (cm):	12-15	40-43	90-93	90-93	73-76	74-77	92-95	20-24	20-24
Curated depth (mbsf):	136.98	137.26	146.00	146.00	165.03	174.64	174.82	183.82	183.30
Rock type:	BR	AD	AD	AD [†]	AD	AD	GD	GD	GD [†]
Alteration style:	GSC	GSC	Sil	Sil	Sil	GSC	Sil	Sil/GSC	Sil/GSC
Ignited rock powder composition*:									
Major element oxide (wt%):									
SiO ₂	61.67	67.19	73.25	72.04	67.55	52.34	70.05	60.53	61.77
TiO ₂	0.76	0.64	0.57	0.57	0.56	0.65	0.53	0.53	0.69
Al ₂ O ₃	14.74	14.43	14.40	14.38	14.42	12.05	14.33	13.86	14.48
Fe ₂ O ₃	9.14	5.79	4.97	4.64	4.90	13.71	5.46	8.77	9.69
MnO	0.13	0.09	0.04	0.05	0.06	0.07	0.03	0.06	0.07
MgO	4.19	2.39	2.61	2.68	1.21	4.68	1.23	5.36	6.38
CaO	4.35	4.13	1.13	1.10	2.65	2.31	2.52	2.89	3.07
Na ₂ O	4.70	4.13	0.68	0.64	4.91	3.12	4.83	0.07	3.25
K ₂ O	0.06	0.33	1.84	1.98	0.29	0.11	0.36	BD	BD
P ₂ O ₅	0.36	0.19	0.12	0.09	0.11	0.39	0.09	0.31	0.30
Total (wt%):	100.09	99.29	99.60	98.19	96.65	89.43	99.43	92.39	99.71
LOI (wt%):	1.93	1.93	4.57	4.57	2.22	5.76	4.04	3.49	3.49
Trace element (ppm):									
Zr	87	112	130	138	131	75	132	81	85
Y	28	31	41	46	38	20	39	26	27
Sr	434	406	117	124	327	265	320	269	307
Zn	158	94	30	23	31	15	9	73	71
Cu	47	22	13	8	303	95	386	7	14
Ba	177	494	713	637	372	97	337	93	112
Whole-rock composition									
Major element oxide (wt%):									
SiO ₂	60.48	65.90	69.90	68.75	66.05	49.33	67.22	58.42	59.62
TiO ₂	0.74	0.62	0.54	0.55	0.55	0.61	0.51	0.51	0.67
Al ₂ O ₃	14.46	14.15	13.74	13.72	14.10	11.36	13.75	13.37	13.97
Fe ₂ O ₃	8.97	5.67	4.75	4.43	4.79	12.92	5.24	8.46	9.36
MnO	0.12	0.09	0.04	0.05	0.06	0.06	0.02	0.06	0.07
MgO	4.11	2.34	2.49	2.56	1.18	4.41	1.18	5.18	6.16
CaO	4.26	4.05	1.08	1.05	2.59	2.17	2.42	2.79	2.97
Na ₂ O	4.61	4.05	0.65	0.61	4.80	2.94	4.64	0.07	3.14
K ₂ O	0.06	0.32	1.76	1.89	0.28	0.11	0.34	BD	BD
P ₂ O ₅	0.35	0.19	0.11	0.09	0.10	0.37	0.08	0.30	0.29
Total S (%):	3.63	2.16	0.99	0.99	0.49	5.98	2.79	0.39	0.39
Total H ₂ O ⁺ (wt%):	0.87	0.68	3.36	3.36	1.44	2.33	2.17	2.18	2.18
S _{water-soluble sulfate} (wt%):	3.40	ND	1.09	ND	ND	6.03	2.82	0.43	ND

Table T12. Total sulfur and water concentration in samples analyzed by ICP-AES and unignited XRD samples, Hole 1188A.

Core, section, interval (cm)	Curated depth (mbsf)	Total Sulfur (wt%)			H ₂ O* unignited (wt%)
		Unignited	Ignited*	Ignited†	
193-1188A-					
2R-1, 9-12	9.69	0.02	ND	ND	1.21
5R-1, 38-40	33.98	0.06	ND	ND	ND
5R-1, 42-45	44.04	0.65	ND	0.02	7.93
7R-1, 62-64	48.82	4.66	0.74	0.36	4.75
7R-1, 92-93	49.12	2.81	ND	ND	ND
7R-1, 119-120	49.39	2.56	ND	ND	ND
7R-1, 145-147	49.65	9.24	ND	ND	ND
7R-2, 39-41	50.09	3.78	0.73	0.20	5.09
7R-2, 51-53	50.21	6.80	ND	ND	ND
8R-1, 66-69	58.56	2.53	0.32	0.15	5.42
8R-1, 124-127	59.14	5.00	0.63	0.20	4.90
8R-1, 147-148	59.37	7.44	ND	ND	ND
9R-1, 13-14	67.73	0.58	ND	ND	ND
9R-1, 67-70	68.27	4.33	0.21	0.09	3.63
9R-2, 79-81	69.89	5.13	ND	0.20	3.34
10R-1, 35-37	77.65	0.93	ND	ND	ND
11R-1, 35-38	87.25	5.47	0.53	0.33	3.49
11R-1, 56-57	87.46	4.75	ND	ND	ND
12R-1, 51-52	97.11	2.68	ND	ND	ND
12R-1, 69-70	97.29	2.88	ND	ND	ND
12R-1, 117-118	97.77	0.33	ND	ND	ND
12R-2, 48-51	98.56	0.63	0.01	ND	1.54
13R-1, 9-12	106.39	1.37	ND	ND	ND
14R-1, 44-45	116.47	3.95	0.69	0.06	3.08
14R-1, 92-93	116.92	1.73	ND	ND	ND
14R-1, 105-108	117.05	2.98	1.09	0.06	2.53
16R-1, 77-78	136.17	3.09	ND	ND	ND
16R-1, 95-98	136.35	3.42	0.56	0.03	3.24
16R-2, 12-15	136.98	3.63	ND	ND	0.87
16R-2, 40-43	137.26	2.16	0.11	BD	0.68
16R-2, 51-52	137.37	2.38	ND	ND	ND
16R-2, 68-69	137.54	2.41	ND	ND	ND
17R-1, 90-93	146.00	0.99	0.01	0.04	3.36
17R-1, 123-124	146.33	4.02	ND	ND	ND
18R-1, 28-29	154.98	1.12	ND	ND	ND
19R-1, 73-76	165.03	0.49	BD	ND	1.44
20R-1, 46-47	174.36	3.99	ND	ND	ND
20R-1, 74-77	174.62	5.98	BD	ND	2.33
20R-1, 75-76	174.64	5.98	BD	ND	2.33
20R-1, 92-95	174.82	2.79	BD	ND	2.17
20R-1, 102-103	174.92	4.23	ND	ND	ND
21R-1, 20-21	183.30	0.39	BD	ND	2.18

Notes: ICP-AES = inductively coupled plasma-atomic emission spectroscopy, XRD = X-ray diffraction. * = ignited at 600°C for 6 hr and then at 1050°C for 1 hr, † = ignited at 600°C for 6 hr and then at 1050°C for 4 hr. Detection limit = 0.01%. Instrument precision = ±0.04%. ND = not determined, BD = below detection. Loss on ignition (LOI) on Hole 1188A samples was carried out at 1050°C for 1 hr. Additionally, total sulfur post-LOI for the ICP-AES samples are reported.

Table T13. Analyses of the cations present in the supernatant and water-soluble sulfate measurements by IC and ICP-AES, Hole 1188A.

Core, section, interval (cm):	193-1188A-				
	8R-1, 124	14R-1, 44	15R-1, 10	16R-2, 12	20R-1, 75
Curated depth (mbsf):	59.14	116.47	125.80	136.98	174.64
Sulfur analysis (wt%):					
TS	5.63	4.64	19.40	3.63	6.31
S in LOI	0.63	0.69	ND	BD	BD
S in soluble sulfate	4.93	3.98	ND	3.39	6.31
S in sulfide	0.77	0.88	ND	0.23	0.33
Major cations associated with sulfates:					
CaO (wt%)	2.05	1.96	ND	3.86	2.31
Ba (ppm)	316	361	ND	170	93
Na ₂ O (wt%)	0.380	0.331	0.120	0.105	0.102
SiO ₂ (wt%)	0.022	0.016	0.002	BD	0.008
Al ₂ O ₃ (wt%)	0.001	ND	0.002	0.001	0.010
MnO (wt%)	0.003	0.001	0.001	BD	BD

Note: IC = ion chromatography, ICP-AES = inductively coupled plasma-atomic emission spectroscopy, TS = total sulfur, LOI = loss on ignition, ND = not determined, BD = below detection.

Table T14. NAA analyses of the bulk samples from Hole 1188A sent to CSIRO for midcruise shore-based analyses.

Element	Unit				Detection limit
Sb	ppm	0.6	<	<	0.1
As	ppm	11.6	6.8	4.2	0.5
Ba	ppm	346	422	325	100
Br	ppm	16.8	11.9	10.3	0.5
Cd	ppm	<	<	<	5
Ca	%	2.5	3.1	3.3	0.5
Ce	ppm	26	22.4	21.2	2
Cs	ppm	<	<	<	0.5
Cr	ppm	18.7	9.6	64.3	2
Co*	ppm	34.6	10	17.9	0.5
Eu	ppm	1.0	0.9	1	0.5
Au	ppb	8.8	2.8	3	2
Hf	ppm	3.3	3.3	2.7	0.5
Ir	ppb	<	<	<	5
Fe	%	3.0	2.5	3.1	0.02
La	ppm	10.2	9.3	8.7	0.5
Lu	ppm	0.5	0.4	0.4	0.2
Hg	ppm	<	<	<	1
Mo	ppm	<	<	<	5
K	%	0.8	0.5	0.4	0.2
Rb	ppm	17.8	18	<	10
Sm	ppm	4.1	3.2	3.3	0.2
Sc	ppm	11.4	9.9	12.6	0.1
Se	ppm	2.2	<	<	2
Ag	ppm	<	<	<	2
Na	%	0.64	1.3	1.76	0.01
Ta	ppm	<	<	<	1
Te	ppm	<	<	<	2

Notes: NAA = neutron activation analysis. CSIRO = Commonwealth Scientific and Industrial Research Organization. * = contamination possible from tungsten carbide mill. < = below detection limit. Analyst: H. Waldron, Becquerel Laboratories, Lucas Heights, Australia.

Table T15. ICP-AES analyses of the bulk samples from Hole 1188A sent to CSIRO for midcruise shore-based analyses.

Shipment number:	1188A-(1)	1188A-(2)	1188A-(3)	
Core 193-1188A-:	7R to 11R	12R to 17R	18R to 23R	
Depth (mbsf):	48.2-96.6	96.6-154.7	154.7-211.6	
CSIRO number:	142645A	142645B	142645C	
				Detection limit
<hr/>				
Oxide (wt%):				
TiO ₂	0.54	0.48	0.61	
Al ₂ O ₃	13.02	12.38	12.57	
Fe ₂ O ₃	4.43	3.69	4.67	
MnO	0.01	0.02	0.04	
MgO	1.35	1.26	2.78	
CaO	3.35	3.91	4.13	
Na ₂ O	0.88	1.78	2.44	
K ₂ O	1.15	1.18	0.84	
P ₂ O ₅	0.12	0.09	0.26	
S(tot)	4.95	3.73	2.71	
<hr/>				
Trace element (ppm):				
Li	<	<	<	5
Be	<	<	<	2
Sc	10	8	11	
V	30	18	92	
Cr	16	7	48	
Co*	31	8	19	
Ni	<	<	21	10
Cu	23	15	19	
Zn	124	14	28	
As	<	<	<	20
Sr	268	377	359	
Y	25	18	18	
Zr	103	89	62	
Mo	<	<	<	5
Ag	<	<	<	5
Sb	<	<	<	20
Ba	266	427	306	
La	10	9	10	
Yb	3	2	2	2
Lu	<	<	<	5
Pb	<	<	<	50
Au (ppb)	<	<	<	200

Notes: ICP-AES = inductively coupled plasma-atomic emission spectroscopy. CSIRO = Commonwealth Scientific and Industrial Research Organization. * = contamination possible from tungsten carbide mill. < = below detection limit. Analyst: L. Dotter, CSIRO, North Ryde, Australia.

Table T16. Major element oxides with selected trace elements by ICP-AES, Hole 1188F. (Continued on next page.)

Core, section: 193-1188F-:	1Z-1	1Z-1	1Z-2	1Z-3	1Z-3	2Z-1	7Z-1	7Z-1	7Z-1	7Z-1	8Z-1	11G-1	11G-1	13Z-1	16Z-1	16Z-1	19Z-1	22Z-1	26Z-1	30Z-1	34Z-1	
Interval (cm):	29-31	87-89	37-39	31-33	85-87	42-44	41-44	76-78	104-107	68-71	53-56	138-141	118-121	41-43	139-141	13-15	123-123	20-23	5-7	5-7		
Curated depth (mbsf):	218.29	218.87	219.57	220.71	221.25	221.92	235.41	235.76	236.04	236.88	NCD	NCD	242.58	255.31	256.29	268.53	283.33	300.30	318.15	336.45		
Rock type:	AD	AD			AD	BR	BR	AD	AD/GD	AD	AD	AD										
Alteration style:	Sil	Sil	Sil	Sil	Sil	Sil	Sil	Sil	GSC	Sil	Sil	Sil										
Ignited rock powder composition*:																						
Major element oxides (wt%):																						
SiO ₂	72.99	81.03	74.28	73.17	69.16	76.63	77.92	71.90	68.61	68.11	74.86	69.97	69.21	76.72	70.06	69.70	66.88	65.56	69.20	73.10		
TiO ₂	0.65	0.65	0.64	0.64	0.60	0.63	0.63	0.64	0.73	0.65	0.61	0.76	0.71	0.54	0.67	0.70	0.75	0.70	0.65	0.67		
Al ₂ O ₃	14.74	13.78	14.73	14.48	15.09	15.36	15.28	15.73	14.83	15.49	15.11	15.12	14.79	14.61	17.68	14.36	15.17	15.05	16.57	14.79		
Fe ₂ O ₃	3.66	2.21	3.11	3.38	8.23	0.29	0.20	2.72	6.98	7.17	0.41	5.16	5.77	4.68	6.11	8.74	6.91	6.32	5.23	5.09		
MnO	0.01	0.01	0.01	0.01	0.04	0.01	0.01	0.02	0.02	0.01	0.01	0.01	0.01	0.01	0.01	0.01	0.04	0.05	0.04	0.01		
MgO	1.06	0.34	0.87	1.67	3.20	0.09	0.13	3.89	3.93	0.49	0.19	0.35	1.77	0.08	0.11	0.18	3.50	3.51	2.46	1.64		
CaO	2.13	1.02	1.61	1.06	0.23	4.34	3.78	1.72	2.25	4.31	4.87	4.62	3.24	0.36	BD	3.37	3.34	3.24	1.18	2.37		
Na ₂ O	0.72	0.75	0.85	0.68	0.62	0.83	0.84	0.66	0.61	1.02	0.99	0.80	0.69	0.83	0.94	0.98	3.45	2.62	2.70	0.57		
K ₂ O	2.89	2.34	2.29	2.29	2.06	1.55	1.39	2.13	1.26	2.23	1.54	2.28	1.46	2.11	2.41	1.85	0.63	0.93	1.71	2.55		
P ₂ O ₅	0.13	0.11	0.14	0.15	0.17	0.15	0.16	0.16	0.31	0.14	0.15	0.29	0.28	0.10	0.07	0.26	0.37	0.30	0.17	0.02		
Total (wt%):	98.97	102.23	98.52	97.54	99.42	99.89	100.34	99.56	99.52	99.63	98.73	99.35	97.94	100.02	98.06	100.15	101.04	98.29	99.91	100.82		
LOI (wt%):	6.16	4.45	5.87	5.77	5.01	7.49	7.28	5.98	8.55	11.06	8.81	16.23	9.16	4.52	5.77	10.42	5.38	4.64	3.11	7.36		
Trace elements (ppm):																						
Zr	138	143	131	134	127	131	126	131	122	133	131	124	124	141	177	117	122	112	171	126		
Y	38	14	41	48	37	37	37	42	34	50	49	37	34	16	21	31	33	32	35	43		
Sr	185	86	125	84	53	674	663	148	185	362	487	466	295	89	70	291	335	285	238	172		
Zn	1	BD	BD	BD	24	BD	48	BD	2	BD	BD	BD	1	39	BD	12	14	14	43	6		
Cu	49	22	56	24	8	4	8	15	83	32	9	45	23	52	87	67	9	4	30	15		
Ba	1417	1332	1054	1096	1048	966	812	1147	450	1309	769	717	492	1003	1427	535	287	318	935	1231		
Whole rock composition:																						
Major element oxides (wt%):																						
SiO ₂	68.50	77.43	69.92	68.95	65.70	70.89	72.24	67.60	62.74	60.58	68.27	58.61	62.87	73.25	66.01	62.44	63.28	62.52	67.05	67.72		
TiO ₂	0.61	0.62	0.60	0.60	0.57	0.58	0.58	0.60	0.67	0.58	0.55	0.64	0.64	0.52	0.63	0.63	0.71	0.67	0.63	0.62		
Al ₂ O ₃	13.83	13.17	13.86	13.65	14.34	14.21	14.17	14.79	13.57	13.78	13.78	12.67	13.43	13.95	16.66	12.86	14.35	14.35	16.06	13.70		
Fe ₂ O ₃	3.43	2.11	2.93	3.19	7.82	0.27	0.19	2.55	6.38	6.37	0.37	4.32	5.24	4.47	5.76	7.83	6.54	6.03	5.07	4.71		
MnO	0.01	0.01	0.01	0.01	0.04	0.01	0.01	0.02	0.02	0.01	0.01	0.01	0.01	0.01	0.01	0.01	0.03	0.05	0.04	0.01		
MgO	0.99	0.33	0.82	1.57	3.04	0.08	0.12	3.65	3.60	0.44	0.17	0.29	1.61	0.07	0.10	0.16	3.31	3.35	2.38	1.52		
CaO	2.00	0.97	1.51	1.00	0.22	4.02	3.51	1.61	2.06	3.83	4.44	3.87	2.94	0.34	BD	3.01	3.16	3.09	1.14	2.20		
Na ₂ O	0.67	0.71	0.80	0.64	0.59	0.77	0.78	0.62	0.56	0.91	0.90	0.67	0.63	0.79	0.88	0.88	3.26	2.50	2.62	0.53		
K ₂ O	2.71	2.23	2.16	2.16	1.96	1.43	1.29	2.00	1.15	1.99	1.40	1.91	1.33	2.02	2.27	1.66	0.59	0.89	1.65	2.36		
P ₂ O ₅	0.12	0.10	0.13	0.14	0.17	0.14	0.14	0.15	0.28	0.12	0.13	0.24	0.25	0.09	0.07	0.23	0.35	0.29	0.16	0.02		
Total S (wt%):	3.43	2.14	3.40	3.23	2.79	1.31	1.57	1.86	6.47	7.71	2.31	5.57	6.82	3.61	5.54	8.25	4.07	2.05	0.78	0.49		
Total H ₂ O ⁺ (wt%):	2.50	2.18	2.74	3.11	3.81	2.33	2.36	3.62	4.03	2.51	2.24	2.26	3.13	2.13	2.77	2.15	2.55	2.61	2.83	1.44		
S _{water-soluble sulfate} (wt%):	0.99	0.55	0.77	0.54	0.05	1.34	1.51	0.66	0.97	0.96	1.80	1.61	ND	0.24	0.04	1.48	0.50	0.58	ND	0.88		

Notes: Rock type: AD = altered dacite, BR = breccia, GD = green dacite. Alteration type: Sil = silicified, GSG = green silica-clay. * = ignited for 6 hr at 600°C and then for 4 hr at 1050°C. LOI = loss on ignition. Total sulfur and post-LOI for the ICP-AES samples are reported. LOI was conducted at 1050°C for 4 hr. BD = below detection, ND = not determined, NCD = no curated depth.

Table T16 (continued).

Core, section: 193-1188F-:	35Z-1	35Z-2	37Z-2	38Z-2	39Z-1	40Z-1	40Z-1	41Z-2	42Z-1	43Z-1	43Z-1
Interval (cm):	46-48	41-43	18-20	90-92	41-43	3-5	36-38	7-10	72-74	3-5	67-69
Curated depth (mbsf):	340.46	341.91	346.00	351.19	353.91	358.03	358.36	363.95	367.72	371.53	372.17
Rock type:	AD	AD	AD	AD/GD	AD	AD	AD	AD	AD	AD	AD
Alteration style:	Sil	Sil	Sil	Sil	Sil	Sil	Sil/GSC	Sil	Sil/GSC	GSC	Sil
Ignited rock powder composition*:											
Major element oxides (wt%):											
SiO ₂	67.09	74.05	68.95	69.19	72.53	66.70	73.01	71.81	69.56	73.78	67.70
TiO ₂	0.66	0.70	0.66	0.76	0.85	0.78	0.48	0.55	0.73	0.56	0.75
Al ₂ O ₃	14.50	14.63	14.20	14.98	15.12	14.78	14.25	14.41	15.20	15.08	15.28
Fe ₂ O ₃	6.85	4.10	7.37	5.47	4.46	7.49	5.61	6.05	6.81	5.05	6.71
MnO	0.03	0.01	0.03	0.05	0.03	0.13	0.03	0.04	0.04	0.05	0.09
MgO	3.25	0.19	2.59	2.47	5.22	3.20	1.72	1.82	4.89	1.72	2.27
CaO	2.84	3.88	2.21	3.38	1.76	3.17	1.17	2.42	1.69	1.99	3.26
Na ₂ O	3.16	1.11	3.78	3.67	0.78	3.55	0.61	2.77	0.64	3.17	3.92
K ₂ O	0.82	2.01	0.68	0.52	1.84	0.29	3.15	1.68	2.23	1.26	0.17
P ₂ O ₅	0.05	BD	0.04	0.04	0.04	0.06	0.02	0.01	0.02	0.02	0.02
Total (wt%):	99.25	100.68	100.51	100.54	102.63	100.14	100.06	101.55	101.79	102.67	100.16
LOI (wt%):	5.44	7.85	3.36	3.66	5.46	3.22	5.19	5.10	7.11	3.32	2.12
Trace elements (ppm):											
Zr	121	126	121	115	115	115	146	141	125	148	121
Y	34	37	33	33	34	34	38	35	32	32	33
Sr	291	309	292	353	121	327	117	257	164	244	372
Zn	15	1	19	14	11	42	90	63	27	34	29
Cu	10	17	11	26	16	30	20	22	14	25	29
Ba	248	319	220	228	390	159	634	354	427	314	242
Whole rock composition:											
Major element oxides (wt%):											
SiO ₂	63.44	68.24	66.63	66.66	68.57	64.55	69.23	68.15	64.61	71.33	66.26
TiO ₂	0.63	0.65	0.64	0.74	0.80	0.75	0.46	0.52	0.67	0.54	0.74
Al ₂ O ₃	13.71	13.49	13.72	14.43	14.30	14.30	13.51	13.68	14.11	14.58	14.95
Fe ₂ O ₃	6.48	3.78	7.12	5.27	4.22	7.25	5.32	5.74	6.32	4.89	6.56
MnO	0.03	0.01	0.03	0.05	0.03	0.13	0.03	0.03	0.04	0.04	0.09
MgO	3.07	0.18	2.50	2.38	4.93	3.10	1.63	1.72	4.55	1.67	2.22
CaO	2.69	3.58	2.14	3.26	1.66	3.07	1.11	2.30	1.57	1.93	3.19
Na ₂ O	2.99	1.02	3.66	3.54	0.74	3.43	0.58	2.63	0.59	3.06	3.84
K ₂ O	0.77	1.85	0.66	0.50	1.74	0.28	2.99	1.59	2.07	1.22	0.17
P ₂ O ₅	0.04	BD	0.04	0.04	0.04	0.06	0.02	0.01	0.01	0.02	0.02
Total S (wt%):	5.03	5.45	4.28	2.85	1.82	1.69	4.28	4.97	4.48	2.81	0.71
Total H ₂ O ⁺ (wt%):	2.08	2.10	1.60	1.67	4.47	2.06	2.34	1.91	4.09	1.67	1.51
S _{water-soluble sulfate} (wt%):	0.54	1.28	0.09	0.43	0.52	0.36	0.49	0.56	0.75	0.27	0.04

Table T17. Total sulfur and water concentration in samples analyzed by ICP-AES and unignited XRD samples, Hole 1188F.

Core, section Interval (cm)	Curated depth (mbsf)	TS unignited (wt%)	TS ignited* (wt%)	H ₂ O+ unignited (wt%)	Core, section Interval (cm)	Curated depth (mbsf)	TS unignited (wt%)	TS ignited* (wt%)	H ₂ O+ unignited (wt%)
193-1188F-					23Z-2, 24-25	288.34	3.25	ND	3.96
1Z-1, 4-5	218.04	3.63	ND	2.02	23Z-2, 45-46	288.55	0.61	ND	3.78
1Z-1, 29-31	218.29	3.43	0.10	2.50	25Z-1, 24-26	295.84	1.58	ND	2.68
1Z-1, 87-89	218.87	2.14	0.00	2.18	26Z-1, 20-23	300.30	2.05	0.00	2.61
1Z-2, 4-5	219.24	1.42	ND	2.43	26Z-2, 60-61	301.78	2.42	ND	4.31
1Z-2, 37-39	219.57	3.40	0.05	2.74	27Z-1, 22-23	304.82	3.04	ND	3.48
1Z-3, 20-21	220.60	3.72	ND	2.33	30Z-1, 5-7	318.15	0.78	0.00	2.83
1Z-3, 31-33	220.71	3.23	0.02	3.11	31Z-1, 1-3	322.61	1.77	ND	1.29
1Z-3, 35-36 rim	220.75	9.96	ND	1.90	31Z-1, 39-42	322.99	0.97	ND	2.95
1Z-3, 35-36 core	220.75	2.73	ND	2.22	34Z-1, 5-7	336.45	4.77	0.42	2.98
1Z-3, 85-87	221.25	2.79	0.00	3.81	34Z-1, 22-23	336.62	4.16	ND	2.26
1Z-3, 106-108	221.46	2.49	ND	3.28	34Z-1, 27-28	336.67	0.78	ND	3.80
1Z-4, 90-91	222.50	4.05	ND	2.25	34Z-1, 40-41	336.80	3.05	ND	3.72
2Z-1, 42-44	221.92	1.31	0.23	2.33	34Z-1, 89-90	337.29	1.05	ND	4.04
2Z-1, 73-74	222.23	1.41	ND	2.37	35Z-1, 5-6	340.05	2.25	ND	2.62
3Z-1, 6-7	222.66	1.12	ND	2.86	35Z-1, 46-48	340.46	5.03	0.06	2.08
3Z-2, 40-41	224.45	5.86	ND	2.56	35Z-2, 41-43	341.77	5.45	0.29	2.10
3Z-2, 150-151	225.55	6.74	ND	2.95	35Z-2, 48-49	341.98	5.87	ND	2.06
6Z-1, 20-21	233.30	4.32	ND	3.70	37Z-1, 6-7	344.56	0.75	ND	1.06
6Z-1, 46-47	233.56	1.31	ND	2.87	37Z-2, 18-20	346.00	4.28	0.02	1.60
6Z-1, 77-78	233.87	2.43	ND	2.31	37Z-2, 31-33	346.13	4.63	ND	6.15
6Z-2, 47-48	234.81	3.65	ND	4.94	37Z-2, 65-68	346.47	2.02	ND	1.58
7Z-1, 41-44	235.41	1.57	0.00	2.36	37Z-2, 120-121	347.02	0.91	ND	2.46
7Z-1, 76-78	235.75	1.86	0.04	3.62	38Z-2, 90-92	351.19	2.85	0.00	1.67
7Z-1, 104-107	236.04	6.47	0.27	4.03	39Z-1, 7-8	353.57	4.25	ND	2.25
7Z-2, 0-36	236.51	2.95	ND	1.97	39Z-1, 41-43	353.91	1.82	0.17	4.47
8Z-1, 68-71	236.88	7.71	0.02	2.51	39Z-2, 18-19	355.10	5.04	ND	2.73
9Z-1, 9-12	237.79	1.03	ND	3.40	40Z-1, 3-5	358.03	1.69	0.00	2.06
11G-1, 53-56	NCD	2.31	0.02	2.24	40Z-1, 36-38	358.36	4.28	0.11	2.34
11G-1, 138-141	NCD	5.57	0.40	2.26	40Z-2, 35-36	359.71	3.19	ND	2.55
13Z-1, 118-121	242.58	6.82	0.15	3.13	41Z-1, 46-47	362.96	2.51	ND	1.19
13Z-2, 51-56	243.27	4.49	ND	2.14	41Z-2, 7-10	363.95	4.97	0.04	1.91
13Z-2, 55-70	243.31	4.76	ND	4.16	42Z-1, 30-31	367.30	2.42	ND	2.14
14Z-1, 134-139	247.24	7.30	ND	2.73	42Z-1, 72-74	367.72	4.48	0.08	4.09
15Z-1, 66-96	251.06	6.73	ND	2.66	43Z-1, 3-5	371.53	2.81	0.03	1.67
15Z-1, 90-95	251.30	3.94	ND	2.70	43Z-1, 6-8	371.56	3.02	ND	3.29
16Z-1, 41-43	255.31	3.61	0.00	2.13	43Z-1, 67-69	372.17	0.71	0.00	1.51
16Z-1, 139-141	256.29	5.54	0.00	2.77	43Z-1, 90-91	372.40	0.79	ND	1.51
19Z-1, 13-15	268.53	8.25	0.00	2.15	44Z-1, 85-86	374.85	0.65	ND	2.23
22Z-1, 63-67	282.73	4.16	ND	2.76					
22Z-1, 123-123	283.33	4.07	0.00	2.55					
23Z-1, 25-26	286.85	2.85	ND	3.18					
23Z-1, 102-103	287.62	2.70	ND	4.13					
23Z-2, 13-14	288.23	23.04	ND	0.32					

Notes: TS = total sulfur. * = ignited at 600°C for 6 hr and then at 1050°C for 4 hr. NCD = no curated depth, BD = below detection, ND = not determined. Detection limit = 0.01%. Accuracy and precision = ± 0.04%.

Table T18. Water chemistry data for downhole water sampler, temperature, and pressure probe sampling of borehole fluids, Holes 1188B and 1188F.

	Hole:	Hole 1188F		Seawater	
		1188B	Sample 1		Sample 2
	Date:	22 Dec	28 Dec	29 Dec	22 Dec
Water depth (mbsf)	3	107	207	Surface	
Temperature (°C)	6	12	21	30	
pH	7.89	8.04	7.74	8.4	
Alkalinity (mmol/L)	2.06	2.277	1.909	2.18	
Salinity (‰)	31	34	35	34	
				IAPSO	
Na ⁺ (mmol/L)	433.3	479.6	470.0	480	
K ⁺ (mmol/L)	9.5	10.4	10.2	10.4	
Mg ²⁺ (mmol/L)	50.2	54.8	54.6	54	
Ca ²⁺ (mmol/L)	11.3	10.0	10.5	10.5	
Cl ⁻ (mmol/L)	506	562	552	559	
SO ₄ ²⁻ (mmol/L)	28.7	29.6	29.1	28.9	
B ³⁺ (μmol/L)	341	438	423	450	
Mn ⁺ (μmol/L)	278	3	4	—	
Fe _{tot} (μmol/L)	7	7	19	—	
Sr ²⁺ (μmol/L)	98	104	101	87	
Ba ²⁺ (μmol/L)	6	6	6	—	
Li ⁺ (μmol/L)	36	26	27	27	

Notes: Fe_{tot} = total iron. IAPSO = seawater standard. — = not analyzed.

Table T19. Total bacterial count and biomass activities.

Hole, core	Depth (mbsf)	Direct count (cells/cm ³)*	ATP (pg/cm ³)†	Active bacterial cells based on ATP content‡ (cells/cm ³)
193-1188A-				
5R	33.77	1.5 x 10 ⁷	65.5	1.3 x 10 ⁶
7R	48.75	5.8 x 10 ⁵	26.0	5.2 x 10 ⁵
8R	59.58	ND	ND	<1 x 10 ⁴
9R	68.97	ND	ND	<1 x 10 ⁴
11R	87.89	ND	ND	<1 x 10 ⁴
12R	97.88	ND	ND	<1 x 10 ⁴
18R	155.19	ND	ND	<1 x 10 ⁴
21R	184.15	ND	ND	<1 x 10 ⁴
193-1188F-				
1Z	222.23	ND	NM	
3Z	224.75	ND	NM	
8Z	236.36	ND	NM	
13Z	242.14	ND	NM	
16Z	255.78	ND	NM	
22Z	282.95	ND	NM	
26Z	301.52	ND	NM	

Notes: * = detection limit of 1 x 10⁵ cells/cm³. ATP = adenosine triphosphate. † = detection limit of 0.5 pg/cm³ (1 x 10⁴ cells/cm³). ‡ = ATP content of a bacteria is ~1 x 10⁻¹⁹ mol/cell. ND = not detected (below detection). NM = not measured.

Table T20. Enrichment cultivation at different culture conditions, Holes 1188A and 1188F.

Hole, core	Depth (mbsf)	Aerobic cultivation			Anaerobic cultivation		
		4°C	25°C	60°C	25°C	60°C	90°C
193-1188A-							
2R	9.6	+	+	-	+	+	+
5R	33.77	-	++	-	+	+	+
7R	48.75	-	-	-	++	-	-
8R	59.58	-	-	-	-	-	-
9R	68.97	-	-	-	-	-	-
193-1188F-							
1Z	222.23	-	+	-	+	-	-
3Z	224.75	-	+	-	-	-	-

Note: - = no growth, + = growth, ++ = more growth.

Table T21. Compressional wave velocity data, Site 1188.

Core, section, interval (cm)	Piece	Depth (mbsf)	Velocity (km/s)	Sil/Qtz	Anh	Cl	Py	Plag	Mt	Vesicles	Alteration	Comments
193-1188A-												
7R-2, 77.5	6	50.48	3.5	30	15	45	10	0	0	0	Vh	Clastic rock with ≤ 2 -cm clasts with flow-banded texture.
10R-2, 61.5	10	79.40	4.7	35	7	23	3	31	0	Tr	Hi	Aphyric sparsely vesicular. Small vein completely filled with quartz-pyrite.
12R-2, 44	4	98.70	3.6	65	Tr	30	2	0	0	0	Cm	Spectacular folded flow banding: chlorite bands with isolated spherulites + light gray clay-rich bands; band thickness = 1–5 mm.
16R-1, 63	9	136.03	4.6	80	1	10	7	2	0	3	Vh	Dark gray, light gray; round vesicles 1–2 mm. Traces of a chlorite.
16R-2, 46	7	137.32	3.9	42	0	15	5	37	0	Tr	Hi	Fine volcanic rock with obvious lamination.
17R-2, 30	6	146.90	4.4	55	20	20	Tr	0	5	0	Cm	Jigsaw breccia, possibly after perlitic texture.
19R-1, 86	16	165.16	3.8	35	1	10	Tr	35	3	5	Hi	Flattened ovoid vesicles, only partly filled by anhydrite. Vesicles mostly <1 mm, varying up to 1 cm (long dimension).
193-1188F-												
13Z-1, 35	2	241.75	4.5	40	1	56	2	1	0	0	Cm	Autoclastic breccia with quartz-filled vesicles.
14Z-1, 61	3	246.51	5.8	45	Tr	42	1	12	Tr	0	Vh	Silicified volcanic rock with quartz-filled, flattened vesicles.
19Z-1, 14	1B	261.54	4.8	26	2	67	5	0	Tr	0	Cm	Silicified volcanic rock with quartz-filled, flattened vesicles.
26Z-1, 21	2	300.31	3.8	65	2	28	Tr	5	Tr	3	Cm	Silicified porphyritic volcanic rock with relict plagioclase phenocrysts.
34Z-1, 46	9A	336.86	5.3	57	0	40	1	0	2	2	Cm	Aphyric volcanic rock with magnetite.
37Z-2, 19	2	346.01	6.3	45	Tr	30	5	20	Tr	0	Hi	Aphyric, sparsely vesicular volcanic rock.
38Z-2, 89	4	351.18	6.2	30	2	35	1	32	Tr	1	Hi	Sparsely plagioclase-phyric volcanic rock.
39Z-1, 42	6	353.92	4.0	60	1	39	Tr	0	Tr	3	Cm	Sparsely plagioclase-phyric volcanic rock.

Notes: Sil/Qtz = silica/quartz, Anh = anhydrite, Cl = clay, Py = pyrite, Plag = plagioclase, Mt = magnetite. Tr = trace. Cm = complete, Vh = very high, Hi = high.

Table T22. Index properties, Holes 1188A and 1188F. (See table note. Continued on next page.)

Core, section, interval (cm)	Piece	Type	Depth (mbsf)	Bulk water content (%)	Density (g/cm ³)			Porosity (%)	Void ratio
					Bulk	Dry	Grain		
193-1188A-									
3R-1, 13-15	3	Minicore	19.33	0.2	2.335	2.331	2.341	0.4	0.004
5R-1, 45-47	8	Minicore	34.05	6.8	1.860	1.733	1.979	12.4	0.142
7R-1, 73-75	12	Minicore	48.93	14.9	2.127	1.811	2.621	30.9	0.447
7R-2, 0-28	1	Rock fragment	49.70	20.6	2.026	1.609	2.712	40.7	0.685
7R-2, 76-78	6	Minicore	50.46	15.7	2.065	1.741	2.547	31.6	0.463
8R-1, 75-97	9	Rock fragment	58.65	14.9	2.078	1.769	2.533	30.2	0.432
9R-1, 24-26	4	Minicore	67.84	22.5	1.996	1.546	2.755	43.9	0.782
9R-2, 37-48	2	Rock fragment	69.47	23.3	1.937	1.485	2.659	44.1	0.790
9R-2, 76-90	6	Rock fragment	69.86	13.3	2.226	1.929	2.717	29.0	0.409
10R-1, 117-119	11	Minicore	78.47	11.9	2.256	1.988	2.694	26.2	0.355
10R-2, 60-62	10	Minicore	79.38	4.8	2.409	2.294	2.586	11.3	0.127
11R-1, 84-100	7	Rock fragment	87.74	10.3	2.300	2.063	2.686	23.2	0.302
12R-2, 0-9	1	Rock fragment	98.08	11.3	2.218	1.967	2.608	24.6	0.326
12R-2, 43-45	11	Minicore	98.51	10.6	2.210	1.976	2.562	22.8	0.296
13R-1, 118-127	15	Rock fragment	107.48	11.9	2.320	2.044	2.797	26.9	0.368
14R-1, 52-56	8	Rock fragment	116.52	18.8	2.130	1.729	2.840	39.1	0.643
14R-1, 102-104	14	Minicore	117.02	20.3	2.031	1.618	2.712	40.3	0.676
15R-1, 73-76	18	Rock fragment	126.43	8.9	2.393	2.180	2.753	20.8	0.263
16R-1, 62-64	9	Minicore	136.02	6.2	2.413	2.264	2.649	14.6	0.170
16R-1, 116-121	18	Rock fragment	136.56	9.3	2.370	2.150	2.740	21.6	0.275
16R-2, 45-47	7	Minicore	137.31	7.7	2.390	2.206	2.691	18.0	0.220
17R-1, 77-86	11	Rock fragment	145.87	9.0	2.341	2.129	2.685	20.7	0.261
17R-1, 108-110	22	Minicore	146.18	12.7	2.234	1.951	2.696	27.6	0.382
17R-2, 29-31	6	Minicore	146.89	9.9	2.329	2.098	2.709	22.5	0.291
18R-1, 87-97	20	Rock fragment	155.57	9.8	2.314	2.088	2.681	22.1	0.284
19R-1, 34-36	7	Rock fragment	164.64	6.1	2.374	2.229	2.597	14.2	0.165
19R-1, 63-65	13	Rock fragment	164.93	4.7	2.384	2.272	2.551	10.9	0.123
19R-1, 85-87	16	Minicore	165.15	7.4	2.329	2.156	2.593	16.9	0.203
20R-1, 41-43	6	Minicore	174.31	17.8	2.102	1.728	2.721	36.5	0.575
20R-1, 82-90	11	Rock fragment	174.72	9.1	2.409	2.189	2.786	21.4	0.273
21R-1, 10-19	2	Rock fragment	183.20	8.1	2.409	2.215	2.734	19.0	0.234
21R-1, 27-29	3	Minicore	183.37	13.0	2.243	1.951	2.727	28.4	0.398
21R-1, 82-84	10	Minicore	183.92	10.1	2.379	2.139	2.795	23.5	0.307
23R-1, 0-19	1	Rock fragment	202.10	17.2	2.125	1.760	2.737	35.7	0.556
193-1188F-									
1Z-1, 84-86	5A	Minicore	218.84	10.5	2.410	2.157	2.865	24.7	0.328
1Z-2, 92-120	4	Rock fragment	220.12	11.0	2.349	2.090	2.798	25.3	0.339
1Z-3, 61-120	3	Rock fragment	221.01	8.6	2.437	2.227	2.799	20.4	0.257
1Z-4, 55-57	1A	Minicore	222.15	9.3	2.370	2.149	2.740	21.6	0.275
1Z-4, 62-120	2	Rock fragment	222.22	7.8	2.509	2.313	2.861	19.1	0.237
2Z-1, 105-107	2H	Minicore	222.55	10.6	2.369	2.118	2.807	24.6	0.325
3Z-1, 22-70	1C	Rock fragment	222.82	7.4	2.515	2.328	2.848	18.3	0.223
3Z-2, 0-51	1A	Rock fragment	224.05	10.2	2.397	2.152	2.827	23.9	0.313
3Z-2, 121-123	2A	Minicore	225.26	9.1	2.391	2.174	2.760	21.2	0.269
6Z-1, 94-124	4B	Rock fragment	234.04	5.8	2.533	2.386	2.787	14.4	0.168
6Z-2, 87-101	3C	Rock fragment	235.21	6.9	2.569	2.391	2.893	17.4	0.210
7Z-1, 57-86	1E	Rock fragment	235.57	7.6	2.477	2.290	2.802	18.3	0.224
7Z-1, 127-150	2D	Rock fragment	236.27	7.3	2.576	2.387	2.926	18.4	0.226
8Z-1, 90-111	2A	Rock fragment	237.10	4.9	2.578	2.451	2.799	12.5	0.142
9Z-1, 21-47	1D	Rock fragment	237.91	6.2	2.610	2.447	2.910	15.9	0.189
11G-1, 66-68	7	Rock fragment	NCD	7.9	2.529	2.330	2.893	19.5	0.242
13Z-1, 34-36	2	Minicore	241.74	7.0	2.247	2.090	2.468	15.3	0.181
13Z-1, 83-105	5A	Rock fragment	242.23	8.0	2.550	2.346	2.929	19.9	0.248
14Z-1, 60-62	1	Minicore	246.50	7.6	2.467	2.280	2.789	18.2	0.223
15Z-1, 62-90	9	Rock fragment	251.02	5.9	2.614	2.459	2.898	15.1	0.178
15Z-1, 142-144	16	Minicore	251.82	11.9	2.388	2.103	2.913	27.8	0.385
15Z-2, 0-12	1	Rock fragment	251.90	9.1	2.416	2.196	2.795	21.4	0.273
16Z-1, 78-92	2	Rock fragment	255.68	6.4	2.761	2.584	3.124	17.3	0.209
17Z-1, 7-9	1	Minicore	259.47	9.4	2.501	2.265	2.943	23.0	0.299
18Z-1, 13-30	1B	Rock fragment	264.03	6.9	2.492	2.319	2.789	16.9	0.203
19Z-1, 13-15	1B	Minicore	268.53	7.2	2.532	2.348	2.861	17.9	0.218
22Z-1, 80-89	11	Rock fragment	282.90	5.7	2.572	2.426	2.829	14.2	0.166
22Z-1, 106-117	14	Rock fragment	283.16	10.1	2.46	2.212	2.921	24.3	0.321
22Z-1, 121-123	15	Minicore	283.31	8.5	2.395	2.192	2.736	19.9	0.249
23Z-1, 9-14	2	Rock fragment	286.69	6.7	2.666	2.487	3.015	17.5	0.212

Table T22 (continued).

Core, section, interval (cm)	Piece	Type	Depth (mbsf)	Bulk water content (%)	Density (g/cm ³)			Porosity (%)	Void ratio
					Bulk	Dry	Grain		
23Z-1, 112-119	11B	Rock fragment	287.72	4.7	2.601	2.479	2.814	11.9	0.135
23Z-2, 69-83	8	Rock fragment	288.79	8.7	2.468	2.254	2.848	20.9	0.264
26Z-1, 20-23	2	Minicore	300.30	8.3	2.435	2.234	2.780	19.7	0.245
26Z-1, 30-93	4	Rock fragment	300.40	6.0	2.557	2.402	2.829	15.1	0.178
31Z-1, 35-37	5	Minicore	322.95	5.6	3.145	2.969	3.585	17.2	0.208
34Z-1, 31-37	7	Rock fragment	336.71	5.4	2.571	2.432	2.813	13.6	0.157
34Z-1, 45-47	14A	Minicore	336.85	4.6	2.574	2.455	2.779	11.6	0.132
34Z-1, 71-88	13A	Rock fragment	337.11	7.9	2.472	2.276	2.814	19.1	0.236
34Z-1, 108-110	14	Minicore	337.48	7.9	2.392	2.204	2.700	18.4	0.225
35Z-1, 23-30	2B	Rock fragment	340.23	6.0	2.503	2.352	2.758	14.7	0.173
35Z-1, 44-46	2D	Minicore	340.44	5.2	2.545	2.411	2.773	13.0	0.150
35Z-2, 28-38	2A	Rock fragment	341.78	11.2	2.377	2.111	2.854	26.0	0.352
37Z-1, 66-123	3	Rock fragment	345.16	8.3	2.356	2.160	2.671	19.1	0.237
37Z-2, 18-20	2	Minicore	346.00	4.7	2.540	2.420	2.741	11.7	0.132
37Z-2, 28-34	3	Rock fragment	346.10	5.2	2.535	2.402	2.760	13.0	0.149
37Z-2, 65-113	7	Rock fragment	346.47	6.4	2.473	2.314	2.738	15.5	0.183
37Z-2, 123-146	9	Rock fragment	347.05	8.2	2.380	2.185	2.698	19.0	0.235
38Z-1, 13-74	2A	Rock fragment	349.13	8.3	2.437	2.235	2.784	19.7	0.246
38Z-2, 0-45	1	Rock fragment	350.29	5.3	2.615	2.476	2.864	13.6	0.157
38Z-2, 88-90	4	Minicore	351.17	4.9	2.540	2.415	2.752	12.2	0.139
39Z-1, 41-43	6A	Minicore	353.91	7.8	2.439	2.249	2.762	18.5	0.228
39Z-1, 46-54	6B	Rock fragment	353.96	7.3	2.499	2.316	2.819	17.8	0.217
39Z-1, 70-76	8A	Rock fragment	354.20	6.7	2.462	2.297	2.738	16.1	0.192
39Z-1, 132-139	12A	Rock fragment	354.82	8.0	2.471	2.273	2.818	19.3	0.240
40Z-1, 3-5	1	Minicore	358.03	7.6	2.403	2.221	2.703	17.8	0.217
40Z-1, 21-28	2B	Rock fragment	358.21	7.9	2.506	2.309	2.859	19.2	0.238
40Z-1, 122-135	3F	Rock fragment	359.22	6.5	2.557	2.392	2.852	16.1	0.192
40Z-2, 65-83	2B	Rock fragment	360.01	5.9	2.571	2.419	2.839	14.8	0.174
41Z-1, 49-59	3D	Rock fragment	362.99	7.4	2.464	2.281	2.778	17.9	0.218
41Z-2, 12-32	2B	Rock fragment	364.00	7.4	2.531	2.344	2.868	18.3	0.224
42Z-1, 75-97	4F	Rock fragment	367.75	5.9	2.521	2.373	2.775	14.5	0.170
43Z-1, 0-54	1	Rock fragment	371.50	5.4	2.609	2.468	2.862	13.8	0.160
43Z-1, 3-5	1	Minicore	371.53	6.1	2.461	2.309	2.709	14.8	0.173
43Z-1, 67-69	3A	Minicore	372.17	5.8	2.486	2.343	2.723	14.0	0.162
44Z-1, 0-40	1	Rock fragment	374.00	4.9	2.592	2.466	2.812	12.3	0.141

Note: NCD = no curated depth.

Table T23. Grain density of powders analyzed by inductively coupled plasma-atomic emission spectroscopy, Holes 1188A and 1188F.

Core, section, interval (cm)	Depth (mbsf)	Grain density (g/cm ³)
193-1188A-		
2R-1, 9-12	9.69	2.48
5R-1, 42-45	34.02	2.23
7R-1, 62-64	48.82	2.83
7R-2, 39-41	50.09	2.62
8R-1, 66-69	58.56	2.45
8R-1, 124-127	59.14	3.13
9R-1, 67-70	68.27	2.71
9R-2, 79-81	69.89	2.83
11R-1, 35-38	87.25	2.74
12R-2, 48-51	98.56	2.70
14R-1, 47-51	116.47	2.84
14R-1, 105-108	117.05	2.50
16R-1, 95-98	136.35	2.70
16R-2, 12-15	136.98	2.81
16R-2, 40-43	137.26	2.70
17R-1, 90-93	146.00	3.22
19R-1, 73-76	165.03	2.67
20R-1, 74-77	174.64	2.95
21R-1, 20-24	183.30	3.45
193-1188F-		
1Z-1, 29-31	218.29	2.82
1Z-1, 87-89	218.87	2.82
1Z-2, 37-39	219.57	2.89
1Z-3, 31-33	220.71	2.93
1Z-3, 85-87	221.25	2.79
2Z-1, 42-44	221.92	2.76
7Z-1, 41-44	235.41	2.83
7Z-1, 76-78	235.76	2.89
7Z-1, 104-107	236.04	2.90
8Z-1, 68-71	236.88	3.18
11G-1, 53-56	NCD	2.79
11G-1, 138-141	NCD	2.79
13Z-1, 118-121	242.58	2.85
16Z-1, 41-43	255.32	2.84
16Z-1, 139-141	256.29	2.79
19Z-1, 13-15	268.53	2.87
22Z-1, 123-123	283.33	2.75
26Z-1, 20-23	300.30	2.85
30Z-1, 5-7	318.15	2.79
34Z-1, 5-7	336.45	2.47
35Z-1, 46-48	340.46	2.48
35Z-2, 41-43	341.91	2.41
37Z-2, 18-20	346.00	2.49
38Z-2, 90-92	351.19	2.35
39Z-1, 41-43	353.91	2.45
40Z-1, 3-5	358.03	2.43
40Z-1, 36-38	358.36	2.51
42Z-1, 72-74	367.72	2.45
43Z-1, 3-5	371.53	2.47
43Z-1, 67-69	372.17	2.42

Note: NCD = no curated depth.

Table T24. Magnetic properties of minicores, Holes 1188A and 1188F.

Number	Core, section, interval (cm)	Depth (mbsf)	Vertically oriented	Volume (cm ³)	NRM (mA/m)	Susceptibility (10 ⁻⁵ SI)	Koenigsberger ratio	Stable inclination (°)	Stable declination (°)	Brief description
193-1188A-										
1	3R-1, 14	19.34	No	9.4	2,760	1,959	48			Black, vesicular
2	5R-1, 46	34.06	No	9.8	823	729	39			Black, massive
3	7R-1, 74	48.94	Yes	13.8	2			-11	180	Gray
4	7R-2, 78	50.48	Yes	11.9	0	13*	1	-4	354	Green, brecciated
5	9R-1, 25	67.85	Yes	11.9	1			-4	289	Gray, massive, vesicular
6	10R-1, 118	78.48	Yes	12.0	94	34*	95	0	99	Gray, massive, vesicular
7	10R-2, 61	79.41	Yes	11.7	446	1,819	8	-16	74	Gray, massive
8	12R-2, 44	98.54	Yes	14.0	86	97	31	-28	69	Gray-light green, brecciated, hard
9	14R-1, 103	117.03	Yes	12.9	19	5*	140	-3	267	White-light gray, brecciated, soft
10	16R-1, 63	136.03	Yes	12.4	507	1,790	10	-15	274	Light-dark gray, fine grain
11	16R-2, 46	137.36	Yes	13.6	97	98	34	-20	198	Gray, hard
12	17R-1, 109	146.19	Yes	12.5	11,610	5,318	75	-21	168	Light-dark gray, fine grain
13	17R-2, 30	146.90	Yes	12.9	4,677	5,430	30	-16	144	Light gray, brecciated
14	19R-1, 86	165.16	Yes	10.9	898	4,343	7	-14	301	Dark gray, fine grained
15	20R-1, 42	183.52	Yes	12.0	2,958	3,778	27	-22	274	Dark gray-light green, soft
16	21R-1, 28	192.98	Yes	14.0	2,266	6,724	12	-5	259	Dark gray-light green, soft
17	21R-1, 83	193.53	Yes	10.3	1,574	11,599	5	18	116	Dark gray-light green, soft
193-1188F-										
18	1Z-1, 85	218.85	No	6.4	60	25	81			Light gray, massive, soft
19	1Z-4, 56	222.16	Yes	16.6	85	44	66	-25	333	Gray, massive, soft
20	2Z-1, 106	222.56	No	11.3	90	33	94			Light gray, massive, soft
21	3Z-2, 122	225.27	Yes	13.2	51	21	85	-14	223	Light gray, massive, soft
22	13Z-1, 32	241.72	No	14.8	45	22	69			Light-moderate gray, massive, hard
23	13Z-1, 35	241.75	No	8.9	38	16	80			Light-moderate gray, massive, hard
24	14Z-1, 61	246.51	Yes	6.5	25	38	23	-17	78	Light-moderate gray, massive, hard
25	15Z-1, 143	251.83	No	13.1	50	56	31			Light-moderate gray, massive, soft
26	17Z-1, 8	259.48	No	16.0	14	5	101			Light-moderate gray, massive, hard
27	19Z-1, 14	268.54	No	12.0	52	17	103			Light-moderate gray, massive, hard
28	22Z-1, 123	283.33	No	10.6	50	44	39			Gray-slightly green, massive, hard
29	25Z-1, 25	295.85	No	12.9	192	250	26			Gray, massive, hard
30	26Z-1, 21	300.31	No	13.0	123	132	32			Gray, massive, hard
31	31Z-1, 36	322.96	No	13.9	199	99	69			Light-moderate gray
32	34Z-1, 46	336.86	No	12.8	12,660	4,799	91			Black-dark gray, brecciated, hard
33	34Z-1, 109	337.49	No	14.0	229	43	184			Light-moderate gray, brecciated, hard
34	35Z-1, 45	340.45	Yes	6.6	153	124	43	-25	59	Gray, massive, hard
35	37Z-2, 19	346.01	No	12.9	473	307	53			Gray, massive, hard
36	38Z-2, 89	351.18	No	11.1	654	174	130			Gray, massive, dark gray spots, hard
37	39Z-1, 42	353.92	No	11.8	148	106	48			Light gray, massive, slightly vesicular
38	40Z-1, 4	358.04	No	11.8	3,977	3,524	39			Gray, massive, dark gray spots, hard
39	43Z-1, 4	371.54	No	15.5	55	22*	84			Light gray-light green, massive, fractures
40	43Z-1, 68	372.18	Yes	12.7	1,660	5,301	11	-16	343	Dark-moderate gray, hard

Notes: * = values that were not taken using a full 15-position measurement. NRM = natural remanent magnetization.

Table T25. Anisotropy of magnetic susceptibility values for the normalized principal susceptibility values and directions.

Core, section, interval (cm)	Depth (mbsf)	k (10^{-5} SI)	k_{\max}			k_{int}			k_{\min}			Error (10^{-5} SI)	P
			Magnitude	Declination ($^{\circ}$)	Inclination ($^{\circ}$)	Magnitude	Declination ($^{\circ}$)	Inclination ($^{\circ}$)	Magnitude	Declination ($^{\circ}$)	Inclination ($^{\circ}$)		
193-1188A-													
3R-1, 14	19.34	1959	1.0409	340	22	0.9843	180	67	0.9747	73	7	12.00	1.0679
5R-1, 46	34.06	729	1.0034	90	36	0.9994	270	54	0.9972	360	1	0.50	1.0063
10R-2, 61	79.41	1819	1.0095	80	14	1.0038	180	35	0.9868	332	52	14.00	1.0230
12R-2, 44	98.54	97	1.0345	81	7	1.0041	180	52	0.9613	346	37	2.51	1.0761
16R-1, 63	136.03	1790	1.0302	350	16	0.9909	180	74	0.9789	82	2	14.60	1.0525
16R-2, 46	137.36	98	1.0090	90	47	1.0014	234	38	0.9895	339	19	0.13	1.0197
17R-1, 109	146.19	5318	1.0160	90	37	1.0145	342	22	0.9695	229	45	30.00	1.0480
17R-2, 30	146.90	5430	1.0788	360	1	0.9888	90	39	0.9323	270	51	50.50	1.1571
19R-1, 86	165.16	4343	1.0100	180	28	1.0042	105	26	0.9857	230	50	10.00	1.0247
20R-1, 42	183.52	3778	1.0091	360	1	1.0059	90	23	0.9849	270	67	37.00	1.0246
21R-1, 28	192.98	6724	1.0180	360	57	1.0135	112	14	0.9684	210	29	11.00	1.0512
21R-1, 83	193.53	11599	1.0154	321	38	0.9923	180	45	0.9923	68	20	16.00	1.0233
193-1188F-													
1Z-1, 85	218.85	25	1.0056	270	54	0.9977	360	1	0.9967	90	36	0.02	1.0090
1Z-4, 56	222.16	44	1.0040	90	67	0.9999	360	1	0.9961	270	23	0.13	1.0079
2Z-1, 106	222.56	33	1.0082	233	41	0.9975	90	43	0.9943	341	19	0.03	1.0140
3Z-2, 122	225.27	21	1.0108	90	41	1.0045	270	49	0.9846	360	1	0.03	1.0266
13Z-1, 32	241.72	22	1.0225	360	51	1.0065	117	20	0.9709	220	32	0.15	1.0531
13Z-1, 35	241.75	16	1.0154	180	55	1.0114	66	16	0.9731	326	30	0.02	1.0435
14Z-1, 61	246.51	38	1.0042	90	84	1.0006	360	1	0.9951	270	6	0.10	1.0092
15Z-1, 143	251.83	56	1.0037	270	58	0.9994	360	1	0.9969	90	32	0.07	1.0069
17Z-1, 8	259.48	5	1.0105	328	21	0.9978	63	12	0.9917	180	66	0.03	1.0189
19Z-1, 4	268.54	17	1.0124	270	55	1.0020	360	1	0.9855	90	35	0.10	1.0273
22Z-1, 123	283.33	44	1.0133	339	33	0.9957	211	43	0.9910	90	29	0.13	1.0225
25Z-1, 25	295.85	250	1.0059	180	50	1.0028	61	22	0.9912	317	31	0.30	1.0148
26Z-1, 21	300.31	132	1.0044	203	18	1.0004	100	36	0.9951	315	48	0.22	1.0094
31Z-1, 36	322.96	99	1.0014	180	14	1.0003	93	14	0.9983	225	70	0.07	1.0032
34Z-1, 46	336.86	4799	1.0206	360	1	1.0053	270	58	0.9742	90	32	36.50	1.0476
34Z-1, 109	337.49	43	1.0023	360	79	0.9999	103	3	0.9978	194	11	0.05	1.0045
35Z-1, 45	340.45	124	1.0139	80	2	1.0116	180	80	0.9744	349	10	0.11	1.0406
37Z-2, 19	346.01	307	1.0233	352	3	1.0001	83	10	0.9765	243	80	3.70	1.0479
38Z-2, 89	351.18	174	1.0244	291	53	0.9902	90	35	0.9854	187	10	0.88	1.0396
39Z-1, 42	353.92	106	1.0170	311	35	0.9931	205	21	0.9899	90	48	0.16	1.0274
40Z-1, 4	358.04	3524	1.0296	180	50	1.0161	69	17	0.9543	326	35	2.50	1.0790
43Z-1, 68	372.18	5301	1.0319	90	61	1.0034	201	12	0.9646	297	26	90.50	1.0698

Notes: Axes of susceptibility ellipsoid: k = volume susceptibility, k_{\max} = maximum, k_{int} = intermediate, and k_{\min} = minimum. P = degree of magnetic anisotropy.

Table T26. Magnetic properties of minicores after alternating-field demagnetization, Hole 1188A. (Continued on next two pages.)

Core, section, interval (cm)	Depth (mbsf)	Demagnetization level (mT)	Declination (°)	Inclination (°)	Intensity (mA/m)
193-1188A- 7R-1, 74	48.94	0	170.8	-11.4	1.76
		10	169.2	-10.1	1.69
		15	170.6	-10.9	1.58
		20	168.0	-11.5	1.47
		25	171.2	-11.1	1.32
		30	169.3	-12.1	1.15
		40	168.8	-11.6	0.92
		50	165.7	-10.9	0.67
		60	167.6	-14.5	0.49
		80	159.4	-4.2	0.29
7R-2, 78	50.48	0	353.9	-3.8	0.36
		10	11.2	-6.7	0.26
		15	5.1	-4.9	0.22
		20	22.6	-6.0	0.25
		25	356.5	2.0	0.18
		30	9.2	-3.9	0.22
		40	0.8	-3.5	0.19
		50	17.2	-12.1	0.15
		60	3.5	-11.1	0.10
		80	13.8	-24.3	0.09
9R-1, 25	67.85	0	288.9	-3.7	1.28
		10	286.8	-0.5	1.09
		15	284.8	-2.1	1.01
		20	279.5	-7.7	1.03
		25	287.3	3.7	0.71
		30	290.6	12.9	0.60
		40	278.8	-5.1	0.51
		50	277.9	-5.3	0.33
		60	272.0	1.4	0.24
		80	263.0	-15.2	0.11
10R-1, 118	78.48	0	98.7	-8.2	94.27
		10	98.7	-0.1	89.84
		15	98.8	3.9	83.40
		20	98.8	5.9	75.27
		25	98.7	6.9	66.16
		30	99.0	6.5	56.64
		40	98.9	6.0	41.85
		50	98.8	5.2	28.13
		60	99.6	4.3	19.15
		80	99.9	2.7	9.05
10R-2, 61	79.39	0	72.6	1.7	445.50
		10	74.4	-15.7	301.80
		15	76.5	-18.3	232.50
		20	78.0	-13.0	179.50
		25	78.9	-10.6	138.80
		30	78.4	-11.6	108.00
		40	78.6	-12.3	71.62
		50	76.9	-11.3	44.69
		60	79.3	-9.5	29.80
		80	64.5	-8.5	17.77
12R-2, 44	98.52	0	74.3	-20.1	86.31
		10	68.9	-27.8	74.25
		15	66.6	-34.7	68.56
		20	64.0	-40.4	64.32
		25	63.2	-40.9	59.91
		30	63.8	-41.6	56.86
		40	62.0	-43.3	51.92
		50	61.6	-43.5	47.98
		60	58.7	-48.0	45.18
		80	54.9	-52.5	41.81
14R-1, 103	117.03	0	266.1	2.4	18.86
		10	266.6	-3.3	17.53
		15	266.7	-8.2	15.64
		20	267.3	-12.2	13.65
		25	267.5	-13.1	11.59
		30	266.5	-13.4	9.59

Table T26 (continued).

Core, section, interval (cm)	Depth (mbsf)	Demagnetization level (mT)	Declination (°)	Inclination (°)	Intensity (mA/m)
		40	268.2	-16.6	6.76
		50	268.1	-18.3	4.50
		60	265.3	-19.1	2.83
		80	268.1	-16.4	1.65
16R-1, 63	136.03	0	275.0	2.4	506.60
		10	274.1	-14.8	423.10
		15	274.6	-17.2	361.00
		20	274.9	-18.7	307.20
		25	275.5	-19.5	258.90
		30	274.8	-20.4	214.30
		40	274.8	-20.9	153.90
		50	275.0	-21.4	103.90
		60	275.2	-20.4	70.29
		80	277.6	-21.7	38.51
16R-2, 46	137.32	0	307.7	-28.0	97.41
		10	198.4	-20.0	166.40
		15	194.6	-18.2	174.90
		20	193.0	-17.6	168.30
		25	192.5	-17.2	154.50
		30	192.0	-17.3	135.60
		40	191.8	-17.2	104.40
		50	192.2	-17.4	73.99
		60	192.2	-17.5	53.39
		80	191.7	-16.9	29.62
17R-1, 109	146.19	0	162.4	-21.8	11610.00
		10	167.5	-20.9	6284.00
		15	168.4	-20.4	3487.00
		20	168.2	-20.2	2181.00
		25	168.5	-19.8	1482.00
		30	169.0	-19.3	1056.00
		40	169.5	-18.8	672.50
		50	170.2	-18.7	437.80
		60	170.8	-18.7	310.80
		80	171.4	-20.2	162.40
17R-2, 30	146.9	0	152.0	-6.8	4677.00
		10	143.6	-16.3	1806.00
		15	143.1	-17.1	1013.00
		20	142.6	-17.6	588.50
		25	141.5	-17.7	366.90
		30	139.4	-17.9	234.30
		40	140.7	-18.2	120.20
		50	141.9	-22.0	56.96
		60	145.0	-26.6	32.98
		80	121.3	-22.1	37.31
19R-1, 86	165.16	0	273.3	18.0	898.00
		10	300.9	-13.6	558.90
		15	301.6	-16.4	427.30
		20	301.6	-17.6	320.20
		25	301.5	-18.8	234.40
		30	301.9	-20.5	168.50
		40	302.8	-21.1	105.40
		50	300.0	-24.0	63.69
		60	301.1	-27.2	46.60
		80	286.1	-35.6	23.68
20R-1, 42	174.32	0	265.8	-12.6	2958.00
		10	274.4	-22.2	1185.00
		15	274.4	-18.8	654.20
		20	274.4	-18.9	435.60
		25	274.4	-19.3	316.20
		30	275.0	-19.4	238.40
		40	274.8	-20.0	153.60
		50	275.0	-20.4	93.35
		60	273.7	-21.8	53.19
		80	275.5	-28.3	18.64
21R-1, 28	183.38	0	247.6	20.1	2266.00
		10	259.2	-4.8	725.90
		15	257.9	-6.4	431.80
		20	262.6	-7.1	301.10

Table T26 (continued).

Core, section, interval (cm)	Depth (mbsf)	Demagnetization level (mT)	Declination (°)	Inclination (°)	Intensity (mA/m)
		25	255.7	-7.9	230.20
		30	261.0	-6.3	174.20
		40	263.7	-5.5	121.30
		50	274.4	-5.1	85.78
		60	264.8	-18.9	63.71
		80	286.4	-12.5	36.68
21R-1, 83	183.93	0	306.1	43.0	1574.00
		10	116.4	18.0	305.50
		15	124.0	17.9	601.00
		20	125.2	18.0	616.90
		25	126.2	17.6	534.40
		30	128.1	18.3	415.60
		40	126.9	18.7	263.50
		50	125.7	16.6	127.20
		60	121.1	10.3	46.13
		80	43.3	-6.6	8.37

Table T27. Magnetic properties of remanence-carrying natural minerals.

Mineral	Composition	Curie temperature (°C)	Saturation magnetization at room temperature
Magnetite	Fe ₃ O ₄	585	93
Ulvospinel	Fe ₂ TiO ₄	-153	—
Hematite	α-Fe ₂ O ₃	675	0.5
Ilmenite	FeTiO ₃	-218	—
Maghemite	γ-Fe ₂ O ₃	~740	85
Pyrrhotite	~Fe ₇ S ₈	~300	~200
Iron	α-Fe	780	200
Goethite	α-FeO·OH	120	~1
Lepidocrocite	γ-FeO·OH	-196	—
Magnesioferrite	MgFe ₂ O ₄	440	21
Jacobsite	MnFe ₂ O ₄	310	77

Notes: — = not applicable. Modified after Thompson and Oldfield (1986).